Forschungszentrum Jülich

Neutron Scattering

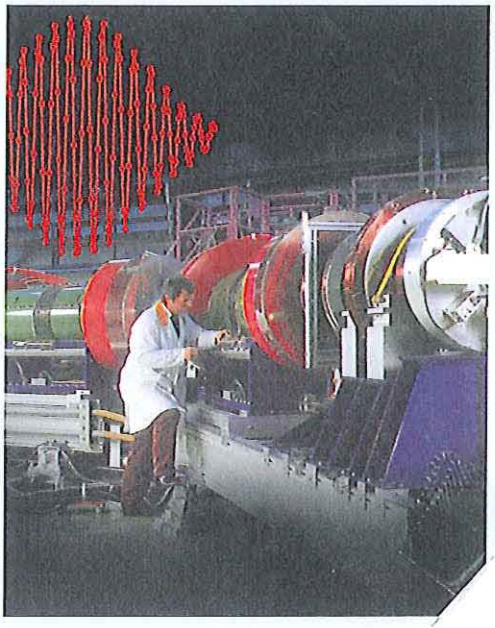

Lectures

RWTH Aachen
University of Bonn
University of Münster

Materie und Material
Matter and Materials

Schriften des Forschungszentrums Jülich
Reihe Materie und Material / Matter and Materials Volume 5

Forschungszentrum Jülich GmbH
Institut für Festkörperforschung

Thomas Brückel, Gernot Heger, Dieter Richter (Editors)

Neutron Scattering

Lectures of the Laboratory Course
held at the Forschungszentrum Jülich
from 26 September to 6 October 2000

In cooperation with
RWTH Aachen, University of Bonn and University of Münster

Schriften des Forschungszentrums Jülich
Reihe Materie und Material / Matter and Materials Volume 5

ISSN 1433-5506 ISBN 3-89336-269-X

Die Deutsche Bibliothek - CIP-Einheitsaufnahme

Neutron Scattering : lectures of the laboratory course held at the Forschungszentrum Jülich from 26 September to 6 October 2000 / Hrsg.: Thomas Brückel ... - Jülich : Forschungszentrum, Zentralbibliothek, 2000

(Schriften des Forschungszentrums Jülich : Materie und Material ; Bd. 5)
ISBN 3-89336-269-X

Herausgeber und Vertrieb:	Forschungszentrum Jülich GmbH ZENTRALBIBLIOTHEK 52425 Jülich Telefon (0 24 61) 61-53 68 · Telefax (0 24 61) 61-61 03 e-mail: zb-publikation@fz-juelich.de Internet: http://www.fz-juelich.de/zb
Umschlaggestaltung:	Grafische Betriebe, Forschungszentrum Jülich GmbH
Druck:	Grafische Betriebe, Forschungszentrum Jülich GmbH
Copyright:	Forschungszentrum Jülich 2000

Schriften des Forschungszentrums Jülich
Reihe Materie und Material / Matter and Materials, Band 5

ISSN 1433-5506
ISBN 3-89336-269-X

Alle Rechte vorbehalten. Kein Teil des Werkes darf in irgendeiner Form (Druck, Fotokopie oder in einem anderen Verfahren) ohne schriftliche Genehmigung des Verlages reproduziert oder unter Verwendung elektronischer Systeme verarbeitet, vervielfältigt oder verbreitet werden.

Lecturers

Dr. M. BRADEN		RWTH Aachen, Institut für Kristallographie
	and	Laboratoire Léon-Brillouin, Saclay (Frankreich)
Prof. Dr. Th. BRÜCKEL		Forschungszentrum Jülich, Institut für Festkörperforschung
	and	RWTH Aachen, Institut für Kristallographie
Dr. H. CONRAD		Forschungszentrum Jülich, Institut für Festkörperforschung
Dr. H. GRIMM		Forschungszentrum Jülich, Institut für Festkörperforschung
Prof. Dr. G. HEGER		RWTH Aachen, Institut für Kristallographie
Dr. M. MONKENBUSCH		Forschungszentrum Jülich, Institut für Festkörperforschung
Dr. M. PRAGER		Forschungszentrum Jülich, Institut für Festkörperforschung
Prof. Dr. D. RICHTER		Forschungszentrum Jülich, Institut für Festkörperforschung
	and	Universität Münster, Institut für Physikalische Chemie
Dr. W. SCHÄFER		Universität Bonn, Mineralogisch-Petrologisches Institut
Dr. D. SCHWAHN		Forschungszentrum Jülich, Institut für Festkörperforschung
Dr. W. SCHWEIKA		Forschungszentrum Jülich, Institut für Festkörperforschung
Dr. O. H. SEECK		Forschungszentrum Jülich, Institut für Festkörperforschung
Dr. R. ZORN		Forschungszentrum Jülich, Institut für Festkörperforschung

Content

1.	Neutron Sources	*H. Conrad*	1-1 - 1-15
2.	Properties of the neutron, elementary scattering processes	*D. Richter*	2-1 - 2-21
3.	Elastic Scattering from Many-Body Systems	*Th. Brückel*	3-1 - 3-28
4.	Polarization analysis	*W. Schweika*	4-1 - 4-19
5.	Correlation Functions Measured By Scattering Experiments	*R. Zorn, D. Richter*	5-1 - 5-24
6.	Continuum description: Grazing Incidence Neutron Scattering	*O. H. Seeck*	6-1 - 6-18
7.	Diffractometer	*G. Heger*	7-1 - 7-13
8.	Small-angle Scattering and Reflectometry	*D. Schwahn*	8-1 - 8-16
9.	Crystal spectrometer: triple-axis and back-scattering spectrometer	*F. Güthoff, H. Grimm*	9-1 - 9-24
10.	Time-of-flight spectrometers	*M. Monkenbusch*	10-1 - 10-23
11.	Neutron spin-echo spectrometer, NSE	*M. Monkenbusch, R. Zorn*	11-1 - 11-18
12.	Structure determination	*G. Heger*	12-1 - 12-16
13.	Inelastic neutron scattering: phonons and magnons	*M. Braden*	13-1 - 13-23
14.	Soft Matter: Structure	*D. Schwahn*	14-1 - 14-18
15.	Polymer Dynamics	*D. Richter*	15-1 - 15-29
16.	Magnetism	*Th. Brückel*	16-1 - 16-19
17.	Translation and Rotation	*M. Prager*	17-1 - 17-20
18.	Texture in Materials and Earth Sciences	*W. Schäfer*	18-1 - 18-17

1. Neutron Sources

Harald Conrad

1.1 Introductory remarks

Slow neutrons are a virtually unique probe for the investigation of structure and dynamics of condensed matter and biomolecules. Neutrons are called *slow*, if their kinetic energy is below 1 keV. As the first neutrons used as microscopic probes were generated in nuclear reactors, historic terms like *thermal neutrons* are also frequently used in the classification of neutrons. In reactor physics the notion *thermal* is used to distinguish these neutrons, which sustain the nuclear chain reaction, from the *fast* fission neutrons with energies of several MeV. *Thermal* neutrons, i.e. with an average kinetic energy of $\overline{E} \cong 25$ meV, are of particular interest in the context of this course. They are in thermal equilibrium with an adequate slowing down medium (moderator) like graphite, light or heavy water at ambient temperature ($k_B T \cong 25$ meV). With the availability of cryogenic moderators, *cold* neutrons ($\overline{E} \cong 3$ meV) became important in recent decades, too. Strictly speaking, cold or so called *hot* neutrons ($\overline{E} \cong 200$ meV) have to be considered as thermal, too, because these are neutron gases in thermal equilibrium with a moderator at a particular temperature. Cold neutrons are in equilibrium with a cryogenic moderator, e.g. liquid hydrogen at 20 K or solid methane at liquid nitrogen temperature, 77 K. Hot neutrons are those in equilibrium with e.g. a graphite block heated to 2000 K, say.

These hot neutrons and the even more energetic, so called *epithermal* neutrons ($E > 1$ eV) may in the future gain importance for scattering experiments, in particular with respect to pulsed accelerator driven neutron sources (see below). But it is important to realize that there are no primary sources known, which directly deliver neutrons in the relevant energy range of typically 10^{-3} eV $< E < 1$ eV. All existing sources emit primary neutrons with energies of about 10^6 eV or above and we are left with the difficult task to reduce the neutron energy between 6 and 9 orders of magnitude (moderation).

1.2 Free Neutrons

Free neutrons are unstable (half life about 12 minutes). As a nuclear constituent they are stable, though, and as bound particles virtually ubiquitous, except in light hydrogen. So, the only means of generating free neutrons are nuclear reactions. There is a variety of possible reactions, mostly forced ones, although spontaneous neutron emission is known to exist as well. A

number of neutron sources is described in the Appendix, in particular with respect to the achievable intensities. There are, of course, other criteria (e.g. cost or technical limitations), but for the neutron scattering experiment the highest possible **signal** (intensity) **at the detector** is decisive. The quality of an experiment strongly depends on the counting statistics, which in turn governs the resolution capability of a neutron diffractometer or spectrometer. This criterion excludes most of the sources described in the Appendix for modern neutron scattering instruments, although electron accelerators for (γ,n)-reactions were successfully utilized for a certain time. For other applications like medical or in nuclear and plasma physics those sources were and still are of importance.

In the following we will explain in greater detail the two most important sources for neutron scattering experiments: the nuclear reactor and the spallation source.

1.3 The nuclear reactor as a neutron source

Fission of a single ^{235}U nucleus with one thermal neutron releases on average 2.5 fast neutrons with energies around 1 MeV. So, this is more than needed to sustain a chain reaction. Therefore we can withdraw typically 1 neutron per fission for purposes like neutron scattering experiments without disturbing the chain reaction. The source strengths Q(n/s), i.e. neutrons emitted per second, achievable with these surplus neutrons are limited in particular by problems of removing the energy released, which is about 200 MeV per fission. Using the relation $1\ eV = 1.6\times10^{-19}$ Ws we get $Q \cong 3\times10^{16}$ n/s per MW reactor power to be removed. As mentioned in the introduction the fast neutrons have to be slowed down to thermal energies to be useful for neutron scattering.

The stochastic nature of the slowing down of neutrons by collisions with light nuclei of the moderator medium (e.g. protons in water) leads to the notion of a neutron flux Φ as a quality criterion for thermal neutron sources. This flux is defined as the number of (thermal) neutrons per second isotropically penetrating a unit area. In order to calculate the flux $\Phi(r)$ for a given source distribution Q(r) (the fuel elements of a reactor core submersed in a moderator medium) we had to solve the general transport (Boltzmann) equation. But there are no analytical solutions possible for realistic geometries of reactor cores [1]. An estimate, however, will be given for simple model: a point source located in the center of a spherical moderator vessel. If the radius of the vessel is equal to the so called slowing down length L_S [2], then 37% of the source neutrons become thermal. Using the definition $\Phi_{th} = \bar{v}_{th} \cdot n$ (average neutron velocity $\bar{v}_{th}$), where the stationary neutron density n is given by a balance equation, viz. $n = q \cdot \tau$ (balance = production rate · life time) with q as the so called slowing down density, we have

$$\Phi_{th} = \bar{\nu}_{th} \cdot q \cdot \tau = \bar{\nu}_{th} \cdot 0.37\, Q / (4\pi L_S^3/3) \cdot \tau, \qquad (1.1)$$

where the slowing down density q is the number of neutrons slowed down to thermal energies (i.e. to about 25 meV) per unit volume and per second. For a point source of strength Q in the center of a spherical moderator volume of radius $r = L_S$ we obtain what we have inserted for q in (2.1). The life time (also called relaxation time) is given by [2] $\tau = (\Sigma_{abs} \cdot \bar{\nu}_{th} + D \cdot B^2)^{-1}$, where Σ_{abs} and D are the coefficients of absorption and diffusion of neutrons, respectively, and $B^2 = (\pi/L_S)^2$ a geometrical factor, the "buckling", which is a measure for the spatial flux distribution. Inserting numerical values, $L_S = 29$ cm, $\Sigma_{abs} = 3\times10^{-5}$ cm^{-1} and $D = 2\times10^5$ cm^2/s for heavy water (Jülich's research reactor FRJ-2 is heavy water moderated), we obtain with the source strength $Q \cong 3\times10^{16}$ n/(s MW) a thermal neutron flux $\Phi_{th} = 1.1\times10^{13}$ n/(cm^{2}s MW). Extrapolating this to 23 MW, the power of the FRJ-2, we obtain $\Phi_{th} = 2.5\times10^{14}$ n/(cm^2 s). This is only 25% too big, a surprisingly good result taking into account the non realistic assumption

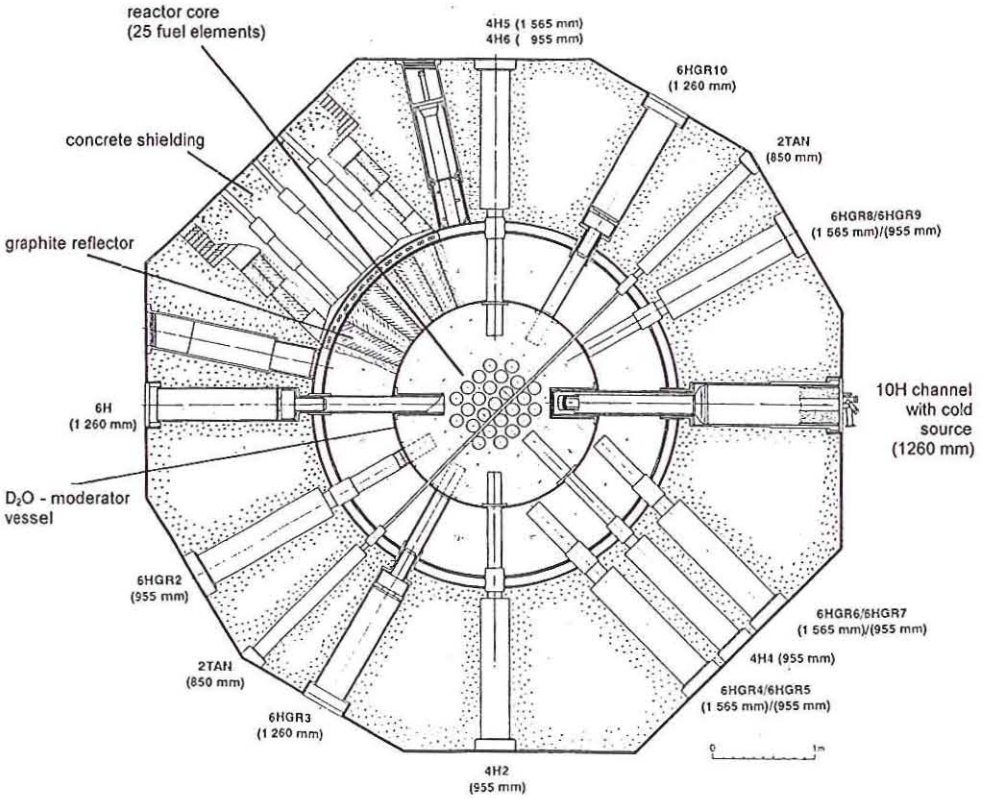

Fig. 1.1 Horizontal cut through the reactor block of the Jülich research reactor FRJ-2.
(The numbers below the acronyms are the beam channel heights above the floor of the experimental hall.)

of the reactor being a point source. In fact the core of the FRJ-2 consists of 25 tubular, 60 cm high fuel elements arranged within a lateral grid of about one meter in diameter. The core is submersed in and cooled by heavy water streaming through the tubes. Figure 1.1 shows a plan cross sectional view of the reactor block.

The FRJ-2 is operated with highly enriched uranium ^{235}U. With the existing relaxed fuel element arrangement an essential neutron flux enhancement, e.g. by an order of magnitude, were only possible with a corresponding but unwanted power increase. A different possibility exists in compacting the core, a solution chosen for the high flux reactor at the Institut Laue-Langevin in Grenoble, France. In fact, its core consists of a single annular fuel element of 40 cm outer and 20 cm inner diameter, respectively. Operated at 57 MW, a disturbed flux at the beam tube noses of $\Phi_{th} = 1.2 \times 10^{15}$ n / (cm^2 s) is obtained.

Technical limitations

We have just established a relation between neutron yield and reactor power released as heat. Disregarding for the moment investment and operation costs, the limiting factor for achievable neutron yields is the power or, to be more precise, the power density in the reactor core. This technically decisive factor, the **power density (MW/liter),** was not included in the number given in the previous section, because it depends on the details of the reactor, in particular the core size, the uranium enrichment and the fuel density in the fuel elements. The size of the primary neutron source (reactor core, target volume, etc.) is important for a high flux of thermal neutrons within the moderator. In Table 1.A.1 of the Appendix a selection of reactions is given and related to its neutron yields and power densities.

It is now well established that power densities in reactor cores cannot substantially be increased without unwanted and impracticable consequences, such as liquid sodium cooling. In particular, the service time of reactor vessel components like beam tube noses or cold sources would become intolerably short due to radiation damage. Experience with the Grenoble High Flux Reactor shows that these service times are of the order of seven years. Ten times higher fluxes would result in impracticable service times under one year.

1.4 Pulsed contra continuous sources

Regarding these arguments, we may ask ourselves, whether high flux reactors have already reached a fundamental limit. This were certainly the case, if we expected a flux increase by another order of magnitude like the one observed in reactor development since the fifties (see Table 1.1).

Period	Example	Flux Φ [10^{13} cm^{-2} s^{-1}]
1950 - 60	FRM-1 München	~ 1
1960 - 70	FRJ-2 Jülich	~ 10
1970 - 80	HFR Grenoble	~ 100
1980 - 90	?	~ 1000 ???

Table 1.1 Development of thermal fluxes of research reactors

A flux increase by a factor of about 6 over that of the Grenoble reactor had been envisaged for a new research reactor in Oak Ridge, USA. This enhancement would have been only possible by a power increase to 350 MW with a simultaneous increase of the average power density by a factor of 4 compared to Grenoble. After ten years of planning, the US Department of Energy decided not to build this so called ANS (Advanced Neutron Source).

At this point we have earnestly to ask, whether the decision was adequate to build ever more powerful but continuously operating reactors. From a technical point of view is was perhaps the easiest path, from the point of view of neutron scattering, on the other hand, it was by no means necessary or economic. In order to accept this we only have to realize that *the* two standard methods of neutron scattering, i.e. crystal and time of flight techniques, in any case only use a minute fraction (10^{-2} ... 10^{-4}) of the source flux. Monochromatization and/or chopping the primary beam as well as collimation and source to detector distance (shielding!) may even reduce the source flux by factors of 10^{-8} to 10^{-11}, depending on resolution requirements.

Time of flight spectroscopy inefficiently utilizes the continuous reactor flux for two reasons, because it requires both a monochromatic and a pulsed beam. Crystal spectrometers and diffractometers use an extremely narrow energy band, too. The rest of the spectrum is literally wasted as heat. Obviously, time of flight techniques with pulsed operation at the same average source power yield gain factors equal to the ratio of peak to average flux. With crystal techniques higher order Bragg reflections can be utilized, because they become distinguishable by their time of flight. In other words, the peak flux will be usable between pulses as well.

So, without increasing the average power density, pulsed sources can deliver much higher peak fluxes, e.g. 50 times the HFR flux. Now, which type of pulsed source is to be preferred: a pulsed reactor or an accelerator driven source? This question is not easy to answer. Possibly it depends on the weights one is willing to assign to the particular arguments. Important arguments are cost, safety, pulse structure or the potential for other uses than neutron scattering.

If we set aside the costs and ask about safety, we can assert that accelerator driven sources (e.g. spallation sources) are inherently safe, because no critical configuration is needed for the neutron production. A pulsed reactor, on the other hand, has to run periodically through a prompt super critical configuration. Therefore the external control mechanisms (absorbers) of the continuously operating reactor will not work. The power excursion must be limited by inherent mechanisms, e.g. by the temperature rise of the fuel. Although it may be unlikely in reality, malfunctions of the necessarily mechanical insertion of excess reactivity (rotating parts of fuel or reflector) may lead to substantial damage of the reactor core. No problems exist in that respect with a spallation neutron source. Furthermore, the proton beam can be shut down within a few milliseconds. Neutron generation by protons enables the shaping of pulse structures (pulse duration below 1 microsecond, arbitrary pulse repetition rates) basically unfeasible with mechanical devices.

1.5 The Spallation Neutron Source

1.5.1 The spallation reaction

For kinetic energies above about 120 MeV, protons (or neutrons) cause a reaction in atomic nuclei, which leads to a release of a large number of neutrons, protons, mesons (if the proton energy is above 400 MeV), nuclear fragments and γ-radiation. This kind of nuclear disintegration has been named spallation, because it resembles spalling of a stone with a hammer.

The spallation reaction is a two stage process, which can be distinguished by the spatial and spectral distribution of the emitted neutrons. This is depicted schematically in Figure 1.2.

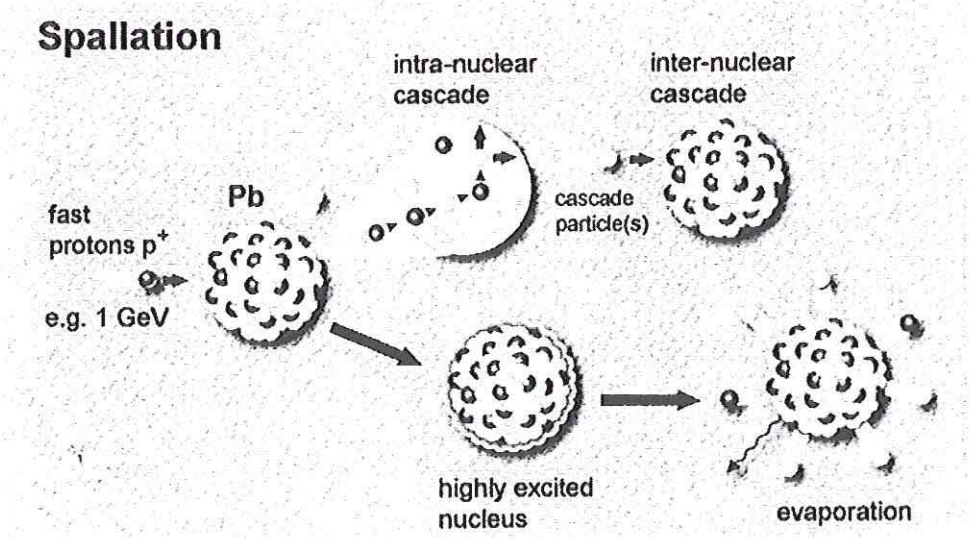

Fig. 1.2 The spallation process

In stage 1 the primary proton knocks on a nucleon, which in turn knocks on another nucleon of the same nucleus (intra-nuclear cascade) or of a different nucleus (inter-nuclear cascade). With increasing energy of the primary particle the nucleons kicked out of the nuclei will for kinematic reasons (transformation from center of mass to laboratory system) be emitted into decreasing solid angles around forward direction. The energy distribution of the cascade particles extends up to the primary proton energy. After emission of the cascade particles the nuclei are in a highly excited state, whose energy is released in stage 2 mainly by evaporation of neutrons, protons, deuterons, α-particles and heavier fragments as well as γ-radiation. Depending on the particular evaporation reaction course, different radioactive nuclei remain. These evaporation neutrons are isotropically emitted. They are the primary source neutrons, in which we are interested in the present context. The spectrum of the evaporation neutrons is very similar to that of nuclear fission and has a maximum at about 2 MeV. This is the very reason, why we can utilize the spallation neutrons as with a fission reactor.

The yield of evaporation neutrons increases with proton energy and depends on the target material. The following expression for the yield has been found empirically

$$Y = f \cdot (A + 20) \cdot (E - b) \quad \text{neutrons / proton,} \qquad (1.2)$$

where A is the mass number of the target material ($9 \leq A \leq 210$), E is the proton energy ($0.2 \leq E \leq 1.5$ GeV) and b = 0.12 GeV. The factor f depends on the target geometry.

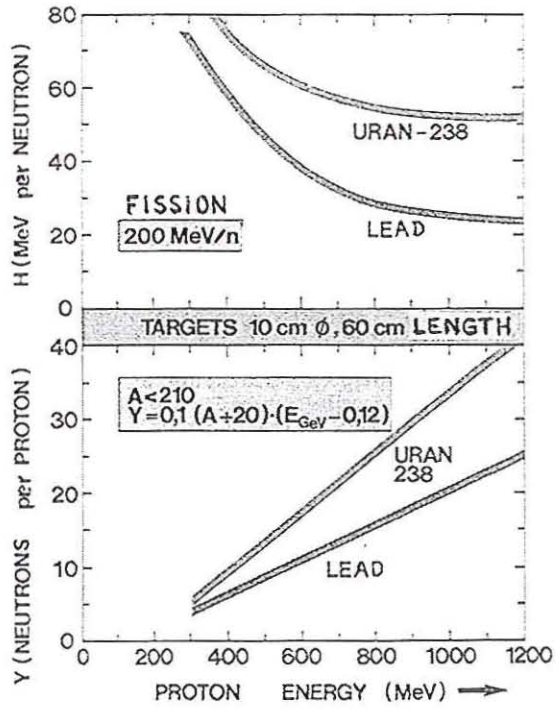

Fig. 1.3

energy deposition H in lead and depleted uranium as a function of proton energy

fast neutron yield Y from lead and depleted uranium as a function of proton energy

For uranium, which releases neutrons by fission as well, b = 0.02 GeV. In Figure 1.3 the yield for lead and uranium is plotted and related to the energy released per neutron. The latter has important consequences as already discussed in section 1.3.

1.5.2 Technical details

A spallation neutron source consists of three important components, the accelerator, the target and the moderators. For reasons discussed in sections 1.3 and 1.4 the planned European Spallation Source (ESS) will be pulsed.

1.5.2.1 The accelerator

The concept of the ESS envisages a pulsed linear accelerator (linac), which will supply the full beam power, and two subsequent storage rings for compressing the pulses from the linac. The ESS design parameters are:

linac proton energy	1.33	GeV,	300 m long (superconducting cavities)
average current	3.75	mA	
average beam power	5	MW	
linac peak current	0.1	A	
ring peak current	100	A	
repetition rate	50	s^{-1}	
linac pulse duration	1	ms	
pulse duration after compression	1	μs	ring diameter: 52 m

It is worthwhile to point out that we need a rather complex machine to accelerate particles from rest to kinetic energies of 1 GeV or above and extract them in pulses of only 1 μs duration. For the case of the ESS we need five stages of acceleration and compression such as

- electrostatic acceleration to 50 keV
- radio frequency quadrupole (RFQ) acceleration from 50 keV to 5 MeV
- drift tube linac (Alvarez-type) from 5 MeV to 70 MeV
- superconducting multiple cavity linac from 70 MeV to 1330 MeV
- two (!) compressor rings (space charge !).

1.5.2.2 The target – solid or liquid?

According to relation (1.2), heavy elements (large mass number A) are favored as target candidate materials, in particular the refractory metals tantalum, tungsten or rhenium, but also lead, bismuth or even uranium. Whatever material is selected, it will be subject to heavy multiple loads. Firstly, about 60% of the 5 MW average beam power is dissipated within the tar-

get as heat, the rest is transported as released radiation to the target vicinity like moderators, reflector and shielding or is converted into nuclear binding energy. Secondly, all materials hit by protons (and fast neutrons) will suffer from radiation damage. Finally, the extremely short proton pulses generate shock-like pressure waves in target and structural materials, which may substantially reduce the target service life. In order to both keep average target temperatures low and reduce specific radiation damage and loads due to dynamic effects from shock waves, a solid rotating target is conceivable and has been proposed for the ESS. As any solid target has to be cooled, it will inevitably be "diluted" by the coolant, whereby the primary source's luminosity will be diminished. One should therefore operate the target in its liquid state avoiding an additional cooling medium. Radiation damage would be no longer a problem with the target, but of course with its container. Obviously, the refractory metals are excluded due to their high melting points. So we are left with elements like lead, bismuth, the Pb-Bi eutectic or - of course - mercury. In fact, mercury has been chosen for the ESS, because it was also shown to exhibit favorable neutron yield conditions as presented in Figure 1.4.

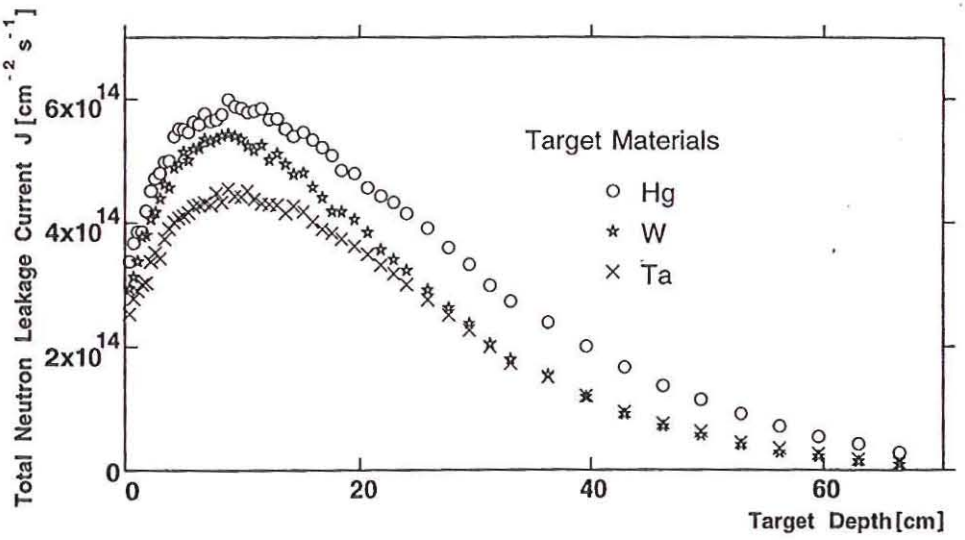

Fig. 1.4 Calculated axial leakage distributions of fast neutrons from a lead-reflected mercury target compared to water cooled tantalum and tungsten targets, respectively.

The dimensions of a target along the beam path will reasonably be chosen according to the range of the protons of given kinetic energy. For mercury and the ESS energy of 1.33 GeV this is about 70 cm. Lateral target dimensions are optimized so that the moderators are not too far from the proton beam axis (solid angle!). A typical target-moderator-reflector configuration is depicted schematically in Figure 1.5.

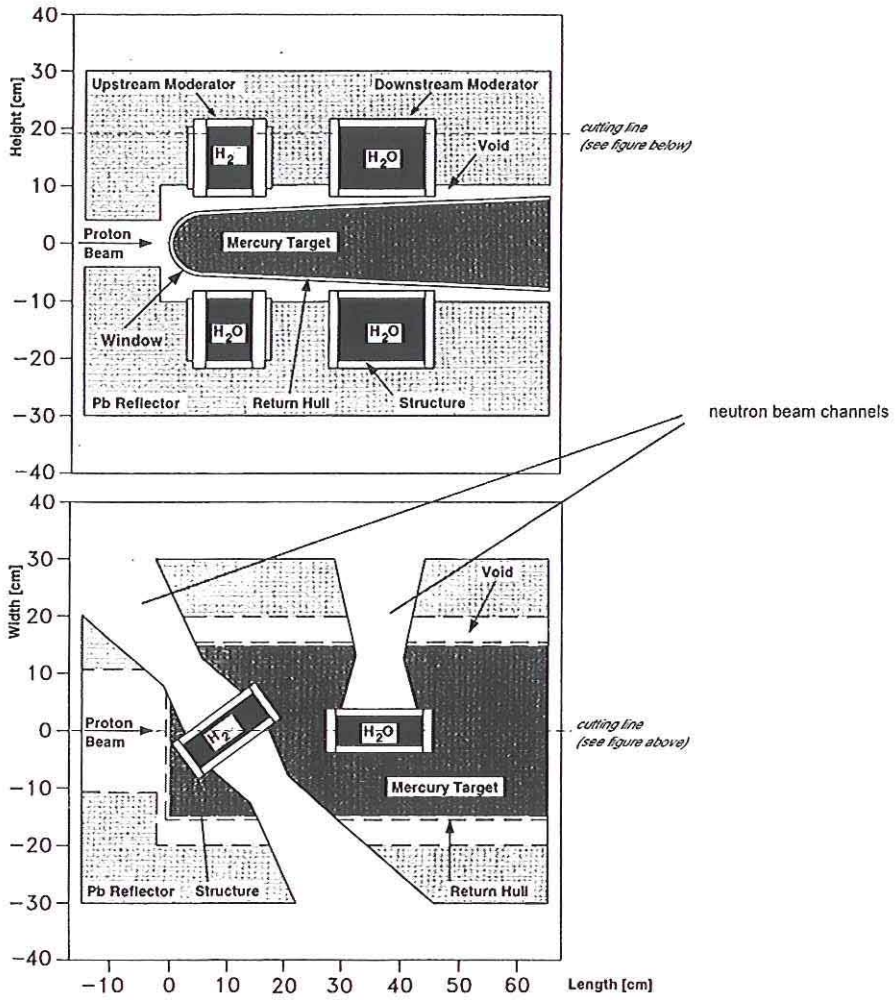

Fig. 1.5 Schematic vertical and horizontal cuts through the inner part of the target block.

1.5.2.3 The moderators

Let us eventually turn to the "heart" of the facility, the moderators, which were just shown in the last figure above in their relative positions next to the target. As the upper and lower faces of the target are equivalent for symmetry reasons with respect to the emission of fast neutrons, it is obvious to exploit both sides with moderators. The question now is, whether we shall use D_2O as the slowing down medium like in all modern medium and high flux reactors or possibly H_2O? As we have discussed in section 1.4, not the highest possible average neutron flux is the only reasonable demand, but rather the highest possible peak flux for a given (or requested) average flux. In that respect, H_2O is the preferred material due to its bigger slowing

down power and stronger absorption for thermal neutrons (see below). The reason for this seemingly paradoxical demand for stronger absorption is that the achievable neutron peak flux is not only proportional to the proton peak current, but also depends on the storage time τ (see below) of thermal neutrons in the moderator. We should point out here that the slowing down time for H_2O and D_2O is small compared to the storage time τ. The neutron peak flux is given by the following expression, which is the result of a convolution of a proton pulse of duration t_p with an exponential decay of the neutron field within the moderator with storage (decay) time τ.

$$\hat{\Phi}_{th} = \overline{\Phi}_{th} \cdot \frac{t_{rep}}{t_p} \cdot (1 - e^{-t_p/\tau}) \qquad (1.3)$$

where $\hat{\Phi}_{th}$, $\overline{\Phi}_{th}$ are peak and average flux, respectively, and t_{rep} is the time between pulses. In the limit $t_p \rightarrow 0$ expression (1.3) reduces to $\hat{\Phi}_{th} = \overline{\Phi}_{th} \cdot t_{rep} / \tau$, i.e. even a δ-shaped current pulse results in a finite neutron peak flux. We see as well that in this case the peak flux is inversely proportional to the moderator storage time. Also with finite current pulses a short storage time is important for obtaining large peak fluxes. The storage time τ of a thermal neutron is a measure of the escape probability from the moderator and is obviously determined by both the geometry of the moderator vessel and the absorption cross section of the moderator medium (see section 1.3) and can be written [2]:

$$\tau = (\bar{v}_{th} \cdot \Sigma_{abs} + 3 D \pi^2 / L^2)^{-1} \qquad (1.4)$$

where $\bar{v}_{th}$ is the average neutron velocity, Σ_{abs} the macroscopic absorption cross section, D the diffusion constant for thermal neutrons and L is a typical moderator dimension. The absorption cross section of H_2O is about 700 times bigger than that of D_2O. If it were only for this reason, an H_2O-moderator had to be small (small L in (1.4)), because we want of course utilize the neutrons that leak from the moderator. So, a short storage time must not entirely be due to self-absorption. As, on the other hand, H_2O possesses the largest known slowing down density (the number of neutrons, which become thermal per cm^3 and s), an H_2O-moderator anyhow does not need to be big. In section 1.3 we have already quoted that within a spherical moderator vessel with its radius equal to the slowing down length L_S (= 18 cm for H_2O), 37% of the fast neutrons emitted from a point source located in the center become thermal. In fact, an H_2O-moderator must not be essentially larger, because within a sphere with r = 23 cm already 80% of the neutrons are lost due to absorption.

For these reasons a pulsed spallation source will have small ($V \cong 1.5$ liter) H_2O-moderators for thermal neutrons. The corresponding storage time of such H_2O-moderators has been measured and is $\tau = 150\ \mu s$ [3], which is in good agreement with the estimate according to (1.4). Small size and absorption diminish in any case the time average neutron yield. In order to improve this without deteriorating the peak fluxes, two tricks are used. Firstly, a moderator is enclosed by a so-called reflector (see Fig. 1.5), a strongly scattering ("reflecting") but non moderating material, i.e. a heavy element with a large scattering cross section like lead. Secondly, the leakage probability from the moderator interior, i.e. a region of higher flux due to geometrical buckling (Chapter 1.3), is enhanced by holes or grooves pointing toward the neutron beam holes. Both measures give gain factors of 2 each, whereby the reflector gain is so to speak "for free", because the anyway necessary lead or iron shielding has the same effect. A reflector can be imagined to effect such that it scatters fast neutrons back, which penetrated the moderator without being or insufficiently slowed down. Similar considerations hold as well for cold moderators employed with spallation sources (Fig. 1.5).

As a final remark let us point out that the overall appearance of a target station can hardly be told from a reactor hall with the respective experimental equipment in place. In both cases neutrons are extracted from the moderators by beam channels or guide tubes and transported to the various scattering instruments.

In the following Table 1.2 the expected and experimentally supported flux data of ESS are shown and compared to those of existing sources.

	High flux reactor (HFR) Grenoble (FR)	**Pulsed reactor IBR-II Dubna (RU)**	**Spallation source ISIS Chilton (UK)**	**ESS Hg-Target H_2O Moderator**
$\hat{\Phi}[cm^{-2}s^{-1}]$	10^{15}	$2 \cdot 10^{16}$	$4.5 \cdot 10^{15}$	$1.4 \cdot 10^{17}$
$\overline{\Phi}[cm^{-2}s^{-1}]$	10^{15}	$2 \cdot 10^{13}$	$7 \cdot 10^{12}$	$0.6 \cdot 10^{15}$
Pulse repetition rate $\nu[s^{-1}]$	-	5	50	50
Pulse duration [10^{-6} s]	-	250	30	165
$\hat{\Phi} \cdot \nu\left[10^{17}\, cm^{-2}s^{-1}\right]$	1*	1	2.2	70

* with neutron chopper 100 s^{-1}

Tab. 1.2 Comparison of the performance of various modern neutron sources

Appendix

Neutron Sources – an overview [4]

1.A.1 Spontaneous nuclear reactions

Although every heavy nucleus is unstable against spontaneous fission, this reaction is generally suppressed by α-decays beforehand. With the advent of nuclear reactors, on the other hand, an exotic isotope, ^{252}Cf, became available in sufficient amount from reprocessing spent nuclear fuel, where 3% of the decays are by spontaneous fission. The rest is α-decay. The data of a **^{252}Cf-source** are:

- yield: 3.75 neutrons / fission
  resp. 2.34×10^{12} neutrons / (gram s)
- half life: 2.65 y (including α-decay)
- average neutron energy: 2.14 MeV (fission spectrum)

1.A.2 Forced nuclear reactions

In this case we can distinguish between reactions initiated by both charged and neutral particles. In this context γ-quanta are regarded as neutral "particles".

1.A.2.1 Reactions with charged particles

Although we will restrict the discussion to light ions such as protons, deuterons and α-particles, a wide field is covered from the historically important radium-beryllium-source to the latest sources like plasma focus or spallation sources.

(α,n)-Reactions

Reaction partners with these sources are either natural (Radium, Polonium) or artificial (Americium, Curium) radioactive isotopes and a light element such as Beryllium as target material. Using a **radium-beryllium-source** Bothe and Becker discovered in 1930 a new particle, which they failed to identify it as the neutron. Two years later Chadwick accomplished this earning him the Nobel prize for this feat. Modern sources employ artificial isotopes alloyed with Beryllium. Yields are between 10^{-4} and 10^{-3} neutrons per particle. The technical parameters of a modern ^{241}Am/Be-source are:

- yield: 0.9×10^{7} neutrons / s per gram ^{241}Am
- half life: 433 y
- neutron energy: a few MeV (complex line spectrum)

(p,n)- and (d,n)-Reactions

Bombarding targets (Be, ... , U) with protons or deuterons of medium energy ($E_{kin} \leq 50$ MeV), either neutrons are released form the target nuclei in the case of protons or the neutrons are stripped from the deuterons during the impact and thereby released. Yields are of the order of 10^{-2} n/p resp. 10^{14} n/s per milli-Ampere.

An interesting special case is the reaction between the two heavy hydrogen isotopes, because it can be exploited in two different ways. One variant is the so-called **neutron generator** utilizing the large reaction cross section of the D-T-reaction, which peaks already at very low deuteron energies (5 barn at 0.1 MeV). With this low particle energy the emitted neutrons are virtually mono-energetic ($E_n = 14$ MeV) and the emission is isotropic. The target may be gaseous or Tritium dissolved in adequate metals (Ti, Zr). The yield for a D-T-neutron generator with $E_{kin}(d^+) = 0.1$ MeV is of the order of 10^{11} neutrons/s per milli-Ampere.

The second variant of exploiting the D-T-reaction is the **plasma source**. In this source both gases are completely ionized by applying high pressure and temperature forming a homogeneous plasma, which releases neutrons via the fusion reaction. In principle, this is the same reaction as with the neutron generator. Such sources operate in a pulsed mode, because the plasma has to be ignited by repeated compression. Due to the need for this compression this special kind of a plasma source is also called the **plasma focus**. Up to now yields of about 3×10^{12} neutrons / s have been obtained experimentally. Planned facilities are expected to deliver 10^{16} neutrons / s.

Chapter 1.5 has already been dedicated in greater detail to (p,n)- or (d,n)-reactions at high particle energies (> 100 MeV), which lead to spalling of the target nuclei ("spallation"). At this point we only want to give a typical number for the neutron yield for comparison with the other reactions quoted in this Appendix:

- yield (for 1 GeV protons on lead):		25 neutrons / proton
	resp.	1.5×10^{17} neutrons / s per milli-Ampere
- average neutron energy:		3 MeV (evaporation spectrum)
		+ cascade neutrons (up to proton energy).

1.A.2.2 Reactions with neutral "particles"

(γ,n)-Reactions (photonuclear reactions)

Gamma radiation of radioactive isotopes can release so called **photoneutrons**, a process, which is indeed exploited in devices analogous to (α,n)-sources. A typically spherical γ-source of a few centimeters in diameter is enclosed by a shell of target material. Due to the extremely high γ-activities needed, even weakest neutron sources (10^6 n/s) can only be hand-

led remotely. It is much more convenient to turn on the source when needed by replacing γ-radiation by bremsstrahlung generated by electron bombardment of a heavy metal target. Using e.g. 35 MeV electrons, we obtain a yield of about 10^{-2} n/e resp. 0.8×10^{14} n/s per mA.

Neutron induced nuclear fission (the nuclear reactor)

Of all neutron sources realized up to now, **nuclear reactors** are still the most intense ones. We had therefore dedicated a detailed chapter for this kind of source (chapter 1.3).

For comparison we have compiled the yields, heat deposition, source strengths and power densities of the various reactions in the following Table 1.A.1.

Reaction	**Yield**	**Heat deposition [MeV / n]**	**Source strength [n/s]**	**Source power Density [MW / Liter]**
Spontaneous fission ^{252}Cf	3.75 n/fission	100	2×10^{12} g^{-1}	0.8 (39 W/g)
^{9}Be (d,n) (15 meV)	1.2×10^{-2} n/d	1200	8×10^{13} mA^{-1}	-
^{3}H (d,n) (0.2 MeV)	8×10^{-5} n/d	2500	5×10^{11} mA^{-1}	-
Spallation 1.33 GeV protons on Hg	28 n/p	20	10^{18}	0.5 (ESS)
Photoproduction W(e,n) (35 MeV)	1.7×10^{-2} n/e	2000	4×10^{14}	5 (Harwell)
^{235}U fission nuclear chain reaction	1 n/fission	200	2×10^{18}	1.2* (HFRGrenoble)

* At the hot spot 3.3 MW/L. For 2×10^{18} source neutrons per second this gives a thermal flux of 10^{15} n cm^{-2} s^{-1}.

Table 1.A.1 *Yield, heat deposition, source strength and power density for selected neutron sources*

Literature

[1] S. Glasstone, A. Sesonske, Nuclear Reactor Engineering; van Nostrand Comp. Inc., 1963

[2] K.H. Beckurts, K.Wirtz, Neutron Physics; Springer-Verlag, 1964

[3] G. Bauer, H. Conrad, K. Friedrich, G. Milleret, H. Spitzer; Proceedings 5th International Conf. on Advanced Neutron Sources, Jül-Conf-45, ISSN 0344-5789, 1981

[4] S. Cierjacks, Neutron Sources for Basic Physics and Applications; Pergamon Press, 1983

2. Properties of the neutron, elementary scattering processes

D. Richter

2.1 A few remarks on history

In 1932 the neutron was discovered by Chadwick. The name results from the observation that the neutron apparently does not possess an electric charge: it is neutral. Today, one knows that the neutron is an ensemble of one up quark and two down quarks. According to the standard theory, the total charge therefore amounts to $2/3\ e^- + 2\ (-1/3\ e^-) = 0$. At present this theoretical statement is proven with a precision of $\sim 10^{-21}\ e^-$!

Only four years later in 1936 Hahn and Meitner observed the first man-made nuclear fission. In the same year also the first neutron scattering experiment was performed. Its set-up is shown in Fig.2.1. Neutrons were taken from a radium beryllium source which was covered by a paraffin moderator. From that moderator neutron beams were extracted such that they hit magnesium oxide single crystals which were mounted on a cylindrical circumference under the appropriate Bragg angle. After reflection they were guided to a detector which was mounted opposite to the radium-beryllium source. In order to avoid any directly penetrating neutrons a big piece of absorber was mounted in between the detector and the source.

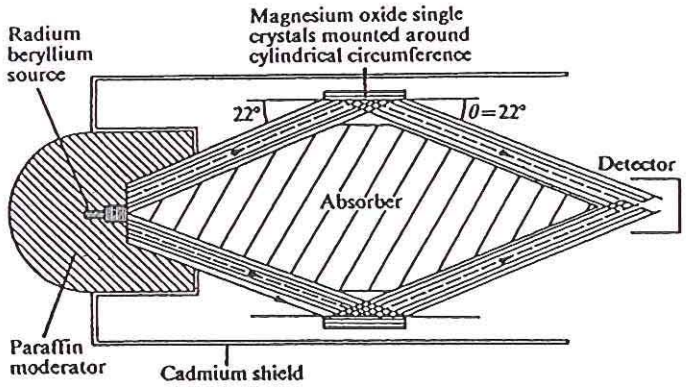

Figure 2.1: Mitchell and Powers's apparatus for demonstrating the diffraction of neutrons (after Mitchell and Powers 1936).

In December 1942 Fermi build his first nuclear reactor in Chicago - the so called Chicago pile - which led to the first controlled nuclear chain reaction. Only one year later the Oak Ridge Graphite Reactor went critical. It had a power of 3.5MW and was originally used for the production of fissionable material. Fig.2.2 shows this reactor which by now is a national historic landmark. At this reactor, Shull build the first neutron diffractometer which became operationally at the end of 1945. At that instrument the first antiferromagnetic structure (MnO_2) was solved (Shull, Noble Price 1994). At the end of the 40's and the beginning of the 50's nuclear reactors for neutron research came into operation in several countries. 1954 the Canadian NRU Reactor in Chalk River was the most powerful neutron source with a flux of $3 \cdot 10^{14} n/cm^{-2}s^{-1}$. There Brockhouse developed the triple axis spectrometer which was designed, in order to observe inelastic neutron scattering and in particular to investigate elementary excitations in solids. For this achievement Brockhouse received the Nobel Price in 1994. Another milestone in neutron scattering was the installation of the first cold source in Harwell (Great Britain). This cold source allowed to moderate neutrons to liquid hydrogen temperatures with the effect that for the first time long wavelength neutrons became available in large quantities.

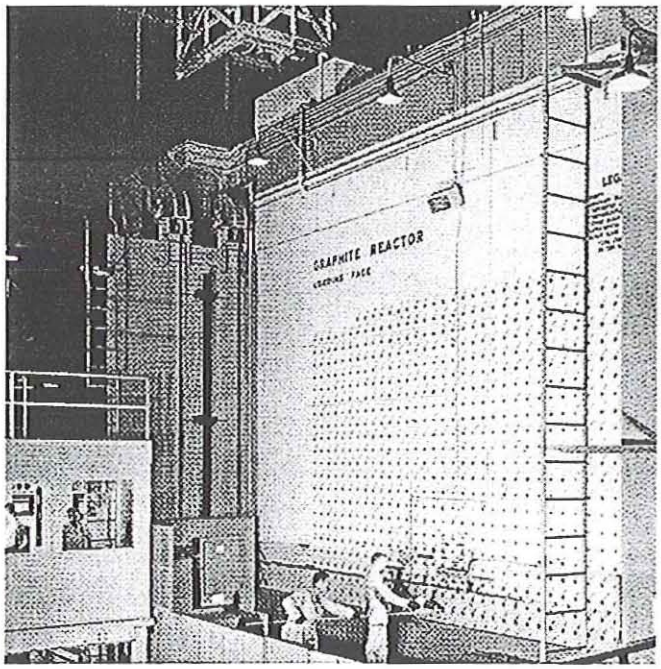

Figure 2.2: View of the Oak Ridge Graphite Reactor.

In the 60's the first high flux reactor specially designed for beam hole experiments became critical in Brookhaven (USA). It provided a flux of 10^{15} n/cm^{-2}s^{-1}. For research reactors this level of flux was not significantly surpassed since then. Finally, 1972 the high flux reactor at the Institute Laue Langevin in Grenoble (France) went into operation. This reactor since then constitutes the most powerful neutron source worldwide.

In parallel using proton accelerators already beginning in the 60's, another path for neutron production was developed. Pioneering work was performed at the Argonne National Laboratory (USA). At present the most powerful Neutron Spallation Source is situated at the Rutherford Laboratory in Great Britain which bases on a proton beam of about 200KW beam power. The future of neutron scattering will most probably go along the lines of spallation sources. At present in the United States the construction of a 2.5MW spallation source has commenced with the aim to get operational in 2005. European plans to build a Megawatt Spallation Source are still under development and hopefully a European decision for the European Spallation Source (ESS) will be reached in the year 2003.

After the war, Germany was late in the development of neutron tools for research. Only in 1955 international agreements allowed a peaceful use of nuclear research. In the same year the first German Research Reactor became critical in Garching. In the early 60's powerful research reactors were build like for example the FRJ-2 reactor in Jülich which provides a flux of $2 \cdot 10^{14}$ n/cm^{-2}s^{-1}. Instrumental developments became a domain of German neutron research. A number of important German contributions in this field are the backscattering spectrometer, the neutron small angle scattering, the instruments for diffuse neutron scattering and high resolution time of flight machines.

2.2 Properties of the neutron

The neutron is a radioactive particle with a mass of $m_n = 1.675 \cdot 10^{-27}$kg. It decays after a mean lifetime of $\tau = 889.1 \pm 1.8$s into a proton, an electron and an antineutrino (β decay).

$$n \rightarrow p^+ + e^- + \bar{\nu} \qquad (+ \ 0.77 \ MeV) \tag{2.1}$$

For any practical application the finite lifetime of the neutron has no consequence. At neutron velocities in the order of 1000m/s and distances in experiments up to 100m lifetime effects are negligible.

The neutron carries a spin of ½ which is accompanied by a magnetic dipole moment

$$\mu_n = -1.913\,\mu_N \tag{2.2}$$

where μ_N is the nuclear magneton. The kinetic energy of the neutron $E_n = \frac{1}{2}\ m_n \cdot \upsilon_n^2$ may be given in different units as follows

1 meV	=	$1.602 \cdot 10^{-22}$	J	$\Rightarrow$	$8.066\ cm^{-1}$
since	E =	$h\nu$	:	1 meV$\Rightarrow$	$0.2418 \cdot 10^{12}$ Hz
since	E =	$k_B T$	:	1 meV$\Rightarrow$	11.60 K

The neutron wavelengths is obtained from the de Broglie relation

$$\lambda_n = h/m_n\,\upsilon_n = h/(2m_n\,E_n)^{1/2} \tag{2.3}$$

According to the conditions for moderation, neutrons in different wavelength regimes are separated into different categories as displayed in Fig.2.3. They are produced by moderation in particular moderators which are kept at different temperatures.

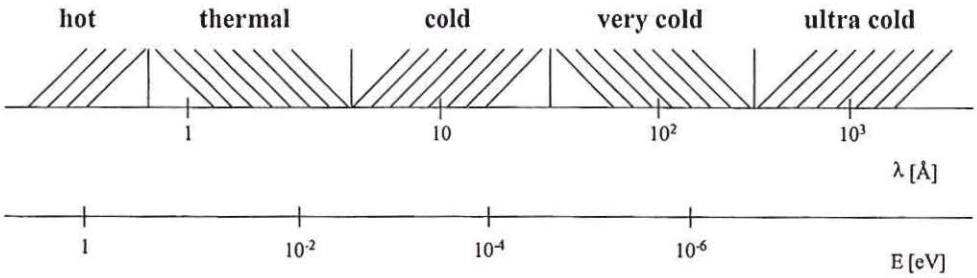

Figure 2.3: Relation between neutron wavelength and their corresponding kinetic energies.

Hot neutrons in reactors are obtained from hot sources at temperatures around 2000K. Thermal neutrons evolve from ambient moderators while cold neutrons are obtained from mainly liquid hydrogen or deuterium moderators. The velocity distribution of the neutrons evolving from such a moderator are given by a Maxwell velocity distribution

$$\phi(\upsilon) = \upsilon^3 \exp\left(-\frac{1}{2}\,\upsilon^2/k_B T\right) \tag{2.4}$$

Thereby, $\Phi(\upsilon)\, d\upsilon$ is the number of neutrons which are emitted through an unit area per second with velocities between υ and $\upsilon+d\upsilon$. Fig.2.4 displays Maxwellian flux distributions for the three types of moderators discussed above.

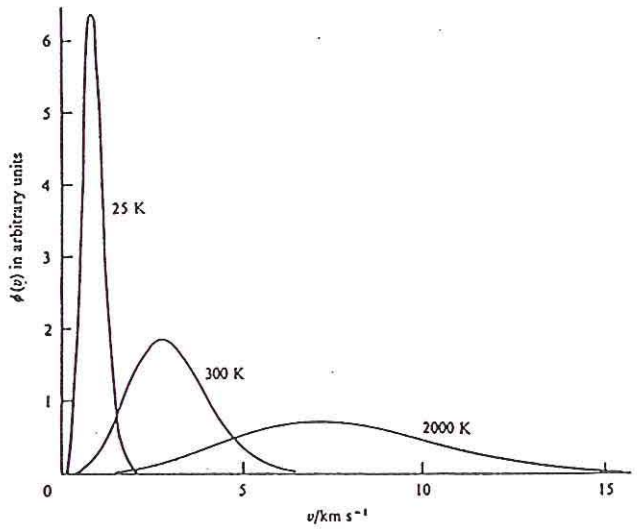

Figure 2.4: Velocity distributions of neutrons from cold (25K), thermal (300K) and hot (2000K) moderators.

Finally, Neutrons as well as X-rays are used for scattering experiments on materials. Table 2.1 compares the most important properties of both radiations.

Table 2.1:
Comparison of X-rays and neutrons

	X-rays are transversal electromagnetic waves	neutrons are particle waves
Mass	$m_{phot} = 0$	$m_n = 1.6749286(10) \cdot 10^{-27}$kg
Charge	0	0
Spin	1	½
Magnetic Moment	0	$\mu_n = -1.91304275(45)\ \mu_N$
Typical Energy	10keV	25meV
Wave length	$\lambda_x = ch/E = 1.24\text{Å}$	$\lambda_n = h/(2E m_n)^{1/2} = 1.8\text{Å}$
Velocity	speed of light	$v_n = \left(\frac{2E}{m_n}\right)^{1/2} = 2200\,m/sec$

2.3 Neutron production

Neutrons are generated by nuclear reactions. For the investigation of matter a large luminosity that means a high flux of neutrons ϕ of the requested energy range is essential. Such fluxes at present can only be obtained through nuclear fission or spallation. Both are schematically displayed in Fig.2.5.

In nuclear fission a thermal neutron is absorbed by an ^{235}U nucleus. The thereby highly excited nucleus fissions into a number of smaller nuclei of middle heavy elements and in addition into 2-5 (on average 2.5) highly energetic fast fission neutrons. Typical energies are in the rage of several MeV. In order to undertain a nuclear chain reaction, on the average 1.5 moderated neutrons are necessary. At a balance a research reactor delivers about 1 neutron per fission event.

The most powerful research reactor worldwide, the HFR at the Institute Laue Langevin in Grenoble, produces a neutron flux of $\Phi_{therm} = 1.5 \cdot 10^{15}$n/cm^{2}s (thermal power 60MW). The

related values for the FRJ-2 reactor in Jülich for comparison are $\Phi_{therm} = 2 \cdot 10^{14}$ n/cm^{2}s at 23 MW.

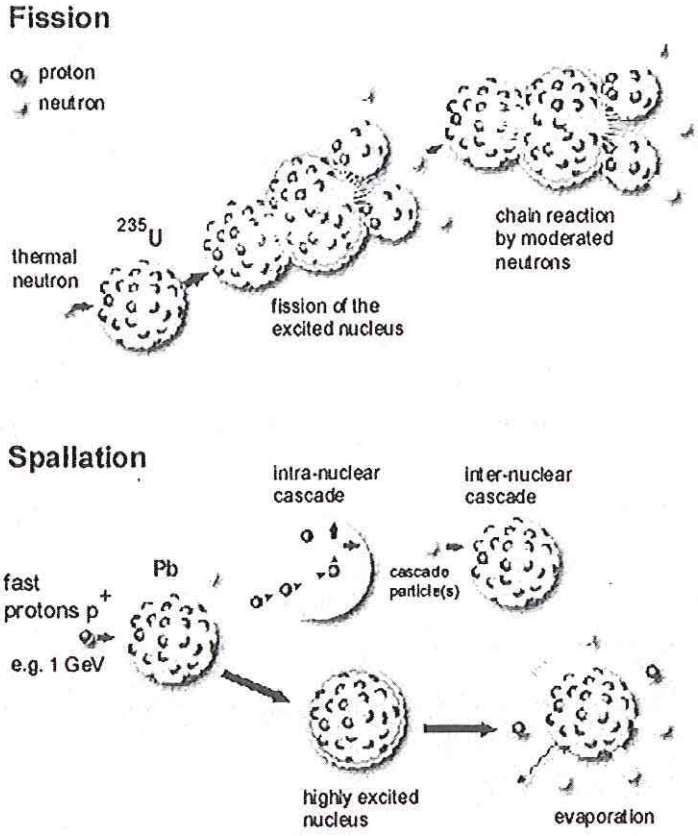

Figure 2.5: Schematic presentation of the fission and spallation process.

In the spallation process highly energetic protons which are typically at energies of about 1GeV hit a target of heavy nuclei like tungsten or tantalum. The proton excites the heavy nucleus strongly and in the event in the order of 20-25 neutrons are evaporated from such a nucleus. The energies of the spallation neutrons are typically in a range from several MeV up to hundreds of MeV. Other than a research reactor, a spallation neutron source can easily be operated in a pulsed mode, where a pulsed proton beam hits a target. At the spallation source ISIS at the Rutherford Laboratory for example, the repetition frequency amounts to 50Hz. In

this way even at a comparatively low average neutron flux very high pulsed fluxes may be obtained. In the thermal range for example, the Rutherford source is able to surpass the ILL with respect to the peak flux significantly. Such pulsed sources can be used in particularly well for time of flight experiments which will be discussed later in the school.

2.4 Neutron detection

Generally the detection of neutrons is performed indirectly through particular nuclear reactions which produce charged particles. A number of possible reactions are listed in Table 2.2.

Proportionality counters operate with a gas volume of ^3He or BF_3 (enriched with ^{10}B). Such counters deliver sensitivities to nearly 100%. Scintillation counters absorb neutrons within a polymer or glass layer which is enriched by ^6Li and ZnS. Neutron absorption then leads to fluorescence radiation which is registered via a photo multiplayer or directly with a photographic film. Finally, fission chambers use the $n + ^{235}U$ reaction and have generally only a low counting probability. They are mainly used in order to control the beam stability and are applied as monitors.

Table 2.2:
Nuclear reactions used for neutron detection.
The cross sections are given in barns (1b = 10^{-28} m^2).

Reaction	Cross Section for 25meV neutrons	Particles generated	Energy [MeV]	Total Energy [MeV]
$n + ^3He$	5333 b	P ^3T	0.57 0.2	0.77
$n + ^6Li$	941 b	^3T ^4He	2.74 2.05	4.79
$n + ^{10}B$	3838 b	^4He ^7Li γ	1.47 0.83 0.48 (93%)	2.30
$n + ^{235}U$	681 b	fission		1 - 2

2.5 Scattering amplitude and cross section, the Born approximation

We now consider the scattering event by a fixed nucleus. The geometry for such a scattering process is sketched in Fig.2.6. The incoming neutrons are described by plane waves e^{ikr} travelling in z-direction. At the target this plane wave interacts with a nucleus and is scattered into a solid angle $\Omega d\Omega$.

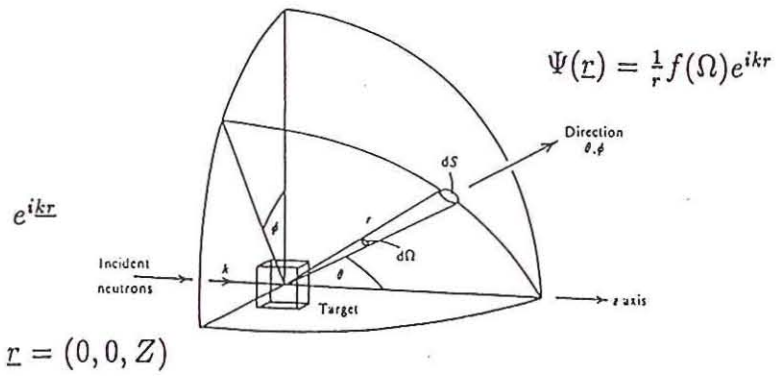

Figure 2.6: Scattering geometry for an incident plane wave scattered at a target.

The partial cross section is defined by

$$\frac{d\sigma}{d\Omega} = \frac{\textit{current of scattered neutrons into } (\Omega,\ d\Omega)}{\textit{current of incident neutrons}} \tag{2.5}$$

Quantum mechanically the current is given by

$$j = \frac{\hbar}{2mi}\left(\psi^* \nabla \psi - \psi \nabla \psi^*\right) \tag{2.6}$$

For an incident plane wave $\psi = e^{ikr}$ Eq.[2.6] leads immediately to $j = \hbar k / m_n \cdot 1/V$, where V is the normalization volume. The scattered spherical wave has the form $\frac{1}{r} f(\Omega) e^{ikr}$ there $f(\Omega)$

describes the solid angle dependent scattering amplitude. Inserting this form for the scattered wave into Eq.[2.6] for large r

$$j_r = \frac{\hbar k'}{m_n} \left| f(\Omega) \right|^2 \quad d\Omega \tag{2.7}$$

is obtained. Finally, inserting the incoming and scattered currents into Eq.[2.5] we obtain for the cross section

$$\frac{d\sigma}{d\Omega} = \frac{\left|\hbar k'/m\right| \left| f \ (\Omega)\right|^2 \quad d\Omega}{\left|\hbar k / m\right| \quad d\Omega} = \left| f(\Omega) \right|^2 \tag{2.8}$$

$\frac{d\sigma}{d\Omega}$ is also called differential cross section. We realize, that a scattering experiment delivers information on the absolute value of the scattering amplitude, but not on $f(\Omega)$ itself. Informations on the phases are lost. The total cross section is obtained by an integration over the solid angle

$$\sigma = \int_{\Omega} d\Omega \, \frac{d\sigma}{d\Omega} \tag{2.9}$$

Our next task is the derivation of $f(\Omega)$ in the so called Born approximation. We start with the Schrödinger equation of the scattering problem

$$\left[-\frac{\hbar^2}{2m} \Delta + V(\underline{r}) \right] \psi = E \psi \tag{2.10}$$

where $V(\underline{r})$ is the scattering potential. We note, that for scattering on a free nucleus the mass term in the kinetic energy has to be replaced by the reduced mass $\mu = \frac{M \cdot m_n}{m_n + M}$. For large distances ($r \to \infty$), $V = 0$ and we have $E = \hbar^2 k^2 / 2m_n$. Inserting into Eq.[2.10] leads to the wave equation

$$\left(\Delta + k^2\right) \ \psi \ = \ u\left(\underline{r}\right) \ \psi \tag{2.11}$$

$$u\left(\underline{r}\right) = \frac{2m_n}{\hbar^2} \ V\left(\underline{r}\right)$$

The wave equation is solved by the appropriate Greenfunction

$$\left(\Delta^2 + k^2\right) G\left(\underline{r} - \underline{r}'\right) = -4\pi\,\delta\left(\underline{r} - \underline{r}'\right) \tag{2.12a}$$

$$G\left(\underline{r} - \underline{r}'\right) \ = \ \frac{e^{ik|\underline{r}-\underline{r}'|}}{\left|\underline{r} - \underline{r}'\right|} \tag{2.12b}$$

$$u(r)\,\psi(r) = \int dr'\,\delta\left(r - r'\right) u(r')\,\psi(r') \tag{2.12c}$$

where $G(\underline{r})$ is the Greenfunction solving the wave equation with the δ-function as inhomogeneity. Using Eq.[2.12c] the wave Eq.[2.11] may be formally solved by

$$\psi\left(\underline{r}\right) \ = \ e^{ik\underline{r}} \ - \ \frac{1}{4\pi} \ \int dr' \ G\left(\underline{r} - \underline{r}'\right) \ u\left(\underline{r}'\right) \ \psi\left(\underline{r}'\right) \tag{2.13}$$

In Eq.[2.13] the first part is the solution of the homogenous equation and the second part the particular solution of the inhomogeneous one. The integral Eq.[2.13] may now be solved by iteration. Starting with the incoming wave $\psi^0 = e^{ikr}$ as the zero order solution, the $\nu+1$ order is obtained from the order ν by

$$\psi^{\nu+1} \ \left(\underline{r}\right) = \ e^{ik\underline{r}} \ - \ \frac{1}{4\pi} \ \int G\left(\underline{r} - \underline{r}'\right) \ u\left(\underline{r}'\right) \ \psi^{\nu}\left(\underline{r}'\right) \ d^3r' \tag{2.14}$$

In the Born approximation we consider the first order solution which describes single scattering processes. All higher order processes are then qualified as multiple scattering events. The Born approximation is valid for weak potentials. $\frac{\sigma_{tot}}{\left(a^2 \cdot \pi\right)} \ll 1$ where a is the size of the scattering object. For a single nucleus this estimation gives about 10^{-7} and the Born approximation is well fulfilled.

We note one important exception, the dynamical scattering theory, which considers the scattering problem close to a Bragg reflection in a crystal. Then multiple beam interferences are important and the Born approximation ceases to apply. For most practical purposes, however, the Born approximation is valid. Under the Born assumption the scattered wave function becomes

$$\psi^1 = e^{i\underline{k}_0\underline{r}} - \frac{1}{4\pi} \int \frac{e^{ik|\underline{r}-\underline{r}'|}}{|\underline{r}-\underline{r}'|} \frac{2m_n}{\hbar^2} V(\underline{r}') e^{i\underline{k}\underline{r}} d^2r' \tag{2.15}$$

In order to arrive at a final expression, we have to expand all expressions containing $\underline{r}$ and $\underline{r}'$ around $\underline{r}$. Thereby, we consider that $\underline{r}'$ is a sample coordinate and small compared to $\underline{r}$. We have

$$\frac{1}{|\underline{r}-\underline{r}'|} \cong \frac{1}{r} + O\left(\frac{1}{r^2}\right) \tag{2.16}$$

$$|\underline{r}-\underline{r}'| \cong r - \underline{r}' \cdot grad\ (\underline{r}) = r - \underline{r}' \cdot \frac{\underline{r}}{|\underline{r}|}$$

Inserting Eq.[2.16] into Eq.[2.15] gives

$$\psi' = e^{i\underline{k}\underline{r}} - \frac{1}{4\pi} \frac{e^{ikr}}{r} \int e^{-ik\frac{\underline{r}}{r}\underline{r}'} \frac{2m_n}{\hbar^2} V(\underline{r}') e^{i\underline{k}\underline{r}} d^3r' \tag{2.17}$$

$k\frac{\underline{r}}{|\underline{r}|}$: direction of the scattered wave k'

Eq.[2.17] may be written as

$$\psi' = e^{i\underline{k}\underline{r}} - \underbrace{\langle k' |V| k \rangle \frac{m_n}{2\pi \hbar^2} \frac{e^{ikr}}{r}}_{f(\Omega)} \tag{2.18}$$

which leads to the final expression for the cross section Eq.[2.8]

$$\frac{d\sigma}{d\Omega} = \left(\frac{m_n}{2\pi\ \hbar^2}\right)^2 \left|\langle k'\ |V|\ k\rangle\right|^2 \tag{2.19}$$

We now also allow for inelastic processes, where the sample undergoes a change of its state from $|\lambda\rangle \rightarrow |\lambda'\rangle$. For the cross section we now also have to consider the changes of state as well as different length of the wave vectors of the incoming and outgoing waves, which lead to factors k' and k in the current calculation.

$$\left(\frac{d\sigma}{d\Omega}\right)_{\left(\rightarrow \frac{k,\lambda}{k',\lambda'}\right)} = \frac{k'}{k}\left(\frac{m_n}{2\pi\ \hbar^2}\right)\left|\langle k'\lambda'\ |V|\ k\lambda\rangle\right|^2 \tag{2.20}$$

The scattering event must fulfill energy and momentum conservation. With that we arrive finally at the double differential cross section

$$\frac{\partial^2\sigma}{\partial\Omega\ \partial\omega} = \frac{k'}{k}\left(\frac{m_n}{2\pi\ \hbar^2}\right)^2 \sum_{\lambda} P_\lambda \sum_{\lambda'} \langle k', \lambda'\ |V|\ k, \lambda\rangle^2\ \delta(\hbar\omega + E_\lambda - E_{\lambda'}) \tag{2.21}$$

The summation over λ is carried out over all possible initial states λ of the system with their appropriate probability P_λ. The sum over λ' is the sum over all final states, the δ-function takes care of the energy conservation, thereby $\hbar\omega$ is the energy transfer of the neutron to the system. This double differential cross section will be discussed in detail in the lecture on correlation functions.

2.6 Elementary scattering processes

2.6.1 The Fermi pseudo potential

The interaction of the neutron with a nucleon occurs under the strong interaction on a length scale of $1.5 \cdot 10^{-15}$m. For that process, the Born criterium is not fulfilled and for the scattering process on a single nucleus the Born series would have to be summed up. Fortunately, this is a problem of nuclear physics and for the purposes of neutron scattering a phenomenological approach suffices. Considering that the wavelengths of thermal neutrons are in the order of 10^{-10}m we realize, that they are much larger than the dimension of a nucleus of about 10^{-15}m.

Therefore, for any scattering event we may perform a separation into partial waves and consider only the isotropic *S*-wave scattering. These scattering processes may be described by one parameter the scattering length $b = b_1 + i \cdot b_2$. Thereby b_1 describes scattering, while b_2 is the absorption part. For thermal neutrons the scattering potential of a single nucleus becomes (Fermi pseudo potential)

$$V(\underline{r}) = \frac{2\pi \ \hbar^2}{m_n} \ b\delta \ (\underline{r} - \underline{R}) \tag{2.22}$$

The scattering lengths b have been measured as a function of neutron energy. For thermal and lower energies the real parts of these scattering lengths are constant and depend in an non-systematic way on the number of nucleons (see Fig.2.7).

We realize, that there are positive as well as negative scattering lengths. Following a convention most of the scattering lengths are positive. In this case, we have potential scattering with a phase shift of 180° between the incoming and scattered wave. Negative values result from resonance scattering where the neutrons penetrate the nuclei and create a compound nucleus. The emitted neutrons do not undergo a phase shift. We also realize strong differences in the scattering lengths for some isotopes. In particular important is the difference in scattering length between hydrogen and deuterium ($b_h = -0.374$, $b_d = +0.667$). This significant difference in scattering length is the basis of all contrast variation experiments in soft condensed matter research as well as in biology (see later lectures). We also note, that the scattering lengths may depend on the relative orientation of the neutron spin with respect to the spin of the scattering nucleus. Again a very prominent example is the hydrogen. There the scattering length for the triplet state, neutron and hydrogen spins are parallel, amounts to $b_{triplet} = 1.04 \cdot 10^{-12}$cm while the scattering length for the singlet situation, neutron and hydrogen spins are antiparallel, is $b_{singlet} = -0.474 \cdot 10^{-12}$cm.

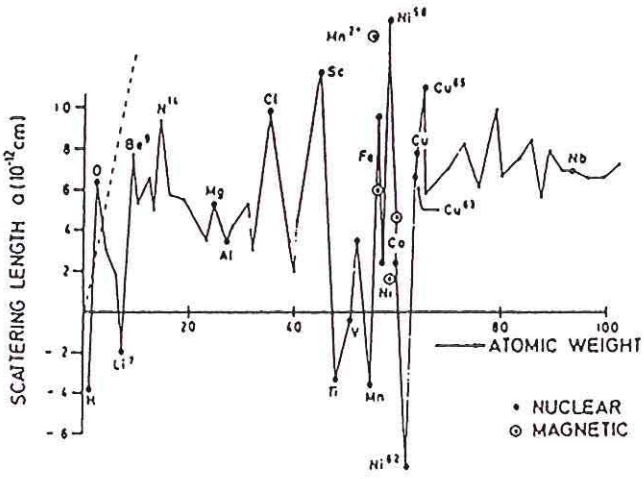

Figure 2.7: Scattering length of nuclei for thermal neutrons as a function of atomic weight.

2.6.2 Coherent and incoherent scattering

The scattering of neutrons depends on the isotope as well as on the relative spin orientations. We now will look into the consequences in regarding the elastic scattering from an ensemble of isotopes with the coordinates and scattering lengths $\{R_l, b_l\}$. The pseudo potential of this ensemble has the form

$$V(\underline{r}) = \frac{2\pi\ \hbar^2}{m_n} \sum_l b_l\, \delta(\underline{r} - \underline{R}_l) \tag{2.23}$$

with Eq.[2.18] we may calculate the matrix element of V between k and k' as

$$\langle k' | V | k \rangle = \frac{2\pi\ \hbar^2}{m} \sum_l b_l \int e^{-i\underline{k}'\underline{r}}\, \delta(r - R_l)\, e^{i\underline{k}\underline{r}}\ d^3\underline{r} \tag{2.24}$$

$$= \frac{2\pi\hbar^2}{m} \sum_l b_l\, e^{i\underline{Q}\underline{R}_l} \qquad \underline{Q} = \underline{k} - \underline{k}'$$

The matrix element is just a Fourier sum over the atomic positions decorated with the appropriate scattering length b_l. The scattering cross section is obtained following Eq.[2.19].

Thereby we now also consider the spin states of the nuclei before and after scattering s and s'. The initial state probabilities are given by P_s.

$$\frac{d\sigma}{d\Omega} = \sum_{ss'} P_s \sum_{ll'} \exp\left(i\underline{Q}\ (\underline{R}_l - \underline{R}_{l'})\right) \left\langle s' \left| b_{l'}^{*}\ b_l \right| s \right\rangle \tag{2.25}$$

We commence with spin independent interactions and assume that spatial coordinates and scattering lengths are not correlated – that means different isotopes are distributed randomly. Then Eq.[2.25] may be evaluated to

$$\frac{d\sigma}{d\Omega} = \sum_{ll'} \left\langle b_{l'}^{*}\ b_l \right\rangle \exp\left(i\underline{Q}\ (\underline{R}_l - \underline{R}_{l'})\right) \tag{2.26}$$

In order to evaluate Eq.[2.26] further, we introduce two scattering lengths averages – the mean square average and the mean scattering length. They are given by

$$\overline{b^2} = \frac{1}{N}\sum_l b_l^2 \ ; \ \bar{b} = \frac{1}{N}\sum_l b_l \tag{2.27}$$

With these definitions, the average product of b_l and b_l' becomes

$$\left\langle b_l\ b_l' \right\rangle = (1-\delta_{ll'})\,\bar{b}^2 + \delta_{ll'}\,\overline{b^2} \tag{2.28}$$

Finally, introducing Eq.[2.28] into the expression for the cross section Eq.[2.26] we obtain

$$\begin{aligned} \frac{d\sigma}{d\Omega} &= \sum_{ll'} \left[(1-\delta_{ll'})\,\bar{b}^2 + \delta_{ll'}\,\bar{b}^2\right] \exp i\underline{Q}(\underline{R}_l - \underline{R}_{l'}) \\ &= N\left(\overline{b^2} - \bar{b}^2\right) + \bar{b}^2 \sum_{ll'} \exp i\underline{Q}(\underline{R}_l - \underline{R}_{l'}) \end{aligned} \tag{2.29}$$

Obviously, the cross section contains two contributions. A coherent one where we have constructive interference of the neutron waves eminating from the different nuclei. This

scattering is observed with the average scattering length $\bar{b}$. In addition there exists incoherent scattering as a result of the isotope disorder. It is not able of interference and isotropic.

We now consider spin dependent scattering from one isotope with the nuclear spin j. Both the nuclear spin as well as the neutron spin are statistically distributed. There exist two compound spin states:

(i) neutron and nuclear spin are parallel: then $I = j + ½$. This spin state has the multiplicity of $2j + 2$. Its scattering length is b^+.

(ii) neutron and nuclear spin are antiparallel $I = j - ½$ the multiplicity is $2j$ and the corresponding scattering length equals b^-. The a priory probabilities for the compound spin states are given by the number of possibilities for their realization divided by the total number.

$$p^+ = \frac{2j + 2}{2j + 2 + 2j} = \frac{j+1}{2j+1} \qquad (2.30)$$

$$p^- = \frac{j}{2j+1}$$

The corresponding average scattering lengths become

$$\bar{b} = p^+ b^+ + p^- b^- \qquad (2.31)$$

$$\overline{b^2} = p^+ b^{+2} + p^- b^{-2}$$

We now consider the proton as an example. Here $j = ½$, $b^+ = 1.04 \cdot 10^{-12}$cm, $b^- = -4.74 \cdot 10^{-12}$cm, $p^+ = ¾$, $p^- = ¼$. Inserting into Eq.[2.31] we find $\bar{b} = -0.375 \cdot 10^{-12}$cm and $\bar{b}^2 = 6.49 \cdot 10^{-24}$cm^2. These values lead to a coherent cross section $\sigma_{coh} = 4\pi \cdot \bar{b}^2 = 1.77 \cdot 10^{-24} cm^2$. For the incoherent cross section, we obtain $\sigma_{inc} = 4\pi \cdot \left(\bar{b}^2 - \overline{b^2}\right) = 79.8 \cdot 10^{-24} cm^2$. This value is the largest incoherent cross sections of all isotopes and makes the hydrogen atom the prime incoherent scatterer which can be exploited for hydrogen containing materials.

2.7 Comparison between X-ray and neutron scattering

Other than neutrons, X-rays are scattered by the electrons, which are distributed in space around the respective nucleus. This spatial distribution leads to an atomic form factor which is the Fourier transformed of the electron density distribution $\rho_j(\underline{r})$. It depends in principle on the degree of ionisation of a nucleus but not on the isotope.

$$f_j\ (\underline{Q}) = \int_V \rho_j\ (\underline{r})\ \exp\ (i\underline{Q}\underline{r})\ dV \tag{2.32}$$

Since the atomic radii (about 10^4 times larger than the radius of a nucleus) are comparable with the wavelength, the scattering amplitude $f_j(Q)$ depends strongly on Q. Thus, with increasing scattering angle the scattering intensity drops significantly. Furthermore, the atom formfactor depends on the number of electrons Z and is given by

$$f_j\ (Q = 0) = Z \tag{2.33}$$

Thereby, Z is the number of electrons of an atom or of an ion. Fig.2.8 displays schematically the atomic formfactor normalized to one as a function of $\frac{\sin\theta}{\lambda}$.

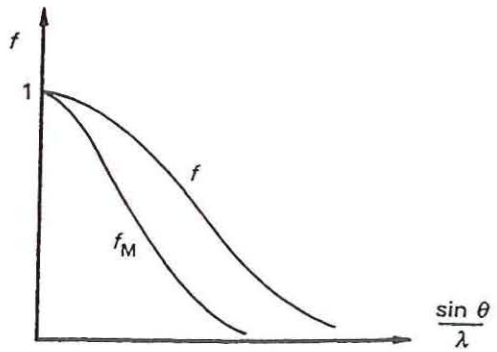

Figure 2.8: Schematic representation of normalized X-ray and magnetic neutron scattering form factors as a function of sin θ/λ.

For a spherical electron distribution $\rho_j(r)$, $f_j(r)$ depend only on the absolute value of Q. For neutral atoms and possible ionic states they has been calculated by Hartree-Fock calculations and may be found tabulated.

Since the atomic form factors depend on the atomic number, the scattering contributions of light atoms for X-rays are only weak. Therefore, in structure determinations the precision of the localization of such important atoms like hydrogen, carbon or oxygen is limited in the presence of heavy atoms. Neutrons do not suffer from this problem since the scattering length for all atoms are about equal.

In particular important is the case of hydrogen. In the bound state the density distribution of the only electron is typically shifted with respect to the proton position and an X-ray structure analysis in principle cannot give the precise hydrogen positions. On the other hand, bonding effects which are important for the understanding of the chemistry, may be precisely studied by X-ray electron density distributions.

Atoms or ions with slightly different atom number like neighbouring elements in the periodic table are difficult to distinguish in X-ray experiments. Again, neutron scattering experiments also by the use of the proper isotope allow a by far better contrast creation. Such effects are in particular important for e.g. the 3d-elements.

The paramagnetic moment of an atom or ion μ_j results form the unpaired electrons. The density distribution of these electrons $\rho_{jm}(\underline{r})$ is also named magnetization density or spin density and is a partial electron density compared to the total electron density $\rho_j(r)$. Because of the magnetic dipole interaction, the amplitude of the magnetic neutron scattering is given in analogy to Eq.[2.32] as the Fourier transformed of the magnetization density $\rho_{jM}(r)$. The normalized scattering amplitude

$$f_{jM}(Q) = \frac{1}{\mu_j} \int \rho_{jM}(r) \exp(iQr)\, dV \qquad (2.34)$$

is also named magnetic form factor. If the spin density distribution is delocalised as e.g. for 3d-elements, the magnetic form factor decays even more strongly than the X-ray analogue.

2.8 Conclusion: Why are neutrons interesting?

Modern materials research together with the traditional scientific interest in the understanding of condensed matter at the atomic scale requires a complete knowledge of the arrangement and the dynamics of the atoms or molecules and of their magnetic properties as well. This information can be obtained by investigating the interaction of the material in question with varies kinds of radiation such as visible light, X-rays or synchrotron radiation, electrons, ions and neutrons. Among them, neutrons play a unique role due to the inherent properties discussed above

- their dynamic dipole moment allows the investigations of the magnetic properties of materials.
- their large mass leads to a simultaneous sensitivity to the spatial and temporal scales that are characteristic of atomic distances and motions.
- neutrons interact differently with different isotopes of the same atomic species. This allows the experimentator to paint selected atoms or molecules by isotopes replacement.
- neutrons can easily penetrate a thick material – an important advantage for material testing.
- the interaction of the neutron with a nucleus has a simple form (Born approximation) which facilitates the direct unambiguous theoretical interpretation of experimental data.

A more thorough introduction to neutron scattering may be found in the following books:

[1] Bacon G.E., *Neutron Diffraction*, Clarendon Press, Oxford (1975)

[2] Bacon G.E. (Ed.), *Fifty Years of Neutron Diffraction: The advent of Neutron Scattering*, Adam Hilger, Bristol (1986)

[3] Bée M., *Quasielastic Neutron Scattering: Principles and Applications in Solid State Chemistry, Biology and Materials Science*, Adam Hilger, Bristol (1988)

[4] Lovesey S.W. and Springer T. (Eds.), *Dynamics of Solids and Liquids by Neutron Scattering*, Topics in Current Physics, Vol. 3, Springer Verlag, Berlin (1977)

[5] Lovesey S.W., *Theory of Neutron Scattering from Condensed Matter*, Vol. 1: *Nuclear Scattering*, Vol. 2: *Polarization Effects and Magnetic Scattering*, Clarendon Press, Oxford (1984)

[6] Sköld K. and Price D.L. (Eds.), *Methods of Experimental Physics*, Vol. 23, Part A, B, C: *Neutron Scattering*, Academic Press, New York (1986)

[7] Springer T., *Quasielastic Neutron Scattering for the Investigation of Diffusive Motions in Solids and Liquids*, Springer Tracts in Modern Physics, Vol. 64, Springer Verlag, Berlin (1972)

[8] Squires G.L., *Introduction to the Theory of Thermal Neutron Scattering*, Cambridge University Press, Cambridge (1978)

[9] Williams W.G., *Polarized Neutrons*, Clarendon Press, Oxford (1988)

[10] Willis B.T. (Ed.), *Chemical Application of Thermal Neutron Scattering*, Oxford University Press, Oxford (1973)

[11] Windsor C.G., *Pulsed Neutron Scattering*, Taylor & Francis, London (1981)

3. Elastic Scattering from Many-Body Systems

Thomas Brückel, IFF, FZ-Jülich

3.1 Introduction

So far we have learnt about the production of neutrons and their interaction with a single atom. In this chapter, we will discuss the scattering of thermal neutrons from a sample containing many atoms. In the first part, we will assume that the atoms are non-magnetic and only the scattering from the nucleus will be considered. In the second part, we will discuss the scattering from the spin- and orbital- angular momentum of the electrons in a magnetic solid.

For simplification, we will assume in this chapter that the atoms are rigidly fixed on equilibrium positions, i. e. they are not able to absorb recoil energy. This assumption is certainly no longer valid, if the neutrons are scattered from a gas, especially in the case of hydrogen, where neutron and the atom have nearly the same mass. In this case, the neutron will change its velocity, respectively its energy, during the scattering event. This is just the process of moderation and without this so-called inelastic scattering (i. e. scattering connected with a change of kinetic energy of the neutron) we would not have thermal neutrons at all. Also when scattered from a solid (glass, polycrystalline or single crystalline material) neutrons can change their velocity for example by creating sound waves (phonons). However, in the case of scattering from a solid, there are always processes in which the recoil energy is being transferred to the sample as a whole, so that the neutron energy change is negligible and the scattering process appears to be elastic. In this chapter we will restrict ourselves to only these scattering processes, during which the energy of the neutron is not changed. In subsequent chapters, we will learn how large the fraction of these elastic scattering processes is, as compared to all scattering processes.

Quantum mechanics tells us that the representation of a neutron by a particle wave field enables us to describe interference effects during scattering. A sketch of the scattering process in the so-called *Fraunhofer* approximation is given in figure 3.1.

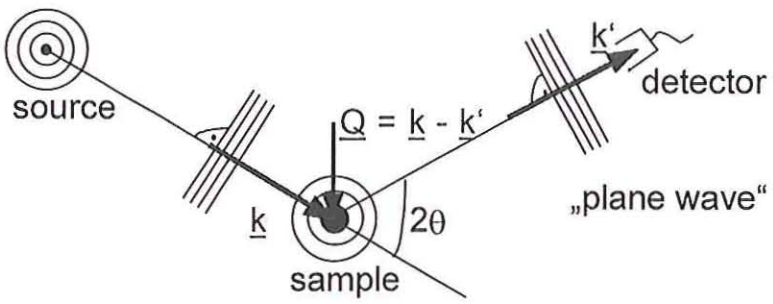

Fig. 3.1: A sketch of the scattering process in the Fraunhofer approximation, in which it is assumed that plane waves are incident on sample and detector due to the fact that the distance source-sample and sample-detector, respectively, is significantly larger than the size of the sample.

In the Fraunhofer approximation it is assumed that the size of the sample is much smaller than the distance between sample and source and the distance between sample and detector, respectively. This assumption holds in most cases for neutron scattering experiments. Then the wave field incident on the sample can be described as plane waves. We will further assume that the source emits neutrons of one given energy. In a real experiment, a so-called *monochromator* will select a certain energy from the white reactor spectrum. Altogether, this means that the incident wave can be completely described by a wave vector $\underline{k}$. The same holds for the wave incident on the detector, which can be described by a vector $\underline{k}'$. In the case of elastic scattering (diffraction), we have:

$$k = |\underline{k}| = |\underline{k}'| = k' = \frac{2\pi}{\lambda} \tag{3.1}$$

Let us define a so-called *scattering vector* by:

$$\boxed{\underline{Q} = \underline{k} - \underline{k}'} \tag{3.2}$$

The magnitude of the scattering vector can be calculated from wave length λ and scattering angle 2θ as follows:

$$Q = |\underline{Q}| = \sqrt{k^2 + k'^2 - 2kk'\cos 2\theta}$$

$$\Rightarrow \boxed{Q = \frac{4\pi}{\lambda}\sin\theta} \qquad (3.3)$$

During a scattering experiment, the intensity distribution is being determined as a function of the scattering vector:

$$I \sim \frac{d\sigma}{d\Omega}(\underline{Q}) \qquad (3.4)$$

The proportionality factors arise from the detailed geometry of the experiment. Our task is to determine the arrangement of the atoms in the sample from the knowledge of the scattering cross section $d\sigma/d\Omega(\underline{Q})$. The relationship between scattered intensity and the structure of the sample is especially simple in the approximation of the so-called *kinematic scattering*. In this case, multiple scattering events and the extinction of the primary beam due to scattering in the sample are being neglected. Following figure 3.2, the phase difference between a wave scattered at the origin of the co-ordinate system and at the position $\underline{r}$ is given by:

$$\underline{k}\cdot\underline{r} - \underline{k}'\cdot\underline{r} = \underline{Q}\cdot\underline{r} \qquad (3.5)$$

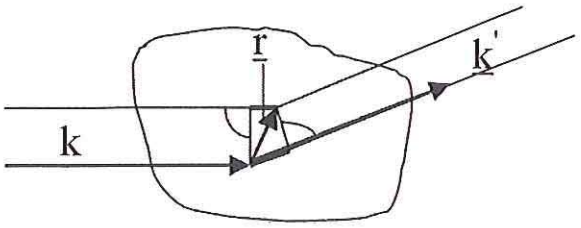

Fig. 3.2: A sketch illustrating the phase difference between a beam being scattered at the origin of the co-ordinate system and a beam scattered at the position $\underline{r}$.

The scattered amplitude at the position $\underline{r}$ is proportional to the *scattering power density* $\rho_s(\underline{r})$. The meaning of ρ_s in the case of neutron scattering will be given later. The total scattered amplitude is given by a coherent superposition of the scattering from all positions $\underline{r}$ within the sample, i. e. by the integral:

$$A = \int \rho_s(\underline{r}) \cdot e^{i\underline{Q}\cdot\underline{r}} d^3r \qquad (3.6)$$

I.e. the scattered amplitude is connected with the scattering power density $\rho_s(\underline{r})$ by a simple Fourier transform:

$$A = F(\ \rho_s\ (\ \underline{r})\ ) \qquad (3.7)$$

A knowledge of the scattering amplitude for all scattering vectors Q allows us to determine via a Fourier transform the scattering power density uniquely. This is the complete information on the sample, which can be obtained by the scattering experiment. Unfortunately, life is not so simple. There is the more technical problem that one is unable to determine the scattering cross section for all values of Q. The more fundamental problem, however, is given the fact that normally the amplitude of the scattered wave is not measurable. Instead only the scattered intensity $I \sim |A|^2$ can be determined. Therefore, the phase information is lost and the simple reconstruction of the scattering power density via a Fourier transform is no longer possible. This is the so-called *phase problem* of scattering.

The question what we can learn about the structure of the sample from a scattering experiment despite this problem will be the subject of the following chapters. For the moment, we will ask ourselves the question, which wavelength we have to choose to achieve atomic resolution. The distance between neighbouring atoms is in the order of a few times 0.1 nm. In the following we will use the "natural atomic length unit" 1 Å = 0.1 nm. To obtain information on this length scale, a phase difference of about $Q \cdot a \approx 2\pi$ has to be achieved, compare (3.5). According to (3.3) $Q \approx \frac{2\pi}{\lambda}$ for typical scattering angles ($2\theta \approx 60°$). Combining these two estimations, we end up with the requirement that the wavelength λ has to be in the order of the inter-atomic distances, i. e. in the order of 1 Å to achieve atomic resolution in a scattering experiment. This condition is ideally fulfilled for thermal neutrons.

3.2 Fundamental Scattering Theory

In this chapter, we will give a simple formulation of scattering theory. Our purpose is to derive (3.7) from fundamental principles. The conditions under which (3.7) holds and the limitations of kinematical scattering theory will thus become clearer. During a first reading this section can be skipped. More details can be found in [1].

In quantum mechanics, neutrons are described as particle wave fields through the Schrödinger equation:

$$H\Psi = \left(-\frac{\hbar^2}{2m_n}\Delta + V \right)\Psi = i\hbar\frac{\partial}{\partial t}\Psi \tag{3.8}$$

ψ is the probability density amplitude, V the interaction potential. In the case of purely elastic scattering E = E', the time dependence can be described by the factor $\exp\left(-i\frac{E}{\hbar}t\right)$. Assuming this time dependence, a wave equation for the spatial part of the probability density amplitude ψ can be derived from (3.8):

$$\Delta\Psi + k^2(\underline{r})\Psi = 0 \tag{3.9}$$

In (3.9) we have introduced a spatially varying wave vector with the magnitude square:

$$k^2(\underline{r}) = \frac{2m_n}{\hbar^2}(E - V(\underline{r})) \tag{3.10}$$

Solutions of (3.8) in empty space can be guessed immediately. They are given by plane waves $\Psi = \Psi_0 \exp\left[i\left(\underline{k}\cdot\underline{r} - \frac{E}{\hbar}t\right)\right]$ with $k^2 = \frac{2m_n}{\hbar^2}E$. The relations between magnitude of the wave vector, wave length and energy of the neutron E can be written in practical units:

$$\boxed{\begin{aligned} k\left[\text{Å}^{-1}\right] &\approx 0.695\sqrt{E\left[meV\right]} \\ \lambda\left[\text{Å}\right] &\approx 9.045/\sqrt{E\left[meV\right]} \\ E\left[meV\right] &\approx 81.8/\lambda^2\left[\text{Å}\right] \end{aligned}} \tag{3.11}$$

To give an example, neutrons of wavelength λ = 2.4 Å have an energy of 14.2 meV with a magnitude of the neutron wave vector of k = 2.6 $Å^{-1}$.

To obtain solutions of the wave equation (3.9) in matter, we reformulate the differential equation by explicitly separating the interaction term:

$$\left(\Delta + k^2\right)\Psi = \frac{2m_n}{\hbar^2} V \cdot \Psi =: \chi \tag{3.12}$$

Here $\underline{k}$ denotes the wave vector for propagation in empty space. The advantage of this formulation is that the solution of the left hand side are already known. They are the plane waves in empty space. Equation (3.12) is a linear partial differential equation, i. e. the superposition principle holds: the general solution can be obtained as a linear combination of a complete set of solution functions. The coefficients in the series are determined by the boundary conditions. To solve (3.12) one can apply a method developed for inhomogeneous linear differential equations. For the moment, we assume that the right hand side is fixed (given as χ). We define a "*Greens-function*" by:

$$\left(\Delta + k^2\right)G(\underline{r},\underline{r}') = \delta(\underline{r} - \underline{r}') \tag{3.13}$$

We can easily verify that a solution of (3.13) is given by:

$$G(\underline{r},\underline{r}') = \frac{e^{ik|\underline{r}-\underline{r}'|}}{4\pi|\underline{r} - \underline{r}'|} \tag{3.14}$$

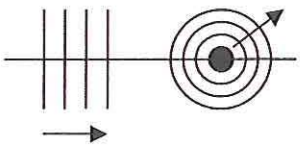

The meaning of (3.14) is immediately clear: the scattering from a point-like scatterer (δ-potential) gives a emitted spherical wave.

Using the "Greens-function" G(r,r'), a formal solution of the wave equation (3.12) can be given:

$$\Psi = \Psi^o + \int G(\underline{r},\underline{r}')\chi(\underline{r}')d^3r' \qquad (3.15)$$

Here, we have taken the initial conditions of a incident plane wave ψ^0 into account. That (3.15) is indeed a solution of (3.12) can be easily verified by substituting (3.15) into (3.12). If we finally substitute the definition of χ, one obtains:

$$\Psi(\underline{r}) = \psi^o(\underline{r}) + \frac{2m_n}{\hbar^2}\int G(\underline{r},\underline{r}')V(\underline{r}')\Psi(\underline{r}')d^3r' \qquad (3.16)$$

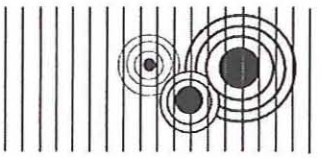

(3.16) has a simple interpretation: the incident plane wave $\psi^0(\underline{r})$ is superimposed by spherical waves emitted from scattering at positions $\underline{r}'$. The intensity of these spherical waves is proportional to the interaction potential $V(\underline{r}')$ and the amplitude of the wave field at the position $\underline{r}'$. To obtain the total scattering amplitude, we have to integrate over the entire sample volume.

However, we still have not solved (3.12): our solution ψ appears again in the integral in (3.16). In other words, we have transformed differential equation (3.12) into an integral equation. The advantage is that for such an integral equation, a solution can be found by iteration. In the zeroth approximation, we neglect the interaction V completely. This gives $\psi = \psi^0$. The next higher approximation for a weak interaction potential is obtained by substituting this solution in the right hand side of (3.16). The first non-trivial approximation can thus be obtained:

$$\Psi^1(\underline{r}) = e^{i\underline{k}\cdot\underline{r}} + \frac{2m_n}{\hbar^2}\int \frac{\exp(ik|\underline{r}-\underline{r}'|)}{4\pi|\underline{r}-\underline{r}'|} V(\underline{r}')e^{i\underline{k}\underline{r}'}d^3r' \qquad (3.17)$$

(3.17) is nothing else but a mathematical formulation of the well-known *Huygens principle* for wave propagation.

The approximation (3.17) assumes that the incident plane wave is only scattered once from the potential V(r'). For a stronger potential and larger sample, multiple scattering processes can occur. Again, this can be deduced from the integral equation (3.16) by further iteration. For simplification we introduce a new version of equation (3.16) by writing the integral over the "Greens function" as operator **G**:

$$\psi = \psi^o + \mathbf{G}V\psi \qquad (3.18)$$

The so-called *first Born approximation*, which gives the *kinematical scattering theory* is obtained by substituting the wave function ψ on the right hand side by ψ^0:

$$\psi^1 = \psi^o + \mathbf{G}V\psi^o \qquad (3.19)$$

This first approximation can be represented by a simple diagram as a sum of an incident plane wave and a wave scattered once from the potential V.

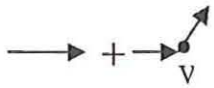

The second approximation is obtained by substituting the solution of the first approximation (3.19) on the right hand side of equation (3.18):

$$\psi^2 = \psi^o + \mathbf{G}V\psi^1$$
$$= \psi^o + \mathbf{G}V\psi^o + \mathbf{G}V\mathbf{G}V\psi^o \qquad (3.20)$$

Or in a diagrammatic form:

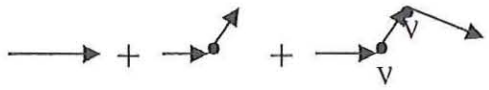

I. e. in the second approximation, processes are being taken into account, in which the neutron is scattered twice by the interaction potential V. In a similar manner, all higher order approximations can be calculated. This gives the so-called *Born series*. For a weak potential and small samples, this series converges rather fast. Often, the first approximation, the kinematic scattering theory, holds very well. This is especially the case for neutron scattering, where the scattering potential is rather weak, as compared to x-ray- or electron- scattering. Due to the strong Coulomb interaction potential, the probability for multiple scattering processes of electrons in solids is extremely high, making the interpretation of electron diffraction experiments very difficult. But even for neutrons, the kinematic scattering theory can break down, for example in the case of Bragg scattering from large ideally perfect single crystals, where the Born series does not converge. The wave equation has to be solved exactly under the boundary conditions given by the crystal geometry. For simple geometries, analytical solutions can be obtained. This is then called the *dynamical scattering theory*. Since for neutrons, the kinematical theory holds in most cases, or multiple scattering events can be corrected for easily, we will no longer discuss dynamical theory in what follows and refer to [1, 2].

Let us return to the first Born approximation (3.17). According to Fraunhofer, we assume in a further approximation that the size of the sample is significantly smaller than the distance sample-detector. The geometry to calculate the far field limit of (3.17) is given in figure 3.3.

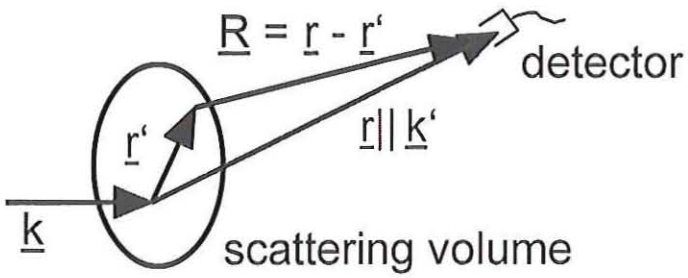

Fig. 3.3: Scattering geometry for the calculation of the far field limit at the detector. In the Fraunhofer approximation, we assume that $|\underline{R}| >> |\underline{r}'|$.

Under the assumption $|\underline{R}| >> |\underline{r}'|$, we can deduce from figure 3.3 the following approximation for the emitted spherical wave:

$$\frac{\exp(ik|\underline{r}-\underline{r}'|)}{|\underline{r}-\underline{r}'|} \approx \frac{\exp(ik(R-\underline{r}'\cdot\hat{\underline{R}}))}{R} \approx \frac{\exp ikR}{R}\cdot e^{-i\underline{k}'\cdot\underline{r}'} \tag{3.21}$$

The probability density amplitude for the scattered wave field in the limit of large distances from the sample is thus given by:

$$\Rightarrow \psi^1(\underline{R}) = e^{i\underline{k}\cdot\underline{R}} + \frac{2m_n}{\hbar^2}\frac{e^{ikR}}{4\pi R}\int V(\underline{r}')e^{i\underline{Q}\cdot\underline{r}'}d^3r' \tag{3.22}$$

This is just the sum of an incident plane wave and a spherical wave emitted from the sample as a whole. The amplitude of the scattered wave is given according to (3.22):

$$\boxed{\begin{aligned} A(\underline{Q}) &= \frac{2m_n}{4\pi\hbar^2}\int V(\underline{r})e^{i\underline{Q}\cdot\underline{r}}d^3r \\ &\sim F[V(\underline{r})] \end{aligned}} \tag{3.23}$$

I. e. the amplitude of the scattered wave is proportional to the Fourier transform of the interaction potential in the sample. In the case of pure nuclear scattering of neutrons, this interaction potential is the *Fermi-pseudo-potential* (see proceeding chapter). Finally, the measured intensity is proportional to the magnitude square of the scattering amplitude:

$$I(\underline{Q}) \sim |A(\underline{Q})|^2 \tag{3.24}$$

3.3 The Patterson- or Pair-Correlation-Function

As already mentioned in the introduction, the phase information is lost during the measurement of the intensity according to (3.24). For this reason, the Fourier transform of the scattering potential is not directly accessible in most scattering experiments (note, however that phase information can be obtained in certain cases). In this section, we will discuss, which information can be obtained from the intensity distribution of a scattering experiment.

The same problem will be dealt with in a more general context in the chapter on correlation functions. Substituting (3.23) into (3.24), we obtain for the magnitude square of the scattering amplitude, a quantity directly accessible in a scattering experiment:

$$\left|A(\underline{Q})\right|^2 \Big/ \left(\frac{2m_n}{4\pi\hbar^2}\right)^2 = \int V(\underline{r}) e^{i\underline{Q}\cdot\underline{r}} d^3r \int V^*(\underline{r}') e^{-i\underline{Q}\cdot\underline{r}'} d^3r'$$

$$= \iint d^3r d^3r' V(\underline{r}) V^*(\underline{r}') e^{i\underline{Q}(\underline{r}-\underline{r}')}$$

$$= \int d^3R \int d^3r V(\underline{R}+\underline{r}) V^*(\underline{r}) e^{i\underline{Q}\cdot\underline{r}}$$

$$\uparrow$$

$$\underline{r}-\underline{r}' =: \underline{R}$$

This shows that the scattered intensity is proportional to the Fourier transform of a function P(R):

$$I(\underline{Q}) \sim \left|A(\underline{Q})\right|^2 \sim F_{\underline{R}}[P(\underline{R})] \tag{3.25}$$

However, this function is not the interaction potential, but the so-called *Patterson-function:*

$$\boxed{P(\underline{R}) = \int d^3r V^*(\underline{r}) V(\underline{r}+\underline{R})} \tag{3.26}$$

This function correlates the value of the interaction potential at position r, with the value at the position r + R, integrated over the entire sample. If, averaged over the sample, no correlation exists between the values of the interaction potential at position R and r + R, then the Patterson function P(R) vanishes. If, however, a periodic arrangement of a pair of atoms exists in the sample with a difference vector for the positions R, then the Patterson function will have an extremum for this vector R. Thus, the Patterson function reproduces all the vectors connecting one atom with an other atom in a periodic arrangement. In fact, the Patterson function is just a special case of the pair correlation functions accessible by scattering.

The meaning of the Patterson function can be illustrated by a simple example. Figure 3.4 shows an arrangement of three atoms in the form of a triangle. We can construct the Patterson function by copying this original pattern and shifting the copy with respect to the original by a difference vector R. In this case of a discrete distribution of the interaction potential V(r) (we also assume that V(r) is real), we can just count how many points of the original and the

translated pattern coincide for this given difference vector R. Only if two or more atoms coincide, will we have a non-vanishing value for P(R) according to (3.26) for this discrete distribution of potentials. In this manner we can construct the Patterson function given in figure 3.4.

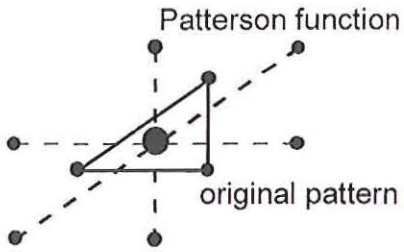

Fig. 3.4: Construction of the Patterson function for a pattern, which consists of three atoms at the corners of a triangle.

It is this function which we would obtain by Fourier transforming the diffraction pattern of a periodic arrangement of our original triangular pattern. One can easily see that in the Patterson function all vectors connecting one atom with any other one in the original pattern can be obtained. In our simple case, the original pattern can be guessed. However, the guess is not unique: we could also choose the mirror image.

3.4 Scattering from a Periodic Lattice in three Dimensions

As an example for the application of formulas (3.23) and (3.24), we will now discuss the scattering of thermal neutrons from a single crystal. More precisely, we will restrict ourselves to the case of a Bravais lattice with one atom at the origin of the unit cell. We further assume that there is only one isotope with scattering length b. The single crystal is finite with N-, M- and P-periods along the basis vectors a, b and c. The scattering potential, which we have to use in (3.23) is a sum over the Fermi-pseudo-potentials of all atoms:

$$V(\underline{r}) = \sum_{n=0}^{N-1} \sum_{m=0}^{M-1} \sum_{p=0}^{P-1} \frac{2\pi\hbar^2}{m_n} \cdot b \cdot \delta(\underline{r} - (n \cdot \underline{a} + m \cdot \underline{b} + p \cdot \underline{c})) \qquad (3.27)$$

The scattering amplitude is the Fourier transform of the scattering potential (compare 3.23):

$$A(\underline{Q}) = \sum_{n,m,p} b \int e^{i\underline{Q}\cdot\underline{r}} \delta(\underline{r} - (n\cdot\underline{a} + m\cdot\underline{b} + p\cdot\underline{c}))\,d^3r$$

$$= b \sum_{n=0}^{N-1} e^{in\underline{Q}\cdot\underline{a}} \sum_{m=0}^{M-1} e^{im\underline{Q}\cdot\underline{b}} \sum_{p=0}^{P-1} e^{ip\underline{Q}\cdot\underline{c}}$$

geometrical series (3.28)

Summing up the geometrical series, we obtain the scattered intensity:

$$I(\underline{Q}) \sim |A(\underline{Q})|^2 = |b|^2 \cdot \frac{\sin^2 \frac{1}{2} N\underline{Q}\cdot\underline{a}}{\sin^2 \frac{1}{2}\underline{Q}\cdot\underline{a}} \cdot \frac{\sin^2 \frac{1}{2} M\underline{Q}\cdot\underline{b}}{\sin^2 \frac{1}{2}\underline{Q}\cdot\underline{b}} \cdot \frac{\sin^2 \frac{1}{2} P\underline{Q}\cdot\underline{c}}{\sin^2 \frac{1}{2}\underline{Q}\cdot\underline{c}} \quad (3.29)$$

As expected, the scattered intensity is proportional to the magnitude square of the scattering length b. The dependence on the scattering vector $\underline{Q}$ is given by the so-called *Laue-function*. The latter is plotted along one lattice direction $\underline{a}$ in figure 3.5.

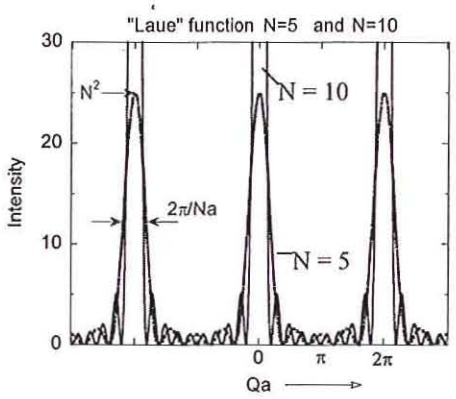

Fig. 3.5: Laue-function along the lattice direction $\underline{a}$ for a lattice with 5 and 10 periods, respectively.

The main maxima are found at the positions $Q = n \cdot \frac{2\pi}{a}$. The maximum intensity scales with the square of the number of periods, the half-width is given approximately by $\frac{2\pi}{N \cdot a}$. The

more periods contribute to coherent scattering, the sharper and higher are the main peaks. Between the main peaks, there are N-2 side maxima. With increasing number of periods N, their intensity becomes rapidly negligible compared to the intensity of the main peaks. The main peaks are of course the well known *Bragg-reflections*, which we obtain when scattering from a crystal lattice. From the position of these Bragg peaks in momentum space, the metric of the unit cell can be deduced (lattice constants a, b, c and unit cell angles α, β, γ). The width of the Bragg peaks is determined by the size of the coherently scattering volume (parameters N, M and P), among other factors. Details will be given in subsequent chapters.

3.5 Coherent and Incoherent Scattering

In the last section, we assumed that we have the same interaction potential for all lattice sites. In the case of x-ray scattering, this can be well realised for a chemically clean sample, for example a Ni single crystal. However, neutrons are scattered from the nuclei and for a given atomic species, there can exist several isotopes with different scattering lengths (five different isotopes for the case of nickel). Moreover, the scattering length depends on the orientation of the nuclear spin relative to the neutron spin. In this section we will discuss the effects of these special properties of the interaction of neutrons and nuclei for the scattering from condensed matter.

Let us assume an arrangement of atoms with scattering lengths b_i on fixed positions $\underline{R}_i$. For this case, the scattering potential writes:

$$V(\underline{r}) = \frac{2\pi\hbar^2}{m_n} \sum_i b_i \delta(\underline{r} - \underline{R}_i) \tag{3.30}$$

The scattering amplitude is obtained from a Fourier transform:

$$A(\underline{Q}) = \sum_i b_i e^{i\underline{Q}\cdot\underline{R}_i} \tag{3.31}$$

When we calculate the scattering cross section, we have to take into account that the different isotopes are distributed randomly over all sites. Also the nuclear spin orientation is random, except for very low temperatures in external magnetic fields. Therefore, we have to average over the random distribution of the scattering length in the sample:

$$\frac{d\sigma}{d\Omega}(\underline{Q}) = \left|A(\underline{Q})\right|^2 = \left\langle \sum_i b_i \; e^{i\underline{Q}\cdot\underline{R}_i} \cdot \sum_j b_j^* e^{-i\underline{Q}\underline{R}_j} \right\rangle$$

average over the random distribution

$$= \sum_i \sum_j \left\langle b_i b_j^* \right\rangle e^{i\underline{Q}(\underline{R}_i - \underline{R}_j)} \qquad (3.32)$$

In calculating the expectation value of the product of the two scattering lengths at sites i and j, we have to take into account that according to the above assumption, the distribution of the scattering length on the different sites is completely uncorrelated. This implies that for $i \neq j$, the expectation value of the product equals to the product of the expectation values. Only for $i = j$, we have a correlation, which gives an additional term describing the mean quadratic deviation from the average:

$$\left\langle b_i b_j \right\rangle = \begin{cases} \langle b \rangle \langle b \rangle = \langle b \rangle^2 & i \neq j \\ \left\langle b^2 \right\rangle = \langle b \rangle^2 + \left\langle (b - \langle b \rangle)^2 \right\rangle & i = j \end{cases}$$

$$\left\langle (b - \langle b \rangle)^2 \right\rangle = \left\langle b^2 - 2b\langle b \rangle + \langle b \rangle^2 \right\rangle = \left\langle b^2 \right\rangle - \langle b \rangle^2 \qquad (3.33)$$

Therefore, we can write the cross section in the following form:

$$\frac{d\sigma}{d\Omega}(\underline{Q}) = \langle b \rangle^2 \left| \sum_i e^{i\underline{Q}\cdot\underline{R}_i} \right|^2 \quad \text{"coherent"}$$
$$+ N\left\langle (b - \langle b \rangle)^2 \right\rangle \quad \text{"incoherent"} \qquad (3.34)$$

The scattering cross section is as a sum of two terms. Only the first term contains the phase factors $e^{i\underline{Q}\cdot\underline{R}}$, which result from the coherent superposition of the scattering from pairs of scatterers. This term takes into account interference effects and is therefore named *coherent scattering*. Only the scattering length averaged over the isotope- and nuclear spin- distribution enters this term. The second term in (3.34) does not contain any phase information and is proportional to the number N of atoms (and not to N^2!). This term is not due to the interference of scattering from different atoms. As we can see from (3.33) (line $i = j$), this

term corresponds to the scattering from single atoms, which subsequently superimpose in an incoherent manner (adding intensities, not amplitudes!). This is the reason for the intensity being proportional to the number N of atoms. Therefore the second term is called *incoherent scattering*. Coherent and incoherent scattering are illustrated in figure 3.6.

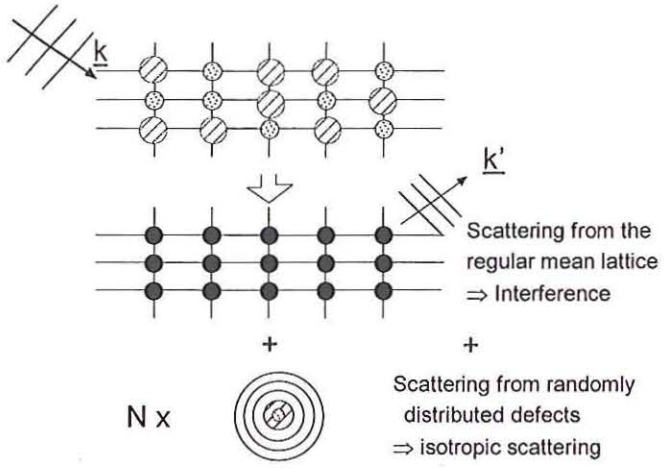

Fig. 3.6: Two-dimensional illustration of the scattering process from a lattice of N atoms of a given chemical species, for which two isotopes (small dotted circles and large hatched circles) exist. The area of the circle represents the scattering cross section of the single isotope. The incident wave (top part of the figure for a special arrangement of the isotopes) is scattered coherently only from the average lattice. This gives rise to Bragg peaks in certain directions. In the coherent scattering only the average scattering length is visible. Besides these interference phenomena, an isotropic background is observed, which is proportional to the number N of atoms and to the mean quadratic deviation from the average scattering length. This incoherent part of the scattering is represented by the lower part of the figure.

The most prominent example for *isotope incoherence* is elementary nickel. The scattering lengths of the nickel isotopes are listed together with their natural abundance in table 3.1 [3]. The differences in the scattering lengths for the various nickel isotopes are enormous. Some isotopes even have negative scattering lengths. This is due to resonant bound states, as compared to the usual potential scattering.

Isotope	Natural Abundance	Nuclear Spin	Scattering Length [fm]
^{58}Ni	68.27 %	0	14.4(1)
^{60}Ni	26.10 %	0	2.8(1)
^{61}Ni	1.13 %	$^3/_2$	7.60(6)
^{62}Ni	3.59 %	0	-8.7(2)
^{64}Ni	0.91 %	0	-0.37(7)
Ni			10.3(1)

Tab. 3.1: The scattering lengths of the nickel isotopes and the resulting scattering length of natural $_{28}Ni$ [3].

Neglecting the less abundant isotopes ^{61}Ni and ^{64}Ni, the average scattering length is calculated as:

$$\langle b \rangle \approx [0.68 \cdot 14.4 + 0.26 \cdot 2.8 + 0.04 \cdot (-8.7)] fm \approx 10.2 fm \tag{3.35}$$

which gives the total coherent cross section of:

$$\Rightarrow \sigma_{coherent} = 4\pi \langle b \rangle^2 \approx 13.1 \, barn \, (exact: 13.3(3) barn) \tag{3.36}$$

The incoherent scattering cross section per nickel atoms is calculated from the mean quadratic deviation:

$$\begin{aligned} \sigma_{incoherent}^{Isotope} = 4\pi \big[& 0.68 \cdot (14.4 - 10.2)^2 + 0.26 \cdot (2.8 - 10.2)^2 \\ & + 0.04 \cdot (-8.7 - 10.2)^2 \big] fm^2 \\ & \approx 5.1 barn \, (exact: 5.2(4) barn) \end{aligned} \tag{3.37}$$

Values in parentheses are the exact values taking into account the isotopes ^{61}Ni and ^{64}Ni and the nuclear spin incoherent scattering (see below). From (3.36) and (3.37), we learn that the incoherent scattering cross section in nickel amounts to more than one third of the coherent scattering cross section.

The most prominent example for *nuclear spin incoherent scattering* is elementary hydrogen. The nucleus of the hydrogen atom, the proton, has the nuclear spin I = ½. The total nuclear spin of the system H + n can therefore adopt two values: J = 0 and J = 1. Each state has its own scattering length: b_- for the singlett state (J = 0) and b_+ for the triplett state (J = 1) - compare table 3.2.

Total Spin	Scattering Length	Abundance
J = 0	$b_- = -47.5$ fm	$\frac{1}{4}$
J = 1	$b_+ = 10.85$ fm	$\frac{3}{4}$
$\langle b \rangle = -3.739(1)$ fm		

Tab. 3.2: Scattering lengths for hydrogen [3].

As in the case of isotope incoherence, the average scattering length can be calculated:

$$\langle b \rangle = \left[\frac{1}{4}(-47.5) + \frac{3}{4}\cdot(10.85)\right] fm = -3.74\, fm \qquad (3.38)$$

This corresponds to a coherent scattering cross section of about ≈ 1.76 barn [3]:

$$\Rightarrow \sigma_{coherent} = 4\pi\langle b \rangle^2 = 1.7568(10)\, barn \qquad (3.39)$$

The nuclear spin incoherent part is again given by the mean quadratic deviation from the average:

$$\sigma_{incoherent}^{nuclear\ spin} = 4\pi\left[\frac{1}{4}(-47.5+3.74)^2 + \frac{3}{4}(10.85+3.74)^2\right] fm^2 = 80.2\, barn$$

$$(exact:\ 80.26(6)\, barn) \qquad (3.40)$$

Comparing (3.39) and (3.40), it is immediately clear that hydrogen scatters mainly incoherently. As a result, we observe a large background for all samples containing hydrogen.

We note immediately that we should avoid all organic glue for fixing our samples to a sample stick. Finally, we note that deuterium with nuclear spin I = 1 has a much more favourable ratio between coherent and incoherent scattering:

$$\sigma^{D}_{coh.} = 5.592(7) barn; \quad \sigma^{D}_{inc.} = 2.05(3) barn \tag{3.41}$$

The coherent scattering lengths of hydrogen (-3.74 fm) and deuterium (6.67 fm) are significantly different. This can be used for contrast variation by isotope substitution in all samples containing hydrogen, i. e. in biological samples or soft condensed matter samples, see corresponding chapters.

A further important element, which shows strong nuclear incoherent scattering, is vanadium. Natural vanadium consists to 99,75 % of the isotope ^{51}V with nuclear spin 7/2. By chance, the ratio between the scattering lengths b_+ and b_- of this isotope are approximately equal to the reciprocal ratio of the abundances. Therefore, the coherent scattering cross section is negligible and the incoherent cross section dominates [3]:

$$\sigma^{V}_{coh} = 0.01838(12)\, barn; \quad \sigma^{V}_{incoh} = 5.08(6)\, barn \tag{3.42}$$

For this reason, Bragg scattering of vanadium is difficult to observe above the large incoherent background. However, since incoherent scattering is isotropic, the scattering from vanadium can be used to calibrate multi-detector arrangements.

Here, we will not discuss scattering lengths for further elements and refer to the values tabulated in [3].

3.6 Magnetic Neutron Scattering

So far, we have only discussed the scattering of neutrons by the atomic nuclei. Apart from nuclear scattering, the next important process is the scattering of neutrons by the magnetic moments of unpaired electrons. This so-called magnetic neutron scattering comes about by the magnetic dipole-dipole interaction between the magnetic dipole moment of the neutron and the magnetic field of the unpaired electrons, which has spin and orbital angular momentum contributions (see figure 3.7).

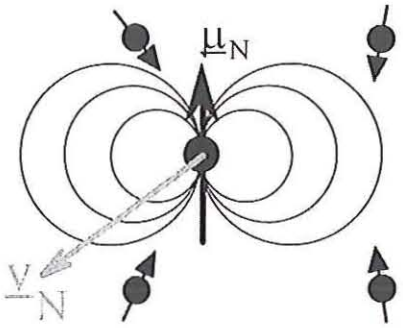

Fig. 3.7: Schematic illustration of the interaction process of a neutron with the atomic magnetic moments via the dipole interaction.

This magnetic neutron scattering allows us to study the magnetic properties of a sample on an atomic level, i. e. with atomic spatial- and atomic energy- resolution. A typical problem studied is the determination of a magnetic structure, i. e. the magnitudes and arrangements of the magnetic moments within the sample. Besides the well-known and simple ferromagnets, for which all moments are parallel, there exists a whole zoo of complicated ferri- and antiferromagnetic structures, such as helical structures, spin density waves, etc. (compare figure 3.8).

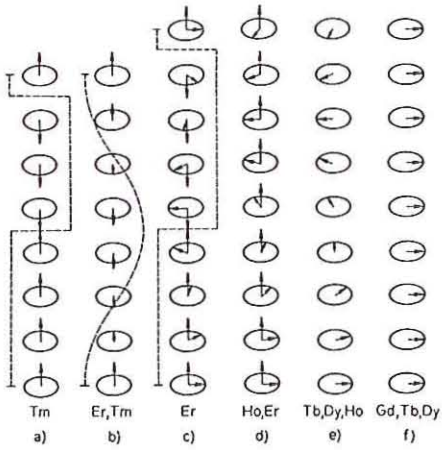

Fig. 3.8: Schematic illustration of the magnetic structures of the hexagonal rare earth metals. Within the hexagonal basal plane, all moments are parallel. The figure shows the sequence of moments in successive planes along the hexagonal c-axis. Besides simple ferromagnetic phases (f), helical (e), conical (d) and c-axis-modulated structures (b) etc. are observed.

These magnetic structures can be understood on the basis of magnetic interactions, which again can be determined by neutron scattering from measurements of the magnetic excitation spectra. Magnetic structures are only stable in a certain range of theromdynamic parameters, such as temperature, pressure or magnetic field. As we approach the limits of a stability region, magnetic phase transitions into a different magnetic phase occur. An example is the transition from a long-range magnetic order at low temperatures to a paramagnetic high temperature phase. By means of neutron scattering, the spectra of magnetisation fluctuations close to a magnetic phase transition can be determined. Such measurements provide the experimental foundation of the famous renormalisation group theory of phase transitions.

In what follows, we will give an introduction into the formalism of magnetic neutron scattering. Again, we will restrict ourselves to the case of elastic magnetic scattering. Examples for magnetic scattering will we given in a later chapter.

To derive the magnetic scattering cross section of thermal neutrons, we consider the situation shown in figure 3.9: a neutron with the nuclear moment μ_N is at position $\underline{R}$ with respect to an electron with spin $\underline{S}$, moving with a velocity $\underline{v}_e$.

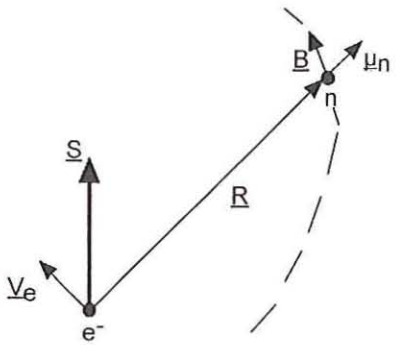

Fig. 3.9: Geometry for the derivation of the interaction between neutron and electron.

Due to its magnetic dipole moment, the neutron interacts with the magnetic field of the electron according to:

$$V_m = -\underline{\mu}_n \cdot \underline{B} \qquad (3.43)$$

Here, the magnetic moment of the neutron is given by:

$$\underline{\mu}_n = -\gamma_n \mu_N \cdot \underline{\sigma} \tag{3.44}$$

$\underline{\sigma}$ denotes the spin operator, μ_N the nuclear magneton and $\gamma_N = -1.913$ the gyromagnetic factor of the neutron. The magnetic field $\underline{B}$ of an electron is due to a spin- and orbital- part $\underline{B} = \underline{B}_S + \underline{B}_L$. The dipole field of the spin moment is given by:

$$\underline{B}_S = \underline{\nabla} \times \left(\frac{\underline{\mu}_e x \underline{R}}{R^3} \right) \quad ; \quad \underline{\mu}_e = -2\mu_B \cdot \underline{S} \tag{3.45}$$

The field due to the movement of the electron is given according to Biot-Savart:

$$\underline{B}_L = \frac{-e}{c} \frac{\underline{v}_e \times \underline{R}}{R^3} \tag{3.46}$$

The magnetic scattering cross section for a process, where the neutron changes its wave vector from $\underline{k}$ to $\underline{k}'$ and the projection of its spin moment to a quantisation axis z from σ_z to σ_z' can be expressed within the first Born approximation:

$$\frac{d\sigma}{d\Omega} = \left(\frac{m_n}{2\pi\hbar^2} \right)^2 \left| \langle \underline{k}' \sigma_z' | \mathrm{V}_m | \underline{k} \sigma_z \rangle \right|^2 \tag{3.47}$$

As mentioned, we only consider the single differential cross section for elastic scattering. Introducing the interaction potential from (3.43) to (3.46) in (3.47), we obtain after a lot of algebra [4, 5]:

$$\frac{d\sigma}{d\Omega} = (\gamma_n r_0)^2 \left| -\frac{1}{2\mu_B} \langle \sigma_z' | \underline{\sigma} \cdot \underline{M}_\perp (\underline{Q}) | \sigma_z \rangle \right|^2 \tag{3.48}$$

The pre-factor $\gamma_n r_0$ has the value $\gamma_n r_0 = 0.539 \cdot 10^{-12}$ cm = 5.39 fm. Here, $\underline{M}_\perp(\underline{Q})$ denotes the component of the Fourier transform of the sample magnetisation, which is perpendicular to the scattering vector $\underline{Q}$:

$$\underline{M}_{\perp}(\underline{Q}) = \hat{\underline{Q}} \times \underline{M}(\underline{Q}) \times \hat{\underline{Q}} \tag{3.49}$$

$$\underline{M}(\underline{Q}) = \int \underline{M}(\underline{r}) e^{i\underline{Q}\cdot\underline{r}} d^3 r \tag{3.50}$$

The total magnetisation is given as a sum of the spin- and orbital-angular- momentum part according to:

$$\underline{M}(\underline{r}) = \underline{M}_S(\underline{r}) + \underline{M}_L(\underline{r})$$
$$\underline{M}_S(\underline{r}) = -2\mu_B \cdot \underline{S}(\underline{r}) = -2\mu_B \sum_i \delta(\underline{r} - \underline{r}_i)\underline{S}_i \tag{3.51}$$

(3.48) tells us that with magnetic neutron scattering, we are able to determine the magnetisation $\underline{M}(\underline{r})$ in microscopic atomic spatial co-ordinates $\underline{r}$. This gives a lot more information as a simple macroscopic measurement, where we obtain the ensemble average of the magnetisation over the entire sample. We also see from (3.48) that the orientation of the nuclear spin momentum of the neutron (represented by σ_z) plays an important role in magnetic scattering. This is not surprising, since magnetism is a vector property of the sample and obviously there should be an interaction with the vector property of the neutron, its nuclear magnetic moment. Therefore, the analysis of the change of the direction of the neutron nuclear moment in the scattering process should give us valuable additional information as compared to a determination of the change of energy and momentum direction of the neutron alone. These so-called polarisation analysis experiments are discussed in the following chapter. For our present purposes, we will completely neglect these dependencies. Finally, to obtain an idea of the size of magnetic scattering relative to nuclear scattering, we can replace the matrix element in (3.48) for a spin ½ particle by the value 1 μ_B. This gives us an "equivalent" scattering length for magnetic scattering of 2.696 fm for a spin ½ particle. This value corresponds quite well to the scattering length of cobalt, which means that magnetic scattering is comparable in magnitude to nuclear scattering.

In contrast to nuclear scattering, we obtain for magnetic scattering a directional term: neutrons only "see" the component of the magnetisation perpendicular to the scattering vector (see figure 3.10).

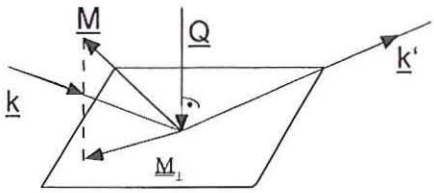

Fig. 3.10: For magnetic neutron scattering, only the component $\underline{M}_\perp$ of the magnetisation perpendicular to the scattering vector $\underline{Q}$ is of relevance.

That only $\underline{M}_\perp$ gives rise to magnetic neutron scattering, can be understood from the notion that neutrons are scattered from the dipolar field of the electrons. This is depicted for two different geometries in figure 3.11. For the case that the magnetisation is parallel to the scattering vector, the planes for equal phase factor cut though the dipolar field in such a way that due to symmetry reasons, the field averaged over these planes vanishes. This is no longer the case, if the magnetisation is perpendicular to the scattering vector. This special directional dependence allows it to determine the orientation of magnetic moments relative to the lattice.

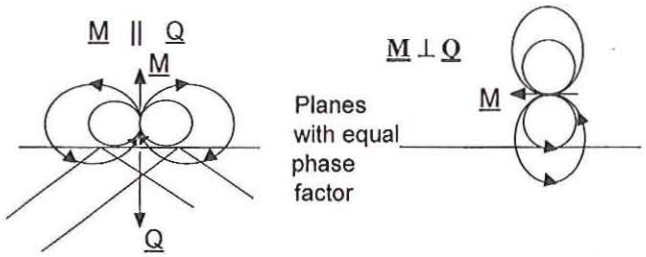

Fig. 3.11: Illustration of the directional dependence for the scattering from a dipolar field: in the case where $\underline{M}$ || $\underline{Q}$ the dipolar field averaged over planes with equal phase factors is zero, so that no magnetic scattering appears.

A second speciality of magnetic scattering as compared to nuclear scattering is the existence of the so-called *form factor*. The form factor describes the fact that the scattering amplitude drops with increasing momentum transfer. This occurs because the object, from which we scatter, namely the electron cloud of an atom, has a size comparable to the wave length of thermal neutrons. Since the distribution of the magnetic field for spin and orbital angular momentum is completely different (compare figure 3.12 for the case of a classical Bohr orbit), different Q-dependencies of the corresponding form factors result (compare figure 3.13).

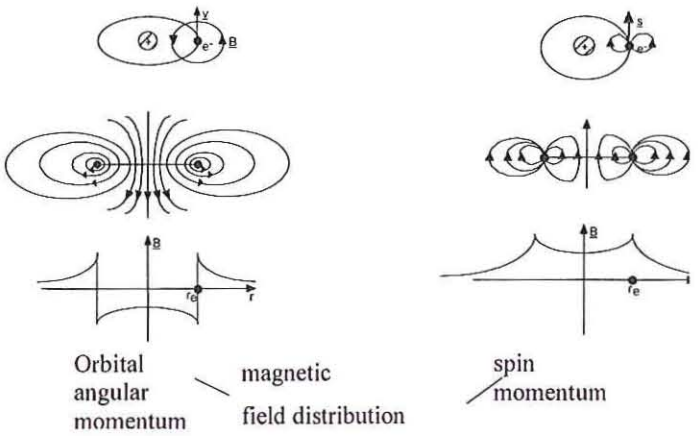

Fig. 3.12: Schematic illustration of the magnetic field distribution due to spin - (S) and orbital- (L) angular momentum in the case of a Bohr orbit. The magnetic field due to the spin moment is much more spread out than the one due to the orbital angular momentum.

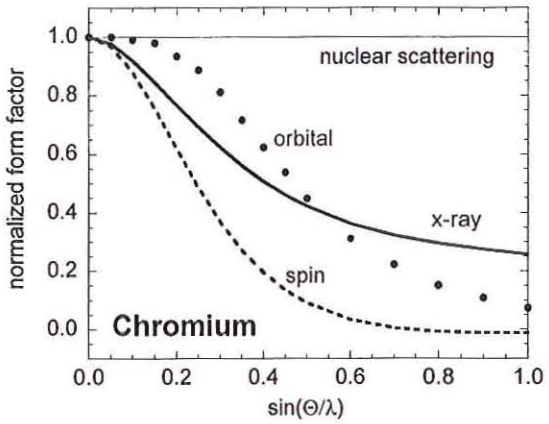

Fig. 3.12: Form-factor of Cr [7, 8]. Due to the different distribution of the magnetic field for S and L according to figure 3.11, a more rapid decrease of the scattering amplitude as a function of momentum transfer results for the spin momentum. For the x-ray form factor, the inner electrons play an important role, too. Therefore, the x-ray form factor drops slower as compared to the magnetic form factor. Finally, on the Å length scale of the thermal neutron wave length, the nucleus is point-like. Therefore, nuclear scattering is independent of the momentum transfer.

Since the scattering amplitude is proportional to a Fourier transform of the scattering power density in direct space, the scattering amplitude decreases faster with momentum transfer if the scattering occurs from a larger object in direct space. Since the unpaired magnetic electrons are located in the outermost electronic shells, the magnetic form factor drops faster than the x-ray form factor. Compared to the natural length scale of the neutron wave length, the nucleus is point-like, which results in a scattering amplitude being independent of momentum transfer. Finally, we want to mention that the magnetic form factor can in general be anisotropic, if the magnetisation density distribution is anisotropic.

How the form factor comes about is most easily understood in the simple case of pure spin scattering, i. e. for atoms with spherical symmetric (L = 0) ground state, such as Mn^{2+} or Fe^{3+}. Moreover, the derivation is simplified for ionic crystals, where the electrons are located around an atom. In figure 3.13 we define the relevant quantities for a derivation.

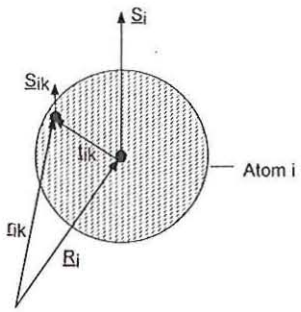

Fig. 3.13: Definition of the relevant quantities for a derivation of the spin-only form factor.

We denote the spin operators of the electrons of atom i with $\underline{s}_{ik}$. The spatial co-ordinates of the electron number k in atom i are $\underline{r}_{ik} = \underline{R}_i + \underline{t}_{ik}$, where $\underline{R}_i$ denotes the position vector to the nucleus of atom i. Now we proceed to separate the intra-atomic quantities. We can write the operator for the magnetisation density as:

$$\underline{M}_S(\underline{r}) = -2\mu_B \sum_{ik} \delta(\underline{r} - \underline{r}_{ik}) \cdot \underline{s}_{ik} \qquad (3.52)$$

The Fourier transform of this magnetisation density is calculated to:

$$\underline{M}(\underline{Q}) = \int \underline{M}_S(\underline{r}) e^{i\underline{Q}\cdot\underline{r}} d^3r = \sum_{ik} e^{i\underline{Q}\cdot\underline{r}_i} \underline{s}_{ik} = \sum_i e^{i\underline{Q}\cdot\underline{R}_i} \sum_k e^{i\underline{Q}\cdot\underline{t}_{ik}} \cdot \underline{s}_{ik} \quad (3.53)$$

To calculate the scattering cross section, we now have to determine the expectation value of this operator for the quantum mechanical state of the sample averaged over the thermodynamic ensemble. This leads to

$$\underline{M}(\underline{Q}) = -2\mu_B \cdot f_m(\underline{Q}) \cdot \sum e^{i\underline{Q}\cdot\underline{R}_i} \cdot \underline{S}_i \quad (3.54)$$

The single differential cross section for elastic scattering is thus given by:

$$\frac{d\sigma}{d\Omega} = (\gamma_n r_0)^2 \left| f_m(\underline{Q}) \sum_i S_{i\perp} e^{i\underline{Q}\underline{R}_i} \right|^2 \quad (3.55)$$

Here, $f_m(\underline{Q})$ denotes the form factor, which is connected with the spin density of the atom via a Fourier transform:

$$f_m(\underline{Q}) = \int_{Atom} \rho_s(\underline{r}) e^{i\underline{Q}\cdot\underline{r}} d^3r \quad (3.56)$$

With the form (3.55), we have expressed the cross section in simple atomic quantities, such as the expectation values of the spin moment at the various atoms. The distribution of the spin density within an atom is reflected in the magnetic form factor (3.56).

For ions with spin and orbital angular momentum, the cross section takes a significantly more complicated form [4, 5]. Under the assumption that spin- and orbital- angular momentum of each atom couple to the total angular momentum $\underline{J}_i$ (L/S-coupling) and for rather small momentum transfers (the reciprocal magnitude of the scattering vector has to be small compared to the size of the electron orbits), we can give a simple expression for this cross section in the so-called *dipole approximation*:

$$\frac{d\sigma}{d\Omega} = (\gamma_n r_o)^2 \cdot \left| \frac{g_J}{2} f_m(Q) \sum_i J_{i\perp} e^{i\underline{Q}\cdot\underline{R}_i} \right|^2 \quad (3.57)$$

Here the magnetic form factor writes:

$$f_m(Q) = \langle j_o(Q) \rangle + C_2 \langle j_2(Q) \rangle \tag{3.58}$$

g_J denotes the Lande g-factor, $C_2 = \frac{2}{g_J} - 1$ and

$$\langle j_l(Q) \rangle = 4\pi \int_0^\infty j_l(Qr) R^2(r) r^2 dr \tag{3.59}$$

are the spherical transforms of the radial density distributions R(r) with the spherical Bessel functions $j_l(Qr)$. For isolated atoms, the radial part R(r) has been determined by Hartree-Fock-calculations and the functions $\langle j_0(Q) \rangle$ and $\langle j_2(Q) \rangle$ in (3.58) have been tabulated [6].

After having introduced the principles of magnetic scattering, we will discuss applications in chapter 16.

References

[1] J. M. Cowley "Diffraction Physics"
North-Holland, Amsterdam 1990

[2] B. W. Batterman, H. Cole "Dynamical Diffraction of X Rays by Perfect Crystals", Reviews of Modern Physics 36, 3, 681 - 717 (1964)

[3] V. F. Sears "Neutron Scattering Length and Cross Sections", Neutron News 3 (1992), 26 - 37

[4] G. L. Squires "Introduction to the theory of thermal neutron scattering" Cambridge University Press, Cambridge (1978)

[5] S. W. Lovesey "Theory of neutron scattering from condensed matter" Volume 2: Polarisation effects and magnetic scattering, Clarendon Press, Oxford (1987)

[6] A. J. Freeman & R. E. Watson, Acta Cryst. 14 (1961), 231

[7] J. Strempfer, Th. Brückel et al Eur. Phys. J. B14 (2000), 63

[8] J. Strempfer, Th. Brückel et al Physica B 267-268 (1999), 56

4. Polarization analysis

W. Schweika

4.1 Introduction

Most typical neutron experiments are concerned only with the intensities related to a specific change in momentum and energy of the neutron in a scattering process yielding information about the structure and dynamics of the considered system of interest. However, since the neutron has a spin it interacts with the magnetic moment of the electron shells, and the scattering amplitude depends also on the nuclear spins of a sample. There are cases where one is able to distinguish magnetic from nuclear scattering, either from the different form factor dependence or from a temperature variation across a magnetic phase transition. Here we shall discuss the technique of using polarized neutrons and the analysis of their final polarization after the scattering process. It is a powerful method for distinguishing the various possible scattering scattering contributions, – *i.e.* magnetic, nuclear coherent, and nuclear spin-incoherent scattering –, and to separate them from each other by *experimental means without further assumptions.* Its application to neutron spin echo techniques will be discussed in chapter 11.

The theoretical foundation for polarized neutron studies has essentially been set by the early works of Halpern and Johnson[1], Maleyev[2], and Blume[3]. A good introduction is given in the classical work of Moon *et al* [7], see also [4, 5]. This lecture will not treat the full complexity of magnetic scattering (see [2, 3]). Emphasis will be given rather to basic ideas following Refs. Schärpf [6] and Moon *et al* [7].

4.2 The motion of the neutron in magnetic fields and experimental devices

The essential characteristics of the motion of a neutron in a magnetic field is the precession mode, which for simplicity can be considered in a classical treatment[6]. In fact, even the quantum mechanical treatment, which introduces Pauli spin matrices into the Schrödinger equation, is effectively a classical treatment considering the origin of these matrices. They result from the problem of mapping three dimensions onto two by intro-

ducing a complex component and were treated by Cayley and Klein (1897) [8] describing the classical problem of a spinning top.

Classical mechanics shows that a torque exerted on a magnetic moment $\underline{\mu}$ by a magnetic field $\underline{\mathrm{H}}$ inclined at an angle θ relative to the magnetic moment causes the magnetic moment of the neutron to precess about the direction of the field with the *Larmor* frequency ω_L. The precession frequency is independent of the angle θ. Different to the motion of a spinning top in a gravity field the neutron's motion shows no nutation, its angular momentum $\underline{L} = \hbar\underline{S}$ and its energy is a constant. $S\ (= \frac{1}{2})$ denotes the spin quantum number of the neutron and $\hbar$ is Planck's constant divided by 2π. The relation between angular momentum $\underline{L}$ and magnetic moment $\underline{\mu}$ defines the *gyromagnetic ratio* γ

$$\underline{\mu} = \gamma\,\underline{L}\,. \tag{4.1}$$

An applied magnetic field will tend to align this magnetic moment and exerts a torque. No force is exerted by a homogeneous field, so that the resulting equation of motion simply says that the change of $\underline{L}$ in time is normal to $\underline{L}$ and $\underline{\mathrm{H}}$, *i.e.* a precession:

$$\dot{\underline{L}} = -\gamma\,\underline{L} \times \underline{\mathrm{H}} = \underline{L} \times \underline{\omega}_L \tag{4.2}$$

$$\text{with} \quad -\gamma\underline{\mathrm{H}} = \underline{\omega}_L \text{and} \quad \gamma/2\pi = -2916.4\mathrm{Hz/Oe}\,.$$

A magnetic *guide field* defines a quantization axis and can be used to maintain the direction the spin and thus the polarization of the neutron beam, see Fig. 4.1. The neutron moments will align either parallel or anti-parallel. Guide fields are typically weak so that the sample magnetization is not significantly influenced, but sufficiently stronger than for instance the magnetic field of the earth or any other stray magnetic fields from the surrounding. Such a guide field may vary is space and two important limits are of interest (see Fig. 4.2):

- *slow field change*: this so-called adiabatic case means that $\underline{\mathrm{H}}$ slowly changes its direction with a frequency that is small compared to the Larmor frequency, $\omega \ll \omega_L$, such that a neutron moving with a velocity $\underline{v}_N$ keeps its precession mode around the spatially varying $\underline{\mathrm{H}}$. This can be achieved by sufficiently long path for the variation of the field or by a sufficiently strong the field H ($\propto \omega_L$).

- *sudden field change*: If the field direction changes suddenly, the polarization of the neutron cannot follow. Two opposite guide fields can be separated by a current

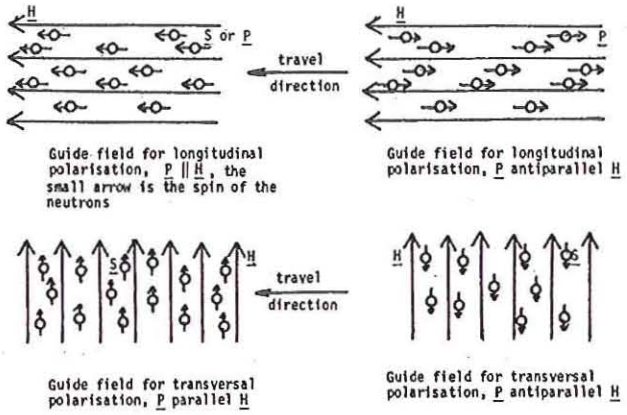

Figure 4.1: Neutrons in a guide field H with spins parallel or anti-parallel[6].

sheet, for example, and polarized neutrons parallel to the first guide field will be kept in an anti-parallel orientation to the second field when passing the sheet. This case $\omega \gg \omega_L$ is also used in coils operating as spin flippers.

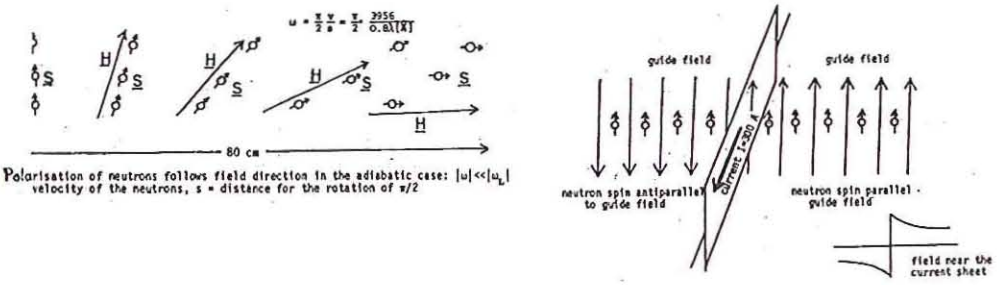

Figure 4.2: Left: $\omega \ll \omega_L$ (adiabatic case), the orientation of the neutron spin follows the field direction; right: $\omega \gg \omega_L$, the neutron spin keeps its orientation for sudden field changes.[6]

In neutron scattering experiments with polarized neutrons, the principle of slow field changes is used, for instance, to align the polarization along a particular direction at the sample position. As will be seen in the examples below, the polarizations perpendicular and parallel to the scattering vector and the magnetization of the sample are of particular interest. Usually, we assume that the field at the sample position is sufficiently weak so that the magnetization of the samples remains undisturbed. Using three (orthogonal)

pairs of coils the polarization can be turned arbitrarily into any direction at the sample position to probe the orientation the magnetization of a sample. While turning the neutron polarization at the sample position by an additional field $\underline{H}$ and thus keeping the neutrons moments in guide fields one can only distinguish scattering processes in which the spin direction is preserved (non-spin flip) or reversed (spin-flip) for a given direction. In general, there may be an arbitrary angle of rotation of the neutron polarization, and it can be measured only if the sample is in a field-free space. Super-conducting sheets are ideal for shielding the sample environment from external magnetic fields (sudden field changes). Such an sample environment with zero-field is realized in a device called *cryopad* ([9] F. Tasset, ILL). It allows one to exploit all possible scattering channels with independent initial and final polarizations along xyz in spin-flip or non-spin flip mode (which takes $3 \times 3 \times 2 = 18$ measurements).

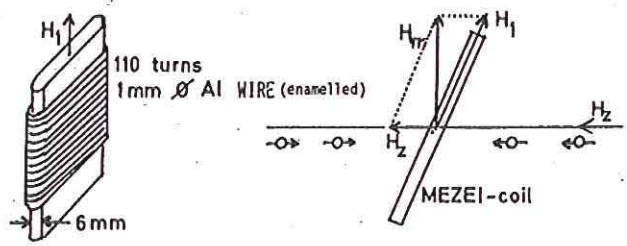

Figure 4.3: Neutron π-spin flipper (Mezei-flipper). The neutrons perform half of a Larmor-precession inside a long rectangular coil. The field $\underline{H}_\pi$ is perpendicular to spin orientation and to the travel direction of the neutron and has to be adjusted to the speed of the neutrons. In order to compensate the guide field one may either tilt the flipper or use a correction coil[10]. (Fig. from [6].)

An important device for working with polarized neutrons is a *spin flipper*, see Fig. 4.3. One can use the Larmor precession in a coil to turn the neutron spin. The so-called Mezei coil is a long rectangular coil. The field inside ($H = N \cdot I/l$) is perpendicular to the polarization and the travel direction of the neutron. Guide fields outside are necessary to avoid depolarization by the earth field or undefined stray fields, but need to be compensated inside the coil. Monochromatic neutrons passing through the coil they experience a sudden field changes at the wires and perform a precession inside. A rotation of 180 degrees (π-flip) is realized by field H_π determined by $\gamma \mathrm{H}_\pi \cdot d/v = \pi$, which gives

$H_\pi = 67.825\,\mathrm{Oe} \cdot (\mathrm{\AA\,cm})/(\lambda\, d) \approx 20\,\mathrm{Oe}$ for $\lambda = 3.4\,\mathrm{\AA}$ and $d = 1\,\mathrm{cm}$. There are other types of spin flippers using for instance radio-frequency resonators.

By experimental means it is possible to choose the initial polarization of the neutron as either spin-up or spin-down, and the polarization analysis requires also the experimental ability to determine the final polarization of the neutron after the scattering process. In practice, there are three types of polarizing devices:

- a crystal monochromator and Bragg reflection, where the interference of the magnetic and nuclear part of the scattering amplitudes is constructive for one spin state and destructive for the opposite spin state;
- super-mirrors with a magnetic layered structure which shows total reflection for one spin state only;
- filters that produce by absorption or extinction a polarized beam in transmission. ^{3}He is of particular importance. It exhibits high absorption for neutrons having their spins anti-parallel aligned to the spin of the ^{3}He nucleus.

Some polarizers using Bragg reflections, for instance the (200) reflection from $Co_{0.92}Fe_{0.08}$ alloy crystals, exhibit a very high degree of polarization (≈ 0.99 for the whole set-up: initial polarization - spin-flipper - final polarization). However, only a narrow band of wavelengths can be used and also the accepted divergence is small, which could be demanding in terms of scattering intensities. An experimental set-up for polarization analysis using the total reflection of long super-mirrors or shorter benders (a stack of such super-mirrors) perform also reasonably well in terms of polarization (typically ≈ 0.95 or better), and in addition a comparatively wide band in wavelength or energy of cold neutrons is accepted (particularly useful for time-of-flight spectrometers). For thermal neutrons ^{3}He-filters seem to be a very appropriate choice. The device does not interfere with the divergence, which has been set otherwise in the experiment. The beam transmission and degree of polarization can be optimized by varying the gas pressure and can be matched to the spectrum of neutron energies. The most efficient performance is, however, a compromise between intensity and a modest degree of neutron polarization (say about 50%). Of course, this requires to perform corrections due to the finite degree of polarization. However, such corrections can easily be performed and the final result for

the scattering intensities depend just on the accuracy with which ones knows the degree of polarization.

4.3 Polarization and scattering processes

4.3.1 Coherent nuclear scattering

Within the first Born approximation the scattering cross-section is determined by

$$\frac{d\sigma}{d\Omega} = \left(\frac{\mathrm{m_n}}{2\pi\hbar}\right)^2 |\langle \underline{\mathrm{k}}' S_z' | \mathbf{V} | \underline{\mathrm{k}} S_z \rangle|^2 \ . \tag{4.3}$$

First, we calculate the matrix element of the interaction potential $\mathbf{V}$ between the initial and final states for pure nuclear scattering at a nucleus with spin $I = 0$, *i.e.* the scattering amplitude $A(\underline{\mathrm{Q}})$ (see chapter 3). With $b(\underline{\mathrm{Q}}) = \sum_i b_i e^{i\underline{\mathrm{Q}}\cdot\underline{\mathrm{r}}_i}$ the matrix element is

$$A(\underline{\mathrm{Q}}) = \langle S_z' \left| b(\underline{\mathrm{Q}}) \right| S_z \rangle = b(\underline{\mathrm{Q}}) \langle S_z' \mid S_z \rangle = \begin{cases} b(\underline{\mathrm{Q}}) & \left\{ \begin{array}{l} + \to + \\ - \to - \end{array} \right\} NSF \\ 0 & \left\{ \begin{array}{l} + \to - \\ - \to + \end{array} \right\} SF \end{cases} \tag{4.4}$$

It follows that *the nuclear scattering for nuclei with zero spin is purely "non-spin-flip" scattering, i.e.* there are no scattering processes that turn the neutron spin around. In particular this is valid for all isotopic-incoherent scattering and coherent nuclear scattering. Since the coherent scattering amplitude represents the average non-fluctuating part of the total actual scattering amplitude, it is the part that is also independent even of any possibly existing nuclear spin.

4.3.2 Magnetic scattering

The matrix element of the interaction potential for pure magnetic scattering between the states $\underline{\mathrm{k}}$ and $\underline{\mathrm{k}}'$ has already been introduced in the previous chapter 3. The scattering amplitude results to

$$\mathrm{A}(\underline{\mathrm{Q}}) = \langle S_z' | \frac{-\gamma_n r_o}{2\mu_B} \underline{\sigma} \cdot \underline{\mathrm{M}}_\perp(\underline{\mathrm{Q}}) | S_z \rangle = \frac{-\gamma_n r_o}{2\mu_B} \sum_\alpha \langle S_z' | \underline{\sigma}_\alpha | S_z \rangle \, \underline{\mathrm{M}}_{\perp\alpha}(\underline{\mathrm{Q}}) \ . \tag{4.5}$$

Here $\gamma_n = -1.913$ denotes the magnetic dipole moment of the neutron expressed in nuclear magnetons $\mu_N = 5.051 \cdot 10^{-27} J/T$, and $r_0 = \frac{e^2}{m_e c^2}$ is the classical electron radius.

$\underline{\underline{\sigma}}_\alpha$ denotes the Pauli-spin matrices:

$$\underline{\underline{\sigma}}_x = \begin{pmatrix} 0 & 1 \\ 1 & 0 \end{pmatrix}, \underline{\underline{\sigma}}_y = \begin{pmatrix} 0 & -i \\ i & 0 \end{pmatrix}, \underline{\underline{\sigma}}_z = \begin{pmatrix} 1 & 0 \\ 0 & -1 \end{pmatrix}. \tag{4.6}$$

Writing briefly the spin-up and down states as $|+\rangle = \begin{pmatrix} 1 \\ 0 \end{pmatrix}$ and $|-\rangle = \begin{pmatrix} 0 \\ 1 \end{pmatrix}$ respectively, we obtain the following relations:

$$\begin{aligned} \underline{\underline{\sigma}}_x|+\rangle &= \ |-\rangle \ , \ \underline{\underline{\sigma}}_x|-\rangle = \ \ |+\rangle \\ \underline{\underline{\sigma}}_y|+\rangle &= i\,|-\rangle \ , \ \underline{\underline{\sigma}}_y|-\rangle = -i\,|+\rangle \\ \underline{\underline{\sigma}}_z|+\rangle &= \ |+\rangle \ , \ \underline{\underline{\sigma}}_z|-\rangle = \ -|-\rangle \, . \end{aligned} \tag{4.7}$$

Inserting these relations into Eq. (4.5) we obtain the matrix elements (scattering amplitudes) for spin-flip and non-spin flip scattering:

$$A(\underline{Q}) = \frac{-\gamma_n r_o}{2\mu_B} \times \begin{cases} -\underline{M}_{\perp z}(\underline{Q}) \\ +\underline{M}_{\perp z}(\underline{Q}) \\ -(\underline{M}_{\perp x}(\underline{Q}) + i\,\underline{M}_{\perp y}(\underline{Q})) \\ -(\underline{M}_{\perp x}(\underline{Q}) - i\,\underline{M}_{\perp y}(\underline{Q})) \end{cases} \text{for} \begin{cases} + \to + \quad \text{(NSF)} \\ - \to - \quad \text{(NSF)} \\ + \to - \quad \text{(SF)} \\ - \to + \quad \text{(SF)} \end{cases} \tag{4.8}$$

Different to the coherent nuclear scattering now we can also observe "spin-flip" processes that reverse the neutron spin direction. Recall that $\underline{M}_\perp(\underline{Q})$ is the perpendicular component of $\underline{M}$ with respect to the scattering vector $\underline{Q}$, and the neutron polarization has been chosen parallel to an external field $\underline{H}_z$. We obtain two rules for the magnetic scattering:

The "spin-flip" processes are observed for the component $\underline{M}_\perp(\underline{Q})$ that is perpendicular to the neutron polarization. The "non-spin flip" processes are observed for the component of $\underline{M}_\perp(\underline{Q})$ that is parallel to the neutron polarization.

4.3.3 Nuclear spin-dependent scattering

If the neutron is scattered from a nucleus with non-zero spin the compound may form a singulett or triplett state where the neutron spin $\underline{\sigma}$ is anti-parallel or parallel to the nuclear spin $\underline{I}$ with different scattering lengths b_- and b_+ respectively. The case of nuclear spin-dependent scattering can be formally treated in analogy to the magnetic scattering

by introducing the scattering length operator

$$\mathbf{b} = A + B\,\sigma \cdot \mathbf{I} \tag{4.9}$$

$$\text{with } A = \frac{(\mathrm{I}+1)\,b_+ + \mathrm{I}\,b_-}{2\mathrm{I}+1} \text{ and } B = \frac{b_+ - b_-}{2\mathrm{I}+1},$$

where I and σ denote the nuclear spin operator and the neutron spin operator respectively.

The scattering amplitude $\mathrm{A}(\underline{\mathrm{Q}})$ will have the same form as given in Eq. (4.8) only $\underline{\mathrm{M}}_\perp(\underline{\mathrm{Q}})$ has to be replaced by the nuclear spin operator I.

$$\mathrm{A}(\underline{\mathrm{Q}}) = \langle \mathrm{S}'_{(z)} | A + B\,\sigma \cdot \mathrm{I} | \mathrm{S}_{(z)} \rangle = \begin{cases} A + B\,\mathrm{I}_z & \left\{ \begin{matrix} + \to + \\ - \to - \end{matrix} \right\} NSF \\ B\,(\mathrm{I}_x + \mathrm{i}\,\mathrm{I}_y) & \left\{ \begin{matrix} + \to - \\ - \to + \end{matrix} \right\} SF \end{cases} \tag{4.10}$$

While in Eq. (4.5) $\underline{\mathrm{M}}_\perp$ is assumed to represent the thermodynamic expectation value, the thermal average has to be calculated now for the different nuclear spin orientations and for the first matrix element in Eq. (4.10). Except for some unusual cases, we may expect that the orientation of nuclear spins is given by a random distribution, *i.e.* :

$$\langle \mathrm{I}_x \rangle = \langle \mathrm{I}_y \rangle = \langle \mathrm{I}_z \rangle = 0 \tag{4.11}$$

Therefore the non-spin flip matrix elements equal to A, and (as derived before) the coherent nuclear scattering is proportional to the square of b^2_{coh}, identifying $A = \bar{b} = b_{coh}$.

$$\frac{d\sigma}{d\Omega}^{\left(\begin{smallmatrix} + \to + \\ - \to - \end{smallmatrix}, NSF\right)}_{coherent} = \bar{b}^2 \sum_{\underline{\mathrm{r}},\underline{\mathrm{r}}'} \mathrm{e}^{\mathrm{i}\underline{\mathrm{Q}}\cdot(\underline{\mathrm{r}}' - \underline{\mathrm{r}})} \tag{4.12}$$

The non-spin flip matrix elements vanish, however, for the incoherent scattering, which is proportional to $\bar{b^2} - \bar{b}^2$, and we have to consider the thermal average of the squares of the matrix elements. Since

$$\langle \mathrm{I}_x^2 \rangle = \langle \mathrm{I}_y^2 \rangle = \langle \mathrm{I}_z^2 \rangle = \frac{1}{3}\mathrm{I}\langle|\mathrm{I}+1\rangle \tag{4.13}$$

from Eq. (4.10) one obtains the spin-incoherent scattering (per atom):

$$\frac{d\sigma}{d\Omega}^{\left(\begin{smallmatrix} + \to + \\ - \to - \end{smallmatrix}, NSF\right)}_{spin-incoherent} = (\bar{b^2} - \bar{b}^2)^{NSF} = \frac{1}{3}\langle B^2\mathrm{I}(\mathrm{I}+1)\rangle \tag{4.14}$$

$$\frac{d\sigma}{d\Omega}^{\left(\begin{smallmatrix} + \to - \\ - \to + \end{smallmatrix}, SF\right)}_{spin-incoherent} = (\bar{b^2} - \bar{b}^2)^{SF} = \frac{2}{3}\langle B^2\mathrm{I}(\mathrm{I}+1)\rangle \tag{4.15}$$

1/3 of the spin-incoherent part of the nuclear scattering is non-spin flip scattering and 2/3 of it is spin-flip scattering independent of the (direction) of an external field $\underline{H}$.

In analogy to the coherent scattering amplitude b_{coh}, one may define the (spin-) incoherent scattering amplitude $b_{inc} = \sqrt{B^2 I(I+1)}$.

4.3.4 Rules for separation

From the preceding discussion we can summarize some useful rules for separating different scattering contributions. If we may neglect magnetic scattering, the coherent and spin-incoherent scattering is obtained from the spin-flip and non-spin flip scattering:

$$\frac{d\sigma}{d\Omega}_{coherent} = \frac{d\sigma}{d\Omega}^{NSF} - \frac{1}{2}\frac{d\sigma}{d\Omega}^{SF} \tag{4.16}$$

$$\frac{d\sigma}{d\Omega}_{spin-incoherent} = \frac{3}{2}\frac{d\sigma}{d\Omega}^{SF} \tag{4.17}$$

If a part of the scattering is of magnetic origin, a field variation is required (perpendicular and parallel to $\underline{Q}$) to separate the magnetic cross-section:

field/polarization	spin-flip intensities	non-spin flip intensities
$\underline{H} \parallel \underline{Q}$	$\sigma_{mag} + \frac{2}{3}\sigma_{inc} + \sigma_{BG}$	$\sigma_{coh} + 0\sigma_{mag} + \frac{1}{3}\sigma_{inc} + \sigma_{BG}$
$\underline{H} \perp \underline{Q}$	$\frac{1}{2}\sigma_{mag} + \frac{2}{3}\sigma_{inc} + \sigma_{BG}$	$\sigma_{coh} + \frac{1}{2}\sigma_{mag} + \frac{1}{3}\sigma_{inc} + \sigma_{BG}$

where σ_{BG} denotes the background.

Hence, the magnetic cross-section is separated by

$$\frac{d\sigma}{d\Omega}_{mag} = 2\left(\frac{d\sigma}{d\Omega}_{\perp}^{NSF} - \frac{d\sigma}{d\Omega}_{\parallel}^{NSF}\right) = 2\left(\frac{d\sigma}{d\Omega}_{\parallel}^{SF} - \frac{d\sigma}{d\Omega}_{\perp}^{SF}\right) \tag{4.18}$$

and all nuclear scattering contributions and the background cancel in the differences of Eq. (4.18), since they are independent of the magnetic field[11].

For a multi-detector instrument it is possible to fulfill the condition $\underline{P} \perp \underline{Q}$ with $\underline{P} = P_z$ perpendicular to the scattering plane, however, $\underline{P} \parallel \underline{Q}$ cannot be realized simultaneously for all different scattering angles. However, a similar expression has been obtained for *paramagnetic scattering* [12]. Therefore, two measurements are required with the two polarizations P_x and P_y lying in the scattering plane perpendicular to each other. Using $\langle M_x M_x \rangle = \langle M_y M_y \rangle = \langle M_z M_z \rangle$ and $\cos^2\alpha + \sin^2\alpha = 1$, we may substitute (valid for both spin-flip and non-spin flip term)

$$\frac{d\sigma}{d\Omega}_{\parallel} + \frac{d\sigma}{d\Omega}_{\perp} = \frac{d\sigma}{d\Omega}_{x} + \frac{d\sigma}{d\Omega}_{y} \tag{4.19}$$

(trivial, if x lies in direction of $\underline{Q}$). Hence, the paramagnetic scattering is given by [12]:

$$\begin{aligned}\frac{d^2\sigma}{d\Omega d\omega}_{paramagnetic} &= 2\left(\frac{d^2\sigma}{d\Omega d\omega_x}^{SF} + \frac{d^2\sigma}{d\Omega d\omega_y}^{SF} - 2\frac{d^2\sigma}{d\Omega d\omega_z}^{SF}\right) \\ &= -2\left(\frac{d^2\sigma}{d\Omega d\omega_x}^{NSF} + \frac{d^2\sigma}{d\Omega d\omega_y}^{NSF} - 2\frac{d^2\sigma}{d\Omega d\omega_z}^{NSF}\right) ,\end{aligned} \tag{4.20}$$

Furthermore, the coherent scattering and the spin-incoherent scattering can be separated from each other and from paramagnetic scattering by the following useful combinations [12]:

$$\frac{d^2\sigma}{d\Omega d\omega}_{coherent} = \frac{d^2\sigma}{d\Omega d\omega_z}^{NSF} - \frac{1}{2}\frac{d^2\sigma}{d\Omega d\omega}_{paramagnetic} - \frac{1}{3}\frac{d^2\sigma}{d\Omega d\omega}_{spin-incoherent} \tag{4.21}$$

$$\frac{d^2\sigma}{d\Omega d\omega}_{spin-incoherent} = \frac{3}{2}\left(3\frac{d^2\sigma}{d\Omega d\omega_z}^{SF} - \frac{d^2\sigma}{d\Omega d\omega_x}^{SF} - \frac{d^2\sigma}{d\Omega d\omega_y}^{SF}\right) . \tag{4.22}$$

One may note, however, that – different from the separation for (para-)magnetic scattering – the above relations do not compensate for possible background contributions. Furthermore, the above equations hold for ideal experimental conditions for polarization and flipping ratio. In general, depolarizing effects may occur at all experimental devices, and appropriate corrections need to be taken into account. Fig. 4.4 illustrates that the corrections for the ideal case can easily be performed. The example is given for the case of coherent scattering and spin-incoherent scattering. From the flipping ratio of non-spin flip scattering to spin-flip scattering from either a purely coherent scatterer or a purely incoherent scatterer the polarization factor of the experimental set-up can be determined. One should note that multiple scattering may alter the expected ideal final polarization as soon as spin-flip processes are involved. Since from polarization analysis the information on both scattering channels is available, the possible corrections for multiple scattering are more reliable as compared to unpolarized experiments.

Furthermore, one should mention the possible interference of nuclear and magnetic scattering amplitudes; an example will be given below. The interference properties are especially of importance for polarizers. Since coherent nuclear scattering is only observed in non-spin flip scattering, the interference term cancels as well for the spin-flip scattering. For specific cases such as spiral ordering, non-collinear ordering, etc., we refer to the literature [2, 3].

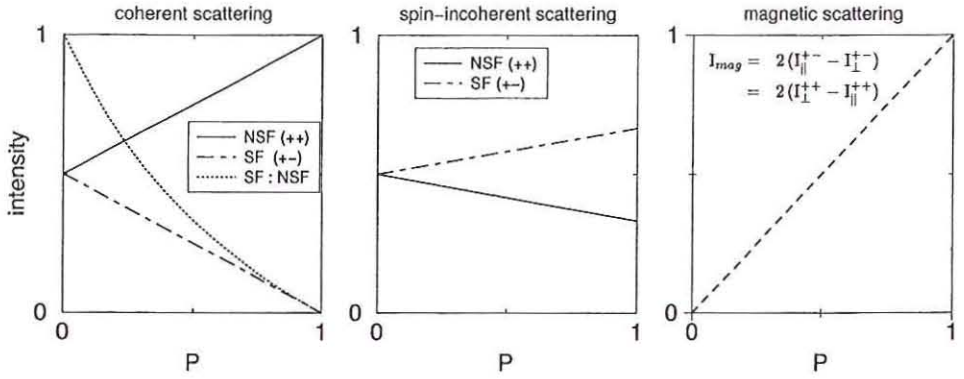

Figure 4.4: Non-ideal experimental conditions for polarization analysis shown for coherent, spin-incoherent and paramagnetic scattering. The polarization factor of the instrument, $P < P_{ideal} = 1$, can be determined from the flipping ratio SF:NSF for a coherent scatterer, and one can extrapolate to the ideal conditions.

4.4 Applications

We now consider examples of experimental studies with polarized neutrons and polarization analysis[7]. A scheme of the experiment is shown in Fig. 4.5.

The first example (Fig. 4.6) shows the isotopic-incoherent scattering from Ni. Since the Ni-isotopes do not produce nuclear spin-dependent scattering it serves as an example for pure non-spin flip scattering. Apparently there are no relevant spin-flip scattering processes.

Actually, this example is not trivial, and it is not so straightforward to reproduce this result. Since at room temperature Ni is a ferromagnet, additional magnetic scattering is to be expected if the magnetization has any component perpendicular to $\underline{Q}$, and a saturating magnetic field has to be applied to avoid any magnetic domain structure. Such inhomogeneities typically cause depolarization effects. A much simpler example for pure non-spin flip scattering would be Bragg scattering which is due to the coherent nuclear scattering amplitude from a non-magnetic material, for instance the Debye-Scherrer rings of aluminum or other materials. In practice, the ratio of NSF- to SF-intensities (*flipping ratio*) for such a measurement is useful to determine the degree of polarization for the experimental set-up.

Fig. 4.7 probably represents the first verification of the spin-flip and non-spin flip scat-

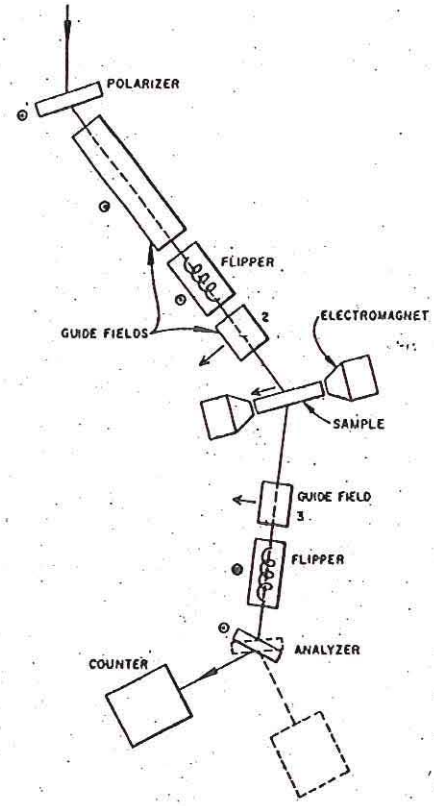

Figure 4.5: The original experimental arrangement of Moon, Riste and Koehler at the Oak Ridge reactor (HFIR): a triple axis instrument with additional equipments for polarization analysis. Co-Fe crystals mounted in the gap of a permanent magnet are used on the first and third axis for the production of the polarized, monochromized beam and for analysis of scattered neutrons in energy and spin. At the second axis with the sample an electromagnet is located with a horizontal rotation axis so that the field is easily changed from vertical to horizontal. Radio-frequency coils with a vertical field are used as flipping devices.[7]

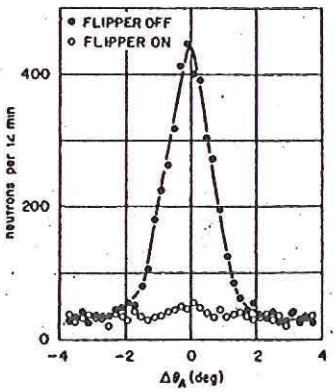

Figure 4.6: Isotopic incoherent scattering from nickel obtained by rocking the analyzer crystal through the elastic position. Essentially all scattering is non-spin flip scattering (++) measured with "flipper off". In flipper on mode the spin-flip data (+−) are taken, In contrast to magnetic scattering the result is independent of the neutron polarization with respect to the scattering vector $\underline{Q}$.[7]

tering from a spin-incoherent scatterer. The example is Vanadium a typical material used for absolute calibrations of neutron measurements. The scattering above the background level shows nearly the ideal intensity ratio 2:1 for spin-flip to non-spin-flip intensities. In particular, hydrogenous materials have large spin incoherent cross sections.

We recall that for a magnetic system the spin-flip and non-spin flip scattering should

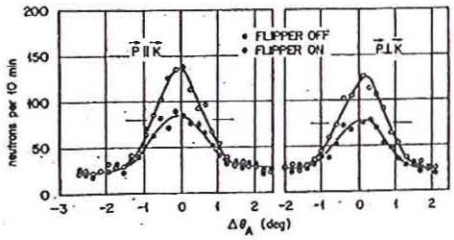

Figure 4.7: Nuclear-spin incoherent scattering from vanadium obtained by rocking the analyzer crystal through the elastic position. The flipper off data are proportional to the (++) cross section and the flipper on data are proportional to the (−) cross section. In contrast to magnetic scattering the result is independent of the neutron polarization with respect to the scattering vector $\underline{Q}$.[7]

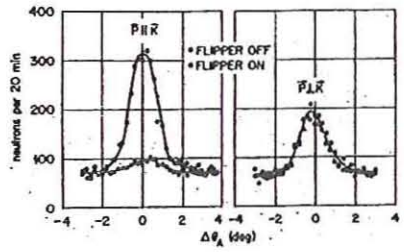

Figure 4.8: Paramagnetic scattering from MnF_2.[7]

depend on the polarization of the neutron with respect to $\underline{Q}$. This field dependence is illustrated in Fig. 4.8 showing the paramagnetic scattering from MnF_2. In general, we expect that the final polarization to vary between 0 and $-\underline{P}_{initial}$. It is obvious that this scattering can be distinguished from spin-incoherent scattering. Indeed, one can easily verify that the difference between the spin-flip scatterings with polarization $\underline{P} \parallel \underline{Q}$ and $\underline{P} \perp \underline{Q}$ is proportional to the (para-)magnetic scattering only, free from any other scattering contributions like coherent nuclear scattering, spin-incoherent scattering and possible background. The same is true for the difference of non-spin flip scatterings with $\underline{P} \parallel \underline{Q}$ and $\underline{P} \perp \underline{Q}$, and Fig. 4.9 shows such a separation of the paramagnetic scattering from MnF_2 powder diffraction data. Measurements with the unpolarized beam show a background intensity decaying with $\underline{Q}$ and various Bragg peaks on top. The Bragg peaks occur only in the non-spin flip channel, which verifies their non-magnetic origin. In the

spin-flip channel we see the paramagnetic scattering with a decay that is characteristic for the form factor of the ion Mn^{2+}.

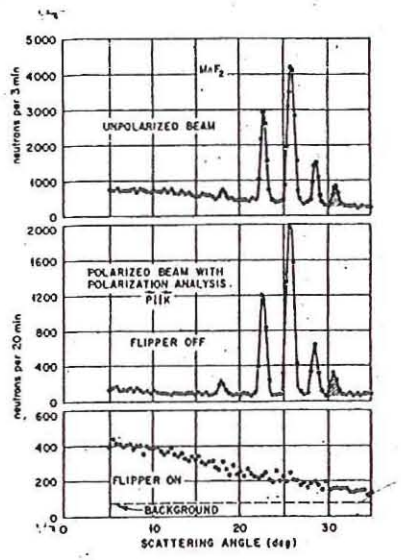

Figure 4.9: Separation of the paramagnetic scattering from MnF_2 in a powder diffraction pattern.[7]

The next example in Fig. 4.10 shows the separation between nuclear and magnetic Bragg peaks for $\alpha - Fe_2O_3$. The magnetic Bragg peaks appear in the spin-flip channel only, while only nuclear Bragg peaks appear in the non-spin-flip channel, if $\underline{P} \parallel \underline{Q}$.

So far we have discussed the nuclear and magnetic scattering separately. However, in general there are possible non-zero matrix elements for both contributions. Therefore interference phenomena may occur but only in the non-spin flip channel. In order to maximize the magnetic signal one chooses the magnetization perpendicular to the scattering plane. In cases where the magnetic scattering amplitude is much weaker than the nuclear amplitude the interference term may be large compared with the pure magnetic intensity. Since the polarization of the scattered beam is not changed, and thus already determined we do not need to perform the polarization analysis in the experiment. A useful application of this effect is the determination of the distribution of magnetization densities. For instance, the form factor of chromium can be measured in the paramagnetic phase, inducing a magnetization by an external magnetic field, as shown in Fig. 4.11. The results for the magnetization density distribution are obtained by Fourier-transformation

and in comparison by a so-called maximum entropy method.

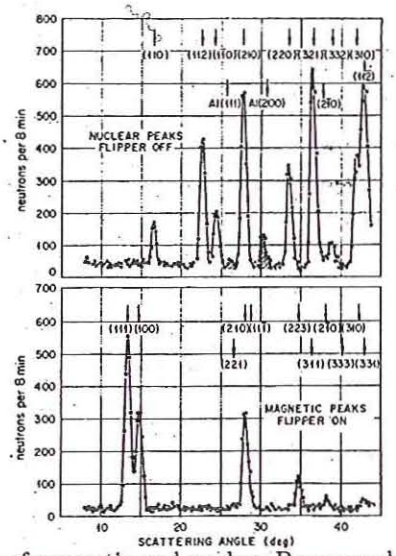

Figure 4.10: Separation of magnetic and nuclear Bragg peaks for powder diffraction data from $\alpha - Fe_2O_3$.[7]

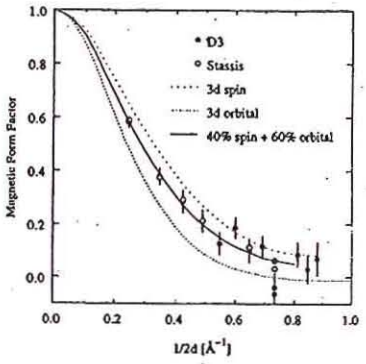

Figure 4.11: Induced magnetic form factor of Cr at a field of 4.6 Tesla. Open and filled circles are experimental data, lines denote theoretical calculations for spin-orbital-, and total magnetic moments [13].

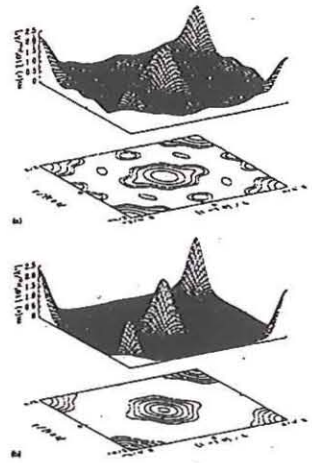

Magnetization density in the (110) plane obtained by Fourier transformation (*top*), and by "Maximum-entropy" reconstruction (*bottom*).

With triple axis instruments one can measure only step-by-step specific dynamic struc-

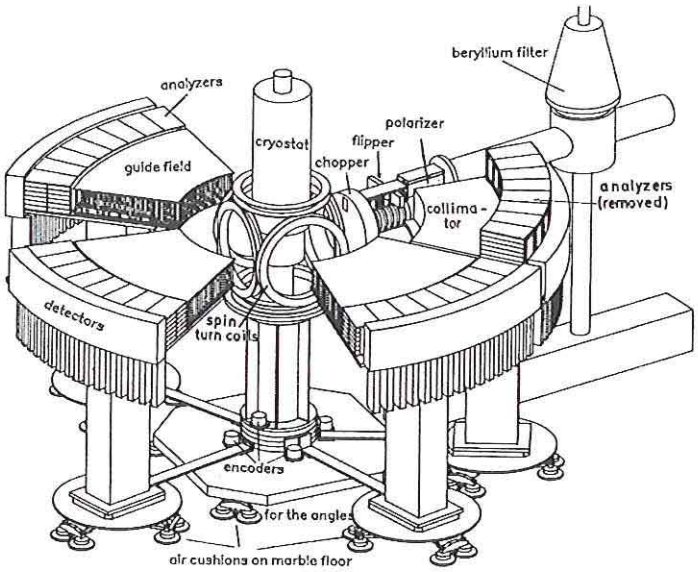

Figure 4.12: The D7 at the ILL, a multi-detector instrument for polarization analysis. On the right hand side one bank is shown in the non-polarizing version with analyzers removed by pneumatic elevators and the collimators inserted instead of the guide fields. With the spin turner coils the polarization of the neutrons can be rotated into the x,y, or z direction.[14]

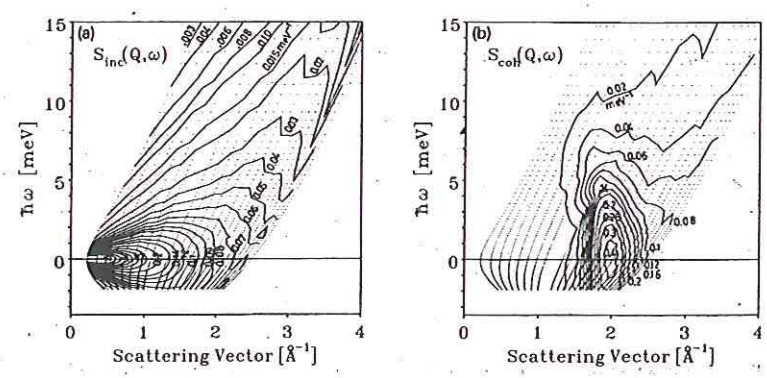

Figure 4.13: Contour plots of (a) the (spin-)incoherent scattering and (b) coherent scattering from liquid sodium at T = 840 K over the plane of energy and momentum transfer as separated by polarization analysis on D7. The incoherent scattering is related to the single particle motion; the coherent scattering is related to the collective motion. [14].

ture factors $S(\underline{Q},\omega)$ of interest. However, multi-detector instruments are more efficient for measuring powders, for time-of-flight spectroscopy, or if larger regions in reciprocal space

need to be measured. The first instrument for such purposes is the D7, see Fig. 4.12, at the high flux reactor at the ILL in Grenoble; 32 detectors are equipped for polarization analysis. The polarizers are benders, curved stacks of polarizing supermirrors, which exhibit good polarization and transmission properties for subthermal neutrons. In order to cover a large solid angle with polarizers in front of the detectors an enormous amount (6000) of magnetic multi-layers had to be produced. A π-flipper (Mezei-type with a Brookhaven correction coil) is used in the incident beam.

The following example [14] of a measurement at D7 demonstrates the capabilities of such an instrument: the dynamic structure factor of liquid sodium, is separated into the coherent and (spin-)incoherent parts. The quasi-elastic incoherent scattering gives information about the single particle motion in space and time, while coherent quasi-elastic scattering is related to collective relaxations of the ensemble. The measurements shown in Fig. 4.13 have been measured on the D7 instrument in time-of-flight spectroscopy, while the presentation is given in the coordinates of energy and momentum transfer. The

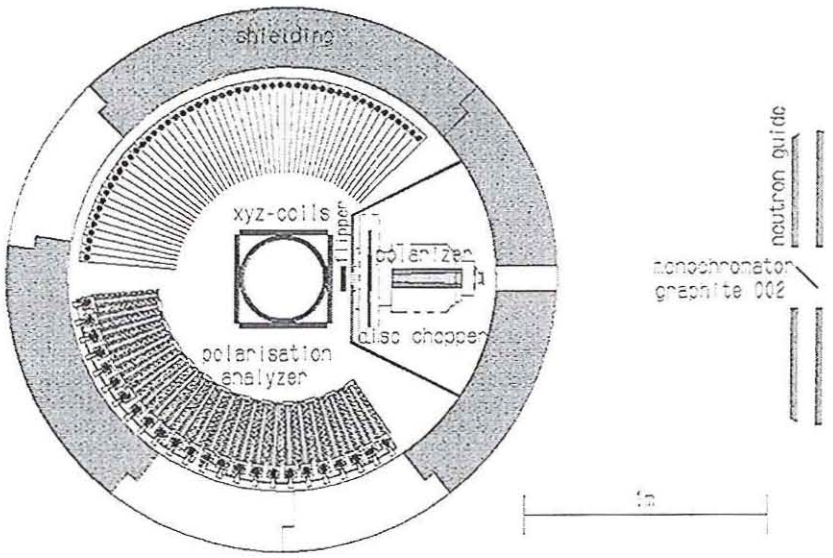

Figure 4.14: The DNS instrument at Jülich equipped for 3-dim polarization analysis. The detector bank to the right of the incoming beam is for unpolarized experiments the one to the left for polarization analysis. A focusing layout has been used for the initial and final polarizers.

instrument DNS (see Fig. 4.14) at the research reactor in Jülich is similar to the D7. Different to the present version of the D7 (there are plans for an upgrade) the polarizers have a geometrical design to use beam focusing on the sample with a substantial gain in intensity. In studies of structural properties of polymer glasses, polarization analysis can be quite useful. Besides separating the coherent and (spin-)incoherent contributions, but the separated incoherent scattering intensities can be used for an intrinsic calibration.

An example is shown in Fig. 4-15. In this experiment[15] one has also used partial isotopic substitution of H by D to mark and to contrast the side-chains and the backbone of different polymers (polyalcylmethacrylates).

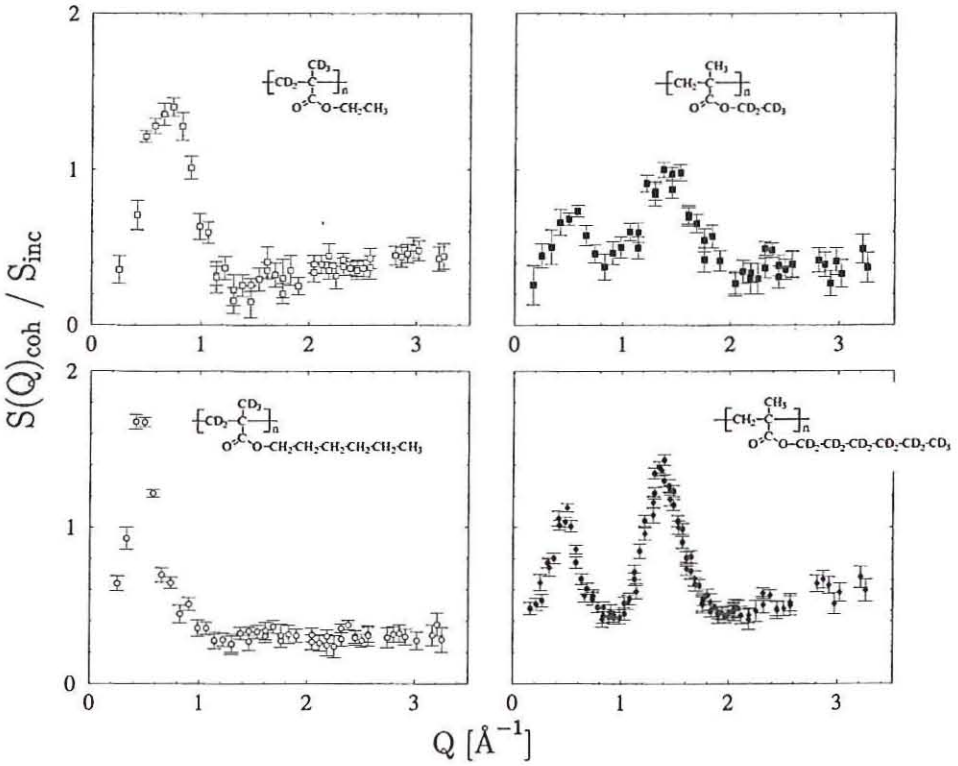

Figure 4.15: Coherent structure factor of a partially deuterated polymer. Note that by separation of the coherent and incoherent scattering one obtains a precise absolute intrinsic calibration. Two measurements are displayed in the figure (*bottom right*) [with $\lambda = 3.3$ Å (diamonds) and $\lambda = 5.3$ Å (circles)] demonstrating the excellent reproducibility of the data. The peak at lower Q is due to inter-chain correlations between different polymer "backbones" and the peak around $Q \approx 1.4 Å^{-1}$ can be related to intra-chain correlations along the polymer, the ones between the side-chains of a polymer.

Appendix

Units:

magnetic field $\underline{H}$:

Ampere/meter (SI) $= 4\pi \times 10^{-3}$ Oersted (cgs)

magnetic induction $\underline{B} = \mu_0 \mu \underline{H}$, $\mu_0 = 1.2566 \times 10^{-6} \mathrm{m\,kg\,C^{-2}}$ (=1 in cgs-units):

Tesla (SI) = kg / ($\sec^2$ Ampere) $= 10^4$ Gauss (cgs)

For cgs-units and vacuum ($\mu = 1$), $\underline{H}$ in Oe corresponds to $\underline{B}$ in Gauss.

Earth magnetic field: ≈ 15 A/m ≈ 0.19 Oe.

References

[1] O. Halpern and M.R. Johnson, Phys. Rev. **55** 898 (1939).

[2] S.V. Maleyev, Zh. Eksperim. i Teor. Fiz. **33**, 129 (1958) [English Translation: Soviet Phys.-JETP **34**, 89 (1958)]; S.V. Maleev, Zh. Eksperim. i Teor. Fiz. **40**, 1224 (1961) [English Translation: Soviet Phys.-JETP **13**, 860 (1961)].

[3] M. Blume, Phys. Rev. **130**, 1670 (1963); Phys. Rev. **133**, A1366 (1964).

[4] G.L. Squires, *Introduction to the theory of thermal neutron scattering*, Cambridge University Press, Cambridge (1978).

[5] S.W. Lovesey *Theory of neutron scattering from condensed matter*, Volume 2: Polarization and magnetic scattering, Clarendon Press, Oxford (1987).

[6] O. Schärpf, in *Neutron Spin Echo*, p. 27-52, Lecture Notes in Physics **128**, Ed. F. Mezei, Springer (1980).

[7] R.M. Moon, T. Riste, W.C. Koehler, Phys. Rev. **181**, 920 (1969).

[8] F. Klein, *The mathematical theory of the top*, Princeton 1897; see also [6] or H. Goldstein, Klassische Mechanik, Akademische Verlagsges. Frankfurt am Main (1974).

[9] F. Tasset, Physica B **241-243**, 177 (1998).

[10] R. Pynn, Rev. Sci. Instrum. **55**, 837 (1984).

[11] G. Shirane, Y.J. Uemura, J.P.Wicksted, Y. Endoh, Y. Ishikawa, Phys. Rev. B **31**, 1227 (1985).

[12] O. Schärpf, H. Capellmann, Phys. Stat. Sol. (a) **135**, 359 (1993).

[13] J. Strempfer, Th. Brückel, G.J. McIntyre, F. Tasset, Th. Zeiske, K. Burger, W. Prandl, Physica B **267-268**, 56 (1999).

[14] O. Schärpf, Physica B **182**, 376 (1992).

[15] G. Meier, U. Pawelzik, W. Schweika, W. Kockelmann, Physica B **276-278**, 369 (2000).

[16] Proceedings of the *Polarized Neutrons for Condensed Matter Investigations 2000* (PNCMI) in Gatchina/St. Petersburg, to appear in Physica B.

5. Correlation Functions Measured By Scattering Experiments

Reiner Zorn, Dieter Richter

In this lecture static and dynamic correlation functions will be introduced. We will start by introducing probability densities, relate those to the scattering cross section and define the pair correlation function. Two examples will be given, one from the physics of liquids and one from polymer physics. The concept of dynamic correlation functions will be explained firstly by the example of correlation spectroscopy. Then the Van Hove correlation function will be introduced which is the basis for the calculation of the double differential scattering cross section. Finally, the concept will be applied to the example of an ideal gas.

5.1 Probability Densities

We start by considering a homogeneous monatomic liquid with N atoms in a volume V. We denote the probability to find a certain atom in a volume element d^3r at $\underline{r}$ by $P(\underline{r})\mathrm{d}^3r$. Because of the homogeneity $P(\underline{r})$ is constant and evidently

$$P(\underline{r}) = \frac{1}{V}\,. \tag{5.1}$$

Then the number density of atoms at $\underline{r}$ is

$$\rho(\underline{r}) = NP(\underline{r}) = \frac{N}{V} \equiv \rho_0\,. \tag{5.2}$$

We call the probability density to find a certain atom at $\underline{r}_1$ and another at $\underline{r}_2$ $P(\underline{r}_1, \underline{r}_2)$. This function fulfills the basic relations

$$P(\underline{r}_1, \underline{r}_2) = P(\underline{r}_2, \underline{r}_1) \text{ and} \tag{5.3}$$

$$\int_V \mathrm{d}^3r_2 P(\underline{r}_1, \underline{r}_2) = P(\underline{r}_1)\,. \tag{5.4}$$

If there is no interaction between the atoms $P(\underline{r}_1, \underline{r}_2)$ factorizes into

$$P(\underline{r}_1, \underline{r}_2) = P(\underline{r}_1)P(\underline{r}_2)\,. \tag{5.5}$$

In real liquids however usually an interaction exists which depends (only) on the distance of the atoms $\underline{r}_{12} = \underline{r}_2 - \underline{r}_1$. We express the deviation from (5.5) by a pair correlation function defined by

$$g(\underline{r}_{12}) \equiv \frac{P(\underline{r}_1, \underline{r}_2)}{P(\underline{r}_1)P(\underline{r}_2)} \,. \tag{5.6}$$

With the pair distribution function $n(\underline{r}_1, \underline{r}_2) = N(N-1)P(\underline{r}_1, \underline{r}_2)$ which expresses the probability density for any pair of atoms to occupy positions $\underline{r}_1$ and $\underline{r}_2$ we obtain

$$g(\underline{r}_{12}) = \frac{n(\underline{r}_1, \underline{r}_2)}{{\rho_0}^2} \tag{5.7}$$

because in the limit of large N we have $N(N-1) \approx N^2$.

The qualitative features of the pair correlation function are shown in figure 5.1. For $r \to 0$ one finds $g(r) = 0$ because two atoms cannot be at the same position. Usually, this is also true for distances $r < r_0$ because the atoms cannot penetrate each other and have a "hard core" radius r_0. For $r \to \infty$ the limit is $g(r) = 1$ because the interactions decay with distance and the $P(\underline{r}_1, \underline{r}_2)$ reverts to its default value 5.5. At intermediate distances $g(r)$ shows a peak because the probability density which is lacking at $r < r_0$ must be compensated. Its location is usually close to the minimum of the interatomic potential, i.e. close to the average next neighbour distance r_{nn}.

Using the pair correlation function one can formulate the differential neutron cross section for a monatomic liquid[1]

$$\left(\frac{\mathrm{d}\sigma}{\mathrm{d}\Omega}\right)_{\mathrm{coh}} = |\bar{b}|^2 \left\langle \sum_{i,j=1}^{N} \exp\left(\mathrm{i}\underline{Q} \cdot \left(\underline{r}_i - \underline{r}_j\right)\right) \right\rangle \,. \tag{5.8}$$

Here $(\mathrm{d}\sigma/\mathrm{d}\Omega)_{\mathrm{coh}}$ denotes the angle dependent coherent scattering cross section and $\bar{b}$ is the average scattering length of the liquid atoms. $\underline{Q}$ is the scattering vector, i.e. the difference between incoming and scattered wave vector of the radiation, $\underline{Q} = \underline{k} - \underline{k}'$. The average in the expression can be evaluated using the pair correlation function (5.7):

$$\left(\frac{\mathrm{d}\sigma}{\mathrm{d}\Omega}\right)_{\mathrm{coh}} = |\bar{b}|^2 \left(1 + \left\langle \sum_{i \neq j}^{N} \exp\left(\mathrm{i}\underline{Q} \cdot \left(\underline{r}_i - \underline{r}_j\right)\right) \right\rangle\right)$$

[1] Exactly speaking, this expression is valid only for mon*isotopic* liquids. Otherwise, there would be an additional incoherent term like the one discussed for the dynamic correlation function in section 5.3. Nevertheless, this term is just a constant and therefore only visible as a flat background in the experiment. The Q dependent (coherent) part of the cross section is still correctly represented by (5.8).

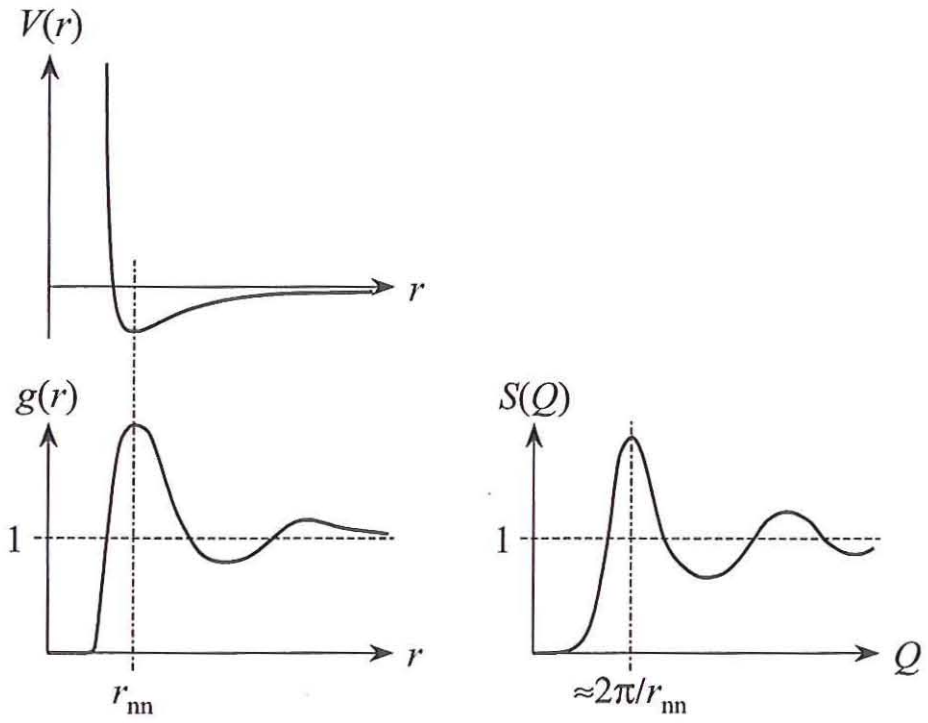

Figure 5.1: Schematic representation of interaction potential $V(r)$, pair correlation function $g(r)$, and scattering function $S(Q)$.

$$
\begin{aligned}
&= |\bar{b}|^2 \left(N + \int_V \mathrm{d}^3 r_1 \int_V \mathrm{d}^3 r_2 n(\underline{r}_1, \underline{r}_2) \exp\left(\mathrm{i}\underline{Q} \cdot (\underline{r}_1 - \underline{r}_2)\right)\right) \\
&= |\bar{b}|^2 \left(N + {\rho_0}^2 V \int_V \mathrm{d}^3 r_{12} g(\underline{r}_{12}) \exp\left(\mathrm{i}\underline{Q} \cdot \underline{r}_{12}\right)\right) \\
&= |\bar{b}|^2 N \left(1 + \rho_0 \int_V \mathrm{d}^3 r_{12} g(\underline{r}_{12}) \exp\left(\mathrm{i}\underline{Q} \cdot \underline{r}_{12}\right)\right) . \qquad (5.9)
\end{aligned}
$$

This equation states that the scattering cross section can be represented as the Fourier transform of the pair correlation function. Assuming isotropy (as is found in the homogeneous liquid discussed here) one can replace $g(\underline{r}_{12})$ by the radial correlation function $g(r)$:

$$
\left(\frac{\mathrm{d}\sigma}{\mathrm{d}\Omega}\right)_{\mathrm{coh}} = |\bar{b}|^2 N \left(1 + 4\pi\rho_0 \int_0^\infty r^2 \mathrm{d}^3 r g(r) \frac{\sin Qr}{Qr} \right) \qquad (5.10)
$$

Equation (5.10) follows from (5.9) by radial averaging of $\exp\left(\mathrm{i}\underline{Q} \cdot \underline{r}_{12}\right)$ (i.e. an average over all possible orientations of $\underline{r}_{12}$).

The term in big parentheses of equations (5.9) and (5.10)

$$S(\underline{Q}) \equiv 1 + \rho_0 \int_V \mathrm{d}^3 r_{12} g(\underline{r}_{12}) \exp\left(\mathrm{i}\underline{Q} \cdot \underline{r}_{12}\right) \tag{5.11}$$

is usually called structure factor or scattering law[2]. $S(Q)$ is solely determined by the properties of the sample and does not depend on the radiation used in examining the sample.

For $Q \to \infty$, $\exp\left(\mathrm{i}\underline{Q} \cdot \underline{r}_{12}\right)$ becomes a rapidly oscillating function and the integral vanishes. Then one has

$$\lim_{Q\to\infty} S(Q) = 1\,. \tag{5.12}$$

For $Q \to 0$, $S(Q)$ measures only the overall density fluctuation, i.e. the fluctuation of the particle number:

$$\lim_{Q\to 0} S(Q) = V^2\langle\delta\rho^2\rangle = \langle N^2\rangle - \langle N\rangle^2 = \rho_0 k_\mathrm{B} T \kappa_T\,. \tag{5.13}$$

Here, k_B denotes the Boltzmann factor, T the temperature and κ_T the isothermal compressibility. At intermediate Q, the structure factor of liquids shows a diminishing series of broad peaks, remainders of the Bragg peaks of a crystalline structure. The first peak occurs at a scattering vector roughly corresponding to the next neighbour distance by $Q_\mathrm{max} = 2\pi/r_\mathrm{nn}$.

[2] The usual definition of the structure factor found in the literature is

$$S'(\underline{Q}) \equiv 1 + \rho_0 \int_V \mathrm{d}^3 r_{12}\,(g(\underline{r}_{12}) - 1) \exp\left(\mathrm{i}\underline{Q} \cdot \underline{r}_{12}\right)$$

subtracting the long distance limit 1 from $g(r)$. Because the Fourier transform of the constant 1 is the delta function the two definitions differ only by a delta function, $S(Q) = S'(Q) + \rho_0\delta(Q)$ in lieu of the local density itself. This means that apart from the unobservable scattering at zero angle ($Q = 0$) both are the same.

The reason for this alternative definition is to avoid the singularity. Another way to accomplish this is to use the density fluctuation $\delta\rho(\underline{r}) = \rho(\underline{r}) - \rho_0$ from the start (equation (5.2)). From this approach it becomes clear that the structure factor at $Q \neq 0$ depends only on the fluctuation of the density but not on its absolute level.

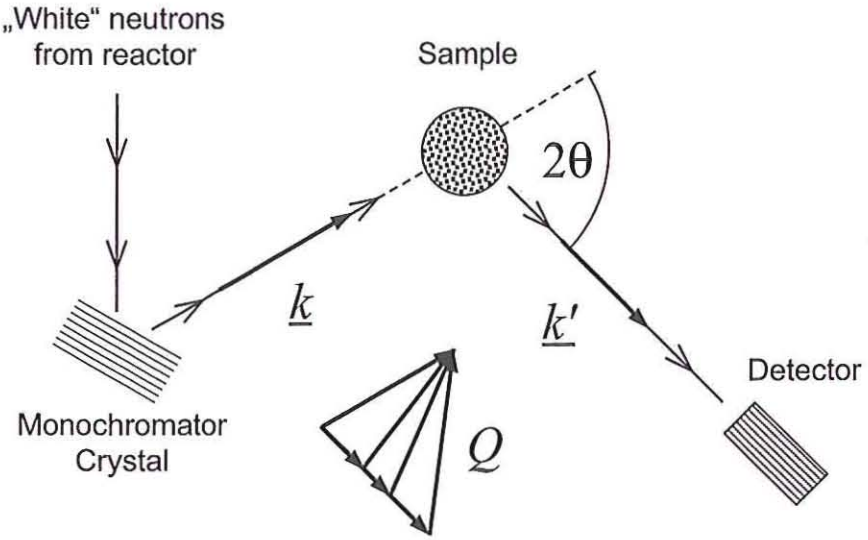

Figure 5.2: Schematic set-up of a diffraction experiment. The inset shows the relation between incident and final wave vectors k, k' and the scattering vector Q.

5.2 Experimental Examples: Static Scattering

5.2.1 Placzek corrections

Figure 5.2 shows the schematics of a scattering experiment for the determination of $S(Q)$. By using a monochromator the incident neutron energy or the wave vector k is fixed. After scattering the intensity is recorded as a function of the scattering angle 2θ without energy discrimination. This means that the diffraction setup fixes only the direction of $\underline{k}_f$ but not its magnitude. Therefore, for a given angle different scattering vectors Q are mixed as figure 5.3 shows.

Strictly speaking, this invalidates the relation $(\mathrm{d}\sigma/\mathrm{d}\Omega)_{\mathrm{coh}} = |\bar{b}|^2 N S(Q)$ between (angle) differential cross section and structure factor.

Nevertheless, for high incident energies it is an excellent approximation as long as the energy transfer due to inelastic scattering is small compared to the incident energy E. This condition is always fulfilled for x-ray scattering because the incident energy lies in the keV range there and the inelasticity of scattering is limited mainly to thermal energies $k_B T$ which are of the order of meV.

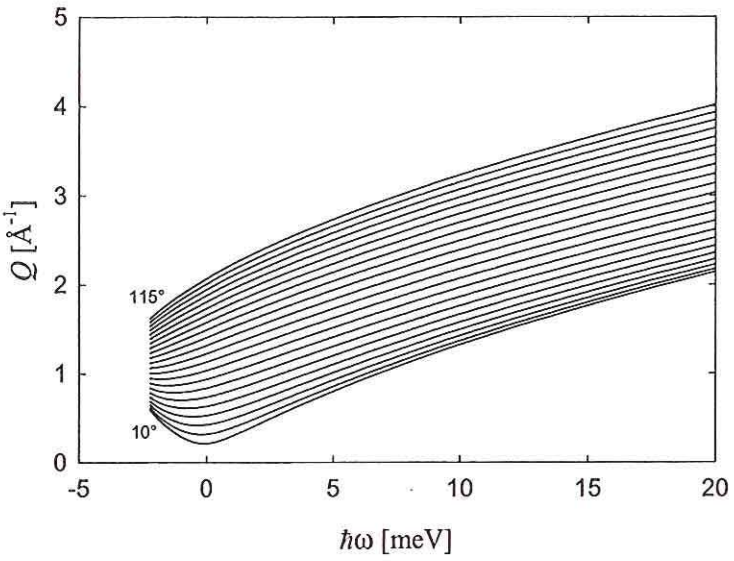

Figure 5.3: Scattering vectors Q accessed by a diffraction experiment with the detector at scattering angles $2\theta = 10 \ldots 115°$ vs. the energy transfer $\hbar\omega$ (incident wavelength $\lambda_i = 5.1$ Å).

For neutrons on the other hand, incident energies are just in the latter range. Fortunately, the errors which occur due to neglect of inelasticity are still not too large. Therefore, it is possible to derive a correction formula by expanding the true differential cross section under constant angle into a series in the ration of the mass of the scattering nucleus and the neutron mass m_n/m_{sc}. In this way Placzek obtained:

$$\left(\frac{d\sigma}{d\Omega}\right)_{2\theta} = |\bar{b}|^2 N \left(S(Q) + f_P(Q)\right) \text{ with } f_P(Q) = \frac{m_n}{m_{sc}} \left(\frac{k_B T}{E} - \left(\frac{Q}{k}\right)^2\right). \tag{5.14}$$

Here, E is the incident energy and $k = \sqrt{2m_n E}/\hbar$ the respective wave vector.

5.2.2 Experiments on Liquid Argon

As an example of the structure factor $S(Q)$ of a monatomic liquid we consider the neutron scattering results of Yarnell et al. [6] from liquid Argon. The result of the experiment is shown in figure 5.4. The wavelength of the incident neutrons was $\lambda = 0.978$ Å. Under this condition the Placzek corrections vary between 0.0012 near $Q = 0$ and -0.0426 at $Q = 9.08\,\text{Å}^{-1}$. The pair correlation function $g(r)$ was obtained by numerical inverse

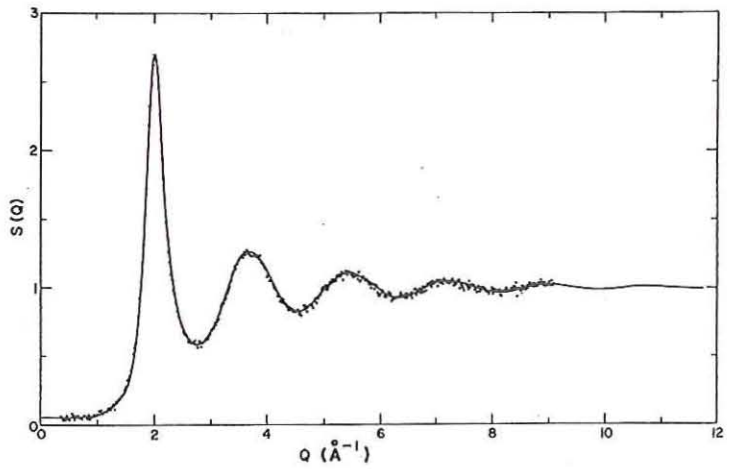

Figure 5.4: Structure factor $Q(Q)$ of liquid ^{36}Ar at 85 K. The points are from a neutron scattering experiment, the curve is generated by a molecular dynamics calculation using a Lennard-Jones potential [6].

Fourier transform of $S(Q) - 1$ and is shon in figure 5.5. The oscillations at small r are a consequence of cut-off effects on the Fourier transform. They occur below the atomic diameter r_0 and therefore do not impede the interpretation. The determination of $g(r)$ is important for the calculation of equilibrium properties of the liquid and allows scrutinization of theoretical models for the interatomic forces.

Two methods of theory based calculation of $g(r)$ have to be emphasized: (1) In Monte Carlo (MC) calculations a large number of possible atomic configurations is created. Their probability is determined by the Boltzmann factor on the basis of interatomic potentials. Finally, the ensemble average is calculated. (2) In Molecular Dynamics (MD) calculations one starts from an initial configuration and solves (numerically) the equations of motions using the interatomic forces. These calculations yield the time average[3]. The solid curve in figure 5.5 shows the result of an MD calculation with a Lennard-Jones-Potential ($V(r) \propto (\sigma/r)^{12} - (\sigma/r)^6$)—the agreement is excellent.

Unfortunately, the pair correlation function is comparatively insensitive to details of the pair potential. To obtain exact information on $V(r)$ it is necessary to do extremely accurate measurements with errors in the per mille range.

[3] The ergodic hypothesis ensures that the results of both methods are the same.

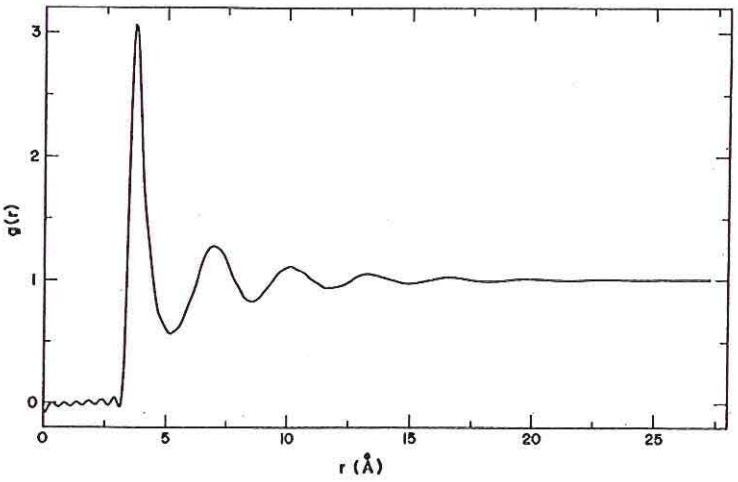

Figure 5.5: The pair correlation function $g(r)$ of liquid Argon calculated by inverse Fourier transform from the data in figure 5.4 [6].

5.2.3 Scattering from a Polymer Chain

We consider a polymer, i.e. a long chain molecule consisting of equal building blocks, the monomers. In the melt the spatial arrangement of the monomers is simply given by a random walk[4]. The mean squared distance between monomers i and j for such a coiled chain is proportional to the difference of indices

$$\langle {r_{ij}}^2 \rangle = \ell^2 |i - j| \tag{5.15}$$

where r_{ij} denotes the monomer distance and ℓ is the characteristic monomer length. This is the same expression as for a random walk but with the time t replaced by $|i - j|$. Because for not too small distances r_{ij} is the sum of many random variable the central limit theorem is applicable and the final distribution of the distance is a Gaussian:

$$g(r_{ij}) = \left(\frac{3}{2\pi \langle {r_{ij}}^2 \rangle} \right)^{3/2} \exp\left(-\frac{3{r_{ij}}^2}{2\langle {r_{ij}}^2 \rangle} \right) . \tag{5.16}$$

[4] This is a result by no means trivial. It was actually confirmed for the first time by the neutron scattering results shown here.

Application of equation (5.8) (radially averaged as (5.10)) yields the so-called form factor[5] of the monomer

$$P(Q) = \frac{1}{\mathcal{N}^2} \sum_{i,j=1}^{\mathcal{N}} 4\pi \int r_{ij}^2 \mathrm{d}^3 r_{ij} \frac{\sin Qr_j}{Qr_{ij}} g(r_{ij}) = \sum_{i,j=1}^{\mathcal{N}} \exp\left(-\frac{Q^2}{6}|i-j|\ell^2\right) \tag{5.17}$$

where $\mathcal{N}$ is now the number of monomers. Analogous to the preceding derivation of (5.9) we take the diagonal part out of the sum and convert the double sum into a single sum over all differences $k \equiv |i-j|$:

$$P(Q) = \frac{1}{\mathcal{N}} \left(1 + 2 \sum_{k=1}^{\mathcal{N}} \left(1 - \frac{k}{\mathcal{N}}\right) \exp\left(-\frac{Q^2}{6} k\ell^2\right)\right) . \tag{5.18}$$

Here it is taken account that in contrast to (5.9) not all pairs are equally probable but an index distance k occurs $2(\mathcal{N}-k)$ times in the chain. Converting this sum into an integral one obtains

$$P(Q) = \frac{2}{z^2}\left(\mathrm{e}^{-z} - 1 + z\right) \equiv D(z) \text{ with } z = \frac{Q^2 N \ell^2}{6} . \tag{5.19}$$

The expression $D(z)$ is usually called the Debye function. It describes the scattering of a single polymer coil in the melt which is labeled e.g. by isotopic contrast. Figure 5.6 shows the scattering cross section of protonated polystyrene in a deuterated polystyrene matrix. The solid curve represents a fit with equation (5.19). At large scattering vectors the leading asymptotic term of $D(z)$ is $2/z$ and $P(Q)$ becomes proportional $1/Q^2$—characteristic for a Gaussian random walk. In a so-called Kratky plot ($Q^2 \cdot \mathrm{d}\sigma/\mathrm{d}\Omega$ vs. Q) one expects a plateau at high scattering vector Q. Figure 5.7 shows this plateau for polystyrene. At very large Q values deviations occur again which signalize the breakdown of Gauss statistics for small distances.

5.3 Dynamical Correlation Function

5.3.1 Correlation Spectroscopy

We consider an observable A of a system which fluctuates randomly because of the thermal motion of the system. A could be e.g. the pressure on the wall exerted by a gas in a cylinder

[5] Here the monomers are simply considered as "big atoms" neglecting their inner structure. One has to keep in mind that the thus obtained results only represent the actual scattering law for small scattering vector when $2\pi/Q$ is larger than the size of a monomer.

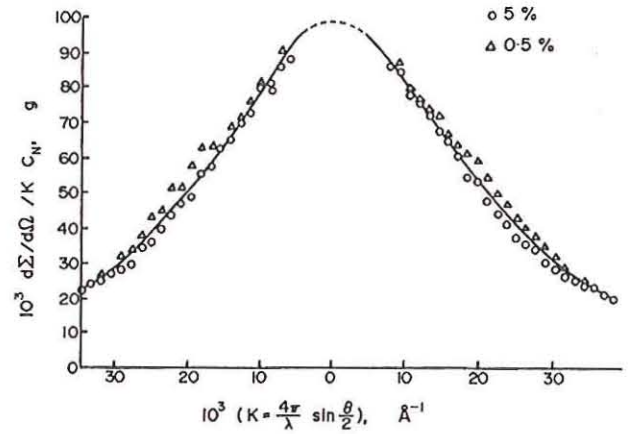

Figure 5.6: Partial differential cross section for protonated polystyrene in a deuterated polystyrene matrix [7]. The concentration of the protonated component is 5% (o) and 0.5% (Δ) respectively. The curve is a fit with the Debye function.

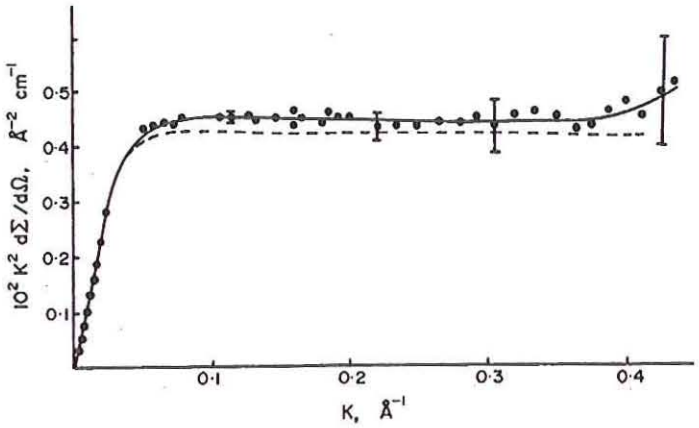

Figure 5.7: Kratky plot of the data from figure 5.6.

or the particle density in a liquid. Figure 5.8 shows exemplarily the time-dependent value of a quatitity A fluctuating around its average value $\langle A \rangle$.

If one takes a time average over a long time interval as compared with the fluctuation periods one obtains a stationary result which is independent of the start of the time interval

$$\lim_{T\to\infty} \frac{1}{T} \int_{t_0}^{t_0+T} dt A(t) = \text{const.} \equiv \langle A \rangle \tag{5.20}$$

but in general $A(t+\tau) \neq A(t)$. If τ is very small compared to typical times of the system

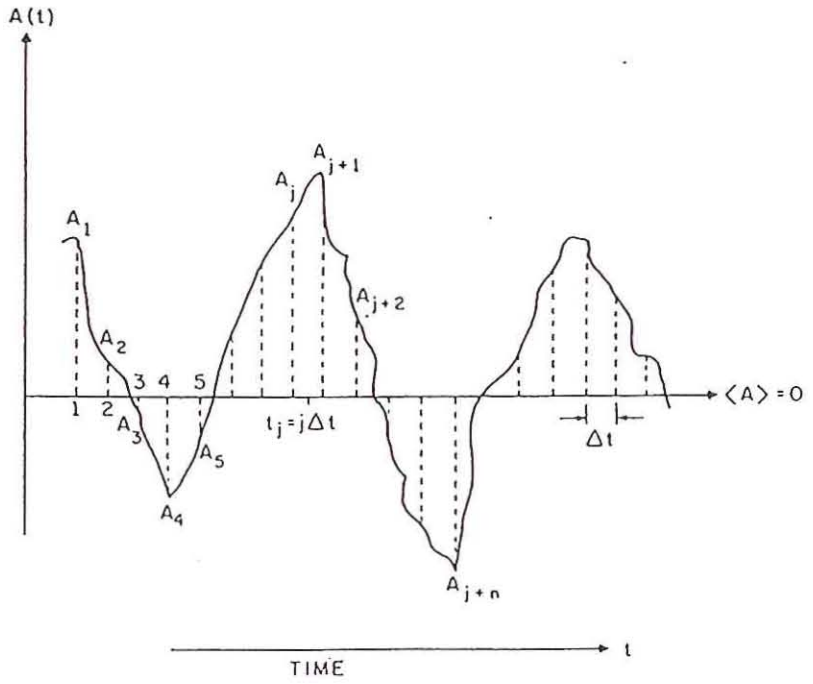

Figure 5.8: Fluctuating observable $A(t)$ of an ensemble of molecules as a function of time. The time axis is subdivided into discrete intervals of length Δt. For simplicity the average $\langle A \rangle$ is set to zero.

$A(t+\tau)$ approaches the value of $A(t)$ which means that the both are correlated in time. As a measure of this correlation the autocorrelation fnction is introduced:

$$\langle A(0)A(\tau)\rangle = \lim_{T\to\infty} \frac{1}{T} \int_{t_0}^{t_0+T} dt A(t)A(t+\tau)\,. \tag{5.21}$$

This function correlates the observable A with itself in a certain time displacement τ and then averages over all starting times.

In a real experiment (figure 5.8) this can be done by sampling values A_i at equidistant times $t_i = i\delta t$. Let j denote the index of the starting time ($t = j\delta t$), n the distance counted in time intervals ($\tau = n\delta t$), and N the number of intervals to be averaged ($T = N\delta t$). Then equation (5.21) can be converted into a sum:

$$\langle A(0)A(\tau)\rangle = \lim_{N\to\infty} \frac{1}{N} \sum_{j=1}^{N} A_j A_{j+n}\,. \tag{5.22}$$

In optical correlation spectroscopy sums like (5.22) are calculated from the photodetector

signal by special purpose computers. In this case A is the number of photons detected per time interval, i.e. the light intensity.

It is easy to see that the autocorrelation function has the following properties

$$\langle A(0)A(\tau)\rangle \leq \langle A(0)A(0)\rangle \equiv \langle A^2\rangle \tag{5.23}$$

$$\lim_{\tau\to\infty}\langle A(0)A(\tau)\rangle = \langle A\rangle^2 . \tag{5.24}$$

As an experimental example we want to consider light scattering experiments on polystyrene spheres in an aqueous dispersion. Figure 5.9a shows the fluctuating intensity scattered from such a dispersion. Figure 5.9b presents the autocorrelation function calculated by (5.22). The correlation function usually decays following a simple exponential law:

$$\langle A(0)A(\tau)\rangle = \langle A\rangle^2 + \left(\langle A^2\rangle - \langle A\rangle^2\right)\exp\left(-\tau/\tau_r\right) \tag{5.25}$$

where τ_r is the correlation time of the system. In general, also more complicated decays, e.g. involving multiple characteristic times, are possible. But the decay always takes places between the limits given by (5.23) and (5.24).

Alternatively, one can consider the fluctuations $\delta A(t) = A(t) - \langle A\rangle$, i.e. the deviations of the observable from its average. For its autocorrelation function follows:

$$\begin{aligned}\langle \delta A(0)\delta A(t)\rangle &= \langle A(0)A(\tau)\rangle \\ &= \langle \delta A^2\rangle \exp\left(-\tau/\tau_r\right) .\end{aligned} \tag{5.26}$$

The general result is that the fluctuation autocorrelation function decays starting from the variance of the observable, $\langle \delta A^2\rangle = \langle A^2\rangle - \langle A\rangle^2$ to zero.

The time-dependent autocorrelation function describes the temporal fluctuation behaviour of the system. In the case presented here of a polymer colloid the characteristic time is directly connected to the diffusion constant: ${\tau_r}^{-1} = DQ^2$.

5.3.2 The Van Hove Correlation Function

In order to consider inelastic scattering generalizes the differential cross section $\mathrm{d}\sigma/\mathrm{d}\Omega$ with respect to its dependence on the energy transfer $\hbar\omega$. This leads to the double

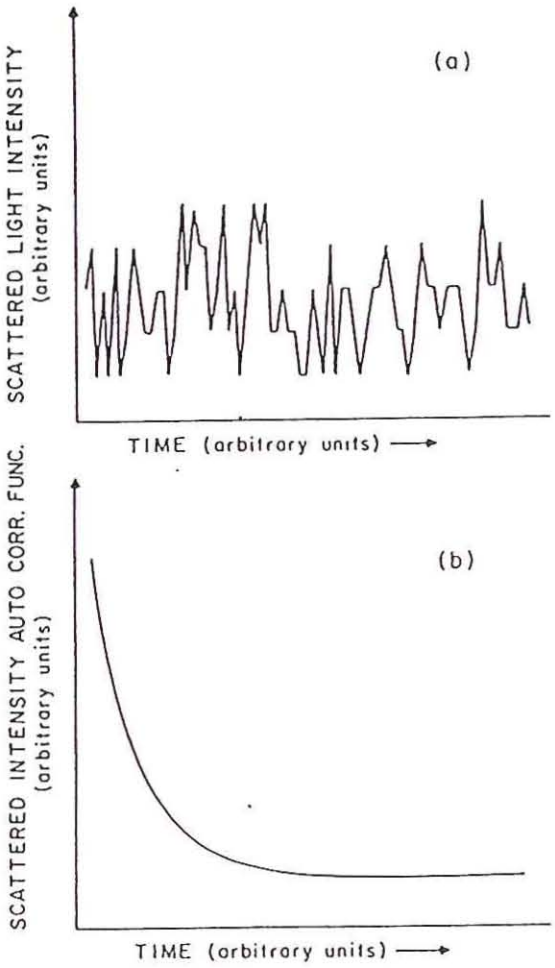

Figure 5.9: (a) Intensity of the light scattered from an aqeous solution of polystyrene spheres with radius $1\,\mu$m as a function of time t. (b) Time averaged autocorrelation function of the scattered intensity shown in (a) as a function of correlation time τ. In both cases the units are arbitrary.

differential cross section in quantum mechanical notation:

$$\frac{\partial^2\sigma}{\partial\Omega\partial\omega} = \frac{k'}{k}\sum_{\lambda,\sigma} P_\lambda P_\sigma \sum_{\lambda',\sigma'} \left|\sum_i \langle\lambda',\sigma'|b_i \exp(\mathrm{i}\underline{Q}\cdot\underline{\mathbf{r}}_i)|\lambda,\sigma\rangle\right|^2 \delta\left(\hbar\omega + E_\lambda - E_{\lambda'}\right) . \qquad (5.27)$$

Here, λ and σ describe the relevant space and spin quantum number respectively in the initial state and λ' and σ' those in the final state. P_λ and P_σ are the respective probabilities for the initial states λ and σ. The inner sum refers to all particles with scattering lengths b_i

and single-particle coordinate operators $\underline{\mathrm{r}}_i$. k and k' are the wave vectors of the incident and scattered neutrons. The delta function expresses energy conservation: the energy transfer of the neutron $\hbar\omega$ is exactly compensated by the energy change of the quantum state of the scattering system $E_{\lambda'} - E_\lambda$. In the following we will neglect the spin coordinates for the sake of simplicity.

The route from expression (5.27) to the Van Hove correlation function starts with an integral representation of the delta function:

$$\delta\left(\hbar\omega + E_\lambda - E_{\lambda'}\right) = \frac{1}{2\pi\hbar}\int_{-\infty}^{\infty} \mathrm{d}t \exp\left(-\mathrm{i}\left(\omega + \frac{E_\lambda - E_{\lambda'}}{\hbar}\right)t\right) \tag{5.28}$$

which results from the fact that the delta function is the Fourier transform of a constant one. With this expression the matrix element in equation (5.27) can be written as a Fourier transform in time:

$$\begin{aligned}
&\left|\sum_i \langle\lambda'|b_i \exp(\mathrm{i}\underline{Q}\cdot\underline{\mathrm{r}}_i)|\lambda\rangle\right|^2 \delta\left(\hbar\omega + E_\lambda - E_{\lambda'}\right) \\
&= \frac{1}{2\pi\hbar}\int_{-\infty}^{\infty} \mathrm{d}t \exp(-\mathrm{i}\omega t) \exp\left(-\mathrm{i}\frac{E_\lambda}{\hbar}t\right) \exp\left(-\mathrm{i}\frac{E_{\lambda'}}{\hbar}t\right) \\
&\qquad \sum_i b_i \langle\lambda'|\exp(\mathrm{i}\underline{Q}\cdot\underline{\mathrm{r}}_i)|\lambda\rangle \sum_j b_j^* \langle\lambda|\exp(-\mathrm{i}\underline{Q}\cdot\underline{\mathrm{r}}_j)|\lambda'\rangle \\
&= \frac{1}{2\pi\hbar}\int_{-\infty}^{\infty} \mathrm{d}t \exp(-\mathrm{i}\omega t) \sum_{i,j} b_i b_j^* \langle\lambda|\exp(-\mathrm{i}\underline{Q}\cdot\underline{\mathrm{r}}_j)|\lambda'\rangle \\
&\qquad\qquad \langle\lambda'|\exp(\mathrm{i}E_{\lambda'}t/\hbar)\exp(\mathrm{i}\underline{Q}\cdot\underline{\mathrm{r}}_i)\exp(-\mathrm{i}E_\lambda t/\hbar)|\lambda\rangle
\end{aligned} \tag{5.29}$$

If $\mathbf{H}$ is the Hamiltonian of the scattering system, the fact that $|\lambda\rangle$ are energy eigenstates is expressed by

$$\mathbf{H}|\lambda\rangle = E_\lambda|\lambda\rangle\,. \tag{5.30}$$

Iterating this equation n times yields:

$$\mathbf{H}^n|\lambda\rangle = E_\lambda{}^n|\lambda\rangle\,. \tag{5.31}$$

By expanding the exponential into a power series one finally obtains from this relation

$$\exp(\mathrm{i}\mathbf{H}t/\hbar)|\lambda\rangle = \exp(\mathrm{i}E_\lambda t/\hbar)|\lambda\rangle\,. \tag{5.32}$$

With this result and the analogous one for λ' it is possible to replace the eigenvalues E_λ in (5.29) by the Hamiltonian $\mathbf{H}$:

$$\ldots\langle\lambda'|\exp(\mathrm{i}\mathbf{H}t/\hbar)\exp(\mathrm{i}\underline{Q}\cdot\underline{\mathrm{r}}_i)\exp(-\mathrm{i}\mathbf{H}t/\hbar)|\lambda\rangle\,. \tag{5.33}$$

In the picture of time dependent Heisenberg operators the application of the operator $\exp(\mathrm{i}\mathbf{H}t/\hbar)$ and its conjugate just mean a propagation by time t:

$$\exp\left(\mathrm{i}\underline{Q}\cdot\underline{\mathbf{r}}_i(t)\right) = \exp(\mathrm{i}\mathbf{H}t/\hbar)\exp(\mathrm{i}\underline{Q}\cdot\underline{\mathbf{r}}_i(0))\exp(-\mathrm{i}\mathbf{H}t/\hbar) \tag{5.34}$$

where we can arbitrarily set $\underline{\mathbf{r}}_i = \underline{\mathbf{r}}_i(0)$ because of translation of time invariance. Using this result the final expression for the double differential cross section is obtained:

$$\begin{aligned}\frac{\partial^2\sigma}{\partial\Omega\partial\omega} &= \frac{k'}{k}\frac{1}{2\pi\hbar}\int_{-\infty}^{\infty}\mathrm{d}t\exp(-\mathrm{i}\omega t)\\ &\quad\sum_\lambda P_\lambda\sum_{i,j}b_ib_j^*\left\langle\lambda\left|\exp(-\mathrm{i}\underline{Q}\cdot\underline{\mathbf{r}}_j(0))\exp(\mathrm{i}\underline{Q}\cdot\underline{\mathbf{r}}_i(t))\right|\lambda\right\rangle .\end{aligned} \tag{5.35}$$

This equation averages over the scattering length distribution (which may depend on the spin orientation distribution with respect to the incident neutron's spin). This produces coherent and incoherent scattering as explained in lecture 1. In addition the initial states of the scattering system are averaged weighted with the probability of their occurrence P_λ. The latter is given by the Boltzmann distribution

$$P_\lambda = \frac{1}{Z}\exp\left(-E_\lambda/k_\mathrm{B}T\right)\ \text{with}\ Z = \sum_\lambda\exp\left(-E_\lambda/k_\mathrm{B}T\right) . \tag{5.36}$$

We now denote this thermal average by angular brackets $\langle\ldots\rangle$ while that over the scattering lengths be written as an overline $\overline{\ldots}$. Keeping in mind that for equal indices $b_ib_i^* = |b_i|^2$ has to be averaged while for unequal indices the scattering lengths itself will be averaged we end up with the usual separation into incoherent and coherent part:

$$\begin{aligned}&\frac{\partial^2\sigma}{\partial\Omega\partial\omega} =\\ &\frac{k'}{k}\frac{\overline{|b|^2}-|\bar{b}|^2}{2\pi\hbar}\int_{-\infty}^{\infty}\mathrm{d}t\exp(-\mathrm{i}\omega t)\sum_i\left\langle\lambda\left|\exp(-\mathrm{i}\underline{Q}\cdot\underline{\mathbf{r}}_i(0))\exp(\mathrm{i}\underline{Q}\cdot\underline{\mathbf{r}}_i(t))\right|\lambda\right\rangle\\ &+\frac{k'}{k}\frac{|\bar{b}|^2}{2\pi\hbar}\int_{-\infty}^{\infty}\mathrm{d}t\exp(-\mathrm{i}\omega t)\sum_{i,j}\left\langle\lambda\left|\exp(-\mathrm{i}\underline{Q}\cdot\underline{\mathbf{r}}_i(0))\exp(\mathrm{i}\underline{Q}\cdot\underline{\mathbf{r}}_i(t))\right|\lambda\right\rangle .\end{aligned} \tag{5.37}$$

The first term is the incoherent scattering. It involves the coordinate vector operators of the *same* atom at different times. The second, the coherent term correlates also *different* atoms at different times. The material dependent parts are now defined as the scattering functions

$$S_\mathrm{inc}(Q,\omega) \equiv \frac{1}{2\pi\hbar N}\int_{-\infty}^{\infty}\mathrm{d}t\exp(-\mathrm{i}\omega t)\sum_i\langle\exp(-\mathrm{i}\underline{Q}\cdot\underline{\mathbf{r}}_i(0))\exp(\mathrm{i}\underline{Q}\cdot\underline{\mathbf{r}}_i(t))\rangle \tag{5.38}$$

$$S_\mathrm{coh}(Q,\omega) \equiv \frac{1}{2\pi\hbar N}\int_{-\infty}^{\infty}\mathrm{d}t\exp(-\mathrm{i}\omega t)\sum_{i,j}\langle\exp(-\mathrm{i}\underline{Q}\cdot\underline{\mathbf{r}}_i(0))\exp(\mathrm{i}\underline{Q}\cdot\underline{\mathbf{r}}_j(t))\rangle . \tag{5.39}$$

In terms of the scattering functions the double differential cross section can be written as

$$\frac{\partial^2\sigma}{\partial\Omega\partial\omega} = \frac{k'}{k} N \left(\left(\overline{|b|^2} - |\bar{b}|^2 \right) S_{\text{inc}}(\underline{Q},\omega) + |\bar{b}|^2 S_{\text{coh}}(\underline{Q},\omega) \right) . \tag{5.40}$$

In addition it is often useful to define the intermediate scattering function which denotes the time dependent parts of definitions (5.38) and (5.39) before Fourier transform:

$$S_{\text{inc}}(\underline{Q},t) \equiv \frac{1}{N} \sum_i \langle \exp(-\mathrm{i}\underline{Q}\cdot\underline{\mathbf{r}}_i(0)) \exp(\mathrm{i}\underline{Q}\cdot\underline{\mathbf{r}}_i(t)) \rangle \tag{5.41}$$

$$S_{\text{coh}}(\underline{Q},t) \equiv \frac{1}{N} \sum_{i,j} \langle \exp(-\mathrm{i}\underline{Q}\cdot\underline{\mathbf{r}}_i(0)) \exp(\mathrm{i}\underline{Q}\cdot\underline{\mathbf{r}}_j(t)) \rangle . \tag{5.42}$$

If one compares this result with the definition of the structure factor (5.8–5.11) one recognizes that $S_{\text{coh}}(Q,\omega)$ is in an analogous way the Fourier transform in space and time of a dynamical pair correlation function $G(\underline{r},t)$:

$$G(\underline{r},t) = \left(\frac{1}{2\pi}\right)^3 \int \mathrm{d}^3Q \exp\left(-\mathrm{i}\underline{Q}\cdot\underline{r}\right) \frac{1}{N} \sum_{i,j} \left\langle \exp\left(-\mathrm{i}\underline{Q}\cdot\underline{\mathbf{r}}_i(0)\right) \exp\left(\mathrm{i}\underline{Q}\cdot\underline{\mathbf{r}}_j(t)\right) \right\rangle . \tag{5.43}$$

The derivation of the relation between the coherent dynamical structure factor $S_{\text{coh}}(Q,\omega)$ and the generalized pair correlation function requires a strict quantum mechanical calculation. This problem results from the fact that the coordinate vector operators commute only at identical times. Therefore, in all algebraic manipulations the order of $\underline{\mathbf{r}}_i(0)$ and $\underline{\mathbf{r}}_i(0)$ must not be interchanged.

To begin, one writes the operator $\exp\left(-\mathrm{i}\underline{Q}\cdot\underline{\mathbf{r}}_i(0)\right)$ as the Fourier transform of the delta function:

$$\exp\left(-\mathrm{i}\underline{Q}\cdot\underline{\mathbf{r}}_i(0)\right) = \int \mathrm{d}^3r' \delta\left(\underline{r}' - \underline{\mathbf{r}}_i(0)\right) \exp(-\mathrm{i}\underline{Q}\cdot\underline{r}') . \tag{5.44}$$

Using this expression equation (5.43) can be rewritten as

$$\begin{aligned} G(\underline{r},t) &= \left(\frac{1}{2\pi}\right)^3 \frac{1}{N} \sum_{i,j} \Bigg\langle \int \mathrm{d}^3r' \delta\left(\underline{r}' - \underline{\mathbf{r}}_i(0)\right) \\ &\qquad \underbrace{\int \mathrm{d}^3Q \exp\left(-\mathrm{i}\underline{Q}\cdot\underline{r} - \mathrm{i}\underline{Q}\cdot\underline{r}' + \mathrm{i}\underline{Q}\cdot\underline{\mathbf{r}}_j(t)\right)}_{= (2\pi)^3 \delta\left(\underline{r} + \underline{r}' - \underline{\mathbf{r}}_j(t)\right)} \Bigg\rangle \\ &= \frac{1}{N} \sum_{i,j} \int \mathrm{d}^3r' \left\langle \delta\left(\underline{r} - \underline{r}' + \underline{\mathbf{r}}_i(0)\right) \delta\left(\underline{r}' - \underline{\mathbf{r}}_j(t)\right) \right\rangle \end{aligned} \tag{5.45}$$

without changing the order of the operators at different times.

Now the particle density operator is introduced as a sum over delta functions at the particle position operators:

$$\rho(\underline{r},t) \equiv \sum_i \delta\left(\underline{r} - \underline{\mathbf{r}}_i(t)\right) . \tag{5.46}$$

With this definition the pair correlation function can be written as time-dependent density-density correlation function:

$$G(\underline{r},t) = \frac{1}{N}\int \mathrm{d}^3r' \left\langle \rho(\underline{r}' - \underline{r},0)\rho(\underline{r}',t)\right\rangle . \tag{5.47}$$

With this form of the dynamic pair correlation function the dynamical structure factor can be—analogously to equation (5.11)—written as the double Fourier transform of the correlator of the particle density:

$$S_{\mathrm{coh}}(\underline{Q},\omega) = \int_{-\infty}^{\infty} \mathrm{d}t \exp(-\mathrm{i}\omega t)\int \mathrm{d}^3r \int \mathrm{d}^3r' \exp\left(\mathrm{i}\underline{Q}\cdot\underline{r}\right)\left\langle \rho(\underline{r}' - \underline{r},0)\rho(\underline{r}',t)\right\rangle . \tag{5.48}$$

We now define the density operator in reciprocal space as the Fourier transform of (5.46):

$$\rho_{\underline{Q}}(t) \equiv \sum_i \exp\left(\mathrm{i}\underline{Q}\cdot\underline{\mathbf{r}}_i(t)\right) \tag{5.49}$$

and obtain for the dynamic structure factor

$$S_{\mathrm{coh}}(\underline{Q},\omega) = \frac{1}{2\pi\hbar N}\int_{-\infty}^{\infty} \mathrm{d}t \exp(-\mathrm{i}\omega t)\left\langle \rho_{\underline{Q}}(0)\rho_{-\underline{Q}}(t)\right\rangle . \tag{5.50}$$

Correspondingly, the intermediate scattering function is

$$S_{\mathrm{coh}}(\underline{Q},t) = \frac{1}{N}\left\langle \rho_{\underline{Q}}(0)\rho_{-\underline{Q}}(t)\right\rangle \tag{5.51}$$

which after insertion of (5.49) turns out to be equivalent to (5.42).

Analogously, one can define a self correlation function by setting $i = j$ in the preceding equations leading to

$$G_{\mathrm{s}}(\underline{r},t) = \frac{1}{N}\sum_i \int \mathrm{d}^3r' \left\langle \delta\left(\underline{r} - \underline{r}' + \underline{\mathbf{r}}_i(0)\right)\delta\left(\underline{r}' - \underline{\mathbf{r}}_i(t)\right)\right\rangle \tag{5.52}$$

as the equivalent of (5.45).

The pair correlation function has some general properties:

1. For spatially homogeneous systems the integrand in (5.47) is independent of $\underline{r}'$ which can be arbitrarily set to the origin $\underline{0}$:

$$G(\underline{r},t) = \frac{V}{N}\left\langle \rho(-\underline{r},0)\rho(\underline{0},t)\right\rangle = \frac{1}{\rho_0}\left\langle \rho(\underline{0},0)\rho(\underline{r},t)\right\rangle . \tag{5.53}$$

2. The pair correlation function has the following asymptotic behaviour: For fixed distance and $t \to \infty$ or fixed time and $r \to \infty$ the averages in equation (5.47) can be executed separately and in consequence

$$G(\underline{r}, t) \to \frac{1}{N} \int \mathrm{d}^3 r' \, \langle \rho(\underline{r}' - \underline{r}, 0) \rangle \, \langle \rho(\underline{r}', t) \rangle = \rho_0 \, . \tag{5.54}$$

3. For $t = 0$ the operators commute and the convolution integral of equation (5.47) can be carried out:

$$G(\underline{r}, 0) = \frac{1}{N} \sum_{i,j} \left\langle \delta \left(\underline{r} + \underline{\mathbf{r}}_i(0) - \underline{\mathbf{r}}_j(0) \right) \right\rangle \, . \tag{5.55}$$

For indistinguishable particles the relation to the static pair correlation function as defined in (5.6) can be drawn. Because of the identity of the particles we can set $i = 1$ in (5.55) and drop the average over i:

$$G(\underline{r}, 0) = \sum_{j} \left\langle \delta \left(\underline{r} + \underline{\mathbf{r}}_1(0) - \underline{\mathbf{r}}_j(0) \right) \right\rangle = \delta(\underline{r}) + \sum_{j \neq 1} \left\langle \delta \left(\underline{r} + \underline{\mathbf{r}}_1(0) - \underline{\mathbf{r}}_j(0) \right) \right\rangle \, . \tag{5.56}$$

We now consider the average number of particles $\delta N(\underline{r})$ in a volume δV at a vector distance $\underline{r}$ from a given particle at $\underline{r}_1$. It is obviously given by the integral over the second term in the preceding expression which for small δV can be written as

$$\delta N(\underline{r}) = \delta V \sum_{j \neq 1} \left\langle \delta \left(\underline{r} + \underline{\mathbf{r}}_1(0) - \underline{\mathbf{r}}_j(0) \right) \right\rangle \, . \tag{5.57}$$

Using the definition (5.6) and the expression for the number density in homogeneous fluids (5.2) one can relate $\delta N(\underline{r})$ also to the static pair correlation function:

$$\delta N(\underline{r}) = \rho_0 g(\underline{r}) \delta V \, . \tag{5.58}$$

Finally, by comparison of the last three equations we get a relation between the dynamic correlation function at time zero and its static counterpart:

$$G(\underline{r}, 0) = \delta(\underline{r}) + \rho_0 g(\underline{r}) \, . \tag{5.59}$$

This equation expresses the fact that the diffraction experiment ($g(r)$) gives an average snapshot picture ($G(r, 0)$) of the sample.

In the classical approximation the operators commute always, especially also at different times. Then the integrals of equations (5.45) and (5.52) can be carried out and yield

$$G^{\mathrm{cl}}(\underline{r}, t) = \frac{1}{N} \sum_{i,j} \delta(\underline{r} - \underline{r}_j(t) + \underline{r}_i(0)) \text{ and} \tag{5.60}$$

$$G_{\mathrm{s}}^{\mathrm{cl}}(\underline{r}, t) = \frac{1}{N} \sum_{i} \delta(\underline{r} - \underline{r}_i(t) + \underline{r}_i(0)) \, , \tag{5.61}$$

respectively. The former equation expresses the probability to find *any* particle at a time t in a distance $\underline{r}$ from another at time 0. The latter equation denotes this probability for the *same* particle. It therefore depends only on the particle's displacement during a time interval $\Delta\underline{r}_i(t) = \underline{r}_i(t) - \underline{r}_i(0)$ leading to a simple expression for the intermediate incoherent scattering function:

$$S_{\text{inc}}^{\text{cl}}(\underline{Q}, t) = \frac{1}{N} \sum_i \left\langle \exp\left(-\mathrm{i}\underline{Q} \cdot \Delta\underline{r}_i(t)\right)\right\rangle . \tag{5.62}$$

In certain cases this expression can be further simplified using the "Gaussian approximation":

$$S_{\text{inc}}^{\text{Gauss}}(Q, t) = \exp\left(-\frac{1}{6} Q^2 \langle \Delta r^2(t)\rangle\right) . \tag{5.63}$$

[6] Here $\langle \Delta r^2(t)\rangle$ is the average mean squared displacement which often follows simple laws, e.g. $\langle \Delta r^2(t)\rangle = 6Dt$ for simple diffusion. Because one of the prerequisites of the Gaussian approximation is that all particles move statistically in the same way (dynamic homogeneity) the particle average and the index i vanish. An analogous expression can be derived for the coherent scattering.

In order to decide whether the classical approximation can be used the following rule has to be taken into account: Quantum effects play a rôle if the distance of two particles is of the order of the DeBroglie wavelength $\lambda_{\text{B}} = \hbar/\sqrt{2m_{\text{sc}}k_{\text{B}}T}$ or if the times considered are smaller than $\hbar/k_{\text{B}}T$.

Figure 5.10 schematically shows on the left side the behaviour of the correlation functions $G(r, t)$ and $G_{\text{s}}(r, t)$ for a simple liquid (in classical approximation). On the right side the corresponding intermediate scattering functions $S_{\text{coh}}(Q, t)$ and $S_{\text{inc}}(Q, t)$ are displayed:

- For $t = 0$ the self correlation function is given by a delta function at $r = 0$. The pair correlation function follows the static correlation function $g(r)$. The intermediate scattering functions are constant one for the incoherent and the static structure factor for the coherent.
- For intermediate times the self correlation function broadens to a bell-shaped function while the pair correlation function loses its structure. The intermediate scat-

[6] For solids the long-time limit of this equation is called the Lamb-Mößbauer factor. Its coherent counterpart is the Debye-Waller factor.

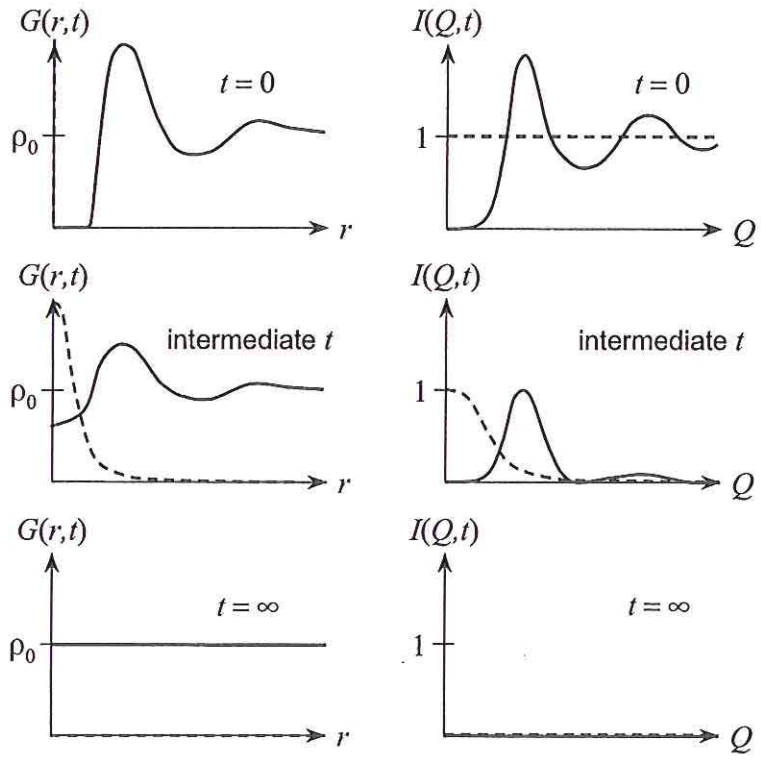

Figure 5.10: Schematic Comparison of the correlation functions $G(r,t)$, $G_s(r,t)$ and the intermediate scattering functions $S_{\text{coh}}(Q,t)$, $S_{\text{inc}}(Q,t)$ for a simple liquid at different times. The solid lines denote the coherent case, the dashed lines the self/incoherent.

tering functions decay with respect to the $t = 0$ value. The decay is faster for higher Q and (in the coherent case) less pronounced at the structure factor maximum.

- The long time limit of the pair correlation function is the average density ρ_0 while the self correlation simply vanishes (in a liquid). In consequence both the coherent and the incoherent intermediate scattering function decay to zero for long times and any Q.

5.4 Scattering from an Ideal Gas

We consider a gas of N atoms in a volume V neglecting the spin coordinates σ and assume that all scattering lengths are identical $b_i = 1$. The wave function of a free atom confined

to a volume V is simply a plane wave with wave vector $\underline{\kappa}$:

$$\Psi_{\underline{\kappa}}(\underline{r}) = \langle \underline{r}|\underline{\kappa}\rangle = \frac{1}{\sqrt{V}} \exp(\mathrm{i}\kappa \cdot \underline{r}) \,. \tag{5.64}$$

Using this expression, the matrix element in the double differential cross section (5.27) can immediately be calculated:

$$\langle \underline{\kappa}'| \exp \mathrm{i}\underline{Q} \cdot \underline{\mathbf{r}}|\underline{\kappa}\rangle = \frac{1}{V} \int_V \mathrm{d}^3 r \exp(\mathrm{i}(\underline{Q} + \underline{\kappa} - \underline{\kappa}') \cdot \underline{r}) = \delta(\underline{Q} + \underline{\kappa} - \underline{\kappa}') \,. \tag{5.65}$$

The resulting delta function expresses the momentum conservation. Only if momentum is conserved the matrix element is 1—otherwise zero.

In the second step we have to consider energy conservation. The energy of the atom with wave vector κ is

$$E_\kappa = \frac{\hbar^2}{m_{\mathrm{sc}}} \kappa^2 \tag{5.66}$$

where m_{sc} is the mass of the scattering atom. For the evaluation of the delta function in (5.27) we need the energy difference between the states κ and κ'. Because of the delta function factor (5.65) only such states with $\underline{\kappa}' = \underline{\kappa} - \underline{Q}$ have to be considered and for those the energy difference is:

$$E_\kappa - E_{\kappa'} = -\frac{\hbar}{2m_{\mathrm{sc}}} \left(Q^2 + 2\underline{Q} \cdot \underline{\kappa}\right) \,. \tag{5.67}$$

With this result one can calculate the scattering function:

$$S(Q,\omega) = \sum_{\underline{\kappa}} P_{\underline{\kappa}} \delta \left(\hbar\omega - \frac{\hbar}{2m_{\mathrm{sc}}} \left(Q^2 + 2\underline{Q} \cdot \underline{\kappa}\right)\right) \,. \tag{5.68}$$

In the limit of a large volume V, $\underline{\kappa}$ becomes a continuous variable. In addition only the component of $\underline{\kappa}$ parallel to Q is relevant. Therefore, (5.68) can be written as a one-dimensional integral:

$$S(Q,\omega) = \int_{-\infty}^{\infty} \mathrm{d}\kappa P_\kappa \delta \left(\hbar\omega - \frac{\hbar}{2m_{\mathrm{sc}}} \left(Q^2 + 2Q\kappa\right)\right) \,. \tag{5.69}$$

The probability of a momentum state κ follows from the Boltzmann distribution:

$$P_\kappa = \frac{1}{Z} \exp\left(-\frac{\hbar^2\kappa^2}{2m_{\mathrm{sc}}k_{\mathrm{B}}T}\right) \tag{5.70}$$

with the state sum being

$$Z = \int_{-\infty}^{\infty} \mathrm{d}\kappa \exp\left(-\frac{\hbar^2\kappa^2}{2m_{\mathrm{sc}}k_{\mathrm{B}}T}\right) = \frac{\sqrt{2\pi m_{\mathrm{sc}}k_{\mathrm{B}}T}}{\hbar} \,. \tag{5.71}$$

Insertion of this result into (5.69) yields:

$$S(Q,\omega) = \frac{\hbar}{\sqrt{2\pi m_{sc} k_B T}} \int_{-\infty}^{\infty} d\kappa \exp\left(-\frac{\hbar^2\kappa^2}{2m_{sc}k_BT}\right) \delta\left(\hbar\omega - \frac{\hbar}{2m_{sc}}\left(Q^2 + 2Q\kappa\right)\right) . \quad (5.72)$$

Substitution of $w \equiv \hbar\omega - \frac{\hbar}{2m_{sc}}(Q^2 + 2Q\kappa)$ into this integral allows the evaluation of the delta function:

$$\begin{aligned} S(Q,\omega) &= \frac{\hbar}{\sqrt{2\pi m_{sc} k_B T}} \\ &\quad \int_{-\infty}^{\infty} dw \frac{m_{sc}}{\hbar^2 Q} \exp\left(-\frac{\hbar^2}{2m_{sc}k_BT}\left(\frac{m_{sc}}{\hbar^2 Q}(\hbar\omega - w) - \frac{Q}{2}\right)^2\right) \delta(w) \\ &= \sqrt{\frac{1}{4\pi E_r k_B T}} \exp\left(-\frac{(\hbar\omega - E_r)^2}{4E_r k_B T}\right) \end{aligned} \quad (5.73)$$

with $E_r = \hbar^2 Q^2/2m_{sc}$ being the recoil energy experienced by the atom during the scattering event. Thus, the dynamical structure factor of an ideal gas is a Gaussian centred around the recoil energy for a given Q. The width of the Gaussian $\sqrt{2E_r k_B T} = \sqrt{k_B T/m_{sc}}\hbar Q$ increases with temperature and scattering vector Q.

Double inverse Fourier transform with respect to ω and Q gives the correlation function $G(r,t)$:

$$\begin{aligned} S(Q,t) &= \hbar \int_{-\infty}^{\infty} d\omega \exp(i\omega t) \sqrt{\frac{1}{4\pi E_r k_B T}} \exp\left(-\frac{(\hbar\omega - E_r)^2}{4E_r k_B T}\right) \\ &= \exp\left(-\frac{Q^2}{2m_{sc}}\left(k_B T t^2 - i\hbar t\right)\right) , \end{aligned} \quad (5.74)$$

$$\begin{aligned} G(r,t) &= \left(\frac{1}{2\pi}\right)^3 \int d^3Q \exp(-i\underline{Q}\cdot\underline{r}) \exp\left(-\frac{Q^2}{2m_{sc}}\left(k_B T t^2 - i\hbar t\right)\right) \\ &= \left(\frac{m_{sc}}{2\pi k_B T t(t - i\hbar/k_B T)}\right)^{3/2} \exp\left(-\frac{m_{sc} r^2}{2k_B T t(t - i\hbar/k_B T)}\right) . \end{aligned} \quad (5.75)$$

Because of the quantum mechanical nature of the underlying dynamics both $S(Q,t)$ and $G(r,t)$ have an imaginary part.

The same result can be obtained via the Van Hove correlation function. For this route we start with equation (5.39) for which we have to calculate $\exp(i\underline{Q}\cdot\underline{r}(t))$ for a free atom. This can be done using the equation of motion

$$i\hbar\frac{d}{dt}\exp(i\underline{Q}\cdot\underline{r}(t)) = \left[\exp(i\underline{Q}\cdot\underline{r}(t)), \mathbf{H}\right] \quad (5.76)$$

where

$$\mathbf{H} = \frac{1}{2m_{sc}}\mathbf{p}^2 \quad (5.77)$$

is the Hamiltonian of a free atom and $\mathbf{p}$ the momentum operator. In the following the time dependent operator $\exp(\mathrm{i}\underline{Q}\cdot\underline{\mathbf{r}}(t))$ shall be calculated. This is done using the equation of motion

$$\mathrm{i}\hbar\frac{\mathrm{d}}{\mathrm{d}t}\exp(\mathrm{i}\underline{Q}\cdot\underline{\mathbf{r}}(t)) = \left[\exp(\mathrm{i}\underline{Q}\cdot\underline{\mathbf{r}}(t)), \mathbf{H}\right] . \tag{5.78}$$

Here, the bracket on the right hand side is the commutator. In analogy to equation (5.34)

$$\frac{1}{2m_{\mathrm{sc}}}\left[\exp(\mathrm{i}\underline{Q}\cdot\underline{\mathbf{r}}(t)), \mathbf{p}^2\right] = \frac{1}{2m_{\mathrm{sc}}}\exp(\mathrm{i}t\mathbf{H})\left[\exp(\mathrm{i}\underline{Q}\cdot\underline{\mathbf{r}}(t)), \mathbf{p}^2\right]\exp(-\mathrm{i}t\mathbf{H}) \tag{5.79}$$

holds. The commutator at equal times on the right hand side of the last equation can easily be calculated. For this purpose one uses the coordinate representation $\underline{\mathbf{p}} = -\mathrm{i}\hbar\underline{\nabla}$. By calculation of the derivatives

$$\left[\exp(\mathrm{i}\underline{Q}\cdot\underline{\mathbf{r}}(t)), \mathbf{p}^2\right] = -\hbar\exp(\mathrm{i}\underline{Q}\cdot\underline{\mathbf{r}}(0))\left(\hbar Q^2 + 2\underline{Q}\cdot\underline{\mathbf{p}}\right) \tag{5.80}$$

follows. Since $\underline{\mathbf{p}}$ commutes with the Hamiltonian in the equation of motion the Hamiltonian can be applied directly on $\underline{\mathbf{r}}(0)$:

$$\mathrm{i}\hbar\frac{\mathrm{d}}{\mathrm{d}t}\exp(\mathrm{i}\underline{Q}\cdot\underline{\mathbf{r}}(t)) = -\frac{\hbar}{2m_{\mathrm{sc}}}\exp(\mathrm{i}\underline{Q}\cdot\underline{\mathbf{r}}(0))\left(\hbar Q^2 + 2\underline{Q}\cdot\underline{\mathbf{p}}\right) \tag{5.81}$$

This differential equation can be solved immediately and one obtains for the time dependent operator:

$$\exp(\mathrm{i}\underline{Q}\cdot\underline{\mathbf{r}}(t)) = \exp(\mathrm{i}\underline{Q}\cdot\underline{\mathbf{r}}(0))\exp\left(\frac{\mathrm{i}t}{2m_{\mathrm{sc}}}\left(\hbar Q^2 + 2\underline{Q}\cdot\underline{\mathbf{p}}\right)\right) . \tag{5.82}$$

With this result the correlator in the scattering function (5.39) can be calculated:

$$\left\langle\exp(-\mathrm{i}\underline{Q}\cdot\underline{\mathbf{r}}(0))\exp(\mathrm{i}\underline{Q}\cdot\underline{\mathbf{r}}(t))\right\rangle = \exp\left(\frac{\mathrm{i}\hbar Q^2}{2m_{\mathrm{sc}}}\right)\left\langle\exp\left(\frac{\mathrm{i}\hbar\underline{Q}\cdot\underline{\mathbf{p}}}{2m_{\mathrm{sc}}}\right)\right\rangle . \tag{5.83}$$

As in equation (5.72) the average is taken by using the Boltzmann factor yielding

$$\left\langle\exp\left(\frac{\mathrm{i}\hbar\underline{Q}\cdot\underline{\mathbf{p}}}{2m_{\mathrm{sc}}}\right)\right\rangle = \exp\left(-\frac{t^2Q^2k_{\mathrm{B}}T}{2m_{\mathrm{sc}}}\right) . \tag{5.84}$$

Insertion into (5.83) gives

$$\left\langle\exp(-\mathrm{i}\underline{Q}\cdot\underline{\mathbf{r}}(0))\exp(\mathrm{i}\underline{Q}\cdot\underline{\mathbf{r}}(t))\right\rangle = \exp\left(-\frac{Q^2}{2m_{\mathrm{sc}}}\left(t^2k_{\mathrm{B}}T - \mathrm{i}\hbar t\right)\right) . \tag{5.85}$$

identical to equation (5.74). Thus using the Van Hove correlation function we obtain the same result as was originally derived directly from the definition of the scattering function.

With this example we can also demonstrate that neglecting the operator character of the position vectors leads to a wrong result. If we write the scattering function using the classical expression (5.60)

$$S^{\mathrm{cl}}(Q,\omega) = \frac{1}{2\pi\hbar}\int_{-\infty}^{\infty} \mathrm{d}t \exp(-\mathrm{i}\omega t)\left\langle \exp\left(-\mathrm{i}\underline{Q}\cdot(\underline{r}(t)-\underline{r}(0))\right)\right\rangle \tag{5.86}$$

is obtained. For a free atom we have $\underline{r}(t) = \underline{r}(0) + t\underline{p}/m_{\mathrm{sc}}$. Inserting this expression into (5.86) and averaging leads to:

$$S^{\mathrm{cl}}(Q,\omega) = \sqrt{\frac{1}{4\pi E_{\mathrm{r}} k_{\mathrm{B}} T}}\exp\left(-\frac{\omega^2 m_{\mathrm{sc}}}{2k_{\mathrm{B}}TQ^2}\right). \tag{5.87}$$

Comparison with (5.73) shows that this result is wrong by neglecting the recoil energy term. Instead of being centred at E_{r} the expression (5.87) is symmetric with respect to $\omega = 0$.

References

[1] G. E. Bacon: "Neutron Diffraction" (Clarendon Press, Oxford, 1975).

[2] G. E. Bacon (ed.): "Fifty Years Of Neutron Diffraction: The Advent Of Neutron Scattering" (Adam Hilger, Bristol, 1986).

[3] S. W. Lovesey: "Theory of Neutron Scattering from Condensed Matter" (Clarendon Press, Oxford, 1984).

[4] G. L. Squires: "Introduction to the theory of thermal neutron scattering" (Cambridge University Press, Cambridge, 1978).

[5] M. Bée: "Quasielastic neutron scattering" (Adam Hilger, Bristol, 1988).

[6] J. L. Yarnell, M. J. Katz, R. G. Wenzel, S. H. Koenig, *Phys. Rev. A* **7** 2130 (1973).

[7] G. D. Wignall, D. G. H. Ballard, J. Schelten, *Eur. Polym. J.* **10** 861 (1973).

6. Continuum description: Grazing Incidence Neutron Scattering

O.H. Seeck, IFF8, FZ Jülich

6.1 Introduction

When studying solids or soft matter the explicit molecular structure is not always of particular importance. Quite often the properties investigated are long ranged and not directly connected with the atoms or their positions. One example is a material with a continuous ferromagnetic phase transition: Far below a well defined temperature (the critical temperature called Curie temperature) the material is in a complete ferromagnetic state. Far above no ferromagnetic behavior can be detected. Close to the critical temperature magnetic fluctuations appear. The typical width of the magnetic areas is in the range of several nanometers up to macroscopic distances depending on the temperature (see Fig. 6.1a). The width is basically independent of the lattice spacing or the particular kind of atoms. Therefore, the knowledge of the detailed molecular structure is not necessary to explain the physical properties of ferromagnets.

Other examples are surfaces or layer systems. The properties of the samples such as film thicknesses or in-plane correlation lengths are usually also long ranged compared to the atomic distances and the information about the exact atomic positions is not relevant (see Fig. 6.1b).

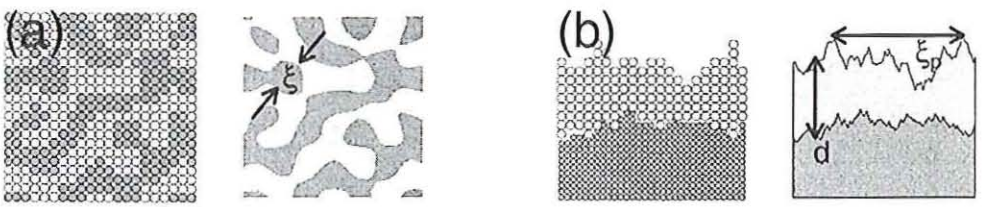

Figure 6.1: *Sketch of systems with relevant mesoscopic or macroscopic properties. (a) Ferromagnet close to the Curie temperature. Ordered regions with a correlation length* ξ *exist. (b) Monolayer system. The layer thickness* d *and the in-plane correlation length of the rough surface* ξ_p *are much larger than the atomic spacing. The left picture of each example shows the real atomic structure the right part the approximation as a continuous system.*

A straightforward method to investigate mesoscopic length scales without taking into account the exact molecular structure of the samples is the small angle scattering. 'Small angle' in this case means that the mean value of the wave vector transfer $|\underline{Q}|$ of the scattered beam is much smaller than the typical reciprocal spacing of the atoms in the sample (e.g., the reciprocal lattice vector $|\underline{a}^*|$ for a crystal with cubic symmetry). In this case the effects of the atomic structure on the scattered signal are negligible. This is schematically explained in Figure 6.2.

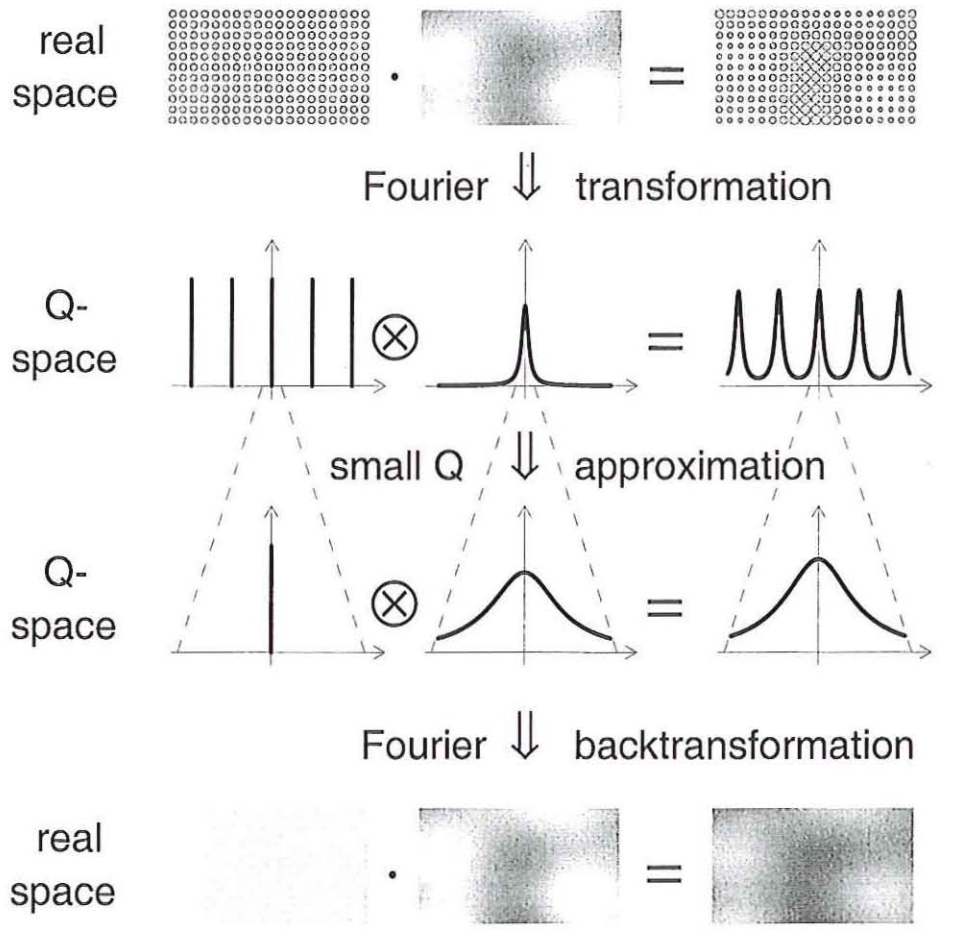

Figure 6.2: *Principles of small angle scattering. The method is not sensitive to the exact atomic structure but only to mesoscopic or macroscopic length scales. Therefore, samples can be treated as continuous systems. The operator ⊗ denotes the convolution of two functions. A more detailed explanation is given in the text.*

Starting point is the exact atomic structure of the sample. In this section a crystal with some density modulations is chosen (Fig. 6.2 top row). The potential $V(\underline{r})$ of such a system can be written as a product of the undisturbed infinite crystal lattice potential $V_{\mathrm{latt}}(\underline{r})$ and the modulation $V_{\mathrm{mod}}(\underline{r})$. As it was shown in previous sections in Born approximation the scattered intensity

$$I(\underline{Q}) \sim |A(\underline{Q})|^2 \sim \left|\int V(\underline{r})\exp(i\underline{Q}\cdot\underline{r})\mathrm{d}^3r\right|^2 = \left|\int V_{\mathrm{latt}}(\underline{r})V_{\mathrm{mod}}(\underline{r})\exp(i\underline{Q}\cdot\underline{r})d^3r\right|^2$$
$$= |\mathbf{F}\{V_{\mathrm{latt}}(\underline{r})V_{\mathrm{mod}}(\underline{r})\}(\underline{Q})|^2 \qquad (6.1)$$

of the sample can be calculated by performing a Fourier transformation $\mathbf{F}\{V(\underline{r})\}$ of $V(\underline{r})$. The convolution theorem for Fourier transformations can be used to modify equation (6.1). This theorem states that the convolution $\otimes$ of two Fourier transformed functions $f_i=\mathbf{F}\{g_i\}$ gives the same result as the Fourier transformation of the product of both functions g_i. Thus,

$$\mathbf{F}\{g_1 \cdot g_2\} = \mathbf{F}\{g_1\} \otimes \mathbf{F}\{g_2\} = f_1 \otimes f_2 = \int f_1(\underline{q}) f_2(\underline{q}-\underline{Q})\mathrm{d}^3q \qquad (6.2)$$

where the integral is the definition of the convolution.

It is also known from previous sections that for an infinite periodic crystal the lattice potential $V_{\mathrm{latt}}(\underline{r})$ can be written as a sum of delta-functions weighted with the scattering length and located at the position of the atoms. The Fourier transformation of $V_{\mathrm{latt}}(\underline{r})$ also yields delta-functions: the Bragg peaks at the reciprocal lattice positions. In contrast, the Fourier transformation of $V_{\mathrm{mod}}(\underline{r})$ is usually a 'smooth' function which is strongly decreasing for large $|\underline{Q}|$. The result of the convolution is depicted in the second row of Figure 6.2.

By doing a small angle scattering experiment only wave vector transfers $\underline{Q}$ with a mean value close to 0 are considered. All other values are omitted. The result of the magnification around $\underline{Q}=0$ is shown in the third row of Figure 6.2. In good approximation it is identical to a convolution of just a **single** delta-function at $\underline{r}=0$ with the Fourier transformation of $V_{\mathrm{mod}}(\underline{r})$. In real space (Fourier backtransformation) a single delta peak corresponds to an infinite sample with homogeneous potential which turns out to be the averaged value of $V_{\mathrm{latt}}(\underline{r})$. The fourth row of Figure 6.2 proofs that no information about the atomic structure is necessary to explain a small angle scattering pattern.

To study the morphology of surfaces or interfaces of thin layer systems such as polymer films on silicon substrates or magnetic multilayer systems some specific kinds of small angle neutron (or x-ray) scattering experiments can be performed. Especially for buried interfaces these surface sensitive methods are the only way to investigate the film properties without destroying the sample. Therefore, they are very frequently applied and have an enormous impact on solid states and soft condensed matter physics in general.

The so-called **specular reflectivity** is a scan with a wave vector transfer Q perpendicular to the sample surface which is defined as the z-direction in this section. Because of the missing Q_x- and Q_y-component the reflectivity is only sensitive to the thickness, the potential and the roughness of each film. In-plane properties of the interfaces such as lateral correlation lengths are accessible with different kinds of **diffuse scattering experiments** where at least one of the components Q_x or Q_y are not vanishing.

In the following, the specular reflectivity and the diffuse scattering are explained in more detail. The usual experimental setup will be shown and the basic theory of specular and diffuse scattering will be presented with some examples.

6.2 Experimental Principals of Surface Sensitive Neutron Scattering

A sketch of a typical neutron surface scattering experiment is displayed in Figure 6.3, a more detailed description is given in other sections. The direction of the primary beam is defined by some slits. Before the primary beam hits the sample the flux is usually monitored. The incident angle θ which is determined with respect to the sample surface is set by rotating the sample in the beam. The scattered beam is detected at an angle θ' (also with respect to the surface) which is determined by θ and the scattering angle $\phi=\theta'+\theta$. In the literature ϕ is sometimes called 2θ (which is actually inaccurate because ϕ is not necessarily equal to $2\cdot\theta$).

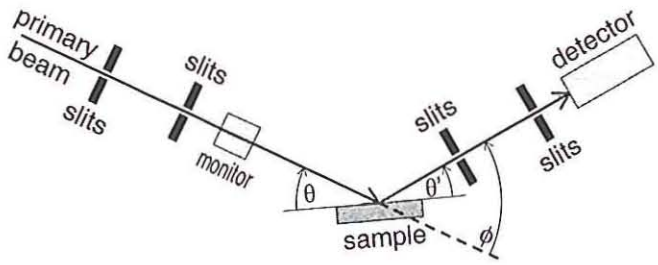

Figure 6.3: *Sketch of a typical surface sensitive neutron scattering experiment. The incident angle is denoted by* θ, *the outgoing angle with respect to the surface by* θ'. *The scattering angle is called* ϕ.

For specular reflectivity measurements the condition θ=θ' holds which is usually not true for diffuse scattering experiments. The mean value of the wave vector transfer is given by

$$|\underline{Q}| = \frac{4\pi}{\lambda}\sin\left(\frac{\phi}{2}\right) \tag{6.3}$$

with the de Broglie wavelength of the neutrons $\lambda = h/(2mE)^{1/2}$. As it was mentioned before for a small angle scattering experiment $|Q|$ has to be much smaller than the typical reciprocal distance of the atoms in the sample. Therefore, ϕ also has to be small. Depending on the chosen wavelength the angle ϕ is almost never larger than a few degrees. For a surface sensitive experiment, which is performed in reflection and not in transmission (see Fig. 6.4), this means that θ and θ' are also small and positive.

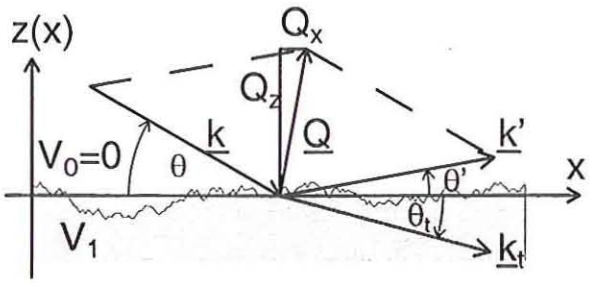

Fig. 6.4: *Sketch of the wave vectors for a surface sensitive experiment. The parameters of the transmitted beam are labeled with the index* t. *The potential of air is denoted by* V_0 *that one of the substrate with* V_1.

From simple geometrical considerations the components of the wave vector transfer can be deduced. They are defined by

$$Q_x = \frac{2\pi}{\lambda}(\cos\theta' - \cos\theta) \qquad Q_y = 0 \qquad Q_z = \frac{2\pi}{\lambda}(\sin\theta' + \sin\theta) \tag{6.4}$$

and can be used to estimate the accessible Q-range of surface sensitive experiments. At a typical wavelength of the neutrons of about 0.2nm=2Å and angles not larger than 1.0 degree Q_z would always be less than 0.1Å^{-1}. $|Q_x|$ would even be restricted to $5\cdot10^{-4}\text{Å}^{-1}$. For comparison: A simple cubic crystal with 3Å lattice spacing has a smallest reciprocal lattice vector of 2.1Å^{-1}.

6.3 Specular Neutron Reflectivity in Born Approximation

For specular reflectivity measurements the exit angle θ' is always identical to the incident angle θ. Therefore, the Q_x-component is equal to zero and the reflectivity data does not contain any particular information about the in-plane structure of the sample. In first order Born approximation [1] the scattered intensity is given by

$$I(Q_z) \sim \frac{1}{Q_z^4}\left|\int \frac{dV(z)}{dz}\exp(-iQ_z z)dz\right|^2 \tag{6.5}$$

which means, that the specular reflectivity is basically determined by the Fourier transformation of the gradient of the potential profile perpendicular to the sample surface. The averaged (continuous) potential of a particular material with N components is defined by

$$V = \frac{2\pi\hbar^2}{m_n}\sum_{j=1}^{N} b_j \rho_j \tag{6.6}$$

where the b_j are the scattering lengths and the ρ_j are the particle number densities of the components. A one-component sample with a perfectly smooth and flat surface which is oriented in the (x,y)-plane would yield a step function for the z-dependent potential:

$$V(z) = \frac{2\pi\hbar^2 b\rho}{m_n}\left(\frac{1}{2} - \frac{1}{2}\Theta(z)\right) = \begin{cases} 0 & : \ z > 0 \\ 2\pi\hbar^2 b\rho / m_n & : \ z \le 0 \end{cases} \tag{6.7}$$

The derivative of $V(z)$ is a delta-function $dV(z)/dz \sim \delta(z)$. With Eq. (6.5) one gets $I(Q_z) \sim Q_z^{-4}$ because the Fourier transformation of a delta-function at $z=0$ is identical to 1.

However, a perfectly smooth and flat surface does not exist. Instead surface roughness or density gradients have to be taken into account [2,3]. As shown in Fig. 6.5 roughness means that the z-position of the surface is locally different from the mean position at $z=0$. Averaging the density in the (x,y)-plane at each z-coordinate gives a smooth profile $V(z)$ perpendicular to the surface. The exact shape of the profile depends on the actual physical and chemical properties close to the surface. For simple rough surfaces in good approximation an error-function

$$V(z) = \frac{V}{2} - \frac{V}{2}\mathrm{erf}\left(\frac{z}{\sqrt{2}\sigma}\right) \qquad \text{with} \qquad \mathrm{erf}(z) = \frac{2}{\sqrt{\pi}}\int_0^z \exp(-t^2)\mathrm{d}t \tag{6.8}$$

is sufficient to model the profile. The parameter σ is called rms-roughness and is a measure for the root mean square width of $V(z)$ given by the gaussian probability function

$$\frac{\mathrm{d}V(z)}{\mathrm{d}z} \sim P(z) = \frac{1}{\sqrt{2\pi}\sigma}\exp\left(-\frac{z^2}{2\sigma^2}\right). \tag{6.9}$$

Figure 6.5 also shows that the profile does not contain any information about the lateral structure of the rough surface. Therefore, the reflectivity is insensitive to different in-plane length scales ξ_p. It even cannot be used to distinguish between a rough interface or a density gradient caused by e.g., interdiffusion. It will be explained later that this can only be done by using diffuse scattering experiments.

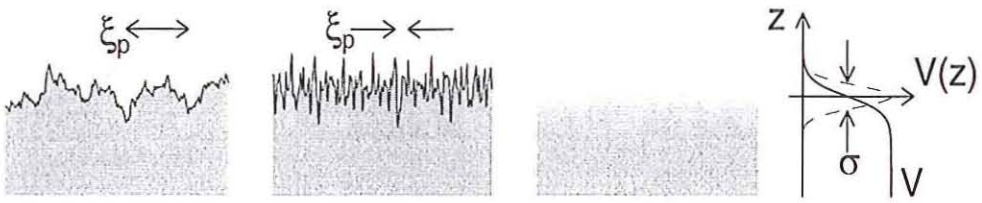

Figure 6.5: *Three different surfaces with the same rms-roughness σ determined by the root mean square width of the probability function (dashed line) of the profile* V(z) *(solid line). The in-plane structure is determined by the lateral correlation length* ξ_p *which is large for the very left example quite small for the rough surface shown in the center and not defined for the density gradient example (right).*

The reflectivity of a rough surfaces with an error function profile can easily be calculated. The derivative of $V(z)$ is determined by the probability function P(z) [see Eq. (6.9)]. With Eq. (6.5) this yields $I(Q_z) \sim Q_z^{-4}\exp(-Q_z^2\sigma^2)$. Compared with the perfectly smooth surface the reflected intensity is damped by a Debye-Waller factor: The rougher the surfaces the less intensity is reflected at large Q_z (see Figure 6.6 left).

Reflectivity scans are not only extremely sensitive to surfaces roughnesses but also to film thicknesses of layer systems. If a thin film with thickness d and an averaged potential V_1 is deposited on a substrate with potential V_2 the density profile $V(z)$ is given by

$$V(z) = \begin{cases} 0 & : \quad z > d \\ 2\pi\hbar^2 b_1\rho_1 / m_n = V_1 & : \quad d \geq z > 0 \\ 2\pi\hbar^2 b_2\rho_2 / m_n = V_2 & : \quad 0 \geq z \end{cases} \tag{6.10}$$

if the interfacial rms-roughnesses σ_1 and σ_2 are neglected. The derivative yields two delta-functions: $dV(z)/dz \sim (b_2\rho_2 - b_1\rho_1)\delta(z) + b_1\rho_1\delta(z-d)$. Using Eq. (6.5), the specularily reflected intensity of a perfectly smooth monolayer system is given by

$$I(Q_z) \sim \frac{1}{Q_z^4}\left[\left(b_2\rho_2 - b_1\rho_1\right)^2 + \left(b_1\rho_1\right)^2 + 2\left(b_2\rho_2 - b_1\rho_1\right)\left(b_1\rho_1\right)\cos\left(Q_z d\right)\right]. \tag{6.11}$$

This means that films cause oscillations in the reflectivity. The period is determined by the film thickness the strength (usually called 'contrast') by the difference of the potentials V_1 and V_2 (see Fig. 6.6 right).

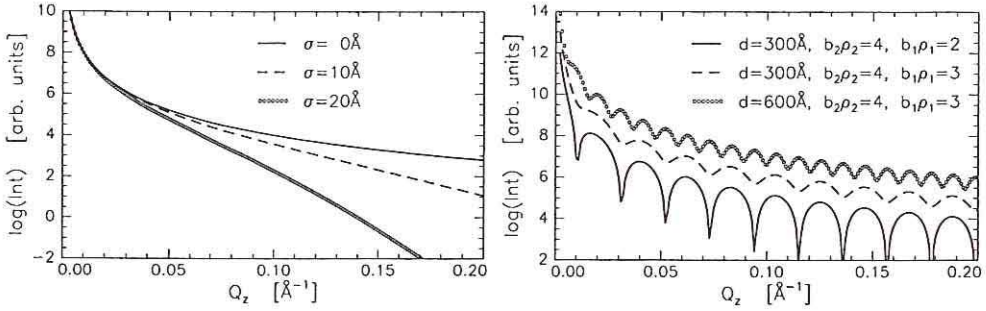

Figure 6.6: *The left graph displays the effect of the surface roughness on the specularily reflected intensity: the rougher the surface the less intensity is reflected at large* Q_z. *The right figure shows reflectivities of perfectly smooth monolayer systems. The curves are shifted in intensity for clarity. The thicker the film the smaller the distance of the so-called Kiessig fringes. The less the contrast (given by* $[b_2\rho_2 - b_1\rho_1]$*) the less pronounced the oscillations are.*

In this way every additional layer appears as an oscillation in the reflectivity curve. Interface roughnesses can also quite easily be included in the theory and yield a typical damping of each oscillation. Multilayer systems with different parameters for each layer generally show very complicate reflectivities. They are usually difficult to analyze especially because of the so-called 'phase problem' which prevents an unambiguous solution of Eq. (6.5). The „phase problem" appears when performing the mean square of the complex function

$F\{dV(z)/dz\}$ to calculate the reflected intensity [see Eq. (6.5)]. The loss of the phase information may end up in identical reflectivities even though the potential profiles are different. E.g., using Eq. (6.11) it can easily be shown, that a monolayer system with $b_2\rho_2=4$ and $b_1\rho_1=3$ exactly results in the same reflectivity as $b_2\rho_2=4$ and $b_1\rho_1=1$, if the film thicknesses are identical.

6.4 Diffuse Neutron Scattering in Born Approximation

Performing a surface scattering experiment it turns out that some intensity is also scattered in directions with $\theta\neq\theta'$. In this case the wave vector transfer $\underline{Q}$ has a component in Q_x-direction (see Fig. 6.4). This off-specular signal is called diffuse scattering and is caused by lateral structures (in-plane, in the (x,y)-plane) of the sample [4]. If the samples are perfectly smooth or if there is no lateral structure (see Fig. 6.5 right) no diffuse scattering is expected.

In general, for rough layer systems the diffuse scattering is sensitive to the correlation function $C_{jk}(\underline{R})$ between two interfaces j and k where $\underline{R}$ is an in-plane vector (x,y). The correlation function is defined by

$$C_{jk}(\underline{R}) = \int z_j(\underline{r}) z_k(\underline{r}+\underline{R}) \mathrm{d}^2 r \tag{6.12}$$

with the local deviation $z_j(\underline{r})$ from the averaged position of the interface j. The correlation function between two different interfaces is usually called 'cross-correlation'. If $j=k$ holds $C_{jk}(\underline{R})=C_{jj}(\underline{R})$ is called 'auto-correlation'. Qualitatively, $C_{jk}(\underline{R})$ is large if two areas of the interfaces j and k, which are $\underline{R}$ apart from each other, 'look similar'. E.g., if the two interfaces contain a periodic structure with the same periodic distance D the correlation function exhibits maxima at D,$2D$,$3D$ ... . For an auto-correlation function of a single rough surfaces one gets a monotone decreasing function: For very small distances the parts of the surface look similar, the larger the distance the more different they become. The width of the curve is connected to the lateral correlation length ξ_p of the interface (see e.g., Fig 6.5) [5].

The diffuse scattering can be used to investigate periodic in-plane structures, in-plane correlation lengths of a single rough interface and correlations between two different interfaces. Figure 6.7 depicts some examples. The complete mathematical formalism to deduce the diffusely scattered intensity is quite complicate [6]. Therefore, the full theory is omitted in this section. Instead, the diffuse scattering is explained using a simple monolayer system.

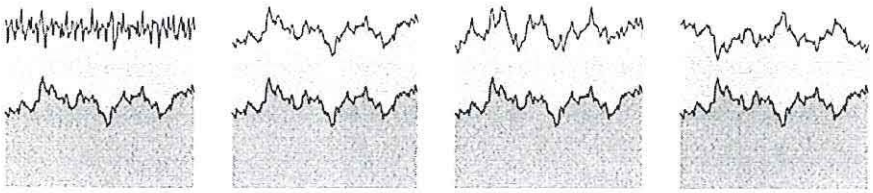

a) b) c) d)

Figure 6.7: *Some examples of monolayer systems with rough surfaces. a) Both interfaces are not correlated at all. b) Perfect cross-correlation between the lower and the upper interface. c) A cross-correlation is visible but it is not perfect: The interfaces do not exactly look the same. d) Perfectly anti-correlated interfaces.*

In Born Approximation the diffusely scattered intensity of a monolayer system with the interfaces j=1,2 and the film thickness d can be calculated by

$$I_{\text{diff}}(Q_x,Q_z) \sim \frac{1}{Q_z^2}\Big[(b_2\rho_2 - b_1\rho_1)^2 \exp\left(-Q_z^2\sigma_2^2\right)S_{22}(Q_x) + (b_1\rho_1)^2 \exp\left(-Q_z^2\sigma_1^2\right)S_{11}(Q_x) + 2(b_2\rho_2 - b_1\rho_1)(b_1\rho_1)\exp\left(-Q_z^2\left[\sigma_2^2+\sigma_1^2\right]/2\right)S_{12}(Q_x)\cos(Q_z d)\Big] \tag{6.13}$$

The rms-roughnesses are given by $\sigma_{1,2}$ and the so-called structure factor by

$$S_{jk}(Q_x) = \int\left(\exp\left[Q_z^2 C_{jk}(x)\right] - 1\right)\exp\left(-iQ_x x\right)\mathrm{d}x\,. \tag{6.14}$$

Eq. (6.13) obviously looks similar to Eq. (6.11) which describes the specular reflectivity. The exponential Debye-Waller functions would also appear in Eq. (6.11) if roughness is taken into account, the only difference are the additional structure factors $S_{jk}(Q_x)$ which modify the scattering due to the in-plane structure of the interfaces.

Some examples of diffuse scattering experiments are depicted in Fig. 6.8. They show that the in-plane correlation length ξ_p of a rough surface (see Fig 6.5) is directly connected with the width of the diffuse scattering in Q_x-direction. Furthermore, a Q_z-scan at fixed Q_x contains the information about cross-correlations of two interfaces. If cross-correlations are present with $S_{jk}\neq 0$ for $j\neq k$ the last term of Eq. (6.13) leads to characteristic oscillations of the diffuse scattering which are in-phase with the specular reflectivity in the case of correlated interfaces and out-of-phase in the case of anti-correlation.

Equation (6.13) also shows that the diffuse scattering can be detected in the whole Q-space even at Q_x=0 which is actually the position of the specularily reflected signal. This means that reflectivity measurements (Q_z-scans at Q_x=0) **always** contain both the specular reflectivity and the diffuse scattering at Q_x=0. To extract the specular reflectivity from the reflectivity measurement the diffuse scattering has to be subtracted. This is usually done by performing a Q_z-scan with a small offset ΔQ_x so that the specular condition is not exactly matched. This so-called longitudinal diffuse scan is subtracted from the measured reflectivity to get the true specular reflectivity.

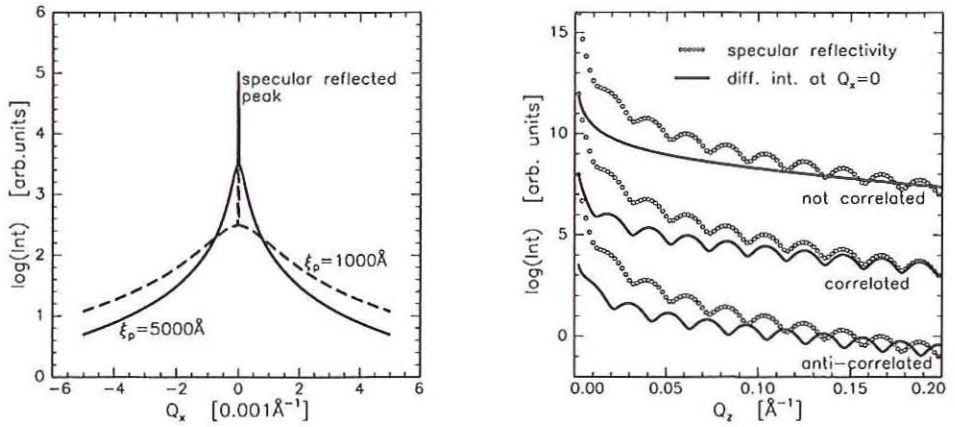

Figure 6.8: *Examples of diffuse scattering experiments. Left:* Q_x*-scan at fixed* Q_z *from a single rough surface. The solid curve corresponds to a sample with an in-plane correlation length of* ξ_p=*5000Å the dashed line to* ξ_p=*1000Å. The peaks at the condition* Q_x=*0 (where* θ=θ'*) are* ***not*** *diffuse scattering but caused by the specular reflectivity. Right: Specular reflectivity (symbols) and diffuse scattering* Q_z*-scans at* Q_x=*0 (solid lines) of a monolayer system with* d=*300Å,* $b_2\rho_2$=*4,* σ_2=*5Å,* $b_1\rho_1$=*3 and* σ_1=*5Å. The diffuse scans show the effect of cross-correlations. The* ***measured*** *reflectivity is determined by the sum of the specular and the diffuse scan.*

Unfortunately, the intensity of the diffuse scattering is usually orders of magnitude smaller than the specularily reflected signal. To get good statistics and reliable data a very high primary flux is necessary. This can easily be achieved with synchrotron radiation x-ray sources but is hardly possibly for neutron sources (see section 6.5). Therefore, it is extremely difficult to extract quantitative information from the neutron diffuse scattering data.

6.5 The Regime of the Total External Reflection: Exact Solution of the Wave Equation

It is obvious that the Born approximation [Eqs. (6.5) and (6.13)] fails for $Q_z \to 0$ because the intensity would become infinite at $Q_z=0$. The reason is that multiple scattering processes are neglected within the Born approximation. For surface sensitive experiments multiple scattering processes become essential at very small angles [7]. An exact description of the scattered intensity can be deduced for a perfectly smooth surface from quantum theory.

Starting point is the Schrödinger equation

$$\left[-\frac{\hbar^2}{2m_n}\Delta + V(\underline{r})\right]\Psi(\underline{r}) = E\Psi(\underline{r}) \tag{6.15}$$

for the wave function of the neutrons $\Psi(\underline{r})$. The energy of the neutrons is given by $E = \hbar^2 k^2 / (2m_n)$ with the mean value $k=2\pi/\lambda$ of the wave vector $\underline{k}$ (the incident and the outgoing beam have identical k because elastic scattering is assumed). For a homogeneous sample the potential is determined by Eq. (6.6), thus

$$\left[\Delta + \left(k^2 - 4\pi\sum_j b_j\rho_j\right)\right]\Psi(\underline{r}) = \left[\Delta + k^2\left(1 - \frac{\lambda^2}{\pi}\sum_j b_j\rho_j\right)\right]\Psi(\underline{r}) = \left[\Delta + k_t^2\right]\Psi(\underline{r}) = 0 \tag{6.16}$$

with the wave vector k_t inside the medium (see Fig. 6.4). From Eq. (6.16) it is justified to introduce the refraction index $n_t=k_t/k$ of the material. In very good approximation one yields

$$n_t = 1 - \frac{\lambda^2}{2\pi}\sum_j b_j\rho_j = 1 - \delta_t \tag{6.17}$$

for the refraction index which is a number close to 1 for neutrons of approximate 1Å wavelength (the correction δ_t is called **dispersion** and is on the order of $10^{-5}...10^{-6}$)

By introducing the refraction index the basic principles of optics can be applied for all further considerations. First of all it is remarkable that for many materials n_t is smaller than 1 (because b_j is usually and ρ_j always positive, thus δ_t is usually positive). This means that the transmitted beam is refracted towards the sample surface ($\theta_t<\theta$, see Fig. 6.4). For values of θ below the so-called **critical angle** θ_c the incoming beam cannot penetrate the sample surface

but is completely reflected. The critical angle can be estimated by $\theta_c \approx (2\delta_t)^{1/2}$ and is on the order of some 0.1 degree depending on the density, the scattering lengths of the atoms and the wavelength of the neutrons. For θ values beyond θ_c the beam can penetrate the sample and is only partly reflected. At the sample surface the reflection and transmission coefficients r_f and t_f are obtained by the Fresnel formulars

$$r_f = \frac{k_z - k_{t,z}}{k_z + k_{t,z}} \qquad \text{and} \qquad t_f = \frac{2k_z}{k_z + k_{t,z}} \tag{6.18}$$

with $k_z = k\sin\theta$ and $k_{t,z} = k_t\sin\theta_t = k(n_t^2 - \cos^2\theta)^{1/2}$ (see Fig. 6.4). The specular reflected intensity $I = |r_f|^2$ is determined by the absolute square of the reflection coefficient. It shows the typical plateau below the critical angle, the regime of the total external reflection, and the rapidly decreasing intensity beyond θ_c. With appropriate approximations one gets $I \approx \delta_t^2/(4\sin^4\theta) \sim Q_z^{-4}$ for incident angles θ larger than $3\delta_t$ which is the confirmation of the Born approximation (see Fig. 6.9).

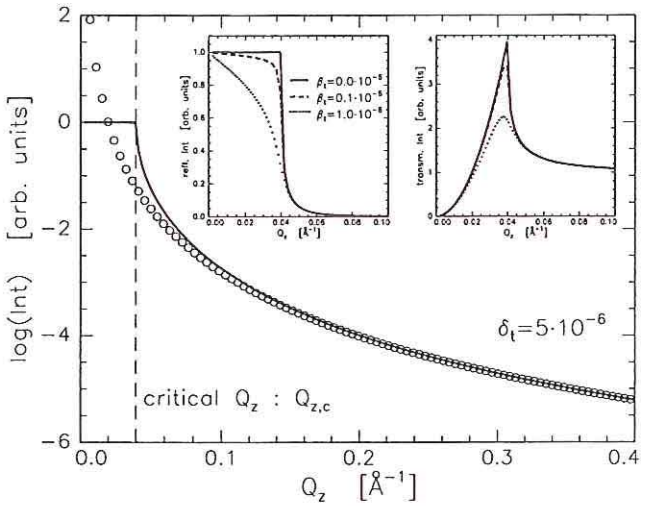

Figure 6.9: *Effect of the total external reflection. The large figure shows a reflectivity of a smooth surface in Born approximation (symbols) and the exact Fresnel form (solid line). The dashed line marks the critical* Q_z. *The left inset displays absorption effects in the reflectivity on a linear scale. The same is depicted for the transmitted intensity in the right inset.*

Not addressed yet in this section is the **absorption** β_t of the neutrons inside the sample. For most materials such as silicon the absorption is negligible but this is not the case for e.g. cadmium or indium. Most straightforward, it can be introduced by including an imaginary part to the refraction index

$$n_t = 1 - \delta_t + i\beta_t . \tag{6.19}$$

The effect of the absorption is shown in Fig. 6.9. It basically smoothes the sharp features of the intensity close the critical angle and also restricts the penetration depth of the neutrons to finite values.

The diffuse scattering is also modified in the regime of the total external reflection [8,9]. In good approximation one gets

$$I_{\text{diff}}(Q_x, Q_z) \sim \left|t_f(\theta)\right|^2 Q_z^{-2} \exp\left(-Q_z^2\sigma_1^2\right) S_{11}(Q_x) \left|t_f(\theta')\right|^2 \tag{6.20}$$

for a single rough surface. For layer systems this expression becomes much more complicate. Eq. (6.20) shows, that the transmission functions of the incoming and the outgoing beam have to be taken into account. The transmission function t_f exhibits a maximum at the critical angle (or the critical Q_z, respectively, see Fig. 6.9) because for incident angles $\theta = \theta_c$ an evanescent wave appears which runs parallel to the surface ($\theta' = 0$) [10]. Therefore, the diffuse scattering also has maxima called Yoneda wings at the positions $\theta=\theta_c$ and $\theta'=\theta_c$ (see Fig.6.10).

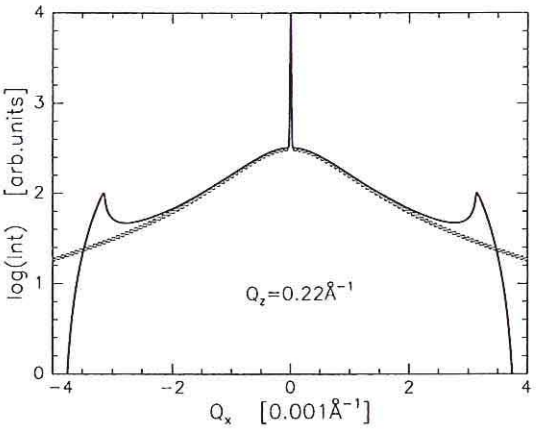

Figure 6.10: *Diffuse scattering scan at fixed* Q_z. *The symbols correspond to the Born approximation (dashed line in Fig. 6.8). The solid line displays the better approximation including the scattering effects due to the total external reflection at* $\theta=\theta_c$ *and* $\theta'=\theta_c$. *They are visible as the Yoneda-maxima at* $|Q_x|\approx 0.0032\text{Å}^{-1}$.
The peak at the center is the specular reflected intensity ($\theta=\theta'$).

In summary, the optical properties of the sample affect the scattering only if the incident or the exit angle is comparable or smaller than the critical angle which is usually smaller than

0.4°. The full dynamical theory can only be deduced for the specular reflectivity. For the diffuse scattering no exact solution exist right now.

6.6 Important Applications of Neutron Reflectrometry

For many standard scattering experiments on layer systems x-rays are much more suitable than neutrons because of the higher flux, the better collimation and the less divergence. In numbers: A standard synchrotron radiation source has a primary beam intensity of about 10^{10} counts/sec at a typical spot size of $(0.2\times1)mm^2$. The beam divergence which determines the Q-space resolution is less than 1/100 of a degree. For a modern neutron source one gets less than 10^7 counts/sec in an area of $(0.5\times20)mm^2$ with a divergence of larger than 0.02°.

However, for some topics of research neutron scattering is superior. One example is the investigation of materials which mainly contain hydrogen, carbon, nitrogen or oxygen such as organic molecules. In this case the electron density [which for x-rays replaces the potential $V(\underline{r})$] is very low and the x-ray contrast becomes very small. In contrast, for neutron $V(\underline{r})$ strongly depends on the isotope of the elements. Therefore, by using deuterated or hydrogenated organic materials the scattering contrast can easily be tuned without changing the chemical properties of the samples. Figure 6.11 shows an example of a polymer bilayer.

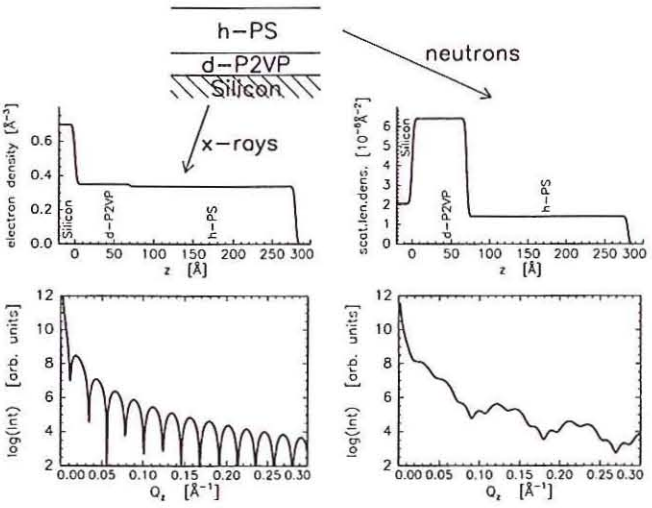

Figure 6.11: *Comparison of an x-ray (left column) and a neutron (right column) reflectivity of a polymer bilayer (210Å polystyrene [PS] on 70Å deuterated polyvinylpyrridine [d-P2VP] on a silicon substrate). The x-ray contrast between the two polymers given by the electron density is only about 5%.*

It can clearly be seen that the x-ray reflectivity only exhibits one significant oscillation period which is due to the whole film thickness. The x-ray contrast at the polymer interface is

too small to modulate the intensity. Advanced analyzing methods have to be used to extract the information of the polymer-polymer interface [11]. This is different for neutrons: By deuterating the bottom polymer the contrast is enhanced dramatically. The reflectivity shows separate oscillations: a long period due to the thin d-P2VP film and a short period which is caused by the h-PS film. The analysis is straightforward and usually very reliable.

Another very important application is the magnetic neutron scattering. Neutrons have a spin of 1/2 which means that they are sensitive to the magnetization of the sample. A sketch of a magnetic neutron reflectivity experiment is depicted in Fig. 6.12. The sample is illuminated with polarized neutrons. The polarization is determined by the direction of the neutron spins with respect to an external field $\underline{H}$: They are usually either parallel or antiparallel to $\underline{H}$.

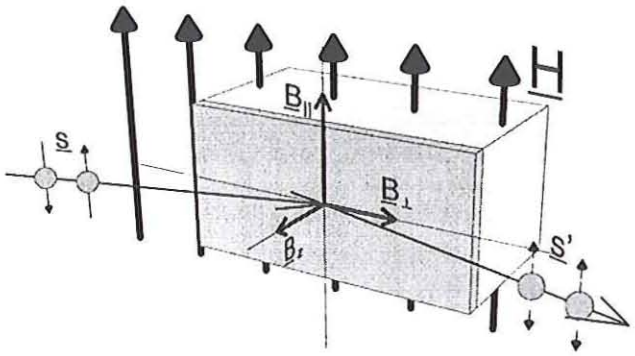

Figure 6.12: *Sketch of a neutron reflectivity experiment on a magnetic layer. The spins of the incident neutrons* $\underline{s}$ *are oriented parallel (either up or down) to an external field* $\underline{H}$. *After the scattering the direction of the spins* $\underline{s}$' *may have flipped depending on* $\underline{B}$ *which is given by the magnetization of the film and* $\underline{H}$.

After the scattering process the spin direction of the neutrons may have flipped. Thus, four different reflectivities can be measured:

- R_{++} : The spins of the incident neutrons are parallel to $\underline{H}$. The spins of the scattered neutrons are also parallel to $\underline{H}$ (non-spin-flip process).
- R_{--} : The spins of the incident neutrons are antiparallel to $\underline{H}$. The spins of the scattered neutrons are also antiparallel to $\underline{H}$ (non-spin-flip process).
- R_{+-} : The spins of the incident neutrons are parallel to $\underline{H}$. The spins of the scattered neutrons are antiparallel to $\underline{H}$ (spin-flip process).
- R_{-+} : The spins of the incident neutrons are antiparallel to $\underline{H}$. The spins of the scattered neutrons are parallel to $\underline{H}$ (spin-flip process).

The four reflectivities can be deduced from the Schrödinger equation considering the external field, the magnetization of the sample and the spin direction of the neutrons [12]. In the following only some qualitative descriptions are given.

1) If no magnetic induction $\underline{B}$ (which is determined by the external field $\underline{H}$ and the magnetization of the sample) is present one yields $R_{++} = R_{--}$ and $R_{+-} = R_{-+} = 0$. Thus, there is no dependence of the scattering on the spin orientation of the incoming neutrons.
2) If $\underline{B} = \underline{B}_z$ (magnetic induction perpendicular to the surface) no magnetic scattering is expected either. The reason are the Maxwell equations which do not allow a change of the mean value of $\underline{B}$ in field direction ($\underline{\nabla} \cdot \underline{B} = 0$). This means that $\underline{B}$ does not change at the sample surfaces. Therefore, $R_{++} = R_{--}$ and $R_{+-} = R_{-+} = 0$.
3) If $\underline{B} = \underline{B}_\parallel$ only non-spin-flip processes appear ($\underline{s} = \underline{s}'$). The reason is the vanishing cross product between $\underline{s}$ and $\underline{B}$. This means that no interaction between the spins and the induction is present so that the spins cannot flip. However, a magnetic contribution to the refraction index has to be added for R_{++} and subtracted for R_{--}. Thus, $R_{++} \neq R_{--}$ but still $R_{+-} = R_{-+} = 0$.
4) If $\underline{B} = \underline{B}_\perp$ the spins can flip during the scattering process. Therefore, non-spin-flip processes appear with $R_{+-} \neq 0$ and $R_{-+} \neq 0$. In contrast to point 3) the non-spin-flip reflectivities are identical ($R_{++} = R_{--}$).

In summary, from all reflectivities R_{++}, R_{--}, R_{+-} and R_{-+} the exact magnitude and orientation of the magnetization profile of the sample can be determined with polarized neutron reflectivity.

References

[1] J. Als-Nielsen, *Topics in Current Physics. Structure and Dynamics of Surfaces* (Springer, Berlin, 1986).

[2] P. Beckmann, A. Spizzichino, *The Scattering of Electromagnetic Waves From Rough Surfaces* (Pergamon, New York, 1963).

[3] L. Névot, P. Croce, Revue de Physique appliqué **15**, 761 (1980).

[4] S.K. Sinha, E.B. Sirota, S. Garoff. H.B. Stanley, Phys. Rev. B **38**, 2297 (1988).

[5] A.L. Barabási, H.E. Stanley, *Fractal Concepts in Surface Growth* (Cambridge University Press, Cambridge, 1995).

[6] V. Holý, J. Kubena, I. Ohlídal, K. Lischka, W. Plotz, Phys. Rev. B **47**, 15896 (1993).

[7] J. Lekner, *Theory of Reflection* (Martinus Nijhoff, Dordrecht, Boston, 1987).

[8] S. Dietrich, A. Haase, Phys. Rep. **260**, 1 (1995).

[9] V. Holý, U. Pietsch, T. Baumbach, *X-Ray Scattering from Thin Films (High Resolution X-Ray Scattering from Crystalline Thin Films)* (Springer Tracts in Modern Physics, Vol. 149, Berlin, 1998).

[10] H. Dosch, *Critical Phenomena at Surfaces and Interfaces (Evanescent X-Ray and Neutron Scattering)* (Springer Tracts in Modern Physics, Vol. 126, Berlin, 1992).

[11] O.H. Seeck, I.D. Kaendler, M. Tolan, K. Shin, M.H. Rafailovich, J. Sokolov, R. Kolb, Appl. Phys. Lett. **76**, 2713 (2000).

[12] C.F. Majkrzak, J.F. Ankner, N.F. Berk, D. Gibbs, *Neutron and X-Ray Diffraction Studies of Magnetic Multilayers* (in: *Magnetic Multilayers*, World Scientific, Singapore, 1994).

7. Diffractometer

G. Heger

7.1 Introduction

For pure elastic scattering the scattering function $S(\underline{Q},\omega)$ is reduced to the special case without energy transfer ($E_0 = E_1$ and $\hbar\omega = E_0 - E_1 = 0$) and equal length of the wave vectors of the incident and scattered beams ($|\underline{k_0}| = |\underline{k_1}|$). $S(\underline{Q},\omega = 0)$ and hence the scattering intensity is only depending on the scattering vector $\underline{Q} = \underline{k_0} - \underline{k_1}$. The coherent elastic neutron scattering (≡ neutron diffraction) yields information on the positions (distribution) of the atomic nuclei and the arrangement of the localised magnetic spins in crystalline solids, the pair correlation function of liquids and glasses, and the conformation of polymer chains.

Depending on the scientific problem to be investigated adequate diffraction methods may be quite different. For fluids and glasses diffraction data of high statistical relevance over a very large $|\underline{Q}|$ range are required. The direction of the scattering vector $\underline{Q}$ is not defined for these non-crystalline states and a good resolution $|\Delta\underline{Q}|/|\underline{Q}|$ is of no importance. Besides of the pure elastic scattering also inelastic contributions are involved.

Completely different are the needs for a diffraction study of crystalline solids. The diffraction at the crystal lattice gives rise to pure elastic scattering localised at the nodes of the so-called reciprocal lattice. The scattering vectors $\underline{Q}$ for the different "Bragg-reflections" are well defined. For the separation of reflections with similar $\underline{Q}$ values a good resolution $\Delta\underline{Q}/\underline{Q}$ is very important. A measured data-set of Bragg-intensities (integrated intensities of Bragg-reflections) as complete as possible over a large $|\underline{Q}|$ range is required. An experimental stability and accuracy leading to a precision of the intensity data of about 2% is desired and may be achieved.

Diffraction measurements on polycrystalline samples depend only on the length of the scattering vector $|\underline{Q}|$. Very small line widths (according to an excellent resolution $|\Delta\underline{Q}|/|\underline{Q}|$) combined with well defined reflection profiles are prerequisites for a quantitative line-profile analysis. The complete powder diagrams resulting from overlapping reflections are described and analysed by means of the Rietveld method.

For all diffraction methods firstly the energy of the incident neutron beam (expressed in another way as its wavelength or velocity) must be specified. In the case of angular dispersive diffraction, the 2-axes diffractometer (see Fig. 1) is equipped with a crystal monochromator to

select a special wavelengths band ($\lambda \pm \Delta\lambda/\lambda$) out of the "white" beam according to the Bragg condition for its scattering plane *(hkl)*

$$2d_{hkl}\cdot\sin\theta_{hkl} = \lambda, \qquad (1)$$

with the interplanar spacing d_{hkl} and the monochromator scattering angle $2\theta_{hkl} = 2\theta_M$. The width of the wavelengths band $\Delta\lambda/\lambda$, which is important for the Q-resolution, depends on the divergences of the beam before and after the monochromator (collimations α_1 and α_2), on the mosaic spread of the monochromator crystal ΔM, and on the monochromator angle $2\theta_M$. In order to increase the intensity of the monochromatic beam at the sample position the monochromator crystal is often bent in vertical direction perpendicular to the diffraction plane of the experiment. In this way the vertical beam divergence is increased leading to a loss of resolution in the reciprocal space. The diffracted intensity from the sample is measured as a function of the scattering angle 2θ and the sample orientation (especially in case of a single crystal):

for a single crystal $\rightarrow$ $I(\underline{Q})$, and for a polycrystalline sample $\rightarrow$ $I(|\underline{Q}|)$.

2θ is defined by the collimators α_2 and α_3. As there is no analysis of the energy of the

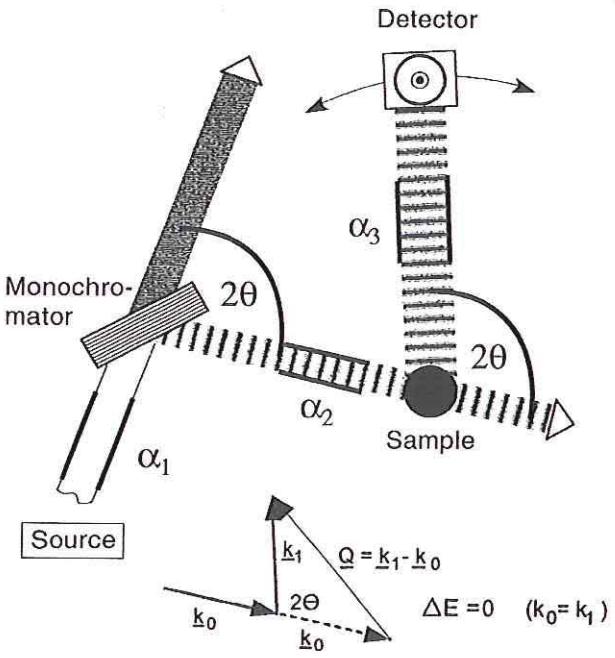

Fig. 1. Schematic representation of a 2-axes diffractometer.

scattered beam behind the sample, the energy resolution $\Delta E/E$ of a 2-axes diffractometer is not well defined (typically of the order of some %). In addition to the dominant elastic scattering also quasi-elastic and some inelastic scattering contributions are to be taken into account. The name 2-axes-diffractometer results from its two axes of rotation, the monochromator axis defining $2\theta_M$ and the sample axis (2θ).

In the case of energy dispersive diffraction, the time-of-flight diffractometer uses the complete energy spectrum of a pulsed neutron beam and the wavelengths of the scattered neutrons are determined by velocity analysis. The measurement of the neutron intensity as a function of velocity at fixed scattering angle 2θ has to be calibrated according to the energy spectrum of the neutron beam. Assuming no energy transfer at the sample the time-of-flight diffraction yields again $I(\underline{Q})$ (and for a polycrystalline sample $I(|\underline{Q}|)$).

7.2 Reciprocal lattice and Ewald construction

Bragg scattering (diffraction) means coherent elastic scattering of a wave by a crystal. The experimental information consists of the scattering function $S(\underline{Q},\omega = 0)$ with no change of energy or wavelength of the diffracted beam. For an ideal crystal and an infinite lattice with the basis vectors $\underline{a}_1$, $\underline{a}_2$, $\underline{a}_3$, there is only diffraction intensity $I(\underline{H})$ at the vectors

$$\underline{H} = h\underline{a}_1^* + k\underline{a}_2^* + l\underline{a}_3^* \qquad (2)$$

of the reciprocal lattice. h,k,l are the integer Miller indices and $\underline{a}_1^*$, $\underline{a}_2^*$, $\underline{a}_3^*$, the basis vectors of the reciprocal lattice, satisfying the two conditions

$$\underline{a}_1^* \cdot \underline{a}_1 = \underline{a}_2^* \cdot \underline{a}_2 = \underline{a}_3^* \cdot \underline{a}_3 = 1 \text{ and } \underline{a}_1^* \cdot \underline{a}_2 = \underline{a}_1^* \cdot \underline{a}_3 = \underline{a}_2^* \cdot \underline{a}_1 = \ldots = 0,$$

or in terms of the Kronecker symbol with i, j and k = 1, 2, 3

$$\delta_{ij} = 0 \text{ for } i \neq j \text{ and } \delta_{ij} = 1 \text{ for } i = j \text{ with } \delta_{ij} = \underline{a}_i^* \cdot \underline{a}_j^*. \qquad (3)$$

The basis vectors of the reciprocal lattice can be calculated from those of the unit cell in real space

$$\underline{a}_i^* = (\underline{a}_j \times \underline{a}_k)/V_c, \qquad (4)$$

where $\times$ means the cross product, and $V_c = \underline{a}_1 \cdot (\underline{a}_2 \times \underline{a}_3)$ is the volume of the unit cell.

Here is a compilation of some properties of the reciprocal lattice:

- The reciprocal lattice vectors are perpendicular to those in real space: $\underline{a}_i^* \perp \underline{a}_j$ and $\underline{a}_k$ $(i \neq j,k)$
- The lengths of the reciprocal lattice vectors are $|\underline{a}_i^*| = 1/V_c \cdot |\underline{a}_j| \cdot |\underline{a}_k| \cdot \sin\angle(\underline{a}_j, \underline{a}_k)$.
- Each point *hkl* in the reciprocal lattice refers to a set of planes (*hkl*) in real space.

• The direction of the reciprocal lattice vector $\underline{H}$ is normal to the (*hkl*) planes and its length is reciprocal to the interplanar spacing d_{hkl}: $|\underline{H}| = 1/d_{hkl}$.

• Duality principle: The reciprocal lattice of the reciprocal lattice is the direct lattice.

From the positions of the nodes of the reciprocal lattice obtained by diffraction experiments one can determine directly the parameters of the unit cell of a crystal.

Although somewhat abstract, the concept of the reciprocal space provides a practical tool to express geometrically the condition for Bragg scattering in the so-called Ewald construction. In this way the different diffraction methods can be discussed.

We consider the reciprocal lattice of a crystal and choose its origin 000. In Fig. 2 the wave vector $\underline{k}_0$ (defined in the crystallographers' convention with $|\underline{k}_0| = 1/\lambda$) of the incident beam is marked with its end at 000 and its origin P. We now draw a sphere of radius $|\underline{k}_0| = 1/\lambda$ around P passing through 000. Now, if any point *hkl* of the reciprocal lattice lies on the surface of this Ewald sphere, then the diffraction condition for the (*hkl*) lattice planes is fulfilled: The wave vector of the diffracted beam $\underline{k}$ (with its origin also at P) for the set of planes (*hkl*), is of the same length as $\underline{k}_0$ ($|\underline{k}| = |\underline{k}_0|$) and the resulting vector diagram satisfies $\underline{k} = \underline{k}_0 + \underline{H}$. Introducing the scattering angle 2θ (and hence the Bragg angle θ_{hkl}),we can deduce immediately from $2|\underline{k}|\cdot\sin\theta = |\underline{H}|$ the Bragg equation:

$$2d_{hkl}\cdot\sin\theta_{hkl} = \lambda. \qquad (5)$$

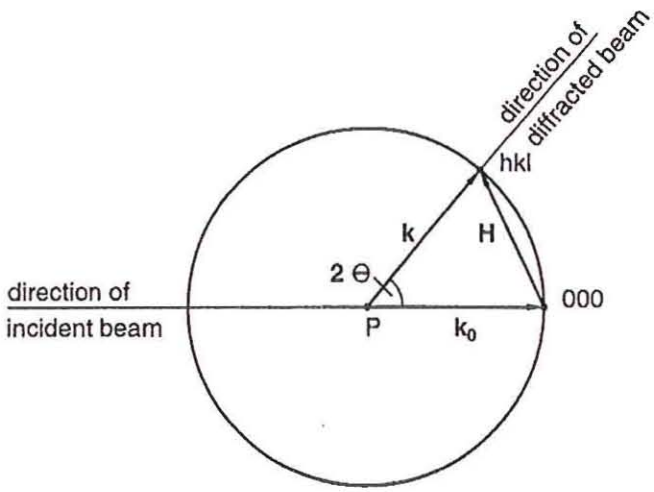

Fig. 2. Ewald construction in reciprocal space, showing the diffraction condition for the *hkl* reflection.

In the case of single crystal diffraction a rotation of the crystal and therefore also of the corresponding reciprocal lattice (which is rigidly attached to the crystal) is often used to set the diffraction conditions for the measurement of intensities $I(\underline{H})$.

If $|\underline{H}| > 2/\lambda$ (then $d_{hkl} < \lambda/2$) the reflection *hkl* cannot be observed. This condition defines the so called limiting sphere, with center at 000 and radius $2/\lambda$: only the points of the reciprocal lattice inside the limiting sphere can be rotated into diffraction positions. Vice versa if $\lambda > 2d_{max}$, where d_{max} is the largest interplanar spacing of the unit cell, then the diameter of the Ewald sphere is smaller then $|\underline{H}|_{min}$. Under these conditions no node of the reciprocal lattice can intercept the Ewald sphere. That is the reason why diffraction of visible light (wavelength $\cong$ 5000 Å) can never be obtained from crystals. λ_{min} determines the amount of information available from a diffraction experiment. In ideal conditions λ_{min} should be short enough to measure all points of the reciprocal lattice with significant diffraction intensities.

For a real crystal of limited perfection and size the infinitely sharp diffraction peaks (delta functions) are to be replaced by broadened line shapes. One reason can be the local variation of the orientation of the crystal lattice (mosaic spread) implying some angular splitting of the vector $\underline{H}$. A spread of interplanar spacings $\Delta d/d$, which may be caused by some inhomogeneities in the chemical composition of the sample, gives rise to a variation of its magnitude $|\underline{H}|$. The ideal diffraction geometry on the other hand is also to be modified. In a real experiment the primary beam has a finite divergence and wavelength spread. The detector aperture is also finite. A gain of intensity, which can be accomplished by increasing the angular divergence and wavelengths bandwidth, has to be paid for by some worsening of the resolution function and hence by a limitation of the ability to separate different Bragg reflections.

All of these influences can be studied by the Ewald construction. The influence of a horizontal beam divergence on the experimental conditions for a measurement of Bragg-intensities of a single crystal is illustrated in Fig. 3 where strictly monochromatised radiation (only one wavelength λ with $\Delta\lambda/\lambda = 0$) is assumed. A so-called ω-scan, where the crystal is rotated around the sample axis perpendicular to the diffraction plane, may be used for a reliable collection of integrated intensities in adapting the detector aperture $\Delta 2\theta$ as a function of the scattering angle 2θ. It is obvious that larger $\Delta 2\theta$-values will give rise to a higher background and may lead to difficulties for the separation of neighboured reflections with similar $\underline{H}$-vectors in the reciprocal lattice. It is shown by this example that a larger beam divergence with an increase in intensity can restrict the resolution conditions.

Bragg-intensities of single crystals are recorded in general by $\omega/n{\cdot}2\theta$-scans ($0 \leq n \leq 1$) with a coupled rotation of the sample and the detector. The mainly used bisectic special case consists of $\omega = \theta$. The horizontal and vertical detector aperture must be chosen in a way to avoid systematic errors from cutting some intensity of a reflection. The pure ω-scan (rocking-scan) records an intensity distribution of reflection almost perpendicular to the scattering vector $\underline{Q} = 2\pi\underline{H}$ – i.e. almost corresponding to a transversal scan. The $\omega/2\theta$-scan represents a longitudinal scan in reciprocal space recording reflection profiles along $\underline{H}$.

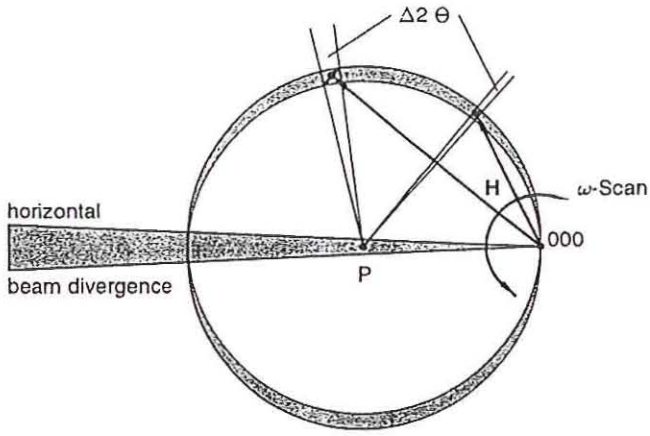

Fig. 3. Ewald-construction: Influence of the horizontal beam divergence on the experimental conditions for the measurement of Bragg-intensities

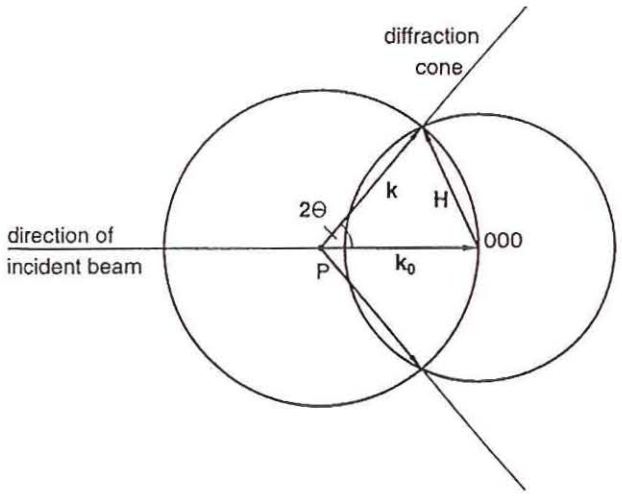

Fig. 4. Ewald-construction in case of powder diffraction

Powder diffraction also may be discussed on the basis of the Ewald-construction. An ideal polycrystalline sample is characterised by a very large number of arbitrary oriented small crystallites. Therefore, for a powder only $|\underline{H}|$ is defined without preferred orientation. In Fig. 4 the corresponding sphere with radius $|\underline{H}| = 1/d_{hkl}$ is drawn around the origin of the reciprocal lattice at 000. For each Bragg-reflection the circle of intersection with the Ewald-sphere yields a diffraction cone. All reflections with equal interplanar spacing are perfectly superposed and cannot be separated.

7. 3 Powder diffractometer

There are two principally different powder diffraction techniques: the angular-dispersive ADP-method and the energy-dispersive EDP-method, better known as time-of-flight method in the case of neutron diffraction. In the ADP measurement the sample is irradiated by a monochromatic beam (λ = const.). To each d_{hkl} belongs a Bragg-angle θ_{hkl}.Most of the neutron powder diffractometers at steady-state reactor sources work according to the ADP method (e. g. the D2B-instrument at the HFR/ILL in Grenoble). The angular resolution of a powder diffraction diagram depends on the beam divergences before and behind the

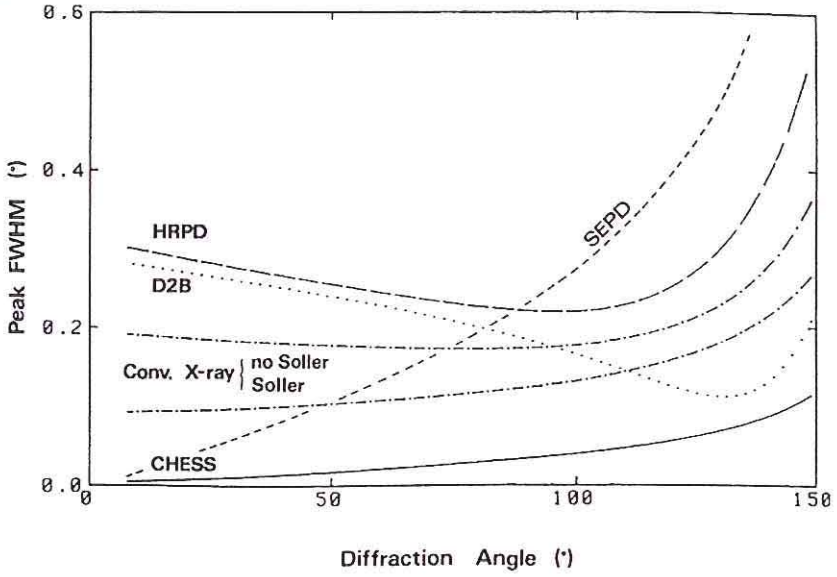

Fig. 5. Comparison of the half-widths of powder lines for selected neutron powder diffractometers: D2B at the HFR/ILL in Grenoble(F), HRPD at NBSR in Lucas Heights (USA), SEPD at ANL in Argonne (USA) – the time-of-flight data of this instrument with $\Delta d/d \approx 1.5 \cdot 10\text{-}3$ are converted in 2θ-values – and X-ray powder diffractometers: conventional and synchrotron facilities (CHESS, USA) [1]

monochromator, on the mosaic spread of the monochromator crystal, and on the monochromator's scattering angle $2\theta_M$. In Fig. 5 for several X-ray- and neutron powder diffractometers the half-width of powder lines (Bragg-reflections) $\Delta 2\theta$ is given as a function of the scattering angle 2θ. A large $2\theta_M$-value can be favourable to realise smaller line widths $\Delta 2\theta$ at higher diffraction angles as can be seen for the D2B-instrument ($2\theta_M = 135°$).

The plan of the E9 instrument at the HMI-reactor BER II in Berlin is shown in Fig. 6. The typical technical data of this new powder diffractometer are:

- collimations $\alpha_1 = 10'$, $\alpha_2 = 20'$, $\alpha_3 = 10'$
- germanium and graphite monochromators with mosaic-spreads $\Delta M(Ge) \approx 20'$ and $\Delta M(PG) \approx 30'$
- monochromator's scattering angle $40° \leq 2\theta_M \leq 140°$
- 64 high pressure gas detectors (^3He, 8 bar) arranged with an angular interval of $\Delta 2\theta = 2.5°$

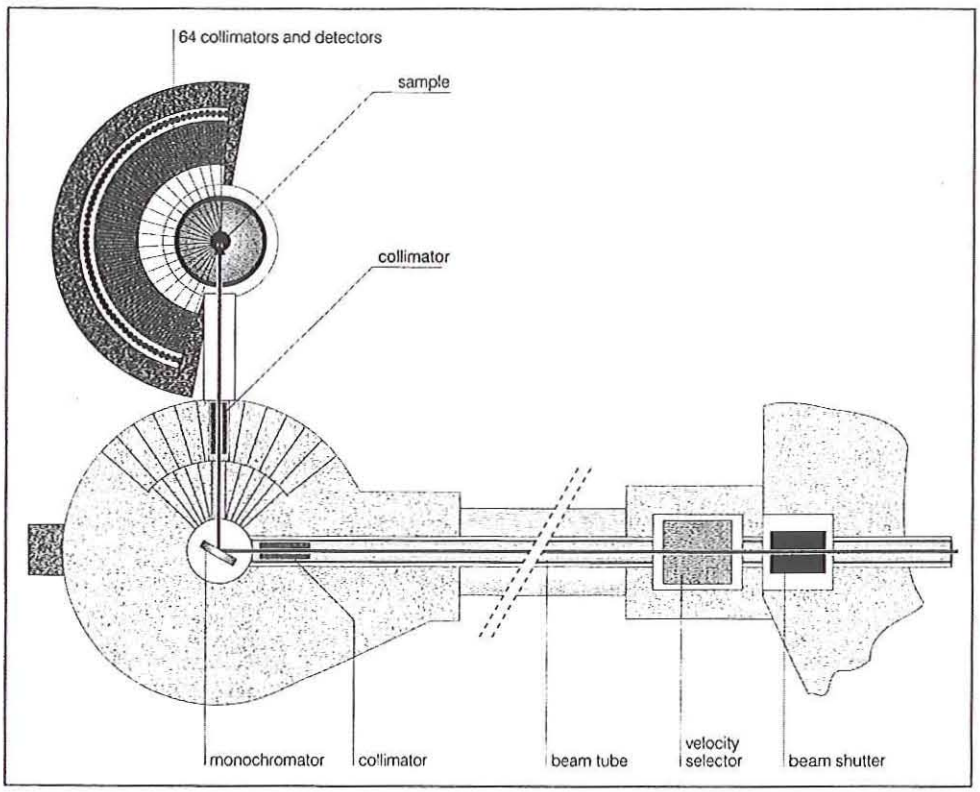

Fig. 6. Plan of the E9 powder diffractometer at BER II/HMI in Berlin.

For a ADP-powder diffractometer the measuring time can be reduced substantially by the simultaneous use of many single detectors or of linear multidetector systems.

As an example for a 2-axes diffractometer specially designed for the investigation of amorphous systems and liquids the 7C2-instrument installed at the hot neutron source of the ORPHEE-reactor in Saclay (F) is shown in Fig. 7. Combined with an exchange of monochromator crystals there are three different standard wavelengths available: λ(Ge(111)) = 1.1 Å, λ(Cu(111)) = 0.7 Å, λ(Ge(311)) = 0.57 Å. The linear multidetector allows a continuous intensity measurement over a range in scattering angle of 128°. The angular resolution of this instrument is limited as there is no collimation in between the sample position and the detector. But the $|\underline{Q}|$-range is very large. For the shortest wavelength λ(Ge(311)) = 0.57 Å the accessible values extend up to $|\underline{Q}|_{max} = 2\pi|\underline{H}|_{max} = 20$ Å^{-1}.

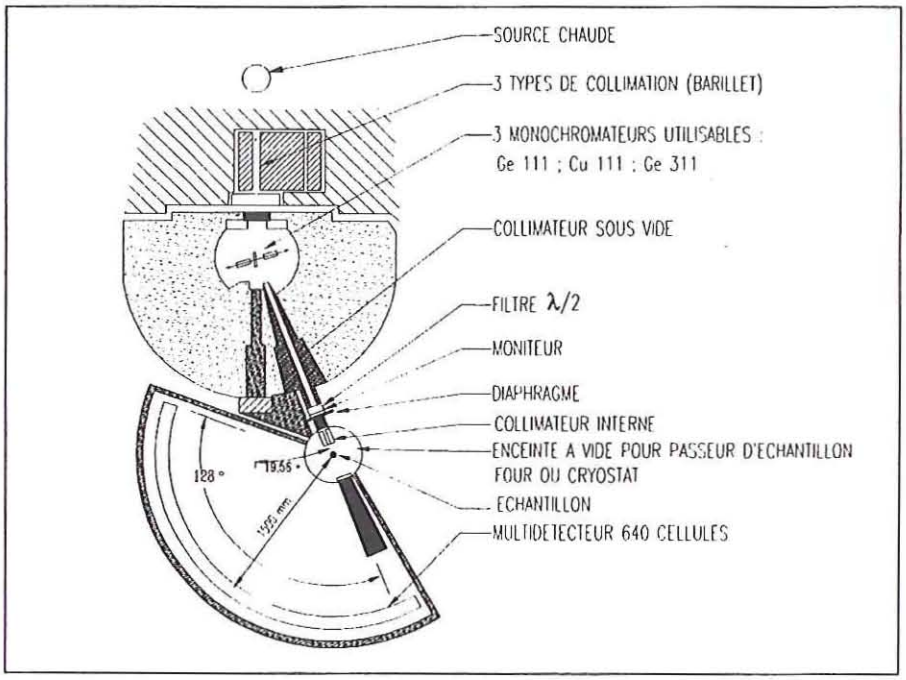

Fig. 7. Plan of the 2-axes diffractometer 7C2 at the hot source of the ORPHEE-reactor in Saclay (F)

In the case of the EDP method a polychromatic white beam is used with the scattering angle being fixed (2θ = const.). The d_{hkl}-values result from the time-of-flight measurement of the neutron velocities – converted to wavelengths - for the *hkl* reflections. This technique is specially suitable for pulsed neutron sources. Moreover, it offers some advantages for

complex sample environments, such as extreme temperatures, magnetic fields, external pressures, etc. due to its fixed scattering geometry. The resolution of the time-of-flight analysis $\Delta t/t$ depends on the wavelength-dependant pulse structure of the moderator, on the length of the flight path, and on the scattering angle 2θ (a back-scattering geometry is recommended). As there are normally relatively short wavelengths in the beam, too, also higher indexed reflections with shorter d_{hkl}-values may be reached. Some typical technical data of the HRPD installed at the spallation source ISIS/RAL in England are shown in Fig. 8. A special feature of this instrument consists in the very long flight path of about 100 m.

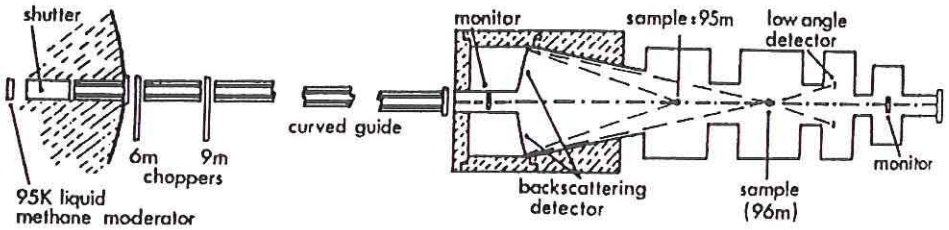

Fig. 8. HRDP (high-resolution powder diffractometer) at the spallation source ISIS/RAL, England. A resolution of $\Delta d/d \approx 4 \cdot 10^{-4}$ is achieved with a sample position at 95 m.

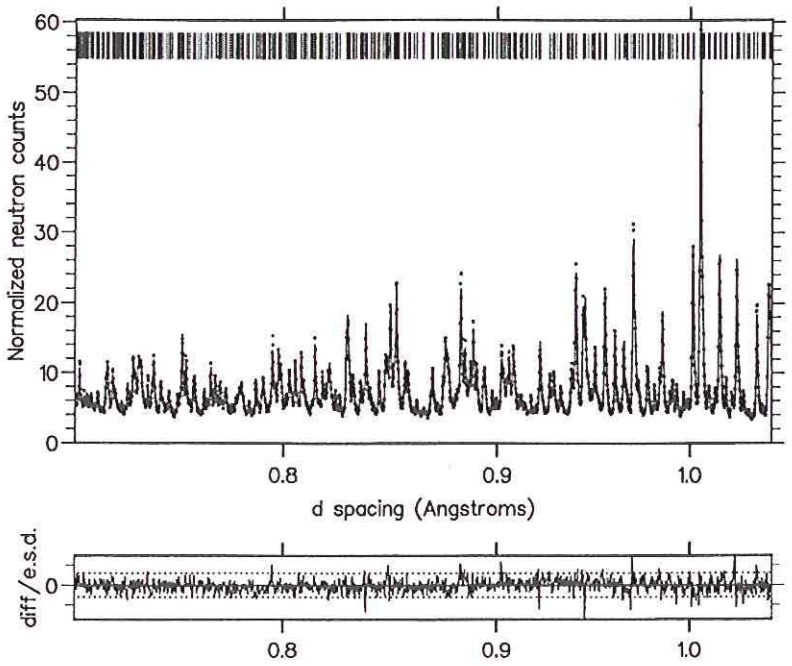

Fig. 9. Powder diffractogram of benzene: (a) section from 0.72 Å ≤ d ≤ 1.03 Å

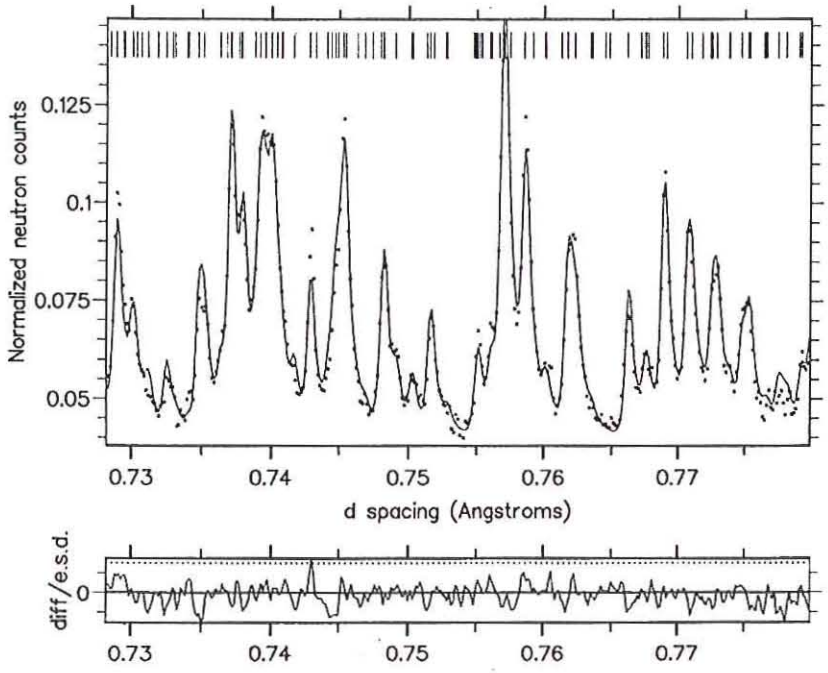

Fig. 9. Powder diffractogram of benzene: (b) enlarged section from 0.73 Å ≤ d ≤ 0.78 Å
The calculated d_{hkl}-values are indicated by the small lines at the top of the upper graph. The quality of the refinement can be judged from the difference in between experimental data and profile calculation in the lower graph.

The excellent resolution of this time-of-flight diffractometer is demonstrated by sections of the powder diffractogram of benzene shown in Fig. 9. The complete rage of 0.5 ≤ d ≤ 2.0 Å was analysed by means of the Rietveld profile method in order to refine the crystal structure of this molecular compound [2] (space group Pbca; lattice parameters: a = 7.3551 Å, b = 9.3712 Å, c = 6.6994 Å).

7.4 Single crystal diffractometer

For neutron diffraction studies on single crystals actually there are in use the Laue-method with 2-dim. positional sensitive detectors (e.g. LADI-instrument with an image-plate detector at HFR/ILL in Grenoble (F)) and 2-axes diffractometers with single detectors. New developments with 2-dim. detection systems become more and more important.

To fulfil the diffraction condition for all vectors $\underline{H}$ of the reciprocal lattice (within $2\sin\theta/\lambda < |\underline{H}|_{max}$) single crystal diffractometers are equipped with a special goniometer consisting of three independant rotations. The eularian cradle in Fig. 10 has in addition to the ω-axis (⊥ to

the diffraction plane) two further rotation axes χ and φ, which are perpendicular to each other. The χ-axis is also perpendicular to the ω-axis. Together with the rotation axis of the detector 2θ ($\parallel$ to the ω-axis) this mechanical unit is called 4-circle goniometer (leading to the name 4-circle diffractometer for this type of single crystal diffractometers). The measurement of integrated intensities $I(\underline{H})$ of individual Bragg-reflections is performed according to the $\omega/n{\cdot}2\theta$-scan techniques described in chapter 7.2. For a computer-controlled automatic data collection a detailed knowledge of the crystal lattice is needed. Therefore, a single crystal diffraction experiment starts by a systematic search of reflections in varying χ and φ, with the restriction $\omega = \theta$ (bisected condition). From the accurate angular positions of typically 20 indexed reflections the lattice constants and the orientation matrix are determined.

As an example for a single crystal neutron diffractometer the P110/5C2-instrument installed at the hot neutron source of the ORPHEE-reactor in Saclay (F) is shown in Fig. 10. The monochromatic neutron flux at the sample position is increased by a monochromator system with vertical focussing. The use of small wavelengths allows the measurement of Bragg-intensities up to large $|\underline{H}|$-values ($|\underline{H}|_{max} = 2\sin\theta_{max}/\lambda = 2.8$ Å^{-1}).

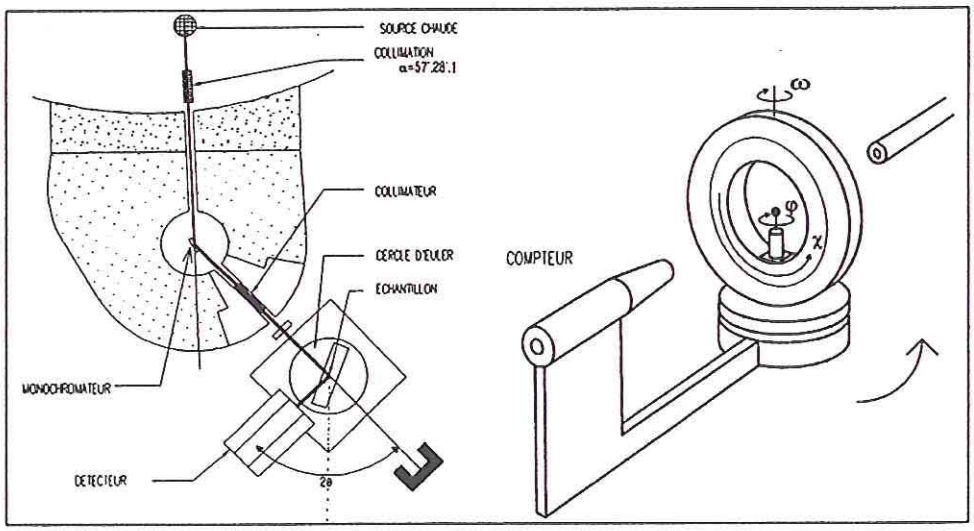

Fig. 10. Single crystal diffractometer P110/5C2 at the hot neutron source of the ORPHEE-reactor in Saclay (F)

Attention: The lengths of both the vector $\underline{H}$ of the reciprocal lattice used in crystallography and the scattering vector $\underline{Q}$ of solid state physics are expressed in Å^{-1}. But there is a factor of 2π which means that $|\underline{H}| = 2.8$ Å^{-1} corresponds to $|\underline{Q}| = 17.6$ Å^{-1}.

The influence of the primary collimation α_1 on the half-width of Bragg-reflections of a perfect Ge crystal is shown in Fig. 11. The resolution curves for two different wavelengths λ(Cu(420)) = 0.525 Å and λ(Cu(220)) = 0.831 Å are plotted as a function of sin θ/λ.

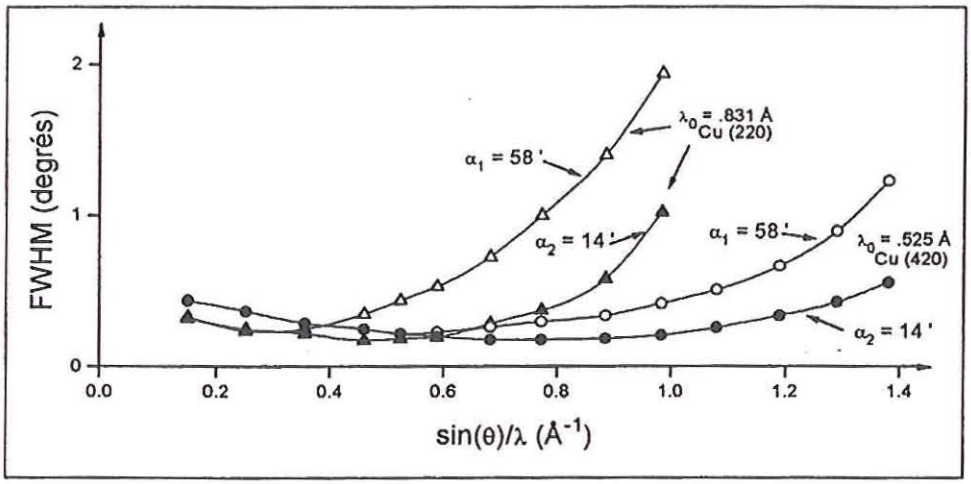

Fig. 11. Resolution curves of the single crystal diffractometer P110/5C2 at the hot neutron source of the ORPHEE-reactor in Saclay (F)

References

[1] R. J. Hill, The Riedveld Method, ed. R. A. Young, Chap. 5, Oxford University Press (1993)

[2] W. I. F. David and J. D. Jorgensen, The Riedveld Method, ed. R. A. Young, Chap. 11, Oxford University Press (1993)

8. Small-angle Scattering and Reflectometry

Dietmar Schwahn

8.1. Introduction

The methods of elastic scattering with neutrons deliver structural information from arrangements of atoms and magnetic moments in condensed material. Those arrangements can be precipitated phases in mixtures of metals, low molecular liquids or polymers and one gets information about size, number density and correlations between the objects. In scattering experiments the intensity of neutrons is measured as a function of momentum transfer Q

$$Q = \frac{4\pi}{\lambda} \sin \Theta \tag{8.1}$$

with the scattering angle 2Θ and the wavelength λ of the neutrons. $\underline{Q}$ is the difference of the wave numbers $\underline{k}$ (absolute value $k = 2\pi/\lambda$) of incoming and scattered neutrons. The momentum transfer is inversely proportional to the length scale of investigation; at Q of the order of $1\,\text{Å}^{-1}$ one measures inter atomic distances and in the region $10^{-1}\,\text{Å}^{-1} - 10^{-4}\,\text{Å}^{-1}$ mesoskopic objects of sizes between $10\text{Å} - 10^{4}\,\text{Å}$. For all these investigations specialized instruments have been developed. In this lecture we will introduce instruments for small angle scattering and reflectometry with neutrons. With these instruments objects within the bulk and at the surface are investigated. The main elements of these elastic methods will be separately introduced in the last part of the lecture. We will discuss instruments working at stationary nuclear research reactors. In future spallation sources will become the more important sources as they show a larger neutron flux with a periodic time structure; those instruments need quite different conditions for optimization.

8.2. Intensity at Sample and Detector

In Fig. 8.1 the traces of neutrons for elastic scattering are depicted in real and reciprocal space. The *intensity at the sample* (in linguistic usage: primary intensity) is determined according to

$$\Delta I_0 = L \cdot F \cdot \Delta\Omega \tag{8.2}$$

by the *luminosity of the source* given in units [$\text{cm}^{-2}\,\text{s}^{-1}$ steradian^{-1}]

$$L=\frac{\Phi}{2\pi}\left(\frac{k}{k_T}\right)^4 e^{-(k/k_T)^2}\,\frac{\Delta k}{k} \tag{8.3}$$

for neutrons with wave vector $\underline{k}$, the irradiated area of the sample F, and the divergency of the primary beam described by the space angle $\Delta\Omega$. The luminosity L is determined by the total

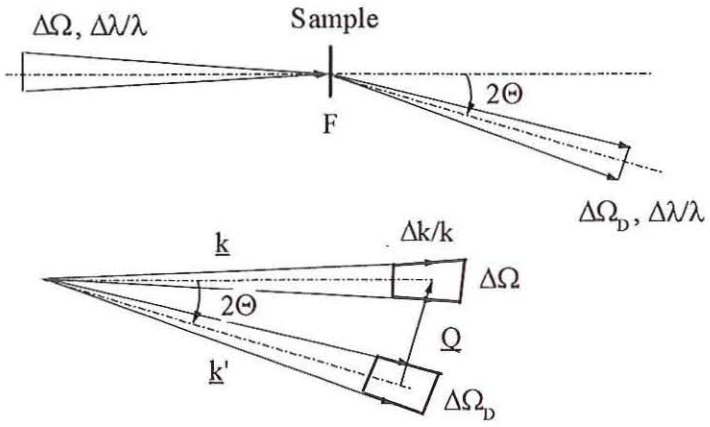

Figure 8.1: *Traces of neutrons in real- und reciprocal space*

thermal flux of the neutrons Φ, the temperature of the moderator $(h/2\pi)^2\, k_T^2/2m = k_B T$ and the resolution of wave length distribution according to $\Delta k/k$ and determined by the monochromator. The scattered intensity in a detector element with space angle $\Delta\Omega_D$ and scattering angle 2Θ or scattering vector $\underline{Q}$ respectively is given as

$$\Delta I_D(\Theta;\underline{Q}) = \Delta I_0 \cdot D \cdot T \cdot \frac{d\Sigma}{d\Omega}(\Theta;\underline{Q}) \cdot \Delta\Omega_D \tag{8.4}$$

with sample thickness D and diminution coefficient T of the primary intensity (transmission). The macroscopic scattering cross section $d\Sigma/d\Omega$ is the experimental result and is usually given in absolute units [1/cm].

8.3. Small Angle Scattering with Neutrons

The method of small angle scattering (SANS) is a broadly used tool in research. There are three different SANS techniques: The pin-hole SANS, the double crystal diffractometer, and the focusing SANS. The first two types of instruments are being used in our laboratory in Jülich, and a first focusing SANS instrument is presently built and will start operation in our laboratory within the next year.

8.3.1. Pin-Hole SANS

The principle lay out of a pin-hole SANS is depicted in Fig. 8.2. After the fission process, thermalization, and a further moderation in the *cold source* the neutrons are guided through *neutron guides* to the instrument. Monochromator and collimator are filters for neutrons with a predetermined wave length and divergency. The collimator consists of two apertures of

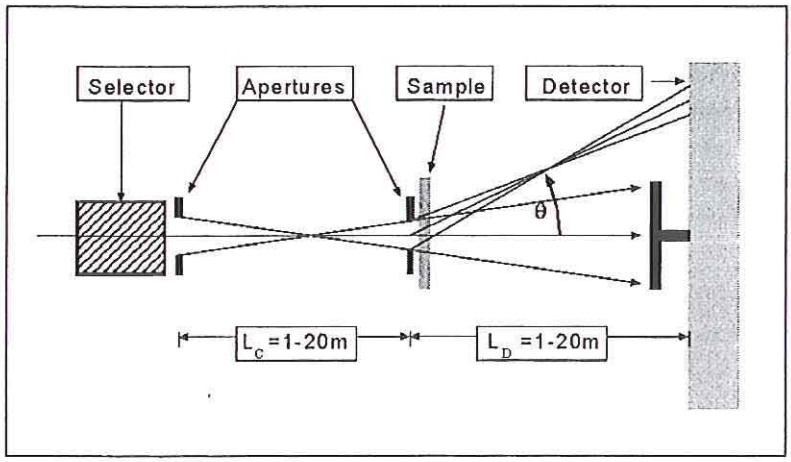

Figure 8.2: *Principle design of pin hole SANS*

neutron absorbing material as f.i. Cd and as monochromator one has a *velocity selector,* delivering a monochromatic beam of wave lengths between 5 and 15 Å with a relative mean square deviation of about $<\delta\lambda^2>^{0.5} / <\lambda> = 0.1$. After passing both apertures the neutrons irradiate the sample and part of the neutrons are scattered. The thickness of the sample should be adjusted in a way, that only about 10% of the neutrons are scattered in order to avoid remarkable effects from multiple scattering. The scattered neutrons are counted in a *two dimensional local sensitive detector.* The neutrons not scattered by the sample remain in the primary beam and are absorbed in the beam stop in front of the detector. The resolution function of this experiment is given as

$$<\delta Q^2> = \frac{k^2}{12}\left[\left(\frac{d_D}{L_D}\right)^2 + \left(\frac{d_E}{L_S}\right)^2 + d_S^2\left(\frac{1}{L_S} + \frac{1}{L_D}\right)^2 + \Theta^2\left(\frac{\delta\lambda}{<\lambda>}\right)^2\right] . \qquad (8.5)$$

The symbols L_S und L_D represent the distances between the two apertures and between sample and detector, the symbols d_D and d_E the diameter of the two apertures. For a given instrumental setting neutrons can be detected in a limited angular interval; the setting is adjusted by the distance between sample and detector between 1.25 und 20 m leading for the

possible neutron wave lengths between 5 and 15 Å to a Q interval of 10^{-3} Å^{-1} – 0.3Å^{-1}. The resolution has always been adjusted to the instrumental setting and which is determined by the length of collimation L_S. The space between selector and first aperture is always bridged by

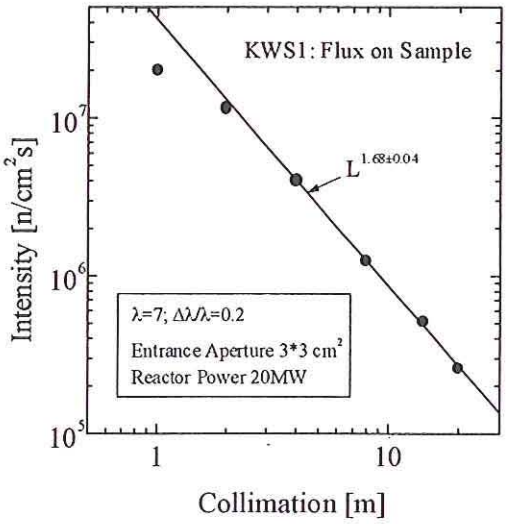

Figure 8.3: *Sample intensity for different length of collimation*

neutron guides which in segments of 1m length can be posed in or out the beam; in this way the primary intensity can be remarkably enhanced by a beam with larger divergency. This is shown in Fig.8.3 where the measured primary intensity is depicted versus the length of collimation. The optimized conditions of the instrument are achieved, when all elements of resolution in Eq.(8.5) contribute the same amount to the „desmearing" of the scattered intensity. Optimal conditions are accordingly obtained for the following instrumental setting:

$$L_D = L_S \qquad \text{und} \qquad d_E = d_D = 2\,d_S\,. \tag{8.6}$$

One always tries to perform measurements with as much intensity as possible with sufficiently good resolution. Such an optimized instrument has a resolution of $\delta Q_{opt.} = (k/\sqrt{3}) \cdot d_E / L_D$ (see Eqs.(8.5) und (8.6)) and delivers an intensity at the sample according to

$$\Delta I_0 = L\,\Delta\Omega \frac{F}{L_D^2} L_D^2 = L\left(\frac{\delta Q}{k}\right)^4 L_D^2\,. \tag{8.7}$$

The last relationship shows that the intensity at the sample is proportional to the square of its length and is the reason of 40m long pin-hole SANS instruments. The upper limit is

determined by the maximum divergence of the neutrons according to the total angle of reflection.

A further important criterion for the quality of a SAS diffractometer is the sharpness of the primary neutron beam prepared by the collimator. In Fig.8.4 primary beam for a given

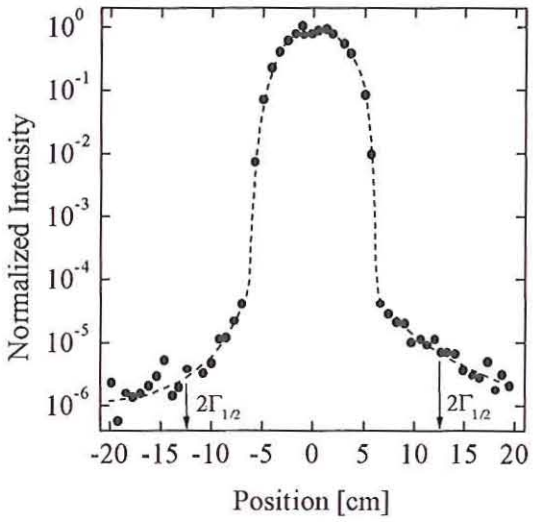

Figure 8.4: *Resolution curve for a given configuration*

configuration has been depicted in a semi-logarithmic presentation. One recognizes, that at twice the full half width the primary intensity has been decreased to values between 10^{-5} und 10^{-6}. This result demonstrates that the instrument is in a good condition; the background near the primary beam is sufficiently small, so that also in this region scattered neutrons can be sensitively detected and analyzed.

8.3.2. Focusing SANS

The principle of a focusing SANS has been depicted in Fig.8.5. The monochromatic neutrons enter the instrument through an aperture with a diameter of about 1mm and enter the focusing mirror with the full divergence of the neutron guide. From the mirror the neutrons are reflected and in the focal point the neutrons are detected from a local sensitive detector. The resolution element of this detector has the same size as the aperture of about 1mm. Just behind the mirror is the position of the sample. The instrument with the lengths given in the

figure and with neutrons of about 15Å wave length covers a Q range of $(10^{-3}-10^{-4})\text{Å}^{-1}$; it measures in the resolution range of light scattering. The intensity at the sample is given as

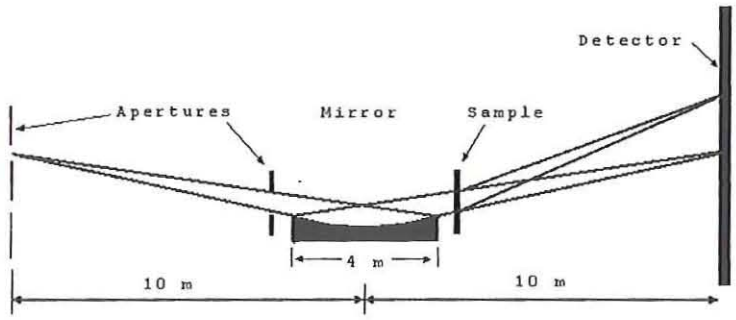

Figure 8.5: Schematic design of a focusing SANS

$$\Delta I_0 = L\,\Delta\Omega\,\frac{F}{L_D^2}\,L_D^2 = L\,(4\gamma_C^2)\,(\frac{\delta Q}{k})^2\,L_D^2 \qquad (8.8)$$

Within these small Q ranges this instrument is superior to the pin-hole instrument because neutrons with the maximum space angle $4\gamma_C^2$ of the neutron guide are used. The concept of

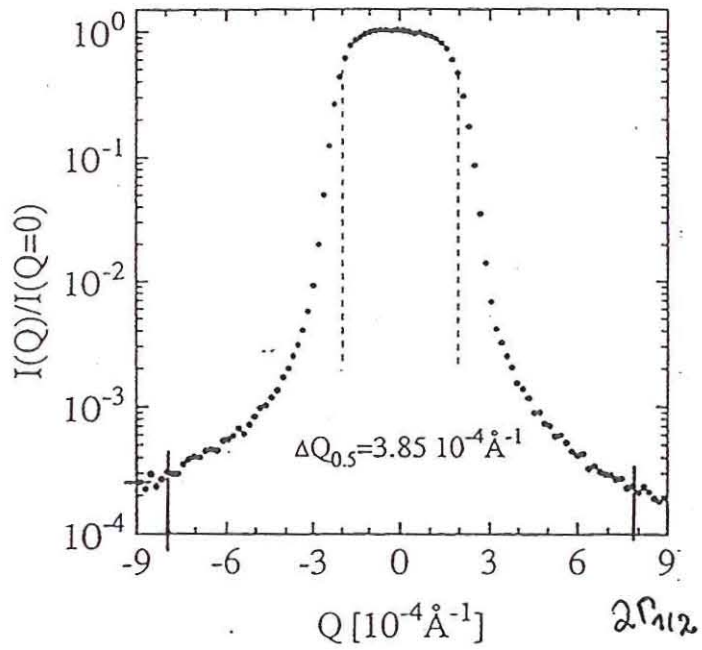

Abb.8.6: *Resolution curve of a focusing SANS*

the focusing SANS is known for long time. However, only quite recently it is possible to build such instruments with the necessary good quality as shown from the experimental resolution curve depicted in Fig. 8.6. The reason is the high demand on the surface quality of the focusing mirror; those mirrors can be built today as the result of an extended project for the development of X-ray satellites.

8.3.3. Double Crystal Diffractometer

From all three SANS instruments the double crystal diffractometer (DCD) has the highest resolution. Its concept is depicted in Fig.8.7. The central part of this instrument are two

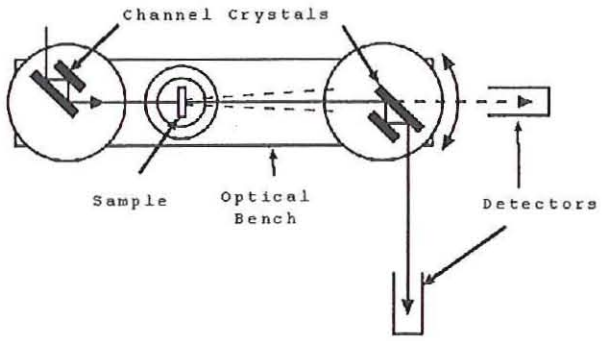

Figure 8.7: *Schematic design of a double crystal diffractometer*

perfect Silicon single crystals, mounted on an optical bench. The reflectivity of a perfect crystal is described by the Darwin curve according to

$$R(y)=\begin{cases}1 & |y|\le 1\\ 1-(1-y^{-2})^{0.5} & |y|>1\end{cases} \qquad (8.9)$$

and depicted in Fig. 8.8. The parameter y is the scattering angle which is normalized in a way that the interval where neutrons are fully reflected are within $|y|\le 1$. The second crystal is rotated with respect to the first one. When the corresponding lattice planes of both crystals are oriented parallel to each other the Darwin curves of both crystals overlap completely and one measures the maximum intensity of the resolution curve as shown in Fig. 8.9 at $\Delta=0$. If the second crystal is rotated, both Darwin curves only partly overlap with the result of a smaller reflected intensity. The rotation of the second crystal is mathematically equivalent with the folding of the two Darwin curves, which gives the resolution curve in

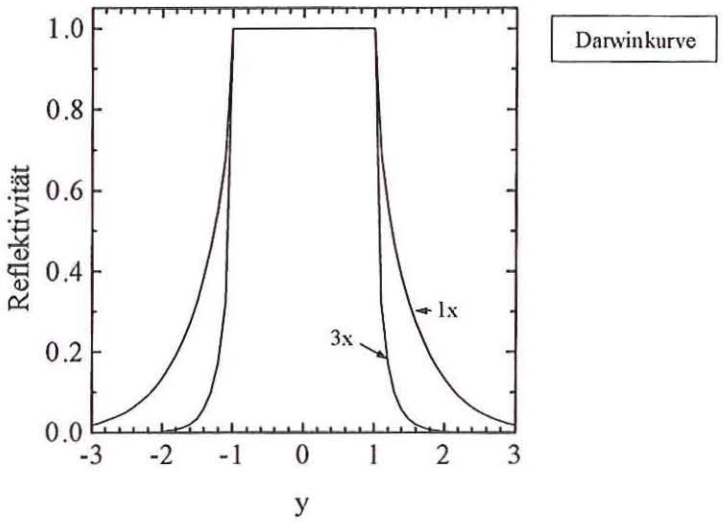

Figure 8.8: *Darwin curve after single and triple reflections.*

Fig.8.9 and which is the scattered intensity from the second crystal. In the region $|y| \leq 1$ the reflectivity is equal one, which means total reflection. The width of total reflection is given as

$$\Delta\Theta = \frac{b_c \, e^{-W} |F| N \lambda^2}{4\pi \sin 2\Theta_B} \qquad (8.10)$$

For instance, for the (331) lattice planes of a Silicon single crystal and λ=1.8Å neutrons the Bragg angle of diffraction is about 45° and the half width of the resolution curve is $\Delta\Theta = 3.2\,\mu\text{rad}$, which corresponds to an angle of slightly more than half a second of arc or a $Q = 1.12 \cdot 10^{-5}\,\text{Å}^{-1}$. This examples shows, that this method measures at very small angles; this demands protections against mechanical vibrations, fluctuations of temperature, and much patience from experimentalist.

The strength of this instrument is its very high resolution, which is even better than of light and its relatively simple and cheap design in comparison with most other neutron scattering instruments. This instrument can also be successfully operated at smaller research reactors. Disadvantages are that it measures in slit geometry, that the experiment points are measured in sequence, and that it is rather poor in intensity. There are, however, improvements possible by special designs of the crystals. So, the relative high background near the primary beam can be strongly improved by so called channel cut crystals. If the neutrons are reflected within the channels of a compact single crystal (Fig.8.7 and Fig.8.8) f.i.

three times, then one measures a Darwin curve multiplied three times with itself and gets a reflection curve as depicted in Fig. 8.9 with the region of total reflection and much sharper

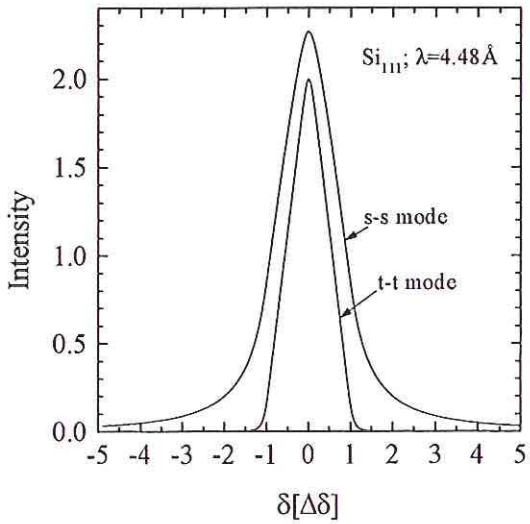

Figure 8.9: *Theoretical curves of resolution of the double crystal diffractometer for single-single (s-s) and triple-triple (t-t) reflections.*

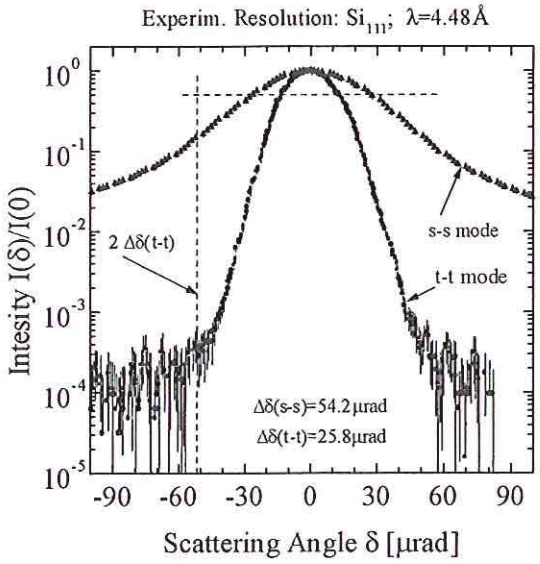

Figure 8.10: *Experimental resolution after single-single and triple-triple reflections within the channel cut crystal.*

tails. This reflection curve leads after folding to a much sharper resolution curve. Experimental resolution curves of single-single and triple-triple reflections are shown in Fig.8.10. One clearly see the effect of multiple reflections.

8.4. Reflectometer

Investigations of surface properties by surface reflection of neutrons or X-rays is a relatively new technique and is presently very active field in research. In Fig. 8.11 the specular

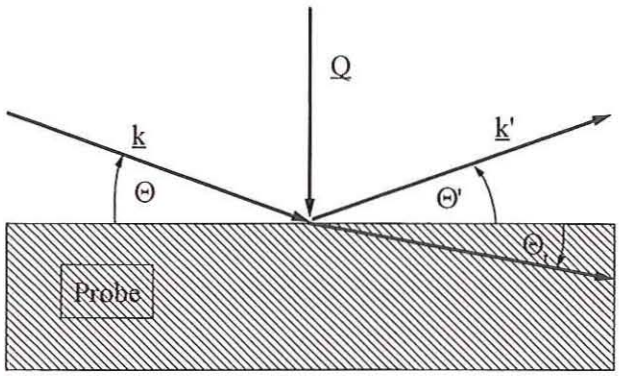

Figure 8.11: *Traces of neutrons and diagram of momentum of specular reflection*

reflection of neutrons at a surface is shown and in Fig. 8.12 a reflectometer for neutrons has been schematically depicted. Similarly to the pin-hole SANS instrument in Fig.8.2 the divergency of the monochromatic neutron primary beam is determined by two apertures. In this example the monochromatic neutron beam is determined by a single crystal within the neutron guides. A linear position detector measures the reflected neutrons. Specular reflection as shown in Fig. 8.11 is defined by the same incoming and outgoing angle. In this case the Q vector has an orientation perpendicular to the surface and only heterogeneities in direction perpendicular to the surface e.g. parallel to Q are measured. An example is shown in Fig. 8.13 giving the reflection profile of a Nickel metallic film coated on glass. In this case one measures the heterogeneities formed between Nickel and glass and in addition the surface roughness between Nickel and vacuum according to the different values of the coherent scattering length densities. The intensity profile shows total reflection at small angles and then at larger angles strongly decreases with periodic oscillations. From this profile one can determine thickness and roughness of the metallic film.

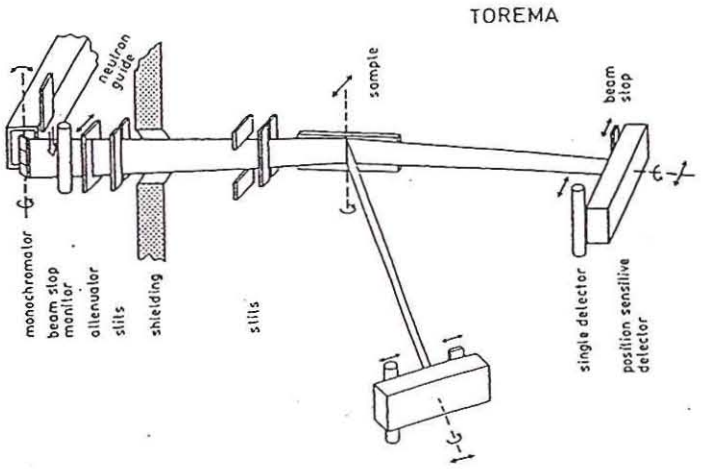

Figure 8.12: *Schematic design of a diffractometer for neutron reflectometry.*

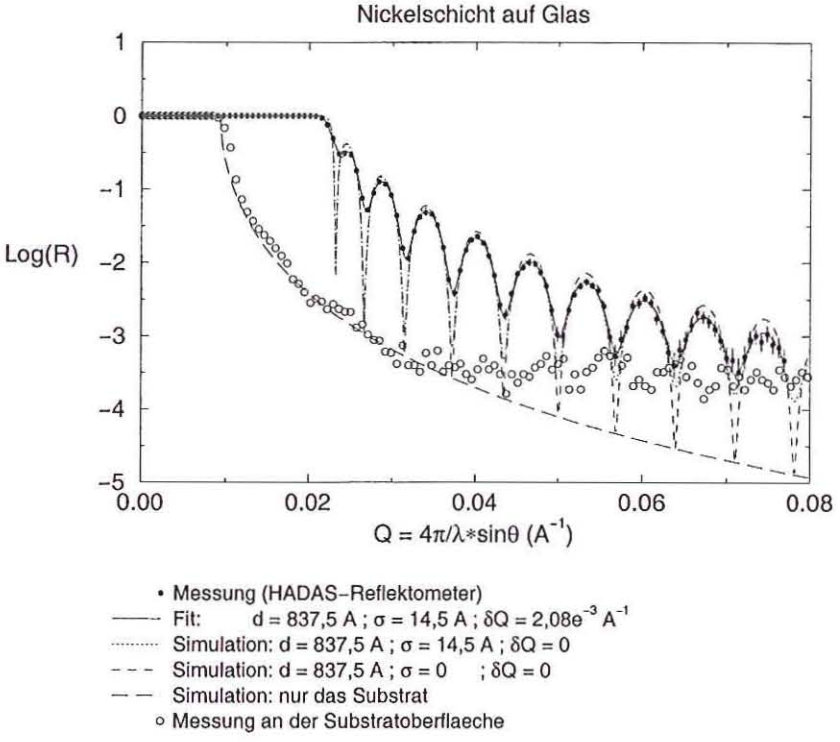

Figure 8.13: *Curve of reflection from a Nickel surface measure at the "HADAS" instrument.*

For the Nickel film one gets a thickness of 838 Å and a roughness of 15 Å. The open dots in Fig. 8.13 show the reflection from glass alone. One clearly observes a smaller angle of total reflection and a decrease equivalent to the Darwin curve in Eq. (8.9). At relatively small intensities of 10^{-3} scattering from background becomes visible.

One can also study heterogeneities within the surface which are f.i. formed by phase separation. In those cases one also observes nonspecular reflection in direction parallel to the surface.

8.5. Important Elements of Small Angle Scattering and Reflection

The most important elements of small angle scattering and reflection are (1) the neutron guides for an effective transport of neutrons, (2) the velocity selector and the perfect single crystals for monochromatization of the neutrons, and (3) the local sensitive detector for a fast determination of the scattering angle.

8.5.1. Neutron Guide

The phenomenon of total reflection is demonstrated in Fig.8.13 on a Nickel film. This effect is used to transport neutrons through neutron guides over long distances without much loses. The angle of total reflection is given as

$$\Theta_c = \lambda\,(\rho/\pi)^{0.5} \qquad (8.11)$$

with the coherent scattering length density ρ. Natural Nickel is a good choice for coating material in order to have a large angle of total reflection (see Figure 8.13); an even better choice is the isotope Nickel 58 because of its large coherent scattering length. So, for natural Nickel one gets a total angular of reflection of $\Theta_c = 6' \cdot \lambda[\text{Å}]$ and for the isotope 58 a $\Theta_c = 7.1' \cdot \lambda[\text{Å}]$. About 30 years ago neutron guides were invented at the research reactor in München; Neutron guides lead to a much broader use of neutron scattering with instruments posed far from the source and with much better conditions.

Neutron guides coated with a so-called super mirror transport neutrons with even larger angles of divergence. In addition to Nickel those mirrors consist of alternating layers of two different metals (their coherent scattering length density must be sufficiently different) with an ingenious sequence of different thickness, in order to excite Bragg scattering in a continuous range of Q perpendicular to the surface. In this way the angle of reflection of Nickel can be increased by more than a factor of two; however, the best achieved reflectivity of super mirrors is still slightly less than one so that one gets appreciably losses of neutrons if transported over long distances..

Neutron guides also enable to transport neutrons on curved traces. The bending radii can be made very small by so-called *bender guides* consisting of several small and parallel channels. Bender with proper materials for the layers are also used as a polariser.

8.5.2. Velocity Selector

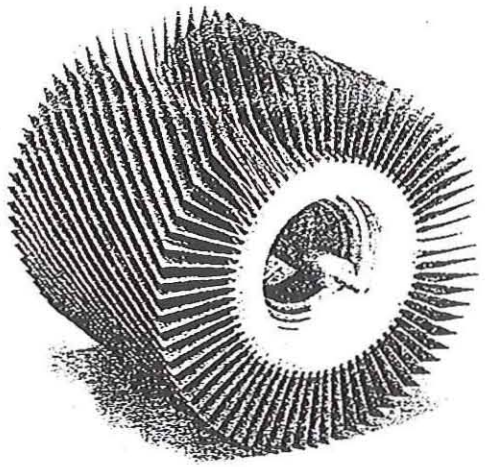

Figure 8.14: *Rotor of a velocity selector built from Dornier.*

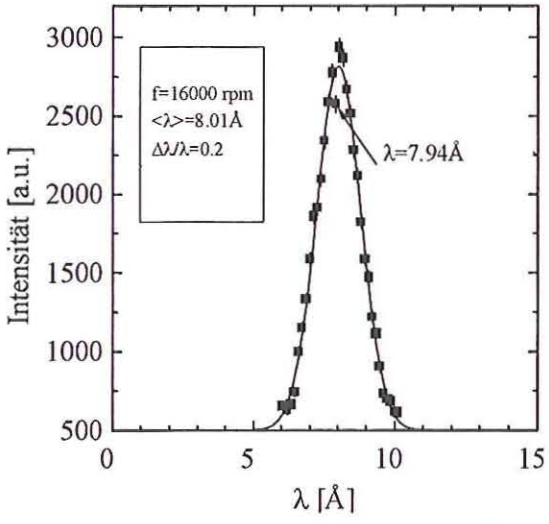

Figure 8.15: *Time-of-flight spectrum from a velocity selector. The neutron wave length is evaluated from the velocity, e.g. from the flight time and the distance between chopper and detector. The small dip in the intensity at 7.94Å is caused from Bragg scattering in the Bismuth filter just behind the cold source and is used as a reference value.*

The rotor of a velocity selector is shown in Figure 8.14. This rotor is mounted in a housing and can rotate with a speed up to 30000 rpm. It is transparent for a given wave length depending on the speed of the rotator. A distribution of neutron wave length after passing the selector is shown in Figure 8.15. The neutron wave length is inversely proportional to the frequency of rotation; the exact relationship and the half width of the wave length distribution is determined by the tilt angle and the width of the channels.

8.5.3. Local sensitive Detectors

Local sensitive detectors are necessary for an optimized use of small angle scattering and reflection instruments. The resolution element of a detector for the pin-hole SANS is typically 0.5-1cm, for the focusing SANS and reflectometer 1mm. A two dimensional local sensitive detector has at least 64x64 resolution elements. There are detectors on the basis of gas- and scintillation detection.

8.5.3.1. Gas Detector

The presently mostly used detector for SANS are ^{3}He gas detectors. The neutron is absorbed by an ^{3}He gas atom which then decomposes according to

$$^3\mathrm{He} + \mathrm{n} \rightarrow {}^3\mathrm{H} + {}^1\mathrm{H} + 0.77\mathrm{MeV} \qquad (8.12)$$

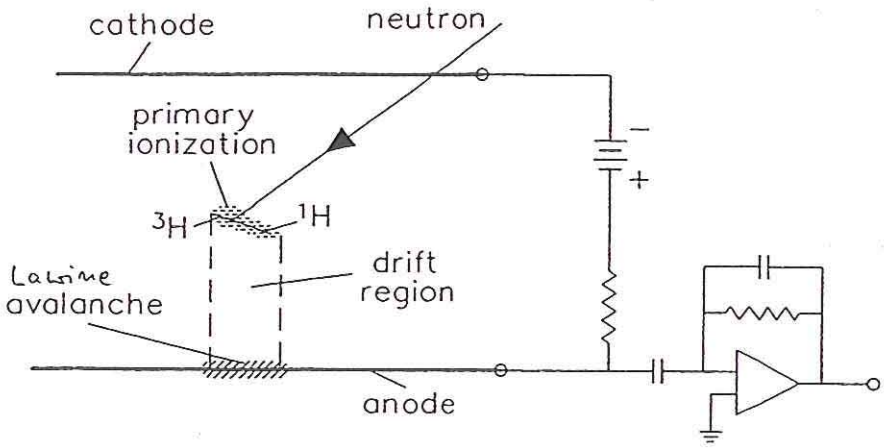

Figure8.17: *Process of detection of the* ^{3}He *gas detector*

into two ionic particles with kinetic energies of 0.573Mev and 0.191Mev for the proton and the ^3H (tritium), respectively. As shown in Figure 8.17, both ions cause a "primary" ionization cloud within the surroundings where the neutron was absorbed. These ions are accelerated by an electric field and produce by a so-called "secondary" ionization process an avalanche of ions. Only the electrons give a signal at the anode because they achieve a much larger acceleration according to their small mass. The size of the voltage pulse at both ends of the anode is used for determination the position of absorption and thereby the scattering angle. In a two-dimensional detector there are two perpendicularly arranged wire lattices, from which by coincidence measurements the position of the absorbed neutron is determined.

8.5.3.2. Scintillation Detector

Another type of detector are solid state detectors using the principle of scintillation. The reaction equation is the following:

$$^6Li + n \rightarrow {}^4He + {}^3H + 4.79MeV \qquad (8.13)$$

A Li glass with 6.6% ^6Li is mixed with Cerium (Ce). By absorbing a neutron in ^6Li two ionic products of reaction are formed, which interacting with Cerium produce about 4000 photons of 400nm wave length per neutron. In the disperser the photons form a light cone of 90° as depicted in Figure 8.18. The light cone is adjusted by the thickness of the disperser and by the slit between scintillator and disperser (total reflection) so that the light overshadows two photo multiplier. The photo multiplier have a diameter of 8cm and in total 8x8 photo

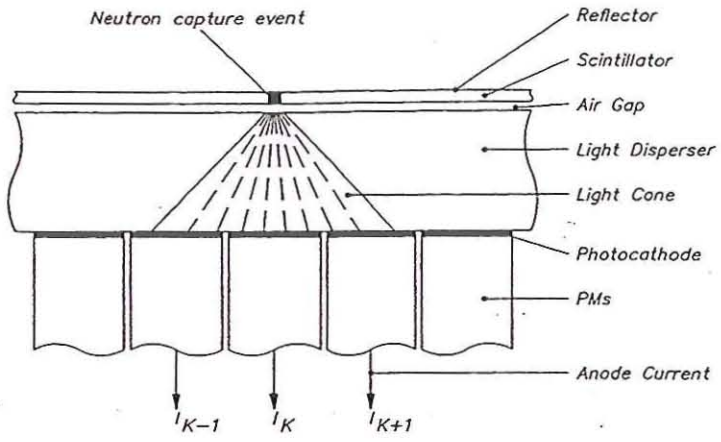

Figure 8.18: *Process of detection of a ^6Li scintillation detector*

multiplier are arranged in a quadratic array. The resolution of one pixel is 0.8 cm. Such a resolution becomes possible by an algorithm calculus from the light intensities of several photo multipliers. In a first stage a rather rude determination with an uncertainty of 8cm is made by the position of the photo multiplier with the largest light intensity. In a second stage he neutron position is determined by also considering the intensity of the neighboring photo multipliers. An important advantage of this detector is the large atomic density of the absorbing material and its consequently large detection probability; a 1mm thick absorbing material of a scintillator has a 93% detection sensitivity of 7 Å neutrons. Such a detector (Anger camera) was developed at the Forschungszentrum Jülich and is used in our KWSI small angle instrument.

References:

Books:

J.S. Higgins und H.C. Benoit, *Polymers and neutron scattering*. Clarendon Press, Oxford (1994)

C.G: Windsor, *Pulsed Neutron Scattering*. Taylor & Francis, London(1981)

P. Convert and J.B. Forsyth (eds.), *Position-Sensitive Detection of Thermal Neutrons*. Academic Press, London (1983)

X.L. Zhou and S.H. Chen, *Theoretical Foundation of X-Ray and Neutron Reflectometry*. Elsevier, Amsterdam (1995)

Articles about single subjects:

W. Schmatz, T. Springer, T. Schelten and K. Ibel, J. Appl. Cryst. 7, 96 (1974)

D. Schwahn, A. Miksovsky, H. Rauch, E. Seidl and G. Zugarek, Nucl. Instrum. Methods, **A239**, 229 (1985)

B. Alefeld, H.J. Fabian, D. Schwahn and T. Springer, Physica, **B156&157**, 602 (1989)

D.Schwahn,, G.Meier and T.Springer, J. Appl. Cryst. **24**, 568 (1991)

M. Heiderich, R. Reinartz, R. Kurz and J. Schelten, Nucl. Instrum. Methods, **A305**, 423 (1991)

9. Crystal spectrometer: triple-axis and back-scattering spectrometer

F. Güthoff, H.Grimm

It has been emphasized in the preceding lectures that thermal neutrons provide wavelengths λ comparable to inter-atomic distances and energies $\hbar\omega$ in the order of collective excitations of condensed matter. In order to determine the properties of a sample - as represented by the scattering function $S(Q,\omega) \propto \mathrm{d}^2\sigma / \mathrm{d}\Omega \mathrm{d}E'$ - a variety of instruments may be used. The evaluation of the single differential cross section represented by $\mathrm{d}\sigma / \mathrm{d}\Omega$ is the topic of diffractometers. However, since – in general – the scattering of neutrons by the sample is connected with an energy transfer it suggests itself to analyze the neutrons scattered into the solid angle $\mathrm{d}\Omega$ in addition with regard to their energy. Introducing and investigating the double differential cross section $\mathrm{d}^2\sigma / \mathrm{d}\Omega \mathrm{d}E'$ thus corresponds to the switching from diffractometer to spectrometer. In order to determine which energy transfer $E - E' = \hbar\omega$ is associated with which momentum transfer Q, the neutrons have to be characterized before hitting the sample by means of the so-called primary spectrometer and after leaving the sample by the secondary spectrometer. It will be shown in the lecture on time-of-flight spectrometers that the energy of neutrons can be determined via selection of velocity and travel time. Recall that thermal neutrons (300K) having an energy of $k_B T = \frac{1}{2} m v^2 \sim 25$ meV travel with a speed of about 2200m/s. According to de Broglie one may associate a wavelength λ to a moving particle with mass m. This fact is used by crystal spectrometers which – by means of Bragg scattering

$$n \cdot \lambda = 2d \sin\Theta \tag{9.1}$$

select neutrons of energy

$$E = \frac{\hbar^2 k^2}{2m} = \frac{h^2}{2m\lambda^2} \tag{9.2}$$

under Bragg angle Θ for given spacing d of the selected atomic planes. The modulus of the wave vector is related to the wavelength by $k = 2\pi / \lambda$.

Two types of crystal spectrometers will be introduced in this lecture. The triple-axes spectrometer represents one of the earliest neutron spectrometer types. It was developed by B. N. Brockhouse. By means of this facility his essential studies [1] resulted by the end of the fifthies laying ground for his winning of the Nobel prize for physics in 1995. In contrast, the backscattering spectrometer is of more recent origin (the first facility of this type was put into operation in Jülich at the beginning of the seventieths by B. Alefeld) and was stimulated by ideas of Maier-Leibnitz [2].

Both types of spectrometers can be – similar to time-of-flight machines – positioned at cold and thermal neutron sources. Especially for triple-axes spectrometers the possibility is realized to use them at hot sources where neutron energies range up to 1eV.

9.1 Common features of crystal spectrometers

One of the most important properties describing and characterizing spectrometers is the resolution function. It is essential to determine and to optimize this function since it determines the type of dynamical behaviour which may successfully be measured. For a substance to be investigated, this might mean that several different spectrometers are to be employed in order to determine the whole range of interesting excitations. According to the expected excitation energies not only a change in the moderation of the neutron source but also switching to a conceptually different spectrometer might become necessary. However, already for a given spectrometer, resolution and flux may be varied by an order of magnitude taking advantage of available measures. Amongst other aspects. the knowledge of the instrumental resolution function is of central importance in view of the rather limited neutron flux, since - for example - the size of the measured signal varies proportional to the inverse fourth power of the chosen average collimation for a triple-axes spectrometer. Thus, for each experiment, a suitable compromises between resolution and intensity have to be chosen. A comparison might elucidate this point: e.g. 10^{17} - 10^{21} quanta/s are typical for a LASER beam whereas a reactor like the DIDO offers normally 10^{6} - 10^{7} neutrons /cm$^{2}\cdot$ s (monochromatic) at the sample position. In order to make the most efficient use of those neutrons, different strategies – discussed below - are pursued by the various crystal spectrometers.

For a crystal spectrometer one may write the measured intensity scattered into the solid angle $\Delta\Omega$ with the energy spread $\Delta\hbar\omega$ in the form:

$$\Delta I = \underbrace{A(k)\cdot k\cdot p(\underline{k})\cdot \Delta V}_{\text{primary side}}\cdot \underbrace{\frac{N\mathrm{d}^2\sigma}{\mathrm{d}\Omega\mathrm{d}\omega}}_{\text{sample}}\cdot \underbrace{p'(\underline{k}')\cdot\Delta\Omega\cdot\Delta\hbar\omega}_{\text{secondary side}}. \tag{9.3}$$

The first part of eq. (9.3) up to the cross section of the sample represents information about the spectrum of the neutron source $A(k)$ and the reflectivity of the monochromator $p(\underline{k})$; the number of scatterers in the sample is N. The last part refers to the signal measured by the secondary spectrometer. Since monochromator (primary side) and analyzer (secondary side) act by the same physical principles it is advantageous to describe the instrumental factors and thus the resolution in eq. (9.3) more symmetrically. To this end we use the already introduced relation between cross section and scattering function

$$\frac{\mathrm{d}^2\sigma}{\mathrm{d}\Omega\mathrm{d}\omega} = \frac{k'}{k}S(\underline{Q},\omega) \tag{9.4}$$

and with the help of $\Delta\Omega\cdot\hbar\Delta\omega = \frac{\Delta k'_{\perp_1}\Delta k'_{\perp_2}}{k'^2}\cdot\frac{\hbar^2}{m}k'\Delta k'_{\parallel} = \frac{\hbar^2\cdot\Delta V'}{m\cdot k'}$ we can rewrite eq. (9.3) to

$$\Delta I \propto A(k)\cdot N\cdot S(\underline{Q},\omega)\cdot p(\underline{k})\Delta V\cdot p'(\underline{k}')\Delta V' , \tag{9.5}$$

where – as will be shown below – the volume elements in wave vector space are given by $\Delta V = \Delta k_{\perp_1}\cdot\Delta k_{\perp_2}\cdot\Delta k_{\parallel}$.

In this section, now, the most important elements for the triple-axis and the backscattering spectrometer shall be introduced. It will become obvious that exploiting an essentially identical principle leads to quite different set-ups and properties. As a first step the general influence of various components on the resolution will be described by means of the triple-axis machine which will be followed by an optimization of the physics involved (one sided in a certain sense) in the shape of the backscattering spectrometer.

9.2 Principle of the crystal spectrometer with three variable axes

Fig.9.1 shows the principle layout of a triple-axis spectrometer. Neutrons of a defined wavelength λ are selected from an incident "white" beam by means of a single crystal (mono-

chromator M, first axis) under the associated angle $2\Theta_M$ according to eq. (9.1). The sample S under inspection is positioned in the diffracted beam. The secondary spectrometer moves around the sample thereby selecting neutrons scattered by an angle $2\Theta_S$ (second axis) which are further sorted with regard to their energy via the angular setting $2\Theta_A$ of an analyzer crystal. A (third axis) and counted by detector D. The scattering vector $\underline{Q}$ as well as the energy transfer $\hbar\omega$ are determined by the angles $2\Theta_S$ and $2\Theta_A$ for given incident wave vector $\underline{k}$ (see also Fig.9.2).

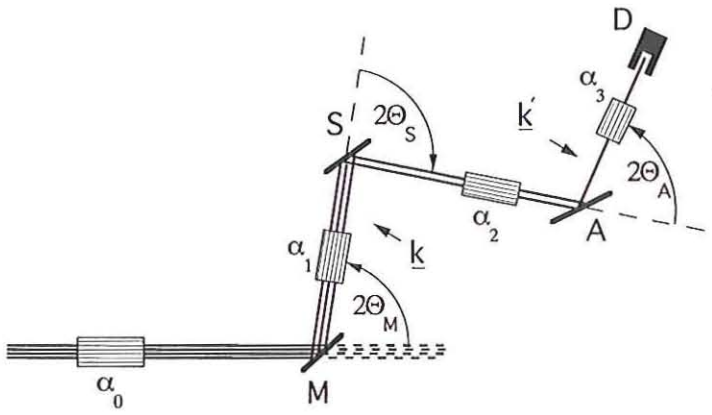

Fig.9.1: Schematic layout of a triple-axis spectrometer with: collimators α_i,, monochromator M, sample S, analyzer A, detector D, incident (scattered) wave vector $\underline{k}$ ($\underline{k}'$)

Thereby, the wave vectors $\underline{k}$ and $\underline{k}'$ are connected with the variables $\underline{Q}$ and $\hbar\omega$ by the conservation of momentum and energy. In the resulting scattering triangle (Fig.9.2) the deviation of the foot F from $\frac{1}{2}Q$ determines the energy transfer $\hbar\omega$. The sense of this deviation determines whether the neutron has gained ($\underline{k} < \underline{k}'$, $E\text{-}E' = \hbar\omega < 0$) or lost energy ($\underline{k} > \underline{k}'$, $\hbar\omega > 0$) by the scattering process. In order to influence the divergence of the neutron beam, collimators α are inserted before and after the crystals by which neutrons are selected. Detection of neutrons is by materials with an exceptionally large absorption cross section. The involved nuclear processes are e.g. $^{10}B(n,\square)$, $^{6}Li(n,\square)$, and $^{3}He(n,p)$. The most common type of detectors is conceived as proportional counter filled with ^{3}He having an absorption cross section

of 5300 barn for neutrons with 25 meV. With the typical active length of about 5 cm and a filling pressure of about 5 bar, the counting probability reaches >95% for thermal neutrons (the absorption cross section is reciprocal to the speed of the neutron).

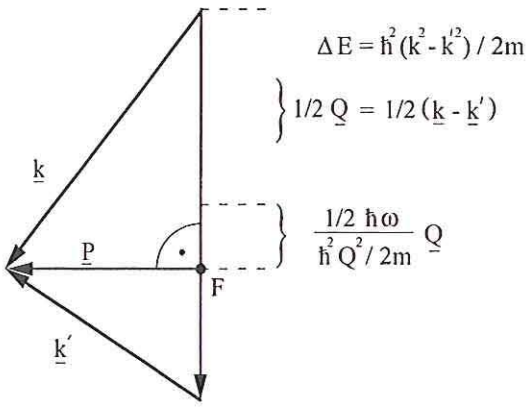

Fig.9.2: Geometrical relation between wave vectors $\underline{k}$ and $\underline{k}'$ on the one hand side to momentum- $\hbar \underline{Q}$ and energy transfer $\hbar\omega$ on the other hand. Since ($\underline{k}$, $\underline{k}'$) represents 6 dimensions, yet ($\underline{Q}, \omega$) 4 dimensions, only, arbitrary solutions of vector $\underline{P}$ on the plane perpendicular to $\underline{Q}$ result for a given ($\underline{Q}, \omega$)-point.

It is meaningful to insert a neutron monitor at the exit of the primary spectrometer. This device is principally similar to a counter absorbing and detecting, however, a small fraction of the incident neutrons, only. The measured spectra may thus be normalized to the number of incident neutrons which is essential for long measuring periods since the neutron flux may undergo appreciable fluctuations. In addition, for a reactor of the type DIDO, the average neutron flux increases by about 10% during a normal cycle.

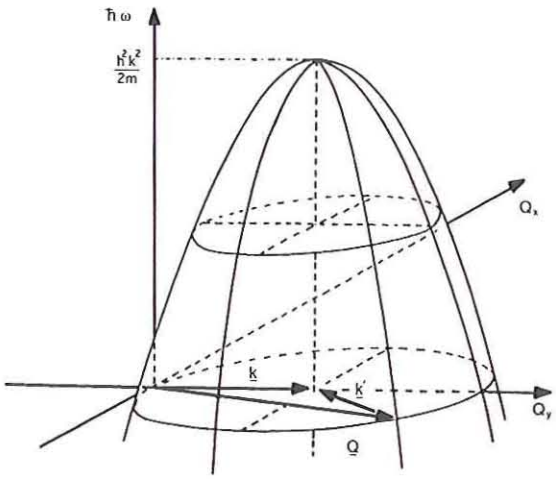

Fig.9.3: Representation of the theoretical measuring range of a neutron spectrometer with fixed incident wave vector $\underline{k}$.

The term triple-axis spectrometer indicates already the versatility of this instrument (not only in real space) which distinguishes this concept from other types of spectrometers. As long as the radius of action is not barred by the radiation shielding, arbitrary points in $\underline{Q}, \omega$ - space may be selected. For fixed incident wave vector, those points belong to a parabolic surface which is defined by momentum- and energy conservation as shown in Fig.9.3).

$$\underline{Q} = \underline{k} - \underline{k}' \tag{9.6}$$

$$\Delta E = \hbar\omega = \tfrac{\hbar^2}{2m}(k^2 - k'^2) \quad . \tag{9.7}$$

9.3 Beam shaping

Due to the fact that neutrons are uncharged and thus may penetrate materials rather easily, neutrons may be bundled or focused to a limited extent, only. This aspect aggravates with increasing neutron energy . Already in the source, there arises the problem to guide a suitable

number of neutrons through "holes" (beam tubes) in the biological shielding to the experimental setup. From the total solid angle of 4π, only the fraction travelling in the direction of the beam tube will contribute to the flux. The used divergence of the beam is can merely be chosen by annihilating all those neutrons by absorbing materials travelling outside a defined angular range. Thus a beam tube represents the simplest version of a collimator. It is comparable to a system of two diaphragms positioned in a distance of some meters. With a typical length of 3 m for the beam tube and a cross section of 0.1 m there results a divergence of about 2° for the neutron beam.

Now it turns out that it is less meaningful to collimate the neutron beam in the vertical plane as tight as in the horizontal (scattering) plane. Tilting the scattering triangle (Fig.9.2) slightly out of the scattering plane influences the selected $(\underline{Q},\omega)$ -point either not at all or in second order, only. If collimation shall be achieved within a short distance, thereby making allowance for a desired anisotropy, one uses a so-called Soller collimator. To this end, a set of coplanar foils coated with absorbing material is mounted vertically with a distance of say 1 to 5 mm. Choosing about 30 cm for the length of the foils, one may achieve a horizontal divergence of the neutron beam in the order of 10 minutes of angle. Yet one has to take into account that switching to half of the divergence entails about the same reduction of the neutron flux! The facts that the foils have a finite thickness and that their absorption is less than 100% modifies the ideal triangular transmission curve by rounding the top and by the appearance of tails beyond the base. This modified curve may well be represented by a normal distribution - a useful property for folding operations. In regard to the interpretation of measured data the more sharply limited resolution triangle as realized by the chopper of a time-of-flight machine would be more desirable. Since a well defined cut-off clearly separates the change from elastic to inelastic scattering the difficulties in interpreting the quasi-elastic transition region which involve the knowledge of the exact shape of the resolution function are greatly reduced.

The anisotropy of the divergence may be exploited by a vertically focusing arrangement of monochromator and/or analyzer crystal in order to increase the neutron flux at the sample as shown in Fig.9.4). It is well known from optics that the inverse focal length is given by $1/f = (\frac{1}{L_1} + \frac{1}{L_2})$ and that the ratios of heights for image and source is equal to that of their distances L_2/L_1. Since, in general, the Bragg angle $\Theta \neq 0°$, the focal length depends on the Bragg angle and the radius of vertical curvature by

$$f = \frac{R}{\sin\Theta} \quad . \tag{9.8}$$

The distances L_1, L_2 for a given spectrometer are to be considered as fixed quantities and thus the curvature R of the crystal has to be variable. This may e.g. be realized by the parallel arrangement of lamellae of single crystals which can be tilted individually. An additional gain factor results from the height ratio of monochromator to source. Depending on the relative heights of sample and crystals an increase of the neutron flux at the sample by a factor of 2 to 6 might be achieved. The possibility of a horizontal focusing – whereby the influence on the resolution is no longer negligible – will be discussed further down.

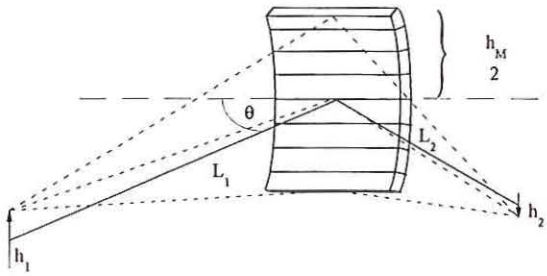

Fig.9.4: Vertical focusing: The gain factor P for the intensity at the sample is given by the ratio of heights for source and image (h_1/h_2) and the height of the deflecting crystal h_M in units of the height of the source by: $P = \frac{crystal_{covered}}{crystal_{free}} = \frac{h_M}{L_2} \cdot \frac{L_1+L_2}{h_1} = \frac{h_M}{h_1}\left(\frac{L_1}{L_2}+1\right)$

Similarly to e.g. light, one may mirror and thus guide neutrons. On the basis of the Fermi pseudo potential V one obtains the index of refraction for neutron by

$$n = \frac{k}{k_0} = \sqrt{1-\frac{V}{E}} = \sqrt{1-\frac{2\pi\hbar^2 m^{-1}\cdot\rho(\underline{r})\cdot b_{coh}(\underline{r})}{\hbar^2 k^2 (2m)^{-1}}} \cong 1-\frac{\lambda^2\rho(\underline{r})\cdot b_{coh}(\underline{r})}{2\pi} \quad . \tag{9.9}$$

where $b_{coh}(\underline{r})$ denotes the average scattering length and $\rho(\underline{r})$ the particle density. The losses due to the total reflection are small even for a rather modest quality of the mirroring surface.

By suitable coating the simple beam tube may become a neutron guide and the $1/r^2$-law is thus circumvented. According to eq. (9.9) one should use materials for such mirrors which possess a large coherent cross section together with a large atomic density which is fulfilled for the isotope ^{58}Ni with $b = 14.4 \cdot 10^{-15}$ m. Since the limiting angle for total reflection is extremely small ($\phi_c / \lambda \approx 0.1°/10^{-10}$m), simple homogeneous coating could be used successfully for cold neutrons, only (the technique to produce super mirrors opened the possibility for guiding neutrons with energies up to the thermal range). By means of the neutron guides instruments having still a high neutron flux can be set up at larger distances from the reactor core. If , in addition, such a neutron guide is slightly curved one can avoid the direct view onto the core which reduces the background. Simultaneously, one obtains an efficient $\lambda/2$-filter by suppressing the unwelcome faster neutrons. A marginal note might be added: in the case of extreme cooling of neutrons one may keep and store them in "bottles" since they are totally reflected under arbitrary angles.

9.4 Resolution for diffraction by a crystal

As we have seen already, single crystals offer the possibility to control the travelling direction of neutrons. Thereby use is made of their coherent, elastic scattering properties which – according to eq. (9.1) - allow for deflecting neutrons from an incident "white" beam under the angle 2Θ. This Bragg scattering becomes possible as soon as the scattering vector corresponds to a reciprocal lattice vector, i.e.

$$\underline{Q} = \underline{k} - \underline{k'} = \underline{G} \tag{9.10}$$

and eq. (9.7) satisfies the condition $\Delta E = 0$, or expressed differently by:

$$G \cdot k = \frac{1}{2} G^2 \quad . \tag{9.11}$$

This case is fulfilled if – as shown in Fig.9.5 – the projection of the wave vectors onto $\underline{G}$ is just equal to $1/2 \cdot G$ and is thus negligible for triple-axis spectrometers.

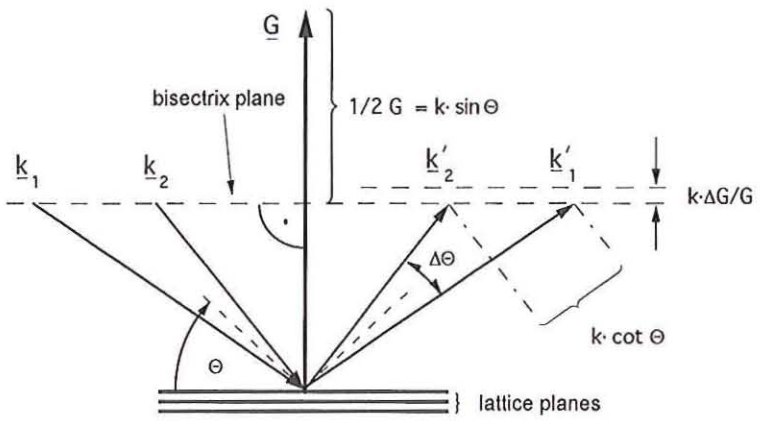

Fig.9.5: Illustration for the selection of scattered wave vectors and their divergence as determined by the modulus G and the scattering angle. $\Delta G/G$ is of the order of 10^{-4}.

The variance of a selected k-vector is given by the derivative of $\frac{1}{2}G = k\sin\Theta$, or

$$\frac{\Delta k}{k} = \frac{\Delta\lambda}{\lambda} = \frac{1}{2}\frac{\Delta E}{E} = \frac{\Delta G}{G} + \cot\Theta \cdot \Delta\Theta \quad . \tag{9.12}$$

With increasing wavelength of the neutron the energy resolution will be improved.

Back to the "bottled" neutrons: in this case it is the half life time of the free neutron of about 13 minutes which finally limits the variance of the energy.

The probability for a k-vector to obey the Bragg condition is both given by the "thickness" of the bisecting plane (constructive interference of the contribution of the lattice planes) and by the variance of the orientation of $\underline{G}$. The former condition means a relative sharpness of the modulus of $\underline{G}$ in the range of 10^{-4} to 10^{-5}, whereas the latter is fulfilled with an accuracy of about 10^{-8} for an illuminated crystal surface in the order of cm^2. Simultaneously, eq. (9.12) expresses the dependence of the resolution on the material of the crystal, i.e. the lattice parameter. This is exemplified in Fig.9.6. The smallest variance in k (or λ) results for a Bragg angle of 90°. This range of $\Theta \cong 90°$ is not accessible for usual triple-axis spectrometers.

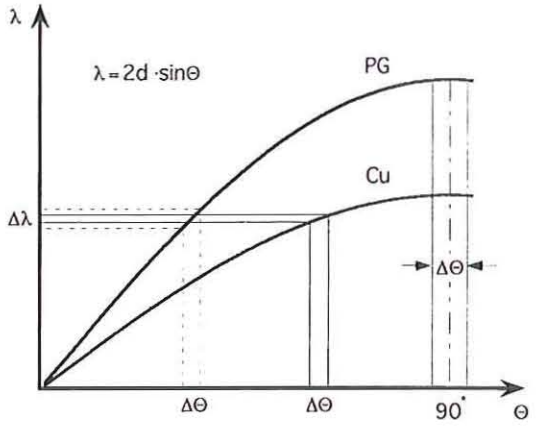

Fig. 9.6: Schematic representation of the variance $\Delta\lambda$ as a function of scattering angle and material

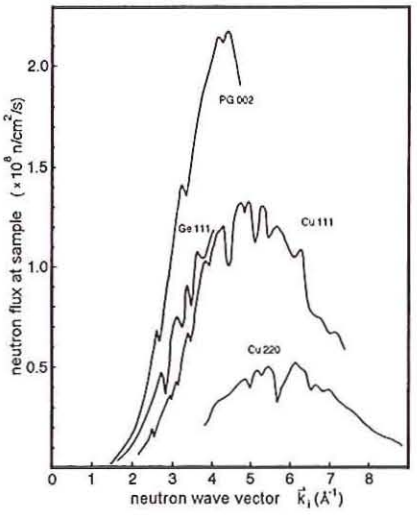

Fig. 9.7: M monochromatic flux at the IN8 (ILL) for various materials as a function of $\underline{k}$ [3]

Ideal crystals would be nearly prohibitive for measurements with the triple-axis spectrometer since their variances in the lattice vector are too small as to reflect sufficient intensity. Therefore, the perfection of the crystals is artificially degraded by various methods. Possible methods are elastic bending of the crystals or a continuous variation of the lattice parameter in so-called gradient crystals. The breakthrough in the successful preparation of gradient crystals which implies a complicated and costly procedure was achieved satisfactorily in 1995 in Berlin-Adlershof with Ge-Si crystals. A comparably wide-spread method is the deformation of perfect crystals, thereby generating an imperfect mosaic crystal by introducing dislocations. On may imagine such a crystal as being composed of small perfectly crystalline blocks – the mosaic pebbles – whose orientation is normally distributed. A common full-width-half-maximum or mosaic spread is in the order of 30′.

Fig.9.8 illustrates the operation of such a crystal as monochromator. The neutron beam incident on the crystal is given a divergence α_0. A perfect crystal would reflect just one wavelength for each angle Θ_M, as expressed by the section of the dashed line (bisecting plane) limited by $\alpha_1 (\leq \alpha_0)$. It is the distribution of bisecting planes (mosaic) which spans the hatched area being proportional to $k^2 \cot\Theta_M$. Together with the vertical divergence β delivering a contribution of βk there results a resolution volume being proportional to $k^3 \cot\Theta_M$. The variance of the scattering angle $\Delta\Theta$ in eq. (9.12) follows to (without derivation):

$$\Delta\Theta = \sqrt{\frac{\alpha_0^2\alpha_1^2 + \alpha_0^2\eta^2 + \alpha_1^2\eta^2}{\alpha_0^2 + \alpha_1^2 + 4\eta^2}} \quad . \tag{9.13}$$

This dependence shows that the gain in intensity by the mosaic crystal is not to be "paid" by a worse energy resolution for $\alpha_0 = \alpha_1$! Generally, the influence of η on $\Delta\Theta$ is weak. (Fig.9.9)

Which crystals should now be used as monochromators for neutron? Apart from the lattice parameters further criteria are to be considered: those are the reflectivity, the suppression of $\lambda/2$-contamination, and last not least the availability as given by the technical and financial effort for their production in suitable quality and size. For example, for the same reflected wavelength, Cu has a better resolution as graphite (PG means pyrolytic deposited graphite), however, an appreciably lower reflectivity (see table 9.1 and Fig.9.7).

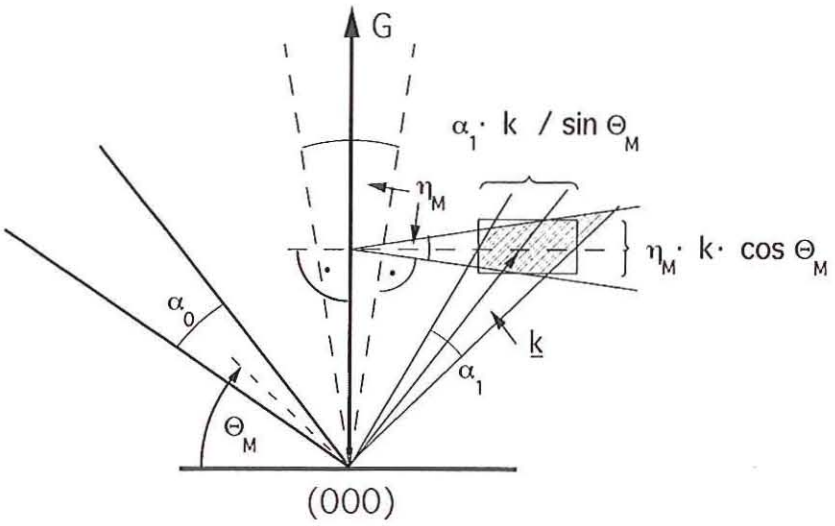

Fig.9.8: Bragg-reflexion by a crystal width mosaic spread η and collimations α_0 und α_1

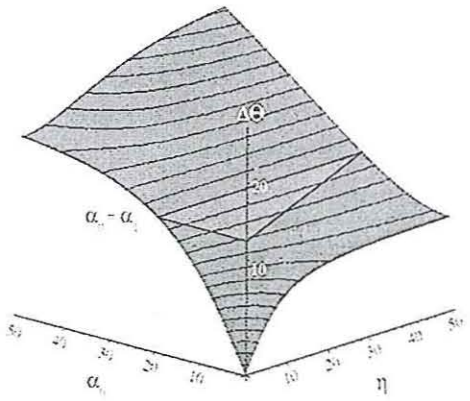

Fig.9.9: Dependence of $\Delta\Theta$ on α_0 and η

The elastic form factor of the crystal

$$F(\underline{Q}) = \sum_n b_n(\underline{Q}) \cdot \exp(i\underline{Q} \cdot \underline{R}_n) \tag{9.14}$$

plays an important role since it represents the coherent scattering length and the extinction rules. Eq. (9.14) delivers for the diamond lattice the form factors:

$$F(\underline{Q}) = b \begin{cases} 2 & \text{h+k+l} = 4n \\ 1 \pm i & = 2n + 1 \\ 0 & = 2(2n + 1) \quad !! \end{cases}$$

Thus Ge and Si have the desired property to suppress the $\lambda/2$-contamination of the reflected beam by means of the forbidden (222)-reflection when using the (111)-reflection.

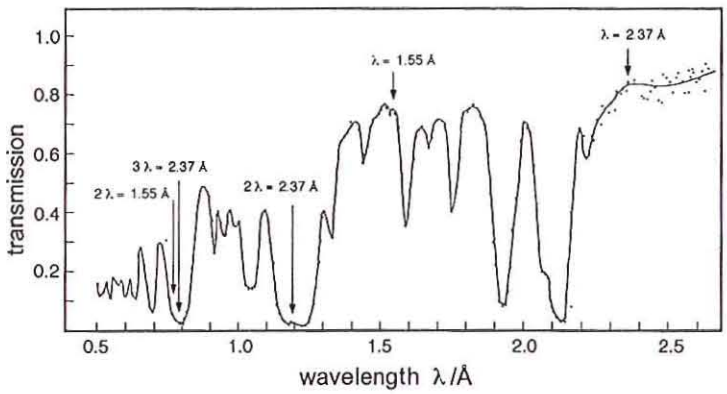

Fig.9.10: Transmission of PG-filters [4]

Choosing PG or Cu one gets contributions of higher order apart from the wavelength scattered first order. It is important to eliminate those contributions carefully in order to avoid any ambiguity of the measured signal. One may circumvent this problem by inserting suitable materials as filter, however, at the expense of weakened intensity. In addition, there result limitations in regard of the freedom to choose the wavelength as can be seen by the example

of the frequently used PG-filter. The corresponding transmission curve is shown in Fig.9.10. The goal is to choose a wavelength λ for which the filter offers an especially large transmission and, however, a large absorption for integer fractions λ/n. With the choice of $\lambda = 2.37 \cdot 10^{-10}$ m, neutrons with 2λ and $3\lambda = 2.37 \cdot 10^{-10}$ m will be largely suppressed. The wavelength $\lambda = 1.55 \cdot 10^{-10}$ m offers itself, as well. Above $\lambda \cong 4 \cdot 10^{-10}$ m , as in the case of a triple-axis spectrometer at a cold source, one uses a Beryllium-filter cooled by liquid nitrogen as a cut-off for shorter wavelengths.

Mosaic distribution of a crystal and beam divergence are not the only means to influence resolution and intensity. Those properties may be varied also directly by the choice of $\underline{k}$. In order to offer more neutrons at the correspondingly large or small incident energies, one shifts the maximum in the energy spectrum of the reactor neutrons by cooling (D_2 at 25 K) or heating (C at 2000 K) of a moderator. A spectrometer placed at a cold source (small $\underline{k}$), has a higher resolution as compared to those placed at thermal or hot sources. Thus, by selecting different moderation, one may vary ΔE between orders of 0.01 meV, 1 meV, and 100 meV.

Table 9.1: Properties of frequently used mosaic crystals

material reflection (hkl)		graphite (PG) (002)	Ge (111)	Cu (220)
λ -range / 10^{-10}m	upper limit ($\approx$2d)	6.708	6.533	2.556
	lower limit (Θ=10°)	1.16	1.13	0.444
peak- reflectivity (%)	$\lambda = 1 \cdot 10^{-10}$ m	-	-	14
	$= 2 \cdot 10^{-10}$ m	74	24	32
	$= 3 \cdot 10^{-10}$ m	82	34	-
	$= 4 \cdot 10^{-10}$ m	87	43	-
absorption		$5 \cdot 10^{-4}$	0.058	0.19
details			(222) forbidden	"bad" mosaic distribution
costs per crystal in DM (coarse)		20000	15000	5000

One notes that nearly all introduced components affect the resolution function of the spectrometer. This function – a four dimensional ellipsoid - results by projecting the product of the volume elements ΔV and $\Delta V'$ onto the $(\underline{Q},\omega)$-space (integration over the two dimensional

vector $\underline{P}$ in Fig.9.2 [5]. In the upper part of Fig.9.11, the orientation of the volume elements with respect to $\underline{k}$ and $\underline{k}'$ are indicated as well as projections of the resolution function. Inclination and widths of the ellipsoids depend strongly on the scattering sense – part (II) of the figure. Part (III) shows that there results an appreciable increase of the wave vector spread for scattering twice in the same sense. It is just those different projections on the various (Q,ω) directions which is exploited for the measurement of phonons. By adapting the slope of the resolution ellipsoid to the slope of the dispersion curve in question one achieves a focusing effect – as shown schematically in Fig.9.12. This exemplifies an important possibility to influence the quality of the measurement. The following two figures shall demonstrate

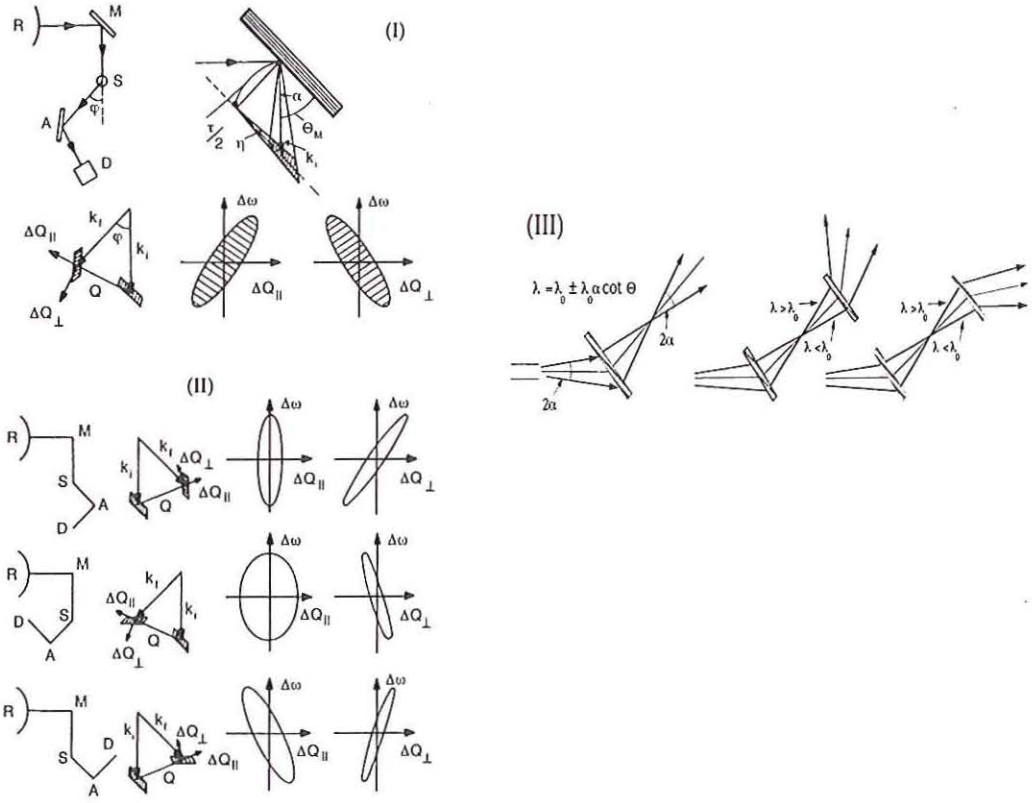

Fig.9.11: Dependence of widths and inclinations of the resolution ellipsoid from the configuration of the spectrometer ((I) and (II) from B. Dorner [6], with $k_i = \underline{k}$ and $k_f = \underline{k}'$)

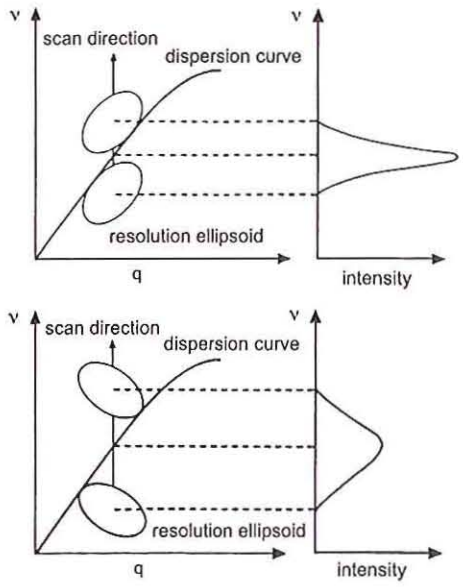

Fig.9.12: Effect of focusing for measurements of phonons. The integrated intensity is the same in both cases. The focused mode (upper part) exhibits a smaller width and a better signal-to-background ratio.

How one can obtain a complete picture of the dispersion surfaces by measuring phonons at selected symmetry direction and making use of a lattice dynamical calculation. In contrast to TOF-instruments recording simultaneously many points on the surface shown in Fig.9.3 (e.g. 128 angles * 1024 time channels), one may measure just one point with a conventional triple axis spectrometer. Fig.9.13a shows a scan in energy direction, i.e. a series of such points, whereby the vector $\underline{Q}$ is kept fixed in the system of the inspected crystal. Thus the widths of the observed peaks represent the frequency or energy width of the phonons folded with the resolution. The scan also demonstrates the general case that several phonons will contribute to a scan according to their dynamical structure factor. In fact, the same peak positions but quite different intensities will be observed at equivalent positions in other Brillouin zones.

On the one hand side this equivalence serves as experimental cross check for the peak positions (eigenvalues) and on the other hand one may derive the eigenvector from the observed intensities for a selected phonon.

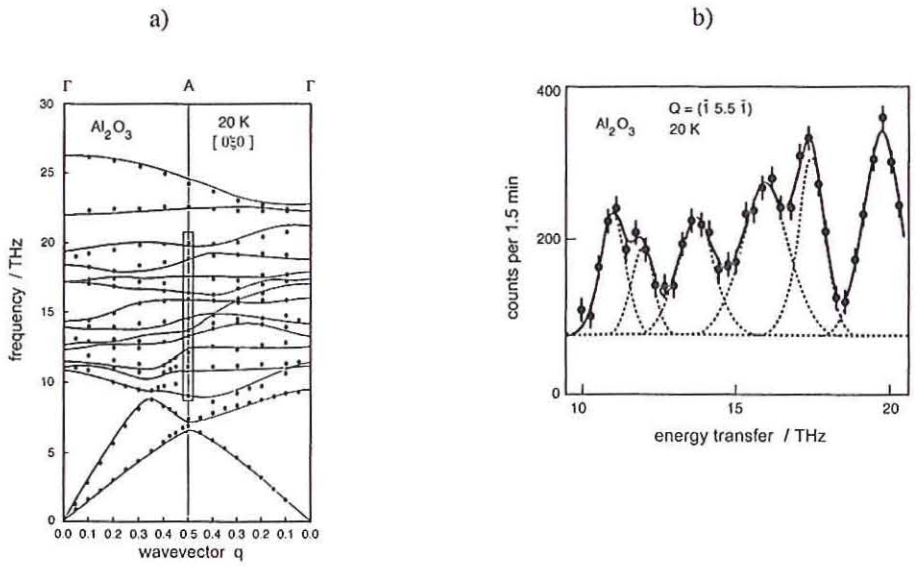

Fig.9.13: Phonon dispersion for Al_2O_3 (sapphire) along the (010)-direction at 20 K. The points (phonons) in a) result from the maxima observed in many separate scans. E.g. the results within the marked region are obtained from scans as shown in b). Such scans display however not always all theoretically expected phonons simultaneously. The solid line in a) represents the fit of the experimentally obtained data to a lattice dynamical model; in b) the line corresponds to the fit of the response funtion broadened by the resolution function of the instrument to the observed scattering intensity (in many cases, a one dimensional folding with a Gaussian is sufficient for fitting the measured spectra). [7].

The dispersion – often illustrated as curves along symmetry directions (e.g. Fig.9.13b) - represent of course dispersion surfaces being periodic with the Brillouin zone. In general, this surface needs not to be determined completely by further scans. One rather fits a lattice dynamical model (see lecture on inelastic neutron scattering) to the observed peaks and may extent this calculation to arbitrary wave vectors which "predictions" might in turn be tested experimentally. The dispersion surface for Barium is shown in Fig.9.14 in the $(0\bar{1}1)$-plane [8]. Directly measured have been the indicated points, only. The remainder results from a fitted lattice dynamical model.

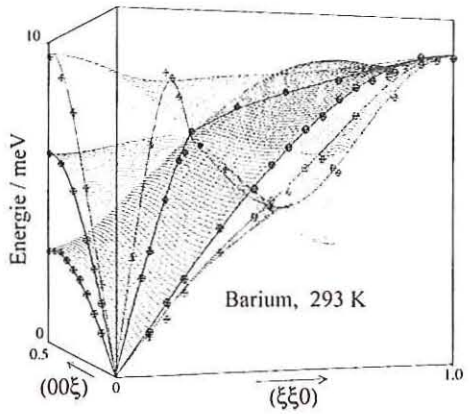

Fig.9.14: Dispersion surfaces for Barium in the $(\bar{1}10)$-plane. The solid lines correspond to the main symmetry directions, the points to the various observed peak positions of intensity. The transition from lighter to darker points corresponds to that from longitudinal to transverse polarisation of the phonons.

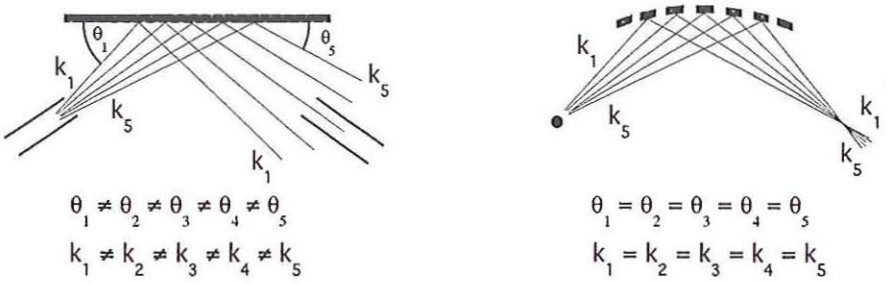

Fig.9.15: Left hand side: energy and resolution are determined by the deflection angle Θ as well as by the collimators absorbing all neutrons travelling outside the accepted divergence. Right hand side: for the so called monochromatic focusing, all deflection angles and thus the energy of the neutrons are equal due to the curved crystal such that the divergent (i.e. relaxed Q-resolution) but monochromatic neutrons merge together at the focusing point. Caution! the average energy of the set-up has now become dependent on the sample position due to the omitted collimators. The resolution will depend on the size of source and sample relative to the radius of curvature.

A final aspect for optimising the spectrometer shall now be mentioned. Considering the dispersion for Barium it becomes obvious that the dependence on wave vector for the so called *acoustic* phonons is not exceedingly large towards the zone boundary. Optical phonons (see the lecture on phonons and magnons) exhibit this property in most cases even more clearly. This means that one could achieve more intensity or shorter measuring times by reducing the $\underline{Q}$ -resolution and keeping the energy resolution constant, i.e. keeping the distinctness of the various phonon branches. This can be achieved by means of a horizontally curved monochromator and/or analyzer as drafted in Fig.9.15. About a factor of five in intensity may be gained by this horizontal arrangement. Experiments using doubly focusing deflection crystals exist since a couple of years requiring, however, a high degree of skill and experience.

9.5 Back-Scattering Spectrometer

It follows from Fig.9.16 and eq. (9.12) that for a given divergence of the neutron beam a crystal will achieve the optimum resolution in the modulus of $\underline{k}$ for the case of backscattering, i.e. for $\Theta = 90°$. This is the basic idea for the backscattering-(π)-spectrometer which realizes this optimum deflection angle both at the monochromator and the analyzer. For the case of backscattering one may rewrite eq. (9.12) to:

$$\left(\frac{\Delta k}{k_0}\right)_{div} = \frac{1}{\cos(\Delta\Theta/2)} - 1 \cong \frac{(\Delta\Theta)^2}{8} \tag{9.15}$$

Assuming that the divergence of the beam is determined by a neutron guide, one gets from eq. (9.9) and for the isotope ^{58}Ni

$$\Delta\Theta_{Ni} = \frac{2\Delta k_{Ni}}{k} = \frac{2\sqrt{(4\pi\rho b_c)}}{k}. \tag{9.16}$$

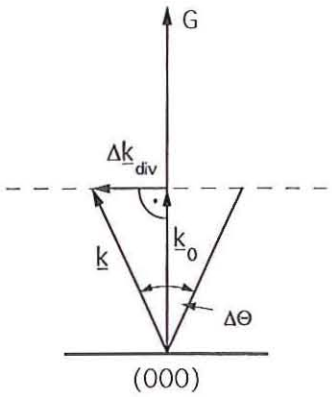

Fig.9.16: Bragg-reflection in the case of near backscattering.

Inserting $\Delta\Theta_{Ni}$ into eq. (9.15) delivers $\left(\Delta k/k_0\right)_{div} \cong 5\cdot 10^{-5}$ and with eq. (9.12) an energy resolution of $\Delta E = \frac{1}{2}\Delta k_{Ni}^{\ 2}\cdot E/k^2 \cong 2.4\cdot 10^{-7}$ eV. This contribution to the energy resolution is thus independent of the selected energy. Even with a triple axis spectrometer at a cold source this extreme value of ΔE is out of question. An additional contribution to the variance of k results from primary extinction, i.e. the fact that a final number of lattice planes contributes to the Bragg-reflection, only. Perfect crystals are used in order to maximise this number. This second variance is expressed in Fig.9.5 by the thickness of the bisecting plane. The primary extinction is proportional to the number of unit cells per volume N_z and the absolute value of the structure factor F_G, and inversely proportional to G^2. For perfect crystals like e.g. Si the additional variance is of about the same order as that due to the divergence of the k-vector. The maximum error for the energy results then from the sum of both contributions, i.e. adding the extinction in eq. (9.15) (without derivation).

$$\frac{\Delta E}{E} = 2\left(\frac{\Delta k}{k_0}\right)_{div} = 2\left(\frac{(\Delta\Theta)^2}{8} + \frac{16\pi N_z F_G}{G^2}\right) \tag{9.17}$$

Yet, how is it now still possible to vary the incident energy at such a spectrometer being restricted to the deflection angles $\Theta = 90°$? To this end one needs – according to eq. (9.1) – a variation of the lattice parameter or the reciprocal lattice vector $\underline{G}$. This can be achieved by heating the monochromator crystal or simply by moving the crystal (periodically) parallel to

the direction of $\underline{G}$ with a velocity v_D. The change of energy (in the laboratory system, Doppler effect) is then

$$\Delta E = 2E \cdot v_D / v_N \tag{9.18}$$

whereby E and v_N denote energy and speed of the backscattered neutrons and v_D die velocity of the Doppler drive. Moving a crystal - set to neutrons with $\lambda \approx 6.3 \cdot 10^{-10}$ m by using the Si(111) reflection – with a velocity amplitude of 2.5 m/s results in an energy range of $\pm$ 15 μ eV. Fig.9.17 now displays the realisation of the above considerations by means of an experimental facility.

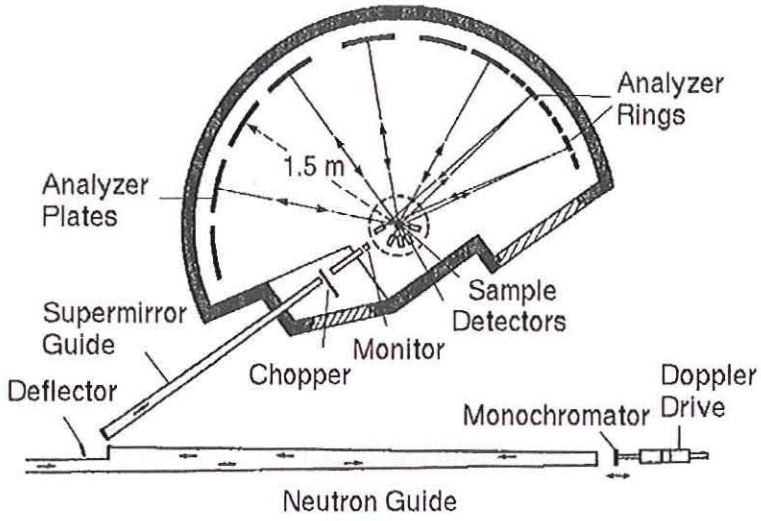

Fig.9.17: Layout of the backscattering spectrometer in Jülich

Not unexpectedly, this set up is quite different from that of triple axis spectrometer. The backscattered and Doppler shifted neutrons have to be deflected by a second crystal off from the neutron guide towards the sample position. This so called deflector is positioned next to the neutron guide which entails a slight deviation from perfect backscattering and thus the optimum energy resolution. Exact backscattering has been attempted in the first experimental set up by placing a deflector covering 1/10th of the beam size inside the neutron guide. Despite

the somewhat better resolution this option results in too a low flux for most applications. After deflection, the neutrons travel through a conical shaped, supermirror coated neutron guide which focuses the beam onto the sample. A chopper with about 50% dead time interrupts the continuous beam and triggers the gate of the counters. Thereby one avoids counting of those neutrons being scattered directly from the sample into the nearby counters, whereas neutrons having passed the analyzers are detected according to the Doppler velocity. The analyzers (elastically curved Si single crystals) are arranged at a fixed radius around the sample and focus the backscattered neutrons on the associated detectors. Note, that the energy resolution of the backscattering instrument also depends on the flight path. It increases with increasing flight path since the detectors have a finite volume which means slightly different detection times. The accuracy of the counting electronic may thereby be considered as perfect.

After all those constraints on the detected neutrons it might astonish that there remains sufficient intensity for measurements. We had learned about the cost of intensity for optimizing the resolution. In order to achieve a useful signal/noise ratio here, one has to relax the resolution in the momentum transfer. Taking the width of 45 cm for an analyzer plate being positioned at a distance of 150 cm to the sample, one gets an angular resolution of about $9°$. For an average $\underline{Q}$ value, given by $Q = {}^{4}\!/_{\lambda} \sin\Theta_s = 1.41 \cdot 10^{10}\ \mathrm{m}^{-1}$ for $\Theta_s = 90°$ and a wavelength $\lambda = 6.3 \cdot 10^{-10}$ m, this means a resolution of $\pm 0.1 \cdot 10^{10}\ \mathrm{m}^{-1}$. For comparison: at the triple axis spectrometer one has a resolution in $\underline{Q}$ of about $0.01 \cdot 10^{10}\ \mathrm{m}^{-1}$. On the other hand, most problems investigated on a backscattering spectrometer exhibit smooth functions on $|\underline{Q}|$, only, which allow for such a relaxed Q –resolution. The isotropic scattering also permits the simultaneous recording of several momentum transfers by arranging many counters and associated analyzer plates around the sample. In this respect the efficiency of a backscattering instrument is higher than that of a triple axis spectrometer which uses on detector, only..

Finally, as an example for a measurement on the backscattering instrument in Jülich, the temperature dependence of the spectrum of Paracetamol is shown in Fig.9.18. In this case, one is interested in the rotational or more exactly – permutational - tunneling of the methyl group of the molecule. Eigenvalues and eigenvectors of the associated hamiltionian result from the Mathieu equation for threefold symmetry.

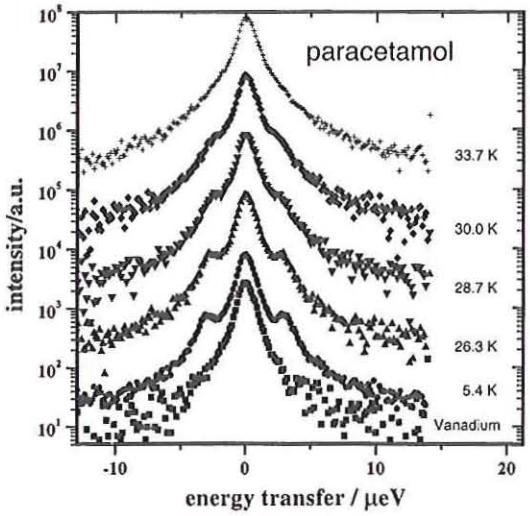

Fig.9.18: Rotational tunneling of the methyl group in Paracetamol.

The goal is to determine those eigenvalues (here about 3□eV for the A ↔ E transition, A = *totally symmetric*, E = *doubly degenerate*) and thus to obtain rather precise information on the intra- and inter-molecular interactions. A remarkable observation thereby is that the excitation energies are much smaller than the thermal energy of say 10 K of the sample (1 □eV ≈ 1/100 K). This may be understood by considering the basically different coupling of phonon (spin = 0) and neutron (spin = ½) to the eigenstates with different symmetries (see lecture on *Translation and Rotation).*

Literature

[1] B. N. Brockhouse, in *Inelastic scattering of neutrons in solids and liquids* (IAEA), Vienna,1961 p. 113

[2] H. Maier-Leibnitz, *Nukleonik*, **8**, 61 (1966)

[3] The Yellow Book, ILL (1988)

[4] V. J. Minkiewicz, G. Shirane, *Nucl Inst. Methods* **89,** 109 (1970)

[5] H. Grimm, *Nucl. Inst. Methods* **219,** 553 (1984)

[6] B. Dorner, *Coherent Inelastic Neutron Scattering in Lattice Dynamics*, Springer Tracts in Modern Physics, **Vol. 93** (1982)

[7] H. Schober, Dissertation, Universität Regensburg (1992)

[8] J. Mizuki, Y. Chen, K.-M. Ho, and C. Stassis, Phys. Rev. B **32**, 666 (1986)

10. Time-of-flight spectrometers

Michael Monkenbusch

10.1 Introduction

The information that may be extracted from a neutron scattering experiment can be expressed in terms of the *scattering function* $S(\underline{Q},\omega)$. All properties accessible by these kinds of scattering experiments are contained in $S(\underline{Q},\omega)$. The resulting intensity represents the double differential cross section:

$$\frac{d^2\sigma}{d\Omega dE'} = N\frac{k'}{k}b^2 S(\underline{Q},\omega) \tag{10.1}$$

where k', k is the modulus of the scattered and incoming neutrons respectively. N denotes the number of atoms in the sample and b is the *scattering length*[1]. The energy transfer during scattering is $\hbar\omega = (E - E')$, here E , E' denote the energies of the incoming and scattered neutrons respectively. The variables of the scattering function depend on $\underline{k}$, $\underline{k}'$; $\underline{Q} = \underline{k} - \underline{k}'$ is the momentum transfer and

$$\hbar\omega = (\hbar^2/2m_n)(k^2 - k'^2) \tag{10.2}$$

the energy transfer that occurred during the scattering process. Since the modulus of the wavevector $\underline{k}$ of the neutron is related as well to the neutron velocity, $\underline{v}$ (momentum) as to the wavelength (1/wavenumber):

$$\underline{v}m_n = \hbar\underline{k} \tag{10.3}$$

$$\frac{2\pi}{\lambda} = k \tag{10.4}$$

it is possible to determine the energy transfer (10.2) as well –by employing the wave properties of the neutron– by analysis of the wavelength λ' as –by using the particle character– by measurement of the velocity v' of the scattered neutrons. The first method is applied in crystal-spectrometers like the classical **triple-axis-spectrometer** or the

[1]For compounds containing different types of atoms (elements or isotopes) the corresponding expression consists of the sum of partial structure factors multiplied by the corresponding scattering lengths $b_i b_j$ in bilinear combination. For the discussion of instruments the simple version is sufficient.

backscattering-π-spectrometer; for details see chapter 10. The second method leads to the spectrometer types that are the topic of this chapter, namely different variants of **time-of-flight (TOF)-spectrometers**. Also the **neutron spin-echo spectrometer, NSE** that is described in the next chapter employs –somewhat less obvious– directly the velocity **change** of the neutrons to infer the energy transfer. The generic geometry of a scattering experiment in reciprocal (i.e. velocity, momentum or wavevector) space is illustrated in Fig. 1. The scattering triangle consisting of the incoming wavevector $\underline{k}$,

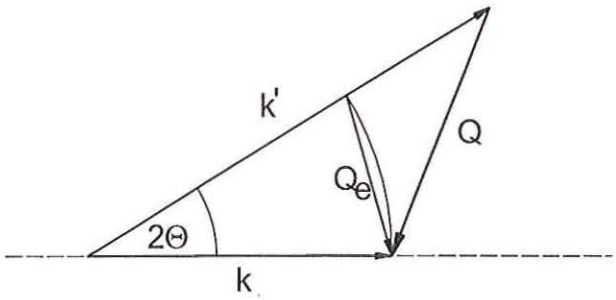

Figure 10.1: Scattering triangle.

the wavevector of the scattered neutrons $\underline{k'}$ and the resulting momentum transfer ($\div\hbar$), $\underline{Q}$, the figure shows the general situation of inelastic scattering (here: energy gain of the neutron). 2Θ is the scattering angle, $\underline{Q}_e$ indicates the momentum transfer for elastic scattering (i.e. **without** energy transfer).

A nuclear research reactor as neutron source basically yields a thermal (Maxwellian) spectrum of neutron velocities, the temperature of the moderator (D_2O-cooling water approx. $60°C$) determines the temperature of the neutron cloud. Many facilities contain additional small moderators of different temperature that supply single beam tubes with neutrons of a different spectral distribution (different temperature). In particular the so called "cold sources" have to be mentioned. In Jülich the "cold source", which supplies the neutron guide hall (ELLA) with long wavelength neutrons, consists of a small volume filled with liquid H_2 corresponding to a temeparture of 20 K. The following table enables a quick survey over the average values of the corresponding neutron spectra.

$T_{\text{Moderator}}/K$	$\sqrt{\overline{v^2}}/\text{m/s}$	λ/nm	$\hbar\omega/\text{eV}$	$\nu = \omega/2\pi/\text{s}^{-1}$
330	2870	0.14	28×10^{-3}	6.87×10^{12}
20	706	0.56	1.7×10^{-3}	0.42×10^{12}
5	177	2.24	0.4×10^{-3}	0.1×10^{12}

For specific experiments of course also neutrons of deviating velocities within a band around the average are employed, however far from that the available number density resp. the flux drops strongly. Typical neutron velocities are in the order of 1000 m/s the corresponding time-of-flight per meter is 1 ms/m, i.e. such neutrons need a couple of milliseconds for their journey through a spectrometer.

10.2 The classic time-of-flight spectrometer

Figure 10.2 illustrates the generic setup of a classical time-of-flight (TOF) instrument.

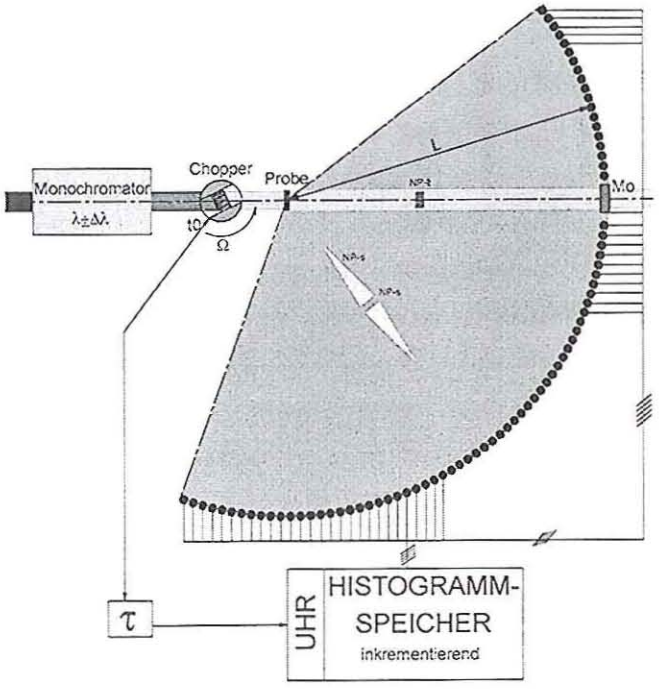

Figure 10.2: Generic setup of a classical TOF instrument.

From the thermal spectrum of the neutron beam entering from the left a monochromator (of any type) filters a limited wavelength band $\lambda \pm \Delta\lambda$. By doing this typically a bandwidth of $\Delta\lambda/\lambda \approx 10^{-2}$ is achieved. The thus monochromatized beam enters a so-called chopper which opens the beam path periodically for a short moment. Typical frequencies are between 20 and 200 Hz, the ratio of time-open:time-closed is around 1:100. The resulting pulse widths are of the order of several (tens) of microseconds. After an as short as possible flight path the neutron bunches hit the sample and are scattered according to the double differential cross section of the sample material. In this process some neutrons exchange kinetic energy with excitations in the sample, i.e. change their velocities. After scattering into different directions the neutrons transverse the flight space between sample and the detectors. The path length between sample and detector is usually kept the same for all detectors placed at the periphery of the flight space. The detectors most often consists of ^{3}He ($\simeq$10 bar) filled counting tubes of $30 \cdots 40$ cm length. Up to 1000 (and more) tubes are used in some installations to cover as much solid angle as possible.

The elastically scattered neutrons (like those from the direct beam) reach the detectors after the time $t_{CP} + t_0 = d_{\text{chopper-sample}}/v_0 + L/v_0$, those scattered inelastically arrive earlier (energy gain of the neutron) or later (energy loss of the neutron). Each pulse from a counting tube causes via the associated electronics an increment of one cell in the histogrammic memory. The address of this cell is derived from the time difference between chopper opening and arrival time of the neutron (pulse), i.e. TOF, and the detector number ($\rightarrow$ scattering angle). Thus the distribution of flight times evolves as a histogram of $512 \cdots 2048$ channels with a width of around 10μs each. For each detector (resp. group of detectors) such an histogramm vs. time is obtained. A monitor (Mo) in the direct beam serves to normalize the histograms to the incoming neutron flux. [2]

[2] A "monitor" is a detection device (counting "tube") that covers the beam cross section and has a high transmission for neutrons (> 90%) and low detection probability ($10^{-3} \cdots 10^{-7}$). In the figure only one monitor behind the sample is shown for clarity. In general another monitor (more important) is located between chopper and sample, it measures the incoming flux without the influence of the sample transmission.

10.2.1 Interpretation of spectra

As displayed in the path-time diagram in fig. 10.3 pulses of neutrons with defined velocity are periodically transmitted by the chopper with the frequency [3] $N\Omega = 1/\tau$. The slope of the dashed lines corresponds to the average velocity v_0. The neutron pulse needs a constant time t_{CP} for the distance from the chopper to the sample $d_{\text{Chopper-Probe}}$. After

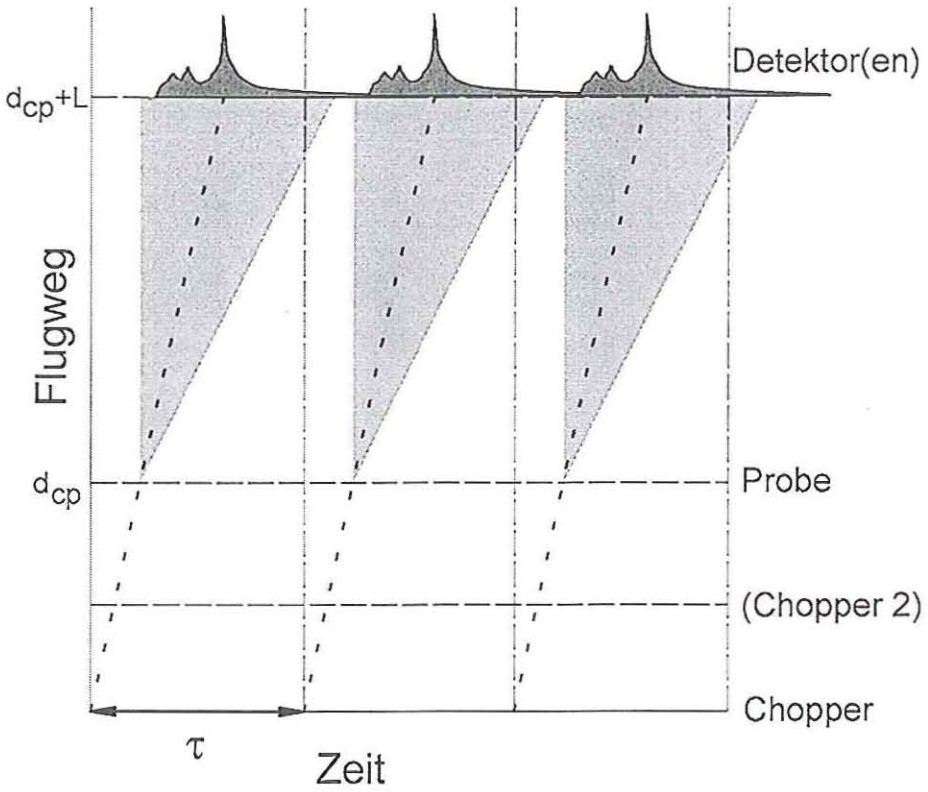

Figure 10.3: Path(Flugweg)-time(Zeit) diagram.

This velocity spread is indicated by the filled grey triangles. The analysis of arrival

[3] According to the technical realization there is an integer factor between rotation frequency of the chopper and pulse repetition frequency; e.g. a Fermi chopper that opens twice per one revolution (see 10.2.4).

times is performed at the detector distance $d_{CP} + L$. A possible resulting "spectrum" is indicated on top of the detector distance line. The extrapolation of the dashed line to the detector position indicates the location of the "elastic line", i.e. the time channel where neutrons without energy transfer arrive [4]. The left vertical edge of the triangle defines the "beginning" of the time-of-flight spectrum, i.e. the earliest possible time of arrival occurring only for nearly infinite energy gain of the neutron. In reality there are no infinite large energy gains and the proper spectrum starts somewhat later. The right edge of the "velocity fan" symbolized by the triangle is less well defined, in principle the neutron may transfer only a part of its energy but also virtually all of its energy to the sample, thus virtually hortizontal path-time curves may result. I.e. strictly speaking the spectrum does **not** end at some maximum channel number. However it is immediately recognizable that fortunately this effect goes along with a corresponding "dilution" of the intensity which becomes virtually structureless on the scale of the histogram channel windows ("frames") causing a constant background in all channels of a "frame" that may be subtracted during data treatment. Thereby it becomes possible to repeat the uptake of a "frame" with a frequency Ω and to accumulate the spectra into the histograms mentioned above. Each chopper pulse resets the clock to time zero and the channels of the histogram cover the time interval τ in terms of bins of width $\Delta\tau_K \approx \tau/N$. If due to resolution requirements [5] or due to other technical demands Ω has to be chosen such that the above discussed "frame"-overlap effect still distorts the spectra, it is possible, as indicated in fig. 10.4, to use an additional coarse chopper to transmit only every 2nd or n-th pulse. By doing this sufficient spacing between "frames" may be gained to collect an undistorted spectrum, however with an n-fold reduction of effective data collection rate.

10.2.2 Time-of-flight spectra

In fig. 10.5 several spectra as they are accumulated in the histogrammic memory are displayed. The time-of-flight scale of the horizontal axis refers to the distance L between sample and detectors. This time-of-flight is directly proportional to the wavelength λ' of the scattered neutrons as is indicated by the diagonal representing this linear relation

[4] Generally the scattering without (sizeable) energy transfer is the most probable process.

[5] The pulse width (opening time) of a chopper depends –for a given design– on its rotation frequency.

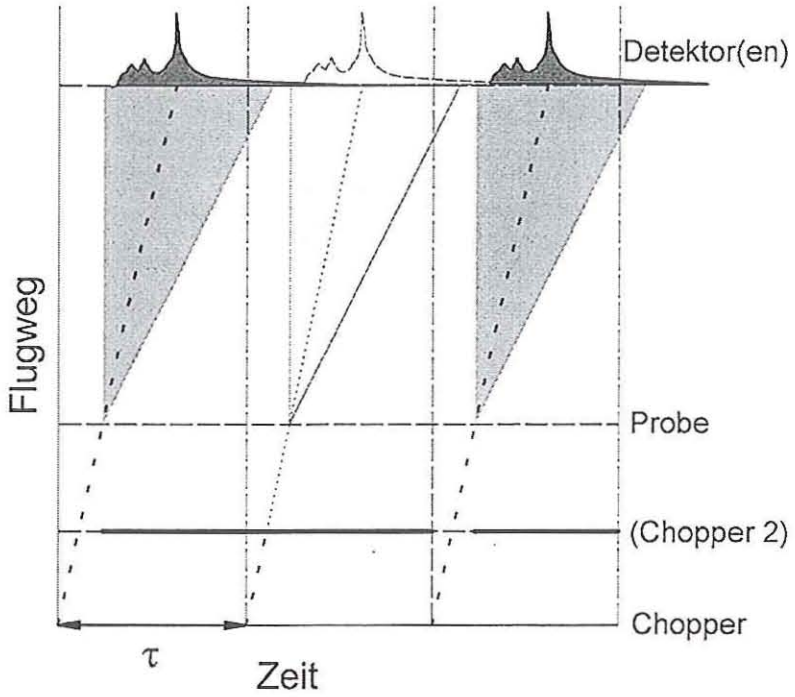

Figure 10.4: Path-time diagram for a configuration with "Frame overlap choppers", chopper 2.

using the right hand vertical scale. This diagonal straight line intersects the level $\lambda_0 = 0.6$nm at the location of the "elastic channel" where neutrons are collected that did not change their velocity during scattering. Since in liquid water which was the sample all molecules may diffuse without restriction only a so called **quasielastic** line is observed which corresponds to a Lorentzian with a width proportional to Q^2. The maximum of intensity is nevertheless at the elastic channel ($\rightarrow$ quasielastic). The difference between a solid with atoms/molecules fixed at lattice sites and a liquid is illustrated by the right part of the figure. Imidazole in the solid state exhibits an intense line at the elastic channel with a width corresponding to the instrumental resolution. In contrast molten imidazole (especially for the relatively large scattering angle displayed here $\rightarrow$ large Q) shows only a broad quasielastic intensity distribution. At shorter times-of-flight corresponding to larger

energy transfers (gains) structures in the spectra are visible that stem from molecular and lattice vibrations. Note the second left scale in combination with the dashed line that illustrates the strongly nonlinear relation between energy and time-of-flight. For energy gains $\Delta E \gg k_B T$ the scattering energy dies out due to the exponential Boltzmann factor. At ambient temperature $k_B T$ is equivalent to 25meV. Well above that energy gain the unavoidable virtually constant background due to "frame overlap" may be determined.

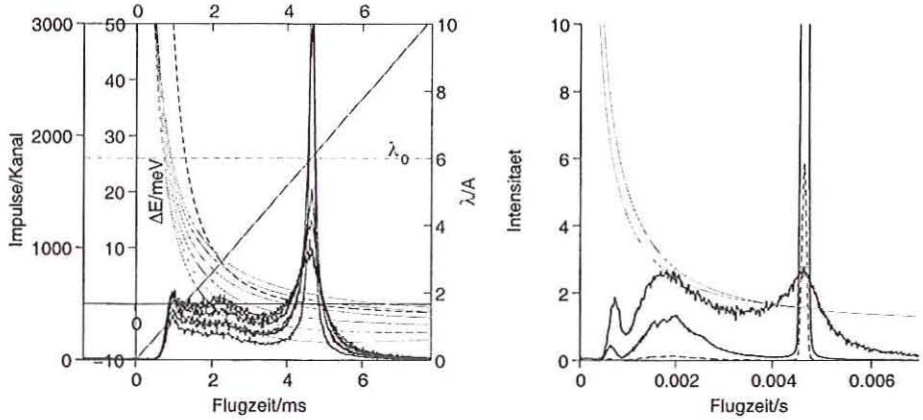

Figure 10.5: Left: TOF-spectra from liquid water at ambient temperature for different scattering angles between 30° and 140°. Parameters: $\lambda_0 = 0.6$nm, $\Delta\tau = 18\mu$s, $L = 3.05$m, $N = 512$. Right: TOF-spectrum from imidazole (C_4H_4NH) as crystalline solid at 300K (the dashed lines displays the same data scaled by $\times 0.1$) and as melt at 403K at a scattering angle of 95°.

Technically a TOF spectrum is accumulated at a fixed scattering angle for each detector. That corresponds to the situation of the scattering triangle as depicted in fig. 10.1. A glimpse on this figure makes clear that different momentum transfers $\underline{Q}_e$ and $\underline{Q}$ (depending on energy transfer) for elastic and inelastic scattering have to be assigned to the different time channels of the histogram from one specific detector. That applies as well for the modulus Q as for the direction of $\underline{Q}$. The sequence of curves in the left figure 10.5 shows the values of Q as function of scattering angle (different curves) and time channel. The property that the values become very similar for large energy gains –also expressed by

the similar intensity distribution of that part of the spectra for different angles– follows from the fact that the main contribution to Q at high energy gain stems from the length difference of k and k' (see fig. 10.1). The variation of $|\underline{Q}|$ may be compensated within certain limits by combining the data from different detectors (angles), however that does not apply for the direction change of $\underline{Q}$. Therefore TOF-instruments –in contrast to triple-axis spectrometers– are better suited for isotropic samples (liquids, powders, amorphous substances) than for single crystals or other highly oriented samples.

10.2.3 Transforms

Since the physics of the systems under investigation is usually expressed in terms of $S(Q,\omega)$, a transformation of the raw data representing $I(2\Theta,t)$ into the (Q,ω)-space is necessary. With $t = L/v'$ and $t_0 = L/v$ inserted in Eqn. 10.2 yields

$$\omega(t) = \frac{m_n}{2\hbar} L^2 \frac{t^2 - t_0^2}{t^2 t_0^2} \tag{10.5}$$

and

$$Q = \frac{m_n}{\hbar} L \sqrt{\frac{t^2 + t_0^2 - 2cos(2\Theta)t_0 t}{t_0^2 t^2}} \tag{10.6}$$

The nonlinear mapping from channels to energy given by Eqn. 10.5 also causes a strongly varying energy-width of TOF-channels, K.

$$I(2\Theta,K) \propto \int_{(K-1)\Delta\tau}^{K\Delta\tau} \frac{k'}{k} 4\pi b^2 S(\underline{Q},\omega(t)) \frac{d\omega}{dt} dt \tag{10.7}$$

or somewhat simpler

$$I(2\Theta,K) \propto \frac{k'}{k} 4\pi b^2 S(\underline{Q},\omega(K\Delta\tau)) \frac{d\omega}{dt} \Delta\tau \tag{10.8}$$

with

$$\frac{k'}{k} = \frac{t_0}{t} \tag{10.9}$$

and

$$\frac{d\omega(t)}{dt} = \frac{m_n}{\hbar} L^2 \frac{1}{t^3} \tag{10.10}$$

the result

$$I(2\Theta,K) \propto S(\underline{Q},\omega(K\Delta\tau)) \ \frac{1}{t^4} \tag{10.11}$$

is obtained, all constant factors are omitted and lumped into a still undetermined proportionality factor [6]. Note the factor t^{-4} between S and I which causes a significant intensity enhancement for the early arriving time channels, however intimately connected with a corresponding loss of energy resolution. Application of the transforms Eqns. 10.5 and 10.11 allows a display of the spectra in terms of $S(2\Theta,\omega)$. Figure 10.6 shows a corresponding $S(2\Theta,\omega)$ derived from the water data (medium angle data in fig. 10.5).

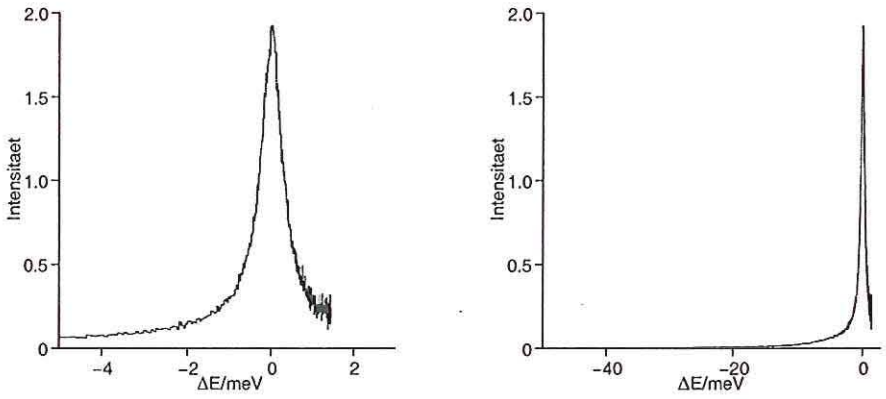

Figure 10.6: TOF spectrum from liquid water (see fig. 10.5) converted to $S(2\Theta,\omega)$ displayed over two different energy ranges.

The diffusion is easily recognizable but the structure due to (internal) vibrations is lost in this type of representation. As soon as a model for $S(Q,\omega)$ is available, it is in most cases more advantageous to apply the inverse transform to that model to compute $I(2\Theta,K)$ and to compare this result with the raw TOF data. This procedures also allows for a simpler more direct application of resolution corrections.

Remark: application of a coordinate transform (here $(Q,\omega) \rightarrow (2\Theta,K)$ resp. $(Q,\omega) \leftarrow (2\Theta,K)$) requires –besides the observation of the (nonlinear) coordinate dependence– the application of a Jacobian determinant as factor to preserve "volume". For the time-frequency part this is also done here (t^{-4}-factor). The transform $2\Theta \rightarrow Q$, however

[6]For practical purposes the proportionality factor is determined by an absolute calibration using a standard sample, e.g. vanadium which is a purely incoherent elastic scatterer.

is performed without Jacobian due to an asymmetry in definitions of $S(Q,\omega)$, namely $d\sigma(2\Theta)/d\Omega = S(Q(2\Theta))$!

10.2.4 Fermi chopper

One possibility to open the beam for a short time to create the required neutron pulse consists in the placement of a short rotating collimator in the beam such that it transmits neutrons only for a narrow interval of the rotation angle. The collimator consists of of a parallel arrangement of neutron absorbing sheets (cadmium, gadolinium, boron). The gaps are filled with a material which is transparent for neutrons (aluminum). Such a chopper is sketched in fig. 10.1, this type of chopper is called "Fermi chopper". The divergence $\Delta\alpha$ is determined by the distance between neigbouring sheets D and their length l in beam direction, $\Delta\alpha_{FWHM} = \arctan(D/l)$ (typical values are $1^\circ \cdots 2^\circ$). The duration of the opening $\Delta\tau$ is given by the rotation frequency Ω

$$\Delta\tau_{FWHM} = \frac{\Delta\alpha_{FWHM}}{2\pi\Omega} \tag{10.12}$$

Note that the neutron pulse frequency for a chopper with straight collimator slits is 2Ω, because the collimator axis is twice per revolution parallel to the beam axis. Since the neutrons have a finite velocity, the chopping collimator must not be too long, because otherwise the transmission direction drops too much even before the neutrons that entered, when the collimator orientation corresponded to transmission, have emerged from the collimator. It is also possible to use a "collimator" with curved slits, which accounts for the above mentioned effect, however such a curved-slit-chopper exhibits a wavelength dependent transmission characteristic. Sometimes this is a desired characteristic to suppress unwanted orders of monochromator Bragg reflections.

10.2.5 Disc choppers

Besides the Fermi choppers also so called "disc choppers" are used. Figure 10.7 shows a front view with respect to the beam direction of such a chopper disc.

The disc is covered by a neutron absorbing layer (dark grey) and contains –for counterbalancing two– window zones, A and B. The beam cross section is indicated as striped area in A. The typical diameter of such discs is $0.5 \cdots 1$m. From the figure it is immediately visible that the ratio pulse width to pulse-pulse distance for a copper of this type is rather

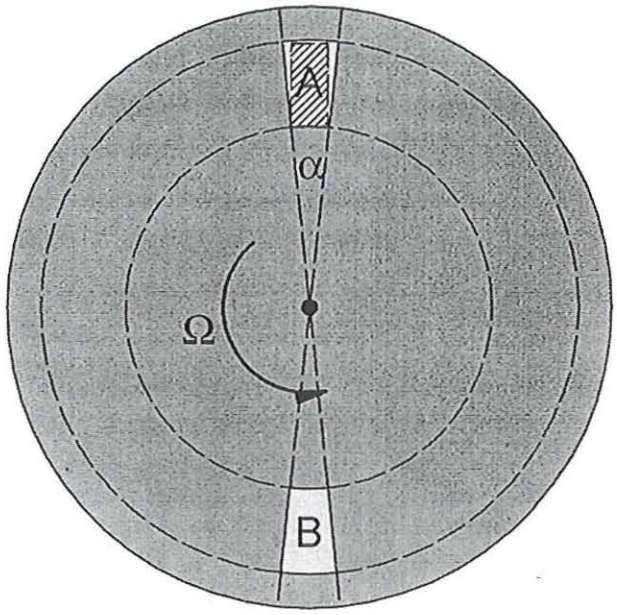

Figure 10.7: Disc chopper.

10% than 1%. A reduction of the window size would not help to improve this ratio, since that would also impose a reduced beam width on the system which would reduce the available intensity to an unacceptable level. To achieve nevertheless a reasonable temporal resolution with the required pulse-pulse distance (to avoid "frame overlap"), it is necessary to combine several disc choppers where slow choppers select only one of several openings of faster ones (rotating with a integer multiple n of the pulse repetion frequency Ω). The resulting pulse has –according to the higher rotation frequency $n\Omega$– a length which is shorter by a factor $1/n$. Also counter rotating discs are employed. The multiple disc chopper technique requires exact electronic control of the relative rotation phases of the choppers.

10.2.6 Crystal monochromators

The monochromator indicated in fig. 10.2 has the function to select neutrons from a narrow band of velocities (approx. 1%) out of the Maxwellian spectrum of the incoming primary beam. It may be realized by different means. First the **crystal monochromator** is described. It uses the matter wave properties of the neutrons to select neutrons of a defined wavelength (i.e. velocity) by interference in a crystal lattice (Bragg reflection). Neutrons with a wavelength of

$$\lambda = \frac{2d}{n} \sin(\Theta_M/2) \tag{10.13}$$

are reflected in direction of the sample; here d is the distance of lattice planes of the monochromator crystal (often pyrolytic graphite 002, $d = 0.6708$nm), n the diffraction order and Θ_M the angle of reflection. I.e. a simple crystal monochromator rotates the beam direction by Θ_M; if the wavelength should be changed the bulky rest of the spectrometer must be rotated around the location of the monochromator crystal. See figure 10.9 in the following section. [7] In addition Eqn. 10.13 implies that generally several diffraction orders are reflected. To suppress the unwanted orders mainly three methods are used:

1. **Filter:** if the desired wavelength λ is long enough it is possible to use a block of polycrystalline material (mostly beryllium) which has negligible neutron absorption. The shorter wavelength neutrons are Bragg reflected by some crystallites in the block and removed from the beam direction while the long wavelength neutrons with $\lambda > 2d_{max}$ are transmitted with low losses.

2. **Curved slit choppers:** by curving the slits of a Fermi chopper it is possible to achieve that the chopper is only transparent for a certain band of neutron velocities. This band may be selected such that only the selected diffraction order is included.

3. **Second (coarse) chopper:** by a second (coarse) chopper at some distance from the main chopper it is possible to select the desired diffraction order via the TOF

[7] This may be avoided by the use of two crystals in a parallel arrangement. The second crystal performs a reflection that restores the original beam direction and rotation and translation of the crystals in such a "double monochromator" are performed such that the direction and position of the monochromatized beam stays the same for all wavelengths. However this advantage is connected with an intensity loss. More about crystal monochromators may be found in the chapter "Crystal spectrometers".

between the two choppers. See also section TOF-TOF.

10.2.7 Time focussing

It seems unsatisfactory that by a TOF spectrometer at a continuous source (reactor) only a small fraction (1%) of the continuous primary beam is utilized. On the other hand the TOF-analysis correlates the energy resolution with the length of the neutron pulses $\Delta\tau$. However there is trick to partly compensate for this correlation and to achieve a multiplication of the intensity without resolution loss (at the elastic line), see fig. 10.8. The chopper opening may last longer if there is a correlation between time and wavelength (velocity) of the neutrons during the opening interval such that all neutrons arrive at the same time at the detector –as indicated in fig. 10.8. By this means the elastic line remains

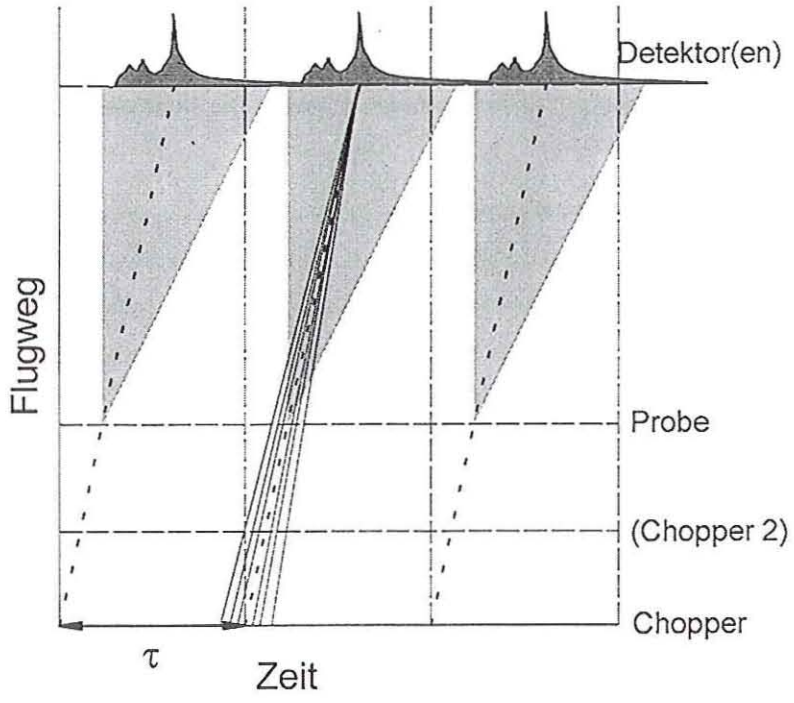

Figure 10.8: Path-time diagram, time focussing.

narrow but the focussing effect depends on energy transfer and becomes ineffective for

larger energy transfers. However it is possible to move the focusing point to some inelastic energy transfer by chosing a different chopper frequency. Figure 10.9 shows a technical realization of the time focussing principle.

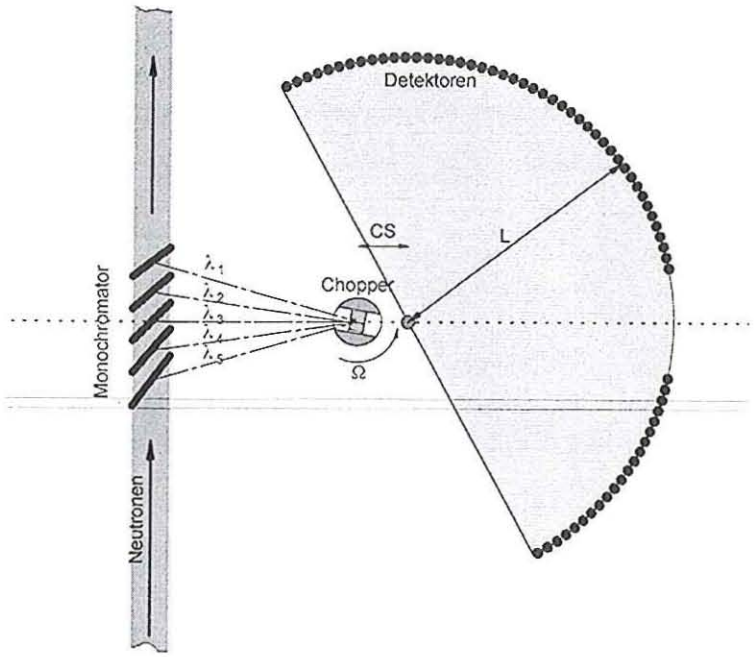

Figure 10.9: TOF-spectrometer with time-focussing.

Instead of only one monochromator crystal several crystals one after the other form the monochromator, each crystal reflects a slightly different wavelength $\lambda_1 > \lambda_2 \cdots > \lambda_5$, such that the slowest neutrons (λ_1) are transmitted first when the chopper channel approaches transmission during a revolution; thereafter the gradually faster neutrons ($\lambda_2 \cdots \lambda_5$) follow subsequently. For a set of matched distances between crystals and between monochromator and chopper and frequency Ω of the chopper a path-time behaviour as illustrated in fig. 10.8 may be achieved. By the use of 5 instead of one crystal about 5 times as much neutrons hit the sample.

10.2.8 TOF-TOF: TOF-monochromator

Instead of a crystal monochromator (see above) the incoming wavelength (velocity) may be equally well selected by the time-of-flight between two choppers (see fig. 10.10), therefore the abbreviation **TOF**(monochromator)-**TOF**(analyzer).

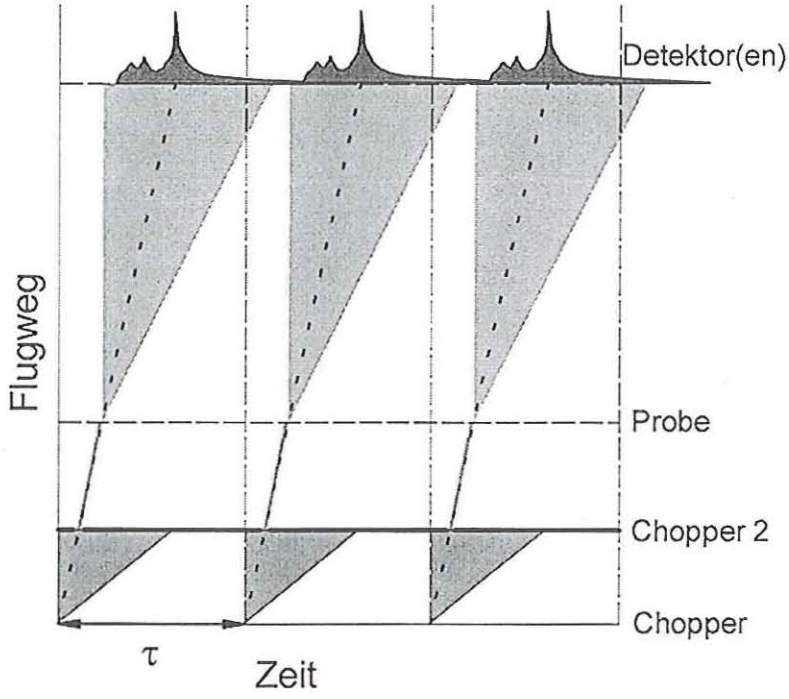

Figure 10.10: Path-time diagram for an instrument with TOF-monochromator.

A technical realization of this principle is e.g. the IN5 spectrometer at the ILL in Grenoble. It is equipped with a system of disc choppers. Besides the flexibility to choose wavelength simply by changing the chopper phasing a better defined resolution function, due to convolution of several real triangular window opening functions, is advantageous. In any case this method of monochromatization automatically yields a pulsed beam hitting on the sample.

10.3 Inverted TOF-spectrometer

In the spectrometer types described above the sample was "illuminated" by pulses of neutrons with a single defined wavelength (velocity) which have been prepared by a chopper-monochromator combination. The analysis of the velocities of the scattered neutrons was effected by TOF-measurement.

It is also possible to **invert** this sequence, the incoming velocity (i.e. wavelength, energy, k) is determined by the TOF between chopper (pulsed source) and sample. Then –to obtain a defined energy and momentum transfer– only scattered neutrons of a given final wavelength that may pass an analyzer are detected.

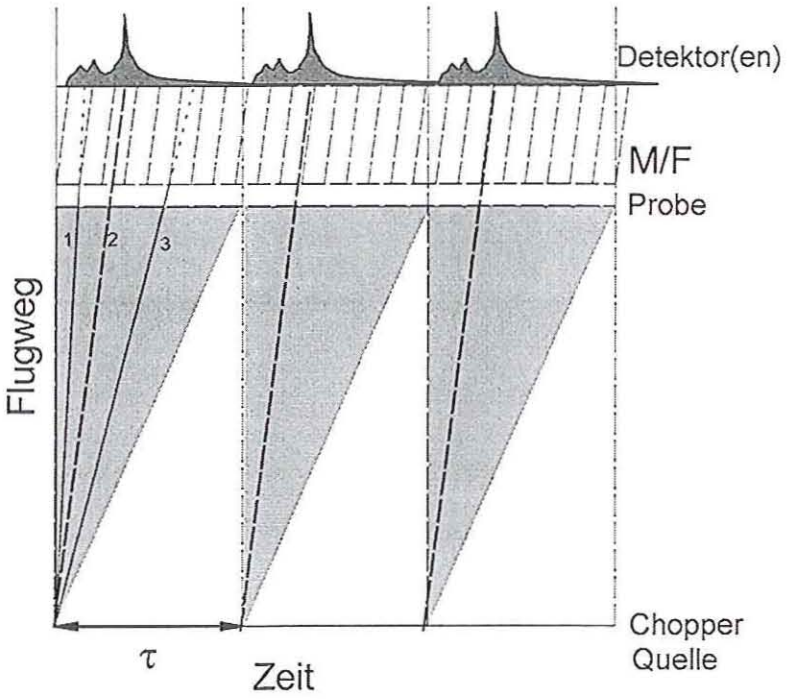

Figure 10.11: Path-time diagram of a TOF spectrometer with inverted geometry.

The corresponding path-time diagram is displayed in figure 10.11. Neutrons emerging the pulsed source fly according to their individual velocity in direction of the sample,

the associated paths are indicated by the grey triangle. The intensity within the range of this triangle is of course not uniform but depends on the spectral properties of the source. [8] Neutrons that have been elastically scattered by the sample (path 2) pass the analyzer/filter M/F and lead to the elastic line in the TOF-histogram. Neutrons that loose energy (path 1) are faster before the sample scattering and arrive earlier at the detector than the elastically scattered ones. Analogously path 3 represents neutrons that gained energy during scattering. Compared to a "normal" TOF instrument the energy gain and energy loss sides of the histogram are reversed. Therefore also high energy excitations that are thermally not occupied may be measured.

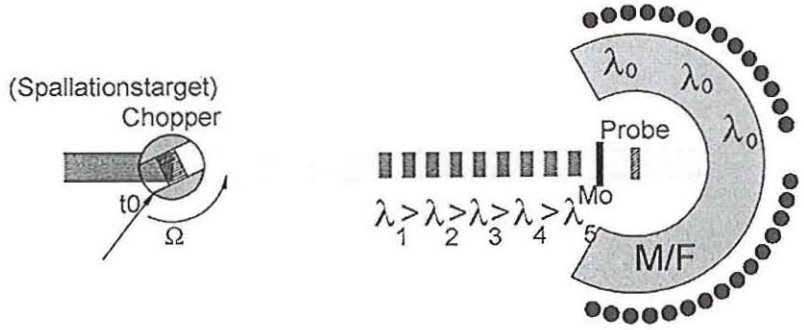

Figure 10.12: Setup of a TOF spectrometer with inverted geometry.

Figure 10.12 shows a corresponding setup. The pulse at the chopper contains neutrons from a broad velocity distribution (Maxwellian spectrum at moderator temperature). During the path from chopper (pulsed source) to sample this pulse separates into different wavelengths λ, resp. different incident energies, that arrive at different times at the sample. Since a wavelength selection (to λ_0) is performed between sample and detectors, all detected neutrons have the same velocity and the distance sample-detector adds a

[8] In particular overlap of the triangles ("frame overlap") may happen, which may be suppressed by filters tayloring the incoming spectrum.

constant offset to the TOF. To be able to correct the TOF-histograms with respect to the spectral distribution of the incoming pulse, it is important to detected the incoming neutron flux by a monitor (Mo) located close to the sample position accumulated in a separate TOF-histogram. This type of TOF-spectrometer is preferentially used at pulsed sources, ideally it may be possible to omit the first chopper by taking the pulse as generated by the pulsed source (spallation target). [9] All neutrons from the pulse (flying into the right direction) are utilized. This method has a few specific advantages and disadvantages, advantages are:

1. The pulse contains neutrons with high incident energy that may perform energy loss scattering, the resolution at high energy loss is relatively good, especially if the pulsed source supplies very short pulses at high neutron energies.

2. If the analyzers are used in near backscattering configuration high resolutions (comparable to those on true backscattering spectrometers, see chapter 9) can be attained.

The utilization of the full spectrum has however also disadvantages:

1. The full "white" pulse enters the shielded sample detector space. Any parasitic scattering and any imperfection of the analyzing filters or failure to absorb neutrons of "unused" final wavelength or direction leads to increased background. In addition the background depends on the sample which makes correcting subtractions difficult.

2. Samples are hit by a higher integral flux and therfore become more radioactive.

In general also "normal" TOF instruments perform better on a pulsed source in comparison with a reactor (if the average fluxes are equal) since by synchronizing source and chopper only a small part of the generated neutrons (with the desired wavelength) are not used. The distance source-chopper may serve at the same time as TOF-monochromator. In total the efficiency is comparable with the inverted type because in both cases on one side of the sample the spectrum is restricted by filters/monochromators and on the other side the full spectrum is utilized and sorted according to the TOF. Energy transfer analysis without filter on any side is impossible.

[9] To suppress background or to prevent "frame overlap" it may be nevertheless advisable to use an additional chopper.

10.3.1 Analysis by filters

The analyzer that is indicated by the grey segment labelled M/F in fig. 10.12 may either consist of an array of crystals reflecting scattered neutrons of the selected wavelength λ_0 onto the associated detectors or of a filter. Especially in the early days of neutron scattering filters made from polycrystalline blocks of Be , BeO etc. were used. These filters are transparent only for neutrons with energies below the "Bragg-edge", i.e. for wavelengths larger than twice the largest lattice spacing. All faster neutrons will be reflected by some crystallite in the block. By integrated absorbing plates the thus reflected neutrons are removed. For the filter to be sufficiently transparent below the Bragg-edge the used material may only have a very low absorption cross section. In addition the thermal diffuse scattering by fluctuating lattice deformations (phonons) has to be suppressed by cooling (liquid nitrogen). Below the Bragg-edge these filters transmit all neutrons from nearly zero energy to the edge energy of a few meV. For the spectroscopy of high energy excitation this is accceptable since the energy transfer is then determined by the incident energy of a few 100 meV. High resolution quasielastic scattering has to be done with other instruments. By employing the difference between data obtained with two different filters (e.g. Be and BeO) the effective window of final energies may be narrowed, however two measurements are needed and the final signal is obtained from a small difference of two larger counting signals with the corresponding statistical errors.

10.4 Resolution and intensity

One important quality of a spectrometer is its resolution in $(\underline{Q},\omega)$-space. For TOF-spectrometers –unlike for triple-axis instruments– for many applications mainly/only the energy resolution is important since the scattering intensity has to be collected and accumulated in a large solid angle anyway to yield a sufficient number of counts. The energy resolution is determined by the accuracy of the TOF-measurement and by the width of the incoming (or analyzed) wavelength band. The latter is given by the beam divergence in combination with the mosaic width of the crystals (see also chapter on triple-axis spectrometres). The TOF-uncertainty is given by the chopper pulse length and the accuracy of the flight path. The flight path cannot be defined with arbitrary accuracy, since finite

sample size of cm and a detection position uncertainty of some mm in the detectors[10]. If all timing uncertainties are lumped into Δt, a classical TOF instruments has the following resolution:

$$\Delta\omega = \sqrt{(\frac{\partial\omega}{\partial t}\Delta t)^2 + (\frac{\partial\omega}{\partial\lambda}\Delta\lambda)^2} \tag{10.14}$$

From Eqns. 10.2 - 10.5 follows:

$$\Delta\omega = \sqrt{(\frac{m_n L}{\hbar t^3}\Delta t)^2 + (\frac{4\pi^2\hbar}{m_n\lambda^3}\Delta\lambda)^2} \tag{10.15}$$

Because $\lambda' \propto 1/v' \propto t$ and close to the elastic line ($\lambda' \approx \lambda$) it follows that $\Delta\omega \propto 1/\lambda^3$, i.e. the most efficient measure to increase the "elastic" resolution is the use of a long neutron wavelength/ For a matched setup the relative timing uncertainty $\Delta t/t_0$ and the relative wavelength width $\Delta\lambda/\lambda$ should be about equal. Eqn.10.15 shows in addition that the timing uncertainty term $\propto \Delta t$ dominates the resolution width for short time t, i.e. large energy gain of the neutron. If path uncertainties ΔL are treated separately, Δt represents only the chopper opening and Eqn. 10.15 reads:

$$\Delta\omega = \sqrt{(\frac{m_n L}{\hbar t^2}\Delta L)^2 + (\frac{m_n L}{\hbar t^3}\Delta t)^2 + (\frac{4\pi^2\hbar}{m_n\lambda^3}\Delta\lambda)^2} \tag{10.16}$$

For the inverted spectrometer the expressions stay the same except for the exchange of λ and λ'.

10.4.1 Intensity

The available neutron sources are rather weak compared to sources of electromagnetic radiation (laser, synchrotron), they emit neutrons in form of a thermalized gas with a broad distribution of velocities and into all directions. Preparation of collimated and monochromatic beams is only possible by selection, i.e. removing all unwanted neutrons. The resulting beams –even at high flux reactors– contain only relatively few neutrons. [11] For this reason the available neutrons have to be utilized as efficient as possible. Even

[10] For sample in form of thin plates the path uncertainty due to scattering position in the sample may be reduced for (only) one scattering angle (region) to the plate thickness.

[11] The typical neutron flux in front of the chopper of a classical TOF instrument is in the order of 10^7n/cm^{2}s, after chopping only 10^5n/cm^{2}s hit the sample and are available for scattering. In comparison a beam of a small 1 mW HeNe laser is strictly collimated and monochromatic and represents an integral flux of 3×10^{15}Photonen/s with a cross section of maybe $1mm^2$, i.e. 3×10^{17}photons/cm^{2}s.

if an increase in resolution may be achieved by stricter wavevector $\underline{k}$ selection (velocity, direction) and by reduction of the chopper pulse length, it is often not advisable to enhance all elements of the resolution up to the technological limits because this goes along with a drastic loss of intensity (detector count rate). Design of (neutron)-spectrometers means the search for the best compromise between resolution and intensity. The optimum depends on the nature of the problem, i.e. the features and structures expected in $S(Q,\omega)$. TOF spectrometers as described in this chapter are preferentially used to investigate isotropic to weakly anisotropic samples with only weak structures in $S(Q)$. This enables the utilization of a large solid angle for detection which compensates for the losses caused by energy analysis. In the schematics of the spectrometers this is already indicated by the large number of detectors. Modern TOF instruments contain more than 1000 single counting tubes covering a detecting area of $30 \times 1\text{cm}^2$ each. The total area coverd by 1000 detectors is about 3m^2, for a flight path of 3 m this corresponds to a solid angle of 0.333 or 1000 degrees squared. Thereby an intesity gain of a factor 500 is obtained compared to a triple axis spectrometer with a detecting area of 2 degrees squared, the loss caused by the fact that the chopper opens only for about 1% of the time is more than compensated. In addition the TOF instrument has a multiple advantage: all energy transfers are detected simultaneously and not sequentially as in the case of a triple-axis spectrometer. However it is seldom useful to sum the data of ALL detectors into one spectrum but different scattering angle regions have to be evaluated separately. Still they are measured all at the same time! Generally the TOF instrument is more efficient than a triple-axis spectrometer for isotropic samples. As soon as single crystals or very anisotropic samples with a strong dependence of the spectra on $\underline{Q}$ are to be investigated the conventional triple-axis spectrometers are better suited.

Contents

10.1 Introduction 10–1

10.2 The classic time-of-flight spectrometer 10–3

10.2.1 Interpretation of spectra 10–5

10.2.2 Time-of-flight spectra 10–6

10.2.3 Transforms 10–9

10.2.4 Fermi chopper 10–11

10.2.5 Disc choppers 10–11

10.2.6 Crystal monochromators 10–13

10.2.7 Time focussing 10–14

10.2.8 TOF-TOF: TOF-monochromator 10–16

10.3 Inverted TOF-spectrometer 10–17

10.3.1 Analysis by filters 10–20

10.4 Resolution and intensity 10–20

10.4.1 Intensity 10–21

11. Neutron spin-echo spectrometer, NSE

Michael Monkenbusch, Reiner Zorn

11.1 Introduction

The attempt to increase the resolution of time-of-flight (TOF) instruments described in chapter 11 far beyond the $\approx 1\%$ of the present realizations would lead to an unacceptable loss of intensity (as expressed in terms of detector count rate). E.g. a factor 0.1 which had to be applied as well to the monochromatization as to the pulse length (chopper opening time) would on the one hand increase the resolution accordingly by a factor of about 10 but at the same time the intensity is reduced by $0.1_{monoch.} \times 0.1_{chopper} = 10^{-2}$. Still other necessary measures to preserve the increased resolution as the reduction of sample size (definition of flight path) are not contained in this reduction factor. The same situation is also given if monochromator and analyzer consist of crystals. In general an improvement of the spectral resolution requires the narrowing of the filter transimssion functions before and after the sample scattering by the desired improvement factor. However this means an intensity reduction by the square of the resolution improvement factor. This situation would immediately improve, if it would be possible to equip each neutron with an individual stop watch which could be read in a way that the run time difference between test tracks before and after the sample is obtained at detection. If this stop watch has a sufficient time resolution it would be possible to observe very small velocity changes even if a beam with a wide range of initial neutron velocities is used. This would allow to escape the intensity trap.

In the neutron spin echo (NSE) spectrometer—with some restrictions (with important consequences for the application)—it is indeed possible to use the neutron spin directions as kind of individual stop watch pointers. The clockwork of this watch is then effected by the precession of the neutron spins in an external magnetic field[1]. The restrictions

[1]It is somewhat involved to extract this analogy starting from a quantum mechanical view with spin eigenstates and eigenvalues. Implicitly we are talking about the behaviour of the ensemble average of the spin vectors which obeys the "classical" Bloch equation concerning its precession in the magnetic field. As long as the kinetic energy of the neutrons is much bigger than the magnetic level splitting the classical

affecting application are caused by the fact that the "spin-stop watch" can only be read up to an unknown integer number of complete precession turns. The reading is performed by the cosine type transmission function of an analyzer and yields only ensemble averages and not individual rotation angles. The intensity at the detector is modulated accordingly. In addition inelastic scattering does not produce only one defined velocity change but Δv is distributed according to $S(Q,\omega \approx k\Delta v)$. The detector signal is then proportional to the integral of intensity contributions modulated by the cosine of the precession angle and weighted according to the Δv of $S(Q,\omega)$. Therefore, the signal of the NSE spectrometer—as explained in this chapter—is completely different from the TOF histograms of classical TOF-spectrometers (chapter 11). Instead it is proportional to the cosine Fourier transform of $S(Q,\omega)$, i.e. the intermediate scattering function $S(Q,t)$. A detailed derivation and discussion is given below. But first of all the actual setup of an NSE spectrometer is presented.

11.2 Setup and Function

Figure 11.1 shows the schematic setup of a NSE spectrometer (upper part) together with the propagation of the neutron spin in the instrument (lower part).

Longitudinally polarized neutrons[2] (i.e. spin expectation value parallel to the beam direction) enter the spectrometer from the left. In the first so-called $\pi/2$-flipper the spin is rotated such that on exit it is orthogonal to the longitudinal magnetic field of the precession path. That defines the start of the "spin stop watch", immediately after the flipper a precession of the spins around the axial magnetic field begins. The precession frequency increases during the approach to the centre of the main precession solenoid where it reaches its maximum of up to a few MHz. The accumulation of precession angle

picture is completely sufficient. It is much easier to understand the NSE spectrometer in this way than a quantum mechanical treatment.

[2]The polarized neutron beam is obtained by reflection by a magnetic multilayer mirror. The layer stack consists of alternating nonmagnetic (e.g. Fe, Si or Ti) and magnetic (Fe or Co) layers. The effective index of refraction of the magnetic layers depends on the relative orientation of magnetization and spins of the neutrons such that there is a modulation of index of refraction for neutrons in one spin state only. Those neutrons are reflected, the others are transmitted. For layer distances of 5 .. 10 nm reflection angles of a few degrees result for wavelengths around 10 Å. Both the reflected and the transmitted beam are polarized (with opposite spin directions).

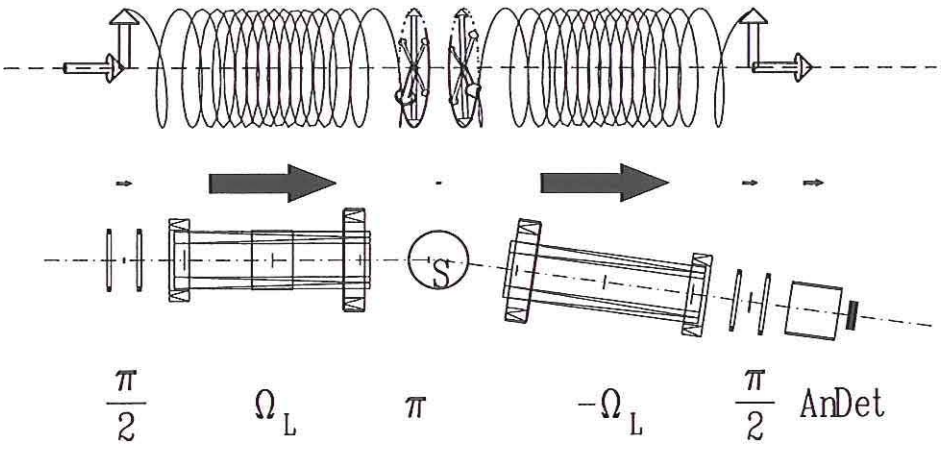

Figure 11.1: Spin rotations and setup of a generic NSE-spectrometer. Upper part: Spin rotation, middle part: magnitude of the magnetic field, lower part: schematic setup of the Jülich NSE-spectrometer.

continues—with decreasing frequency—until the neutrons reach the π-flipper close to the sample (S). The total precession angle at that point is:

$$\Psi = \frac{\gamma}{v}\int_l |B| dl \equiv \alpha \tag{11.1}$$

where $\gamma = 2\pi \times 2913.06598 \times 10^4\,\mathrm{s}^{-1}/\mathrm{Tesla}$ is the gyromagnetic ratio of the neutrons and $|B|$ is the modulus of the magnetic induction along the path l.

The "stop watch" does not proceed uniformly but with a position dependend frequency that is proportional to the local magnetic field along the neutron path, see figure 11.1. This may also be considered as a field dependend distance streching, which releases e.g. the mechanical positioning accuracy requirements for the flippers since they are located in low field regions. The total number of precessions a neutron spin undergoes on passage through one arm of the spectrometer lies between 10 and some 10^4.

Close to the sample (ideally: at the sample position) the so-called π-flipper is located, it rotates the spins by 180° around a vertical axis. In this way the total precession angle is transformed to $\Psi_1 = +\alpha \rightarrow -\alpha$. The precession angle α is—according to equation 11.1—extremely dependent on velocity and therefore very different for different neutrons in a beam with finite width of the wavelength distribution. As a consequence the spin

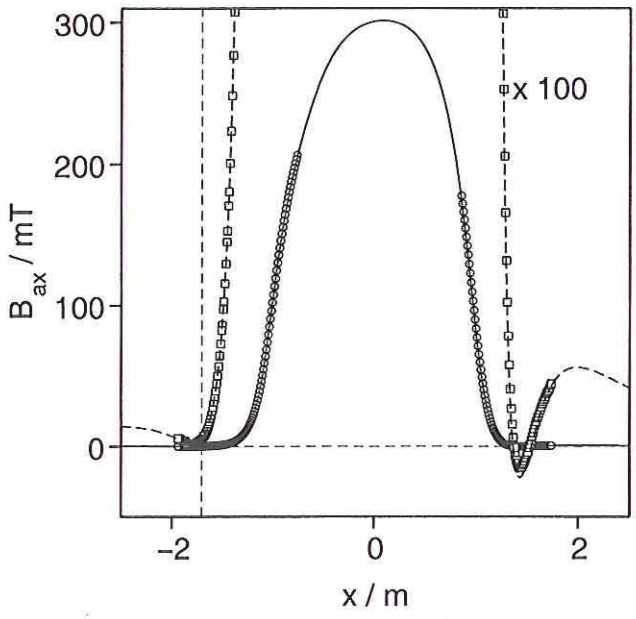

Figure 11.2: Field along the axis of a main precession coil.

vectors at the sample position (π-flipper) are evenly distributed on a disc orthogonal to the field direction. If no velocity change occurs during scattering at the sample (elastic scattering) each neutron enters the secondary arm of the spectrometer with unchanged velocity. The precession field and path length of the secondary arm exactly match the corresponding elements of the primary arm before sample and π-flipper. Accordingly, the precession accumulated in the secondary arm is $\Psi_2 = +\alpha$ and the total precession angle at the second $\pi/2$-flipper is $\Psi_1 + \Psi_2 = -\alpha + \alpha = 0$. I.e. all spins—irrespective of their initial velocity—reassemble at the same vertical position they had at the start point. The rotation imposed by the second $\pi/2$-flipper converts this back to the initial longitudinal polarization that is fully restored. The flippers limit the the two race tracks and realize "start", "time reversal" and "stop" of the "spin stop watches". The second $\pi/2$-flipper is the last element used to manipulate the spins. It converts the average precession angle to a longitudinal polarization component. Since the field after the second $\pi/2$-flipper is again

longitudinal, further precessions do not influence the analyzed longitudinal polarization component (the stop watch is stopped!). The analyzer accepts neutrons of one longitudinal spin state for the detector. After ensemble averaging this means that the count rate at the detector is proportional to $(1 \pm \cos(\overline{\Psi}))/2$ [3], where $\overline{\Psi}$ is the expectation value of the angle between spin and axial direction.

11.2.1 Flippers

Ignoring technical details the main elements needed to perform the spin operations necessary for a NSE spectrometer are:

- $\pi/2$-flipper (start)
- first precessions field
- π-flipper ("time reversal")
- second precessions field
- $\pi/2$-flipper

While in the precession fields the spin vector (its expectation value) continuously rotates around the field vector on a cone with constant angle (angle field-spin, ideal value = 90°) even if the field which the neutron experiences during its flight performs (sufficiently slow, i.e. adiabatic) direction changes[4], the flippers rely on a sudden change in the field direction that gives rise to a new drastically changed cone angle. In figure 11.3 a $\pi/2$-flipper is shown together with the field vectors that have to be generated for an adequate function of the flipper.

[3]The sign in front of the cosine depends on the technical realization of polarizer and analyzer (both reflecting, transmitting, one reflecting one transmitting) and on the orientation of flippers. It may be selected by choosing the signs of the flipper currents.

[4]The cone of precession follows the direction of the precession field quite accurately if the effective frequency of the field rotation is much smaller than the local precession frequency. Such a change in field is called *adiabatic*. In particular this means that faster direction changes are the more adiabatic the larger the field is. For a NSE spectrometer care must be taken that except at the entry and exit of flippers the conditions are adiabatic. The magnetic field of the spectrometer is of course static, however the neutron spins experience a time varying field due to the passage of the neutron through the spectrometer.

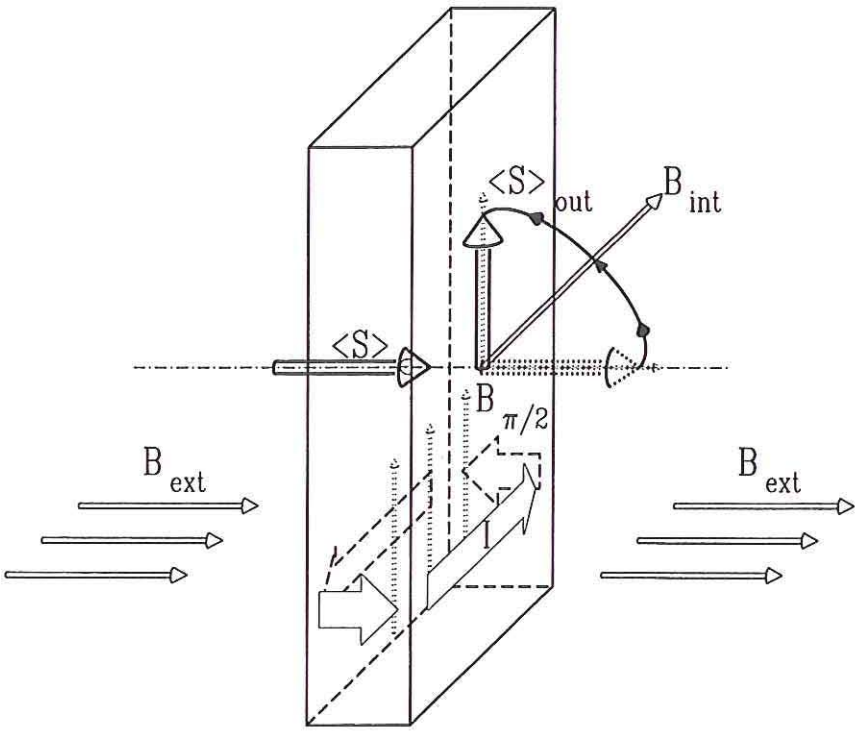

Figure 11.3: Schematics and function of a $\pi/2$-flipper.

The rectangular flipper exposes its large sides to the beam. The box consists of electrically conducting and neutron transparen material (aluminum wire) which carries a current I, as indicated by the broad arrows. All side walls realize a thin homogeneous current density distribution (current sheets) that leads to a homogeneous field $B_{\pi/2}$ in the inside of the flipper. For a sufficient length of the flipper the stray field emerging from the ends of the flipper coil is negligibly small in the beam area in front of the flipper. To obtain the desired operation the $\pi/2$-flipper has to be embedded in an external longitudinal field The resulting field in the interior of the flipper B_{int} has an angle of 45° to the longitudinal axis. The magnitude of the field must be set such that the neutrons perform a precession of exactly 180° during the time they need to transverse the flipper. In this way a longitudinal spin vector is rotated into an orientation perpendicular to the axial field. Then the precession cone has the maximum angle of 90°, i.e. it is a disc (dial of the "stop watch"). For a typical flipper thickness of 1 cm the interior field is in the order of

0.1 mTesla = 10 Gauss (For comparison the earth's magnetic field is $\approx$ 0.5 Gauss). Since a fixed precession angle around B_{int}=const must be accumulated during the passage time of the neutron through the flipper, the flipper function is moderately wavelength dependent. For the ease of setup and stability of operation of the spectrometer it is advantageous that the flippers are embedded in a comparatively small external field ($< 10^{-3}$ of the maximum precession field). I.e. close to the flippers the "spin clock" runs slowly and small path differences due to positioning inaccuracy and thermal expansion only lead to very small errors in precession angle.

The technical realization of the π-flipper is identical to the one of the $\pi/2$-flipper, however its function—as indicated by its name—is different. It performs a 180° rotation around an axis perpendicular to the beam axis (e.g. a vertical axis) which is virtually parallel to the axis of the flipper coil. To do so the internal field has the same magnitude as in the $\pi/2$-flipper however the embedding field is close to zero and therefore the internal field vector is virtually vertical[5].

11.3 The detector signal

As mentioned above the detector signal results from the transmission function of the analyzer shaped as the cosine of the net precession angle in combination with the distribution of net precession angles due to the distribution of velocity changes during scattering. The velocity distribution is proportional to the spectral part of $S(Q,\omega)$. In the following this is derived in terms of mathematical expressions. First the field integrals along the primary

[5]Unfortunately it is not possible to embed the π-flipper in a zero field environment, as everywhere in the beam volume this would lead to a violation of the adiabatic condition. While the beam enters such a zero field region if would suffer uncontrolled inhomogeneous tilts and rotations of the precession cone that would effectively lead to a depolarization. Smallest external stray fields would exert a big influence on the signal. A defined spin operation would not be possible. For that reason a minimal field in the range of a few (1 . . . 2 Gauss) is mandatory not to loose the defined polarization. Without further action the π-flipper function is deteriorated by this finite external field. But by a slight tilt of the flipper or by a tiny extra component of the external field in direction of the flipper axis the ideal function may be restored. The condition to be fulfilled is that the resulting internal field is orthogonal to the embedding field which may be slightly tilted from its horizontal orientation by the added small extra field component.

and secondary paths of precession are defined:

$$J_1 = \int_{l((\pi/2)_1)}^{l(\pi)} |B| dl \tag{11.2}$$

$$J_2 = \int_{l(\pi)}^{l((\pi/2)_2)} |B| dl \tag{11.3}$$

for a symmetric setup $J_1 = J_2$; $l(\pi, (\pi/2)_{1,2})$ denotes the positions of the corresponding flippers. The precession angle accumulated on a path i is

$$\Psi_i = \frac{\gamma J_i}{v} \tag{11.4}$$

where v is the neutron velocity (typically several 100 m/s). Because the π-flipper inverts the sign of Ψ_1, a total precession angle of

$$\Psi_{1,2} = -\frac{\gamma J_1}{v} + \frac{\gamma J_2}{v + \Delta v} \tag{11.5}$$

results, where Δv is the velocity change of the neutron due to inelastic scattering. The transmission function of an (assumedly ideal) analyzer is

$$T_a = \frac{1}{2}\left[1 + \cos\left(-\frac{\gamma J_1}{v} + \frac{\gamma J_2}{v + \Delta v}\right)\right] \tag{11.6}$$

From that the detector intensity

$$I = \eta S(Q) \iint \frac{1}{2}\left[1 \pm \cos\left(-\frac{\gamma J_1}{v} + \frac{\gamma J_2}{v + \Delta v}\right)\right] w_\omega(\Delta v) w_\lambda(v)\, d\Delta v\, dv \tag{11.7}$$

results, where η is an irrelevant calibration factor and w_ω resp. w_λ are normalized distribution functions. w_ω represents the spectrum of the sample as found in the scattering function and w_λ takes account for the fact that the NSE spectrometers usually are operated with a broad incoming wavelength distribution ($\Delta\lambda_{FWHM}/\lambda = 10 \ldots 20\%$). Observing the linear dependences of k, λ and v and series expansion of the squares in the expression for the double differential cross section 10.2 and insertion into equation 11.7 leads to:

$$I = \eta \iint \frac{1}{2}\left[1 \pm \cos\left(-\frac{\gamma J_1}{(h/m_n)\lambda^{-1}} + \frac{\gamma J_2}{(h/m_n)\lambda^{-1} + \lambda\omega/2\pi}\right)\right] S(Q,\omega) w_\lambda(\lambda)\, d\omega\, d\lambda \tag{11.8}$$

11.3.1 Symmetric Case

At the point of symmetry $J_1 = J_2 = J$ it is possible to collect the λ-dependend terms in equation 11.8 and to write them as series expansion for small ω:

$$-\frac{1}{\lambda^{-1}} + \frac{1}{\lambda^{-1} + \lambda(m_n/h)\omega/2\pi} \approx -\lambda^3 \frac{m_n \omega}{h 2\pi} \tag{11.9}$$

To see the salient features of the spectrometer signal more clearly the finite wavelength distribution is temporarily ignored

$$\begin{aligned} I &= \eta \frac{1}{2}\left[S(Q) + \int \cos\left(\underbrace{\gamma J \frac{m_n^2}{h^2 2\pi}\lambda^3}_{\equiv t}\ \omega\right) S(Q,\omega) d\omega\right] \\ &= \frac{\eta}{2}\left(S(Q) + S(Q,t)\right) \end{aligned} \tag{11.10}$$

The underbraced product has the unit "time", the integral in equation 11.10 represents the cosine Fourier transform of $S(Q,\omega)$ with respect to ω, the resulting function is called *intermediate scattering function,* $S(Q,t)$ [6] From equation 11.10 it is further reckognizable that the time parameter $t = \gamma J m_n^2 \lambda^3/(h^2 2\pi)$ depends on the third power of the wavelength λ (i.e. long wavelength $\rightarrow$ very long Fourier times). In addition $t \propto J$, i.e. mainly proportional to the current throught the main precession solenoids. This current usually is the parameter used to stepwise scan the Fourier time during an experiment to get a table of $S(Q,t)$ vs. t.

11.3.2 Elastic Scattering of a Finite Width Wavelength Distribution

For a transmitted beam or elastically scattered neutrons from a reference sample $\omega = 0$ holds, i.e $S(Q,\omega) = \delta(\omega)$. With that equation 11.8 becomes

$$I = \frac{1}{2}\int \left[1 \pm \cos(\lambda \underbrace{\gamma(m_n/h)\{J_2 - J_1\}})\right] w_\lambda(\lambda) d\lambda \tag{11.11}$$

For this case the intensity is proportional to the Fourier transform of the wavelength distribution. Here, the underbraced part is the external control parameter. It contains the difference between the field integrals along the primary and secondary paths $J_2 - J_1$. This difference can be easily controlled by sending a current through an auxiliary coil

[6] Strictly this is only true for a $S(Q,\omega)$ that is symmetric with respect to ω, i.e. in the classical approximation. For any practical problems however this is well fulfilled since the minute energy transfers corresponding to the NSE time scale are very small compared to $k_B T$.

of a few windings around one of the precession solenoids. For a Gaussian wavelength distribution the envelope of the Fourier transform is again a Gaussian whose width is inversely proportional to the width of the wavelength distribution. Since w_λ is centered at a finite nominal wavelength λ_0 the envelope is multiplied by a cosine with a period $\propto 1/\lambda_0$. This function follows immediately from equation 11.11 if $w_\lambda = \delta(\lambda)$ is assumed. Figure 11.4 displays the results of an extensive measurement using the attenuated direct beam with a central wavelength of $\lambda_0 = 0.7\,\mathrm{nm}$ and $\Delta\lambda_{FWHM}/\lambda_0 = 0.1$ compared to a calculation (fit) assuming a Gaussian wavelength distribution.

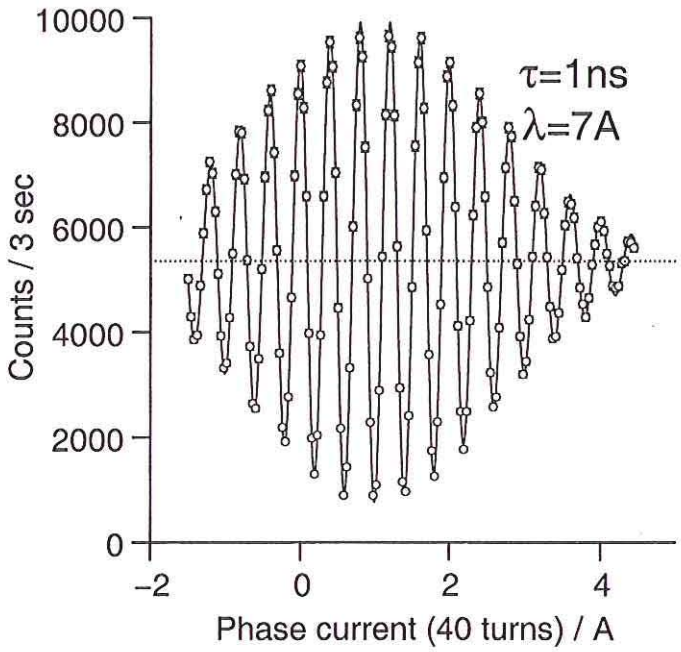

Figure 11.4: Echo shape: count rate as function of the magnetic symmetry ($\propto$ phase coil current).

At the echo point (i.e. a phase coil current close to 1.5 A creating perfect symmetry) the count rate has a minimum. Ideally the count rate should be zero there, but because all elements that contribute to the polarization manipulation and analysis are imperfect a residual intensity is left that has to be determined by calibration measurements. From the

the functional dependence of the intensity on the phase current it is possible to determine the wavelength distribution.

11.4 Experimental Procedures and Evaluation

In principle the information on $S(Q,t)$ according to equation 11.10 is contained in the ratio of the intensities at the symmetry point and the average intensity $(\eta/2)\,S(Q)$. However there are practical reasons that prevent the reliable setting of the symmetry point alone. The location of the symmetry point (i.e. phase zero current in the phase coil) is extremely sensitive to tiny variations of the magnetic environment caused e.g. by displacement of larger iron parts at neighbouring instruments, movement of the crane of the instrument hall and thermal displacements of coils. Therefore, the position of the symmetry point has to be measured as well as the intensity for each Q,t setting. In figure 11.5 the minimum of single countings is indicated, intensity must be determined for three points $P_1 \ldots P_3$ separated by a symmetry change corresponding to a quarter precession each. From these three values it is possible to extract the average intensity $I(Q,0)$, the echo amplitude $I(Q,t)$ and the exact symmetry point location. This also holds if any perturbation shifts the location as indicated by the three hollow circles in the figure.

For an ideal spectrometer $I(Q,t)/I(Q,0) = S(Q,t)/S(Q)$ would be the desired value of the normalized intermediate scattering function. In reality resolution effects and polarization losses reduce the value of $I(Q,t)/I(Q,0)$ compared to $S(Q,t)/S(Q)$.

Figure 11.6 shows data from actual experiments that are used to determine the echo amplitude and average intensity. Here the shape of the echo signal (intensity vs. symmetry current) is sampled for a considerably larger number than the minimum of three points. The parameters amplitude, average and phase zero current are determined by a nonlinear fit. Behind the oscillating echo form there are two further groups of points showing the minimum and maximum of intensity which indicates the efficiency of the polarization analysis. These intensities are measured by deactivating the $\pi/2$-flippers (minimum) and then additional deactivation of the π-flipper (maximum). An ideal spectrometer would have zero transmission in the one case and 100% transmission of neutrons in the other case. The non-ideal behaviour is caused by depolarization effects at the technical elements of the spectrometer, the wavelength dependence of the flipper operations and the finite

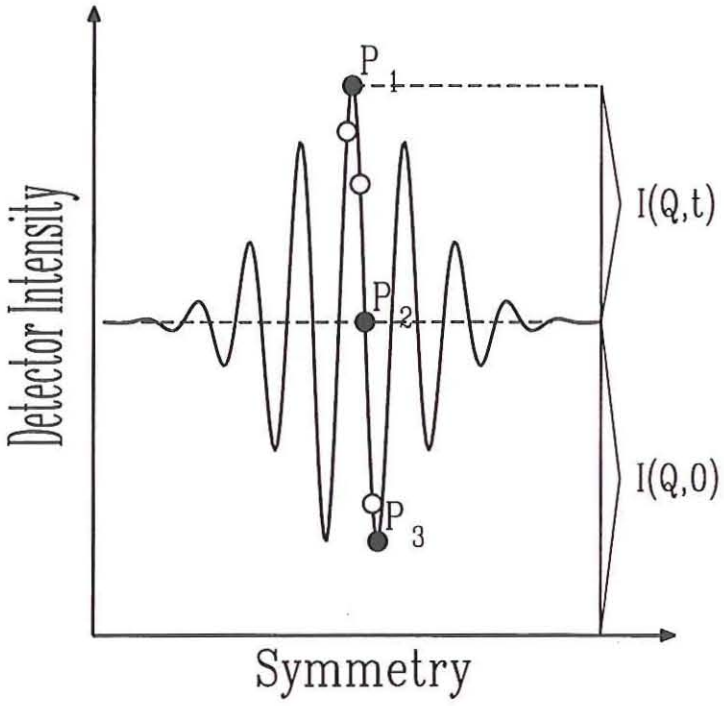

Figure 11.5: Schematic echo form, idealized.

efficiency of polarizers and analyzers. Also for an ideal spectrometer being free from the above effects a finite minimum and less than 100% maximum intensity will result for spin-incoherent scattering which is always accompanied by spin flips for 2/3 of the incoherently scattered neutrons.

To account for the polarization losses the difference between the thus determined "up" and "down" count rates is used to normalize the echo amplitude (instead of taking just the average intensity).

11.5 Field Integral Homogeneity and Resolution

Besides the decay of $S(Q,t)$ as a consequence of the dynamical processes in the sample the measured echo amplitude suffers a further reduction due to resolution effects (different from the above mentioned depolarization effects) that must be accounted for in the data evaluation.

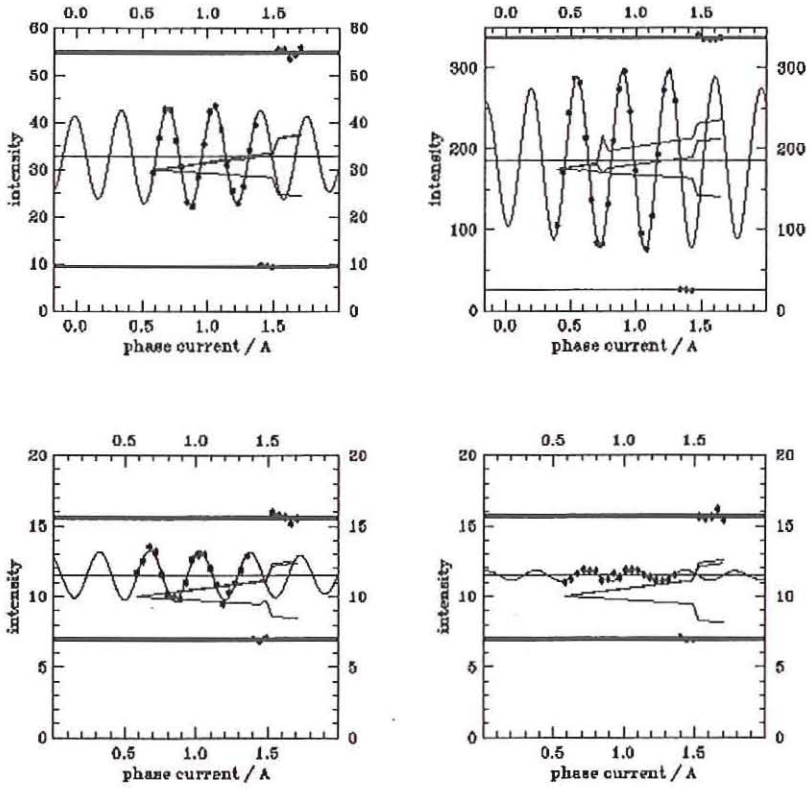

Figure 11.6: "Phase scans" used to determine the echo amplitude at the Jülich NSE spectrometer. Symbols indicate count rates normalized to a monitor rate. The oscillating lines are "fitted" echo signals (assuming Gaussian distribution of wavelengths). At the end of the scans groups of points corresponding to the minimal ($\pi/2$-flippers off, π-flipper on) and maximal (all flippers off) obtainable count rates are located. The horizontal lines correspond to the average and the minimum and maximum intensities. The experimental value of interest is computed from the ratio of the echo amplitude and the maximum possible up-down difference. The lines starting at one point at the beginning of the scan are measured magnetic field components (differences to the starting value) at the sample position, they serve to monitor variations of the magnetic environment.

Up to this point we tacitly assumed that the values of J_1 and J_2 are the same for all neutrons in the primary and scattered beams. This would however only be approximately true for very narrow beams which therefore would carry only very few neutrons. Useable beams must have a width of several cm and contain neutrons of different direction (divergence). In particular the use of a large area sensitive detector leads to rather divergent rays in the secondary arm. Note that a field of 1000 Gauss=0.1 Tesla acting along a track of 2 m yields 3000 Hz/Gauss $\times$ 1000 Gauss $\times$ 2 m / 400 m/s = 15000 full precessions for neutrons with a velocity of 400 m/s ($\lambda = 1.0$nm). The condition that the precession angle accumulated along different rays in the beam must be equal within 0.1 precessions then translates into the requirement that the field integrals along the different rays must be same within $1 : 10^5$. As soon as the precession angles resulting from different rays differ by 180° the signal ist lost completely. Simple cylindrical precession coils fall behind the required homogeneity by a factor 100. Only by use of special correcting elements ("Fresnel" coils) the required homogeneity may be achieved. The correction elements positioned in the neutron beam have to realize radial current distributions around the magnetic axis. Three radial elements per arm in principle allow for a full correction. However the making of such elements that are transparent for neutrons and are able to carry the required high current densities with the required accuracy is difficult. Currently the improvement by a factor of 100, sufficient for operation with the above parameters, is barely achievable.

Fig. 11.7 shows the shape of the radial correction elements which are used in the Jülich NSE. The uncorrected inhomogeneity is proportional to the main precession fields and therefore proportional to the Fourier time t. In the current setup the residual inhomogeneity (after correction) sets the limit for the maximum Fourier time.

Figure 11.8 illustrates how the echo amplitude decreases due to resolution effects even with correction elements. Without correction the amplitude would drop to values below 0.1 above Fourier times of a few ns. The resolution functions as show in figure 11.8 can be determined using the scattering from a reference sample which is known to exhibit elastic scattering only ($> 99.9\%$), here: microcrystalline MgO. The experimental results (normalized echo amplitudes) of all samples have to be divided by the normalized echo amplitudes from the reference sample to yield $S(Q,t)/S(Q)$. An example for the final result of a typical experiment is shown in figure 11.9.

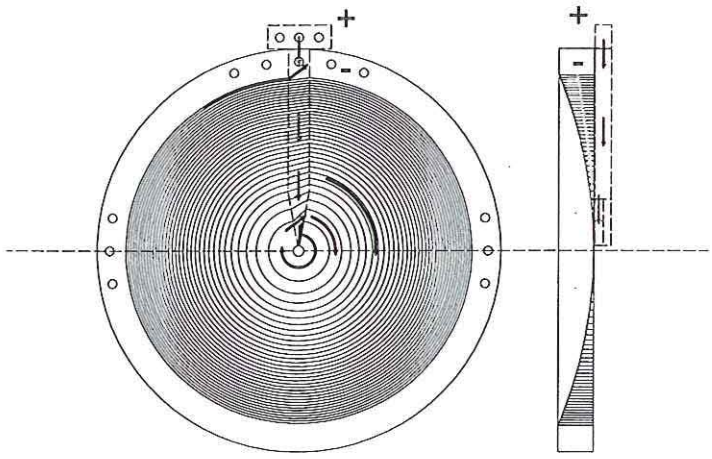

Figure 11.7: Correction element for the field integral homogenization, material: aluminum.

11.6 Practical Aspects, Peculiarities

From the above description it follows that the NSE spectrometer measures the Fourier transform $S(Q,t)$ of the spectral part of $S(Q,\omega)$ directly. As a consequence the average count rate at the detector corresponds to half of all neutrons scattered from the sample into the solid angle of the detector (Fourier*integral*). Therefore weak spectral features are buried under the noise due to counting statistics. However the method is perfectly adapted to relaxations that are performed by most of the scattering structure since the relaxation functions are measured in the time domain directly and resolution correction consists of a division instead a deconvolution in the frequency space.

One very important field for NSE investigations are "soft matter" problems. These comprise polymer melts and solutions and other complex fluids. The NSE methods opens a dynamics window in the SANS scattering vector regime. Since in that regime the dynamics is determined by the balance between elastic (entropic) forces and friction and in comparison inertial forces are negligible the observed fluctuations are pure relaxations and well suited for investigation by NSE.

Many isotopes—especially normal hydrogen (protons)—scatter neutrons incoherently.

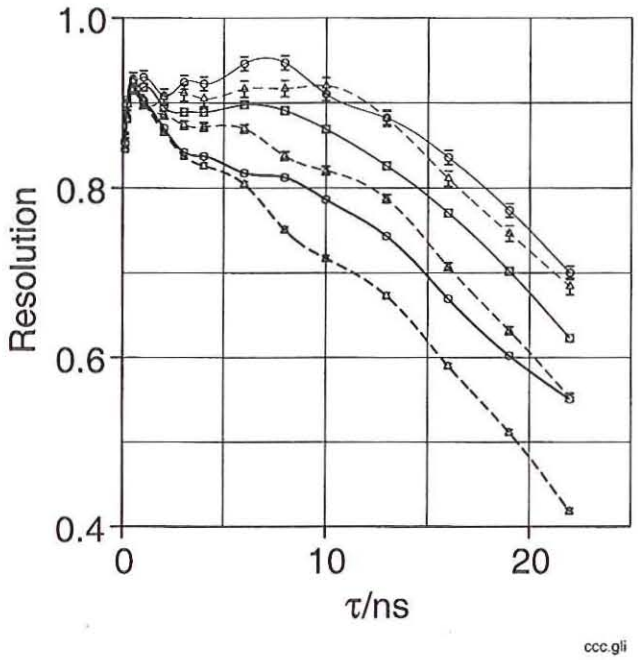

Figure 11.8: Resolution function of the Jülich NSE for beams of different divergence. Solid lines: configuration with three correction coils, dashed lines: only two correction coils.

This is often utilized in TOF investigations since the incoherent scattering from hydrogen is dominant and more easy to interpret than the coherent. The spin incoherent scattering is caused by the dependence of the scattering length on the relative orientation of nuclear and neutron spins. The fluctuating part of the scattering length due to random spin orientation contains no interference of scattering from different nuclei, i.e. the scattering intensity distributes evenly over 4π solid angle and is "diluted" accordingly. The intensity is very small compared to typical SANS intensities. The dynamics of the incoherent scattering reflects the tagged particle motion (self correlation). For the NSE method it is important to note that the spin-dependent scattering flips 2/3 of the neutron spins. This means that a considerable loss of polarization is encountered, only 1/3 of the neutrons contribute to the echo signal—the rest is background. This 1/3 stems form the spin

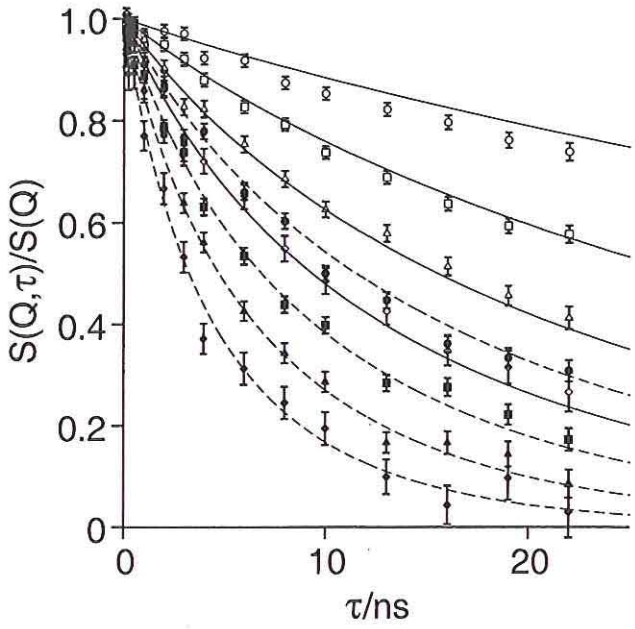

Figure 11.9: $S(Q,t)/S(Q)$ of a 2.5 % polymer solution with a fit to the Zimm model that theoretically describes $S(Q,t)$ for a dilute polymer solution. The data have been measured using the area detector at only two angular positions of the secondary spectrometer arm within 8 h time. The hollow symbols have been obtained at an arm setting of $\bar{Q} = 0.05\text{Å}^{-1}$ and correspond to $Q/\text{Å}^{-1} = 0.038, 0.05, 0.061, 0.072$. The filled symbols were measured at $\bar{Q} = 0.08\text{Å}^{-1}$ and correspond to $Q/\text{Å}^{-1} = 0.067, 0.08, 0.09, 0.102$.

flipped neutrons, i.e. the echo amplitude is also inverted (negative). It is evident that for this reason NSE experiments with incoherent scattering are much more difficult to perform. If coherent and incoherent scattering contributions are simultaneously present this may lead to peculiar effects since the amplitudes may cancel each other depending on their—potentially different—dynamics.

Contents

11.1 Introduction 11–1

11.2 Setup and Function 11–2

11.2.1 Flippers 11–5

11.3 The detector signal 11–7

11.3.1 Symmetric Case 11–9

11.3.2 Elastic Scattering of a Finite Width Wavelength Distribution 11–9

11.4 Experimental Procedures and Evaluation 11–11

11.5 Field Integral Homogeneity and Resolution 11–12

11.6 Practical Aspects, Peculiarities 11–15

12. Structure determination

G. Heger

12.1 Introduction

The analysis of crystal structure and magnetic ordering is usually based on diffraction phenomena caused by the interaction of matter with X-rays, neutrons, or electrons. Even though electron microscopy can achieve atomic resolution, more detailed information on the 3dim. atomic arrangement of crystals with its symmetry and chemical bonding as well as magnetic structures and spin densities requires diffraction methods. The basic theory of diffraction is the same for all types of radiation. Complementary information is achieved due to the different character of X-rays, neutrons and electrons, and hence their different interactions with matter and further practical aspects.

Considering only X-rays and thermal neutrons one finds that their wavelengths are similar (0.5 Å $< \lambda <$ 2.4 Å). While the electromagnetic X-ray radiation yields the total electron density distribution, the nuclear scattering of neutrons probes the density distribution of the nuclei and the magnetic neutron scattering the spin density of unpaired electrons.

X-ray diffraction using conventional laboratory equipment and/or synchrotron installations is the most important method for structure analyses. The purpose of this paper is to discuss special cases, for which, in addition to this indispensable part, neutrons are required to solve structural problems. Even though the huge intensity of modern synchrotron sources allows in principle the study of magnetic X-ray scattering the investigation of magnetic structures is still one of the most important applications of neutron diffraction.

12.2 Structure factor and Bragg intensities

The characteristic feature of the crystalline state consists of its periodic ordering, which may be represented by a (translational) lattice. In the 3dim. case three basis vectors $\underline{a}$, $\underline{b}$, and $\underline{c}$ define a parallelepiped, called unit cell. The general lattice vector

$$\underline{\tau} = u\underline{a} + v\underline{b} + w\underline{c} \qquad (1)$$

results from a linear combination of the basis vectors with coefficients u, v, and w being positive or negative integers (incl. 0). According to their point-symmetry properties seven crystal systems are distinguished:

Triclinic, *Monoclinic*, *Orthorhombic*, *Tetragonal*, *Trigonal*, *Hexagonal*, and *Cubic*.

Besides of the related seven primitive lattices, with only one lattice point per unit cell, multiple lattices with centred unit cells are possible. In this way a total of 14 Bravais lattices is defined.

The position of atom j in the unit cell is given by the vector

$$\underline{r}_j = x_j\underline{a} + y_j\underline{b} + z_j\underline{c}. \quad (2)$$

The coefficients x_j, y_j, and z_j are called atomic coordinates ($0 \le x_j < 1$; $0 \le y_j < 1$; $0 \le z_j < 1$).

Lattice planes (that means a set of parallel planes containing lattice points) defined by three integers (*hkl*) called Miller indices have the characteristic interplanar spacing d_{hkl}.

For scattering studies of crystals the concept of the reciprocal lattice with the basis vectors $\underline{a}^*$, $\underline{b}^*$, and $\underline{c}^*$ was developed. The lattice vector of the reciprocal lattice is defined in crystallography by

$$\underline{H} = h\underline{a}^* + k\underline{b}^* + l\underline{c}^*. \quad (3)$$

In solid state physics instead of $\underline{H} = 1/d_{hkl}$ there is normally used the scattering vector

$$\underline{Q} = 2\pi\underline{H}. \quad (4)$$

12.2.1 Nuclear scattering

In kinematical approximation, assuming that the magnitude of the incident wave amplitude is the same at all points in the specimen (this implies a small sample size, weak scattering intensities, no multiple diffraction and neglecting of absorption), the diffracted intensity is proportional to the square of the amplitude of the scattered wave for each individual reflection; it can be regarded as a weight ascribed to the reciprocal lattice nodes

$$I(\underline{H}) \sim |F(\underline{H})|^2. \quad (5)$$

The structure factor $F(\underline{H})$, in terms of the Fourier transform, contains the complete information on the distribution of the scatterer density in the unit cell, including the atomic coordinates x_j, y_j, and z_j,

$$F(\underline{H}) = \sum_j b_j \exp[2\pi i(\underline{H}\cdot\underline{r}_j)]\cdot T_j(\underline{H}) = |F(\underline{H})|\cdot\exp[i\varphi(\underline{H})]. \quad (6)$$

In the case of nuclear scattering of neutrons the structure factor has the dimension of a length, as has the scattering length $b_j(\underline{H}) = b_j$ = const. of nucleus j. $T_j(\underline{H})$ is the Debye-Waller factor which takes into account dynamical and static displacements of the nucleus j from its average position $\underline{r}_j$ (see Eq. 2) in the unit cell. With the fractional coordinates x_j, y_j and z_j the scalar product in the exponential function can be written as

$$\underline{H}\cdot\underline{r}_j = hx_j + ky_j + lz_j. \quad (7)$$

Important: The measured Bragg intensities $I(\underline{H})$ from diffraction experiments yield only the modulus of the structure factors, $|F(\underline{H})| \propto \sqrt{I(\underline{H})}$, and not their phases $\varphi(\underline{H})$ (see Eq. 5), which would be required for the inverse Fourier transform of the data (Fourier synthesis) to give directly the arrangement of the atoms in the unit cell. The lack of the phase information is known as the phase problem of crystallography.

In a diffraction experiment normally only relative Bragg intensities are measured. A SCALE factor is assumed to be rigorously the same for all reflections of one data set. For merely nuclear neutron scattering and single crystals the integrated relative intensities are given by

$$I(\underline{H}) = \text{SCALE}\cdot L\cdot A\cdot|F(\underline{H})|^2. \quad (8)$$

The Lorentz factor L is instrument specific. The absorption correction A depends on the geometry and linear absorption coefficient of the sample.

The geometrical diffraction conditions and hence the reciprocal lattice yield the periodicity of a crystal. Information on the crystal system, the Bravais lattice type and the basis vectors $\underline{a}$, $\underline{b}$, $\underline{c}$ of the unit cell (lattice constants a, b, c, α, β, γ) may be directly deduced from the reciprocal lattice. The $|F(\underline{H})|^2$ values associated as weights to the nodes of the reciprocal lattice give the diffraction symbol and hence valuable information on the space-group symmetry. Here systematic absences (zero structure factors) can be related to the choice of a non-primitive Bravais lattice, or to the presence of non-symmorphic symmetry operations (symmetry operations with translation components).

12.2. 2 Magnetic scattering

The dipolar interaction between the neutron magnetic moments and the magnetic moments of atoms/ions (and nuclei) $\underline{m}_j$ leads to the magnetic neutron scattering in addition to the nuclear contribution. In the case of an ordering of the magnetic moments over the whole crystal (periodic magnetic structure) the magnetic structure factor is given by

$$F_M(\underline{H}) = \sum_j b_{Mj}(\underline{H})\cdot\exp[2\pi i(\underline{H}\cdot\underline{r}_j)]\cdot T_j(\underline{H}) \quad (9)$$

with the magnetic scattering amplitude

$$b_{Mj}(\underline{H}) = (e^2\gamma/2m_ec^2)\cdot f_{Mj}(\underline{H})\cdot\sigma\cdot\underline{m}_{\perp j}(\underline{H}). \quad (10)$$

½σ is the neutron spin operator and $\underline{m}_{\perp j}(\underline{H})$ the projection of the magnetic moment $\underline{m}_j$ onto the scattering plane (*hkl*). The magnetic form factor $f_{Mj}(\underline{H})$ is the Fourier transform of the normalised magnetisation density $M_j(\underline{r})$ of the atom or ion j

$$f_{Mj}(\underline{H}) = \int_V M_j(\underline{r}) \cdot \exp[2\pi i(\underline{H} \cdot \underline{r})] \cdot d\underline{r} \qquad (11)$$

with $f_M(0) = \int_V M_j(\underline{r}) \cdot d\underline{r} = 1$.

This is a function of the reciprocal lattice vector $\underline{H}$, whereas the atomic scattering factor f_j of X-ray diffraction

$$f_j(|\underline{H}|) = \int_V \rho_j(r) \cdot \exp[2\pi i(\underline{H} \cdot \underline{r})] \cdot d\underline{r}, \qquad (12)$$

for a spherical electron density $\rho_j(r)$, depends only on the length of $\underline{H}$.

The intensity of magnetic and nuclear neutron scattering is of the same order of magnitude. For unpolarised neutrons the Bragg intensity of nuclear and magnetic neutron diffraction is simply an incoherent superposition

$$I(\underline{H}) = I_N(\underline{H}) + I_M(\underline{H}) \sim |F_N(\underline{H})|^2 + |F_M(\underline{H})|^2. \qquad (13)$$

For polarised neutrons on the other hand the coherent superposition gives

$$[|F(\underline{H})|^2]^{\pm} = |F_N(\underline{H}) \pm F_M(\underline{H})|^2 \qquad (14)$$

with the interference terms $\pm\, 2 \cdot |F_N(\underline{H}) \cdot F_M(\underline{H})|$ according to the two possible directions of polarisation (+ and -). In measuring the flipping ratio at superimposed Bragg reflections, that means the ratio of the intensities for the two polarisations up and down, even small magnetic structure factors can be determined quite accurately.

The analysis of a magnetic structure starts with the determination of its periodicity with respect to that of the crystal structure. The identification of magnetic reflections is usually accomplished by a careful comparison of powder diagrams recorded below and above the magnetic phase transition temperatures. A more detailed study of the scattering vectors, e.g. for incommensurate structures, may require also single-crystal experiments. The nuclear structure factors $F_N(\underline{H})$ can be calculated from the known crystal structure. In this way the SCALE factor of the data set can be obtained and the absolute values of the magnitudes of the magnetic structure factors $|F_M(\underline{H})|$ can be determined. The individual orientations of the magnetic moments $\underline{m}_j$ with respect to the basis vectors of the crystal lattice and their magnitudes are then to be calculated.

12.3 Contrast variation

Neutron diffraction can be used for an experimental distinction of atoms/ions with almost equal X-ray scattering amplitudes. In the case of mixed systems it is furthermore possible to determine a fractional site occupation. Another application of neutron diffraction is the determination of accurate atomic parameters (positional and thermal parameters, site occupations) of lighter elements in the presence of heavy ones.

The contrast in conventional X-ray diffraction is directly related to the ratio of the number of electrons Z_j of the different atoms or ions j involved. The atomic scattering factor f_j in the structure-factor formula, which represents the Fourier transform of the atomic electron density distribution, is proportional to Z_j ($f_j = Z_j$ for $\sin\theta/\lambda = 0$). Standard X-ray techniques can hardly differentiate between atoms/ions of a similar number of electrons, and only an average structure - including a total occupation probability of mixed occupied sites - may be obtained in such cases.

For neutrons the atomic scattering factor f_j is replaced by the nuclear scattering length (or coherent scattering amplitude) b_j, which is of the same order of magnitude for all nuclei but varies from nucleus to nucleus in a non-systematic way. b_j values, which can be either positive or negative, depend on the isotopes and nuclear spin states of the element j. A nucleus of an isotope with spin I may have two different neutron scattering lengths: one for the combined spin state $J = I + ½$ and one with $J = I - ½$. An important and fundamental example is provided by the simplest of all nuclei, the proton with spin $I = ½$. The two spin states, $J = 1$ (triplet) and $J = 0$ (singlet), with statistical weights ¾ and ¼ respectively, have the scattering lengths for a *free* proton:

$$b^s_H = -23.7 \text{ fm}, \; b^t_H = +5.38 \text{ fm}, \; b_{freeH} = ¼b^s_H + ¾b^t_H = -1.89 \text{ fm (with } 10^{-15} \text{ m} = 1 \text{ fm)}.$$

The value for the *bound* proton in a crystal structure, which is to be used in the structure factor calculations, amounts to $b_H = 2 \cdot b_{freeH} = -3.741$ fm.

The natural isotope mixture and a statistical spin-state distribution lead to the commonly used general formula $b_j = \alpha \cdot b_{j\alpha} + ß \cdot b_{jß} + \gamma \cdot b_{j\gamma} + \ldots$ with the sum of the different isotope fractions $\alpha + ß + \gamma + \ldots = 1$ ($b_{j\alpha}$, $b_{jß}$, $b_{j\gamma}$ being the individual scattering lengths of the different isotopes of the element j). The natural nickel isotopes, for instance, have extremely different coherent scattering amplitudes:

$b(^{58}Ni) = +14.4$ fm, $b(^{60}Ni) = +3.0$ fm, $b(^{61}Ni) = +7.6$ fm, $b(^{62}Ni) = -8.7$ fm, $b(^{64}Ni) = -0.37$ fm resulting in an overall scattering length $b_{Ni} = +10.34$ fm.

Neutron experiments frequently make use of compounds containing single isotope elements, like fully deuterated samples. Incoherent scattering due to a statistical distribution of isotopes and nuclear spin states is not discussed here. It may influence the effective absorption and the background conditions of neutron diffraction studies.

12.3.1 Example of contrast variation:

Crystal structure and magnetic ordering of $(Mn_{1-x}Cr_x)_{1+\delta}Sb$

A special possibility of contrast variation, the combination of X-ray and neutron diffraction information, is demonstrated for the example of the intermetallic compounds $(Mn_{1-x}Cr_x)_{1+\delta}Sb$, with $0 \leq x \leq 1$ [1]. This mixed system is of special interest due to its magnetic properties: competing magnetic interactions with isotropic ferromagnetic behaviour for $Mn_{1+\delta}Sb$ and an uniaxial antiferromagnetic structure for $Cr_{1+\delta}Sb$. It crystallises in the hexagonal NiAs-type structure (space group: $P6_3/mmc$) with some additional partial occupation (≤ 0.14) of the interstitial site 2(d) (see Fig. 1):

2(a) - 0,0,0; 0,0,1/2 and 2(d) - 2/3,1/3,1/4; 1/3,2/3,3/4.

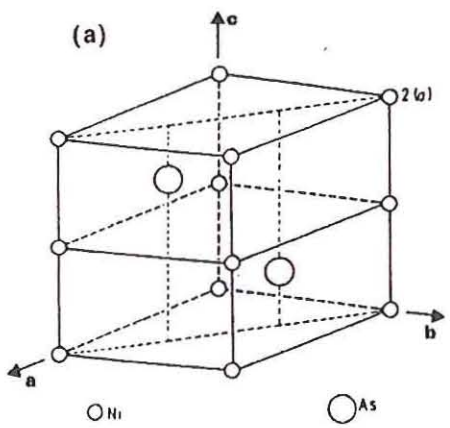

Fig. 1a. NiAs structure

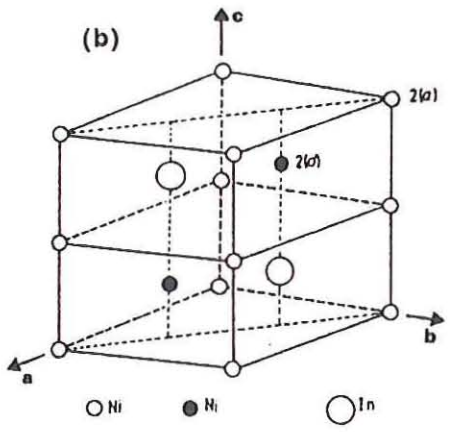

Fig. 1b. Ni_2In structure (filled NiAs-type)

Conventional X-ray diffraction cannot differentiate between chromium (Z_{Cr}= 24) and manganese (Z_{Mn}= 25) on these sites but yields important information on their overall occupation probabilities M = (Mn,Cr): M_aM_dSb, where M_a stands for the occupation probability of site 2(a) and M_d for that of site 2(d). The Sb position is assumed to be fully occupied, thus serving as an internal standard.

The corresponding nuclear scattering lengths of neutron diffraction are extremely different with a negative sign for manganese: $b_{Cr} = +3.52$ fm and $b_{Mn} = -3.73$ fm.

Remember: A positive value of b_j means that there is a phase shift of 180° between the incident and scattered neutron waves as a consequence of predominant potential scattering. The few negative b_j values - no phase change - result from resonant scattering.

The knowledge of the overall occupation probabilities M_a and M_d - from conventional X-ray studies - allows the evaluation of the Cr : Mn ratios of the different sites 2(a) and 2(d) from the corresponding effective scattering lengths determined by neutron diffraction. In the structure analyses based on the neutron data $b_{eff} = b_{Mn} \cdot PP$ is obtained individually for the two sites

($PP_a = a$ and $PP_d = d$ stands for refined pseudo-occupation probabilities). According to

$$b_{eff}(2a) = a[(1-y)\cdot b_{Mn} + y\cdot b_{Cr}] \quad \text{and} \quad b_{eff}(2d) = d[(1-z)\cdot b_{Mn} + z\cdot b_{Cr}]$$

we can calculate

$$y = [b_{eff}(2a)/a - b_{Mn}] / [b_{Cr} - b_{Mn}] \quad \text{and} \quad z = [b_{eff}(2d)/d - b_{Mn}] / [b_{Cr} - b_{Mn}].$$

The detailed site occupations lead to the general formula

$$(Mn_{1-y}Cr_y)_a(Mn_{1-z}Cr_z)_dSb$$

site 2(a) site 2(d)

corresponding to a chemical composition of $Mn_{[(1-y)a + (1-z)d]}Cr_{[ya + zd]}Sb$. It is evident, that the individual (Cr,Mn) distribution on the two crystallographically different sites 2(a) and 2(d) is not accessible merely by a chemical analysis. For most of the samples studied, the site 2(a) was found to be fully occupied: $a \approx 1.0$. But the formula $(Mn_{1-x}Cr_x)_{1+\delta}Sb$ used normally is only correct for the special case of equal Cr : Mn ratios on both sites:

$$x = y = z \quad \text{and} \quad 1+\delta = a+d.$$

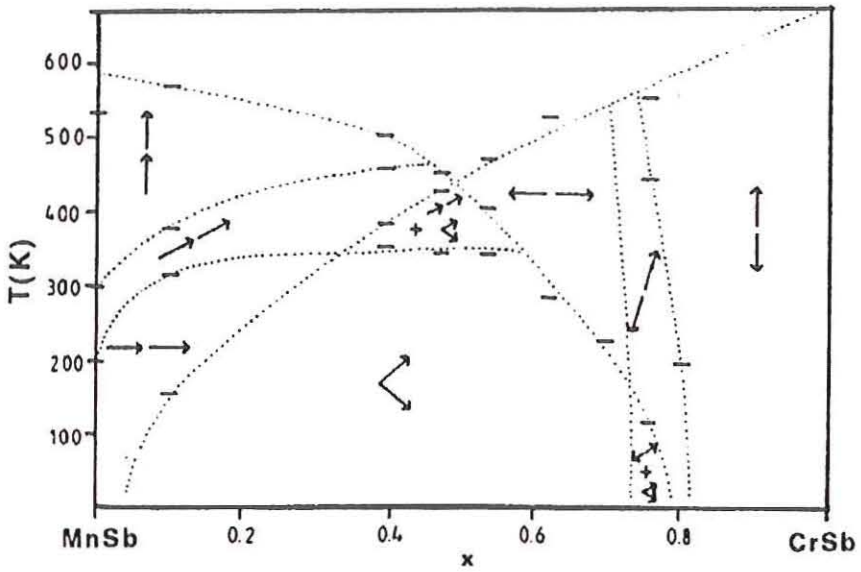

Fig. 2. Magnetic phase diagram of the system MnSb – CrSb. The vectors indicate the spin orientations in the different magnetic structures.

The detailed information on the (Cr,Mn) distribution is needed to explain the magnetic properties of these intermetallic compounds, for which only the spins localised on the 2(a) sites are involved in the magnetic ordering leading to a complex magnetic phase diagram of the MnSb – CrSb system (see Fig. 2). An overall Cr : Mn ratio from chemical analysis is not sufficient. The ferromagnetic $Mn_{1+\delta}Sb$ changes its axis of easy magnetisation from parallel to the hexagonal c-axis at high temperatures to $\perp \underline{c}$ at low temperatures. The magnetic spins of the uniaxial antiferromagnetic $Cr_{1+\delta}Sb$ are oriented parallel (or antiparallel) to $\underline{c}$. For mixed crystals $(Mn_{1-x}Cr_x)_{1+\delta}Sb$ in between the pure end members there exist various ferro- and antiferromagnetic states with inclined spin orientations, with non-colinear magnetic arrangements, and regions with co-existing magnetic ordering.

In general, a mixed occupation of one crystallographic site with <u>three</u> kinds of scatterers - e.g. Mn, Cr, and "vacancies" - requires at least <u>two</u> independent and sufficiently different experimental data to determine the fractional occupancies.

12.4 The hydrogen problem in structure analysis

The determination of the structure parameters of hydrogen atoms is a special problem involving different aspects of X-ray and neutron diffraction. It is obvious that H/D atoms with Z = 1 give only a small contribution to the electron density and, therefore, they are hardly

visible in X-ray structure analyses. This holds especially when heavy atoms are present. But there is a more general problem: the single electron of H/D is engaged in the chemical bonding and is not localised at the proton/deuteron position. This position, however, is of importance when hydrogen bonds - eventually related to the lattice dynamics or structural phase transitions - are discussed.

X-ray studies of electron densities of simple molecular crystals, for which theoretical calculations for isolated molecules are possible, are of special interest in order to compare experimental and theoretical results for a better understanding of chemical bonding in crystalline solids. Molecular crystals consist normally of light atoms often including hydrogen. A combination with neutron diffraction experiments is important to determine the structure parameters of the H/D atoms properly. More generally, the structure analysis by neutron diffraction yields separately and independently from the X-ray data the structure parameters of all atoms including the mean square displacements due to static and dynamic (even anharmonic) effects. This complete information can be used in a so-called X-N synthesis to obtain experimental electron deformation densities from the measured X-ray Bragg intensities.

12.4.1 Example of the determination of H/D positions:

Study of hydrogen bonds in $Na_2S{\cdot}9D_2O$

One of the most important fields of application of neutron diffraction is the determination of H/D sites and of their Debye-Waller factors. As an example for a study of a variety of hydrogen bonds, where the structure model was established by conventional X-ray analysis and neutron diffraction served especially to localise the hydrogen atoms, the case of fully deuterated $Na_2S{\cdot}9D_2O$ was chosen [2]. Its crystal structure (non-centrosymmetric space group: $P4_122$ or $P4_322$) is dominated by discrete $[Na(D_2O)_5]$ and $[Na(D_2O)_4]$ spiral chains of $Na(D_2O)_6$ octahedra (see Fig. 3). There are five different water molecules (see Fig. 4) with O-D distances between 0.949 Å and 0.983 Å, and D-O-D angles from 104.6° to 107.5°. These water molecules are furthermore involved in six different O-D...S bridges to the S^{2-} ions. Details of the various O-D...O/S hydrogen bonds (given in Table I) were combined with results from Raman spectroscopy from which the uncoupled O-D(H) stretching frequencies could be reasonably well assigned to the nine different O-D(H) groups of the crystal structure.

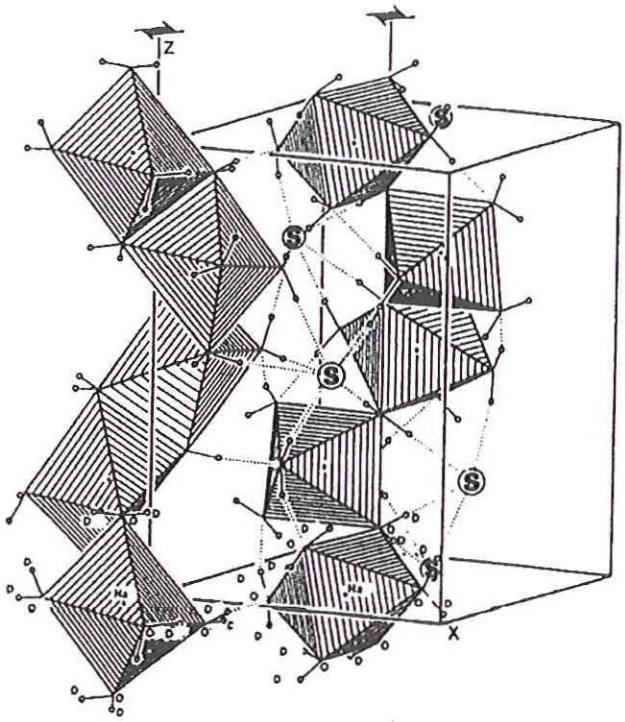

Fig. 3. $Na_2S{\cdot}9D_2O$: A partial view of the crystal structure

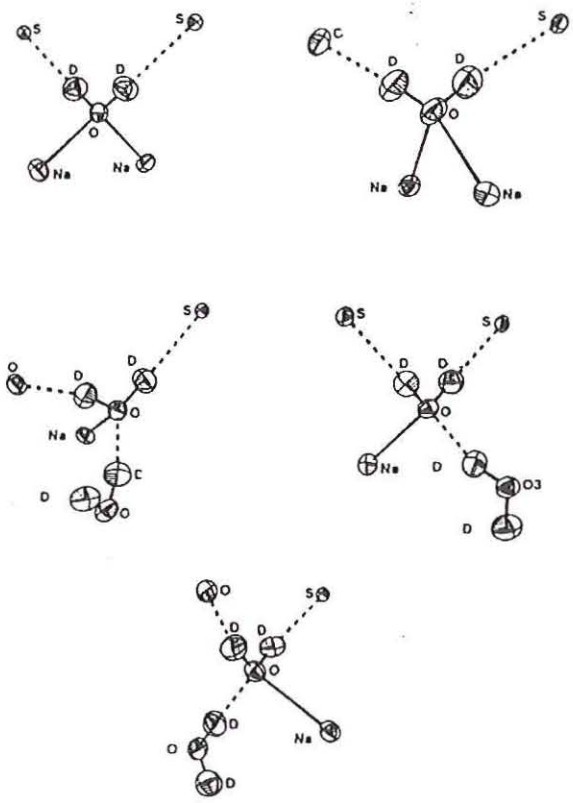

Fig. 4. Coordination of the D_2O molecules in $Na_2S \cdot 9D_2O$.

A	B C	A-B	B-C	A-C	∠BAC	∠ABC	∠BAB'	∠CAC'	L	A-L	∠LAL'
O(1)	-D(1)...S	0.961(7)	2.359(5)	3.319(5)	1.4(4)	178.0(6)	106.3(7)	103.4(2)	Na(1)	2.411(4)	116.1(2)
	-D(1')...S	0.961(7)	2.359(5)	3.319(5)	1.4(4)	178.0(6)			Na(1')	2.411(4)	
O(2)	-D(21)...O(5)	0.964(7)	1.793(7)	2.752(7)	4.9(4)	172.4(6)	106.1(7)	111.5(2)	Na(2)	2.588(5)	97.6(2)
	-D(22)...S	0.962(7)	2.550(6)	3.506(5)	5.2(4)	172.8(6)			Na(2')	2.380(5)	
O(3)	-D(31)...S	0.977(7)	2.311(5)	3.284(5)	4.7(4)	173.3(5)	107.5(7)	116.9(2)	Na(1)	2.397(5)	104.8(2)
	-D(32)...O(4)	0.953(7)	1.797(7)	2.730(7)	9.6(4)	165.3(6)			O(5)	2.768(7)	
O(4)	-D(41)...S	0.983(7)	2.294(5)	3.274(4)	3.4(4)	175.1(5)	104.6(6)	104.1(2)	Na(2)	2.418(5)	105.5(2)
	-D(42)...S'	0.973(7)	2.359(5)	3.333(5)	0.3(4)	179.6(5)			O(3)	2.730(7)	
O(5)	-D(51)...O(3)	0.949(7)	1.838(7)	2.768(7)	9.2(4)	166.1(6)	105.5(6)	103.4(2)	Na(1)	2.485(5)	101.7(2)
	-D(52)...S	0.967(7)	2.441(5)	3.401(5)	5.7(4)	172.1(5)			O(2)	2.752(7)	
mean values		0.965					106.0	107.9	<Na-O>	2.447	
mean values O-D...O		0.955	1.809	2.750		167.9					
mean values O-D...S		0.970	2.386	3.353		175.2					

Table I. Interatomic distances (Å) and angles (°) for the hydrogen bonds and the ligands to the water molecules in $Na_2S \cdot 9D_2O$.

Remember: The scattering lengths of the proton and the deuteron are b_H = -3.74 fm and b_D = +6.67 fm, respectively. Their magnitudes are comparable to the average of all b_j magnitudes and, therefore, H/D can be considered as "normal" atoms for neutron diffraction. The different signs of b_H and b_D may be of interest in Fourier maps for contrast reasons. Experimental conditions like background and effective absorption are strongly affected by the huge and exceptional incoherent neutron scattering cross-section of hydrogen ($\sigma_{inc}(H)$ = 79.7 barns as compared to $\sigma_{inc}(D)$ = 2.0 barns).Very often deuterated compounds are preferred in order to profit from the larger b_D value, but mainly to reduce the background from incoherent scattering. This volume-dependent background may become crucial for neutron powder diffraction experiments, for which normally sample volumes of more than 1 cm^3 are required.

12.4.2 Example of a study of H/D ordering:

Ferroelectric phase transition in KH_2PO_4 (KDP)

The hydrogen problem is of special importance for structural phase transitions driven by proton ordering. As a well known example the ferroelectric transition in KH_2PO_4 (KDP) is presented. A characteristic feature of its crystal structure consists of the PO_4 groups linked by strong hydrogen bonds (see Fig. 5). At room temperature KDP crystallises in a tetragonal phase (space group: I $\bar{4}$2d), where the protons in the O···H···O bonds are dynamically disordered according to a double-well potential. At T_C = 122 K, KDP transforms to a

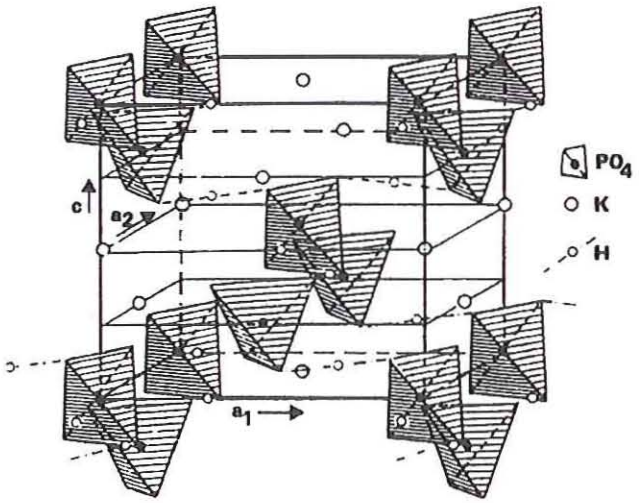

Fig. 5. Crystal structure of KH_2PO_4.

ferroelectric phase of orthorhombic symmetry (space group: Fdd2) in which the protons order in short asymmetric O-H...O bonds [3]. The contour plots of the proton distribution at different temperatures are shown in Fig. 6.

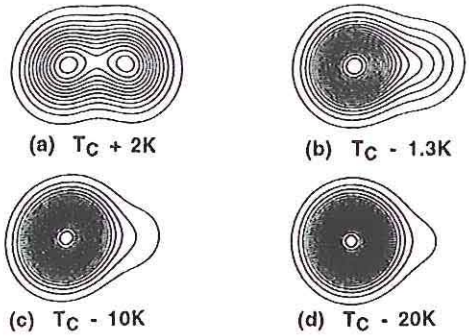

Fig. 6. Contour plots of the refined proton distributions in KH_2PO_4 at:
(a) $T_C + 2$ K, (b) $T_C - 1.3$ K, (c) $T_C - 10$ K, (d) $T_C - 20$ K.

12.5 Molecular disorder

Disordered structures and pseudosymmetries related to dynamical reorientation and/or structural phase transitions are of great current interest. In principal, the dynamical disorder of molecules is due to the fact that the intermolecular bonds are very much stronger than the external ones between the molecular groups and the surrounding crystalline frame. It is obvious that the chemical bonding scheme predicts the symmetry of a crystal structure, and not the other way around. We can state, however, that in the case of an incompatible point-group symmetry of a molecule with respect to its site symmetry in the crystal structure, molecular disorder is the necessary consequence. In order to modellize the atomic density distributions correctly in a way to obtain physically meaningful potentials, very accurate Bragg intensities over a large $\sin\theta/\lambda$ range are required. X-ray experiments are generally more restricted than neutron studies because of the $\sin\theta/\lambda$ dependence of the atomic scattering factor f_j.

12.5.1 Example of molecular disorder:

Almost free rotation of NH_3 groups in the crystal structure of $Ni(NH_3)_6I_2$

As an example, related to the H/D problem, the dynamical disorder of the NH_3 group in the cubic high temperature phase of the metal hexamine halide $Ni(NH_3)_6I_2$ (space group: Fm3m) is presented. The corresponding crystal structure is shown in Fig. 7. With the NH_3 tetrahedra

(3m symmetry) on crystallographic sites of 4mm symmetry it is obvious that they must be orientationally disordered. At 19.7 K, $Ni(NH_3)_6I_2$ undergoes a first order phase transition to a probably ordered rhombohedral low temperature modification [4].

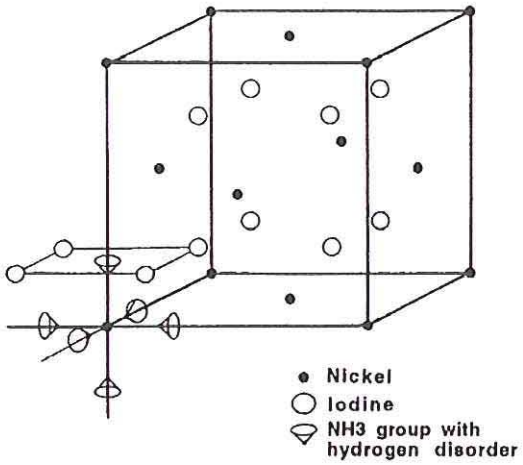

Fig. 7. High temperature structure of $Ni(NH_3)_6I_2$ The hexamine coordination is shown only for the Ni atom at the origin.

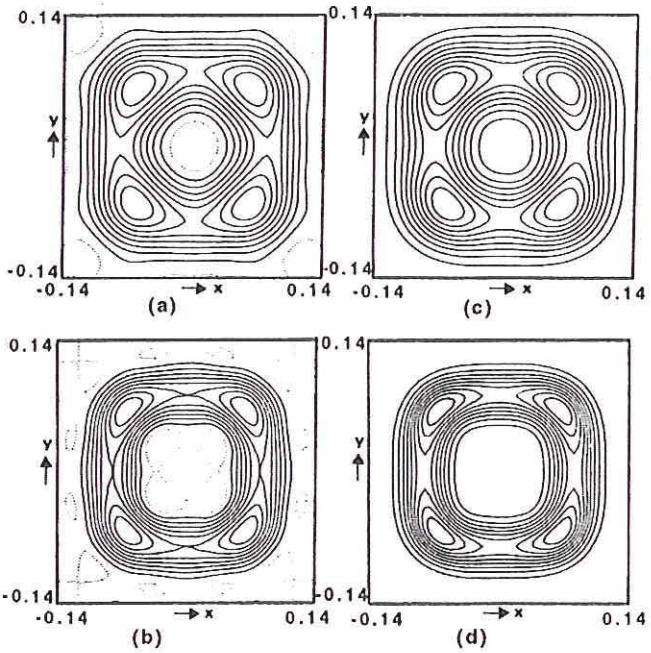

Fig. 8. $Ni(NH_3)_6I_2$: Proton density in a [001] section at z = 0.23;
(a) and (b) experimental results at 295 K and 35 K,

(c) and (d) calculated densities at 295 K and 35 K.

Single crystal neutron diffraction studies at 35 K and 295 K [5] revealed a planar proton density distribution perpendicular to the four-fold axes (see Fig. 8). Its four maxima are directed towards the neighbouring iodines according to the influence of N-H...I bonding. This proton density can be explained as a consequence of a coupled rotational-translational motion of the ammine group.

12.6 Spin densities in magnetic molecular compounds

Molecular magnetic compounds are of great actual interest due to both, applicational perspectives and fundamental research. The spin density distribution is an essential information for the understanding of the magnetic properties of these materials; it yields the localisation of the magnetic electrons and give rise to the microscopic magnetic interactions. Polarised neutron diffraction on single crystals is presently the most powerful tool for determining the spin densities in molecular compounds [6]. Results obtained from a data treatment by the maximum-entropy reconstruction method are presented for the purely organic ferromagnet, β-4,4,5,5-tetramethyl-2-*p*-(nitro-phenyl)-3-oxido-4,5-dihydroimidazolium 1-oxyl (*p*NPNN) [7].

References

1. W. Reimers, E. Hellner, W. Treutmann, and G. Heger, J. Phys. C: Solid State Phys. **15**, 3597 (1982).
2. A. Preisinger, K. Mereiter, O. Baumgartner, G. Heger, W. Mikenda, and H. Steidl, Inorg. Chem. Acta **57**, 237 (1982).
3. R. J. Nelmes, W. F. Kuhs, C. J. Howard, J. E. Tibballs, and T. W. Ryan, J. Phys. C: Solid State Phys. **18**, L711 (1985).
4. J. Eckert and W. Press, J. Chem. Phys. **73**, 451 (1980).
5. P. Schiebel, A. Hoser, W. Prandl, G. Heger, and P. Schweiss, J. Phys. I France **3**, 987 (1993).
6. J. Schweizer, Physica B **234-236**, 772 (1997).
7. P. Schleger, A. Puig-Molina, E. Ressouche, O. Rutty and J. Schweizer, Acta Cryst. **A53**, 426 (1997).

Textbooks

G. E. Bacon, Neutron Diffraction, Clarendon Press, Oxford (1975).

HERCULES: Neutron and Synchrotron Radiation for Condensed Matter Studies, Vol. I and II (edited by J. Baruchel, J. L. Hodeau, M. S. Lehmann, J. R. Regnard and C. Schlenker), Les Editions de Physique, Les Ulis & Springer-Verlag, Berlin (1993-1994).

L. Dobrzynski and K. Blinowski, Neutrons and Solid State Physics, Ellis Horwood Series in Physics and its Applications, New York (1994)

13. Inelastic neutron scattering : phonons and magnons

Markus Braden

Forschungszentrum Karlsruhe, IFP, Postfach 3640, D-76021 Karlsruhe

Laboratoire Léon Brillouin, CE-Saclay, F-91191 Gif-sur-Yvette Cedex

braden@bali.saclay.cea.fr

13.1 Interaction and scattering law

13.1.1 Basic concepts of scattering experiments

Scattering experiments are performed with almost all types of radiation on various systems (solids, liquids, gases, atoms, nuclei, ...). The radiation with well defined initial properties (wavevector $\underline{k}$; energy E) hits the sample, gets scattered and may be detected again with well defined final properties (wavevector $\underline{k'}$; energy E') in the angular segment $r^2 d\Omega$, the schematic picture of the scattering arrangement is drawn in figure 1. Aim of any scattering experiment is to obtain information on the states of the sample by use of the knowledge of the interaction between the radiation (for example neutrons) and the particles forming the sample. In this chapter we deal with the inelastic neutron scattering in solids which is till today the most efficient way to study dispersion relations of lattice vibrations and magnetic excitations.

The initial and final states of the neutron may be denoted by σ_i and σ', those of the sample by λ_i and λ'. σ_i is characterized by the wavevector $\underline{k}$ and the energy $E = \frac{\hbar^2}{2m}k^2$, σ' respectively. The momentum transferred to the sample crystal, $\underline{Q}$, and the energy transfer, $E = \hbar\omega$, have to fulfill the conservation laws, $\underline{Q} = \underline{k} - \underline{k'}$ and $\omega = \hbar(\frac{1}{2m})^2(k^2 - k'^2)$. The probability to observe a scattered neutron in the angular segment $d\Omega$ and in the energy interval dE' is described by the partial differential cross section which may be obtained within the Born-approximation, which is a perturbation theory of first order, i.e. one considers the interaction between radiation and sample crystal to be small.

$$\frac{d^2\sigma}{d\Omega dE'} = (k'/k)(m/2\pi)^2 \sum_{\lambda_i,\sigma_i} P_{\lambda_i} P_{\sigma_i} \sum_{\lambda',\sigma'} \qquad (13.1)$$

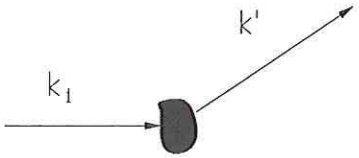

Figure1 Schematical drawing of a general scattering experiment.

$$| < \sigma'\lambda' | \int d^3r \; exp(i\underline{k}' \cdot \underline{r}) \hat{V}(r) exp(i\underline{k} \cdot \underline{r}) | \sigma_i \lambda_i > |^2$$
$$* \delta(\omega + E' - E)$$

The cross section in equation (13.1) is given by the sum of the transition matrix elements between initial states $\sigma_i\lambda_i$ and the final states $\sigma'\lambda'$ weighted by the probabilities of the initial states. In order to calculate the cross section and the observable intensity distribution, one needs the interaction potential $\hat{V}(\underline{r})$ and detailed knowledge of the states in the sample λ_i. In the inverse way one may use a measured intensity distribution in order to characterize the sample states, for example the phonons. This is the usual way of the interpretation of any scattering experiment. The sample states may be characterized by specific parameters, for example the frequencies and the polarization patterns in case of phonons, which with the aid of equation (13.1) will be deduced from the experimental intensity distribution.

13.1.2 Nuclear interaction – phonons

The nuclear interaction between the neutron and the core of the atoms is characterized by an extension of 10^{-5}Å, which is extremely small in comparison to the wavelength of thermal neutrons. Therefore, the scattering is isotrope and may be described by only one parameter, the scattering length. The interaction with the hole crystal is given by the sum over the atoms :

$$\hat{V}(\underline{r}) = \frac{2\pi}{m} \sum_j b_j \delta(\underline{r} - \underline{R}_j) \qquad (13.2),$$

where b_j and $\underline{R}_j$ are the scattering length and the position of the j-th atom. The mixing of different isotopes at the same atom site in the crystallographic lattice yields a further complication, since different isotopes have different scattering lengths. This means

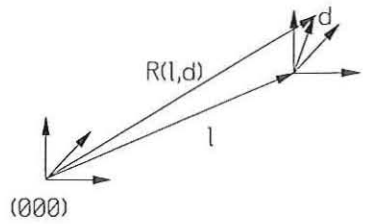

Figure 2 Schematic drawing of the vectors determining the position of an atom in the crystal lattice.

that the interaction potential (13.2) does not show the full translation symmetry of the crystal lattice. The local variation of the scattering length splits the differential cross section into two contributions :

$$\frac{d^2\sigma}{d\Omega dE'} = (\frac{d^2\sigma}{d\Omega dE'})_{coh.} + (\frac{d^2\sigma}{d\Omega dE'})_{incoh.} \qquad (13.3).$$

The coherent contribution is determined by the mean scattering length, whereas the incoherent contribution is given by the root mean square deviation to the averaged scattering length.

In order to calculate the differential cross section in (13.1) it is necessary to know the states in the sample or at least to parameterize them. The sum over the states λ_i in (13.1) may be transformed to the correlation function, in which one has to introduce the parameterized Eigen-states of the system. In order to achieve this transformation in case of the phonons we consider the vibrations of a crystal in harmonic approximation.

– *Description of lattice dynamics in harmonic approximation* – A crystal consists of N unit cells with n atoms within each of them, the equilibrium position of any atom is given by the position of the unit cell to which it belongs, $\underline{l}$, and by the position of the atomic site in the unit cell, $\underline{d}$. At a certain time the atom may be displaced from its equilibrium position by $\underline{u}(\underline{l},\underline{d})$. The instantaneous position is hence given by $\underline{R}_{\underline{l},\underline{d}} = \underline{l}+\underline{d}+\underline{u}(\underline{l},\underline{d})$ (see figure 2).

For simplification we consider first a lattice with only one atom in the unit cell, $\underline{d} = \underline{0}$; $\underline{l}$ describes then the equilibrium position of the atom. The interaction potential between two atoms $\underline{l}$ and $\underline{l}'$, $\Phi(\underline{l},\underline{l}')$, may be expanded at the equilibrium position in terms of $\underline{u}(\underline{l})$=$\underline{u}(\underline{l}')$=0. The constant term does not give any contribution to the equations of movement, it is relevant only for the total energy of the crystal structure. Since at the

equilibrium position the atom is in rest, terms of first order are not allowed. In harmonic approximation one assumes the expansion till the second order to be sufficient. This assumption is essential for the following analysis, since already the presence of third order terms prohibits to solve the equations of movement in the general case. In most solids anharmonic contributions to the potential are, however, small justifying the assumption. If the anharmonic effects have to be taken into consideration (for example close to the melting of the crystal lattice), perturbation theory is the usual technique.

Using the definition :

$$D_{\alpha,\beta}(\underline{l},\underline{l}') = \frac{d^2\Phi(\underline{l},\underline{l}')}{du_\alpha(\underline{l})du_\beta(\underline{l}')} \qquad (13.4)$$

one obtains the equations of movement $(\alpha, \beta = x, y, z)$ to :

$$M\ddot{u}_\alpha(\underline{l}) = -\sum_{\beta,\underline{l}'} D_{\alpha,\beta}(\underline{l},\underline{l}')u_\beta(\underline{l}') \qquad (13.5).$$

The displacement of the atom $\underline{l}'$ in β-direction yields a force on the atom $\underline{l}$ in α-direction of strength $D_{\alpha,\beta}(\underline{l},\underline{l}')u_\beta(\underline{l}')$, $D_{\alpha,\beta}(\underline{l},\underline{l}')$ are therefore called the force-constants. The real problem in treating lattice dynamics consists in the large number of these equations, there are 3N equations to be solved with N being of the order of 10^{23}. In order to avoid this complexity one makes the Ansatz of plane waves : the movements of all atoms are given by the displacement in one unit cell at time zero propagating in time and space as a wave :

$$u_\alpha(\underline{l}) = e_\alpha M^{-1/2} \cdot exp(i\underline{q}\underline{l} - \omega_0 t) \qquad (13.6).$$

Figure 3 shows the displacement pattern of a plane wave characterized by the wave vector $\underline{q}$, reflecting the propagation of the wave (planes perpendicular to $\underline{q}$ are always identically displaced), the vibration frequency ω_0 of each atom and the direction of the oscillation given by the polarization vector $\underline{e}$. In the single atom lattice there are only acoustic modes, they are called longitudinal (LA) if $\underline{q}$ is parallel to $\underline{e}$ and transversal (TA) for $\underline{q}$ perpendicular to $\underline{e}$.

The plane wave Ansatz (13.6) for the equations of movement yields a system of three equations for each $\underline{q}$-value :

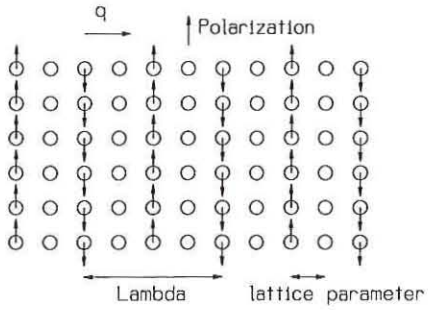

Figure 3 Scheme of the displacements in a transversal plane wave.

$$\omega_0^2 e_\alpha = 1/M \sum_{\underline{l},\beta} D_{\alpha,\beta}(\underline{l},0) exp(-i\underline{q}\underline{l}) e_\beta \qquad (13.7).$$

Here we use that the force constants depend only on the distance in real space $(\underline{l}-\underline{l}')$ and not on the particular values of $\underline{l}$ and $\underline{l}'$. With (13.7) one gets an easily solvable system; the original complexity of the problem is transferred to the number of these 3-dimensional problems. For a complete solution of the crystal dynamics one would need to solve the problem (13.7) for each of the N$\sim 10^{23}$ allowed $\underline{q}$-values. In reality, however, one has to analyze only a few different $\underline{q}$-values. In general it is sufficient to study only $\underline{q}$-values within the first Brillouin-zone.

We may define the dynamical matrix as

$$\bar{D}_{\alpha,\beta}(\underline{q}) = 1/M \sum_{\underline{l},\beta} D_{\alpha,\beta}(\underline{l},0) exp(-i\underline{q}\underline{l}) \qquad (13.8),$$

which allows to rewrite the equations (13.7) in matrix form :

$$\omega_0^2 \underline{e} = \bar{D} \cdot \underline{e} \qquad (13.9).$$

The system (13.9) is just a three-dimensional Eigen-value problem.

For fixed $\underline{q}$ one has to determine the three Eigen-vectors $\underline{e}_j$, j=1,2,3, together with the three corresponding Eigen-values, $\omega_j(\underline{q})$. This may be achieved with the standard numerical techniques. The dependence of the Eigen-frequencies on the wave-vector, $\omega_j(\underline{q})$ with $j = 1, 2, 3$, is called the dispersion relation.

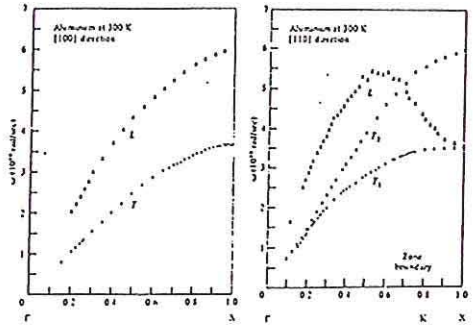

Figure 4 Phonon dispersion of Al along the [100] and [011]-directions (from reference [1]).

The extension to a system with n Atoms in the primitive cell can be easily done, one gets for each $\underline{q}$ an Eigen-value problem in $3n$ dimensions. The Eigen-vectors have the dimension $3n$ and the dynamical matrix is $3n * 3n$ dimensional. For each $\underline{q}$ one finds hence $3n$ Eigen-modes, therefore the complete phonon dispersion consists of $3n$ branches, three of which have zero frequency for $q \rightarrow 0$. The latter branches are called acoustic since they are associated with the propagation of sound. The figure 4 shows the typical presentation ω against wave-vector $\underline{q}$ for the phonon dispersion of aluminum.

The plane waves according to the Eigen-frequencies and to the Eigen-vectors to each of the allowed $\underline{q}$-values form a complete set of functions for the displacements of the N times n atoms in the crystal. Any distortion can be represented as a linear combination of these plane waves. Obviously it is rather favorable to use this set for calculating the differential cross section. However, for this purpose it is necessary to convert the lattice vibrations into quantum mechanics, the corresponding quasi-particle being the phonon. A one-phonon process is shown in the schematic figure 5. The momentum transfer $\underline{Q} = \underline{k} - \underline{k'}$ consists of the sum of a reciprocal lattice vector $\underline{\tau}$ and the wave-vector $\underline{q}$, which lies within the first Brillouin-zone. Only $\underline{q}$ determines the wave vector of the contributing phonons, however $\underline{Q}$ determines the differential cross section, i.e. the intensity.

The exact scattering may be deduced from the correlation function. In the following we only want to discuss the meaning of the different terms in the cross section :

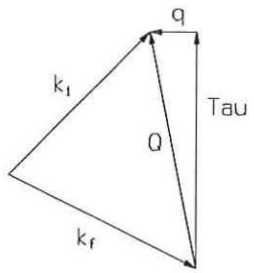

Figure 5 Scattering triangle corresponding to the observation of a phonon mode with wave vector $\underline{q}$ at the reciprocal lattice vector $\underline{\tau}$.

$$\left(\frac{d^2\sigma}{d\Omega dE'}\right)^{\pm} = (k'/k)\frac{(2\pi)^3}{2v_0}\sum_{\underline{\tau}}\sum_{j,\underline{q}} |G_j(\underline{q},\underline{Q})|^2 \qquad (13.10.a)$$

$$\cdot\frac{1}{\omega_j(\underline{q})} \qquad (13.10.b)$$

$$\cdot(n(\omega_j(\underline{q})) + 1/2 \pm 1/2) \qquad (13.10.c)$$

$$\cdot\delta(\omega \mp \omega_j(\underline{q}))\cdot\delta(\underline{Q} \mp \underline{q} - \underline{\tau}) \qquad (13.10.d),$$

with v_0 the volume of the reciprocal unit cell. Equation (13.10) describing the intensity of a one-phonon measurement at specific $\underline{Q}$ closely resembles the elastic structure factor of the Bragg reflection intensity, a part of expression (13.10) is called dynamic structure factor. The intensity is given by the sum over all reciprocal lattice and all wave vectors; however only the combination $\underline{q}+\underline{\tau} = \underline{Q}$ may contribute due to the δ-function in (13.10.d). The second δ-function in (13.10.d) reflects the law of energy conservation, however, one has to take into account that the scattering processes may lead to a creation as well as to an annihilation of a single phonon, corresponding to the upper and the lower signs respectively. There are two more general factors determining the intensity of the phonon observation by neutron scattering. The term (13.10b) indicates, independently of all other terms, that the intensity is inversely proportional to the frequency of the mode. High energy modes are always more difficult to observe than the low lying ones. Since neutron experiments suffer from the low flux of the existing sources, this effect frequently prohibits the study of the high energy part of the phonon dispersion. The term (13.10.b)

results from the quantum mechanics of a single harmonic oscillator : the square of the amplitude is proportional to $\frac{1}{\omega_j(\underline{q})}$.

The term (13.10.c) results from the Bose-statistics of the singular mode with frequency $\omega_j(q)$, the occupation number is given by the Bose-function:

$$n(\omega_j(\underline{q})) = \frac{1}{exp(\frac{\hbar\omega_j(\underline{q})}{kT}) - 1} \qquad (13.11).$$

$n(\omega_j(\underline{q}))$ tends for $T \to 0$ towards zero, the phonons are frozen. For $T \to \infty$, $n(\omega_j(\underline{q}))$ approaches $(\frac{\hbar\omega_j(q)}{kT})$, i.e. the classical relation. The term (13.10.c) indicates that the Bose-function is increased by +1 only in case of phonon creation. At low temperature where $n(\omega_j(\underline{q}))$ is close to zero, the phonon may be observed only in the creation mode, the cross section for the annihilation process becomes vanishing since the phonon states are no longer occupied. At finite temperature the Bose-statistics further simplifies the observation of phonons with low frequencies.

The complex term in (13.10.a) is given by the dynamical structure factor:

$$G_j(\underline{q}, \underline{Q}) = \sum_d \frac{b_d}{\sqrt{m_d}} \cdot exp(-W_d(\underline{Q}) + i\underline{Q}\underline{d}_d) \cdot (\underline{Q} \cdot \underline{e}_d^j(\underline{q})) \qquad (13.12),$$

where the sum is extending to the atoms, numbered by the scalar d, in the primitive cell. They have the mass m_d scattering length b_d and a three dimensional polarization vector $\underline{e}_d^j(q)$, the equilibrium position in the unit cell is given by $\underline{d}_d$. Without the last part equation (13.12) corresponds to the elastic structure factor, in particular one finds the same Debye-Waller-factor $exp(-W_d(\underline{Q}))$. The whole term in the exponential function determines whether the interference between atoms is constructive or destructive. In the dynamical structure factor there is in addition to the elastic one the polarization term (last parenthesis); for instance only those atoms may contribute whose polarization vector, $\underline{e}_d^j(\underline{q})$, possesses a component parallel to $\underline{Q}$. Since $\underline{Q}$ enters this term directly, the structure factor increases with $|Q|$; the intensity is proportional to Q^2. The interference and the polarization term in (13.12) cannot be separated in general, therefore one has to calculate the structure factors precisely.

In addition to the interpretation of the frequency data the prediction of the intensity is an important out-coming of model calculations. Only with the help of these predictions a neutron scattering experiment aiming at the lattice dynamics of a complex material can

be performed in an efficient manner.

Some easy examples may illustrate the significance of the terms in (13.12). Let us consider a longitudinal acoustic mode polarized in the [100]-direction; for this mode all $\underline{e}_d$ are parallel to [100]. The polarization term becomes maximum for $\underline{Q}$=(h+ξ 0 0) and can be extracted from the sum. The remaining interference sum corresponds for small ξ to the elastic structure-factor of (h00), The dynamic structure becomes hence strong for strong Bragg-reflections. In general acoustic phonons have to be measured close to the strong Bragg-reflections. Since for optical modes the atoms may be displaced in opposite directions, the polarization term can change sign yielding a rather distinct sum of the interference term. In a simple two-atomic structure the optical mode has only a weak dynamical structure factor close to the strong Bragg-reflections (this argument is no longer valid in case of negative scattering lengths).

Why does inelastic neutron scattering play such a dominant role in the study of lattice dynamics? The central point is certainly due to similar masses of atoms and the neutron. This yields the possibility of elastic as well as that of inelastic scattering and renders the wave-vectors of thermal neutrons comparable to the wave-vectors of the phonons. Inelastic neutron scattering allows to determine the phonon dispersion over the whole Brillouin zone, whereas optical techniques (Raman and Infra-Red-scattering) yields only the analysis of modes at the zone center.

Recently there are serious efforts to perform lattice dynamical studies using synchrotron radiation. In case of thermal neutrons the energies amount to 1–100 meV and correspond to the typical phonon energies. For comparison, CuK_α-radiation has an energy of $8 \cdot 10^6$meV. In order to determine phonon frequencies, one needs a relative energy resolution of $10^{-6} - 10^{-7}$, which may be achieved only by extreme experimental effort. The concomitant loss of intensity permits these measurements only at the most powerful synchrotron sources, and even then the measurements remain slow. We have seen that the one-phonon process yields an intensity proportional to Q^2, this may be used in case of neutron scattering due to the nuclear interaction. In case of the x-rays the large $\underline{Q}$-range is not at disposition since the form-factor strongly reduces the interaction. In the closer future one may not expect, that inelastic x-ray scattering will supply results comparable to neutron studies concerning the efficiency. The x-ray measurements, however, may become valuable in cases where the neutron scattering is hampered either by sample size or

by absorption.

13.1.3 Magnetic interaction – magnetic excitations

The neutron has a spin 1/2 which yields a coupling to the magnetic fields. The interaction operator is given by :

$$-\gamma_n \mu_N \hat{\sigma} \cdot \underline{H} \qquad (13.13);$$

here γ_n=1.913 is the magnetic moment of the neutron, expressed in μ_N, the nuclear magneton, $\hat{\sigma}$ the Pauli-spin operator and $\underline{H}$ the magnetic field induced by the electrons in the sample. $\underline{H}$ may arise from the velocity of the electrons as well as from their magnetic moment. In the following we limit the discussion to the latter contribution.

Furthermore we assume, that the orbital moment has vanished. This assumption is justified in case of quenching by crystal fields or for a half-filled shell (Mn^{2+}, Fe^{3+}, Gd^{3+}).

The Fourier-component of the interaction potential is :

$$\hat{V}(\underline{Q}) = \frac{2\pi}{m} \frac{\gamma_n e^2}{M_e c^2} \hat{\sigma} \hat{D}_\perp(\underline{Q}) \qquad (13.14)$$

with

$$\hat{D}_\perp(\underline{Q}) = \sum_{\underline{l},d} (1/2) \gamma_d F_d(Q) \hat{\sigma} \hat{S}_\perp(\underline{l}, d) exp(i\underline{Q} \cdot \underline{R}_{\underline{l}d}) \qquad (13.15),$$

here γ_d is the gyro-magnetic factor, $F_d(\underline{Q})$ the form-factor of the atom d and $S_\perp(\underline{l}, d) = \underline{Q} \times (\hat{S}_{\underline{l}d} \times \underline{Q})$ with $\hat{S}(\underline{l}d)$ being the spin-operator of the atom.

There are two important differences between the magnetic and the nuclear interaction of the neutron with the atom. Due to the extension of the electron cloud, which causes the magnetic moment, the interaction is non-local. Described by the form-factor, $F(Q)$, the interaction gradually decreases towards large $\underline{Q}$. The detailed dependence of $F(Q)$ is determined by the single atom. Rare earths show, due to the strong localization of the 4f-electrons, a less pronounced decrease when compared to the transition metal ions with more delocalized electrons. In the latter case the decrease may be quite strong limiting any measurement to the first Brillouin-zones. The dependence of the magnetic interaction due to the form-factor may be used to separate magnetic and nuclear contributions. Furthermore, the magnetic interaction is mediated by vector-operators. Only those magnetic

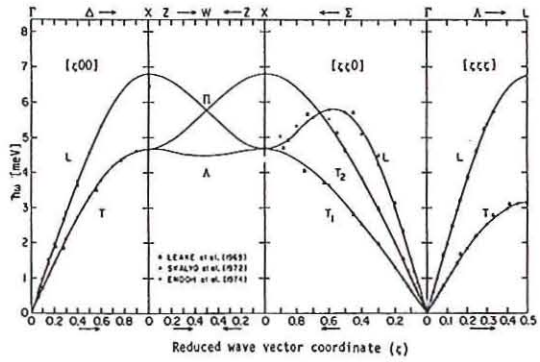

Figure 6 Phonon dispersion of Ne along the three main symmetry directions (from Ref. [2]).

moments may contribute to the interaction, which have a component perpendicular to $\underline{Q}$. This yields the possibility to determine not only the size but also the direction of magnetic moments.

13.2 Analysis of lattice vibrations

13.2.1 Lattice dynamics in simple structures

For a simple crystal lattice one may determine the polarization patterns without detailed model calculations. The lattice dynamics of such a system may then be studied experimentally without particular effort.

In figure 6 we show the phonon dispersion of Ne in the three main symmetry directions, which according the common use are labeled Δ, Σ and Λ. Ne crystallizes in a fcc-lattice with only one atom in the primitive cell, therefore one expects only three acoustic branches per $\underline{q}$-value. One observes the three distinct branches only in the [xx0]-direction, whereas there are only single transverse branches along [x00] and [xxx]. In the [x00]-direction these acoustic polarization patterns may be easily understood. In the longitudinal mode atoms are vibrating in [100]-direction, i.e. parallel to the wave vector. The two transverse modes are characterized by displacements in [010] or in [001]-directions, i.e. perpendicular to the wave-vector. Since [100] represents a four-fold axis in the fcc lattice, the latter two modes cannot be distinguished; they are degenerate. The same situation is found along the [111]-direction which is a three-fold axis of the lattice. This behavior is a simple example of the general relation between crystal symmetry and the phonon dispersion. The crystal

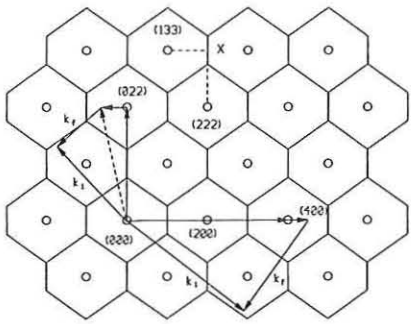

Figure 7 The plane in reciprocal space spanned by the (100) and (011) vectors for a fcc-lattice; the scattering triangle indicates the observation of Δ-modes.

symmetry yields constraints for the phonon modes which may be necessarily degenerate at certain points or - like in the Ne-structure - along a direction. In the case of more complex structures it is essential to profit from the predictions of the symmetry analysis. The [110]-direction represents only a two-fold axis since [1-10] and [001] are not identical, as consequence the corresponding transverse acoustic branches are not equivalent.

In addition figure 6 shows that at X=(100)=(011) Δ and Σ-branches are coinciding, which may be explained due to the shape of the Brollouin-zone. Figure 7 presents the plane of the reciprocal space spanned by (100) and (011); one recognizes that starting at the zone-center, Γ, in the figure (133), in the [100]-direction one will reach the zone-boundary at (233)$\equiv$(100)=X. Similar, one will reach this point when starting at the neighboring point (222) in [011]-direction. However, in this path one finds the border of the Brillouin-zone earlier and continues the last part on the zone boundary. (100) and (011) are equivalent points in reciprocal space; they are connected by a reciprocal lattice vector, (-1 1 1). For the phonon branches we conclude that Δ- and Σ-branches have to coincide. The symmetry further determines which branches coincide : for example the longitudinal Σ-branch with the transversal Δ-branch. Again, similar considerations in more complex systems may decisively contribute to the identification of the branches.

Figure 7 further shows how to measure the Δ-branches. One may observe the longitudinal branch in the (400)-zone passing to (4+x 0 0) (the (400)-zone has to be preferred to (200) due to the larger value of Q^2), whereas one may determine the transverse frequencies in the (022)-zone at (x 2 2).

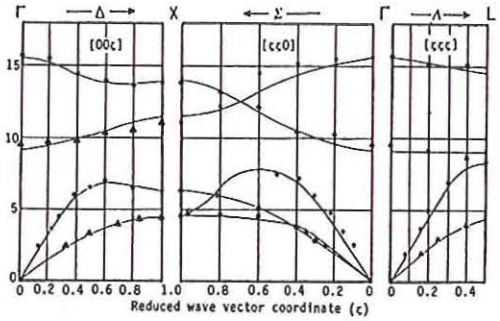

Figure 8 Dispersion curves and crystal structure of FeO (from reference [2]).

– *NaCl-structure* – The NaCl-structure represents one of the most simple possible crystal structures with two atoms per primitive cell. It consists of two fcc-lattices shifted against each other by (0.5 0.5 0.5). The entire crystal structure possesses fcc-symmetry too. Figure 8 shows the dispersion curves of FeO.

The six branches expected for the two-atomic structure are observed only in [xx0]-direction. Like in case of the fcc Ne-lattice the transverse Δ- and Λ-branches are doubly degenerate. Also in other aspects, there is some resemblance with the Ne-phonon dispersion; in both cases LA-Δ and TA-Σ branches coincide at the zone boundary.

A more detailed discussion is needed in order to understand the optical modes at Γ. The polarization pattern of an optical mode corresponds to an anti-phase axial movement of the ion pairs connected in [100], [010] or [001] direction. The three vibrations polarized in the crystal directions should, however, be degenerate due to the cubic symmetry; one might expect only one optical frequency. The optical vibration in the ionic lattice possesses a polar character, i.e. there is a local polarization due to the opposite shifts of cations and anions. For large wave-length, i.e. close to the zone-center, the local polarization adds to a macroscopic polarization only in case of the longitudinal mode. This macroscopic polarization requires an additional energy, the longitudinal optic (LO) mode is always higher in frequency than the trnaversal optic (TO) mode (note, that these modes are only defined as the limit for $\underline{q}$ tending to zero. The splitting between LO and TO-mode frequencies is called Lydane-Sachs-Teller (LST) splitting and is related by the LST-relation to the dielectrical constant. Polar mode frequencies may be easily

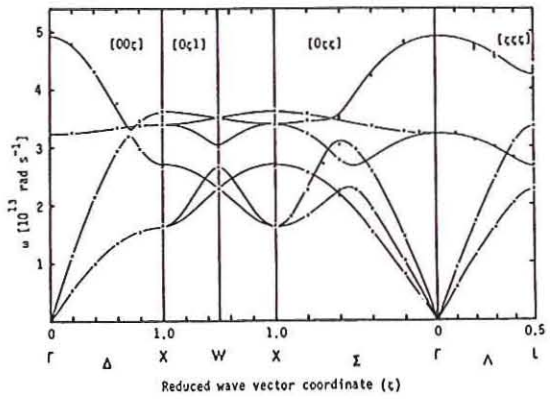

Figure 9 Phonon dispersion of NaCl (from reference [2]).

determined by Infra-Red techniques; due to the form of the resolution ellipsoid neutron scattering on this topic is frequently difficult. In metallic materials electric fields are screened due to the free charge carriers at least for macroscopic distances. As consequence the LST-splitting disappears. The phonon dispersion may then give information on the efficiency of the metallic screening.

Figure 9 shows the phonon dispersion in NaCl, which is isostructural to FeO. Compared to the latter one recognizes the perturbation of the curves arising mainly from the lower optical frequencies. Within the Brillouin-zone it is no longer possible to separate optical and acoustic modes, the branches tend to cross each other but there is always a small gap between branches of the same symmetry. This represents a general property : branches of the same symmetry may not cross. By mixing the polarization patterns it is always possible to yield a gap reducing the total energy of the system. Whether this gap is small or large depends on the similarity between the polarization patterns of the two branches. Similar branches may induce larger gaps, they are called to strongly interact.

13.2.2 Model calculations

The examples discussed above are characterized through their simplicity, which permits to analyze the polarization patterns without detailed calculations. In actual topics one has to deal with systems of more than 10 atoms per primitive cell. Already during an experiment one may identify the multiplicity of the phonon modes only by the predictions

of model calculations.

As discussed above the lattice dynamics is described by the $3n$-dimensional dynamical matrix :

$$\omega^2 \underline{e} = \tilde{D}\underline{e} \qquad (13.16)$$

$$D_{\alpha,\beta}(d,d') = \frac{1}{(m_d m_{d'})^{1/2}} \sum_{\underline{l'}} \Phi_{\alpha,\beta}(\underline{0}d, \underline{l'}d') exp(i\underline{q}\underline{l'}) \qquad (13.17).$$

$\Phi_{\alpha,\beta}(0d, l'd')$ denote the force constants between the atoms d and d' in by $\underline{l}$ shifted cells. The determination of the force constants represents the real problem in lattice dynamics, in particular the question which constants are relevant.

Already by symmetry, the nine parameters per atom-pair are significantly reduced. Furthermore, one may reduce the analysis to the closer neighbors, as far as no long range force is involved. The next step consists in the development of potentials, from which one may obtain the force constants for many pairs inducing only a few free parameters.

Frequently it is sufficient to consider axial-symmetric potentials with $V(\underline{l}d, \underline{l'}d') = V(r)$, i.e. the potential depends only on the distance between the two atoms. Such a potential yields only two force constants, a radial and a transversal one :

$$\Phi_R(\underline{l}d, \underline{l'}d') = \frac{\partial^2 V}{\partial r^2}|_{r=r_o} \qquad (13.18),$$

$$\Phi_T(\underline{l}d, \underline{l'}d') = 1/r \frac{\partial V}{\partial r}|_{r=r_o} \qquad (13.19).$$

In the most simple model one may only introduce these radial and transverse force constants for the close neighbors (Born-von-Kàrmàn Model). However, extending more and more shells will rapidly increase the number of parameters. In particular the lattice dynamics of ionic compounds with the long range Coulomb-interaction, can only be poorly described by such a model.

Even when parameterizing the Coulomb-potential $V(r) \propto \frac{Z_d Z_{d'} e^2}{r}$ by the charges, $Z_d, Z_{d'}$, in order to deduce the respective force constants, the problem of the long range persists. It is not possible to cut the sum at a certain distance, since the sums do not converge. The satisfying solution of this problem consists in the Ewald-method [1].

The Coulomb-potentials in an ionic crystal yields an attractive potential, which has to be compensated by a repulsive one. If the electron clouds of two ions of opposite charge start to overlap upon decrease of their distance, this repulsive potential will increase rapidly. One may describe this interaction by a Born-Mayer-potential $V(r) = B \cdot exp(-r/r_o)$, inducing only two parameters for one type of ionic pair, B and r_0. Amongst the various extensions of this type of model, called "rigid ion", we mention only the shell model, where the polarizability of the ions is described by a separation between an electron cloud (the shell) and the cores. There are many different ways to couple the cores and the clouds by force constants.

In order to prepare an inelastic neutron scattering study on the lattice dynamics of a complex material, even a simple and un-adapted model may be helpful, as long as the crystal structure and therefore the symmetry is correctly entered. By symmetry, degenerations are fixed for certain points or even for lines in reciprocal space, and frequently the structure factors follow some inelastic extinction rules. In principle these predictions may also be found by a careful analysis through group theory; however, the use of a simple model which does not need to describe the frequencies well is much less time demanding. Some of these aspects have already been illustrated for the example of the NaCl structure. Concerning the dynamic structure factors one may add, that one will observe the optical modes close to Γ best at the odd reciprocal lattice vectors (for example (333)) independently of the forces involved.

13.2.3 Structural phase transitions and soft mode behavior

Structural phase transitions form still a topic of actual interest, where information about the underlying microscopic mechanism may frequently be achieved only by inelastic neutron scattering.

In figure 10 one finds the representation of a fictive structural phase transition in a two-dimensional crystal structure with two atoms in the primitive cell. In the high symmetry high temperature phase the black ion in the middle occupies a site with inversion symmetry. This symmetry is broken at the phase transition due to the displacement of the black ion. The right part of figure 10 shows the corresponding dispersion curve, here the polarization pattern of the Γ-mode corresponds to the static distortion below the transition temperature, T_c. The phonon frequency of this mode softens upon approaching the phase transition and is therefore called a "soft-mode". The structural instability,

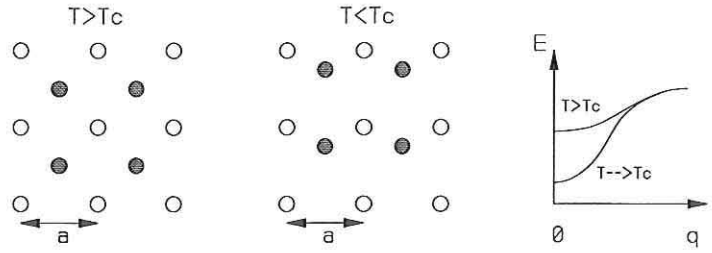

Figure 10 Schematic picture of a displacive phase transition occuring at the zone center and the corresponding dispersion curve.

however, can be also seen in the dispersion quite above T_c : the frequency of the relevant mode at Γ is lower than those of modes with $\underline{q}$-values in the Brillouin-zone.

In addition to the phonon softening one expects a broadening of the line width in frequency; finally the width of the phonon mode may surpass its frequency. Such over-damped modes may no longer be described in the harmonic approximation.

The best studied example for a zone-center phase transition may be found in the ferroelectric transition in perovskites, for example $PbTiO_3$ see figure 11. In the low temperature phase the anions are deplaced against the cations, Pb, Ti, the corresponding phonon frequency vanishes almost completely. This polarization pattern has a strong polar character and is connected to the dielectric constant through the LST-relation. The softening of the TO mode induces a divergence in the dielectric constant, which explains the interest of the phenomena for technical applications.

A structural phase transition may also lead to an enlargement of the unit cell. Here, the equivalent atoms in neighboring cells are not displaced identically; a schematic picture is given in figure 12, where neighboring black ions are shifting in opposite direction. The phonon mode associated with such a displacement pattern necessarily has a finite wave-vector, since the translation symmetry is broken. In case of figure 12, $\underline{q}$ is situated on the zone boundary. But like for the zone-center transition one one may find a softening for the zone-boundary mode too. The most known example for such a transition can again be found amongst the perovskites ABO_3. The perovskite structure consists of BO_6 octahedra with partially covalent and quite hard bonds; the octahedra are connected only through their corners. Therefore, all these systems are more or less unstable against a

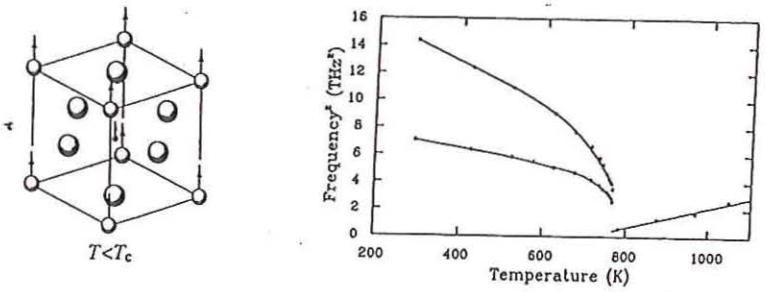

Figure 11 Structure and displacement pattern of the ferrroelectric transition in the perovskite $PbTiO_3$ (left) small black dots in the center designate Ti the small and the large open spheres Pb and O respectively; square of the corresponding phonon frequency as function of temperature from reference [3] (right).

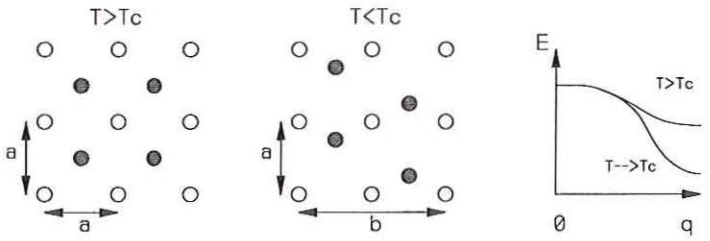

Figure 12 Schematic picture of a displacive phase transition corresponding to a zone-boundary mode.

rotation of the octahedra around an arbitrary axis. Only the strength of this instability and therefore the question whether a transition occurs or not, depends on the composition. For example the octahedron in $SrTiO_3$ below 105 K is rotated around a [100]-direction. The coupling of rotations around different directions leads to a variety of distinct low temperature symmetries.

Recently the rotation phase transitions in the perovskites have regained interest, since they seem to be closely connected in the manganates to the electronic properties in particular their colossal-magneto-resistivity. Also the high-T_c-cuprates show similar transitions.

13.2.4 Electron phonon interaction

The study of the electron phonon interaction represents an important field in lattice

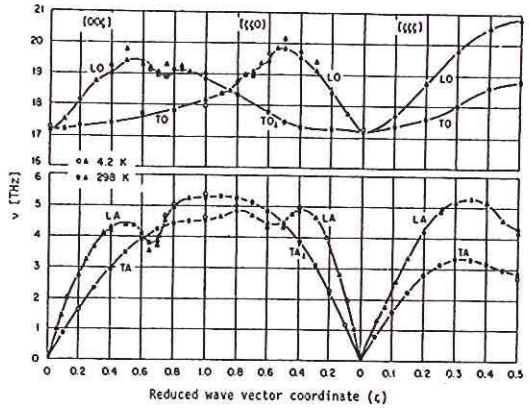

Figure 13 Phonon dispersion of TaC, the dips, for example at (0 0 0.7) andd at (0.6 0.6 0), indicate modes renormalized through the electron phonon coupling, from reference [2].

dynamics, which is analyzed almost exclusively by inelastic neutron scattering since the largest effects are expected in the Brillouin-zone.

The screening of the inter-atomic potentials through free charge carriers is determined by the topology of the Fermi-surface. In particular there are singularities in the electronic susceptibility when parts of the Fermi-surface are parallel and may, hence, be connected by a single nesting vector. The susceptibility at this vector will be essentially increased and may renormalize the phonon frequency of a mode just at this wave vector. In most cases this type of electron phonon coupling leads to a reduction of the phonon frequency, which shows up as a dip in the dispersion curve, called a Kohn-anomaly. In particular the conventional superconductors, for example TaC in Figure 13, exhibit such effects. The phonon dispersion of TaC shows pronounced dips, which are not observed in the phonon dispersion of normal metals. The study and interpretation of similar anomalies in the high-T_c-cuprates is subject of present research. However, in this case the analysis gets rather complicated due to the large number of atoms in these systems.

13.3 Magnetic excitations

13.3.1 Spin waves in a ferromagnet

Like the crystal structure, magnetic order may be disturbed at finite temperature with the perturbation propagating through the crystal. Analogous to the phonons, the

Figure 14 Schematic drawing of a simple ferromagnet : a) ground state, b) one spin being flipped c) in a spin-wave the spins precess on cones (from reference. [4]).

quantisized excitations are called magnons.

The ground state of a ferromagnet results from the interaction between spins of neighboring atoms, which favors a parallel alignment. The energy of a neighboring pair, $\underline{S}_i, \underline{S}_j$, depending on the relative orientation of the spins is described within the Heisenberg-model by $e = -J\underline{S}_i \cdot \underline{S}_j$, where J is the Heisenberg exchange constant. For a chain of coupled spins the energy of the magnetic interaction amounts to :

$$U = -2J \sum_{p=1}^{N} S_p \cdot S_{p+1} \qquad (13.20).$$

In the ground state all spins are parallel and $U_0 = -2NJS^2$, this corresponds to figure 14a. A possible excitation might consist in the flip of just one spin, like it is shown in figure 14b. This perturbation yields a finite increase in energy of $8JS^2$. However, the temperature dependence of several macroscopic properties like specific heat or magnetization does not correspond to an exponential law, as it has to be expected for a finite excitation energy. Spin waves (magnons) must have a much smaller energy than the single spin flip, like phonons may have lower energy than an ionic vacancy for instance.

The distortion of the magnetic order corresponds to a plane magnetic wave (with propagation vector $\underline{q}$ and frequency ω) and is drawn in Figure 14c. Spins are precessing around the direction of magnetic order (here z) with components :

$$S_p^x = u \cdot exp[i(pqa - \omega t)] \qquad (13.21),$$

$$S_p^y = v \cdot exp[i(pqa - \omega t)] \qquad (13.22),$$

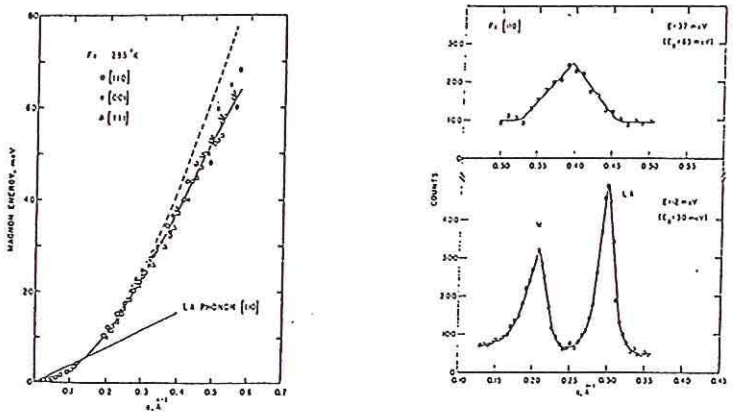

Figure 15 Magnon- and phonon dispersion curves in Fe at room temperature and two $\underline{Q}$-scans at constant energy , reference [5].

where a designates the lattice constant and b is numbering the spins.

Like in the case of the phonon dispersion one may deduce the magnon relation. In case of a simple chain one yields :

$$\hbar\omega(q) = 4JS(1 - cos(qa)) \qquad (13.23),$$

which may be approximated for small $\underline{q}$ by $\hbar\omega(q) = 2JS(qa)^2$, i.e. a quadratic relation. In contrast an acoustic phonon dispersion is always linear in that $\underline{q}$-range. Equation (13.23) may be extended to the three-dimensional case, in all cubic systems the relation $\hbar\omega(\underline{q}) = 2JS(qa)^2$ remains valid for small q.

Figure 15 shows the magnon dispersion measured in Fe, from which one may obtain the exchange constant J; for comparison the linear dispersion relation of the LA branch is added. One may note, that in the case of Fe the magnon frequencies extend to higher energies than those of the phonons. Due to the special form of the resolution ellipsoid in the triple axis spectrometer, it is favorable to perform scans at constant energy revealing both the phonon and the magnon, which exhibit approximately the same intensities, see right part of figure 15.

Since magnons are bosons, their occupation is given by Bose-statistics like that of the phonons, equation (13.11). Also for the differential cross section one may deduce a

formula similar to equation (13.10) valid for phonons :

$$(\frac{d^2\sigma}{d\Omega dE'})^{\pm} = (k'/k) \cdot S \cdot const. \cdot exp(-2W(\underline{Q}))F^2(Q)(1 + \frac{Q_z^2}{Q^2}) \cdot \sum_{\tau \underline{q}}(n(\omega_{\underline{q}}) + 1/2 \pm 1/2) \cdot \delta(\omega \mp \omega_j(\underline{q})) \cdot \delta(\underline{Q} \mp \underline{q} - \underline{\tau}) \qquad (13.24).$$

One recognizes the terms for momentum and energy conservation as well as the Bose-factor, which is increased by one in case of magnon creation. Furthermore the intensity is modulated by the same Debye-Waller-factor as the phonons. However, there is no term equivalent to the dynamic structure factor, the intensity is determined just by the spin S, the form factor $F(Q)$ and the direction of the momentum transfer.

Ferromagnetic materials are still of considerable interest due to their enormous technical potential in the context of data storage media. Attempts to optimize the technical properties lead to binary or ternary compounds, where the complexity of the magnetic order is considerably increased. In all cases the study of the magnon dispersion gives an almost unique insight to the microscopic coupling terms.

13.3.2 Antiferromagnetic Excitations

Antiferromagnetic order results from a negative exchange constant J in $U = -2J \sum_p \underline{S}_p \cdot \underline{S}_{p+1}$. The anti-parallel alignment of neighboring spins (↑↓↑↓↑↓↑↓↑), however, leads to a magnetic cell which is larger than the nuclear one. A classical example is given by the antiferromagnetic order observed in MnO at 120 K (Shull et al. 1951). Again one may find excitations in an antiferromagnet, which have lower energy than the simple flip of a single spin. Again each spin deviates from the ordered position by a component given by a plane wave. The calculation of the antiferromagnetic dispersion more closely resembles that of the phonon case :

$$\omega^2(\underline{q}) = (\frac{4JS}{\hbar})^2(1 - cos^2(\underline{q} \cdot a)) \quad \omega(\underline{q} = -\frac{4JS}{\hbar}|sin(\underline{q} \cdot a)| \qquad (13.25).$$

In contrast to the ferromagnetically ordered structure and in close similarity to the acoustic phonons, the frequency becomes linear in $\underline{q}$ for sufficiently small $\underline{q}$. Figure 16 shows the magnon dispersion observed in $RbMnF_3$.

In general both dispersion relations (13.23) and (13.25) are not gaped, the magnon energy vanishes for $\underline{q}$ approaching the zone center, like in case of an acoustic phonon. For

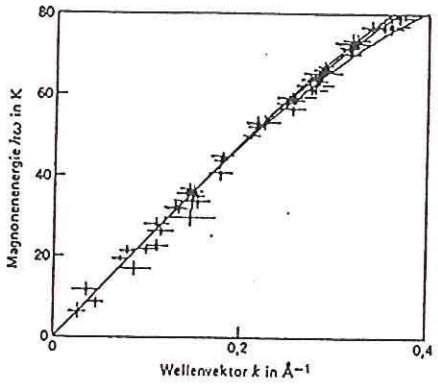

Figure 16 Magnon dispersion in $RbMnF_3$ (from reference [4]).

the acoustic phonon the zone-center limit corresponds to an infinitely small translation of the entire crystal which does not cost any energy, since no force constant is stretched. In case of the magnons the limit corresponds to a rotation of the ordered moment, which in the Heisenberg-model does not involve any energy shift (the interaction depends only on the relative orientation). However, in general this model is not sufficient, there are always interactions favoring the orientation of a certain spin direction. These interactions yield a finite gap in the excitation spectrum, however much smaller than the spin flip energy.

Antiferromagnetic materials have much less technical importance compared to ferromagnetism. However, antiferromagnetic correlations in metallic systems are often essential for the understanding of the electronic properties. For instance the physics of high-temperature cuprate superconductors seems to be determined by the closelyness of the antiferromagnetic order in the insulating parent compounds.

13.3.3 Crystal field excitations for rare earth ions

In the rare earth series one finds unpaired electrons in the 4f-shell, which are strongly localized and therefore screened from the surrounding ions. In consequence the total momentum J remains a good quantum number. For a free ion the the ground state would be $(2J+1)$ times degenerate. In a crystal this degeneracy is partially lifted due to the – weak – Coulomb-fields of the surrounding ionic charges. The transitions between the single levels may be observed by inelastic neutron scattering. (This is valid for the

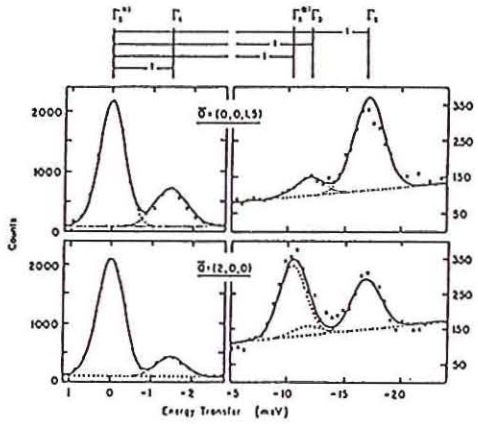

Figure 17 Crystal field scheme and measured energy scans in PrB_3 (T=1.5 K), from reference [6].

crystal field splittings in transition metals too, but due to the larger overlap of the d-orbitals the excited levels in these compounds are usually to high in energy.) If the rare earth ions are sufficiently diluted, interactions amongst them may be neglected. The level frequencies show then no dispersion and may be studied with time of flight methods on a polycristalline sample.

In figure 17 we show the observed spectrum compared to the crystal field scheme for PrB_3. The levels of Pr^{3+} with a J of 4 may split into not more than 9 levels. The local symmetry of the site occupied by the ion in the lattice determines which levels may exist with which multiplicity. However, the symmetry cannot predict the sequence of the levels, for this purpose one needs a quantitative information for the surrounding fields. The single levels are designated according to the irreducible representations of the local symmetry group by Γ_i. In close resemblance to equations (13.10) and (13.24) the differential cross section arises from the sum of transition probabilities $\Gamma_i \rightarrow \Gamma_j$; these matrix elements may be calculated within point charge models.

13.4 Conclusions

Inelastic neutron scattering is almost the unique technique to observe lattice vibrations and magnetic excitations throughout the whole Brillouin-zone. The main part of our knowledge on these topics has indeed been achieved by neutron studies.

Also the subjects of present interest, like high-T_c-superconductors, heavy fermions, quasi-crystals, C_{60} and compounds with colossal magneto-resistivity demand a detailed analysis of their lattice dynamics as well as of their magnetism. Frequently the materials of current interest exhibit a large complexity; therefore their study requires a continuous development of the experimental facilities as well as of the analysis methods.

References

1 N.W. Ashcroft and N.D. Mermin, Solid State Physics, Holt-Saunders International Editions, Philadelphia (1976).

2 H. Bilz and W. Kress, Phonon Dispersion Relations in Insulators, Springer Verlag, Berlin Heidelberg New-York (1979).

3 M.T. Dove, Introduction to Lattice Dynamics, Cambridge University Press, Cambridge (1993).

4 C. Kittel, Einführung in die Festkörperphysik, R. Oldenbourg Verlag, München (1983).

5 G. Shirane, V.J. Minkiewiecz and R. Nathans, Journal of Appl. Physics 39, 3833 (1968).

6 A. Furrer, Magnetic Neutron Scattering, World Scientific, Singapore (1995).

further suggestions

- P. Brüesch, Phonons: Theory and Experiments I, II, III, Springer Verlag, Berlin Heidelberg New-York (1982).

- Landolt-Börnstein Band 13, Metalle, Phononenzustände, Elektronenustände and Fermiflächen, Springer Verlag, Berlin Heidelberg New-York (1981).

- E. Balcar and S.W. Lovesey, Theory of Magnetic Neutron and Photon Scattering, Oxford Science Publications, Clarendon Press, Oxford (1989).

- G.L. Squires, Thermal Neutron Scattering, Cambridge University Press, Cambridge (1978).

14. Soft Matter: Structure

Dietmar Schwahn

14.1. Introduction

The methods of small angle scattering (SAS) with neutrons and X-rays are broadly used for investigations of mesoscopic structures in condensed materials. Whenever, atomic density or chemical composition inhomogeneities of mesoscopic length scale exist in a sample, this method can in principle be applied. SAS is a complimentary method to transmission electron microscopy (TEM); TEM makes visible the microstructure in real space while the SAS methods measure in reciprocal space and give quantitative data averaged over macroscopic large volumes.

In this lecture the theoretical basis of small angle scattering with neutrons (SANS) should be developed for the topic of the physics of polymers or, as it is said today, of "soft" matter und should be clarified with simple experimental examples. Since the end of 1939 the method of SAS was mainly developed by Guinier and Kratky and applied for questions in metal physics. In one of Guinier's first experiments scattering from copper precipitates in aluminum was correctly interpreted and the precipitates were identified as the origin of hardening in so-called Duralumin. This type of precipitation are so-called Guinier-Preston zones; they are still subject of active research. Today, neutron small angle scattering technique is mainly used for soft matter; the main reason might be the relatively simple possibilities of contrast variation using hydrogen and deuterium, which scatter neutrons quite differently but do not change the chemistry of the polymer.

14.2. Diffraction of Neutrons at 3-Dimensional Particles

In this part the basic equations of small angle scattering are discussed. For qualitatively understanding in Figure 14.1 two neutron pencils of rays are depicted in two spheres of different size. From this figure it becomes clear that diffraction from the larger sphere occurs into smaller angles and therefore smaller scattering vectors Q. The basic equation of small angle scattering is given in Eq.(14.1).

$$\frac{d\Sigma}{d\Omega}(\underline{Q}) = \frac{1}{V}\left|\sum_{i=1}^{N} b_i \, e^{i\underline{Q}\underline{r}_i}\right|^2 \qquad (14.1)$$

with the macroscopic scattering cross-section $d\Sigma/d\Omega$ in units of [cm^{-1}], the sample volume V, the number N of atoms in the sample and the coherent scattering length b_i of the atom i at the position $\underline{r}_i$. One can consider the resultant diffraction pattern as a coherent superposition of spherical waves, emanating from single atoms with an amplitude determined by the

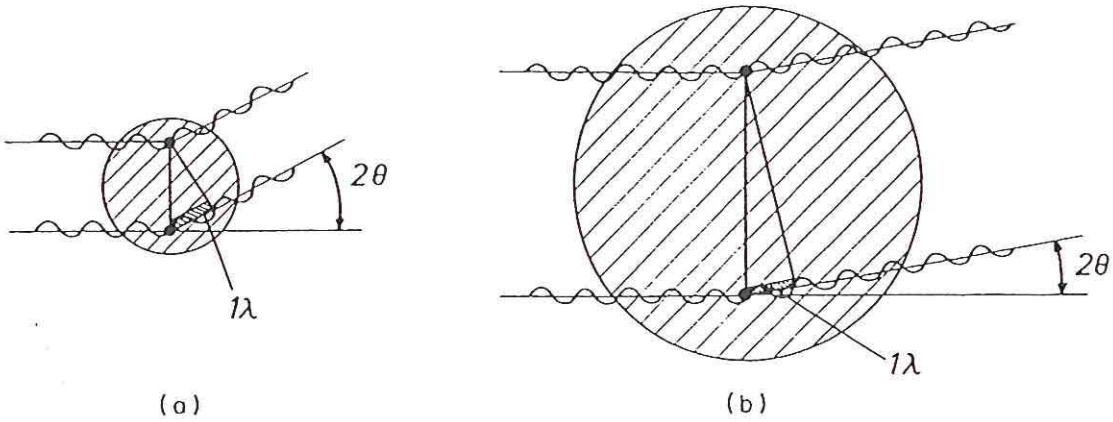

Fig. 14.1: *Two pencils of rays of the scattering probe in two particles of different size*

coherent scattering length. In the region of small angle scattering the relation $Q<2\pi/a$ is always fulfilled with the lattice constant a. Then the sum in Eq.(14.1) can be approximated according to

$$\sum_i b_i e^{i\underline{Q}\underline{r}_i} \quad \rightarrow \quad \int d_3\underline{r}\,\rho(\underline{r})\,e^{i\underline{Q}\underline{r}}$$

by an integral of the coherent scattering length density $\rho(\underline{r}) = b_i/\Omega$ (atomic volume Ω) and the phase factor. In this approximation one get the *basic relationship for SANS*:

$$\frac{d\Sigma}{d\Omega}(\underline{Q}) = \frac{1}{V}\left|\int_V d_3\underline{r}\,\rho(\underline{r})e^{i\underline{Q}\underline{r}}\right|^2 \qquad (14.2)$$

In a *first example* we consider an homogeneous sample with the constant coherent scattering length density $\rho(\underline{r})=\bar{\rho}$ and volume V. From Eq.(14.2) one gets

be approximated by a Delta function. Diffraction caused by the mean coherent scattering length density of a sample against vacuum occurs in the 1/cm Q region and is usually subtracted from the cross-section. So, one gets the expression for the cross-section according to:

$$\frac{d\Sigma}{d\Omega}(\underline{Q}) = \frac{1}{V}\left|\int_V d_3\underline{r}\left(\rho(\underline{r}) - \bar{\rho}\right) e^{i\underline{Q}\underline{r}}\right|^2 \qquad (14.3)$$

This form of the scattering cross-section f.i. is the starting equation for the analysis of micellar structures, which we will not discuss in this lecture.

14.3. Theory of Small Angle Scattering from linear Polymers

We now consider the main features of diffraction from linear polymer chains.

14.3.1 Diffraction from a linear homo polymer

As a model of a linear chain one considers a polygon of z vectors $\underline{r}_i$, whose directions are statistically independent. Such a polygon of a freely joint chain is depicted in Figure 14.2.

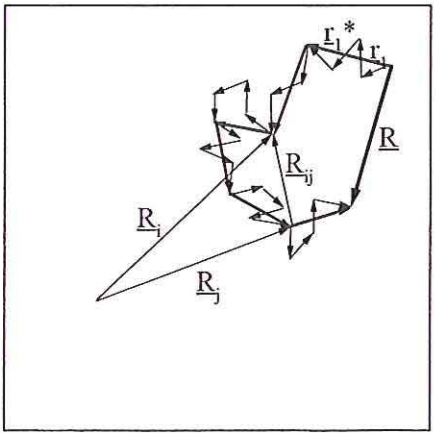

Figure 14.2: *Model of a freely joint linear chain*

Each vector $\underline{r}_i$ represents a monomer, which the chemical unit of a polymer of segment length b. Such a chain can also be represented by another polygon with larger vectors $\underline{r}_i^*$ representing several monomers. Both polygons correctly represent the global properties of the chain as the end-to-end vector $\underline{R}$, which is evaluated from the sum of all vectors according to

$$\underline{R} = \sum_i^z \underline{r}_i = \sum_i^{\tilde{z}} \underline{r}^*_i \,. \qquad (14.4)$$

The probability that a freely joint chain with z monomers takes a conformation with the end-to-end vector $\underline{R}$, is determined by the Gaussian distribution according to

$$W(R,z)=\left(\frac{3}{2\pi z b^2}\right)^{3/2}\exp\left(-\frac{3R^2}{2zb^2}\right). \qquad (14.5)$$

On the statistical average the mean end-to-end distance is zero and its mean square deviation is linear proportional to the number of monomers z.

$$<\underline{R}>=0 \qquad <R^2>=R_L^2=b^2 z$$

The radius of gyration is given as $R_g^2=R_L^2/6$. A linear "real" chain is different from a freely joint chain in so far as neighboring monomers are correlated. This effect is considered by the parameter c_z in $R_g^2=c_z b^2 z/6$ or expressed by the statistical segment length according to $\sigma=b\sqrt{c_z}$ and the radius of gyration $R_g^2=\sigma^2 z/6$ or respectively the mean square end-to-end distance $R_L^2=\sigma^2 z$ determined from scattering experiments. So, a statistical segment length of polystyrene is determined as σ_{PS} = 6.8Å. As in Figure 14.2 a realistic chains can therefore be represented by a polygon with vectors of segment length σ.

The form factor of a linear chain measured in a SANS experiment is determined from the sum of the phase factors from the monomers and an averaging over all possible chain configurations according to

$$P(Q)=\frac{1}{z^2}\sum_{ij}^{z}<\exp i\underline{Q}(\underline{R}_i-\underline{R}_j)> \qquad (14.6)$$

The meaning of the vectors $\underline{R}_i$ becomes clear from Figure 14.2. In a macroscopically large sample the number of polymers is sufficiently large, in order to describe the polymer conformation with the probability distribution of Eq.(14.5). The average value of the phase factors between the positions i and j within the chain is calculated according to

$$<\exp i\underline{Q}\underline{R}_{ij}>=\int d_3\underline{R}_{ij}\, w(R_{ij}|i-j|)\exp(i\underline{Q}\underline{R}_{ij})=W_{ij}(\underline{Q})$$

$$Wij(Q)=\exp(-|i-j|\frac{b^2}{6}Q^2)=W_{12}{}^{|i-j|}.$$

For the form factor one gets

$$P(Q) = \frac{1}{z^2}\sum_{ij}^{z} \exp(-|i-j|\frac{b^2}{6}Q^2) \qquad (14.7)$$

and after some calculation one gets the well known Debye formula

$$P_{Debye\,(Db)}(Q) = \frac{2}{x^2}[x-1+\exp(-x)] \qquad (14.8)$$

with $x = R_g^2Q^2$. In Figure14.3 the form factor according to Debye's formula has been plotted.

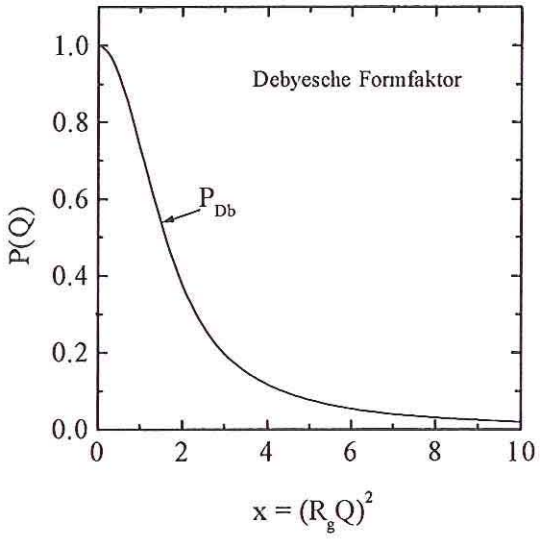

Figure 14.3: *Debye form factor of a linear chain*

The symbol beside Eq.(14.6) represents the form factor of a linear chain determined exclusively by *intramolecular* phase factors. Such symbols should help to make transparent the meaning of scattering laws of more complex polymers.

There are expressions for the form factor in Eq.(14.6) being approximately valid in the regions of small and large scattering vector if compared with the inverse size of the polymer; they have a much simpler form and can easily be used for the analysis of the scattering data. So in the region of small Q, e.g. $Q << 1/R_g$ one finds

$$P_{Db} \cong 1-\frac{1}{3}R_g^2Q^2 \qquad \text{or the Zimm approximation:} \quad P_{Db}^{-1} \cong 1+\frac{1}{3}R_g^2Q^2 \qquad (14.9)$$

as depicted in Figure 14.4a. From this plot one gets the radius of gyration and the scattering in forward direction according to Eq.(14.9), delivering the polymer molar volume and volume

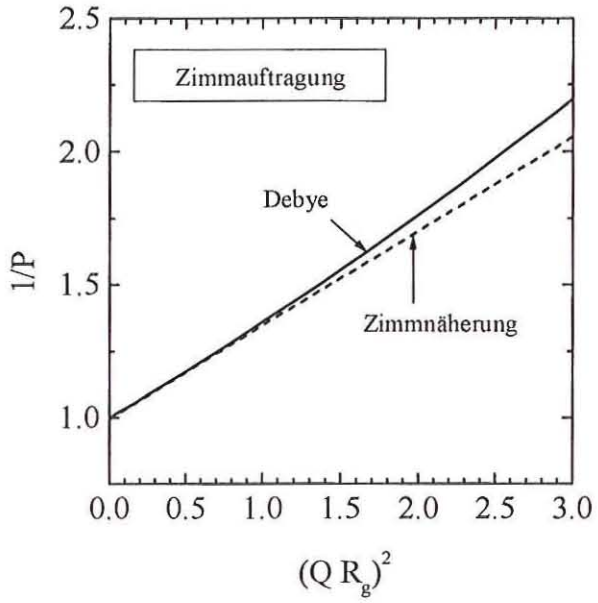

Figure14.4a: *So-called Zimm representation: Within the Zimm approximation the plot of 1/P versus* Q^2 *gives a straight for the Debye form factor. The slope of the straight line is proportional to* R_g.

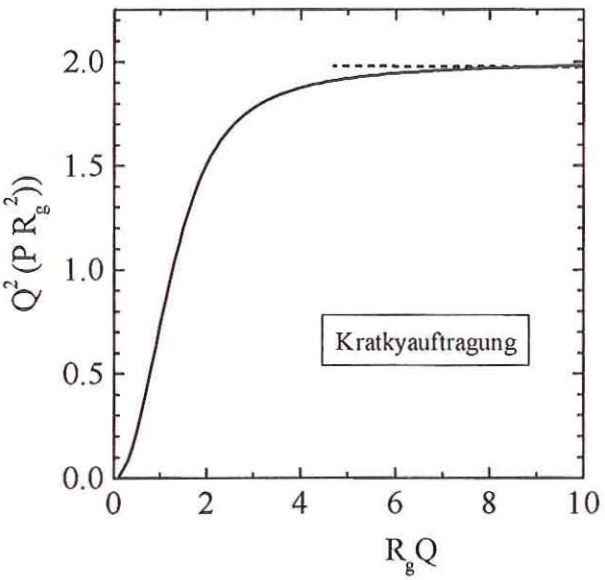

Figure 14.4b: *"Kratky plot" of Debye's form factor:At large Q the representation of* $Q^2 \cdot P(Q)$ *versus Q gives a constant value.*

fraction. In the region of large Q one gets the expression for $Q>>1/R_g$

$$P_{Db} \cong 2/(Q \cdot R_g)^2 \tag{14.10}$$

and according to the representation in Figure14.4b a power law or scaling law with a slope of –2. The scaling law in Eq.(14.10) shows a so-called fractal dimensionality D=2.

14.3.2. Polymer melts

We now consider a melt consisting of n linear polymers within a sample volume V_s. The polymers are of the same type and consist of z monomers with the coherent scattering length b. In the sample there are in total $N = n \cdot z$ monomers. The scattering cross section is derived from Eq. (14.1) and averaged over all conformations according to

$$\frac{d\Sigma}{d\Omega} = \frac{b^2}{Vs} < \left| \sum_i^N e^{i\underline{Q}\underline{r}_i} \right|^2 > = \frac{b^2}{Vs} \sum_{ij}^N < e^{i\underline{Q}\underline{r}_{ij}} > \tag{14.11}$$

Now, Eq.(14.11) can be splitted into an *intramolecular* and *intermolecular* interference terms P(Q) und W(Q) according to

$$\frac{d\Sigma}{d\Omega} = \frac{b^2}{Vs} \left[\underbrace{n \sum_{ij}^z < e^{i\underline{Q}\underline{r}_{ij}} >}_{z^2 P(Q)} + \underbrace{n(n-1)}_{\cong n^2} \underbrace{\sum_{ij}^z < e^{i\underline{Q}\underline{r}_{ij}} >}_{z^2 W(Q)} \right] \tag{14.12}$$

and

$$\frac{d\Sigma}{d\Omega}(Q) = V \frac{\rho^2}{N_A} [P(Q) + nW(Q)] \tag{14.13}$$

with the coherent scattering length density $\rho = b/\Omega$, molar volume V, the Avogadro number N_A and the molar volume Ω of the monomers. The corresponding symbol for inter molecular interference is the following

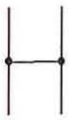

Equations (14.12) and (14.13) are determined by intra- und intermolecular interferences as also made visible by the accompanying symbol.

14.3.3. Babinet Principal

Incompressible melts show no thermal density fluctuations and therefore no diffraction can occur in such a single type polymer melt. The scattering cross section must be zero and following Eq. (14.13) one therefore gets the following relationship

$$P(Q) = -nW(Q) \tag{14.14}$$

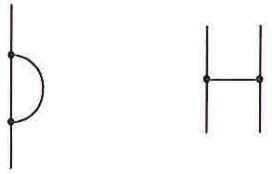

representing the Babinet principal.

14.3.4. Melt of deuterated and protonated polymers with chemically identical monomers of same segment length.

We now discuss a blend of chemically identical polymers whose components are either protonated or deuterated. For further theoretical consideration we introduce an occupation operator σ_i with the following meaning

$$\sigma_i = \begin{cases} 1 & b_i = b_D \\ 0 & b_i = b_H \end{cases}. \tag{14.15}$$

The operator is $\sigma_i = 1$ and $\sigma_i = 0$, if the monomer at the position i is deuterated and protonated, respectively. The coherent scattering length of a monomer at the position i is then described as

$$b_i = \sigma_i (b_D - b_H) + b_H = \sigma_i \cdot \Delta b + b_H \tag{14.16}$$

This expression inserted into Eq.(14.1) gives

$$\frac{d\Sigma}{d\Omega}(Q) = \frac{1}{V_s} < \Delta b \sum_{i=1}^{N} \sigma_i e^{i\underline{Q}\underline{r}_i} + b_H \underbrace{\sum_{i=1}^{N} e^{i\underline{Q}\underline{r}_i}}_{\cong \delta(Q)} \Big|^2 > \tag{14.17}$$

and finally

$$\frac{d\Sigma}{d\Omega}(Q) = \frac{\Delta b^2}{V_s} \underbrace{\sum_{ij}^{N} < \sigma_i \sigma_j e^{i\underline{Q} r_{ij}} >}_{S_{DD}} \tag{14.18}$$

with the partial structure factor S_{DD}. The symbol for S_{DD} has the following form

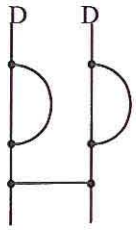

and describes the intra- and intermolecular interferences between the deuterated monomers. Quite generally, the scattering cross section can be described as a sum of the *partial structure factors* according to

$$\frac{d\Sigma}{d\Omega}(Q) = \frac{1}{V_S}\left[b_D^2 S_{DD} + 2b_D b_H S_{DH} + b_H^2 S_{HH}\right] \tag{14.19}$$

with the corresponding symbols

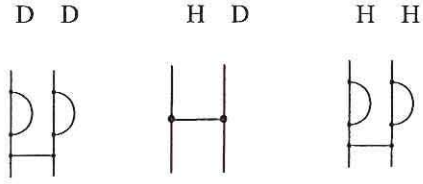

In case of an *incompressible melt* the partial structure factors are related according to

$$S_{DD} = S_{HH} = -S_{DH} \tag{14.20}$$

and thus one gets in correspondence with Eq.(14.18)

$$\frac{d\Sigma}{d\Omega}(Q) = \frac{\Delta b^2}{Vs} S_{DD}\,. \tag{14.21}$$

The definition of the occupation operators in Eq.(14.15) implicitly contains the condition of incompressibility, as no free volume is included. The partial structure factor of the deuterated monomers is given

$$S_{DD} = \Phi n z^2 P(Q) + \Phi^2 n^2 z^2 W(Q) \tag{14.22}$$

with volume fraction Φ of the polymer component D. Because of the Babinet principal one has $z\,P(Q) = -\,nW$ and one gets

$$\frac{d\Sigma}{d\Omega}(Q)=\underbrace{\frac{\Delta\rho^2}{N_A}}_{K}\underbrace{\Phi(1-\Phi)V\,P(Q)}_{S(Q)} \tag{14.23}$$

with the structure factor

$$S(Q)=\Phi(1-\Phi)\,V\,P_{Db}(Q). \tag{14.24}$$

So, the variation of contrast of chemically identical polymers enables the experimental determination of the form factor of a single chain in a melt of chemically identical polymers. In Figure 14.5 an *experimental example* is shown for a polystyrene melt.

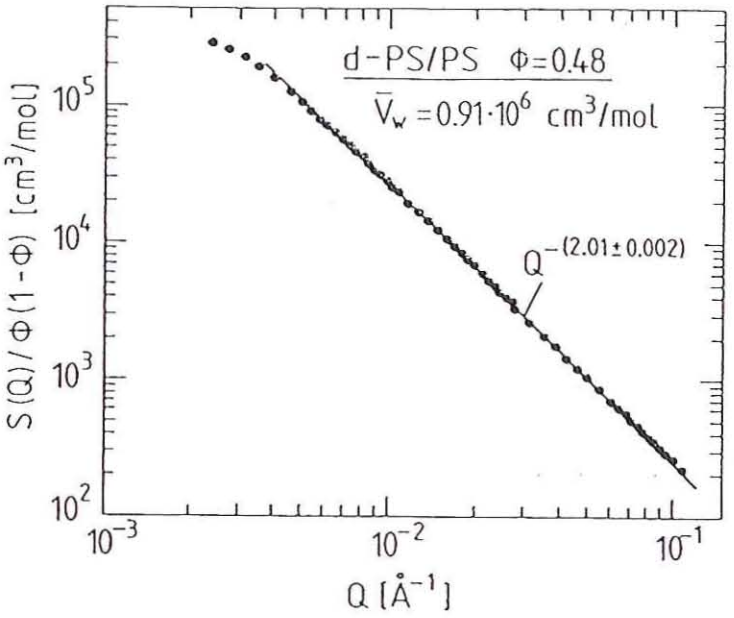

Figure14.5: *Structure factor of a 50% mixture of polystyrene in double logarithmic representation. The power law behavior at large is described by statistical chain*

14.4. H-D Polymer blend in solution

Next we derive the scattering law of an isotopic polymer blend in solution. Again we introduce occupation operators with the meaning

$$\sigma_D(\underline{r}_i)=\begin{cases}1 & b_i = b_D \\ 0 & b_i = b_H \text{ oder } b_O\end{cases} \tag{14.25}$$

$$\sigma_H(\underline{r}_i)=\begin{cases}1 & b_i = b_H \\ 0 & b_i = b_D \text{ oder } b_0\end{cases}$$

and which lead to the scattering cross section

$$\frac{d\Sigma}{d\Omega}(Q)=\frac{1}{V_s}<\left|\sum_{i=1}^{N}\left(b_D\sigma_D(\underline{r}_i)+b_H\sigma_H(\underline{r}_i)+b_0(1-\sigma_D(\underline{r}_i)-\sigma_H(\underline{r}_i))\right)e^{i\underline{Q}\underline{r}_i}\right|^2>$$

which after some calculation leads to the form

$$\frac{d\Sigma}{d\Omega}(Q)=\frac{1}{V_s}<\sum_{i=1}^{N}\left[(b_D-b_0)\sigma_D(\underline{r}_i)+(b_H-b_0)\sigma_H(\underline{r}_i)+\underbrace{b_0}_{\cong 0}\right]e^{i\underline{Q}\underline{r}_i}\Big|^2> \qquad (14.26)$$

and, finally, to a sum of partial structure factors weighted with corresponding contrast factors according to.

$$\frac{d\Sigma}{d\Omega}(Q)=\frac{1}{V_s}\left[\Delta b_D^2 S_{DD}+2\Delta b_D\Delta b_H S_{DH}+\Delta b_H^2 S_{HH}\right] \qquad (14.27)$$

The partial structure factors are given as:

D(H) D(H)

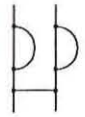

$$S_{DD}=\Phi n z^2 P(Q)+\Phi^2 n^2 z^2 W(Q) \qquad (14.28)$$

$$S_{HH}=(1-\Phi)n z^2 P(Q)+\Phi^2 n^2 z^2 W(Q) \qquad (14.29)$$

$$S_{DH}=\Phi(1-\Phi)n^2 z^2\, W(Q) \qquad (14.30)$$

H D

and finally one delivers the following scattering law

$$\frac{d\Sigma}{d\Omega}(Q)=\frac{1}{V_s}\left\{(b_D-b_H)^2\Phi(1-\Phi)n z^2 P(Q)+\left(\bar{b}_{Poly}-b_0\right)^2\left[n z^2 P(Q)+n^2 z^2 W(Q)\right]\right\} \qquad (14.31)$$

For this systems the Babinet principal is not valid as it contains polymers and solvent molecules. If one matches the scattering length of the solvents and the averaged one of the polymers ($\bar{b}_{Poly}=\Phi b_D+(1-\Phi)b_H$) according to $\bar{b}_{Poly}=b_0$ („zero" contrast), the second term in Eq.(14.31) does not contribute to the scattering and, consequently, one again determines the form factor of a single chain according to

$$\frac{d\Sigma}{d\Omega}(Q)=c\cdot\Phi(1-\Phi)V P(Q)K \qquad (14.32)$$

with c the volume fraction of polymers in solution and the contrast factor K. This again is a demonstration of the possibilities of contrast variation with neutrons allowing to measure the form factor P(Q) of a polymer chain in solution.

14.5 Scattering from a Block Copolymer

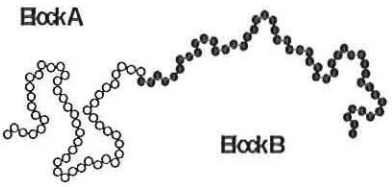

Figure 14.6: *Presentation of a Diblock Copolymer*

We now derive the scattering law of a linear polymer, consisting of the two blocks „A" and „B" of different polymers and which are symmetric with respect to the number of the monomers $z = 2z_D = 2z_H$. The scattering cross section is given as

$$\frac{d\Sigma}{d\Omega} = \frac{1}{V_s}\Delta b^2 S_{DD} \tag{14.33}$$

with the relationship $S_{DD} = S_{HH} = -S_{DH}$ because of assuming an incompressible melt. The various partial structure factors are given as:

$$S_{DD} = n\left(\frac{z}{2}\right)^2 P_{DD} + n^2\left(\frac{z}{2}\right)^2 W_{DD} \tag{14.34}$$

$$S_{DH} = n\left(\frac{z}{2}\right)^2 P_{DH} + n^2\left(\frac{z}{2}\right)^2 W_{DH} \tag{14.35}$$

$$S_{HH} = n\left(\frac{z}{2}\right)^2 P_{HH} + n^2\left(\frac{z}{2}\right)^2 W_{HH} \tag{14.36}$$

The symbolic representation of the structure factor of diblock copolymers has the form

For the intramolecular and intermolecular terms of interference one has $P_{DD} = P_{HH}$ and $W_T = W_{DD} = W_{HH} = W_{DH}$. Because of $z^2 P_T = 2(z/2)^2 P_{DD} + 2(z/2)^2 P_{DH}$ the form factor of the total chain is given as

$$2P_T = P_{DD} + P_{DH} \tag{14.37}$$

which with $nW_T = -P_T$ (Babinet principal) finally leads to the partial structure factor

$$S_{DD} = n\left(\frac{z}{2}\right)^2 [P_{DD} - P_T] \tag{14.38}$$

and the scattering cross section

$$\frac{d\Sigma}{d\Omega}(Q) = K\frac{V}{4}[P_{DD}(Q) - P_T(Q)], \tag{14.39}$$

described as the difference of the intramolecular form factor of a single block ($P_{DD}; P_{DH}$) and the total chain (P_T). These form factors of a symmetrical diblock copolymer are plotted in Figure14.7. An interference peak is observed whose position is according to $Q^* \cdot R_g = 1.9$ related to the radius of gyration and Q* therefore has to be observed at $1.9 \cdot 10^{-2}$ Å^{-1}. The observation of an interference peak in diblock copolymers becomes plausible from the consideration, that composition fluctuations of the blocks A and B can only occur on the length scale of the polymer. As an experimental example we show the structure factor of a melt.

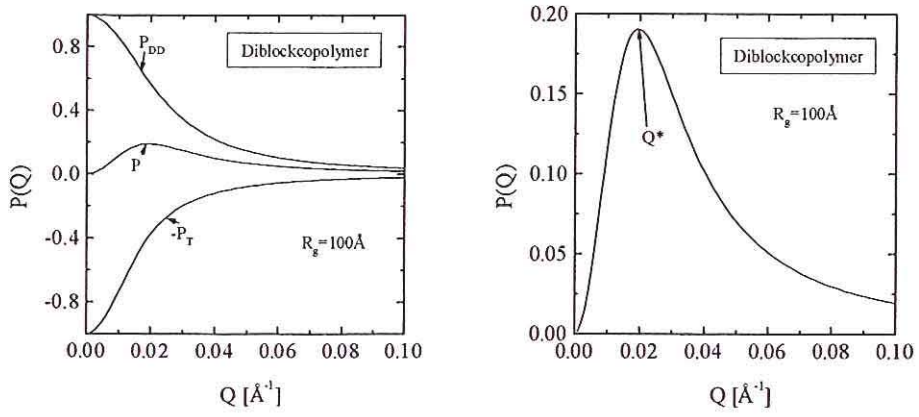

Figure 14.7: *Form factor of a symmetrical diblock copolymer*

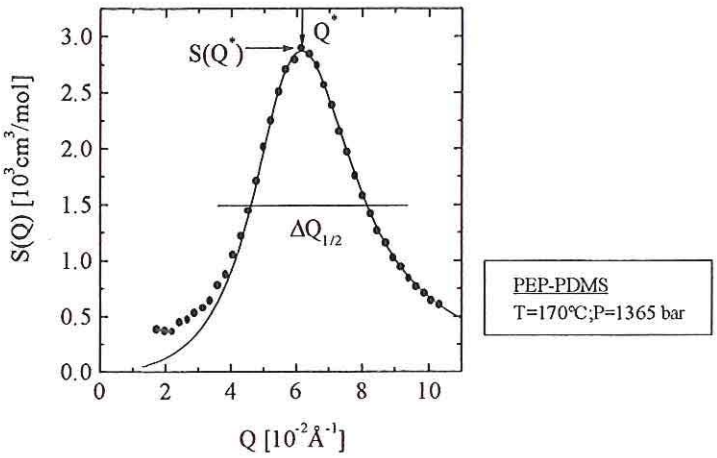

Figure 14.8: *Structur factor of a PEP-PDMS diblock copolymer*

14.6. Binary Melt with different Polymers

The structure factor of an ideal binary melt is evaluated within the "random phase" approximation (RPA) according to

$$S_0^{-1}(Q) = \frac{1}{\Phi V_D P_{Db}^D(Q)} + \frac{1}{(1-\Phi)V_H P_{Db}^H(Q)} \tag{14.40}$$

The inverse structure factor is obtained from the sum of the inverse form factors of both „ideal" chains weighted with their molar volumes and volume fractions. Eq. (14.40) corresponds to an ideal solution of two components with mixing energy being zero and therefore no phase transition phenomena. Those ideal solution are usually not found in reality; as demonstrated in Figure14.9 even isotopic mixtures of chemically identical polymers show phase decomposition at low temperatures because of a small but finite mixing interaction energy. For polymer blends such interaction is described by the Flory-Huggins (F-H) parameter

$$\Gamma = \frac{\Gamma_h}{T} - \Gamma_\sigma . \tag{14.41}$$

The FH-parameter has the meaning of a free enthalpy of mixing with the enthalpic and entropic terms Γ_h and Γ_σ, respectively. In the RPA approximation the interaction parameter added according to

$$S^{-1}(Q) = S_0^{-1}(Q) - 2\Gamma \tag{14.42}$$

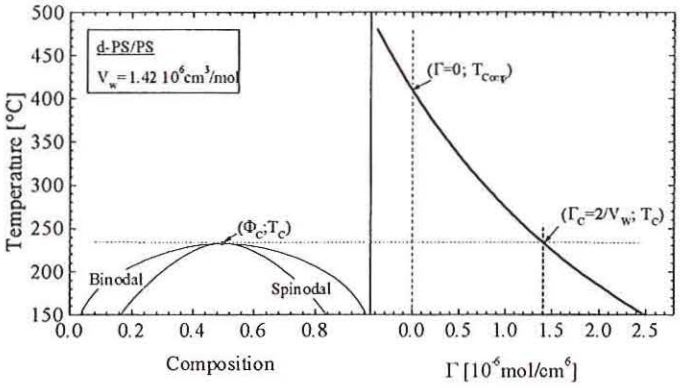

Figure14.9: *Phase diagram and Flory-Huggins interaction parameter of an isotopic d-PS/PS blend*

the structure factor of an ideal mixture. For small Q Eq. (14.42) can be approximated in *Zimm approximation* according to

$$S^{-1}(Q) = S^{-1}(0) + AQ^2 \tag{14.43}$$

with the inverse structure factor $S^{-1}(0) = 2[\Gamma_s - \Gamma]$ at Q=0 and the FH-parameter at the spinodal temperature, $2\Gamma_s = \frac{1}{\Phi V_D} + \frac{1}{(1-\Phi)V_H}$, being inversely proportional to both chain molar volumes and being related to the translatorial entropy of mixing. In experimental reality one tries to measure at sufficiently small Q in order to be able to use Eq.(14.43) for analysis of the scattering data. As shown in Figure 14.9, the spinodal temperature represents the phase boundary between the metastable und unstable two-phase regions and the unstable region touches the stable one-phase region at the critical point. In the single homogeneous phase at high temperatures the FH-parameter is smaller than $\Gamma_c = 2/V$ in accordance with the Gibbs condition of stability of a positive S(0); S(0) represents a susceptibility which according to the fluctuation-dissipation theorem is related with the free enthalpy of mixing ΔG according to

$$S^{-1}(0) = \frac{\partial^2(\Delta G/RT)}{\partial \Phi^2}. \tag{14.44}$$

In case of $\Gamma > \Gamma_c$ the system decomposes with the mechanism of spinodal decomposition in two macroscopically large phases which one polymer component dominating. The free enthalpy of mixing of polymer blends was originally formulated within the mean field approximation by Flory and Huggins, it gives the same result as the random-phase

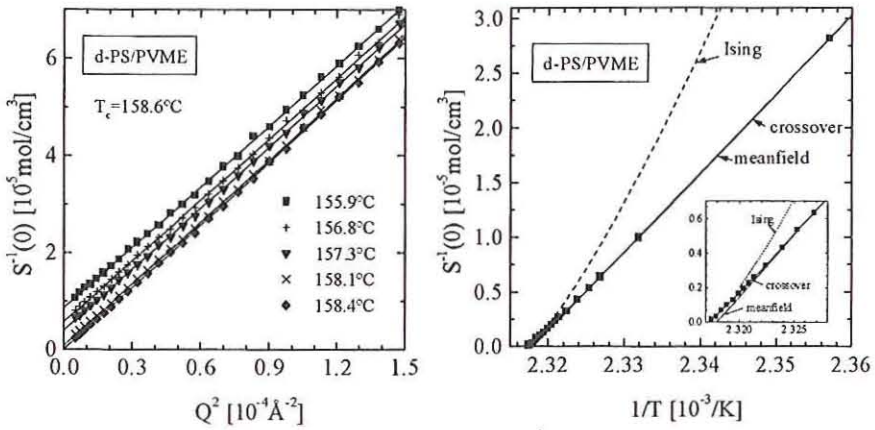

Figure 14.10a: *Structure factor S(Q) in Zimm representation of a critical mixture dPS/PVME polymer blend at various temperatures.*

Figure14.10b: $S^{-1}(0)$ *plotted versus 1/T. The solid lines describe the critical behavior of the thermal composition fluctuations. Near the critical temperature one observes deviations from the mean field behavior. The spinodal and critical temperatures are determined from the extrapolation* $S^{-1}(0)=0$; $S^{-1}(0)=0$ *means an infinite susceptibily.*

approximation being a mean field approximation as well. According to RPA the slope A in Eq.(14.43) is related to the square of the radius of gyration of both chains assumed as being undisturbed.

Next we discuss an experimental example of a binary blend of a deuterated polystyrene (d-PS) und polyvinylmethylether (PVME). This mixture shows the specialty being miscible at low temperatures and decomposes in two macroscopic phases at high temperatures. The reasons are a preferred interaction between PS und PVME ($\Gamma_h < 0$) and an increase of the total free volume during decomposition ($\Gamma_\sigma < 0$). The free volume is related with the entropy Γ_σ and in case of $\Gamma_\sigma > \Gamma_C$ becomes dominant and the driving force for the process of decomposition at high temperatures. The SANS experiments were exclusively performed within the homogeneous one-phase region. In Figure 14.10 S(Q) is plotted in Zimm representation (a) and 1/S(0) versus 1/T in (b). One clearly realizes the increasing scattering at higher temperatures (the inverse S(Q) is of course decreasing), from which one can conclude to stronger thermal composition fluctuations. The inverse susceptibility is linearly proportional to 1/T, it is zero at the spinodal respectively at the critical point, and its slope directly gives Γ_h. The observed linear shape of $S^{-1}(0)$ with 1/T is representative for the

scaling behavior of the susceptibility within the universality class of mean field approximation (the corresponding critical exponent is $\gamma = 1$).

This experiment follows the mean field approximation quite well and can be sufficiently well interpreted with the theoretical approach presented here. The reason is the relatively large molar volume of several $10^5 \, cm^3 / mol$, which allows observations of deviation from the mean field approximation only very near (about 1K) the critical temperature, when the thermal composition fluctuations are sufficiently large.

References

Text books:

[1] A. Guinier und G. Fournet, *Small angle scattering of X-rays*. Wiley, New York (1956)

[2] A. Guinier, Chapter 10 in *X-ray diffraction*. W.H. Freeman & Company, San Francisco (1963)

[3] O. Glatter and O. Kratky (ed.), *Small angle scattering*. Academic Press (1982)

[4] J.S. Higgins and H.C. Benoit, *Polymers and neutron scattering*. Clarendon Press, Oxford (1994)

Review articles:

[5] P.G. de Gennes, *Scaling concepts in polymer physics*. Cornell University Press, New York (1979)

[6] K. Binder, Advances in Polymer Science **112**, 181 (1994)

[7] F.S. Bates, G.H. Fredrickson, Ann. Rev. Phys. Chem. **41**, 525 (1990)

[8] G. Wignall: *Neutron Scattering* in Encyclopedia of Polymer Sciences and Engineering **10** (1987) 112

[9] Dietmar Schwahn and Kell Mortensen: Thermal *Composition Fluctuations in Polymer Blends Studied with Small Angle Neutron Scattering*, Chapter 8 in Scattering in Polymeric and Colloidal Systems, eds. W. Brown and K. Mortensen, Gordon and Breach Publishers (2000)

Articles:

[10] D. Schwahn, K. Mortensen, H. Yee-Madeira, Phys. Rev. Lett. **58**, 1544 (1987)

[11] D. Schwahn, K. Mortensen, T. Springer, H. Yee-Madeira, R. Thomas J. Chem. Phys. **87**, 6078 (1987)

[12] D. Schwahn, S. Janßen, T. Springer, J. Chem. Phys. **97**, 8775 (1992)

[13] D. Schwahn, G. Meier, K. Mortensen and S. Janßen, J. Phys.II (France) **4**, 837 (1994)

[14] D. Schwahn, H. Frielinghaus, K. Mortensen, and K. Almdal, Phys. Rev. Lett. **77**, 3153 (1996);

[15] H. Frielinghaus, D. Schwahn, K. Mortensen, K. Almdal, T. Springer, Macromolecules **29**, 3263 (1996)

[16] L. Leibler, Macromolecules **13**, 1602 (1980)

15. Polymer Dynamics

D. Richter

15.1 Introduction

In our every day life plastics or polymers play a very important role. Polymeric materials are used, because they are durable, cheaply to produce, easily to process and because they exhibit very versatile and favorable mechanical properties, e.g. depending on temperature or time the same polymer may be viscose, rubber elastic, very tough with high impact strength or even brittle. In the simplest case polymers are long linear chain molecules, build from one repeating unit, the monomer; such polymers are called linear homopolymers.

Since in general rotational isomers may be easily formed at each bond of the chain backbone, long chain polymers possess a very large number of internal degrees of freedom which contribute importantly to the entropic part of the molecules free energy. At length scales somewhat larger than the size of the monomer, the detailed chemical structure of the chain building blocks ceases to be of importance and very general properties determined by the statistical mechanics of the chains prevail, e.g. the conformational entropy follows from the number of possible arrangements of a chain sequence in space. According to the central limit theorem the most probable arrangement is that of a *Gaussian* coil, e.g. the polymer chain performs a random walk in space. If pieces of the chain are now stretched an entropic force arises and acts on these stretched segments endeavouring to restore them to the most probable contorted state. Such forces are the basis of rubber elasticity.

This lecture aims to identify general principles of chain motion on a molecular scale which underlie the macroscopic mechanical properties, and presents concepts and experimental results on these motional mechanisms in space and time. Thereby, we restrict ourselves to melts of homopolymers.

Neutron scattering with its space time sensitivity on a molecular and atomic scale unravels the details of the molecular motions in question. Commencing at the scale of the single bond, where movements take place at a pace as in normal liquids, quasielastic neutron scattering (QENS) provides insight into local relaxation processes. At longer length scales first the entropy driven Rouse motion and at even larger distances the effect of entanglement

constraints due to the mutual interpenetration of chains comes into the observation range. The most powerful technique suitable for these investigations, the neutron spin echo spectroscopy (NSE) operates in the time domain and uncovers a time range from about *2ps* to *200ns* and accesses momentum transfers between 0.01Å^{-1} and 3Å^{-1}. The second important high resolution technique is neutron backscattering providing an energy resolution of about $1\mu eV$ and covering a Q-range $0.1 \leq Q \leq 2\text{Å}^{-1}$.

This lecture naturally is not able to review exhaustively the contribution of high resolution neutron scattering to the field of polymer melt dynamics, but rather wants in an exemplary way to display important contributions by example. First in Chapter 2 we will discuss neutron results on the local chain dynamics, addressing self and pair correlation functions. These experiments are of importance in connection with the glass transition in polymer melts. Then in Chapter 3 we deal with the entropy driven dynamics, the Rouse motion. Chapter 4 discusses the large scale chain motion eluding to the reptation process and Chapter 5 finally concludes this lecture.

15.2 Local dynamics

The classical relaxation processes in polymers, the α- and β-relaxations, have been studied since more than 50 years by spectroscopic techniques, like dielectric spectroscopy, mechanical spectroscopy and NMR. Fig.15.1 displays a typical outcome of such experiments for the case of polybutadiene (PB) $[\text{-C}_4\ \text{H}_6\text{-}]_n$. The dominant relaxation process, the α-relaxation, is related to the macroscopic flow and freezes at a finite temperature, the glass transition temperature T_g. Aside from this process a secondary relaxation, β_{slow}, departs from the α-relaxation at a temperature about 20% above T_g. This relaxation displays an Arrhenius behaviour and passes unchanged through the glass transition.

As already mentioned, the α-relaxation is behind the viscous flow of polymers. Its relaxation function may be phenomenologically described by a stretched exponential

$$\phi_\alpha(t) = \exp\left\{-\left(\frac{t}{\tau_{KWW}}\right)^{\beta}\right\} \tag{15.1}$$

τ_{KWW} is the Kohlrausch-William-Watts relaxation time and $\beta < 1$ the stretching exponent. τ_{KWW} in good approximation follows a Vogel-Fulcher temperature dependence.

$$\tau_{KWW}(T) \approx \exp\left\{\frac{A}{T - T_0}\right\} \tag{15.2}$$

The temperature offset in the denominator of the exponent leads to a divergence of τ_{KWW} at T_0, a temperature below T_g which, however, may never be reached in equilibrium.

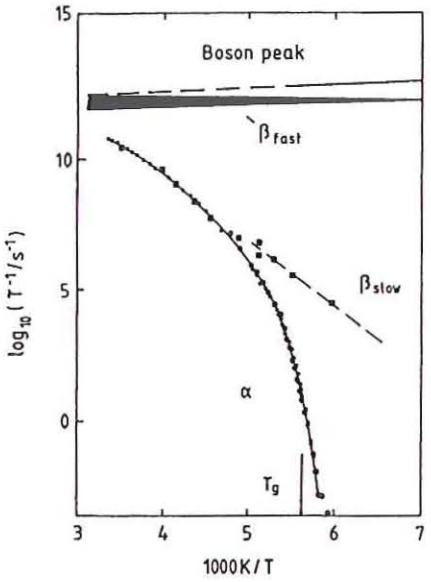

Figure 15.1: Relaxation landscape of PB. α and β_{slow} correspond to the classical relaxation processes and are treated here.

The dielectric β-relaxation is considered to be a result of a partial reorientation of the molecular dipoles in the substance. It is interpreted as a local activated process, where the dipole hops between two positions separated by an activation energy E. The relaxation time follows an Arrhenius behaviour

$$\tau_\beta(E) = \tau_0^\beta \exp\left[\frac{E}{k_B T}\right] \tag{15.3}$$

due to the disorder in the material the activation energies E are distributed around an average value E_0. For the distribution function in general a *Gaussian* is assumed.

$$g(E) \approx \exp\left\{-\left(\frac{E-E_0}{\sigma}\right)^2\right\} \tag{15.4}$$

Empirically it is found that the width $\sigma(T)$ decreases with increasing temperature. Though such processes have been investigated well by spectroscopic techniques, their molecular origin is still unclear. Here QENS with its ability to provide space time resolution on the proper scales contributes to a further exploration of the molecular mechanisms behind these relaxations.

15.2.1 Dynamic structure factors

We commence with the derivation of the dynamic structure factor for the β-process which we consider as a hopping process between two adjacent sites. For such a process the self correlation function has been derived in the lecture on quasielastic scattering, it is given by a sum of two contributions.

$$S_s(Q,t) = \frac{1}{2}\underbrace{\left[1+\frac{\sin(Qd)}{Qd}\right]}_{S^{el}} + \frac{1}{2}\underbrace{\left[1-\frac{\sin(Qd)}{Qd}\right]}_{S^{inel}} \exp\left(-\frac{2t}{\tau(E)}\right) \tag{15.5}$$

Here d is the distance between the two sites and $\tau(E)$ is the jump time corresponding to an activation energy E. The complete scattering function is obtained in averaging Eq.[15.5] with the barrier distribution function $g(E)$ obtained e.g. by dielectric spectroscopy. The Q-dependence of the two contributions to Eq.[15.5] is displayed in Fig.15.2 as a function of Q (d = 1.5Å). From the oscillation of both contributions with Q the jump distance may be obtained. The associated time scale may be found from the time decay of the inelastic part.

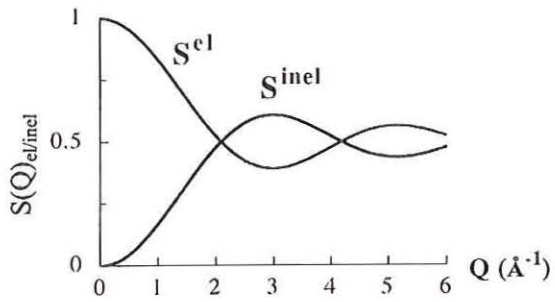

Figure 15.2: Elastic and inelastic contribution to the incoherent scattering function for jump motion between two site. The Figure assumes a jump distance of 1.5Å.

The associated pair correlation function is more difficult to obtain, since now we have to deal with a change of configurations of atoms rather than with single atom jumps. The conceptual difference between the pair and the self correlation function for jump processes may be visualized most easily considering rotational jumps. Let us regard e.g. the 120° rotational jumps of a methyl group around its symmetry axis. An incoherent study would reveal the atomic jumps of the associated hydrogens. The pair correlation function reflects the change of atomic configurations before and after the jump. Since a 120° jump does not change the configuration, a coherent scattering experiment would not reveal anything.

Back to the pair correlation function for the β-process, where we will introduce a simple approximation. We know that for $t = 0$ the pair correlation function is reflected by the static structure factor $S(Q)$. Therefore for $t = 0$ the corresponding pair correlation function for the β-process must reveal $S(Q)$. We now assume that the inelastic scattering is related to uncorrelated jumps of the different atoms. Then all interferences for the inelastic process are destructive and the inelastic form factor should be identical to that of the self correlation function. For the normalized dynamic structure factor for the β-process we arrive at

$$\frac{S(Q,t)_\beta}{S(Q)} = \left\langle \frac{S(Q) - S^{inel}(Q)}{S(Q)} + \frac{S^{inel}(Q)}{S(Q)} e^{-2i/\tau(E)} \right\rangle_{g(E)} \qquad (15.6)$$

This incoherent approximation does not reveal e.g. symmetry related cancellations, but displays a major feature of the corresponding dynamic structure factor, namely the relative suppression of the inelastic contributions from local jump processes at the maximum of the structure factor. Fig.15.3 displays the situation for polybutadiene. There a β-process corresponding to a jump length of d = 1.5Å has been found. The corresponding inelastic dynamic structure factor is strongly reduced at the position of the first peak, while it contributes strongly at higher Q. Fig.15.3 suggests a Q selectivity for the different relaxation processes: at the structure factor maximum local jump processes should not contribute and the relaxation due to flow should dominate. On the other hand at larger Q, in particular in the minimum of the structure factor, the secondary relaxation should reveal itself.

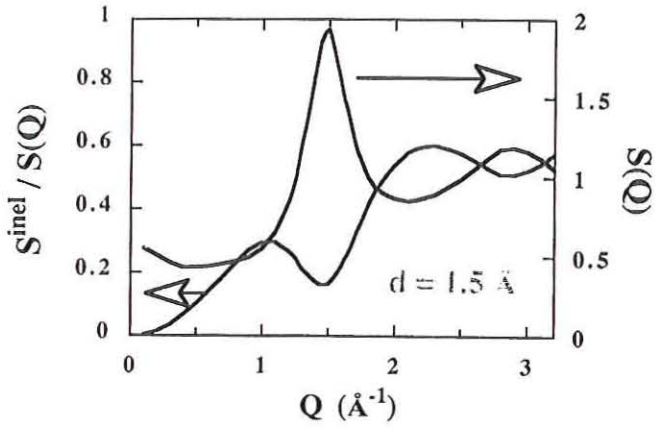

Figure 15.3: Static structure factor $S(Q)$ and normalized inelastic contribution $\frac{S_{inel}}{S(Q)}$ to $S(Q,\omega)/S(Q)$ for PB.

We now assume that the α- and the β-relaxation are statistically independent. Then, in real space the joint correlation function is given by a convolution of the corresponding functions for both separated processes. In Q-space this convolution becomes a product and we may write the total scattering function as a product of the structure factor due to the α- and β-processes.

$$\frac{S(Q,t)}{S(Q)} = S^{\alpha}(Q,t)S_{\beta}(Q,t)/S(Q) \tag{15.7}$$

The approximation behind Eq.[15.7] is called Vinyard approximation and approximates the proper pair correlation function by its self counter part. The self correlation function for a diffusive process relates directly to the mean square displacement.

$$S^{self}(Q,t) = \exp\left\{-\frac{Q^2}{6}\left\langle r^2(t)\right\rangle\right\} \tag{15.8}$$

where $\left\langle r^2(t)\right\rangle$ is the mean square displacement of the flowing particle. According to Eq.[15.1] this should be described by a stretched exponential with the consequence

$$\left\langle r^2(t)\right\rangle = \tilde{D}\ t^{\beta}$$

and

$$\tau_{KWW} = Q^{2/\beta}\tilde{D}^{-1/\beta} \tag{15.9}$$

the combination of Eq.[15.8] and [15.9] invokes sublinear diffusion of the polymer segments as the underlying reason for the stretched exponential behaviour. Its signature is a power law dependence of the Kohlrausch-William-Watts relaxation times τ_{KWW} with an exponent $2/\beta$.

15.2.2 Experimental results

15.2.2.1 Self correlation function

We commence with the secondary relaxation taking polyisobutylene as an example. Fig.15.4 presents the relaxation map of PIB. The solid line corresponds to the dielectric β-relaxation, the dashed line named δ represents NMR results interpreted as a methyl group rotation. γ and γ' are theoretically predicted relaxation mechanisms. In the dynamic regime, where the α-relaxation is too slow to contribute, neutron backscattering has been employed, in order to unravel details of the β-process in this polymer. Fig.15.5 presents as an example a spectrum taken at T = 270K and Q = 1.7Å^{-1}. The spectrum is characterized by a narrow peak, which nearly coincides with the instrumental resolution function (dashed line) and a broad foot revealing the relaxational behaviour. Such a spectral shape is typical for broad distributions of relaxation times, where only a part of it is resolved in the spectrum.

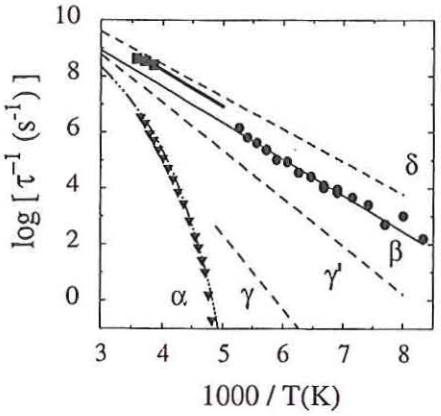

Figure 15.4: Relaxation map for PIB. ▼ marks the α-trace, ● relates to dielectric relaxation experiments on the β-relaxation, ■ results from QENS-experiments.

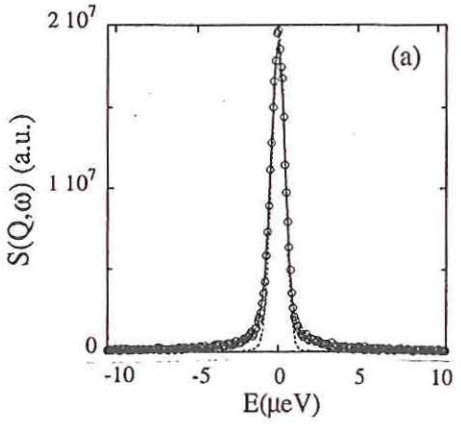

Figure 15.5: Backscattering spectrum from PIB at 270K at a Q-value Q = 1.7Å. The dashed line gives the resolution function, while the solid line displays the fit with the model (see text).

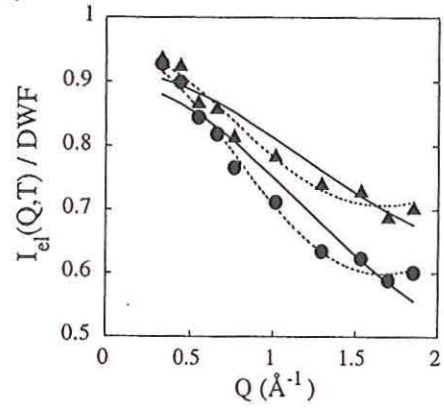

Figure 15.6: EISF for PIB (▲: 250K, ●: 270K). Solid lines: EISF for methylgroup rotation, dashed lines: fit result for a jump distance d = 2.7Å.

Fig.15.6 displays the elastic intensity observed for PIB as a function of Q. The data were corrected for multiple scattering and fitted with Eq.[15.5]. This elastic incoherent structure factor (EISF) (see lecture Quasielastic Scattering) reveals a jump distance d = 2.7Å. For comparison the solid lines display the prediction for methyl group rotation, which was invoked by NMR spectroscopy. Obviously the neutron data point into the direction of a larger motional amplitude.

The squares in Fig.15.4 display the neutron results for the β time scale. Within a factor of 2 they agree with the dielectric spectroscopy results. Since the underlying process has an amplitude of 2.7Å and is also dielectrically active, it cannot be understood as due to a methylgroup rotation alone. A possible interpretation is a combined backbone and methyl motion which is also supported by simulation results.

We now turn to the α-relaxation and ask, whether the sub linear diffusion argument is supported by quasielastic neutron scattering. Fig.15.7 displays Kohlrausch-William-Watts relaxation rates obtained for four different polymers, polyvinylether (PVE) at 340K, polyisobutylene (PIB) at 365K, polybutadiene (PB) at 280K and polyisoprene (PI) at 340K.

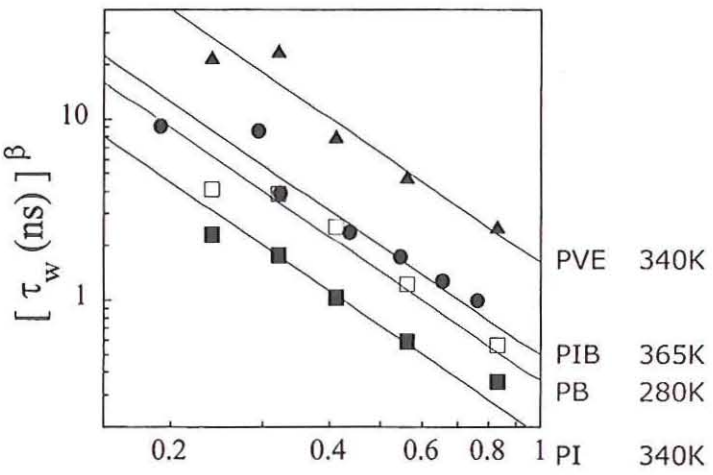

Figure 15.7: $(\tau_{KWW})^{\beta}$ for 4 different polymers as a function of Q. The solid lines display a Q^2 power law.

In order to test Eq.[15.9] the relaxation rates have been exponentiated with the exponent β, obtained from the stretching of the relaxation functions in these polymers in dielectric spectroscopy. According to Eq.[15.9], τ^{β} should be proportional to Q^2. The solid lines in Fig.15.7 display this power law relation. As may be seen, in all cases within experimental error the experimental relaxation times again obtained by backscattering spectroscopy follow the predicted power law behaviour. Thus, the experimental evidence supports a sub linear diffusion process as underlying the α-relaxation. We remark that this result is in disagreement with assertions that the stretched exponential relaxation function of the α-process originates from heterogeneous motional processes, where polymer segments in different parts of the sample would relax at different relaxation rates.

15.2.3 Pair correlation function

The dynamic pair correlation function for polymer relaxation has been studied thoroughly on polybutadiene as a function of temperature and momentum transfer. Fig.15.8 gives a synopsis of these results. The dynamic data presented have been taken at the positions of the first and second peaks in the static structure factor of this polymer. As may be seen from the middle part of Fig.15.8 the first peak of the static structure factor moves strongly with temperature. This peak originates from interchain correlations, where weak v. d. Waals interactions lead to thermal expansion. The second peak relates mainly to intrachain correlations as may be seen from the temperature independence of its position indicative for covalent bonds. The temperature dependent relaxation spectra were rescaled in their time dependence with the characteristic time for viscosity relaxation τ_η (actually the time dependent monomeric friction coefficient was used, see next paragraph). By this procedure the time correlation functions at the first peak assemble to a master curve, showing that the dynamics at the interchain distance follows the same relaxational behaviour as the macroscopic flow. On the other hand as evidenced by the lower part of Fig.15.8 at the second structure peak, such a scaling does not reassemble the data points to a master curve. Obviously the dynamics at the second peak at higher Q follows different dynamics.

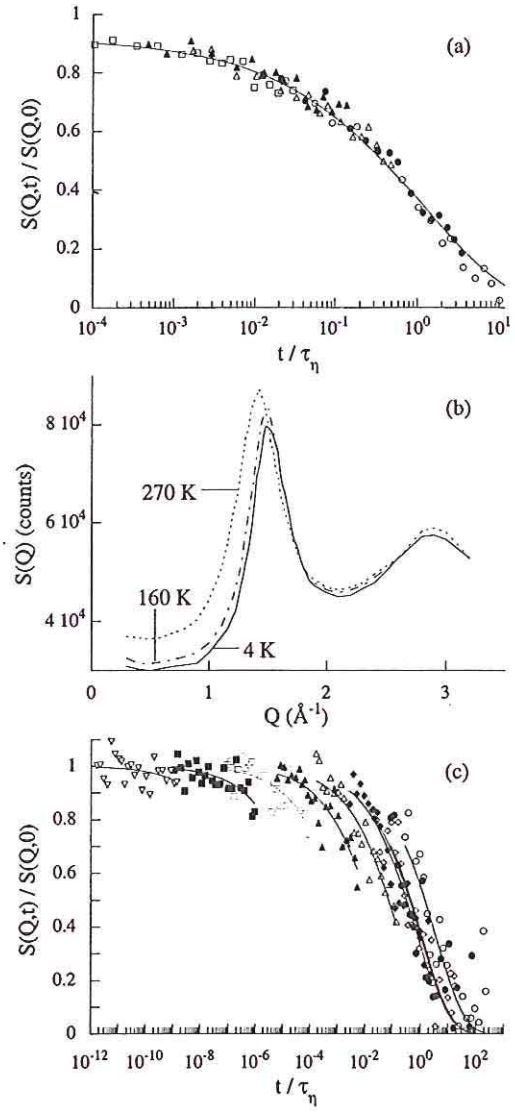

Figure 15.8: NSE spectra from PB taken at the first and second structure factor peak. The time is rescaled with the temperature dependence from flow relaxation. Center: $S(Q)$ for different temperatures.

Fig.15.9 displays the temperature dependence of the corresponding relaxation rates. While the data at the first peak nicely agree with the temperature dependence of the α-relaxation, as already evidenced by the scaling, the relaxation rates taken at the second peak follow an

Arrhenius temperature dependence with a same activation energy as that of the corresponding dielectric β-process.

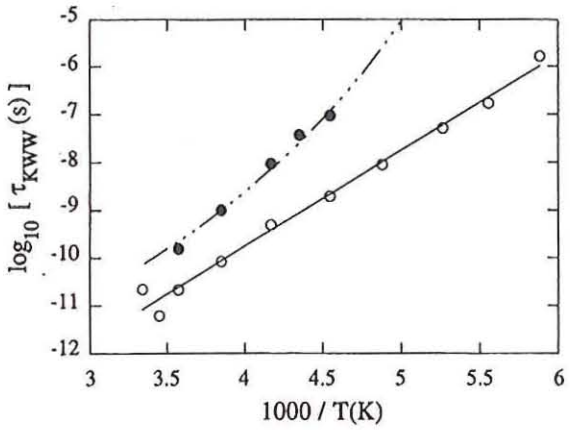

Figure 15.9: Relaxation rates at the first and second structure factor peak of PB in an Arrhenius representation. Solid lines: α- and β traces for this polymers.

An evaluation of the structure factor following Eq. [15.6] and [15.7] reveals a jump distance for the β-process of d = 1.5Å. It also shows that the assumption of statistically independent α- and β-relaxations is supported by the temperature and momentum transfer dependent spectra.

15.3 Entropy driven dynamics – the Rouse regime

As outlined in the introduction, the conformational entropy of a chain acts as a resource for restoring forces for chain conformations, deviating from thermal equilibrium. In this Chapter we deal with these entropy driven dynamics in terms of the Rouse model and present NSE results on the space-time evolution of the Rouse relaxation and finally discuss recent molecular dynamic simulations which have been performed in parallel to NSE experiments, in order to explore the limits of the Rouse picture.

15.3.1 Entropic forces – the Rouse model

As the simplest model for chain relaxation, the Rouse model considers a Gaussian chain in a heat bath. The building blocks of such a *Gaussian* chain are segments consisting of several monomers, so that their end to end distance follows a Gaussian distribution. Their conformations are described by vectors $\underline{a}_n = \underline{r}_n - \underline{r}_{n+1}$ along the chain. Thereby $\underline{r}_n$ is the position vector of the segment *"n"*. The chain is described by a succession of freely connected segments of length ℓ. We are interested in the motion of these segments on a length scale

$\ell < r < R_e$, where $R_e^2 = n\,\ell^2$ is the end to end distance of the chain. The motion is described by a Langevin equation

$$\zeta_0 \frac{d\underline{r}_n}{dt} = \nabla_n F(\underline{r}_n) + \underline{f}_n(t) \,, \tag{15.10}$$

where ζ_0 is the monomeric friction coefficient. For the stochastic force $\underline{f}_n(t)$ we have $\langle \underline{f}_n(t) \rangle = 0$ and $\langle f_{n\alpha}(t) f_{m\beta}(0) \rangle = 2k_B T\ \zeta_0\, \delta_{nm}\delta_{\alpha\beta}\delta(t-t')$ α, and β denote the Cartesian components of $\underline{r}$. $F(\underline{r}_n)$ is the free energy of the polymer chain. The force term in Eq.[15.10] is dominated by the conformational entropy of the chain

$$S = k_B \ell n\ W(\{\underline{r}_n\})$$

where $W(\{\underline{r}_n\})$ is the probability for a chain conformation $\{\underline{r}_n\}$ of a Gaussian chain of n-segments.

$$W(\{\underline{r}_n\}) = \prod_{i=1}^{N} \left\{\frac{3}{2\pi\ \ell^2}\right\}^{3/2} \exp\left\{\frac{-3\ (\underline{r}_i - \underline{r}_{i-1})^2}{2\ell^2}\right\} \tag{15.11}$$

With the boundary conditions of force free ends Eq.[15.10] is readily solved by cosine Fourier transformation, resulting in a spectrum of normal modes. These solutions are similar to e.g. the transverse vibrational modes of a linear chain except that relaxational motions are involved instead of periodic vibrations. The dispersion of the relaxation rates $1/\tau_p$ is quadratic in the number of knots p along the chain.

$$\frac{1}{\tau_p} = \frac{3k_BT}{\zeta_0 \ell^2}\frac{\pi^2}{N^2}p^2 = W\frac{\pi^2}{N^2}p^2 = \frac{p^2}{\tau_R}\,, \tag{15.12}$$

where τ_R is the Rouse time - the longest time in the relaxations spectrum – and W is the elementary Rouse rate. The mode correlation function for the Rouse modes is obtained as

$$\left\langle x_p^\alpha(t)\;\; x_q^\beta(0)\right\rangle = \delta_{\alpha\beta}\delta_{pq}\frac{N\ell^2}{6\pi^2 p^2}\;\; \exp\left(-t/\tau_p\right) \tag{15.13}$$

$$\left\langle x_0^\alpha(t)\;\; x_0^\beta\;\;(0)\right\rangle = \delta_{\alpha\beta}\frac{2k_BT}{N\zeta_0}t$$

Thereby x_p^α is the α-component of the number p normal mode and x_0^α is the centre of mass coordinate. In order to study Brownian motion, the segment correlation functions in the real space $\Delta r_{nm}^2(t) = \left\langle \left(r_m(t) - r_n(0)\right)^2 \right\rangle$ are required. They are obtained by retransformation of the normal coordinates leading to

$$\Delta r_{nm}^2(t) = 6D_R t + |n-m|\;\; \ell^2$$
$$+\frac{4N\ell^2}{\pi^2}\sum_{p=1}^{N}\frac{1}{p^2}\cos\left(\frac{p\pi\;\; m}{N}\right)\cos\left(\frac{p\pi\;\; m}{N}\right)\left(1-\exp\left(-\frac{p^2 t}{\tau_R}\right)\right) \tag{15.14}$$

in Eq.[15.14] we use the fact that the mean square displacement of the centre of mass provides the diffusion constant. For the special case of the self correlation function *(n = m)* $\Delta r_{nn}(t)$ reveals the mean square displacement of a polymer segment. We obtain

$$\Delta r_{nn}^2(t) = 2\ell^2\left(\frac{3k_BTt}{\pi\zeta_0\ell^2}\right)^{1/2} \tag{15.15}$$

In contrast to normal diffusion Δr_{nn}^2 does not grow linearly, but with the square route of time. For the translational diffusion coefficient $D_R = k_BT/N\zeta_0$ is obtained. D_R is inversely proportional to the number of friction performing segments.

By means of neutron scattering two different correlation functions may be accessed. In the case of coherent scattering, all partial waves emanating from different scattering centres are capable of interference – the *Fourier* transform of the pair correlation function of a single chain is measured. In contrast incoherent scattering, where the interferences from partial waves of different scatterers are destructive, measures the self correlation function. The self correlation function leads directly to the mean square displacement of the diffusing segments. In Gaussian approximation for $t < \tau_R$ we have

$$S_{inc}(Q,t) = \exp\left\{-\frac{2}{\sqrt{\pi}}\left(\frac{k_B T \ell^2}{12\zeta_0} Q^4 t\right)^{1/2}\right\} \tag{15.16}$$

in the case of coherent scattering, which observes the pair correlation function, interferences from scattering waves emanating for various segments complicate the scattering function. With Eq.[15.14] we obtain

$$S(Q,t) = \frac{1}{N}\exp\left[-Q^2 D_R t\right] \sum_{nm} \exp\left\{-\frac{1}{6}|n-m|\ Q^2\ell^2\right\} \tag{15.17}$$

$$-\frac{2}{3}\frac{R_E^2 Q^2}{\pi^2} \sum_p \frac{1}{p^2}\left\{\cos\left(\frac{p\pi\ m}{N}\right)\cos\left(\frac{p\ \pi n}{N}\right)\left(1-\exp\left(-\frac{tp^2}{\tau_R}\right)\right)\right\}$$

for small Q $(QR_E < 1)$ the second and third terms are negligible and $S(Q,t)$ describes the centre of mass diffusion of the chain.

$$S(Q,t) = N\ \exp\left(-D_R t\right) \tag{15.18}$$

For $QR_E > 1$ and $t < \tau_R$ the internal relaxations dominate. Converting the sums in Eq.[15.17] to integrals and after some algebra de Gennes has derived an expression for the dynamic structure factor.

$$S(Q,t)=\frac{12}{Q^2\ell^2}\int_0^\infty du\ \exp\left\{-u-(\Omega_R t)^{1/2}\,h\left(u(\Omega_R t)^{-1/2}\right)\right\} \tag{15.19}$$

$$h(y)=\frac{2}{\pi}\int_0^\infty dx\,\frac{\cos(xy)}{x^2}\left(1-\exp(-x^2)\right)$$

We observe that in spite of the complicated functional form *S(Q,t)*, like the self correlation function, only depends on one variable, the Rouse variable.

$$(\Omega_R t)^{1/2}=\frac{Q^2}{6}\sqrt{\frac{3k_BT\ell^2 t}{\zeta_0}}=\frac{Q^2\ell^2}{6}\sqrt{Wt} \tag{15.20}$$

Since there is no length scale in the problem, for different momentum transfers the dynamic structure factors are predicted to collapse to one master curve, if they are represented as a function of the Rouse variable.

15.3.2 Neutron spin echo results

The self correlation function of a Rouse chain was first observed on polydimethylsiloxane (PDMS). Since a straight forward study of the incoherent scattering by NSE is very difficult – due to spin flip scattering a severe loss of polarization occurs leading to very weak signals – the measurements of the self correlation function were performed on high molecular weight deuterated PDMS chains which contained short protonated labels at random positions. In such a sample the scattering essentially originates from the contrast between the protonated sequence and a deuterated environment and therefore is coherent. On the other hand the sequences are randomly distributed, so that there is no constructive interference of partial waves arising from different sequences. Under these conditions the scattering experiments measures the self correlation function.

In Fig.15.10 the corresponding NSE spectra are plotted against the scaling variable of the Rouse model. The results for the different momentum transfers follow a common straight line. In Gaussian approximation for the case of the self correlation function the scattering function directly measures the mean square segment displacement, which according to Eq.[15.15] obeys a square root law in time. This behaviour may be directly read off from Fig.15.10.

The pair correlation function arising from the segment motion within one given chain is observed, if some protonated chains are dissolved in a deuterated matrix. Fig.15.11 displays the observed spectra from polyethylethylene (90% dPEE, 10% hPEE) at a molecular weight of M_W = 20.000. The solid lines give the prediction of the dynamic structure factor of Eq.[15.19]. Obviously very good agreement is achieved.

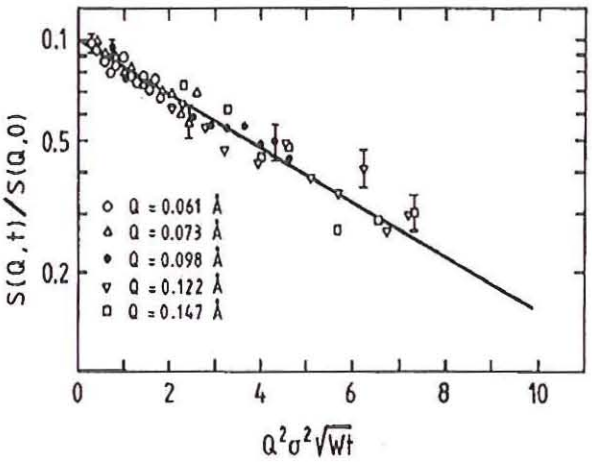

Figure 15.10: Self correlation for a PDMS melt T = 100C. The data at different momentum transfers are plotted us the scaling variable of the Rouse model ($\sigma \equiv \ell$).

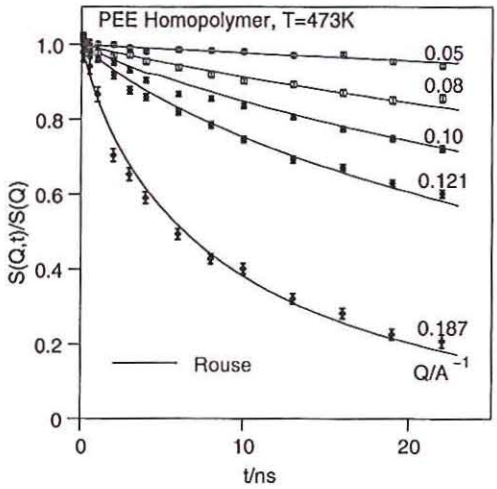

Figure 15.11: Single chain structure factor from a PEE melt at 473K. The solid lines represent a joint fit with the Rouse model.

We now use these data, in order to investigate the scaling prediction inherent in Eq.[15.19]. Fig.15.12 presents a plot of the data of Fig.15.11, now as a function of the Rouse scaling variable (Eq.[15.20]).

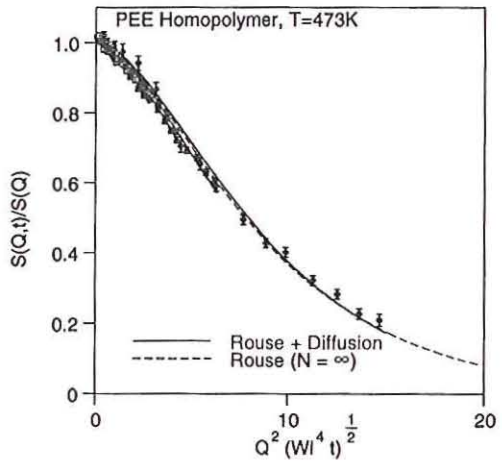

Figure 15.12: Single chain structure factor from PEE melts as a function of the Rouse scaling variable.

The data follow with satisfying precision the scaling prediction. The small deviations are related to the translational diffusion of the chains. This becomes evident from Fig.15.13, where the obtained relaxation rates $\Gamma(Q)$ are plotted versus Q in a double logarithmic fashion.

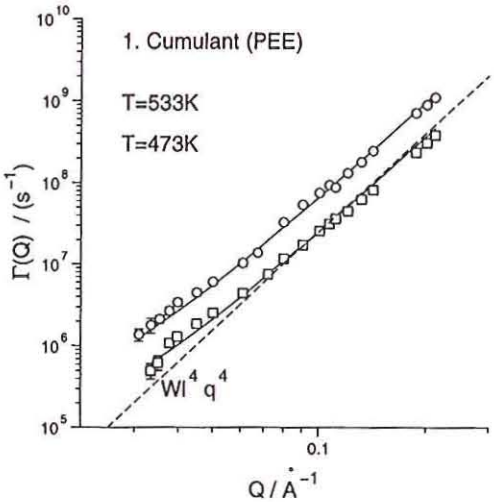

Figure 15.13: Relaxation rates from PEE melts vs. Q for two different temperatures.

The dashed line gives the Rouse prediction $\Gamma \propto W\ell^4 Q^4$. While at larger momentum transfers the experimental results follow very well this prediction, towards lower Q, a systematic relative increase of the relaxation rate is observed. Including the diffusion, we have

$$\Gamma(Q) = Q^2\left[D + Q^2\frac{W\ell^4}{6}\right] \tag{15.21}$$

the solid lines in Fig.15.13 represents the prediction of Eq.[15.21]. Perfect agreement is obtained.

15.3.3 Computer simulation

In order to learn about the limits of the Rouse model, recently a detailed quantitative comparison of molecular dynamics (MD) computer simulations on a 100 C-atom polyethylene chain (PE) with NSE experiments on PE chains of similar molecular weight has been performed. Both, the experiment and the simulation were carried out at T = 509K. Simulations were undertaken, both for an explicit *(ea)* as well as for an united *(ua)* atom model. In the latter the *H*-atoms are not explicitly taken into account but reinserted when calculating the dynamic structure factor. The potential parameters for the MD-simulation were either based on quantum chemical calculations or taken from literature. No adjusting parameter was introduced. Fig.15.14 compares the results from the MD-simulation (solid and broken lines) with the NSE-spectra. The time axis thereby is scaled with the centre of mass diffusion coefficient, in order to correct for the slightly different overall time scales of experiment and simulation. From Fig.15.14 quantitative agreement between both results is evident. Fig.15.15 compares the same experimental data, which agreed quantitatively with the simulations with a best fit to the Rouse model (Eq.[15.17]. Here a good description is observed for small Q-values ($Q \lesssim 0.14\text{Å}^{-1}$), while at higher Q important deviations appear. Similarly also the simulations cannot be fit in detail with a Rouse structure factor.

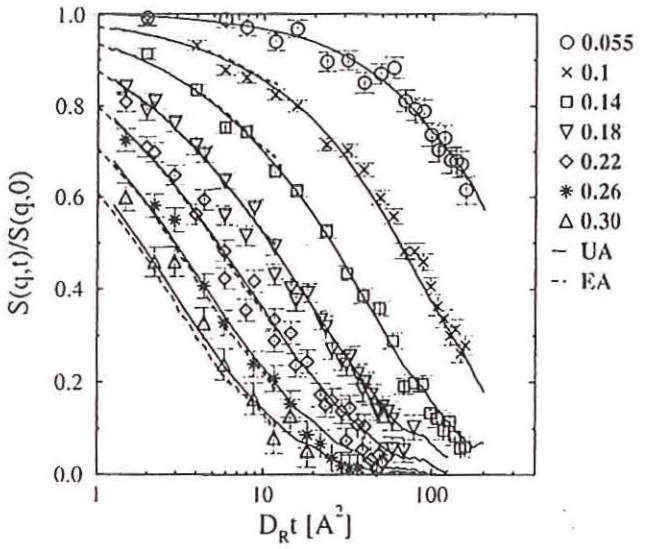

Figure 15.14: NSE data from PE melts vs. computer simulations (see text).

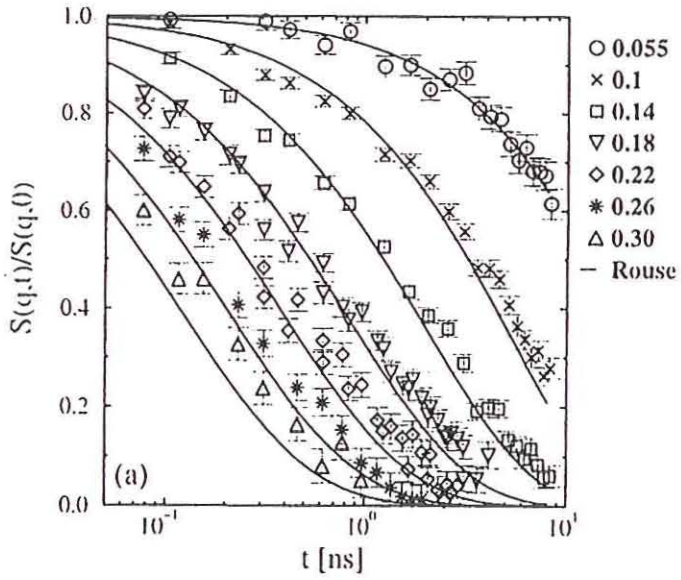

Figure 15.15: NSE data from PE melts in comparison to a best fit with the Rouse model (see text).

Having obtained very good agreement between experiment and simulation, the simulations which contain complete information about the atomic trajectories may be further exploited, in order to rationalize the origin for the discrepancies with the Rouse model. A number of deviations evolve.

1. According to the Rouse model the mode correlators (Eq.[15.13] should decay in a single exponential fashion. A direct evaluation from the atomic trajectories shows that the 3 contributing Rouse modes decay with stretched exponentials displaying stretching exponents β of *(1:$\beta = 0.96$ and 2,3:$\beta = 0.86$)*

2. A detailed scrutiny of the *Gaussian* assumption (see e.g. (Eq.[15.16] and [15.17]) reveals that for $t < \tau_R$ deviations occur.

3. While the Rouse model predicts a linear time evolution of the mean squared centre of mass coordinate (Eq.[15.17]), within the time window of the simulation *($t < 9ns$)* a sublinear diffusion in form of a stretched exponential with the stretching exponent of $\beta = 0.83$ is found. A detailed inspection of the time dependent mean squared amplitudes reveals that the sublinear diffusion mainly originates from motions at short times $t < \tau_R = 2ns$.

The prediction of a time dependent centre of mass diffusion coefficient has recently been corroborated by NSE-experiments on short chain polybutadienes. Fig.15.16 displays the mean square centre of mass displacement from simulation compared to the same quantity obtained from the dynamic structure factor at various Q-values. Both the simulation as well as the experimental data consistently lead to a weaker than linear time dependence of the mean square centre of mass displacement.

The overall picture emerging from this combined simulational and experimental effort is, that for chains, which should be ideal Rouse chains, the model is capable of quantitatively describing the behaviour only on time scales of the order of the Rouse time or larger and therefore on length scales of the order of the radius of gyration of the chains or larger and in the regime, where the chains actually show Fickian diffusion. The self diffusion behaviour for times smaller than the Rouse time and the relaxation of the internal modes of the chains show

small but systematic deviations from the Rouse prediction. The origin of these discrepancies are traced to interchain interactions.

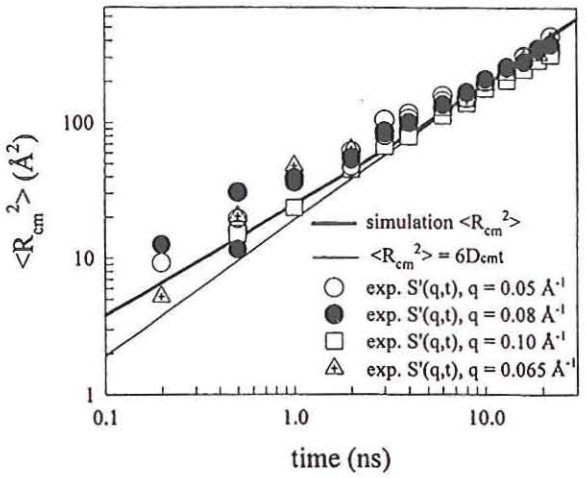

Figure 15.16: Mean square center of mass displacement for PB chains in the melt obtained from $\langle r^2(t)\rangle = -\frac{6}{Q^2}\,\ell n\, S(Q,t)$. Solid line: simulation result; dashed line $\langle r^2(t)\rangle = D_e t$.

15.4 Topological interactions - Reptation

The reptation model of de Gennes, Doi and Edwards proceeds from the intuitive concept that the motions of a chain in a melt are heavily impeded in directions lateral to their own profile by the other chains encircling them. The dominant diffusive motion proceeds along the chain profile. A chain twists and turns through a melt like a snake. The lateral restrictions are modelled by a tube with a diameter d, parallel to the chain profile, whereby d relates to the plateau modulus of the melt. The restrictions of the motion through other chains are not effective on a monomer scale, but rather permits lateral excursions on intermediate length scales *($d \cong 50....Å$)*. The experimental observations for viscosity and diffusion can be made directly comprehensible in this simple intuitive model.

As it concerns the motion of an individual polymer, large scale lateral diffusion is quenched during the life time τ_d of the tube constrains. Initially for short times the chain relaxes according to the Rouse picture until the mean square displacement reaches about the tube

diameter d. At that time (τ_e) the chain has explored the lateral confinement $\tau_e \cong \frac{N_e^2}{\pi^2} W$; with ($d^2 = N_e \ell^2$). For longer times $t \lesssim \tau_R$ the Rouse modes relax along the tube (local reptation). Thereafter longitudinal creep governed by the Rouse diffusion coefficient D_R along the tube dominates. This process takes place until the chain has left its original confinement at a time $\tau_d \cong \frac{1}{W} N^3$. Beyond that time normal diffusion takes over.

For the mean square segment displacement the reptation mechanism invokes a sequence of power laws in the time variable. For short times $t < \tau_e$ Rouse motion prevails and $\Delta r^2 \propto t^{1/2}$ holds. Then in the regime of local reptation we deal with Rouse modes occurring along a contorted Gaussian tube. The segment displacement along the tube follows a $t^{1/2}$ law, in real space considering the random walk nature of the tube, this transforms to a $t^{1/4}$ law. After all Rouse modes have relaxed, Rouse diffusion along the contorted tube takes place. A similar argument as before leads to a power law $\Delta r^2 \propto t^{1/2}$ and only for times longer than τ_d, the lifetime of the tube constraints, $\Delta r^2 \propto t$ holds.

The tube constraints also provoke a strong retardation for the single chain relaxations causing a near plateau regime in the time dependent single chain correlation function. Neglecting the initial free Rouse process de Gennes has formulated a tractable expression for the dynamic structure factor which is valid for $t > \tau_e$, i.e. once confinement effects become important. In the large Q limit the dynamic structure factor assumes the form

$$\frac{S(Q,t)}{S(Q,0)} = \left\{1 - \exp\left[-\left(\frac{Qd}{6}\right)^2\right]\right\} \exp(t/\tau_0)\ erfc\left(\sqrt{t/\tau_0}\right) + \frac{8}{\pi^2} \exp\left(-\left(\frac{Qd}{6}\right)^2\right) \sum_{n_{odd}} \frac{1}{n^2} \exp\left(-n^2 t/\tau_d\right) \tag{15.22}$$

For short times $S(Q,t)$ decays mainly due to local reptation (first term), while for longer times (and low Q) the second term resulting from the creep motion dominates. The two time scales are given by $\tau_0 = \frac{36}{W \ell^4 Q^4}$ *and* $\tau_d = \frac{3N^3 \ell^2}{\pi^2 W d^2}$. Since the ratio of these time scales is proportional to N^3 for long chains at intermediate times $\tau_e < t < \tau_d$ a pronounced plateau in

$S(Q,t)$ is predicted. Such a plateau is a signature for confined motion and relates not only to the reptation concept. Besides the reptation model also other entanglement models have been broad forward. We discuss them briefly by categories.

1. In generalized Rouse models, the effect of topological hindrance is described by a memory function. In the border line case of long chains the dynamic structure factor can be explicitly calculated in the time domain of the NSE experiment. In this class fall entanglement models by Ronca, Hess, Chaterjee and Loring.

2. Rubber like models take entanglements literally as temporary cross links. Such an approach has been brought forward recently by des Cloiseaux. He assumes that the entanglement points between chains are fixed as in a rubber and that under the boundary condition of fixed entanglements the chains perform Rouse motion. This rubber like model is conceptually closest to the idea of a temporary network.

3. Recently in a mode coupling approach a microscopic theory describing the polymer motion in entangled melts has been developed. While these theories describe well the different time regimes for segmental motion, unfortunately as a consequence of the necessary approximations up to now a dynamic structure factor could not yet been derived.

15.4.1 Experimental observations

Fig.15.17 presents measurements on alternating polyethylene propylene copolymer melts at 496K. The dynamic structure factors are plotted linearly against time and qualitatively obey the expectation set by the reptation or other confinement models. For short times $S(Q,t)$ shows fast relaxation which is transformed into a slightly sloping plateau above about 15ns. The broken line demonstrates the expected relaxation in the Rouse model.

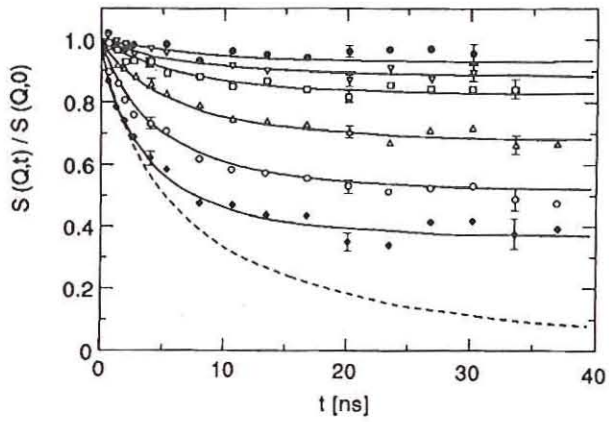

Figure 15.17: Dynamic structure factor of a PEP melt for different Q-values. Solid lines: Ronca model; dashed line: Rouse model at the largest Q-value.

In Fig.15.18 the same data are plotted versus the scaling variable of the Rouse model (Eq.[15.20]). In contrast to Fig.15.12 the scaled data do not follow a common curve but are rather split into Q dependent branches after an initial common course. This splitting is a consequence of the existence of a dynamic length scale which invalidates the Rouse scaling properties. We note, that this length is of purely dynamical character and cannot be observed in static experiments. In order to distinguish between different models measurements up to Fourier times 3 or 4 times larger than τ_e are not enough. Here, the recent development of an ultra high resolution NSE spectrometer (IN15 at the ILL in Grenoble opened new ground in pushing the time limit of NSE up to about 200ns).

Fig.15.19 displays recent experimental results on a polyethylene melt (M_w = 36.000) which were carried over a time regime of 170ns. The data are compared with the dynamic structure factors of the reptation model as well as the models of de Cloizeaux and Ronca. It is apparent that these data clearly favour the reptation model which appears to be the only so far existing model yielding a dynamic structure factor which is in quantitative agreement with this NSE data. The model of Ronca produces a plateau which is too flat. From Fig.15.19 it is also apparent that the Rubber like model of de Cloizeaux leads to an inconsistent Q dependence which is most apparent at the larger Q values. We note that the fits were preformed varying

only one single parameter, the tube diameter d, while the Rouse rate was determined from earlier NSE data taken at short times. With this one parameter it is possible to achieve quantitative agreement both with respect to the Q and the time dependence of the dynamic structure factor.

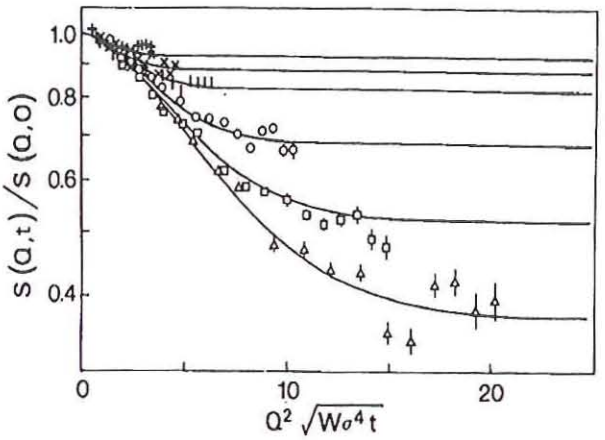

Figure 15.18: Data from Fig.15.17 in a scaling representation as a fact of the Rouse variable ($\sigma \equiv \ell$)

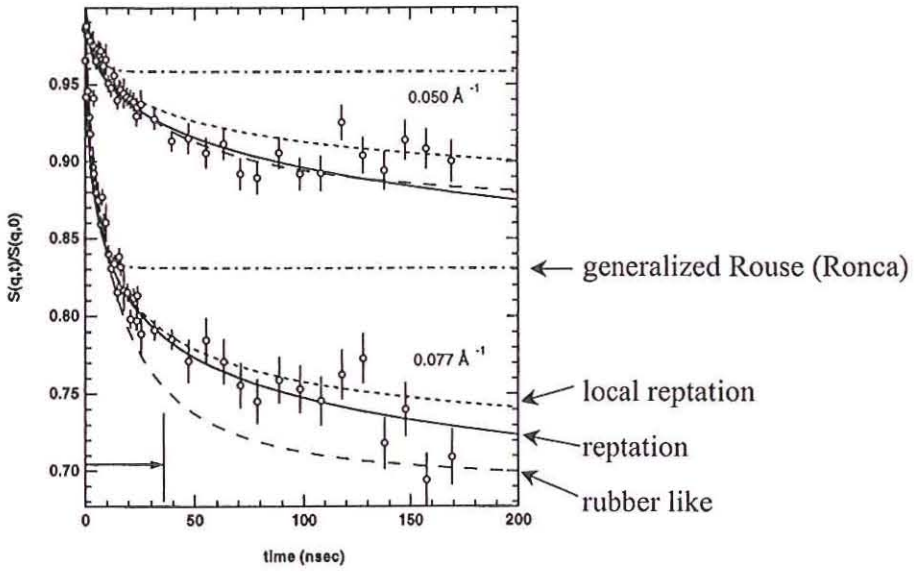

Figure 15.19: NSE data from PE melts at 509K compared to various models.

Finally, one may test whether only local reptation or also the creep motion along the tube is important on this experimental time scale. Local reptation corresponds to $\tau_d = \infty$ and indeed (Fig.15.19) at low Q a difference between local reptation only and the global reptation mechanism appears to become distinguishable indicating the presence of τ_d. Here future experimental work will have to set in. As it stands NSE spectroscopy accessing quantitatively the dynamic structure factor has by now seen clear and unambiguous signature of reptation in a flexible linear polymer chain. The data cover a region of the time domain where reptation is in principle applicable. Compared with other phenomenological approaches reptation is by now the only approach providing a consistent description of all NSE data. It implies that reptation must emerge from any successful microscopic theory of polymer relaxation.

15.5 Summary

High resolution neutron spectroscopy permits to access the molecular motions simultaneously in space and time. Restricting itself to the dynamics of homopolymers melts this lecture attempted to transmit a flavour of what can be achieved in particular by NSE. Choosing different time and length scales, we covered the range of molecular motions, commencing at the scale of a few bonds to large scale motions reaching the scale of the entire chain.

In the regime of the 'classical relaxations' of polymers neutron spectroscopy informs on the geometrical evolution of the motions in question. We have seen, that the α-relaxation may be understood as a sublinear diffusion process while the β-relaxation is in good agreement with a local jump process of a few angstrom distances. Both processes may be considered with good approximation as statistically independent. At scales where the detailed chemical structure of the monomers ceases to be of importance, NSE measurements have by and large confirmed the predictions of the entropy governed Rouse dynamics both for the self and the pair correlation function. Recently, an in depth comparison of specially designed NSE experiments with computer simulation also pointed out the limits of this approach.

The dynamics of polymer melts under the influence of topological interactions which result from the mutually interpenetrating chains poses high demands both conceptually and also experimentally. NSE experiments on the single chain dynamic structure factor of long chain melts, established experimentally the essential prediction of local reptation namely the tube

confinement of the relaxation of large scale Rouse modes. Presently there exists no other theory providing a dynamic structure factor, which is in agreement with this data.

References

A. Review Articles and books

[1] M. Doi, S.F. Edwards, The Theory of Polymer Dynamics, Clarendon Press, Oxford (1986)

[2] B. Ewen, D. Richter, Advances in Polymer Science 134, Springer, Berlin (1997)

[3] D. Richter, Polymer Dynamics by Neutron Spin Echo Spectroscopy in "Scattering in Polymeric and Colloidal Systems" Ed by Wyn Brown and Kell Mortensen, Gordon and Breach, London (2000)

[4] D. Richter, Visoelasticity and microscopic motion in dense polymer systems, Review article in Diffusion in Condensed Matter, Eds: J. Kärger, P. Heitjans, R. Haberlandt (Vieweg, Braunschweig (1998))

B. Experimental work

[5] A. Arbe, U. Buchenau, L. Willner, D. Richter, Study of the Dynamic Structure Factor in the β-Relaxation Regime of Polybutadiene, Phys. Rev. Lett. **76**, 1872 (1996)

[6] A. Arbe, D. Richter, J. Colmenero, B. Farago, The Merging of the α- and β-Relaxations in Polybutadiene; A Neutron Spin Echo and Dielectric Study, Phys. Rev. E. **54**, 3853 (1996)

[7] A. Arbe, J. Colmenero, M. Monkenbusch, D. Richter, Dynamics of glass-forming polymers: homogeneous vs. heterogeneous scenario, Phys. Rev. Lett. **81**, 590 (1998)

[8] D. Richter, M. Monkenbusch, A. Arbe, J. Colmenero, R. Faust, Space Time Observation of the α-Process in Polymers by Quasielastic Neutron Scattering, J. Phys. Condens. Matter **11**, A297 (1999)

[9] A. Arbe, J. Colmenero, B. Frick, M. Monkenbusch, D. Richter, Investigation of the dielectric β-process in Polyisobutylene by incoherent quasielastic neutron scattering, Macromolecules **29**, 4926 (1998)

[10] D. Richter, M. Monkenbusch, J. Allgaier, A. Arbe, J. Colmenero, B. Farago, Y. Cheol Bae, R. Faust, From Rouse Dynamics to Local Relaxation - A Neutron Spin Echo Study of Polyisobutylene Melts, J. Chemical Physics 111, 6107 (1999)

[11] W. Paul, G.D. Smith, D.Y. Yoon, B. Farago, S. Rathgeber, A. Zirkel, L. Willner, D. Richter, Chain Motion in an Unentangled Polymer Melt: A Critical Test of the Rouse Model by Molecular Dynamics Simulations and Neutron Spin Echo Spectroscopy, Phys. Rev. Lett. **80**, 2346 (1998)

[12] P. Schleger, B. Farago, A. Kollmar, C. Lartigue, D. Richter, Clear Evidence of reptation in polyethylene from neutron spin echo spectroscopy, Phys. Rev. Lett. **81**, 124 (1998)

[13] H. Montes, M. Monkenbusch, L. Willner, S. Rathgeber, L.J. Fetters, D. Richter, Neutron Spin Echo Investigations of Concentration fluctuations dynamics in melts of diblock-copolymers, J. Chemical Physics **110**, 10188 (1999)

C. Theoretical Work

[14] G. Ronca, Frequency spectrum and dynamic correlations of concentrated polymer liquids, J. Chem. Phys. **79**, 1031 (1983)

[15] A. Chatterjee, R. Loring, Calculation of the dynamic structure factor in polymer melts, J. Chem. Phys. **101**, 1595 (1994)

[16] J. des Cloizeaux, Dynamic form function of a long polymer constrained by entanglement in a polymer melt, J. Phys. I. (France) **3**, 1523 (1993)

[17] K.S. Schweizer, G. Szamel, Crossover to entangled dynamics in polymer solutions and melts, J. Chem. Phys. **103**, 1934 (1995)

16 Magnetism

Thomas Brückel, IFF, FZ-Jülich

16.1 Introduction

Magnetism is a very active and challenging subject of solid state science since it represents a typical many-body problem and a complex application of quantum-mechanics, statistical physics and electromagnetism. During the last decades, new discoveries have emerged in this field due to the synthesis of new classes of magnetic materials, due to improved or new powerful techniques or due to advancements in solid state theory. Let us mention a few examples of materials of current interest: the high temperature superconductors and the colossal magneto-resistance manganite compounds, both of which have structures derived from the perovskite structure, the rare-earth nickel-born carbide compounds with a coexistence of magnetism and superconductivity, the large class of Kondo systems and heavy fermion compounds, spin glasses and spin liquids or new and rather complex hard magnetic materials, just to mention a few. Besides bulk materials, magnetism of thin films and surfaces became a topic of great current interest, mainly due to the improved preparation techniques. Driven by pure curiosity, scientists have discovered many fundamental effects of thin film devices, such as the oscillating interlayer coupling or the giant magneto-resistance effects. Within less than ten years from their initial discovery, these effects found their applications for example in read heads of computer hard disks. A promising new field of application emerges, so-called magneto-electronics with spin transistors or magnetic random access memories MROM. This should serve us as an excellent example, how curiosity driven fundamental research can find new applications of an effect known since 2500 years (the discovery of the magnetism of magnetite) which are able to change our modern life. This progress is largely due to new experimental methods and again we just want to mention a few: developments in the field of polarised neutron scattering, such as the ^{3}He-polarisation filter or zero-field neutron polarimetry, the development of the spin resonance techniques, resonant nuclear scattering of synchrotron radiation or magnetic x-ray diffraction. Finally, all this experimental progress would be in vain without the improvements of the theory, which provide us with a deeper understanding of correlated electron systems. Probably the most powerful technique that has emerged during the last years is the density functional theory which allows one to calculate

the ground state of metallic magnets. Numerical methods such as Monte-Carlo simulation allows us to test models of complex disordered magnetic systems.

After having motivated the interest in solid state magnetism, let us come back to the basic magnetic properties. Quite generally, a magnetic system can be described by its magnetisation, which denotes the total magnetic moment per unit volume. The magnetisation of a sample can vary in space and time: $\underline{M}(\underline{r},t)$. The magnetisation is coupled to the conjugate magnetic field $\underline{H}(\underline{r},t)$. If the excitation $\underline{H}$ is very small, the response will, to a good approximation, be linear. In the framework of this linear response theory, we can define a magnetic susceptibility χ by:

$$\underline{M} = \underline{\underline{\chi}} \cdot \underline{H} \tag{16.1}$$

Here, $\underline{\underline{\chi}}$ is written as a tensor to describe anisotropic magnetic response. In isotropic systems, $\underline{M}$ will align parallel to $\underline{H}$ and χ reduces to a scalar quantity. More generally, for a spatially and temporally varying magnetic field, we can write:

$$\underline{M}(\underline{r},t) = \iint d^3r'dt' \underline{\underline{\chi}}(\underline{r}-\underline{r}',t-t') \cdot \underline{H}(\underline{r}',t') \tag{16.2}$$

Every material shows a magnetic response. Most materials are diamagnetic with a negative susceptibility χ, which expresses Lenz's rule that the induced magnetisation $\underline{M}$ is anti-parallel to the magnetic field H. Of greater interest are materials, in which χ is positive. Here, two classes of materials have to be distinguished: localised electron systems (e. g. ionic compounds) and itinerant electron systems (metals). Localised electron systems with $\chi > 0$ have open shells with unpaired electrons. Spin- S, orbital- L, and total- angular momentum J for the free ion are determined by Hund's rules. These values can be modified by solid state effects such as the crystalline field or spin transfer into covalent bonds. In itinerant electron systems, the conduction electrons carry the magnetic moment. Within a simple band picture, magnetism arises from an unequal population of spin-up and spin-down bands. At elevated temperatures, systems with $\chi > 0$ show paramagnetic behaviour with strongly fluctuating magnetic moments. As the temperature is lowered interaction between the moments becomes more and more important. In general magnetic dipole-dipole interactions play only a minor

role, compared to the stronger exchange interactions, which result from Coulomb interaction and the Pauli principle. In ionic compounds, we observe direct exchange, if the orbitals of two magnetic ions overlap or super-exchange and double exchange, if the interaction is mediated via an intervening anion. In itinerant electron systems, the interaction is mediated by the conduction electrons and has an oscillating character. This indirect coupling of magnetic moments by conduction electrons is referred to the Rudermann-Kittel-Kasaya-Yosida (RKKY) interaction. If the energy equivalent kT is in the order of the interaction energy, a phase transition from the paramagnetic high temperature state to a magnetically long-range ordered low temperature state can eventually take place. Systems with spontaneous macroscopic magnetisations such as ferromagnets (FM) and ferrimagnets have to be distinguished from antiferromagnets (AF), for which the zero-field magnetisation vanishes. The microscopic arrangement of spin- and orbital- magnetic moments, the so-called magnetic structure, can be rather complex, especially in the case of antiferromagnets.

Neutron scattering is a most powerful technique for the investigation of magnetism due to the magnetic dipole interaction between the magnetic moments of the electrons in the sample and the nuclear magnetic moment of the neutron. We have seen in chapter 3 that for elastic events, the neutron scattering cross section is directly related to the Fourier transform of the magnetic moment density distribution. For the inelastic case, one can show that the double differential cross section for magnetic neutron scattering is connected with the most fundamental quantity, the Fourier transform of the linear response function or susceptibility (16.2) $\chi(\underline{r},t)$ in microscopic space and time variables $\underline{r}$ and t, respectively. In contrast to macroscopic methods it allows one to study magnetic structures, fluctuations and excitations with a spatial and energy resolution well adapted to atomic dimensions. Traditionally neutron scattering is the method to study magnetism on an atomic level, only recently complemented by the new technique of magnetic x-ray scattering.

In what follows, we will give a few examples for applications of neutron scattering in magnetism. Obviously it is completely impossible to give an representative overview within the limited time, nor is it possible to reproduce the full formalism. Therefore we will just quote a few results and concentrate on the most simple examples. Even so polarisation analysis experiments are extremely important in the field, we will not discuss these rather complex experiments and refer to chapter 4.

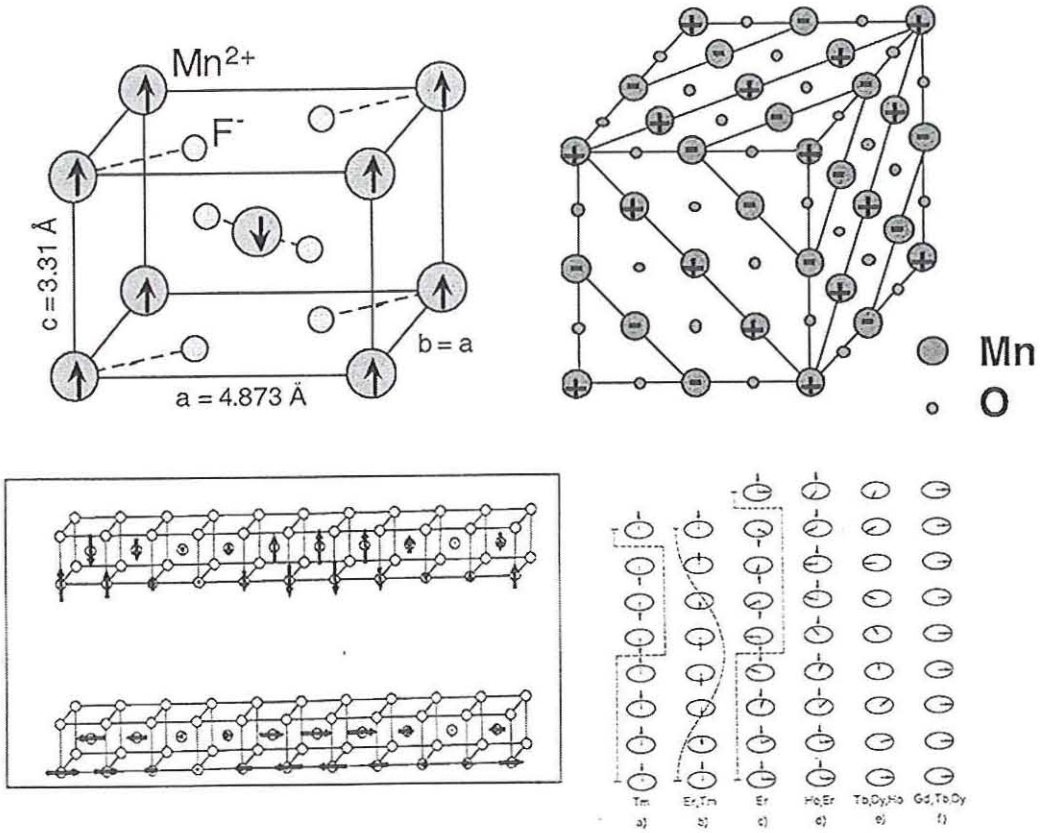

Fig. 16.1: Some examples of magnetic structures: a) The collinear antiferromagnetic structure of MnF_2. The spin moments at the corners of the tetragonal unit cell point along the c-direction, the spin moment in the centre of the unit cell is antiparallel to the moments at the corners. b) The MnO-type magnetic structure on a fcc lattice. Spins within 111 planes are parallel, adjacent planes are coupled antiferromagnetically. c) The spin density wave of chromium, which can be described by an amplitude variation along one of the cubic 001 axis. The spin density wave can be longitudinal or transversally polarised. d) Schematic representation of the magnetic structures of the hexagonal rare-earth metals. Spins in the hexagonal basal plane are always parallel. The figure shows, how successive planes along the c-directions are coupled. One can distinguish a simple ferromagnetic phase, a c-axis modulated phase, helix and cone phases. In reality, the magnetic structures are much more complex with spin slip or multi-k structures. A recent review is given by [1].

16.2 Magnetic Structure Determination

As mentioned in the introduction, the magnetic structure of a substance exhibiting magnetic long range order can be very complex. In general a magnetic structure can be described by its Fourier-components in the form

$$\underline{m}_{l,j} = \sum_{\underline{q}} \underline{m}_{\underline{q}j} \cdot \exp\left(-i\underline{q} \cdot \underline{R}_l\right) \tag{16.3}$$

where $\underline{m}_{l,j}$ denotes the moment of atom j in cell l and $\underline{q}$ is the so called magnetic propagation vector. Some examples for magnetic structures are given in figure 16.1.

Magnetic neutron scattering is the classical method to determine magnetic structures. As neutral particles, neutrons penetrate deep into most materials and allow to study bulk properties. Thermal neutrons have wavelengths in the vicinity of 1 Å, which is well adapted to studies with atomic resolution. Neutrons carry a magnetic dipole moment

$$\underline{\mu}_n = -\gamma\mu_N \cdot \underline{\sigma} \tag{16.4}$$

with the gyromagnetic ratio $\gamma = -1.913$ of the neutron and the nuclear magneton $\mu_N = 5.051 \cdot 10^{-27}\,\mathrm{J/T}$. This magnetic moment of the neutron can interact with the magnetic field created by the spin or orbital angular momentum of unpaired electrons within the solid, see chapter 3. If we restrict ourselves to elastic scattering of unpolarised neutrons, the purely magnetic scattering cross section is given by

$$\left(\frac{d\sigma}{d\Omega}\right)_{el,mag} = \left(\frac{\gamma r_0}{2}\right)^2 \left|\left\langle M_\perp(\underline{Q})/\mu_B \right\rangle\right|^2 = \left(\frac{\gamma r_0}{2}\right)^2 \left|\left\langle 2S_\perp(\underline{Q}) + L_\perp(\underline{Q}) \right\rangle\right|^2 \tag{16.5}$$

with $\frac{\gamma r_0}{2} = 2.696\,\mathrm{fm}$. $\mathrm{M}_\perp(\underline{\mathrm{Q}})$ is the component of the Fourier transform of the sample magnetisation perpendicular to the scattering vector. $\underline{\mathrm{S}}(\mathrm{Q})$ and $\underline{\mathrm{L}}(\mathrm{Q})$ are the Fourier transform of the spin- and orbital- angular momentum density, respectively. The index $\perp$ denotes the component of the corresponding quantity perpendicular to the scattering vector. Neutrons

only "see" this component and not the component of the magnetisation along the scattering vector Q (compare chapter 3). This directional dependence allows one to determine the spin direction, while the magnetic propagation vector can be determined from the position of the magnetic Bragg reflections. Finally, the magnitude of the magnetic moment can be determined by comparing the intensities of the magnetic Bragg reflections with the intensities of nuclear reflections. The scattering amplitude of neutrons by a single fixed nucleus is given by the scattering lengths tabulated in [2]. As an example, the scattering length for cobalt amounts to 2.49 fm, which is comparable to the equivalent magnetic scattering amplitude for spin = 1/2 of 2.696 fm. The formalism for magnetic neutron scattering is detailed by Squires [3] and Lovesey [4], the determination of magnetic structures is described by Rossat-Mignod [5].

Here we want to discuss the most simple example, the determination of the magnetic structure of MnF_2. For simplicity, we will neglect the scattering of the fluorine atoms completely. Then our problem reduces to magnetic Bragg diffraction from a tetragonal body centred antiferromagnet. In the so called antiferromagnetic order of type I, shown in figure 16.2, all spins at the corners of the unit cell are parallel, while the spin in the centre is anti-parallel to the spins at the corners. We assume that due to some anisotropy, e.g. the crystal field effects, all moments are aligned along ±c.

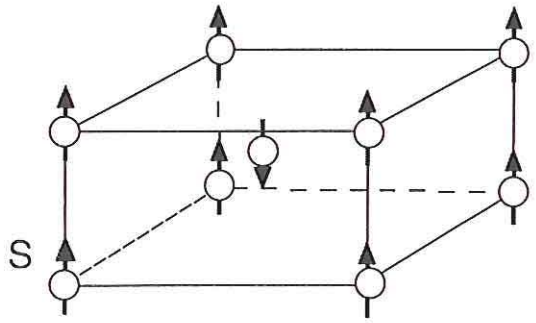

Fig. 16.2: Magnetic structure of a type I antiferromagnet on a body-centred tetragonal lattice. In the figure is assumed that c is the easy axis, i.e. all spins are aligned along c.

The scattering power density can be calculated as a convolution of an infinite three dimensional lattice, which describes the position of the origin of all unit cells, with the scattering power density of a pair of atoms located at the origin and at the centre of the unit cell. Therefore, when calculating the scattered intensity as the Fourier transform of the scattering power density, it is given as a product of the Fourier transform of the lattice and the Fourier transform of the scattering power density of a pair of atoms. The Fourier transform of the lattice is the well known Laue function (compare chapter 3). It gives rise to the Bragg reflections at integer h, k, l. The intensity of these Bragg reflections is being modulated by the Fourier transform of the scattering power density within the unit cell (here of the atom pair), the so called *elastic structure factor*. The structure factor for the pure nuclear scattering is given by:

$$\begin{aligned} S_N(h,k,l) &= b(1+e^{2\pi i(h\cdot\frac{1}{2}+k\cdot\frac{1}{2}+l\cdot\frac{1}{2})}) \\ &= b(1+(-1)^{h+k+l}) = \begin{cases} 0 & h+k+l \quad uneven \\ 2b & h+k+l \quad even \end{cases} \end{aligned} \tag{16.6}$$

The body centring gives rise to an extinction of all reflections with index h+k+l uneven, while all reflections with h+k+l even have the same intensity. In complete analogy to (16.6), the magnetic structure factor can be calculated. We only have to take into account that the spin direction in the centre is opposite to the spin directions at the corners, which can be described by a different sign for the two spins:

$$\begin{aligned} S_M(h,k,l) &= \gamma_n r_o f_m S(1-e^{2\pi i(h\cdot\frac{1}{2}+k\cdot\frac{1}{2}+l\cdot\frac{1}{2})}) \\ &= \gamma_n r_o f_m S(1-(-1)^{h+k+l}) = \begin{cases} 2\gamma_n r_o f_m S & h+k+l \ uneven. \\ 0 & h+k+l \ even \end{cases} \end{aligned} \tag{16.7}$$

The magnetic structure is „anti body centred": all reflections with index h+k+l even vanish, while reflections with h+k+l uneven are present. In the diffraction pattern, a magnetic Bragg reflection appears right between two nuclear ones. The intensity of the magnetic reflections decreases with increasing momentum transfer due to the magnetic form factor (see chapter 3), while the nuclear reflections have constant intensity, if we neglect the temperature factor – see figure 16.3.

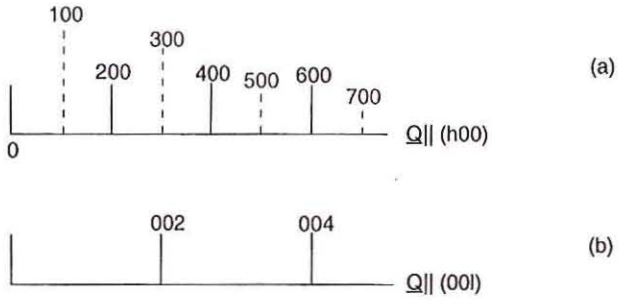

Fig. 16.3: Schematic plot of a neutron diffraction diagram for the antiferromagnet of fig. 16.2. Top: along the (h00) direction; bottom: along (00l). Magnetic Bragg reflections are indicated by the broken lines. The height of the lines is representative for the scattered intensity.

We can determine the direction of the magnetic moments with the help of the directional factor in eq. (16.5). If one measures along the tetragonal a or b directions, one obtains the magnetic Bragg reflections of figure 16.3 a. However, if one measures along c, $\underline{S} \parallel \underline{Q}$ holds, i.e. all magnetic reflections of type 0 0 l are extinct and one obtains the diffraction pattern depicted in figure 16.3 b. In this simple case, one can directly deduce the spin direction along c from the extinction of the 0 0 l reflections. Finally one can obtain the magnitude of the spin moment by comparing the intensities of the magnetic Bragg reflections with the intensities of the nuclear ones.

16.3 Magnetic Form Factors; Magnetisation Densities

For the magnetic structure determination we used a predetermined form factor, e.g. from Hartree-Fock calculations of electronic wave functions for the free atom [6]. Each atomic site was characterised by just one integral variable, the atomic magnetic moment. A scattering experiment can, however, give much more information, if sufficient Fourier components can be measured. We can then obtain the magnetisation density within each atom, which will show deviations from the density of the free atom due to solid state effects. Magnetisation density can be transferred to neighbouring atoms by covalent bonds. In metallic magnetic systems, the "magnetic" electrons are itinerant and the magnetisation density is strongly de-localised. We learned in chapter 3 that the magnetic form factor is the Fourier transform of

the magnetisation density of one atom. Therefore magnetic form factor measurements give us all the important information about such solid state effects.

To illustrate the kind of information we can obtain from such measurements let us quote some recent studies of high temperature superconductors or molecular magnets. There are theories of high temperature superconductivity, which propose a magnetic coupling mechanism for the Cooper-pairs. While no long range ordered magnetic structure is observed in the super-conducting state, dynamic magnetic fluctuations have been searched for with neutron scattering [7,8]. If one wants to detect, which atomic sites are susceptible to magnetism, one can study the magnetisation density induced in the material by an external magnetic field [9]. Molecular magnets are another active field of current interest, due to their very high potential for applications, but also due to fundamental interest. These are organic compounds, where the magnetism is not due to intra-atomic exchange ("Hund's rules"), as in the case of 3d or 4f metal ions, but due to the specific arrangement of bonds. The magnetisation density is distributed over many atomic sites. A neutron study of it's distribution can give us insight to the mechanism giving rise to the magnetic coupling and thus guide us in the search for new, optimised materials [10].

The most efficient way to measure weak magnetic signals is to use the interference between magnetic and nuclear scattering. Using this interference effect, we can even determine the phase of the magnetic structure factors, in addition to their magnitude. In this special case we have then solved the phase problem of crystallography.

We have learned in chapter 4 that this interference term can only be measured with polarised neutrons and cancels for unpolarised neutron diffraction. An interference between nuclear and magnetic scattering can only occur, if both types of scattering are allowed, i.e. the interference can only appear in the "non-spin flip" channel, if the nuclear as well as the magnetic structure factor are non- vanishing. To maximise the magnetic signal, one chooses a diffraction geometry as in figure 16.4, for which the magnetisation is perpendicular to the diffraction plane. This condition can be enforced by applying a strong magnetic field along this direction.

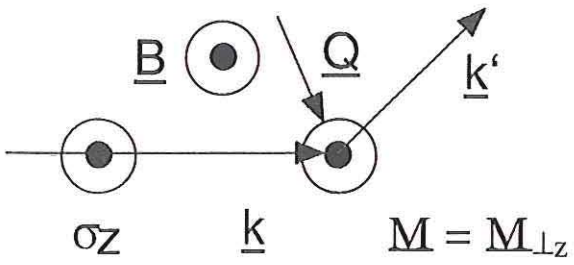

Fig. 16.4: Scattering geometry for measuring the interference term between nuclear- and magnetic scattering with polarised neutrons, but without polarisation analysis.

The relevant cross sections to measure the interference term in this geometry are:

$$\left(\frac{d\sigma}{d\Omega}\right)_{++} = \left|b(\underline{Q}) - \frac{\gamma_n r_o}{2\mu_B} M(\underline{Q})\right|^2 = b^2 - 2\frac{\gamma_n r_o}{2\mu_B} bM + \left(\frac{\gamma_n r_o}{2\mu_B}\right)^2 M^2 \qquad (16.8)$$

b,M real

$$\left(\frac{d\sigma}{d\Omega}\right)_{--} = \left|b(\underline{Q}) + \frac{\gamma_n r_o}{2\mu_B} M(\underline{Q})\right|^2 = b^2 + 2\frac{\gamma_n r_o}{2\mu_B} bM + \left(\frac{\gamma_n r_o}{2\mu_B}\right)^2 M^2 \qquad (16.9)$$

Besides the magnitude square of the amplitude for nuclear- and magnetic- scattering, respectively, these cross sections contain one term, in which a product of the magnetic- and nuclear- amplitudes appears. This interference term is especially useful, if the amplitude of magnetic scattering is much smaller than the amplitude of nuclear scattering:

$$\left|\frac{\gamma_n r_o}{2\mu_B} M\right| << |b| \qquad (16.10)$$

This is for example the case, if an external magnetic field induces a weak magnetisation in the paramagnetic state, when the ration between magnetic- and nuclear- amplitude is often below 10^{-3}. This implies that the contribution from magnetic scattering to the total signal is in the order of 10^{-6} or less, and thus no longer measurable. However, if we take data in two measurements, once with the neutron polarisation parallel and once anti-parallel to the magnetic field, we can determine the so-called *flipping ratio*:

$$R(\underline{Q}) = \frac{(d\sigma/d\Omega)_{++}}{(d\sigma/d\Omega)_{--}} = \frac{1 - \frac{\gamma_n r_o}{\mu_B}\frac{M}{b} + \ldots}{1 + \frac{\gamma_n r_o}{\mu_B}\frac{M}{b} + \ldots} \approx 1 - 4\frac{\gamma_n r_o}{2\mu_B}\frac{M(\underline{Q})}{b(\underline{Q})} \qquad (16.11)$$

Note that the polarisation of the scattered beam is known a priori (only non-spin flip processes can occur), so that the experiment is being done with a polarised beam, but without polarisation analysis. The flipping ration (16.11) depends linearly on the magnetic structure factor, instead of quadratic as the scattered intensity. Therefore much smaller values of the magnetic structure factor can be determined. If the nuclear structure factor is known (e.g. from a prior neutron diffraction experiment), these measurements of the flipping ratio give access to a highly precise determination of the phase and magnitude of the magnetic structure factor.

An example is given by the measurement of the form factor of chromium. Cr is the archetypal itinerant antiferromagnet. Therefore the magnetisation density is very de-localised. As a consequence, the magnetic form factor drops extremely rapidly with increasing momentum transfer. In a recent synchrotron x-ray experiment, we could demonstrate that this form factor is spin only [11]. However, in a polarised neutron diffraction experiment we could show [12], that a magnetisation induced in the paramagnetic state by an external magnetic field is much more localised around the individual atoms. Therefore, the field-induced form factor decreases much slower, compare figure 16.6. It has a large contribution (60 %) of orbital angular momentum, quite in contrast to the form factor in the ordered state. By means of a Fourier transform or with the so-called *Maximum Entropy Method* a magnetisation density distribution within the unit cell can be reconstructed (compare figure 16.7). Such data are of utmost importance to test and improve modern band theories, such as the fully relativistic *density functional theory* and thus to obtain a better understanding of the metallic state.

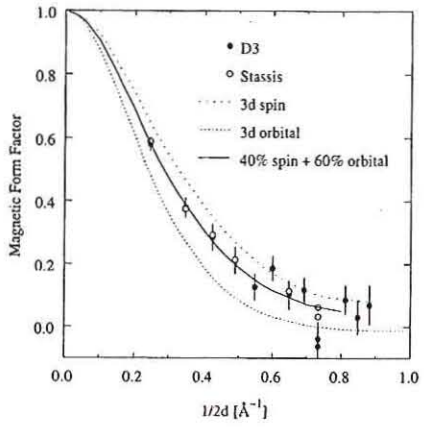

Fig. 16.6: Induced magnetic form factor of Cr for a field of 4.6 T. Open and filled circles are experimental values, the Lines are calculations for spin-, Orbital- and total moment.

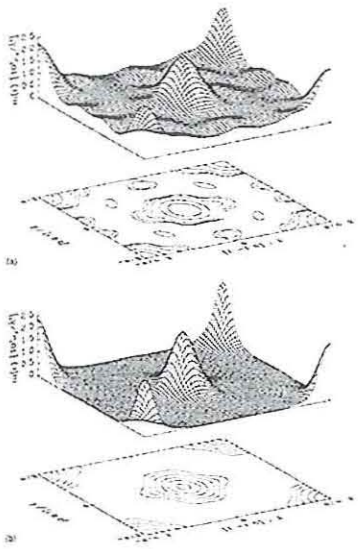

Fig. 16.7: Projection of the induced magnetisation density distribution onto the <110> plane. above: Fourier transform Below: Maximum entropy reconstruction

16.4 Magnetic Phase Transitions

Phase transitions can occur between different magnetic phases as a function of various thermodynamic parameters, such as magnetic field, temperature or pressure. Here we will restrict ourselves to the most simple case of a transition from a low temperature ferromagnetic (FM) or antiferromagnetic (AF) phase to a high temperature paramagnetic (PM) phase. First, we will discuss this phenomenon qualitatively, then introduce the quantitative description and finally show just one example of a neutron diffraction study.

The magnetic long range order discussed in section 16.2 can only be stable, as long as the thermal energy k_BT is small enough compared to the exchange interactions giving rise to magnetic order. At sufficiently high temperatures, entropy wins and the magnetic moments

fluctuate in space and time. A phase transition has occurred at a critical temperature, called *Curie temperature* T_C for ferromagnets or *Néel temperature* T_N for antiferromagnets, from a long range ordered state at low temperatures to a paramagnetic high temperature phase. The two phases are characterised by an *order parameter*, such as the magnetisation for ferromagnets or the sublattice magnetisation for antiferromagnets. In the paramagnetic phase this order parameter vanishes, while in the low temperature phase it increases towards a saturation value, when the temperature is lowered. Depending on whether the order parameter changes discontinuously or continuously at the critical temperature, the phase transition is of *first-* or *second- order*, respectively. At least for local moment systems, the magnetic interactions and moments are still present in the paramagnetic phase. Therefore above the critical temperature, magnetic correlations persist. This magnetic short range order fluctuates in time and extends over regions with characteristic linear dimensions, called the *correlation length*. When we decrease the temperature in the paramagnetic phase towards the transition temperature, the correlation length increases. Larger and larger regions develop which show short range order characteristic for the low temperature phase. The larger these correlated regions, the slower the fluctuation-dynamics. At the critical temperature of a second order phase transition, the correlation length and the magnetic susceptibility diverges, while the dynamics exhibits a critical slowing down.

Besides the magnetic phase transitions, there exist also structural phase transitions. However, experiments on magnetic model systems provided the basis for our modern understanding of this complex co-operative effect. Th reason is that magnetic model systems can often be described by some very simple Hamiltonian, such as the Heisenberg (16.12), the x-y (16.13) or the Ising model (16.14), depending whether the system is isotropic, has a strong planar- or a strong uniaxial anisotropy, respectively:

Heisenberg: $$H = \sum_{i,j} J_{ij} \underline{S}_i \cdot \underline{S}_j \qquad (16.12)$$

x-y: $$H = \sum_{i,j} J_{ij} \left(S_{ix} S_{jx} + S_{iy} S_{jy} \right) \qquad (16.13)$$

Ising: $$H = \sum_{ij} J_{ij} S_{iz} S_{jz} \qquad (16.14)$$

Here, J_{ij} denotes the exchange constant between atoms i and j, $S_{i\alpha}$ is the component α (=x, y or z) of the spin operator $\underline{S}_i$ of atom i. If the Hamiltonian depends on three- (Heisenberg-model, 16.12), two- (x-y-model, 16.13) or one- (Ising-model, 16.14) components of the spin operator, one can define a three-, two- or one dimensional order parameter. Moreover, there are crystal structures, where the magnetic atoms are aligned along well separated chains or planes, so that besides the usual three dimensional lattice, there exist magnetic model systems in one and two space dimensions. Finally, depending on whether the system shows covalent or metallic bonding, the exchange interactions can be short- or long ranged, respectively.

The experimental investigation of continuous (second order) phase transitions in many magnetic model systems revealed a quite surprising behaviour in a critical region (a temperature range around the ordering temperature with a width of by and large 10 % of the ordering temperature) close to the phase transition: independent of the precise nature of the system under investigation, the phase transition shows universal behaviour. These experimental results laid the foundations for the formulation of a modern theory of second order phase transitions, the *renormalisation group theory*.

If we define a *reduced temperature* as

$$\tau = \frac{T - T_C}{T_C} \tag{16.15}$$

then all relevant thermodynamical parameters show a power-law behaviour close to the second order phase transition:

specific heat:	$c_H \propto \tau^{-\alpha}$	(16.16)
order parameter ($T<T_C$):	$m \propto (-\tau)^{\beta}$	(16.17)
susceptibility:	$\chi \propto \tau^{-\gamma}$	(16.18)
correlation length:	$\xi \propto \tau^{-\nu}$	(16.19)

The surprising discovery was that all systems can be classified into *universality classes*. Within a given universality class, the values of the *critical exponents* α, β, γ and ν are the

same and do not depend on the detailed nature of the system. Moreover, the critical exponents for a given system are not independent, but fulfil certain *scaling relations*, see e.g. [13]. To which universality class a system belongs is determined by three criteria:

Dimensionality of the order parameter n

Space dimensionality d

Range of the interactions (long- or short ranged)

Table 16.1 lists values of the critical exponents for some universality classes.

n	1	1	2	3
d	2	3	3	3
α	0	0.106	-0.01	-0.121
β	0.125	0.326	0.345	0.367
γ	1.75	1.238	1.316	1.388
ν	1	0.631	0.669	0.707

Tab. 16.1: Values of the critical exponents for a few universality classes according to [13].

As an example we have selected a rather unusual magnetic phase transition, which turns out to be of first order (discontinuous) and thus cannot be classified by the above criteria. Let us briefly discuss the AF-PM phase transition of MnS_2 [14].

The magnetic semiconductor MnS_2 orders with the type-III antiferromagnetic structure on the fcc lattice with the wave vector $\underline{q}$=(1,1/2,0) (compare (16.3)). The antiferromagnetic phase transition at T_N = 48.2 K is found to be of first order, quite in contrast to the classical behaviour for such a compound. We performed a neutron scattering study in a search for the driving mechanism. Figure 16.8 shows a contour plot of the magnetic diffuse scattering in the (001) plane in the paramagnetic phase about 17K above T_N. One can clearly see, how the magnetic diffuse scattering is concentrated at the positions (1,1/2,0), (1,3/2,0), (3/2,1,0) etc, where in the long range ordered phase the magnetic Bragg reflections appear. However, a closer examination shows that the positions at which the diffuse scattering is centred, are not the rational positions listed above.

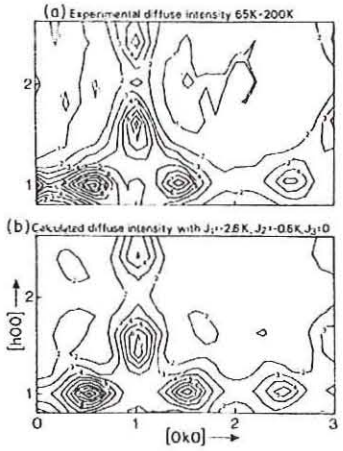

Fig. 16.8: Contour plot of the magnetic diffuse scattering intensity of MnS_2 in the (001) plane at 65 K. Above: measurement; below: calculation

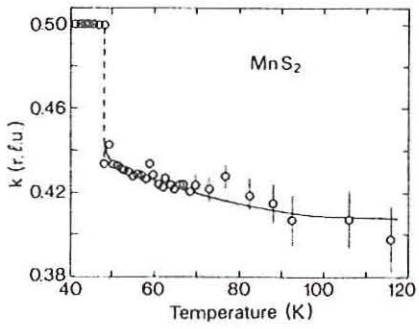

Fig. 16.9: Temperature variation of the incommensurate component.

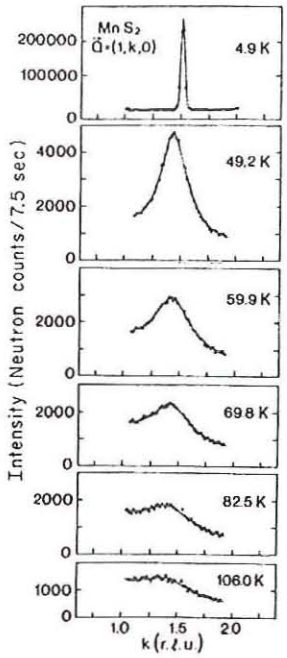

Fig. 16.10: Magnetic diffuse neutron scattering of MnS_2 in reciprocal lattice scans parallel to the modulation vector.

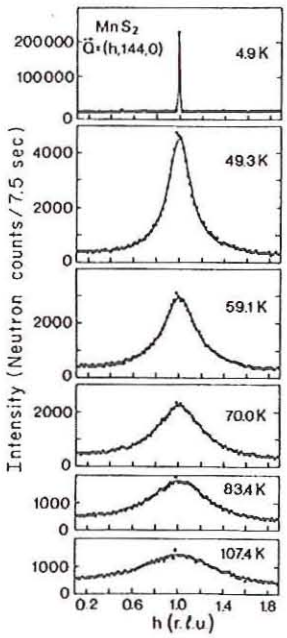

Fig. 16.11: Magnetic diffuse neutron scattering of MnS_2 in reciprocal lattice scans perpendicular to the modulation vector.

Figures 16.10 and 16.11 show the magnetic diffuse neutron scattering of MnS_2 at different temperatures above T_N and the magnetic Bragg peak at 4.9 K (topmost figure). We can clearly observe, how with decreasing temperature the diffuse scattering becomes sharper in reciprocal space and how the peak intensity increases strongly. However, for scans along (1,k,0) the diffuse scattering is not centred at the low temperature Bragg position, while it is centred for the perpendicular scans in the (h,k,0) plane. The magnetic short range order is "*incommensurate*" with the lattice. This means that the periodicity observed in the diffuse magnetic scattering is not just a simple rational multiple of the chemical unit cell periodicity. Figure 16.9 shows the temperature variation of the incommensurate component of the vector at which the diffuse scattering is centred. Note the jump characteristic for a first order transition. Figure 16.9 demonstrates that we can understand the paramagnetic-antiferromagnetic phase transition in MnS_2 as a transition from incommensurate short range order to commensurate long range order. Now it is well established that such "*lock-in-transitions*" are of first order, which explains the unusual behaviour of MnS_2. The problem remains which interaction leads to the shift of the diffuse peak as compared to the Bragg reflection. This question can be solved with model calculations, such as the ones depicted in figure 16.8 [14]. It turns out that an anisotropy term in the Hamiltonian can give rise to the observed effect.

Finally we want to show an example for a true "classical" second order transition, the PM-AF transition in MnF_2. In this case, we have performed the measurements with high energy synchrotron x-rays due to the better reciprocal space resolution as compared to neutrons [15]. Figure 16.12 shows a double logarithmic plot of the reduced sublattice magnetisation m ($m = M/M_S$, where M_S is the saturation value of the magnetisation) versus the reduces temperature τ, defined in eq. (16.15). In this plot, the data points nicely line up along a straight line, corresponding to a power law behaviour as expected from (16.7). The critical exponent β of the sub-lattice magnetisation can be obtained to great precision: $\beta = 0.333$ (3), corresponding roughly to the exponent expected for an Ising system (n=1, d=3) according to table 16.1. However, the calculated and measured value do not quite coincide, at least to within two standard deviations, which demonstrates that the precise values of the critical exponents are still not very well established.

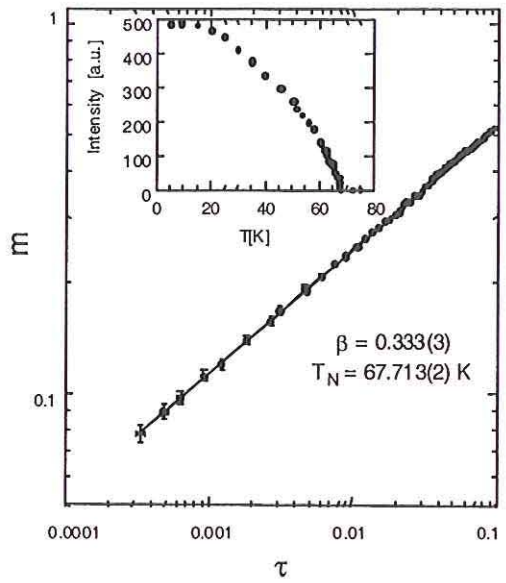

Fig. 16.12: Magnetic Bragg diffraction from MnF_2. The inset shows the temperature dependence of the intensity of the magnetic 300 reflection from 5 to 80K. In the main graph is plotted the reduced sub-lattice magnetisation as a function of reduced temperature on a double logarithmic scale together with a fit employing a power-law function.

16.5 Summary

We have given a few examples of the applications of neutron scattering in magnetism. We have seen how neutrons can be used to investigate the magnetisation density distribution on an atomic level. Besides the rather new technique of magnetic x-ray scattering, no other method can provide the same information on magnetic structure and magnetisation density. Neutrons are ideally suited to study magnetic phase transitions, which are model examples of co-operative phenomena in many body systems. Unfortunately, we were not able to cover other subjects, such as the important fields of magnetic excitations or thin film magnetism. Neutron scattering is the technique to measure spin wave dispersion relations used to determine magnetic interaction parameters (exchange interaction, anisotropy) – see chapter on excitations. In itinerant systems, the transition from collective spin wave like excitations to single particle like "Stoner" excitations could be observed with neutrons. Currently, more "exotic" excitations are in the centre of attention, such as the "resonance peak" in high

temperature superconductors, or excitations in low dimensional magnets. Finally, thin film magnetism is of high current interest due to it's applications in "magnetoelectronics". In this field, neutrons provide the crucial information about the magnetic structure and morphology of thin film devices, compare chapter on reflectometry. While we could not give a comprehensive review, the Jülich group is active in all these fields and we refer to our web page [16] for further information.

References

[1] J. Jensen & A. R. Mackintosh, "Rare Earth Magnetism", Clarendon Press, Oxford (1991)

[2] V. F. Sears, Neutron News 3 (1992) 26

[3] G. L. Squires, "Thermal Neutron Scattering", Cambridge University Press, Cambridge (1978)

[4] S. W. Lovesey, "Theory of Neutron Scattering from Condensed Matter", Clarendon Press, Oxford (1987)

[5] J. Rossat-Mignod, "Magnetic Structures" in: K. Sköld, D. L. Price: "Neutron Scattering", Academic Press, New York (1987)

[6] A. J. Freeman & R. E. Watson, Acta Cryst. 14 (1961), 231

[7] Th. Brückel, H.Capellmann, W. Just, O. Schärpf, S. Kemmler-Sack, R. Kiemel & W. Schäfer; Europhysics Letters 4 (1987) 1189

[8] B. Keimer et al, Physica B 234-236 (1997), 821

[9] J.X. Boucherle et al; Physica B192 (1993), 25

[10] Y.Pontillon et al, Physica B 267-268 (1999), 51

[11] J. Strempfer, Th. Brückel, W. Caliebe, A. Vernes, H. Ebert, W. Prandl & J.R. Schneider; Eur. Phys. J. B14 (2000), 63

[12] J. Strempfer, Th. Brückel, G. J. McIntyre, F. Tasset, Th. Zeiske, K. Burger, W. Prandl, Physica B 267 - 268 (1999), 56

[13] M.F. Collins "Magnetic Critical Scattering", Oxford University Press, Oxford 1989

[14] T. Chattopadhyay, Th. Brückel & P. Burlet; Phys. Rev. B44 (1991), 7394

[15] J. Strempfer, Th. Brückel, U. Rütt, J.R. Schneider, K.-D. Liss & Th. Tschentscher; Acta Cryst. A52 (1996), 438

[16] http://www.fz-juelich.de/iff/Institute/ism/

17. Translation and Rotation

M. Prager

17.1 Introduction

Atomic and molecular motions in liquids and solids are driven by the thermal energy of the sample. Fluctuations may concentrate kinetic energy on one atom, which then is able to cross a potential barrier into a new site. Such transport or orientational jumps occur randomly and give rise to quasielastic scattering.

At low temperature the classical motion dies out on the timescale of neutron spectrometers. The (classical) potentials are still present, however. They now characterise the quantummechanical excitations of the lattice object: librations and tunnelling. Theories used are mostly single particle or mean field theories.

By studying both, classical quasielastic scattering and quantum excitations a detailed information on the shape and the strength of potential barriers can be obtained since neutron properties allow a resolution in space and time. If the crystal structure of a material is known one can calculate the potentials from fundamental intermolecular interactions. The concept of "transferable pair interactions" may finally allow to predict potentials of new materials.

Stochastic motions occur in many materials some of which attract technical interest. Hydrogen in metals is used for energy storage, microporous framework structures as zeolithes offer catalytically active surfaces, polymers can aggregate to secondary structures like micelles with sometimes technically interesting properties. They mix or phase separate by diffusion. Adsorbates, intercalates, molecular and liquid crystals, matrix isolated species and liquids may be studied this way. It was especially the invention of high resolution neutron scattering instruments (since ~1972) which gave an impact to this topic which still holds.

17.1.1 Gaussian approximation

The scattering function of a rare gas can be calculated exactly on the basis of plane wave functions and transition matrix elements. It happens to have the shape of a Gaussian. With $\beta = \frac{1}{k_B T}$ and the recoil energy $E_r = \frac{\hbar^2 Q^2}{2M}$

$$S(Q,\omega) = (\frac{\beta}{4\pi E_r})^{\frac{1}{2}} exp(-\frac{\beta}{4E_r}(\hbar\omega - E_r)^2) \tag{17.1}$$

Fouriertransformation in space and time yields the correlation function (Chapter 5):

$$G_s^{cl}(r,t) = (2\pi\sigma^2(t))^{-\frac{3}{2}} exp(-\frac{r^2}{2\sigma^2(t)}) \tag{17.2}$$

with

$$\sigma^2(t) = t(t - i\hbar\beta)/M\beta \tag{17.3}$$

σ^2 is related to the mean square displacement. The theory yields the generally valid relation

$$\langle r^2(t)\rangle = 3\sigma^2(t) = 4\pi \int_o^\infty r^2 G_s^{cl}(r,t)dr \tag{17.4}$$

In the gaussian approximation one uses this relation also for any other translational or rotational motion despite they have time dependences $\sigma(t)$ different to that of a rare gas. The problem is thus reduced to determine the mean square displacement of a dynamical process. The justification of the gaussian approximation is that it works.

17.2 Translation

The simplest translation is that of a rare gas. Hydrogen on interstitial sites in a metal is often treated as a lattice gas. Self diffusion close to the melting point via vacancies has a similar character. Atomic liquids represent the simplest example for diffusion. But the most common liquids are made up by molecules which show additional rotational degrees of freedom.

17.2.1 Macroscopic diffusion

Diffusion of a monoatomic liquid obeys macroscopically Fick's law

$$\frac{\partial n(\underline{r},t)}{\partial t} = D\nabla^2 n(\underline{r},t) \tag{17.5}$$

with the number density $n(\underline{r},t) \sim G_s(r,t)$ and the diffusion constant D. For isotropic diffusion

$$\nabla^2 = \frac{\partial^2}{\partial r^2} + \frac{2}{r}\frac{\partial}{\partial r} \tag{17.6}$$

in spherical coordinates. $G_s(r,t)$ from (17.2) is a solution of 17.5 if

$$\begin{aligned} \frac{d}{dt}\sigma^2(t) &= 2D \\ \sigma^2(t) &= 2D \mid t \mid + c \end{aligned} \tag{17.7}$$

For long times (small energy transfer $\Delta\hbar\omega$) c can be neglected and Fourier-transformation (FT) in space and time yields the scattering function

$$S(Q,\omega) = \frac{1}{\pi\hbar}\frac{DQ^2}{\omega^2 + (DQ^2)^2} \tag{17.8}$$

Both, half width and scattering intensity of this Lorentzian allow a determination of the diffusion coefficient D via

$$\begin{aligned} \Gamma &= 2\hbar DQ^2 \\ \frac{1}{S(Q,0)} &= \pi\hbar DQ^2. \end{aligned} \tag{17.9}$$

17.2.2 Diffusion, microscopic approach: Langevin equation

For atomic distances and short times the above continuum theory has to be modified. A microscopic model leads to the Langevin equation. A particle of mass M in a thermal bath is exposed to stochastic kicks $\underline{F}(t)$. After the kick it is slowed down by internal friction proportional to its velocity with the viscosity η as proportionality factor.

$$\begin{aligned} M\frac{d\underline{v}}{dt} &= -\frac{\underline{v}}{B} + \underline{F}(t) \\ \frac{d\underline{v}}{dt} &= -\eta\underline{v} + \underline{f}(t) \end{aligned} \tag{17.10}$$

To keep the energy of the system constant the two terms on the right hand side are related by the fluctuation-dissipation theorem

$$\langle f(t)f(0)\rangle = \frac{2k_BT}{M}\eta\delta(t) \tag{17.11}$$

which means in words, that the stochastic force takes its energy from friction losses. Integration of (17.10) yields

$$\underline{v}(t) = exp(-\eta t)\int_{-\infty}^{t} exp(\eta t')f(t')dt' \tag{17.12}$$

This result is used to calculate the velocity-velocity correlation function. For one component it is

$$\begin{aligned} \langle v(t)v(0)\rangle &= exp(-\eta t)\langle\int_{-\infty}^{t} dt'\int_{-\infty}^{0} dt''exp(\eta t')f(t')exp(\eta t'')f(t'')\rangle \\ &= exp(-\eta t)\int_{-\infty}^{t} dt'\int_{-\infty}^{0} dt''\langle f(t')f(t'')\rangle exp(\eta(t'-t'') \end{aligned}$$

and using (17.11) (factor 3 for vectors)

$$\langle\underline{v}(t)\underline{v}(0)\rangle = \frac{3k_BT}{M}exp(-\eta t) \tag{17.13}$$

Integrating the velocity-velocity correlation function yields the mean square displacement [1]

$$\begin{aligned} \gamma(t) &= \frac{1}{3}\int_0^t (t-t_1)\langle\underline{v}(t_1)\underline{v}(0)\rangle dt_1 \\ &= \frac{1}{3}\int_0^t (t-t_1)\frac{3k_BT}{M}exp(-\eta t)dt_1 \\ &= \frac{k_BT}{M\eta}\left(t - \frac{1}{\eta}(1-exp(-\eta t))\right) \\ &= D(t-\tau_r(1-exp(-\frac{t}{\tau_r})) \end{aligned} \tag{17.14}$$

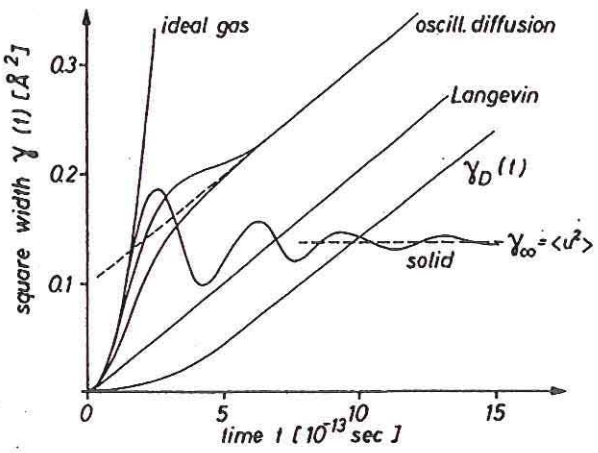

Figure 17.1: Mean square displacement $\gamma(t)$ of a Gaussian self correlation function for the ideal gas, Fick's (oscill.) diffusion, Langevin dynamics. For comparison the case of an atom in a solid is presented too.

The fig. 17.1 summarizes the mean square displacements of various translational motions in Gaussian approximation. We consider the limits:
$t \gg \tau_r$: The exponential term can be neglected. Compared to Fick's law the Langevin equation yields a retardation of the diffusion process.
$t \ll \tau_r$: having expanded the exponential function one gets $\gamma(t) = \frac{k_B T}{2M} t^2$. The mean square displacement is proportional to t^2 (free flight) like in the ideal gas.

As an example we take water [2]. The fig.17.2 shows the broadening of the Lorentzian with Q^2. From the initial slope one gets the diffusion constant $D = 1.9 \cdot 10^{-5} \frac{cm^2}{sec}$.

17.2.3 Jump diffusion on a Bravais lattice

Diffusion in the solid state occurs in many cases by jumps on interstitial sites. That's why the mobile species can and is called a lattice gas. The simplest system is hydrogen in fcc palladium. Hydrogen occupies octahedral sites. All sites are equivalent and form a cubic Bravais lattice with Z=6 neighbour sites (fig. 17.3).

At low concentration all neighbour sites are empty. We call $P(\underline{r}, t)$ the probability of finding a proton at time t on site $\underline{r}$. The change of population is the difference between

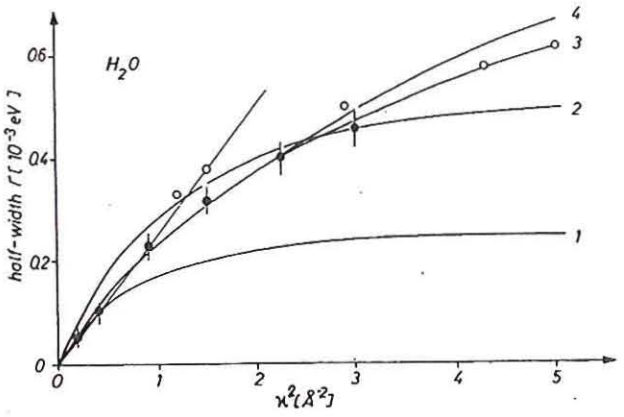

Figure 17.2: Full width at half maximum of the Lorentzian for water at T=300K. The diffusions coefficient follows from the initial slope. The best description at large Q is given by a jump model with a continuous distribution of jump lengths.

all jumps into and out off the site and is determined by the rate equation

$$\frac{\partial}{\partial t}P(\underline{r},t) = \frac{1}{Z}\sum_{k=1}^{Z}\frac{1}{\tau_k}\left(P(\underline{r}+\underline{s}_k,t) - P(\underline{r},t)\right) \tag{17.15}$$

$\underline{s}_k$ and τ_k represents possible jump vectors and residence times connecting the actual hydrogen site with possible neighbour sites. If all sites are equivalent there is a unique characteristic residence time $\tau = \tau_k$. $P(\underline{r},t)$ represents directly the correlation function $G_s(\underline{r},t)$. With the initial condition

$$P(\underline{r},0) = \delta(\underline{r}) \tag{17.16}$$

the infinite system of coupled differential equations (17.15) is solved by Fourier transformation. FT of with respect to space leads to the intermediate scattering function

$$\frac{\partial}{\partial t}I(\underline{Q},t) = \frac{1}{Z\tau}\sum_{k=1}^{Z}\left(exp(-i\underline{Q}\underline{s}_k)I(\underline{Q},t) - I(\underline{Q},t)\right) \tag{17.17}$$

The initial conditions $I(\underline{Q},0) = 1$ means that the proton exists somewhere in the sample. We make the exponential ansatz

$$I(\underline{Q},t) = exp(-f(\underline{Q})\frac{t}{\tau}) \tag{17.18}$$

with

$$f(\underline{Q}) = \frac{1}{Z}\sum(1 - exp(-i\underline{Q}\underline{s}_k)) \tag{17.19}$$

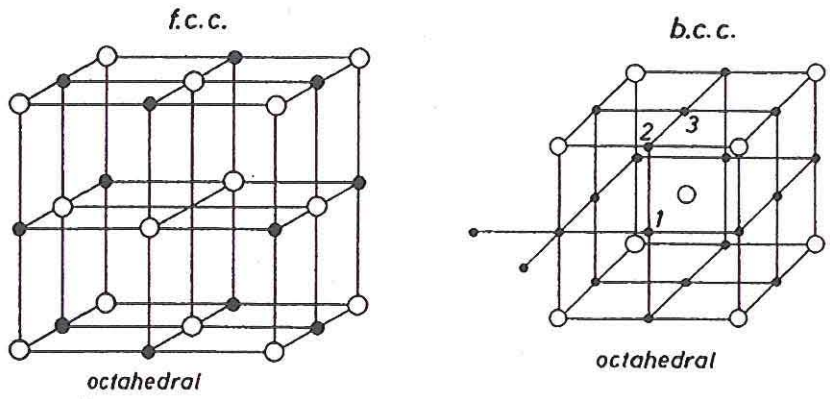

Figure 17.3: Left: Unit cell of fcc-Pd (○) with octahedral hydrogen interstitial sites (●). Right: octahedral sites in a bcc lattice for comparison.

FT in time yields as scattering function a pure Lorentzian

$$S(\underline{Q},\omega) = \frac{1}{\pi}\frac{\frac{f(\underline{Q})}{\tau}}{\omega^2 + (\frac{f(\underline{Q})}{\tau})^2} \tag{17.20}$$

The lack of an elastic term means, that the proton never returns to its starting point.

The scattering function of a polycrystal is obtained by averaging over all crystal orientations

$$S(\underline{Q},\omega) = \frac{1}{\pi}\frac{\Gamma}{\omega^2 + \Gamma^2} \tag{17.21}$$

For small momentum transfers $\underline{Q}\underline{s}_k << 1$ one can expand $f(\underline{Q})$ and obtains

$$\Gamma = 2Q^2\frac{s^2}{6\tau} = 2Q^2D \tag{17.22}$$

The second relation allows an interpretation of the macroscopic diffusion coefficient D of (17.5) by the microscopic jump rate. While for small Q the macroscopic behaviour with the Q^2 dependence of the linewidth is observed the data at large Q show the elementary step of a diffusion process. The fig. 17.4 shows results for H in Pd.

Transport jumps are thermally activated and follow an Arrhenius law

$$\tau = \tau_0 exp(-\frac{E_a}{k_BT}) \tag{17.23}$$

From this relation the barrier height between neighbour sites is obtained from the temperature dependence of the linewidth $\Gamma \sim \frac{1}{\tau}$.

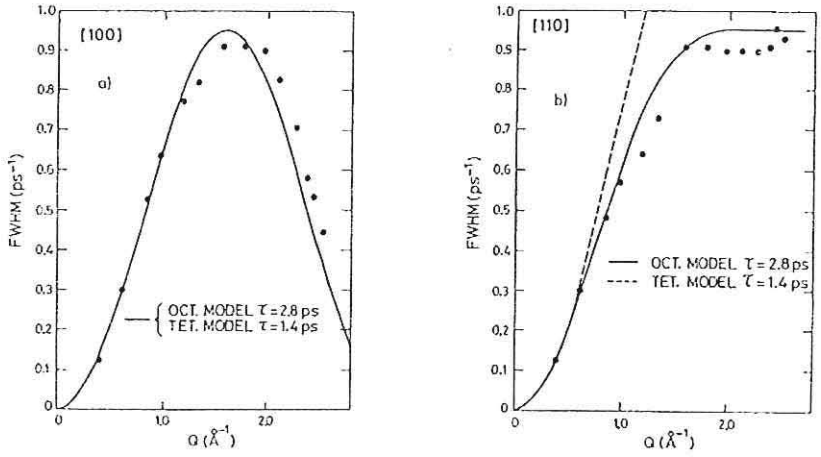

Figure 17.4: Q-dependence of the quasielastic linewidth in a PdH_x single crystal in (100) und (110) direction. The data confirm a diffusion on octahedral interstitial sites.

17.2.4 More complex cases

More than one sublattice

For bcc metals (fig. 17.3), intermetallic compounds or metallic glasses one finds non equivalent hydrogen sites with different coordination numbers and jump rates. In case of bcc lattices protons may occupy octahedral or different types of tetrahedral sites. The scattering function requires the integration over the many possible different starting configurations. $S(Q,\omega)$ consists now of a number of Lorentzians with different widths and partly rate dependent intensities [3]. The formalisme is more complex but basically identical.

Blocking

With increasing hydrogen concentration the diffusion changes since some jump directions may be blocked by a hydrogen neighbour. "Blocking" leads also to an increased probability of back jumps, since the starting site is with certainty empty after the jump.

Phonon-assisted Tunnelling

In some cases like $NbH_{0.02}$ the temperature dependence of the diffusion coefficient deviates from classical behaviour. The observation of an increased jump rate at low temperature lead to the idea of "phonon-assisted tunnelling": phonons of suited symmetry can increase temporarily the distance between the atoms of the host lattice which determine the jump barrier. The decreased barrier increases the probability for quantum mechanical tunnelling of the proton and thus accelerates the diffusion process.

Diffusion in the presence of traps

Hydrogen traps in a metal lattice can be created by chemical impurities. In a lattice with traps the proton dynamics splits into a local motion around the trap and a diffusion between traps. A corresponding two state model [3] yields a scattering function consisting of 2 Lorentzians. At small Q diffusion, at large Q jumps around the trap dominate scattering. Since jumps around a trap are qualitatively very similar to rotations of a molecule around its center of mass the same theory can be applied to get classical jump rates and local librations.

17.2.5 Librations

Usually the 3-dimensional potential of a proton at equilibrium site is expanded harmonically and completed by anharmonic terms consistent with symmetry requirements. It determines its eigenenergies. Vice versa the librations allow to deduce the potential. This information refines the potential beyond the pure knowledge of the barrier height obtained from QNS.

17.2.6 Translational tunnelling

At low temperatures the proton localises in a pocket of the potential. If the barrier between such pockets is weak, the proton wavefunctions of neighbouring pockets overlap and the degenerate librational states split into tunnelling substates. This translational tunnelling is formally almost equivalent to the rotational tunnelling to be described below.

$NbO_{0.001}H_{0.001}$ (Fig. 17.5) represents an especially clear case. The oxygen defect distorts the lattice locally and makes exactly two hydrogen sites - almost - equivalent. Almost: the presence of the particle itself in one minimum introduces an asymmetry. Thus one has to calculate the scattering function of an atom in an asymmetric double minimum [3]. Wave functions Ψ are set up from basis functions $|01>$ and $|10>$ which describe the two possible proton sites. The two configurations can transform into each other by tunnelling due to a finite tunnel matrix element t. The corresponding Schrödinger equation $H\Psi = E\Psi$ in matrix form leads to the eigenvalues problem (symmetric case assumed for simplicity!)

$$\begin{pmatrix} -\lambda & t \\ t & -\lambda \end{pmatrix}$$

The characteristic polynom yields eigenvalues $\lambda_{1,2} = \pm t$. They are connected with the totally symmetric eigenvectorr $\underline{e}^{(1)} = \frac{1}{\sqrt{2}}(|\ 1,0> + |\ 0,1>)$ and the antisymmetric eigenvector $\underline{e}^{(2)}\frac{1}{\sqrt{2}}(|\ 1,0> - |\ 0,1>)$, respectively. Under the assumption of a special

shape of the double minimum potential, e.g. [4],

$$V(x) = x^4 - ax^2 \tag{17.24}$$

one can relate the phenomenological tunnel matrix element t with the parameters of the potential. The observed tunnel transition is $\hbar\omega = 2t$. The full calculation yields for a polycrystalline sample a scattering function

$$S_{inc}(Q,\omega) = \frac{1}{2}(1 - j_0(Qd))F\frac{1}{\pi}\frac{\Gamma}{(\omega - 2t)^2 + \Gamma^2} \tag{17.25}$$

Here F is a complex expression of the order 1, which takes into account the different and temperature dependent populations of the two minima in the asymmetric potential. This

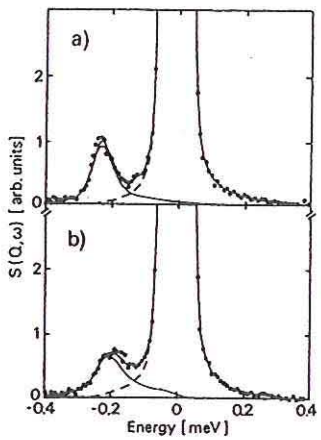

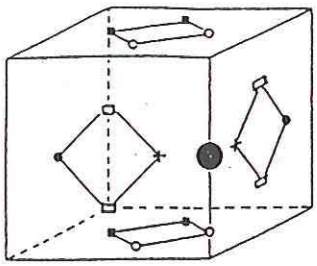

Figure 17.5: Left: Tunnel spectrum of H trapped by O in $Nb(OH)_{0.002}$. T=0.1K. Instrument: IN6, ILL. Top: superconducting, bottom: normal conducting state.
Right: Possible hydrogen-sites around an oxygen-defect (•). Tunnelling can occur between each equivalent sites, e.g. ○.

scattering function is almost identical with that of an $O-H$ group which can assume two equilibrium orientations. It is more or less a semantic question to call a tunnel process translational or rotational.

With the outlined matrix technique it is also possible to get the tunnelling sublevel structure of librational states of more complex potential geometries.

17.3 Rotation

Molecules represent - in first approximation rigid - ensembles of atoms and allow rotation as new degree of freedom. In the simplest approach the environment is represented as a potential which determines the single particle excitations. The potential must show at least the symmetry of the molecule. - A classical motion is fully characterized by the motion of a single proton.

17.3.1 Jump rotation: methyl group in a 3-fold potential

Often the rotational potential is rather strong and forces the molecule to stay most time in an equilibrium orientations. The dynamics consists in this case of jumps between equivalent orientations. We call the atomic positions $\underline{r}_j$, the average time between two jumps τ and neglect the jump time itself. The self correlation function $G_s(\underline{r},t)$ is the conditional probability of finding an atom at time t at site $\underline{r}$ if it was at time t=0 at site $\underline{r}$=0.

$$G_s(\underline{r},t) = \sum_{j=1} N p_j(t) \delta(\underline{r} - \underline{r}_j) \tag{17.26}$$

$p_j(t)$ is the occupation probability of site j at time t. The sum averages over all possible starting conditions = sites of the atom. For uncorrelated jumps the occupation probabilities obey a finite system of coupled differential equations, the so-called rate equations

$$\frac{d}{dt} p_j(t) = \frac{1}{\tau} \left(\frac{1}{N} \sum_{\lambda=1}^{N} p_\lambda(t) - p_j(t) \right) \tag{17.27}$$

The first term describes the all possible jumps into a site, the second the jumps out of this site. For simplicity it is assumed that all sites show the same population and that jump times between any two sites are identical. The considered atom is in the sample:

$$\sum_{j=1}^{N} p_j = 1 \tag{17.28}$$

A simple example is the methyl group. Here N=3 and proton position are $\underline{r}_1$ =(0,0,0)d, $\underline{r}_2$ =(1,0,0)d, $\underline{r}_3 = (\frac{1}{2}, \frac{\sqrt{3}}{2}, 0)$d with the proton proton distance d=1.76Å. With $\nu = \frac{1}{\tau}$ the rate equation for site 1 is

$$\frac{d}{dt} p_1 = -\nu p_1 + \frac{\nu}{2} p_2 + \frac{\nu}{2} p_3 \tag{17.29}$$

and m.m. with cyclic permutation. The ansatz ($\underline{p} = (p_1, p_2, p_3)$)

$$\underline{p} = \underline{q} exp(\lambda t) \tag{17.30}$$

leads to the eigenvalue problem

$$\lambda \underline{q} = \begin{pmatrix} -\nu & \frac{\nu}{2} & \frac{\nu}{2} \\ \frac{\nu}{2} & -\nu & \frac{\nu}{2} \\ \frac{\nu}{2} & \frac{\nu}{2} & -\nu \end{pmatrix} \underline{q}$$

The eigenvalues and eigenvectors of this 3x3 matrix are

$$\lambda_1 = 0; \lambda_{2/3} = -\frac{2}{3}\nu$$

$$\underline{q}_1 = \frac{1}{3}(1,1,1); \underline{q}_2 = \frac{1}{3}(1,\epsilon,\epsilon^*), \underline{q}_3 = \frac{1}{3}(1,\epsilon^*,\epsilon) \tag{17.31}$$

with phasefactors $\epsilon = exp(\frac{2\pi}{3})$ and ϵ^* complex conjugated. Initial conditions are equal population. Including normalization yields

$$p_1(t) = \frac{1}{3} + \frac{2}{3}exp(-\frac{3}{2}\nu t) \tag{17.32}$$

$$p_2(t) = p_3(t) = \frac{1}{2}(1 - p_1(t)) \tag{17.33}$$

For t=∞ all sites are indeed equally populated. The corresponding average proton density distribution represents the jump geometry. The density distribution is also dynamically stable, since jumps into and out off the site are in equilibrium.

Omitting the index at p the first term of the self correlation function is for $\underline{r}_1$

$$G_s(\underline{r},t) = \delta(\underline{r})p(t) + \frac{1}{2}\left(\delta(\underline{r} - \underline{r}_{12}) + \delta(\underline{r} - \underline{r}_{13})\right)(1 - p(t)) \tag{17.34}$$

The FT of $G_s(\underline{r},t)$ with respect to space yields the intermediate scattering function

$$I_s(\underline{Q},t) = p(t) + \frac{1}{3}(1 - p(t))A(\underline{Q}) \tag{17.35}$$

Using abbreviations $\underline{r}_{12} = \underline{r}_2 - \underline{r}_1$ the structure factor is

$$A(\underline{Q}) = cos(\underline{Q}\underline{r}_{12}) + cos(\underline{Q}\underline{r}_{23}) + cos(\underline{Q}\underline{r}_{31}) \tag{17.36}$$

FT with respect to time yields the scattering function of a single crystal. It depends on the orientation of the methyl group, $\underline{r}_{ij}$, with respect to the scattering vector $\underline{Q}$

$$S_{inc}(\underline{Q},\omega) = (\frac{1}{3} + \frac{2}{9}A(\underline{Q}))\delta(\omega) + (\frac{2}{3} - \frac{2}{9}A(\underline{Q}))\frac{1}{\pi}\frac{\frac{3}{2}\nu}{\omega^2 + (\frac{3}{2}\nu)^2} \tag{17.37}$$

In general samples are polycrystals. Powder averaging yields

$$S_{inc}(Q,\omega) = (\frac{1}{3} + \frac{2}{3}j_0(Qd))\delta(\omega) + (\frac{2}{3} - \frac{2}{3}j_0(Qd))\frac{1}{\pi}\frac{\frac{3}{2}\nu}{\omega^2 + (\frac{3}{2}\nu)^2} \tag{17.38}$$

with the Bessel function $j_0(Qd) = \frac{sin(Qd)}{Qd}$.

$\lambda_1 = 0$ represents the totally symmetric stationary solution. The prefactor of this purely elastic term is called elastic incoherent structure factor (EISF). It only depends on the jump geometry and allows to discern between different jump models. The presence of a purely elastic term shows that the jumping atom remains localized around the molecule - in contrast to translational processes. Quasielastic scattering is related to the degenerate eigenvalues $\lambda_{2,3}$. The two phase factors represent clockwise and anticlockwise jumps. The prefactor is now the inelastic incoherent structure factor (IISF). It has its maximum at $Qd \sim \frac{3\pi}{2}$ and thus gives access to the jump distance. The Lorentzian width yields the jump rate.

More complex motions

A transition to potentials of higher multiplicity, e.g. V_6, introduces different jump dis-

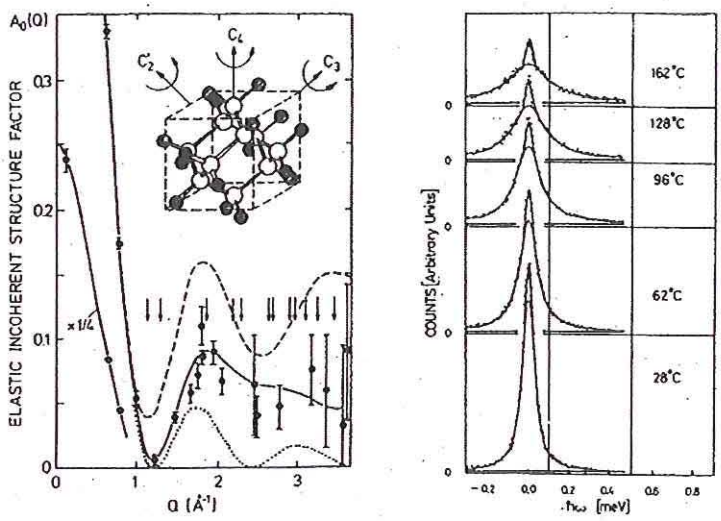

Figure 17.6: QNS-spektra (right) and EISF (left) of adamantan. Spektrometer: IN5, ILL. Inset, right: The molecule and its rotation axes.
Solid line: 90° jumps about all C_4 axes. Dashed: 120° jumps about all C_3 axes.

tances and jump times. Correspondingly the scattering function contains more than one Lorentzian with different IISFs [5, 6]. The unhindered motion (multiplicity=∞) allows for any orientation. This rotational diffusion and is characterized like in the case of translation by a rotational diffusion coefficient [8].

Fig. 17.6 shows quasielastic spectra of adamantan. The large dimensions of the

molecule allow a good determination of the EISF in the accessible Q range. Thus precise conclusions on the possible rotations can be drawn.

Rotational jumps are thermally activated and obey the Arrhenius law (17.23). $\nu_0 = \frac{1}{\tau_0}$ is called attempt frequency. Its inverse is about the time required by the atom at room temperature to pass the jump distance. For a methyl group $\nu_0 \sim 10^{13} sec^{-1}$. The exponential factor represents the succes rate: the larger the barrier E_a, the rarer a crossing. If the shape of a potential is given one gets the potential from the activation energy E_a. It is assumed that the potential does not change with temperature.

In general a large Q range is required at good energy resolution to get conclusive answers. Adamantan (fig. 17.6) is an exceptionally good example. Best suited are backscattering instruments. Time-of-flight spectrometers suffer from a small Q-range. More complex 3-dimensional jump models involve jump matrices of higher dimensions [6].

Possible reasons for wrong conclusions may be the occurrence of multiple jumps. The neutron distinghuishes only the starting and the final orientation. Double jumps about an easy axis may look as a single jump about a high barrier [7]. The scattering function is calculated on the assumption of single jumps, however. Monte Carlo simulations can clarify discrepancies.

17.3.2 Rotational tunnelling: single particle model

Stochastic motions take their energy from a thermal bath. At low temperature they die out and a classical description fails. A quantummechanical theory is needed. In quantum mechanics the indistinghuishable protons of a molecule are connected by a common wave function. This introduces coherence effects. Eigenenergies of rotation are the so-called librations in the meV regime - similar to harmonic oscillations - and the new low energy tunnelling modes in the μeV regime. A "pocket states" formalisme - described in more detail below for methyl groups - gives a qualitative picture. The molecule can exist in three possible orientations $|123>, |231>$ and $|312>$. If the barrier between these orientations is large, the orientational subgroups are decoupled and molecules can perform almost harmonic oscillations only (threefold degenerate). For lower barrier the orientational substates are coupled. In quantum mechanical language: the wave functions overlap and the librational states split by tunnelling. Thus rotational tunnelling is not a dynamical event. Only if one could prepare a system in a Gedanken experiment in a single orientation it would move into a new orientation within a time $t \sim \frac{1}{\omega_t}$. Tunnelling energies $\hbar\omega$ are of the order of μeV. Monographs are [4, 8, 9].

The 1d rotor: solution based on 'free rotor' functions

The canonical strategy diagonalizes the hamiltonian matrix. It is important to chose an appropriate set of basis functions [4].

The simplest molecule consists of two atoms and allows two orientations in a double minimum potential ($H_2, H_2O..$). The case was already considered in the section "Translational tunnelling". Here we want to consider a methyl group, the most intensively studied system. It is characterized by its momentum of inertia Θ around its symmetry axis or - equivalently - by its rotational constant $B = \frac{\hbar^2}{2\Theta}$.

An obvious set of basis functions are the free rotor functions $exp(im\varphi)$. In the single particle model the interaction with the surrounding is reflected in a static rotational potential V. To get the Hamiltonian H the kinetic rotational energy has to be added

$$\begin{aligned} H &= \frac{1}{2}\Theta \mathbf{J^2} + V \\ &= -\frac{\hbar^2}{2\Theta}\frac{d^2}{d\varphi^2} + V \\ &= -B\frac{d^2}{d\varphi^2} + V \end{aligned} \tag{17.39}$$

A dimensionless representation of the eigenvalue (Schrödinger) equation is

$$\frac{H}{B}\Psi = \frac{E}{B}\Psi \tag{17.40}$$

with the scaled rotational potential $V' = \frac{V}{B}$

$$V'(\varphi) = \sum_{n=1}^{N} V'_{3n}(1 - cos(3n\varphi)) \tag{17.41}$$

The eigenfunctions are expanded into free rotor functions up to the order 2M+1

$$\underline{\Psi} = \sum_{m=-M}^{M} a_m exp(im\varphi) \tag{17.42}$$

with eigenvectors $\underline{a}$. Only a few matrix elements deviate from zero. They follow from orthognality relation of the angular functions

$$\begin{aligned} \int exp(in\varphi)V(\varphi)exp(im\varphi)d\varphi &= \frac{V_n}{2}\delta_{nm} \\ \int exp(in\varphi)V(\varphi)exp(im\varphi)d\varphi &= \frac{V_n}{4}\delta_{n(m\pm3)} \\ \int exp(in\varphi)\frac{d^2}{d\varphi^2}exp(im\varphi)d\varphi &= -m^2\delta_{nm} \end{aligned} \tag{17.43}$$

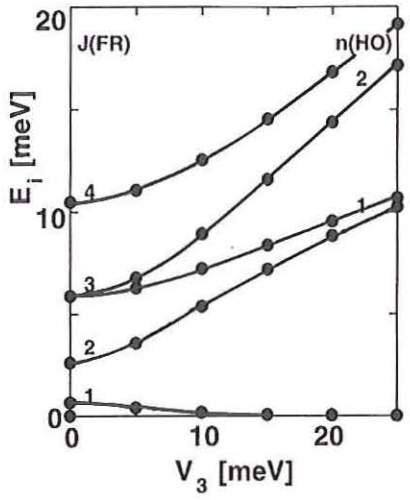

Figure 17.7: Eigenenergies of a tunnelling methyl groups. The potential V_3=0 represents the free rotor with quantum number J. Strong V_3 approaches a harmonic oscillator model - quantum number n - with equidistant librational modes (not yet reached at $V_3 = 25meV$).

For a purely 3-fold potential one obtains the (2M+1) dimensional Hamilton matrix

$$\underline{\underline{H}} = \begin{pmatrix} \ddots & \vdots & \vdots & \vdots & \vdots & \vdots & \vdots & \vdots & \\ \dots & 9+\frac{V_3'}{2} & 0 & 0 & \frac{V_3'}{4} & 0 & 0 & 0 & \dots \\ \dots & 0 & 4+\frac{V_3'}{2} & 0 & 0 & \frac{V_3'}{4} & 0 & 0 & \dots \\ \dots & 0 & 0 & 1+\frac{V_3'}{2} & 0 & 0 & \frac{V_3'}{4} & 0 & \dots \\ \dots & \frac{V_3'}{4} & 0 & 0 & \frac{V_3'}{2} & 0 & 0 & \frac{V_3}{4} & \dots \\ \dots & 0 & \frac{V_3'}{4} & 0 & 0 & 1+\frac{V_3'}{2} & 0 & 0 & \dots \\ \dots & 0 & 0 & \frac{V_3'}{4} & 0 & 0 & 4+\frac{V_3'}{2} & 0 & \dots \\ \dots & 0 & 0 & 0 & \frac{V_3'}{4} & 0 & 0 & 9+\frac{V_3'}{2} & \dots \\ & \vdots & \vdots & \vdots & \vdots & \vdots & \vdots & \vdots & \ddots \end{pmatrix}$$

Such band matrices are easily diagonalised by standard programs. The resulting eigenenergies represent librations split by the tunnel effect.

With increasing librational quantum number the tunnel splitting increases due to the increasing overlap of wavefunctions in excited states. Fig.17.7 shows the eigenenergies as a function of increasing strength V_3' of the hindering potential. One recognizes a huge isotope effect with deuteration ($B_D = \frac{B_H}{2}$) due a doubling of the scaled potential V' (17.41).

For zero potential the Hamilton matrix is already diagonal and the eigenvalues are

those of the free rotor J^2B.

The 1d rotor: pocket state formalisme

Pocket states are useful basis functions for stronger potentials. They represent a single orientation of a molecule. Thus $\psi = \mid 123 >$ means that proton 1 of the methyl group is at position 1, 2 at 2, 3 at 3. A rotation is represented by cyclic permutation. We consider the groundstate only. As outlined for translational tunnelling pocket states are no eigenstates of the problem. They overlap and thus can transform into each other. Since wave functions decay exponentially into a potential wall (Gamow factor) the overlap or tunnelling matrix element is very sensitive to the strength of the potential. The eigenvalue matrix obtained from the Hamiltonian is

	$\mid 123 >$	$\mid 231 >$	$\mid 312 >$
$\mid 123 >$	λ	t	t
$\mid 231 >$	t	λ	t
$\mid 312 >$	t	t	λ

The characteristic polynom yields a unique eigenvalue $\lambda = 2t$ related to the totally symmetric A groundstate and a doubly degenerate eigenvalue $\lambda = -t$ related to the right and left handed E states, respectively. The matrix is formally identical to a jump matrix. The meaning of the eigenvalues is very different, however.

A tetrahedron like methane requires 12 pocket states. The 9 eigenvalues are partially degenerate depending on the environmental symmetry. The mathematics becomes more complicated.

To obtain the scattering function including intensities of transitions the influence of proton spins via the Pauli principle has to be taken into account. The complete theory with inclusion of spin wavefunctions is found in ref.[8]. The resulting scattering function is normalized to the number of protons in the rotor

$$\begin{aligned} S_{inc}(Q,\omega) &= (1 + 2j_0(Qd))\delta(\omega) + (\frac{2}{3} - \frac{2}{3}j_0(Qd))\delta(\omega) \\ &+ (\frac{2}{3} - \frac{2}{3}j_0(Qd))(\delta(\omega + \omega_t) + \delta(\omega - \omega_t)) \end{aligned} \tag{17.44}$$

The first term represents purely elastic scattering. Its intensity is called elastic incoherent structure factor (EISF). The second term is due to transitions between different but degenerate E-states. Finally there are inelastic $A \rightleftharpoons E$ transitions between tunnelling substates. The latter terms are δ-functions only at low temperature. By coupling to phonons they broaden and shift [10] until they merge into the single classical quasielastic Lorentzian. The width of tunnelling lines can be interpreted as a lifetime broadening

due to transitions into the first excited librational level E_{01} of the same symmetry. E_{01} acts as activation energy and can be obtained from an Arrhenius plot. The fig.17.8 shows this transition for acetamide CH_3CONH_2, the most simple molecule containing the biologically important peptide group. The transition is an especially nice example of

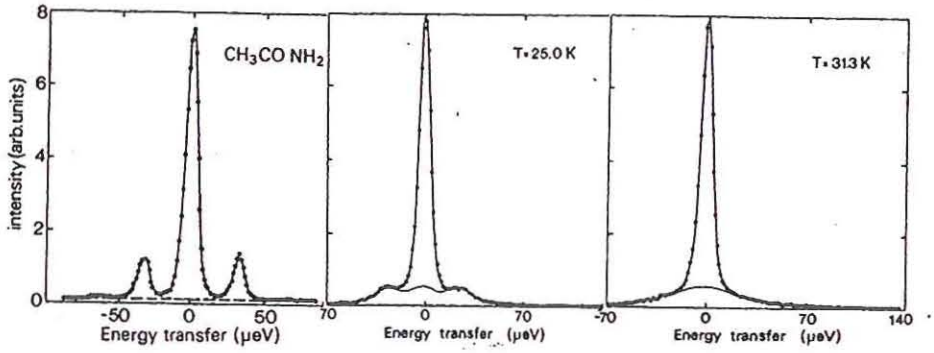

Figure 17.8: High resolution spectra of acetamide at 3 temperatures: transition from methyl rotational tunnelling to classical jump reorientation.

Bohr's correspondance Principle.

Here the question arises, why the tunnelling energy itself does not appear as activation energy. This is a remarquable consequence of the Pauli principle: with change of the spatial symmetry the spin state symmetry has to change too to conserve the symmetry of the total wave function. Thus A groundstate and E tunnel level show different total spin. The spinless phonons cannot induce this transition (spin conservation). Thats the reason why the very small tunnel splittings are not smeared out at $k_BT \gg \hbar\omega_t$.

Structural information

Tunnel spectra of materials with many methyl groups may show many tunnelling transitions due to the different rotational potentials. Like in Raman spectroscopy conclusions may be drawn on structural properties as molecules per unit cell or site symmetries.

17.3.3 Multidimensional tunnelling

Not always a rotation is a pure mode. It might couple to other degrees of freedom. Correspondingly the single particle model is no longer applicable. Well established is so far a combined rotation of the molecule and its center of mass [11]. This type of dynamics is called rotation-translation-coupling. It is a special case of many possible types of multidimensional tunnelling. Each new model of coupled motion requires the

diagonalisation of a new hamiltonian matrix which is always much more complex than the SPM. This is hard and sometimes impossible work. The single particle model is such attractive because it involves only properties of the rotating group and can be applied in any environment.

17.4 Calculation of potentials 'ab-initio'

The result of an analysis of tunnelling spectra, librational (E_{01}) and activation (E_a) energies is the rotational potential up to some order of its Fourier components. The exponential dependence of the tunnel splitting on the barrier height makes this probe especially important.

The determination of rotational potentials is a value in itself. However, a deeper understanding requires its deduction from more fundamental quantities. A step towards this goal is a parametrisation of interactions in a solid by atom-atom potentials

$$V_{ij} = a_{ij} exp(-\alpha_{ij} r) - \frac{b_{ij}}{r^6} + \frac{q_i q_j}{r} \tag{17.45}$$

The first term represents the repulsive, the second the attractive van-der-Waals interactions. In addition electrostatic terms may be added. The total potential energy is given as the sum over all pair potentials. One important postulate/property of atom-atom potentials is their *tranferability* - at least within certain classes of chemically related compounds. Thus the dynamic properties of an unknown material should be calculable on the basis of the structure using established pair potentials. This technique is used in studying reaction pathes in chemistry or functionalities in biology and pharmacy.

With the more and more increasing power of computers it is possible to do energy calculations really 'ab initio'. Quantum chemistry programs like GAUSSIAN98 minimize the energy of the elctronic wave functions of a system of atoms. The aim is the same like with the pair potential: e.g. to probe paths of a synthesis and thus avoid expensive practical tests in preparative chemistry.

Contents

17.1 Introduction 17–1
17.1.1 Gaussian approximation 17–1
17.2 Translation 17–2
17.2.1 Macroscopic diffusion 17–2
17.2.2 Diffusion, microscopic approach: Langevin equation 17–3
17.2.3 Jump diffusion on a Bravais lattice 17–4
17.2.4 More complex cases 17–7
17.2.5 Librations 17–8
17.2.6 Translational tunnelling 17–8
17.3 Rotation 17–10
17.3.1 Jump rotation: methyl group in a 3-fold potential 17–10
17.3.2 Rotational tunnelling: single particle model 17–13
17.3.3 Multidimensional tunnelling 17–17
17.4 Calculation of potentials 'ab-initio' 17–18

References

[1] T. Springer, *Quasielastic neutron scattering for the investigation of diffusive motions in solids and liquids*, Springer Tracts in Modern Physics, Vol. 64, Springer, Berlin, 1972

[2] F. Franks, J. Ravenhill, P.A. Egelstaff, D.I. Page, Proc. Roy. Soc. (London) **A319**,189(1970)

[3] D. Richter, Neutronenstreupraktikum 1998, Forschungszentrum Jülich

[4] D.G. Lister, J.N. MacDonald, N.L. Owen, *Internal Rotation and Inversion*, Academic Press, London, 1978

[5] J.D. Barnes, J. Chem. Phys. **58**5193(1973)

[6] M. Bée, *Quasielastic neutron scattering*, Adam Hilger, Bristol, 1988

[7] R. Gerling, A. Hüller, Z. Phys. **40**,209(1980)

[8] W. Press, *Single Particle Rotations in Molecular Crystals*, Springer Tracts in Modern Physics, Vol. 81, Springer, Berlin 1981

[9] M. Prager, A. Heidemann, Chem. Rev. **97**,2933(1997)

[10] A.C. Hewson, J. Phys. **C15**, 3841 and 3855 (1985)

[11] P. Schiebel, A. Hoser, W. Prandl, G. Heger, W. Paulus, P. Schweiß, J. Phys. Condens. Matter **6**,10989(1994)

18. Texture in Materials and Earth Sciences

Wolfgang Schäfer

Mineralogisch-Petrologisches Institut, University of Bonn
Forschungszentrum Jülich, MIN/ZFR, 52425 Jülich

1.0 Introduction

The topic ‚texture' has to be assigned to the contributions about elastic neutron scattering and the determination of crystal and magnetic structures by means of Bragg scattering using either polycrystalline or single crystalline samples (compare Fig.18.1a and 18.1d, resp.). When performing powder diffraction for the purpose of refinements or even determinations of crystal (or magnetic) structures, one initially assumes statistical distributions of all crystallite orientations inside the polycrystalline material, thus ensuring that for the measurement of each Bragg reflection hkl an almost equal and, with respect to statistical relevance, a sufficient number of crystallites (small single crystals) is in reflection position. This is the prerequisite for an even intensity distribution on the Debye-Scherrer cones of a powder measurement (see Fig. 18.1a). Non-statistical distributions of crystallites, e.g. in case of plate- or rod-like cystal grains or for non-powderized bulk sample material, result in preferred orientations of special scattering planes hkl and cause uneven (orientation dependent) intensity distributions on the Debye-Scherrer cones (see Fig. 18.1b and 18.1c) appraoching the appearance of single crystal spots (Fig. 18.1d). The evolution of experimental intensities in crystal structure analysis is generally hampered by the presence of preferred orientation. For instance, special correction terms have to be applied during structure refinement calculations.

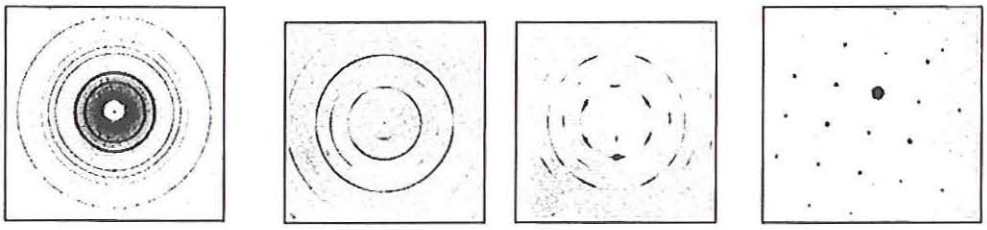

(a) (b) (c) (d)

Fig. 18.1: hkl diffraction maxima (here X-ray scattering) shown as sections from Debye-Scherrer cones obtained from polycrystalline material of random crystallite orientations (a), weak (b) and strong (c) preferred orientations. (d) shows single crystal diffraction spots.

In this contribution, however, we will exclusively focus on the positive aspects of preferred orientations in polycrystalline material in view of the characterization and changes of the bulk

material properties. In material science, mechanical treatment and deformation is artificially applied to generate preferred orientation and, thus, well defined material properties. In earth sciences, preferred orientation exists in rocks by natural deformations over millions of years and, thus, bears important information on longtime geological processes. The study of preferred orientations in bulk polycrystalline material is an independent scientific discipline; the texture analysis [1, 2].

2.0 Anisotropy by Structure and Texture

Texture is a property of condensed crystalline matter. In our daily life, we are often in contact with solid state, crystalline matter, e.g. minerals and rocks being the fundamental components of the earth's crust, or metals and ceramics which are manufactured and used as technological products. Crystalline matter is characterized by its specific crystal structure which is defined by a unit cell with its symmetrical atomic arangement and by its three-dimensional periodicity. This crystal structure essentially determines the physical, chemical and technological properties of a material, at least on a microscopic scale. The microscopic unit is considered to be a monocrystalline aggregate.

Generally, the properties of a single crystal are anisotropic, i.e. they are different in different crystallographic directions. The thermal conductivity of graphite represents a typical example of such a direction-dependent crystalline property. The sheet-like hexagonal crystal structure built up by plane layers of carbon atoms with small interatomic distances inside the layers and large distances between neighbouring layers (Fig. 18.2) is responsible for a strong anisotropy. The thermal conductivity within the layers is about four times larger compared to the conductivity perpendicular to the layers along the hexagonal axis.

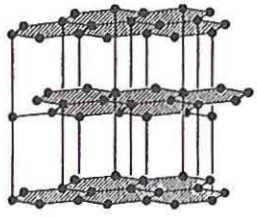

Fig. 18.2: *Graphite structure built up by plane sheets of C atoms (hatched) arranged perdendicular to the hexagonal c-axis*

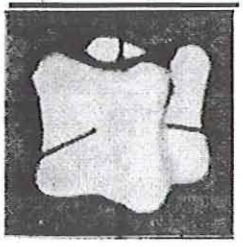

Fig. 18.3: *Property surface of the Young modulus of iron (left) for any directions [hkl] of the cubic crystal system (right)*

Further important structure related anisotropic properties of special technological relevance are e.g. mechanical hardness, elasticity, thermal expansion, electrical conductivity, magnetic induction or corrosive resistance. The single-crystalline anisotropy may be

described by a direction dependent three-dimensional property-specific surface as shown in Fig. 18.3 for the linear (elastic) Young modulus of iron with its cubic crystal structure. The directional dependence of a property E is a function of well-defined crystallographic directions h:

$$E(g) = f(\underline{h}) = f(hkl) \qquad (1)$$

With repect to any direction g in the three-dimensional space, the directional dependence of E can be expressed mathematically as a series of spherical harmonics T with parameters λ, μ and ν and its coefficients e according to

$$E(g) = \sum_{\lambda}\sum_{\mu}\sum_{\nu} e_{\lambda}^{\mu\nu} T_{\lambda}^{\mu\nu}(g) \qquad (2)$$

The vast majority of solid crystalline matter, however, does not exist in form of single crystals but is of polycrystalline nature. The material is built up macroscopically by a multitude of crystallites or grains which can be arranged in many different orientations (compare Fig. 18.4). In case of a statistical orientation distribution of the crystallites the structure-specific orientation dependences of the properties disappear macroscopically and the material becomes quasi-isotropic.

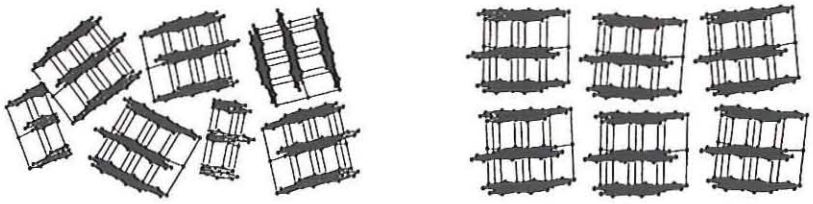

Fig. 18.4: *Schematic representation of random (left) and preferred orientations (right) of graphit-type crystallites (compare Fig. 18.2)*

This loss of anisotropy can be compensated for by the existence or the generation of texture. Texture is defined by the spatial orientation distribution of crystallites in polycrystalline matter. In case of a statistical orientation distribution one speaks of a random texture. The above definition of texture which is widely accepted and used today disregards any effects due to different shapes or sizes of the crystallites. A (non-random) texture performs a transfer of structure relevant microscopic single-crystalline anisotropies to the polycrystalline bulk material. Texture is an important parameter in view of the properties of condensed crystalline matter, besides of other material parameters as structure, phase composition, grain boundaries, or strain [3]. The formation and changes of texture are driven or controlled by outer influences, either already during cystallization by e.g. the existence of non-hydrostatic conditions during crystal growth or after crystallization by natural deformation due to tectonic

events with regard to geological material or, with regard to manufactured materials, by artificial deformation of products by mechanical treatments like rolling or casting.

The mean value of a property $\overline{E}$ of a texturized polycrystal is expressed, according to equation (2), by an integration of over all crystallite orientations with the aid of a so-called orientation distribution function f(g):

$$\overline{E} = \int E(g) f(g) dg = \sum_{\lambda} \sum_{\mu} \sum_{\nu} \frac{1}{2\lambda+1} e_{\lambda}^{\mu\nu} C_{\lambda}^{\mu\nu} \qquad (3).$$

Thus, $\overline{E}$ is expressed mathematically by a folding of structural coefficients e and texture coefficients C. The full mathematical decription of this so-called harmonic series expansion method has been developed by H.J. Bunge [4]. The actual goal of a texture analysis is the experimental determination of the orientation distribution function by diffraction measurements.

3. Orientation Distribution Function

The texture of a polycrystalline sample is expressed by its orientation distribution function f(g), generally abbreviated as ODF, according to the definition

$$f(g) = \frac{1}{V} \frac{dV}{dg} \qquad (4).$$

Thus, the ODF is defined by the volume fraction of crystallites that have the orientation g within a certain infinitesimal orientation element dg. The orientation g can be described by a transformation matrix $[g_{ik}]$ representing the orientation of the individual crystallites (coordinate system K_K) with reference to a common sample coordinate system K_P (Fig. 18.5). The axes of the cartesian K_P coordinate system are selected in accordance with external (or visible) deformation or texture characteristics of the sample. Some commonly used orientations of the sample coordinate system are shown in Fig. 18.6.

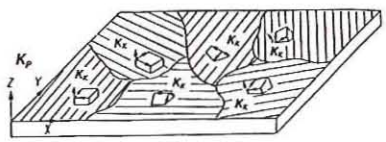

Fig. 18.5: *Schematic representation of a texturized sample in a coordinate system K_P with individual orientation of crystallites and their coordinate system K_K*

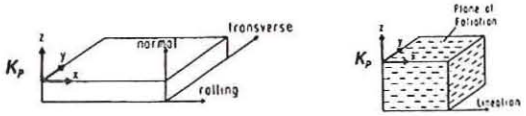

Fig. 18.6: *Usual definitions of coordinate axes of cartesian coordinate systems K_P for rolled metal samples (left) and geomaterial (right) by direction and plane of rolling and by lineation and plane of foliation, respectively.*

For material/metal textures the Euler space is traditionally used as orientation space by describing the orientation g of the crystallites by the three Eulerian angles φ_1, Φ, φ_2. The

corresponding coordinate transformation is performed by three subsequent rotations about the Eulerian angles in the sample coordinate system as depicted in Fig. 18.7. It is then

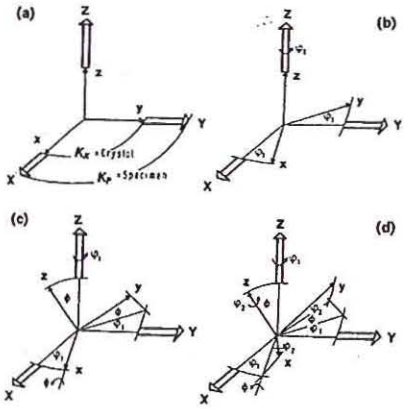

Fig. 18.7: *Definition of the Eulerian angles φ_1, Φ, φ_2 and transformations of sample (K_P) and crystal (K_K) coordinate sytems:*
(a) identical orientation of the axes of K_P and K_K
(b) rotation of the z-axis of K_K by φ_1
(c) rotation of the x-axis of K_K by Φ
(d) rotation of the z-axis of K_K bei φ

convenient to plot these Eulerian parameters as cartesian coordinates in a three-dimensional space which is called the Euler (orientation) space (Fig. 18.8). Each crystal orientation is represented by a point in the Euler space. The orientations of all crystallites of the ensemble are then represented by a point distribution in Euler space. A texture obtained as a continuous distribution function can be represented by equilevel contour lines (Fig. 18.8) which may be completed to equilevel surfaces as it is shown in the example in Fig. 18.9. and its planar sections in Fig. 18.10. The Euler space is a distorted space with a metric quite different from the usual three-dimensional space. Textures of geological samples are usually visualized by other, more descriptive representations which are closer to common sense (see chapter 5.1.).

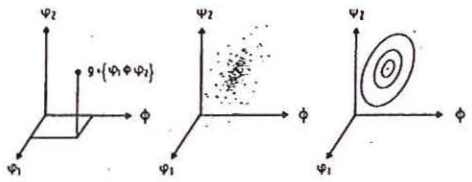

Fig. 18.8: *Crystallite orientations in Eulerian angles: one crystallie (left), all crystallites (middle) with equilevel contour lines (right)*

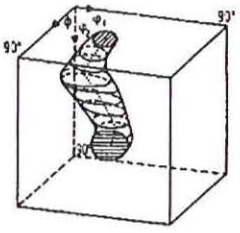

Fig. 18.9: *ODF of a Cu rolling texture represented by an equilevel orientation surface in the 3-dim Eulerian space*

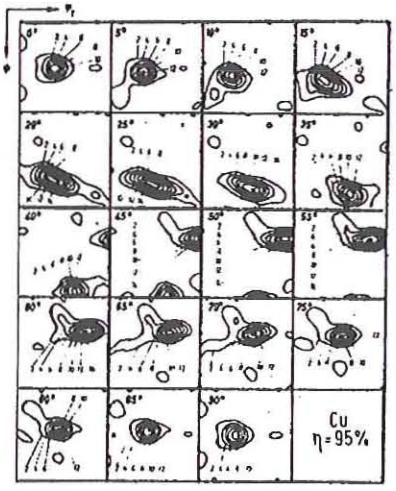

Fig. 18.10: *ODF representation of Fig. 18.9 by a sequence of const. φ_2-sections*

4.0 Experimental Texture Analysis

The material texture and its ODF cannot be measured directly without destroying the specimen. The ODF can only be constructed. Two different types of measurements are applied. The traditional method is the single grain analysis based on optical methods where the orientations of representative single grains are directly observed using universal stage microscopy on a polished sample surface. A faster and much more efficient alternative to the rather painstaking single grain analysis are diffraction methods using either neutrons or X-rays. Bragg scattering intensities are measured as a function of the sample orientation.

4.1 Definition of a Pole Figure

A pole figure represents the orientation distribution of a particular crystal direction [hkl] or the normal to the scattering plane (hkl) of the sample. The crystal direction is first projected onto a sphere of unit radius around the sample. The prenetrating point P on the sphere (Fig. 18.11) is defined by two angles, a pole distance α and an azimuth β. This sphere is then projected onto a plane in order to represent the pole on paper. Various spherical projections are in use, the most common in texture analysis is the stereographic projection (see Fig. 18.11). Fig. 18.12 shows examples of some crystal plane distributions and their associated pole figure representation.

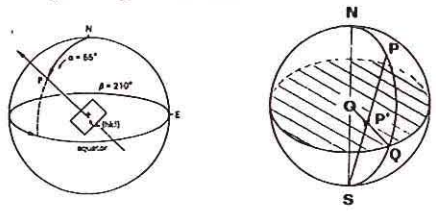

Fig. 18.11: *Representation of a plane (hkl) by its normal and its pole on the surrounding sphere P defined by polar coordiantes α, β (left). Stereographic projection of P into P* inside the (hatched) equatorial plane (right)*

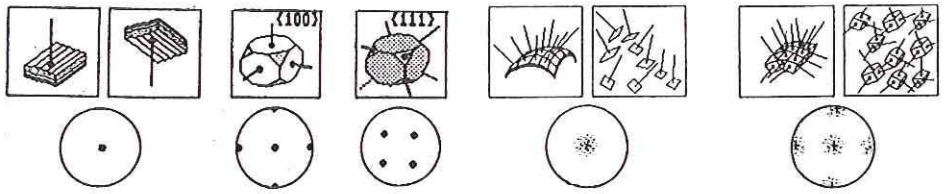

Fig. 18.12: *Examples of crystallographic planes (top) and their accessory pole figures (bottom) for a two-dimensional (a) and a three-dimensional (b) single crystal with one fixed pole per plane and for a polycrystalline sample (c and d) with a scatter of poles;*
(a) (001)-plane and its counterpart (00-1) (north-south normal directions)
(b) cubic basis planes (100), (010), (001) (left) and body diagonal planes {111} (right)
(c) spread of differently oriented (001) planes
(d) spread of differently oriented cubic basis planes {100}

4.2 Experimental Pole figures

An experimental (hkl) pole figure is obtained by diffraction methods by measuring the intensity of a Bragg reflection (hkl) for a variety of different sample orientations. Usually, at least so far, one uses monochromatic neutrons (or X-rays). The simplest instrumental setup is that of a four-circle diffractometer equipped with a Eulerian cradle (φ, χ rotation axes) as sample goniometer (Fig. 18.13) and a simple counting tube, i.e. an instrument as used for single crystal structure investigations. A stationary detector is positioned in the peak maximum of a reflection, and sample orientation dependent measurements are performed, e.g. in a step scanning mode, realizing an equal area pole figure grid (Fig. 18.13).

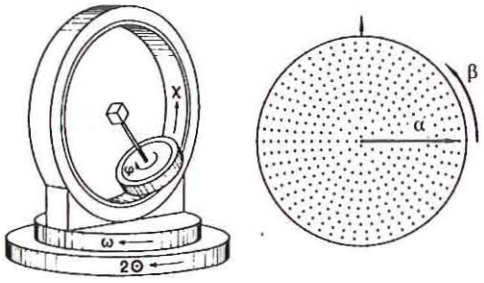

Fig. 18.13: *Eulerian cradle with rotation axes φ, χ ($\omega = 2\Theta/2$ position) (left) and typical (α,β)- pole figure scanning grid (right)*

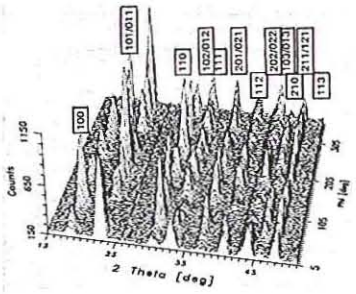

Fig. 18.14: *Variation of reflection intensities with φ rotation (χ fixed) of a quartzit sample measured with a large linear detector in Jülich*

Rather than using a single counting tube it is more efficient to employ a large position-sensitive detector which covers a wide scattering range 2Θ and which allows the simultaneous measurement of many (hkl) reflections (see Fig. 18.14) and, thus, the collection of experimental data for many pole figures in only one sample scan. The pole figures are constructed (1) by conversion of the individual sample orientations (φ, χ) into pole figure coordinates (α, β), (2) by interpolation for points of an almost equispaced (α, β)-grid in the pole figure projection (see Fig. 18.13) and (3) by graphically representing the pole figures with the corresponding reflection intensities (compare Fig. 18.15).

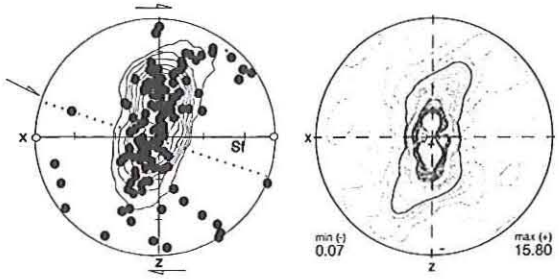

Fig. 18.15: *Comparison of c-axis pole figures (0001) of a texturized quartzite obtained from single grain analysis by U-stage microscopy (left) and neutron diffraction (right) based on investigations of about one hundred and one million grains, respectively.*

4.3 Pole Figures from Neutrons and X-Rays

The advantages and drawbacks of both neutron and X-ray diffraction for texture analysis are obvious. Texture is a statistical description of crystallite orientations and therefore requires a large number of crystallites or grains in order to get a meaningful sampling. Reproducible pole figures require numbers of 10^4 to 10^5 grains are good figures. The knwon properties of X-rays (large absorption in the sample and a small beam diameter) limit its use to (1) flat, thin samples, and (2) fine grained material with grain sizes in the order of 10 to about 100 µm. These limitations allow to study only a surface of a sample because the X-rays penetrate the sample just a few microns. X-rays therefore probe the local texture at the sample surface. Due to the high and orientation dependent absorption and limitations due to defocusing if a flat sample is rotated (see Fig. 18.16), only incomplete pole figures can be obtained.

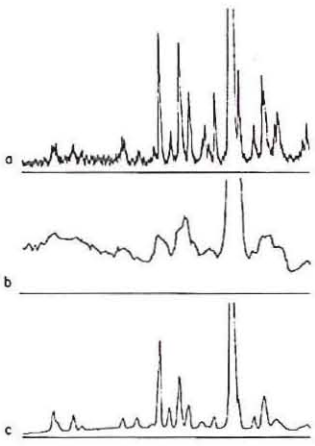

Fig. 18.16: *X-ray diffraction patterns of a flat anorthosit sample in two different orientations (a and b) and mean neutron diffraction diagram (c) of all orientations*

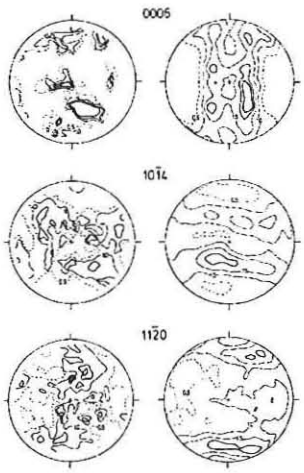

Fig. 18.17: *Comparison of X-ray (left) and neutron pole figures (right) of a coarse grained deformed marble specimen [5]*

Neutron beams, on the other hand, are large up to 100 x 50 mm^2 cross section, and in general weakly absorbed by most materials. Compared to X-ray photons, neutrons are absorbed by less than three orders of magnitude and are therefore in need of large samples. While this may be a drawback in many investigations, it is of great advantage in texture analysis where the global texture of the total volume has to be explored. Due to their ability to penetrate matter, neutrons are well suited for the analysis of the bulk of a thick sample with several cm in diameter. Thus it is possible to study also coarse grained material with reasonable grain statistics even if grain sizes range up to millimeters in diameter (Fig. 18.17). Neutron measurements can be performed in transmission geometry on spherical, cylindrical or even

irregular shaped specimens and complete pole figures are obtained without applying any intensity corrections. Neutron diffraction measurements can be carried out at a much higher degree of accuracy than other techniques to calculate the orientation distribution function.

5.0 Pole Figures and ODF

An experimental pole figure P_{hkl} yields the orientation distribution of the crystallites with respect to one particular crystallographic direction [hkl] which represents the actual scattering vector $\underline{\varepsilon}$ of the diffraction experiment. There is no information, however, on the orientation of

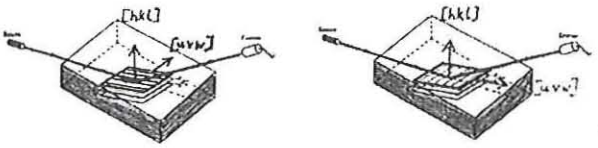

Fig. 19.18: *Scattering experiment with scattering vector $\underline{\varepsilon}$ = [hkl] perpendicular to scattering plane (hkl) (hatched) yields no information on the orientation of any [uvw] inside the plane*

the crystallites perpendicular to the scattering vector, i.e. inside the plane (hkl) (compare Fig. 18.18). As the pole figure represents a two-dimensional orientation distribution, it is thus an integral of the three-dimensional orientation distribution function f(g) taken over a rotation about scattering vector $\underline{\varepsilon}$ = [hkl]:

$$P_{hkl}(y) = \frac{1}{2\pi} \int_{y \perp (hkl)} f(g)d\psi \quad \text{with } y = \{\alpha, \beta\} \tag{5}.$$

Equation (5) may be called the fundamental relation of texture analysis. It is evident that the ODF f(g) is generally not completely determined by one pole figure. One needs the additional information of other crystallographic directions, i.e. other pole figures. The factor $1/2\pi$ in equation (5) results from a normalization with respect to the definition of a statistical orientation distribution:

$$f(g)_{statistical} = 1, \quad \int f(g)d\gamma = 1, \quad P_{hkl}(\alpha, \beta)_{statistical} = 1 \tag{6}.$$

Pole densities are expressed in multiples of the random density (m.r.d.).

5.1 Pole Figure Inversion

The determination of the ODF f(g) from equation (5) is called pole figure inversion. Different mathematical procedures have been developed to calculate the ODF from experimental pole figures. Depending on the method, the calculated ODF is a continuous or a step function. A widely applied method in texture analyses of high symmetry materials (metals) is the series-

expansion or harmonic method developed by H. J. Bunge [6] (compare chapter 3.0). Analogous to the classical procedure in single crystal structure determination, the ODF is expanded into its corresponding Fourier orthogonal series using surface spherical harmonic functions with coefficients C (see equation (2)). A similar expansion is performed with the experimental pole densities P yielding the coefficients F(hkl). A system of linear equations and appropriate transformations of coefficients are used to determine the unknown coefficients C from the experimentally known coefficients F. Routine computer programs are available to perform these calculations. The calculated coefficients C are those texture coefficients C which have been used in equation (3) to describe the anisotropy of macroscopic physical properties of a texturized polycrystal.

After the ODF has been determined it is possible to calculate pole figures of all planes (hkl), also of those which have not been or cannot been measured, for instance, because of extinction. It is also useful to recalculate experimental pole figures from the ODF in order to estimate or control the reliability of the texture analysis performed.

A different mathematical approach to the ODF calculation is the discretization method based on the maximum entropy concept [7] using a finit series expansion into indicator functions. This method was introduced into the program MENTEX by H. Schaeben [8]. The so-called WIMV-method [9] which is rather common in geological texture analysis is based on certain probability assumptions of f(g) which may then be further improved by iterative refnements.

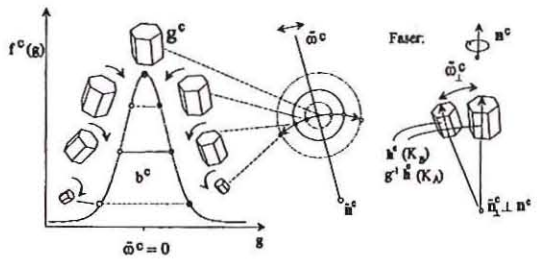

Fig. 18.19: *Representation of a texture component g^c by a Gaussian distribution function $f^c(g)$ of halfwidth b^c. ω^c denotes the deviation of crystalltie orientations from g^c (at $\omega^c = 0°$). n^c represents a sample fixed axis (see [10])*

Apart from the global description of the texture in the total orientation space, texture can also be described by a certain number of texture model components, although this description includes only restricted areas of the orientation space. Each component to be described, for instance, by a Gaussian distribution curve is given by (1) a preferred orientation g^c locally restricted in orientation space, (2) a halfwidth b^c characterizing the spread around g^c (see Fig. 18.19) and (3) an intensity I^c indicating the volume share of all crystallites belonging to that component. The ODF approximation by means of texture components is expressed by

$$f(g) = R + \Sigma I^c f^c(g) \qquad (7).$$

The quantity R gives the volume fraction of the randomly oriented crystallites, i.e. which are not restricted in the orientation space. The component method [10] can be applied to composite experimental pole figures, also of multi-phase geological material of any crystallographic symmetry.

5.2 Inverse Pole Figures

The mathematical procedure of pole figure inversion includes also the calculation of coefficients H of so-called inverse pole figures. While the pole figures discussed so far are defined for one particular crystallographic direction [hkl] and variable sample orientations (compare equation (5)), the inverse pole figures represent shares of main crystallographic directions, e.g. basis axis, face and body diagonal of the cubic crystal system, in a fixed sample orientation (Fig. 18.20). Usually, the inverse pole figure is represented as stereographic projection with respect to the crystal coordinate system K_K, while the ‚standard' pole figure is defined as stereographic projection with respect to the sample coordinate system K_P (compare Fig. 18.5).

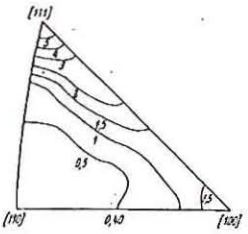

Fig. 18.20: *Inverse pole figure of a cold drawn Al wire (see [2]) by representation of the preferred orientations of the most relevant crystallographic directions (cubic axis [100], face-diagonal [110] and body-diagonal [111]) inside the sample. Pole densities are shown by equilevel contour lines in m.r.d.*

6.0 Examples of Texture Analyses

Texture appears in a great variety. A multitude of different types is kown according to different mechanisms of texture formation during crystallization (grain growth) and recrystallization (generation of dislocations), by deformation during materials processing (plastic deformation, slip and twinning) and as complex superpositions in the course of natural seismic processes in geological texture development.

6.1 Types of Preferred Orientation

One frequently occuring special type of texture are the so-called fibre textures. A fibre texture is typically found in a sample form which is characterized by a main axis (e.g. a cylinder or a wire) with strong preferred orientation of the crystallites along this fibre axis and a 360° rotation symmetry around this axis, i.e. no preferred orientation perpendicular to the fibre axis. For instance, the texture of cold drawn metal wires with fcc structure is a <111> fibre

texture where cubic <111> directions (zone axis) are oriented parallel to the wire axis. Another texture type are preferred orientations of special planes, e.g. the hexagonal basis plane of graphite (see Fig. 18.4), stacked parallel to each other on a surface plane, e.g. a motor piston, but without any preferred orientation within this plane (graphite as lubricant for better gliding).

More general types comprise both the orientation of a plane (hkl) and a zone axis [uvw]. Such a system of glide deformation texture is represented by (hkl)[uvw] or more general {hkl}<uvw>. There is a preferred orientation of a special crystallographic direction <uvw> within the (hkl) planes which are oriented parallel to each other. The deformation of a fcc metal results in a {111}<110> texture, where cubic {111} planes glide along <110> directions. Geological deformation textures are described by mineral specific glide systems.

6.2 General Ojectives .

The major objectives of texture analysis are different in materials and earth sciences. While in material sciences the major emphasis is on the development and control of required preferred orientations under well defined experimental conditions of materials processing in order to evaluate specific (anisotropic) macroscopic physical properties for special technological applications , the problem in geosciences is just the opposite and much more complex. The geologist begins with the end product, the rock as it occurs in nature, and attempts to reconstruct the processes by which the texture has been formed. The texture is a fingerprint of the earth's history and, simultaneously, informs on anisotropies of elastic, magnetic and thermal properties of rocks constituting the crust and the upper mantle. Anisotropy needs to be taken into account in the interpretation of seismic data, development of geological models, and geophysical prospecting.

In the following, two experimental examples of texture analysis are given based on results from the Jülich neutron texture diffractometer.

6.3 Rolling and Recystallization Texture of Copper

One project in the field of applications of neutrons in materials science was concerned with investigations on the longtime stability of copper textures [11]. The rolling texture of copper (Fig. 18.21) is characterized by three main components [12]: the ‚copper'- {112}<111>, the ‚brass'- {110}<112> and the ‚S'-component {123}<634>. The main component of recrystallized copper is the ‚cube'-component {001}<100> and a minor component {122}<212> (Fig. 18.22).

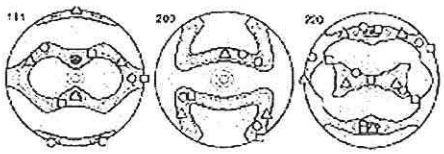

Fig. 18.21: *Measured pole figues of a Cu rolling texture; indicated are ideal orientations of the copper (triangle), the brass (square) and the S-component (circle)*

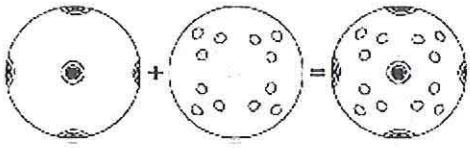

Fig. 18.22: *Modelling of a Cu recrystallization texture by superposition of the main and the minor components {001}<100> (left) and {122}<212> (center), respectively*

A high purity copper sheet was cold rolled to a final thickness reduction of 95%. This sheet of 1 mm thickness was cut into plates of 10x10 mm^2. A part of these plates was annealed at 300°C for 20 min to achieve recrystallization. Two cubes, each of 10 mm edge length, of purely rolled copper and purely recystallized copper where then prepared by glueing ten plates of the respective materials on top of each other. Identical orientations of the individual plates was taken care of. Neutron diffraction pole figures (Fig. 18.23) have been repeatedly performed on both specimens over a period of about six years in which no further treatment of the specimens was undertaken.

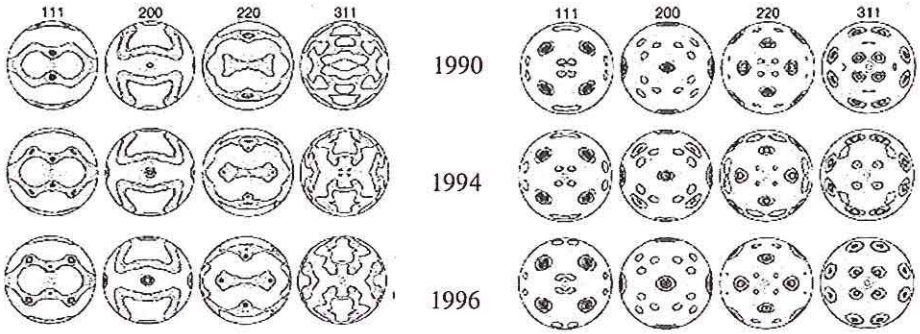

Fig. 18.23: *Experimental neutron pole figures of a rolled (left) and a recrystallized (right) copper specimen in 1990, 1994, and 1996 without any treatment in between*

The textures, quantitatively analysed by model calculations are found unstable over the time of investigation. All quantitative results are summarized in Table 1. The initially almost complete rolling texture recedes by about 30% in sample volume in favour of recrystallization. In the recrystallized specimen, the initial amount of recrystallization texture is reduced from 89% to 66% in favour of a randomly oriented portion. The somewhat surprising findings of ‚living textures' are remarkable with respect to the kinematics of the physical processes involved, and also with respect to the desired longtime stability of material properties in technological applications.

Table 1: *Longtime variations of the texture of rolled (top) and recrystallized copper (bottom) as measured by neutron diffraction and analysed by the component method using the program MULTEX [ ]. Texture parameters are given in Vol% of the main components. The orientation deviations of the crystallites from the various fibre axes are given the full width at half maximum (FWHM) of Gaussian distributions.*

Rolled Cu-specimen

Component	„S“		„copper“		„brass“		„cube“	
Year	Vol %	FWHM	Vol %	FWHM	Vol %	FWHM	Vol %	FWHM
1990	36	13	24	11	22	13	3	10
1994	27	13	19	11	20	13	21	11
1996	24	13	15	11	17	13	28	11

Recrystallized Cu-specimen

Component	„cube“		{112}<212>		random
Year	Vol %	FWHM	Vol %	FWHM	Vol %
1990	61	9	28	13	11
1994	54	10	32	11	14
1996	50	9	16	11	34

The neutron diffraction pole figures of the starting material have been used for a calculation of a three-dimensional ODF according to the series expansion method (Fig. 18.24).

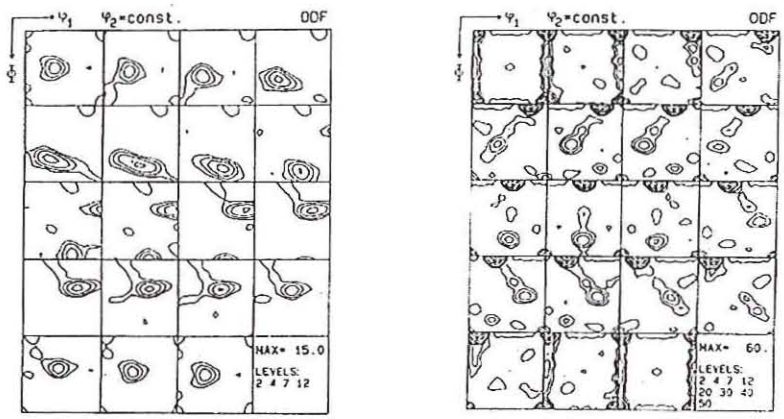

Fig. 18.24: *ODFs of rolled and recrystallized copper according to neutron pole figure data. The ODFs are represented by sections of const. φ_2 in the three-dimensoinal Eulerian space*

6.4 Natural Deformation Texture of Quartz

Quartz (SiO_2) is the most naturally occuring mineral. Among all minerals naturally deformed quartzites display the largest variety of texture types [13]. The variation has been associated with conditions of metamorphic grade and with the deformation history. Quartzites bear information on the tectonic deformation mechanisms by the formation of intracrystalline glide systems which are temperature dependent and strongly influenced by water. Due to its optical

properties, quartz can be investigated by single grain analysis using optical microscopy (compare chapter 4.0). U-stage results can be compared with neutron diffraction pole figures on the global texture (see Fig. 18.15).

The Jülich neutron texture diffractometer has been used for texture studies on quartzites originating from different geological zones [14]. The quartzite to be discussed here was collected from the (late Proterozoic to early Papaeozoic) Pan-African Nosib quartzite of the Tomakas area in the Kaoko belt, North-West Namibia, a 560 million years old geological formation [15]. Pole figure measurements have been performed on a cube-shaped specimen of 20 mm edge size. Grain sizes varied between 0.03 and 0.83 mm.

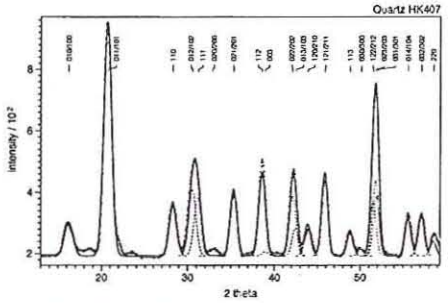

Fig. 18.25: *Experimental neutron diffraction pattern (points)of a quartzite specimen as mean diagram of about 500 different sample orientations during pole figure scanning and full-pattern profile fit (solid line) for separation of overlapping peaks (dotted curves). The indexing is acoording to the hexagonal quartz structure.*

The pole figure data processing, which is adapted to the special potential of the position-sensitive detector and the automatic recording of complete diffraction patterns for each sample orientation, is performed stepwise in a semi-automatic way by (1) adding up all diagrams and preparing a mean diagram of all sample orientations, (2) profile fitting the sum diagram (Fig. 18.25) in order to separate overlapping reflections and to determine orientation-independent reflection parameters, i.e. peak positions and halfwidths, (3) profile fitting the individual diagrams for the determination of the integrated peak intensities, i.e. the orientation-dependent pole densities, and (4) graphical representation of the pole densities in stereographic projection using a normalized grid in multiples of random distribution. The experimental pole figures are shown in Fig. 18.26.

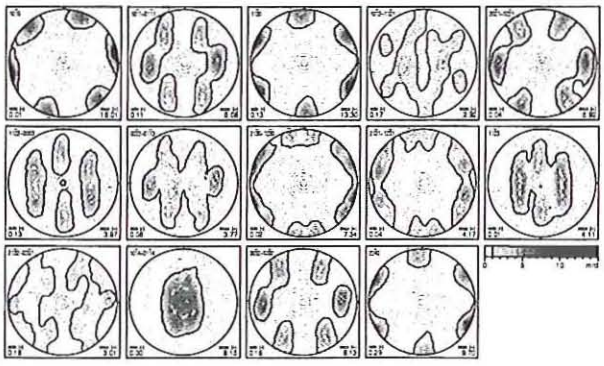

Fig. 18.26: *Experimental pole figures of a naturally deformed quartzite. A total of 14 pole figures is obtained simultaneously from a single pole figure scan at the texture diffractometer SV7-b at the FRJ-2 reactor in Jülich. The instrument is equipped with a large linear detector.*

Pole figure inversion and ODF calculations has been performed using the program MENTEX [8]. Experimental and calculated pole figures of some hkl are presented in Fig. 18.27. The (001) pole figure is of special importance for the quartz structure, because (001) informs on the orientation distribution of the optically relevant hexagonal [001] axes and thus permits a comparison to an individual grain analysis at an U-stage (see Fig. 18.15). While the optical data are confined to this [001] direction, the neutron data permit an overall description of the quartz texture by additional information on preferred orientation of other quartz-relevant planes and forms like prisms and rhombs. The interpretation of the quartz texture is given in the typical nomenclature of a geologist (compare Fig. 18.27):

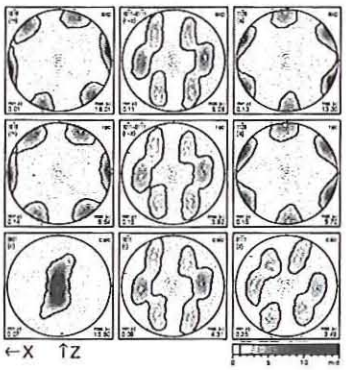

Fig. 18.27: *Observed and calculated neutron pole figures (X, Y: see text). Top row: experimental pole figures {m}, {r+z} and {a} (see text). Second row: corresponding model pole figures recalculated from the ODF. Bottom row: calculation sof the ‚unobserved' pole figures {c}, {r} and {z} (see text).*

(1) The{c} pole figure (0001) shows a concentration of c-axes around Y (direction perpendicular to the diection X of maximum elongation and perpendicular to the direction Z of maximum shortening) and a girdle close to the YZ-plane (plane of foliation) indicating that the investigated rock was predominantly deformed by a prism slip mechanism with a contribution of the slip along rhomb and basal planes.

(2) The pole figure of the crystallographic {a} prisms (11-20) exhibits two nearly separated concentrations around linear fabric and the shear direction. The a-axis maximum is at the margin of the pole figure with an angle of about 25° to the foliation plane.

(3) Preferred orientations of the first order prisms {m} (10-10) show a pronounced concentration parallel to the lineation direction.

(4) Poles of the positive and negative rhombs {r} (10-11) and {z} (01-11) show a tendency of symmetry in their alignment with respect to the shear plane.

Structural geologists compare those local quartzite textures (1) with the texture of other rocks of the same region in order to recognize the regional tectonic transport direction (which in our example was east – east south east), and (2) with the texture of quartzites of different geological origin in order to recognize quartz-specific deformation mechanisms.

References

[1] H.J. Bunge, Texture Analysis in Materials Science, Butterworth & Co., 1982.

[2] H.-R. Wenk, Preferred Orientation in Deformed Metals and Rocks: An Introduction to Modern Texture Analysis, Academic Press, 1985.

[3] U.F. Kocks, C.N. Tomé, H.-R. Wenk, Texture and Anisotropy: Cambridge U. Press, 1998

[4] H.J. Bunge, Directional Properties of Materials, DGM Informationsgesellschaft, 1987.

[5] H.-R. Wenk, H. Kern, W. Schäfer, G. Will, J. Structural Geology 6 (1984) 687.

[6] H.J. Bunge, Theoretical Methods of Texture Analysis, Verlag DGM Informationsg. 1987.

[7] D. Ruer, R. Baro, J. Appl. Cryst. 10 (1977) 458;

[8] H. Schaeben, „Diskrete mathematische Methoden zur Berechnung und Interpretation von kristallographischen Orientierungsdichten", Verlag DGM Informationsgesellschaft, 1994.

[9] S. Matthies, H.-R. Wenk, G.W. Vinel, J. Appl. Cryst. 21 (1988) 285.

[10] K. Helming, Texturapproximation durch Modellkomponneten, Cuvillier-Verlag, 1996.

[11] E. Jansen, W. Schäfer, A. Kirfel, J. Palacios, Mat. Science Forum 278-281 (1998) 502.

[12] H. Mecking in [2] pp. 267-306

[13] K. Helming, H.R. Wenk, C.S. Choi, W. Schäfer, in Textures of Geological Materials (ed. H.J. Bunge et al.), Verlag DGM Informationsgesellschaft, 1994, pp. 303-325.

[14] W. Schäfer, E. Jansen, P. Merz, G. Will, H.R. Wenk, Physica B 180 & 181 (1992) 1035.

[15] H. Ghildiyal, E. Jansen, A. Kirfel, Textures and Microstructures 31 (1999) 239.

List of most important symbols

$\langle ... \rangle$	Thermal average
$\underline{a}^* = 2\pi \cdot \frac{\underline{b} \times \underline{c}}{\underline{a} \cdot (\underline{b} \times \underline{c})}$, $\underline{b}^* = ...$, $\underline{c}^* = ...$	Basis vectors of the reciprocal lattice
$\underline{a}, \underline{b}, \underline{c}, \alpha, \beta, \gamma$	Basis vectors of the unit cell and angles
$\underline{A}$	Vector potential
$\underline{A} \cdot \underline{p}$	Dipole operator
$b, b_{coh}, b_{inc}, b_+, b.$	Neutron scattering length, coherent, incoherent, $J=I+\frac{1}{2}$; $J=I-\frac{1}{2}$; unit: $f_m=10^{-15}$m
2θ	Scattering angle $\angle(\underline{k}, \underline{k}')$
θ	Incident angle ≡ angle between $\underline{k}$ and the surface
θ'	Scattered angle ≡ angle between $\underline{k}'$ and the surface
θ_c	Angle of total reflection
θ_t	Angle of transmitted beam ≡ angle between $\underline{k}_t$ and the surface
$c = 2.9979246 \cdot 10^8$ m/s	Velocity of light
d, d_{hkl}	Inter-lattice plane distance
δ (E-E')	Delta function
$\frac{d\sigma}{d\Omega}, \frac{d^2\sigma}{d\Omega dE'}$	Single- and double-differential cross section
E, E´	Energy of incident/scattered particle, unit: eV (meV, μeV)
$\underline{E}$	Electric field
$f(Q) = f' + if'', f_M(Q)$	Form factor, magnetic form factor
$\gamma_n = -1.913$	Magnetic dipole moment of the neutron expressed in nuclear magnetons
$\gamma = -1.833 \cdot 10^8 \frac{rad}{s \cdot T}$	Gyromagnetic ratio of the neutron
$\underline{G} = h\underline{a}^* + k\underline{b}^* + l\underline{c}^*$	Reciprocal lattice vector
$G(\underline{r},t), G_s(\underline{r},t)$	Pair-, self-correlation function
$\underline{H}$	Magnetic field
$h = 6.626 \cdot 10^{-34}$ Js; $\hbar = \frac{h}{2\pi} = 6.582 \cdot 10^{-16} eVs$	Planck's quantum of action (reduced)
$\hbar\omega = E - E'$	Energy transfer of the scattering process
$\underline{k}_t$	Wave vector of the transmitted wave (reflectometry)
$\underline{k}'$	Wave vector of the scattered wave
$\underline{k} = \frac{2\pi}{\lambda} \cdot \hat{\underline{k}}$	Wave vector (in general: of the incident wave)
$\underline{k}_n$	Wave vector in matter with index of refraction n
$k_B = 1.381 \cdot 10^{-23}$ J/K	Boltzmann's constant
λ	Wave length, unit: nm = 10^{-9} m
$\lambda_c = {}^{h}/_{mc} = 2.426$ pm	Compton wave length
L, **L**	Quantum number of orbital momentum and its operator
m_n, m_e	Neutron mass, electron mass

$\underline{M}$	Vector of magnetisation
$\mu_B = 9.274 \cdot 10^{-24}$ J / T	Bohr's magneton
$\underline{\mu}_n$	Vector of the magnetic dipole moment of the neutron
$\mu_N = 5.051 \cdot 10^{-27}$ J / T	Nuclear magneton
n	Index of refraction
$\Omega, \Delta\Omega$	Solid angle and its element
P, P′	Polarisation before/after scattering
Ψ	Quantum mechanical probability amplitude
$\langle\psi_i\| \|\psi_f\rangle$	Wave functions of the initial and final state
$\underline{Q} = \underline{k} - \underline{k}'$	Scattering vector
R	Reflectivity
$\underline{R}_{ld}$	Position vector of atom d in cell l
$r_o = \frac{e^2}{m_e c^2} = 2.8179$ fm	Classic radius of the electron
$\underline{\sigma}$	Pauli's spin matrix
σ_A	Absorption cross section
σ_{coh}, σ_{inc}	Coherent and incoherent cross section
σ_{tot}	Total cross section (absorption and scattering)
$S_{coh}(Q, \omega)$, $S_{inc}(Q, \omega)$	Coherent and incoherent scattering function
$S(Q)$, $S_M(Q)$, $S_N(Q)$, $S_C(Q)$	Structure factor (static), magnetic, nuclear charge structure factor
$S(Q, t)$	Intermediate scattering function
$S(Q, \omega)$	Scattering function, dynamic structure factor
S, **S**	Spin quantum number and its operator
T	Transmissivity
V(r)	Interaction potential

General conventions:

s	Scalar
$\underline{v}$	Vector
$\underline{\hat{v}}$	Unit vector
$\underline{\underline{M}}$	Matrix
O	Operator

Schriften des Forschungszentrums Jülich. Reihe Materie und Material:

1. **Physik der Nanostrukturen**
   Vorlesungsmanuskripte des 29. IFF-Ferienkurses vom 9. bis 20.3.1998
   (1998), ca. 1000 Seiten
   ISBN 3-89336-217-7

2. **Magnetische Schichtsysteme**
   Vorlesungsmanuskripte des 30. IFF-Ferienkurses vom 1. bis 12.3.1999
   (1999), ca. 1300 Seiten, zahlreiche z.T. farb. Abb.
   ISBN 3-89336-235-5

3. **Femtosekunden und Nano-eV: Dynamik in kondensierter Materie**
   Vorlesungsmanuskripte des 31. IFF-Ferienkurses vom 13. bis 24.3.2000
   (2000), ca. 1000 Seiten, zahlreiche z. T. farb. Abb.
   ISBN 3-89336-205-3 (Hardcover)

4. **Massenspektrometrische Verfahren der Elementspurenanalyse**
   Kurzfassungen der Vorträge und Poster des 5. Symposiums und des 12. ICP-MS-
   Anwendertreffens vom 18. bis 21. September 2000 in Jülich
   zusammengestellt von H.-J. Dietze, J. S. Becker (2000), ca. 100 Seiten
   ISBN 3-89336-267-3

5. **Neutron Scattering**
   Lectures of the Laboratory Course
   held at the Forschungszentrum Jülich from 26 September to 6 October 2000
   herausgegeben von Th. Brückel, G. Heger, D. Richter (2000), 382 Seiten
   ISBN 3-89336-269-X

Forschungszentrum Jülich

Band / Volume 5
ISBN 3-89336-269-X

Materie und Material
Matter and Materials